Physics of the Solid State, Vol. 45, No. 2, 2003, pp. 201–206. Translated from Fizika Tverdogo Tela, Vol. 45, No. 2, 2003, pp. 193–197.
Original Russian Text Copyright © 2003 by Kurganskiĭ, Pereslavtseva, Levitskaya.

SEMICONDUCTORS AND DIELECTRICS

Fermi Surface and Electrical Characteristics of Molybdenum Disilicide

S. I. Kurganskiĭ, N. S. Pereslavtseva, and E. V. Levitskaya
Voronezh State University, Universitetskaya pl. 1, Voronezh, 394006 Russia
e-mail: phssd18@main.vsu.ru

Received April 9, 2002

Abstract—Semirelativistic self-consistent calculations of the electronic structure of $MoSi_2$ are performed within the framework of the linearized augmented-plane-wave (APW) method in the local density functional approximation. The results of investigations of the band structure, the Fermi surface, and electrical characteristics (effective cyclotron masses, the conductivity anisotropy constant, the mean free path, and the coefficient γ of the heat capacity component linear in temperature) are reported. The Fermi surface consists of two sheets, namely, an electron sheet and a hole sheet. The extreme sectional areas of the Fermi surface agree well with the experimental data on the de Haas–van Alphen effect. The results of first-principles calculations need no additional correction. *© 2003 MAIK "Nauka/Interperiodica".*

1. INTRODUCTION

Molybdenum disilicide possesses high microhardness [1], resistance to oxidation during heating both in air and in an oxygen flow [1], high thermal stability [2], temperature-independent high thermoelectric power [3], low resistance [4–9], and good technological properties. This compound has long been in use in many fields of science and engineering. Initially, molybdenum disilicide compounds were used as antirust coatings. However, considerable advances made in micro- and nanotechnologies substantially extended the field of application of $MoSi_2$ materials. In recent years, molybdenum disilicide has been used in the fabrication of diffusion barriers [10], protective coatings for intermetallic compounds at elevated temperatures [11], high-temperature thermocouples deposited on electrodes [3], silicon integrated circuits [1], coatings for aircraft structures [12], and high-temperature turbine blades [13]. Such a wide spectrum of application of $MoSi_2$ stems from the high stability of its properties. The nature of these properties cannot be understood without detailed investigation of the electronic structure.

At present, the electronic structure of $MoSi_2$ has been extensively investigated using experimental and theoretical techniques. Among the experimental methods are x-ray emission [14–16] and photoelectron [17, 18] spectroscopies. The Fermi surface has been experimentally studied in terms of the de Haas–van Alphen effect [19]. The electronic structure of $MoSi_2$ has been treated theoretically in the framework of the self-consistent relativistic pseudopotential approach [20], the linear muffin-tin orbital formalism [21–24], and the augmented-spherical-wave (ASW) method [17]. These calculations were performed in the local density functional approximation, specifically for the band structure [20, 21, 24], densities of states [17, 20–24], and the Fermi surface [22, 24]. However, none of the first-principles calculations of the Fermi surface [22, 24] agrees in full measure with the experiment [19]. It turned out that the results of direct calculations of the extreme sectional areas of the Fermi surface [22, 24], which depend on the direction of the magnetic field, considerably exceed the experimental values [19]. This discrepancy was explained as resulting from the use of the local density functional approximation. In order to achieve better agreement between the calculation and the experiment [19], the results of the direct calculations performed in [22, 24] were corrected by fitting to the experimental Fermi surface. In particular, Andersen *et al.* [24] displaced the Mo $d_{x^2-y^2}$ states to the Fermi level by 0.41 eV and the Mo d_{xy} states to the valence band bottom by 0.21 eV. As a result, the initially obtained density of states at the Fermi level (0.31 states/eV per unit cell) decreased by approximately 20% and almost reached the experimental value (0.24 states/eV per unit cell) [25]). Antonov *et al.* [22] applied a correction according to the same scheme. However, the results of these corrections are ambiguous: the corrected data in [24] are in better agreement with the experiment [19] than those obtained in [22].

This paper reports on the results of direct theoretical investigations of the electronic structure of body-centered tetragonal $MoSi_2$. In the present work, we calculated the band structure, the Fermi surface, and electrical characteristics, such as the effective cyclotron masses, the conductivity anisotropy constant, the mean free path, and the coefficient γ of the heat capacity component linear in temperature. Our results are in satisfactory agreement with the available calculated [20–22,

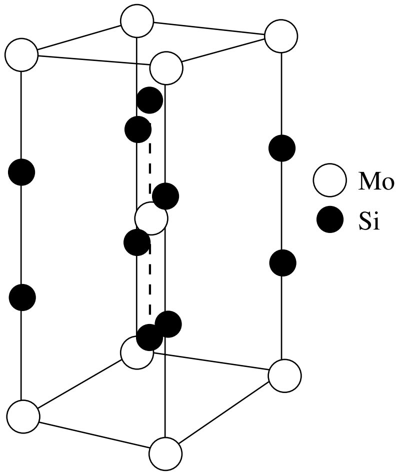

Fig. 1. Crystal structure of $MoSi_2$.

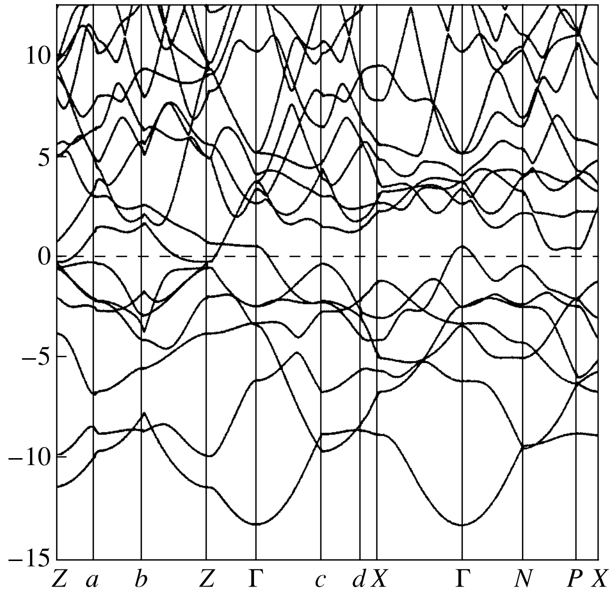

Fig. 2. Band structure of $MoSi_2$.

24] and experimental [4, 19, 25, 26] data. However, no additional correction, such as that performed in [22, 24], was needed in our case.

2. COMPUTATIONAL TECHNIQUE

The electronic structure of an $MoSi_2$ crystal was calculated in the local density functional approximation using an exchange correlation potential within the approach proposed in [27]. The energy spectrum was calculated by the self-consistent linearized augmented-plane-wave (APW) method in terms of the formalism used in [28] within the scalar relativistic approximation [29], which includes all relativistic effects, except for spin–orbit splitting. The linearized APW method was described in detail in [30]. The low-temperature phase of $MoSi_2$ crystallizes in a body-centered tetragonal structure (Fig. 1) (space group D_{4h}^{17}–$I4/mmm$) with the unit cell parameters $a = b = 0.3202$ nm, $c = 0.7852$ nm, and $c/a = 2.452$ [31]. The calculation was performed in the basis set of 176 linearized augmented plane waves. The basis function was expanded in spherical harmonics up to terms with $l = 7$.

3. RESULTS AND DISCUSSION

3.1. Band Structure and the Fermi Surface

Figure 2 represents the band structure of $MoSi_2$. According to the calculation, the valence band is equal to 13.4 eV. The energy bands at the valence band bottom are attributed to the Si *s* electron states. The region from –0.3 to –4.7 eV is determined primarily by the Mo *d* states with an admixture of Si *p* states. This is in good agreement with the available calculated data on the density of states [17, 20–24]. The density of states at the Fermi level (E_F) is relatively low [$N(N_F)$ = 0.28 states/eV per unit cell], which indicates that the compound is stable. This value is less than that determined prior to the fitting of the results in [24] (0.31 states/eV per unit cell) but is closer to the experimental value obtained in [25] (0.24 states/eV per unit cell). The Fermi level is crossed by two energy bands, namely, by the seventh and eighth energy bands counted off from the valence band bottom. The seventh band passes through the Fermi level E_F near the Γ point of the Brillouin zone and is empty in this vicinity. The eighth band crosses the Fermi level in the vicinity of the *Z* point. In this part of the Brillouin zone, the eighth band is characterized by occupied states. These bands form the Fermi surface of $MoSi_2$ (Fig. 3). The intersection of the seventh band with the Fermi level generates a hole sheet on the Fermi surface (Fig. 3a). This sheet has the shape of a cylinder that is slightly widened both in the upper and lower half and is then narrowed in the bases along the ΓZ direction. The eighth band forms an electron sheet on the Fermi surface (Fig. 3b) having the shape of a *Z*-centered rosette. A comparison showed that the results of our calculations of the Fermi surface are in good agreement with the theoretical investigations performed in [22, 24] and the experimental data on the de Haas–van Alphen effect [19]. Nonetheless, there are some differences. As follows from our calculation, the seventh and eighth bands are degenerate in the ΓZ direction. Consequently, the electron and hole sheets of the Fermi level in the ΓZ direction touch each other at a point. However, according to [22, 24], the electron and hole sheets are separated by a gap. This difference stems from the fact that our calculation ignores the spin–orbit splitting, which relieves the degeneracy of these bands. As was shown in [20, 21], the spin–orbit splitting of energy levels in $MoSi_2$ is a small quantity; as a result, there arises a gap of 0.007 bohr^{-1} between the electron and hole sheets of the Fermi surface [20]. This value is less than 2% of the characteristic size of the Fermi surface. Therefore, the error introduced by this neglect is small compared to the contributions made by other factors (for example, the potentials used in the calculations) and does not change the topology of the calculated Fermi surface.

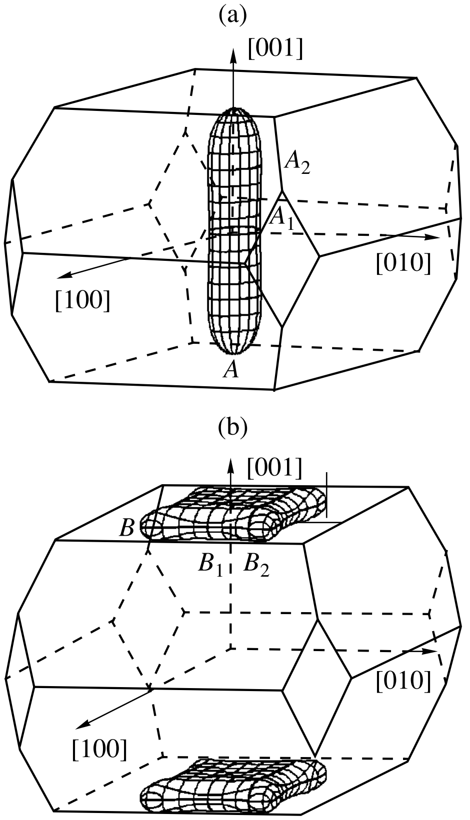

Fig. 3. Fermi surface of $MoSi_2$: (a) hole sheet of the Fermi surface and (b) electron sheet of the Fermi surface. Heavy lines indicate extreme orbits.

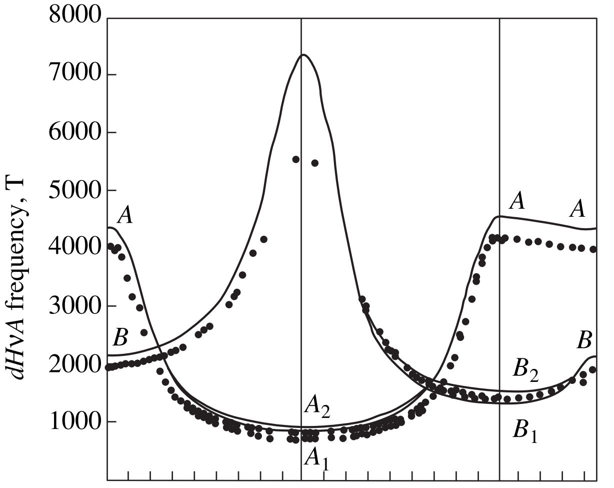

Fig. 4. Angular dependences of the extreme sectional areas of the Fermi surface for $MoSi_2$ according to our calculations (solid line) and experimental data taken from [19] (points).

It was expedient to analyze quantitatively the topology of the Fermi surface and to compare our results with the experimental data [19] on the de Haas–van Alphen effect. For this purpose, we calculated the area of the extreme section of the Fermi surface as a function of the direction of the magnetic field (Fig. 4). In order to compare the available calculated [22, 24] and experimental [19] data with our results, the areas of the extreme sections formed on the Fermi surface by planes orthogonal to four crystallographic directions are presented in Table 1. The values taken from [22, 24] refer to the data obtained after the fitting of the calculation to the experiment, because the initial results differ appreciably from the experimental data. We revealed two extreme sections for the electron and hole parts of the Fermi surface (Fig. 3), which can be associated with the specific features of their structures. The branch *A* corresponds to the seventh band, whereas the branch *B* is attributed to the eighth band. The minimal orbit A_1 is centered at the Γ point, and the maximal orbit A_2 is separated by a distance of 0.1928 bohr^{-1} from the Γ point. The extreme orbits are located in the hole part of the Fermi surface (Fig. 3a) in the planes orthogonal to the [001] crystallographic direction. These two orbits merge into a single branch *A* when the direction of the magnetic field deviates from the [001] direction by an angle greater than 50° (Fig. 4). The electron sheet of the Fermi surface also has two extreme orbits (Fig. 3b); they are aligned with the planes perpendicular to the [100] direction. The minimal orbit B_1 is centered at the *Z* point, and the maximal orbit B_2 is separated by a distance of 0.1475 bohr^{-1} from the *Z* point. These are extreme orbits that merge into a single branch *B* in the case when the magnetic field deviates by an angle greater than 33° from the [100] direction toward the [110] direction and by an angle greater than 57° toward the [001] direction (Fig. 4). The calculations demonstrated that the areas covered by the orbits B_1 and B_2 are very close in magnitude (Table 1); as a result, it is rather difficult to differentiate these orbits experimentally. In their experiments, van Ruitenbeek *et al.* [19] did not obtain a clearly defined splitting of the orbit *B* into a minimal orbit B_1 and a maximal orbit B_2 in the section orthogonal to the [100] direction. These authors noted only a splitting of the orbit *B* into two or three closely located spectral or satellite peaks along this direction [19]. However, they could not assert unambiguously that the orbit *B* is split into minimal and maximal branches. As follows from first-principles calculations [22, 24], considerable splitting of the orbit *B* occurs in the section perpendicular to the [100] direction. However, after the correction, the calculations performed in [22] and [24] offered different results. Andersen *et al.* [24] fitted the calculated data in such a manner that the separation between the branches B_1 and B_2 decreased

Table 1. Extreme sectional areas of the Fermi surface and effective cyclotron masses for $MoSi_2$

Field direction	Orbit	Extreme sectional areas (*T*)				Effective cyclotron masses (m^*/m_0)			
		our calculation	[22]	[24]	experiment [19]	our calculation	[22]	[24]	experiment [19]
[100]	A	4581	4623	4511	4230	0.94	0.82	0.96	1.0
[110]	A	4375	4256	4325	4060	0.85	0.85	0.89	0.91
[001]	A_1	863	664	690	735	0.29	0.29	0.27	0.31
	A_2	942	826	949	830	0.31	0.21	0.31	0.33
[002]	A_1	1397	1188	1148	1165	0.48	0.39	0.45	0.51
	A_2	1431	1248	1385	1235	0.47	0.38	0.46	0.50
[100]	B_1	1369	921	1486	1450	0.55	0.47	0.49	0.53
	B_2	1592	1425	1516		0.65	0.33	0.55	
[110]	B	2177	1656	2016	1970	0.88	0.55	0.77	0.69
[001]	B	7347	8481	6364	5600	1.85	1.11	1.57	–
[102]	B_1	1745	1134	1921	1900	0.71	0.28	0.63	0.65
	B_2	1929	1710	1927		0.76	0.62	0.64	

Table 2. Ratios of extreme sectional areas of the Fermi surface for $MoSi_2$

Sections	Our calculation	[22]	[24]	Experiment [19]	Θ, deg	1/cosΘ
$A_1[102]/A_1[001]$	1.61	1.79	1.66	1.59	50.8	1.58
$A_2[102]/A_2[001]$	1.52	1.51	1.46	1.49		
$B_1[102]/B_1[100]$	1.27	1.23	1.29	1.31	39.2	1.29
$B_2[102]/B_2[100]$	1.21	1.20	1.27			

substantially (Table 1); consequently, their calculation is in close agreement with the experiment [19]. The correction made by Antonov *et al.* [22] gave other results (Table 1): the separation between the orbits B_1 and B_2 was significant, which would unlikely remain imperceptible in the experiment.

The dependence of the extreme sectional area on the angle Θ (where Θ is the angle between the direction of the magnetic field and the [001] axis for the hole part of the Fermi surface and the [100] direction for the electron part of this surface) is well approximated by the law 1/cosΘ. Therefore, the Fermi surface in the vicinity of the extreme sections can be considered to be nearly cylindrical to a good approximation. The calculated and experimental ratios of the areas corresponding to the dependence of the extreme section on the angle Θ are listed in Table 2. It can be seen from Table 2 that, compared to the maximal orbits, the minimal orbits are better approximated by a cylinder.

3.2. Electrical Characteristics

The majority of the electrical properties of the materials depend on the composition and the structure of the Fermi surface. Specifically, the Fermi surface determines the effective cyclotron masses

$$m^*(E, k_2) = \frac{\hbar^2}{2\pi}\frac{\partial A(E, k_z)}{\partial E}, \tag{1}$$

where $A(E, k_z)$ is the area of the extreme section of the Fermi surface. Table 1 presents the effective cyclotron masses according to our results, data taken from [22, 24], and experimental data taken from [19]. Most of the values obtained for the four crystallographic directions ([100], [110], [001], [102]) are less than unity.

The electrical conductivity also depends on the structural features of the Fermi surface. In the approxi-

Table 3. Resistivities [4–9] and the mean free paths for $MoSi_2$

References	$\rho \times 10^8$, Ω m	λ_0, nm
Laborde *et al.* [4]	$E \parallel x$16.56	4.01
	$E \parallel z$11.42	4.55
Machizuki *et al.* [5]	21.8	2.38
Crowder and Zirinsky [6]	21.5	2.42
Murarka *et al.* [7]	21.6	2.41
Crow and Steckl [8]	21.5	2.42
Saraswat [9]	21.8	2.38

mation of the relaxation time, the electrical conductivity can be represented by the expression [32]

$$\sigma = \frac{e^2}{4\pi^3\hbar}\int l_0 \cos^2\theta dS, \qquad (2)$$

where the integration is performed over the entire Fermi surface, θ is the angle between the direction of the electron velocity and the electric field, and l_0 is the mean free path. As a rough approximation, l_0 was considered to be constant. The conductivity anisotropy $\sigma_z/\sigma_x = 1.28$, which was obtained from expression (2), is in good agreement both with the experimental value (1.3–1.45) [4, 26] and with the estimate (1.3) [19].

The mean free path l_0 was estimated from formula (2) using several experimental values of the resistivity [4–9]. The experimental resistivities for $MoSi_2$ [4–9] and the mean free paths calculated from these values are presented in Table 3. According to the calculation, the experimental data on the resistivity of $MoSi_2$, for the most part, lead to a mean free path close to that for alkali metals (the mean free paths for Na, K, Rb, and Cs are equal to 3.38, 3.56, 2.26, and 1.55 nm, respectively [32]). However, Laborde *et al.* [4] obtained a resistivity that was lower than the values given in other works. In this case, the resistivity was measured for different directions of the electric field (the electric field E was aligned parallel either to the x axis or to the z axis). As a consequence, the σ_z/σ_x value calculated from these data turned out to be comparable to the mean free path for noble metals (the mean free paths for Cu, Ag, and Au are equal to 4.2, 5.56, and 4.09 nm, respectively [32]).

The heat capacity of a solid at low temperatures contains the electronic and lattice contributions [32]:

$$c_V = \gamma T + AT^3. \qquad (3)$$

At low temperatures, the coefficient γ for the electronic component of the heat capacity is determined by the density of states at the Fermi level [32]:

$$\gamma = \frac{\pi^2}{3}k_B^2 N(E_F), \qquad (4)$$

where k_B is the Boltzmann constant. Upon substituting the calculated value $N(E_F) = 0.28$ states/eV per unit cell into expression (4), we obtained the coefficient $\gamma = 0.66$ μJ/(mol K^2), which agrees well with experimental values of 0.57 [25] and 0.71 μJ/(mol K^2) [19].

REFERENCES

1. S. Murarka, *Silicides for VLSI Applications* (Academic, New York, 1983; Mir, Moscow, 1986).
2. V. N. Svechnikov, Yu. A. Kocherzhinskiĭ, and L. M. Yupko, Dokl. Akad. Nauk Ukr. SSR, Ser. A, No. 6, 553 (1970).
3. G. V. Samsonov, L. A. Dvorina, and B. M. Rud’, *Silicides* (Metallurgiya, Moscow, 1979).
4. O. Laborde, O. Thomas, J. P. Senateur, and R. Madar, J. Phys. F **16** (11), 1745 (1986).
5. T. Machizuki, K. Shibata, T. Inoue, and K. Ohuchi, Jpn. J. Appl. Phys., Suppl. **17** (1), 37 (1978).
6. B. L. Crowder and S. Zirinsky, IEEE J. Solid-State Circuits **14**, 291 (1979).
7. S. P. Murarka, D. B. Fraser, T. F. Retajczyk, and T. T. Sheng, J. Appl. Phys. **51** (9), 5380 (1980).
8. T. P. Crow and A. J. Steckl, in *Technical Digest* (IEEE, New York, 1979), p. 458.
9. K. C. Saraswat, in *Technical Digest* (IEEE, New York, 1979), p. 462.
10. A. Franciosi, J. H. Weaver, and F. A. Schmidt, Phys. Rev. B **27** (6), 3554 (1983).
11. S. Ignat, P. Sallamand, A. Nichici, *et al.*, Opt. Laser Technol. **33**, 461 (2001).
12. R. E. Regan, W. A. Baginski, and C. A. Krier, Am. Ceram. Soc. Bull. **46** (5), 502 (1976).
13. M. Alouani, R. C. Albers, and M. Methfessel, Phys. Rev. B **43** (8), 6500 (1991).
14. V. V. Nemoshkalenko, A. P. Shpak, V. P. Krivitskiĭ, *et al.*, Izv. Akad. Nauk SSSR, Ser. Fiz. **38** (3), 639 (1974).
15. A. S. Shulakov, T. M. Zimkina, V. A. Fomichev, and V. S. Neshpor, Izv. Akad. Nauk SSSR, Ser. Fiz. **41** (1), 216 (1977).
16. E. P. Domashevskaya and Yu. A. Yrakov, J. Electron. Spectrosc. Relat. Phenom. **96**, 195 (1998).
17. J. H. Weaver, V. L. Moruzzi, and F. A. Schmidt, Phys. Rev. B **23** (6), 2916 (1981).
18. W. Spier, E. V. Leuken, J. C. Fuggle, *et al.*, Phys. Rev. B **39** (9), 6008 (1989).
19. J. M. van Ruitenbeek, W. Joss, and R. Pauthenet, Phys. Rev. B **35** (15), 7936 (1987).
20. B. K. Bhattacharyya, D. M. Bylander, and L. Kleinman, Phys. Rev. B **32** (12), 7973 (1985).
21. Shaoping Tang and Zhang Kaiming, J. Phys. C **21** (8), 1496 (1988).

22. V. N. Antonov, B. Yu. Yavorsky, A. P. Shpak, and A. Yu. Perlov, Fiz. Nizk. Temp. **20** (9), 934 (1994).
23. A. K. McMahan, J. E. Klepeis, M. van Schilfgaarde, and M. Methfessel, Phys. Rev. B **50** (15), 10742 (1994).
24. O. K. Andersen, O. Jepsen, Vl. N. Antonov, *et al.*, Physica B (Amsterdam) **204**, 65 (1995).
25. J. C. Lasjaunias, M. Saint-Paul, O. Laborde, *et al.*, Phys. Rev. B **37** (17), 10364 (1988).
26. O. Thomas, J. P. Senateur, R. Madar, *et al.*, Solid State Commun. **55** (7), 629 (1985).
27. S. N. Vosko, L. Wilk, and M. Nusair, Can. J. Phys. **58** (8), 1200 (1980).
28. D. D. Koelling and G. O. Arbman, J. Phys. F **5** (11), 2041 (1975).
29. A. H. MacDonald, W. E. Pickett, and D. D. Koelling, J. Phys. C **13** (14), 2675 (1980).
30. S. I. Kurganskiĭ and N. S. Pereslavtseva, Kondens. Sredy Mezhfaz. Granitsy **3** (3), 251 (2001).
31. H. J. Goldschmidt, *Interstitial Compounds* (Plenum, New York, 1967).
32. N. W. Ashcroft and N. D. Mermin, *Solid State Physics* (Holt, Rinehart and Winston, New York, 1976; Mir, Moscow, 1979), Vol. 1.

Translated by N. Korovin

Physics of the Solid State, Vol. 45, No. 2, 2003, pp. 207–213. Translated from Fizika Tverdogo Tela, Vol. 45, No. 2, 2003, pp. 198–204.
Original Russian Text Copyright © 2003 by Ganeev, Ryasnyanskiĭ, Usmanov.

SEMICONDUCTORS AND DIELECTRICS

Effect of Nonlinear Refraction and Two-Photon Absorption on the Optical Limiting in Amorphous Chalcogenide Films

R. A. Ganeev*, A. I. Ryasnyanskiĭ, and T. Usmanov***
** Akadempribor Research and Production Association, Academy of Sciences of Uzbekistan, Tashkent, 700143 Uzbekistan*
*** Samarkand State University, Samarkand, 703004 Uzbekistan*
e-mail: ryasn2000@yahoo.com

Received June 20, 2002

Abstract—This paper reports on the results of investigations into the nonlinear optical characteristics of chalcogenide films (As_2S_3, $As_{20}S_{80}$, $2As_2S_3/As_2Se_3$, $3As_2S_3/As_2Se_3$). The nonlinear refractive indices and two-photon absorption coefficients for these films are measured using the *Z*-scan technique at wavelengths of a picosecond Nd : YAG laser (λ = 1064 and 532 nm). The optical limiting due to Kerr-type nonlinearities is analyzed. *© 2003 MAIK "Nauka/Interperiodica".*

1. INTRODUCTION

The possibility of using semiconductors to solve various problems in laser physics depends on a number of nonlinear optical characteristics, specifically on the nonlinear refractive index n_2 and the two-photon absorption coefficient β. This circumstance has stimulated extensive investigations into nonlinear refraction and nonlinear absorption in semiconductors [1–3]. In recent years, particular interest has been expressed by many researchers in amorphous chalcogenide structures. These materials hold promise for use in data processing systems owing to their large nonlinearity, high transparency in the IR range, and good workability. The potential fields of application of amorphous chalcogenides involve phase conjugation, polarization holography, optical image processing, optical switching, integrated optical devices, holographic optical elements, etc. Smektala *et al.* [4] analyzed the nonlinear refractive indices and nonlinear absorption coefficients for a number of chalcogenide glasses. Chalcogenide glasses are characterized by different positions of the absorption edge (depending on the composition of these materials). The composition of glasses also affects the nonlinear susceptibilities at appropriate wavelengths. For example, the replacement of germanium and sulfur atoms by arsenic and selenium atoms leads to an increase in the nonlinear response in these structures. In particular, Kanbara *et al.* [5] proved that an increase in the fraction of selenium atoms is an efficient way to increase the nonlinear susceptibilities of chalcogenide glasses. Moreover, these materials exhibit a pronounced spectral dependence of the nonlinear optical parameters. Indeed, at the wavelength $\lambda = 633$ nm, the nonlinear refractive index γ (expressed in SI units) and the nonlinear absorption coefficient are equal to 7.6×10^{-5} cm^2 W^{-1} and 1.6 cm W^{-1}, respectively [6]. In the IR spectral range, these parameters at $\lambda = 1064$ nm are equal to 5.7×10^{-14} cm^2 W^{-1} and 2.6×10^{-10} cm W^{-1}, respectively [7], and $\gamma = 1.7 \times 10^{-14}$ cm^2 W^{-1} at $\lambda = 1319$ nm [8].

Considerable recent attention has been focused on chalcogenide materials prepared in the form of thin films [6]. The characteristics of these structures substantially depend on the growth conditions and external factors. The effect of irradiation on the optical properties of As_2S_3 amorphous thin films was studied by Dawar *et al.* [9]. The investigation performed by Kwak *et al.* [6] demonstrated that amorphous chalcogenide thin films (including As_2S_3 films) offer promise as materials for optical limiters.

The optical limiting effects are of special interest in nonlinear optics and optoelectronics owing to their possible application for the protection of eyes and sensitive detectors against intense radiation. The mechanisms responsible for optical limiting are of different natures. The reverse saturable absorption, which is associated with a large cross section of absorption from excited levels, brings about optical limiting effects in colloidal

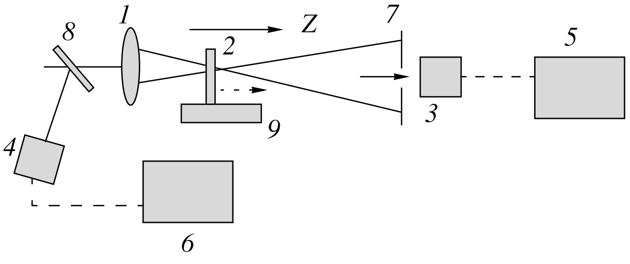

Fig. 1. Schematic diagram of a *Z*-scan experimental setup for investigation of optical limiting: (*1*) focusing lens, (*2*) chalcogenide films, (*3*, *4*) FD-24K photodiodes, (*5*, *6*) V4-17 digital voltmeters, (*7*) limiting aperture, (*8*) reflecting plate, and (*9*) micrometric table.

1063-7834/03/4502-0207$24.00 © 2003 MAIK "Nauka/Interperiodica"

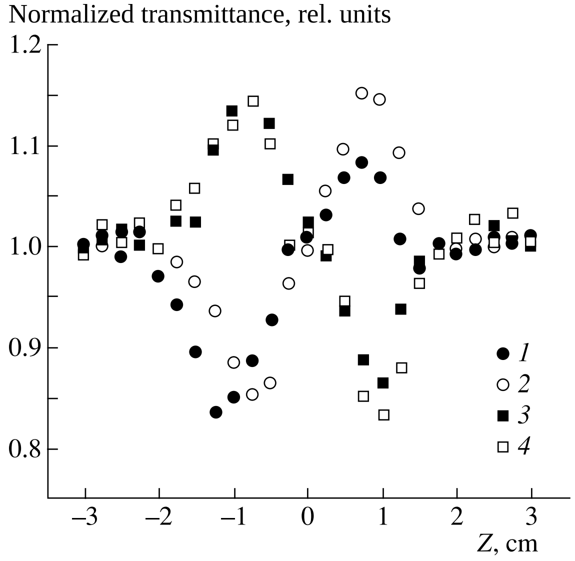

Fig. 2. Normalized transmittance as a function of the position of (*1*) $As_{20}S_{80}$, (*2*) As_2S_3, (*3*) $2As_2S_3/As_2Se_3$, and (*4*) $3As_2S_3/As_2Se_3$ chalcogenide films in the scheme with a limiting aperture at wavelengths of (*1*) 532 and (*2–4*) 1064 nm.

metals [10], fullerenes [11], and phthalocyanines [12]. The optical limiting in inorganic clusters is caused by strong nonlinear refraction [13], whereas the optical limiting in semiconductor structures is governed by two-photon absorption [14].

The purpose of this work was to elucidate how the nonlinear refraction and nonlinear absorption affect the optical limiting of picosecond laser radiation in a number of chalcogenide films (As_2S_3, $As_{20}S_{80}$, $2As_2S_3/As_2Se_3$, $3As_2S_3/As_2Se_3$). We measured the nonlinear refractive indices and the two-photon absorption coefficients of the films under investigation. Moreover, we examined the optical limiting associated with the Kerr-type nonlinearities in amorphous chalcogenide films.

2. EXPERIMENTAL TECHNIQUE

The optical characteristics of chalcogenide films were investigated using a conventional *Z*-scan technique [14] at wavelengths $\lambda = 1064$ and 532 nm. The experimental scheme was similar to that described in our previous work [15]. In the experiments, we used an Nd : YAG laser emitting a train of picosecond pulses. A single 42-ps pulse (at an intensity level of $1/e$) separated out from a train was focused through a lens *1* with a focal distance of 25 cm (Fig. 1). The beam diameters (at an intensity level of $1/e^2$) in the focal waists for the first and second harmonics were equal to 90 and 75 μm, respectively. The diameters of the focused beams in the focal waists were also compared with the experimentally measured parameter $\Delta Z = 1.7z_0$ [14]. Here, ΔZ is the distance between the positions of the studied sample at which the normalized transmittance reaches the maximum and minimum values, $z_0 = kw_0^2/2$ is the diffraction length of the laser beam, $k = 2\pi/\lambda$ is the wave number, and w_0 is the radius beam at the focal point (at a level of $1/e^2$ in the spatial intensity distribution). In our case, ΔZ was equal to 2 cm for radiation with wavelength $\lambda = 1064$ nm (see below). The calculated value of w_0 was 45 μm. The laser pulse energy was recorded with a calibrated FD-24K photodiode *4* and measured on a V4-17 digital voltmeter *5*. Calibrated neutral filters were used for measuring the laser radiation energy. Chalcogenide films *2* were transferred using a micrometric table *9* along the *Z* optical axis when scanning the focal region.

An aperture 1 mm in diameter, which was placed at a distance of 150 cm from the focal region, transmitted ~3% laser radiation (the so-called scheme with a limiting aperture). The signal from an FD-24K photodiode *3*, which was positioned behind the aperture, was sent to a V4-17 digital voltmeter *6*. In order to eliminate the effect of instability of the output energy laser parameters on the results of measurements, the signal detected by photodiode *3* was normalized to the signal detected by photodiode *4*. Each point in the graphs was obtained by averaging over the results of five measurements. The scheme with the limiting aperture enabled us to determine both the sign and the magnitude of the nonlinear refractive index of chalcogenide films. When measuring the nonlinear absorption coefficients, the limiting aperture *7* was removed and the transmittance of the film under investigation was measured as a function of the position of the cell with respect to the focal point (the so-called scheme with an open aperture). In the experiments, special care was taken to prevent optical breakdown in the medium. The thresholds of optical breakdown in the semiconductor films at wavelengths of the first and second harmonics were equal to 8×10^9 and 2×10^9 W cm^{-2}, respectively. The maximum radiation intensities used at these wavelengths did not exceed 10^9 and 8×10^8 W cm^{-2}, respectively.

The experiments were performed using the As_2S_3, $As_{20}S_{80}$, $2As_2S_3/As_2Se_3$, and $3As_2S_3/As_2Se_3$ chalcogenide films. The films were prepared through vacuum evaporation of ground components of the chalcogenide glasses (As_2S_3, $As_{20}S_{80}$, As_2Se_3) onto the surface of BK-7 glass plates. The evaporation rate was equal to 0.5 nm/s. This rate provided evaporation of the film whose parameters were close to those of the initial bulk material (the coincidence of the stoichiometric compositions was confirmed using electron microscopy). The $2As_2S_3/As_2Se_3$ and $3As_2S_3/As_2Se_3$ amorphous multilayer films were produced by successive evaporation of the As_2S_3 and As_2Se_3 compounds. The thickness ratios of individual layers in these films were equal to 20 : 10 nm for $2As_2S_3/As_2Se_3$ films and 30 : 10 nm for

$3As_2S_3/As_2Se_3$ films. The thickness of all the films was equal to 10 μm.

3. RESULTS AND DISCUSSION

The dependences of the normalized transmittance T on the position of the chalcogenide films in the scheme with a limiting aperture are shown in Fig. 2. This scheme is particularly suited to the measurements of nonlinear refraction. The measurements were performed under the conditions when the observed processes were caused by the third-order nonlinearities. Below, these conditions will be considered in greater detail.

One of the advantages of the Z-scan technique is the possibility of determining the sign of n_2 directly from the dependence $T(Z)$. The presence of a minimum ahead of the focal point ($Z = 0$) and a maximum behind this point in the dependence $T(Z)$ indicates that the medium possesses self-focusing properties. For example, it immediately follows from the results obtained that the $2As_2S_3/As_2Se_3$ and $3As_2S_3/As_2Se_3$ films have negative nonlinear refractive indices, which leads to self-defocusing in these materials. At the same time, the As_2S_3 and $As_{20}S_{80}$ films are characterized by positive indices; i.e., these films experience self-focusing processes. From the dependences depicted in Fig. 2, the parameter ΔT_{p-v} can be easily determined as the difference between the maximum and minimum normalized transmittances in the dependence $T(Z)$.

The change in the refractive index of the medium in an electromagnetic wave field (when only the third-order nonlinear optical processes are taken into account) can be represented by the relationship

$$\Delta n = \gamma I_\omega = n_2 \frac{|E_\omega|^2}{2}, \qquad (1)$$

where I_ω and E_ω are the intensity and the electrical field strength of the wave with frequency ω, respectively. The nonlinear refractive indices n_2 and γ, which describe the same process in different units of measurement, are related by the expression n_2 [esu] = $(c \times n/40\pi)\gamma$ [SI]. Here, c is the velocity of light and n is the linear refractive index of the medium.

The nonlinear optical characteristics of the films were determined using the relationship [14]

$$\Delta T_{p-v} = 0.404(1-S)^{0.25}\left|\frac{2\pi\gamma I_0[1-\exp(-\alpha L)]}{\alpha\lambda}\right|, \qquad (2)$$

where I_0 is the radiation intensity at the focal point, S is the aperture transmittance (the portion of the radiation incident on the photodiode), L is the sample thickness, and α is the linear absorption coefficient of the film.

In our experiments, the nonlinear optical characteristics were investigated with the use of picosecond radiation, whose intensity at the focal point was less than the critical intensity at which free carriers arising from two-photon absorption begin to affect the linear refraction and absorption. At low intensities of laser radiation, the third-order nonlinearity is due to the nonlinear refraction caused by bound electrons [16]. At high intensities of laser radiation, a considerable contribution is made by the nonlinear refraction associated with free carriers generated during two-photon absorption. In particular, Smektala *et al.* [17] showed that the nonlinear refractive indices n_2 for As_2S_3 and As_2Se_3 glasses decrease by factors of five and nine with an increase in the intensity of probe radiation (at 1064 nm) from 2×10^8 W cm^{-2} to ~3–7 GW cm^{-2}. In [17], the authors assumed that, in this case, the five-order nonlinearity corresponding to a negative nonlinear addition to the refractive index can also make a noticeable contribution. For this reason, in our work, the nonlinear absorption coefficients were determined for laser radiation intensities at which the nonlinear absorption is of little consequence. Specifically, the nonlinear absorption coefficients n_2 were determined using the radiation intensity $I_0 = 2 \times 10^8$ W cm^{-2}, at which the change in the refractive index is associated only with the third-order nonlinearity. The fact that free charge carriers do not contribute to the change in the refractive index is indirectly confirmed by the symmetric dependences $T(Z)$ (Fig. 2), which was obtained in the scheme with a limiting aperture for all the studied films, except for $As_{20}S_{80}$. The use of low intensities in analyzing the nonlinearities observed in the films made it possible to avoid the influence of the higher order nonlinearities (in particular, the fifth-order nonlinearity) on the Z-scan results. It has been just this effect which, in a number of cases, led to different interpretations of the experimental data on nonlinear optical parameters of semiconduc-

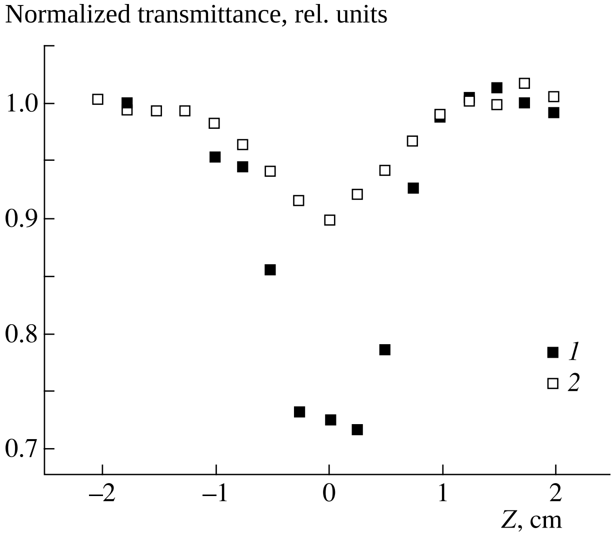

Fig. 3. Normalized transmittance as a function of the position of the (*1*) GaAs semiconductor wafer and (*2*) $As_{20}S_{80}$ chalcogenide film in the scheme with an open aperture at wavelengths of (*1*) 1064 and (*2*) 532 nm.

tors. Most likely, this effect is responsible for the contradictions in the available experimental data on the two-photon absorption coefficients (for GaAs, the absorption coefficients differ by a factor of 2–5 or more [18, 19]) and the nonlinear refractive indices γ.

Our measurements showed that chalcogenide films are characterized by large values of n_2. For example, the value of n_2 for the $As_{20}S_{80}$ film is equal to 1.3×10^{-8} esu at a wavelength of 532 nm. The measurement error in these experiments was 30%. The largest nonlinear refractive index $n_2 = -2.6 \times 10^{-8}$ esu at a wavelength of 1064 nm is observed for the $2As_2S_3/As_2Se_3$ film.

It is found that all the semiconductor structures under investigation are characterized by two-photon absorption. Figure 3 depicts the experimental dependence of the normalized transmittance on the position of the $As_{20}S_{80}$ film in the scheme with an open aperture. For comparison, Fig. 3 shows the dependence $T(Z)$ for a 0.4-mm-thick GaAs wafer at a radiation intensity of 1.3×10^9 W cm^{-2} at the focal point. In the above cases, the dominant contribution to the absorption is made by the nonlinear absorption. The linear absorption in the chalcogenide films is insignificant. In particular, the linear absorption coefficient for the As_2S_3 film at a wavelength of 1064 nm is equal to 0.095 cm^{-1}.

The normalized transmittance in the case of the scheme with an open aperture is defined by the relationship [20, 21]

$$T(z) = \frac{\ln(1+q_0)}{q_0}, \tag{3}$$

where

$$q_0 = \beta \frac{I_0[1-\exp(-\alpha L)]}{\left(1+\left(\frac{z}{z_0}\right)^2\right)\alpha}. \tag{4}$$

Here, $z_0 = kr^2/2$ and r is the beam radius in the focal waist. By determining the minimum normalized transmittance at the focal point ($z = 0$) in the scheme with an open aperture, the nonlinear absorption coefficient of the medium under investigation can be obtained from relationships (3) and (4). By this means, the nonlinear absorption coefficient β for GaAs is found to be equal to 31×10^{-9} cm W^{-1}, which is in good agreement with the experimental data obtained earlier (26×10^{-9} cm W^{-1} [18]). The measured values of β for chalcogenide films $As_{20}S_{80}$ ($\beta = 3 \times 10^{-6}$ cm W^{-1} at $\lambda = 532$ nm and $I_0 = 4 \times 10^8$ W cm^{-2}) and $3As_2S_3/As_2Se_3$ ($\beta = 10^{-7}$ cm W^{-1} at $\lambda = 1064$ nm and $I_0 = 3 \times 10^8$ W cm^{-2}) indicate that chalcogenide thin films have large nonlinear absorption coefficients.

The optical properties of amorphous chalcogenides can be controlled by varying their stoichiometric composition. For this purpose, amorphous chalcogenide films can be easily prepared through vacuum evaporation. It can be expected that a change in the optical parameters of these films should also be attended by variations in their nonlinear optical characteristics. However, to date, only the optical properties of chalcogenide multilayer films have been investigated experimentally [22–24]. The size effects in $As_{40}Se_{60}/Ge_{25}Se_{75}$ amorphous multilayer films were studied by Ogino and Mizushima [22] with the use of optical absorption methods. Similar investigations were carried for $Se_{0.85}Te_{0.15}/CdSe$ and Se/CdSe multilayer structures [23] and As_2Se_3/As_2S_8 chalcogenide films [24]. However, the problem associated with the relation between the nonlinear optical properties of multilayer films and the nonlinear optical parameters of their components was not studied earlier.

The nonlinearities of chalcogenide composite films can be evaluated from the nonlinear hyperpolarizabilities of individual components [25]. Examination of the results obtained in the investigation of the nonlinear refractive index for the As_2S_3 film revealed that, at the given intensities, the sign of this index (as could be expected) is identical to that of the index n_2 for the bulk material. This result also agrees with the analysis of the Kramers–Kronig relations, according to which the positive sign of the nonlinear refractive index should be observed for semiconductors with the ratio $\omega/E_g < 0.69$ [19]. Here, ω is the circular frequency of the laser radiation and E_g is the band gap. For As_2S_3, the band gap E_g is equal to 2.37 eV [26] and the ratio $\hbar\omega/E_g$ at the wavelength $\lambda = 1064$ nm is 0.49.

The situation is different for the $As_{20}Se_{80}$ film. The band gap E_g of this film is equal to 2.5 eV [24]. The ratio ω/E_g at the wavelength $\lambda = 532$ nm is 0.93. Therefore, the medium should possess self-defocusing properties. However, according to our data, the nonlinear refractive index n_2 for this film has positive sign.

A similar situation is observed for $2As_2S_3/As_2Se_3$ and $3As_2S_3/As_2Se_3$ multilayer films. Earlier investigations of the optical spectra of individual components (similar to the aforementioned chalcogenide structures) in the vicinity of the absorption edges demonstrated that the band gaps of arsenic sulfide and arsenic selenide single-component films are equal to 2.5 eV for As_2S_3 and 1.78 eV for As_2Se_3. However, the optical absorption edges of multilayer structures of the $2As_2S_3/As_2Se_3$ and $8As_2S_3/As_2Se_3$ types are shifted toward the high-energy range with respect to the optical absorption edge of As_2Se_3 (and, correspondingly, the band gaps increase) by 0.19 and 0.25 eV, respectively [24]. Consequently, the band gaps of the aforementioned multilayer composite films lie in the range between the band gaps E_g of their chalcogenide glass components. Note that the band gap E_g only slightly increases even in the case when the fraction of As_2S_3 in the multicomponent film considerably exceeds the fraction of As_2Se_3. The band gaps calculated for the $2As_2S_3/As_2Se_3$ and $3As_2S_3/As_2Se_3$ multicomponent films (with due regard for the extrapolation of the data taken from [24]) are equal to 1.97 and 1.99 eV, respectively. For the above values of E_g and the ratios ω/E_g equal to 0.59 for $2As_2S_3/As_2Se_3$ and $3As_2S_3/As_2Se_3$, these films at the wavelength $\lambda = 1064$ nm should possess self-focusing properties ($n_2 > 0$). However, according to our results, the $2As_2S_3/As_2Se_3$ and $3As_2S_3/As_2Se_3$ films are characterized by the self-defocusing properties (Fig. 2).

The origin of this self-defocusing is not quite clear. We can only assume that free carriers (generated by two-photon absorption, which makes an insignificant contribution at the intensities used) affect the general pattern of the phase relationships of the radiation passing through the film. As is known, a change in the refractive index in the general case is determined by the expression [18]

$$\Delta n = \gamma I + \sigma_r N. \qquad (5)$$

Here, the second term of the sum describes the change in the refractive index due to the effect of free charge carriers. The parameter σ_r characterizes the change in the refractive index caused by a single free charge carrier formed in photoexcitation and ionization processes that lead to the appearance of a cloud of charge carriers with density N. Note that the parameter σ_r for the majority of semiconductors has negative sign; as a result, this value can compensate for and even exceed the positive contribution to the refractive index due to the effect of bound electrons [18]. Consequently, the behavior of the laser radiation can change when passing through a similar medium (i.e., there occurs a crossover from self-focusing to self-defocusing). Another reason for the above findings could be interference in the thin films. This phenomenon can be responsible for an increase in the local field factor, the two-photon absorption, and the effect of free charge carriers on the refractive index of the medium. The observed processes of self-defocusing in multilayer films and self-focusing of the radiation with $\lambda = 532$ nm in the $As_{20}S_{80}$ film call for further investigation.

Now, let us now consider in more detail the As_2S_3, $As_{20}S_{80}$, $2As_2S_3/As_2Se_3$, and $3As_2S_3/As_2Se_3$ chalcogenide films, because their use as materials for optical limiters has been poorly investigated. The characteristics of optical limiting for chalcogenides of this type were studied earlier only for As_2S_3 glasses [6]. A theoretical treatment of the optical limiting associated with the Kerr-type nonlinearities in the aforementioned four films is given below.

We used a standard procedure for calculating the Z-scan with a limiting aperture [14] in order to evaluate the optical limiting caused by the Kerr-type nonlinearities in chalcogenide films. The film position is fixed in the region corresponding to a minimum transmittance [ahead of the focal point in the case of self-focusing and behind the focal point in the case of self-defocusing (see Fig. 2)] when two-photon absorption processes are of little significance. In this case, the minimum transmittance T_V is proportional to the laser radiation intensity and the nonlinear refractive index; that is,

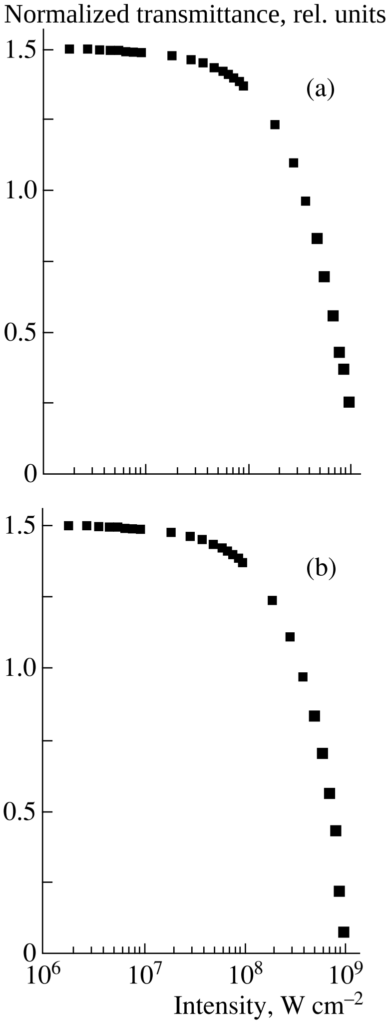

Fig. 4. Calculated normalized transmittance as a function of the laser radiation intensity for (a) $3As_2S_3/As_2Se_3$ and (b) $2As_2S_3/As_2Se_3$ chalcogenide films.

$$T_V = BI_0\gamma, \qquad (6)$$

where B is the parameter independent of laser radiation intensity. The range of the analyzed intensities is chosen from the following considerations. The lower boundary should correspond to the intensity at which the dependence $T(Z)$ in the scheme with a limiting aperture still exhibits a characteristic behavior, and the upper boundary should correspond to the intensity at which the optical breakdown has not yet occurred in the semiconductor.

Figure 4 shows the calculated dependences of the normalized transmittance for $3As_2S_3/As_2Se_3$ (Fig. 4a) and $2As_2S_3/As_2Se_3$ (Fig. 4b) chalcogenide films. The

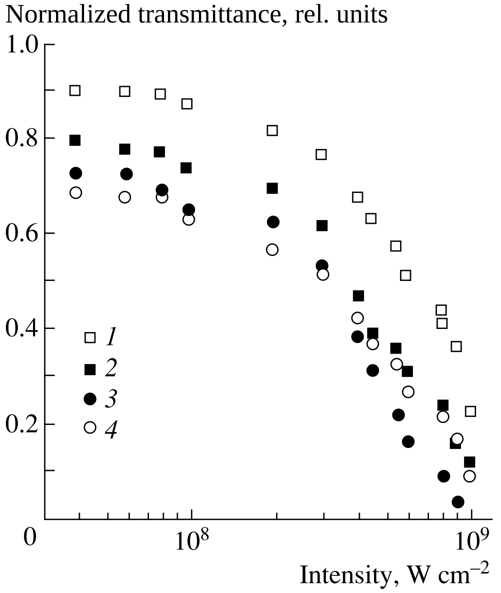

Fig. 5. Normalized transmittance as a function of the incident radiation intensity for (*1*) $As_{20}S_{80}$, (*2*) $2As_2S_3/As_2Se_3$, (*3*) As_2S_3, and (*4*) $3As_2S_3/As_2Se_3$ chalcogenide films in the scheme with an open aperture at wavelengths of (*1*) 532 and (*2*–*4*) 1064 nm.

largest limiting (by a factor of 12.5) is observed for the $2As_2S_3/As_2Se_3$ film. The As_2S_3 and $As_{20}S_{80}$ films are characterized by a fivefold limiting, and the $3As_2S_3/As_2Se_3$ film exhibits a threefold limiting. For all the films, the limiting process is observed in the intensity range 10^7–10^9 W cm^{-2}.

As in the case of nonlinear absorption, the experimental investigation of the optical limiting in semiconductors was performed using the scheme with an open aperture. The dependences of the transmittance on the laser radiation intensity for the studied films are shown in Fig. 5. The sample position corresponds to a minimum transmittance; i.e., the sample is located at the focal point. In this case, the optical limiting is due to two-photon absorption. The largest limiting (by a factor of 25) is observed in the As_2S_3 film.

As was noted above, the two-photon absorption in semiconductors is accompanied by the generation of free charge carriers, which also contribute to the nonlinear propagation of radiation in these media. This effect has found application for the case of using semiconductors (GaAs, GaP, CdSe) as passive elements in generators of extended pulse trains with passive negative feedback [27, 28]. Although these generators are very simple in design, they make it possible to generate compressed picosecond pulses with stable energy and time characteristics, which is a very important and necessary condition for the performance of nonlinear optical experiments. Our investigations demonstrated that chalcogenide films, such as $2As_2S_3/As_2Se_3$ and $3As_2S_3/As_2Se_3$, hold promise for use as intracavity elements for the compression of picosecond pulses.

It should be noted that, up to now, there has been no analysis performed to compare the nonlinear optical characteristics of films and bulk samples of amorphous chalcogenides, nor for their characteristics of optical limiting over the wide range of laser radiation intensities at which higher order nonlinearities (in particular, five-order nonlinearities) make a considerable contribution. The possibility of island structures appearing during epitaxial growth of films can lead to the formation of two-dimensional clusters, which, in turn, can result in an enhancement of the optical nonlinearities caused by the local field effect [29]. The appearance of so-called “hot regions,” in which the field amplitude exceeds the mean field amplitude by several orders of magnitude, brings about a substantial increase in the nonlinearities [30]. Possibly, this is the reason for the rather large nonlinear response observed in our experiments with chalcogenide thin films.

4. CONCLUSIONS

Thus, we investigated the nonlinear optical characteristics and the optical limiting in As_2S_3, $As_{20}S_{80}$, $2As_2S_3/As_2Se_3$, and $3As_2S_3/As_2Se_3$ chalcogenide films. The nonlinear refractive indices and the two-photon absorption coefficients of these films were measured using the *Z*-scan technique at wavelengths of a picosecond Nd : YAG laser ($\lambda = 1064$ and 532 nm). The optical limiting associated with the Kerr-type nonlinearities was analyzed for the amorphous chalcogenide films. It was demonstrated that the $2As_2S_3/As_2Se_3$ film is characterized by a 12.5-fold optical limiting. The optical limiting due to two-photon absorption was investigated experimentally. It was found that the As_2S_3 film exhibits a 25-fold optical limiting.

ACKNOWLEDGMENTS

R.A. Ganeev and T. Usmanov acknowledge the support of the Uzbek Research and Technical Center (project no. Uzb-20). A.I. Ryasnyanskiĭ acknowledges the support of the Uzbek State Committee of Science and Engineering (project no. 7/01).

REFERENCES

1. M. Dabbicco and I. M. Catalano, Opt. Commun. **178**, 117 (2000).
2. K. Y. Tseng, K. S. Wong, and G. K. L. Wong, Opt. Lett. **21**, 180 (1996).
3. K. S. Bindra, R. Chari, V. Shukla, *et al.*, Pure Appl. Opt. **1**, 73 (1999).
4. F. Smektala, C. Quemard, L. Leneindre, *et al.*, J. Non-Cryst. Solids **239**, 139 (1998).
5. H. Kanbara, S. Fujiwara, K. Tanaka, *et al.*, Appl. Phys. Lett. **70**, 925 (1997).

6. C. H. Kwak, Y. L. Lee, and S. G. Kim, J. Opt. Soc. Am. B **16**, 600 (1999).
7. R. Range-Rojo, T. Kasa, R. Hajto, *et al.*, Opt. Commun. **109**, 145 (1994).
8. M. Asobe, K. Suzuki, T. Kanamori, and K. Kubodera, Appl. Phys. Lett. **60**, 1153 (1992).
9. A. L. Dawar, P. K. Shishodia, G. Chauhan, *et al.*, Appl. Opt. **29**, 1971 (1999).
10. R. A. Ganeev, A. I. Ryasnyansky, S. R. Kamalov, *et al.*, J. Phys. D: Appl. Phys. **34**, 1602 (2001).
11. R. A. Ganeev, A. I. Ryasnyansky, M. K. Kodirov, and T. Usmanov, Opt. Commun. **185**, 473 (2000).
12. L. W. Tutt and A. Kost, Nature **356**, 224 (1992).
13. Z. R. Chen, H. W. Hou, X. Q. Xin, *et al.*, J. Phys. Chem. **99**, 8717 (1995).
14. M. Sheik-Bahae, A. A. Said, T. Wei, *et al.*, IEEE J. Quantum Electron. **26**, 760 (1990).
15. R. G. Ganeev, A. I. Ryasnyanskiĭ, Sh. R. Kamalov, *et al.*, Opt. Spektrosk. **90**, 640 (2001) [Opt. Spectrosc. **90**, 568 (2001)].
16. M. Sheik-Bahae, D. J. Hagan, and E. W. Van Stryland, Phys. Rev. Lett. **65**, 96 (1990).
17. F. Smektala, C. Quemard, V. Couders, and A. Barthelemy, J. Non-Cryst. Solids **274**, 232 (2000).
18. A. A. Said, M. Sheik-Bahae, D. J. Hagan, *et al.*, J. Opt. Soc. Am. B **9**, 405 (1992).
19. M. Sheik-Bahae, D. C. Hutchings, D. J. Hagan, and E. W. Van Stryland, IEEE J. Quantum Electron. **27**, 1296 (1991).
20. J. P. Rakovich, M. V. Artemyev, A. G. Rolo, *et al.*, Phys. Status Solidi B **224**, 319 (2001).
21. P. B. Capple, J. Staromlynska, J. A. Hermann, and T. J. Mckay, J. Nonlinear Opt. Phys. Mater. **6**, 251 (1997).
22. T. Ogino and Y. Mizushima, Jpn. J. Appl. Phys. **22**, 1647 (1983).
23. R. Ionov, D. Nesheva, and D. Arsova, J. Non-Cryst. Solids **137–138**, 1151 (1991).
24. H. Hamanaka, S. Konagai, K. Murayama, *et al.*, J. Non-Cryst. Solids **198–200**, 808 (1996).
25. R. Adair, L. L. Chase, and S. A. Payne, Phys. Rev. B **39**, 3337 (1989).
26. J. B. Ramírez-Malo, E. Márquez, C. Corrales, *et al.*, Mater. Sci. Eng. B **25**, 53 (1994).
27. A. Agnessi, A. Del Corno, P. Di Trapani, *et al.*, IEEE J. Quantum Electron. **28**, 7120 (1992).
28. R. A. Ganeev and T. Usmanov, Jpn. J. Appl. Phys. **39**, 5111 (2000).
29. V. M. Shalaev, E. Y. Polyakov, and V. A. Markel, Phys. Rev. B **53**, 2437 (1996).
30. A. E. Neeves and M. N. Birnboim, J. Opt. Soc. Am. B **6**, 787 (1989).

Translated by O. Borovik-Romanova

Physics of the Solid State, Vol. 45, No. 2, 2003, pp. 214–223. Translated from Fizika Tverdogo Tela, Vol. 45, No. 2, 2003, pp. 205–214.
Original Russian Text Copyright © 2003 by I.G. Kuleev, I.I. Kuleev.

SEMICONDUCTORS AND DIELECTRICS

Γ_8-Band Electron Momentum Relaxation Involving a Mixed-Valence Iron Ion System, and Electronic Transport in HgSe : Fe at Low Temperatures

I. G. Kuleev and I. I. Kuleev
Institute of Metal Physics, Ural Division, Russian Academy of Sciences,
ul. S. Kovalevskoĭ 18, Yekaterinburg, 620219 Russia
e-mail: kuleev@imp.uran.ru

Received June 20, 2002

Abstract—Specific features of Γ_8-band electron scattering on a spatially correlated mixed-valence iron ion system in HgSe : Fe crystals are investigated. The *s–p* hybridization and Bloch wave function amplitudes are taken into account in calculating the probability of electron scattering by mixed-valence iron ions. The relaxation time and mobility of Γ_8-band electrons in HgSe and HgSe : Fe at low temperatures are calculated, and the energy dependence of the electron relaxation time is analyzed. This dependence for Γ_8-band electrons is shown to change radically when mixed-valence iron ions are ordered in space. *© 2003 MAIK “Nauka/Interperiodica”.*

1. INTRODUCTION

Studies into electron transport phenomena in iron-doped HgSe crystals are of importance because these materials exhibit unusual physical properties [1–12]. One of these surprising properties is a significant increase in the mobility of electrons observed to occur in the region of liquid-helium temperatures as the iron concentration is increased from $N_{\mathrm{Fe}} = N^* = 4.5 \times 10^{18}$ to $(1–2) \times 10^{19}$ cm^{-3} [1–4]. It has been shown [1–12] that the anomalies in the electron transport in HgSe : Fe crystals at low temperatures are associated with the formation of a mixed-valence (MV) state (Fe^{2+}–Fe^{3+}) of iron ions at the Fermi level and with a spatial ordering of positively charged iron ions due to their Coulomb repulsion.

When interpreting the transport phenomena in these compounds, the dispersion law of carriers in the Γ_8 conduction band is assumed to be nonparabolic, but the wave functions can be approximated by plane waves. In effect, this approach corresponds to the Γ_6 band and an infinitely wide band gap $\varepsilon_g \longrightarrow \infty$; the *s–p* hybridization (characteristic of the Γ_8 band) and the Bloch amplitudes of wave functions are ignored. However, it is well known [13–16] that the scattering of Γ_8-band conduction electrons by charged centers can be significantly weaker than that of Γ_6-band electrons. Therefore, it is of interest to elucidate how this weakened scattering of Bloch electrons and the calculations performed in [6, 17, 18] without regard for the *s–p* hybridization will be affected if the spatial correlation of Fe^{3+} ions and the *s–p* hybridization of the wave functions are taken into account. On the other hand, due to the dependence of the Bloch amplitudes on the electron energy, the energy dependence of the relaxation time $\tau(\varepsilon)$ of electrons can also be affected. Since the thermomagnetic effects, such as the longitudinal and transverse Nernst–Ettingshausen effects, are proportional to the energy derivative of the relaxation time $d\tau(\varepsilon)/d\varepsilon$, allowance for the structure of the Γ_8-band wave functions can change these effects and can be of importance in explaining the unusual dependences of the thermomagnetic effects on temperature and iron impurity concentration [9–11]. Under hydrostatic pressure applied to an HgSe crystal, the energy gap ε_g between the Γ_8 conduction band and the Γ_6 band changes, which should affect the Bloch amplitudes. This effect must be taken into account in interpreting the experimental data on the influence of hydrostatic pressure on the electrical conductivity of HgSe : Fe crystals at low temperatures. These issues are discussed in the present paper.

In Section 2, we calculate the electron momentum relaxation time due to scattering by MV iron ions in HgSe crystals. In Section 3, the dependence of the electron mobility on the iron impurity concentration is analyzed. In Section 4, the energy dependence of the relaxation time of Γ_8-band electrons is discussed and a comparison is made with the results of calculations made in [9, 10] with the Bloch amplitudes ignored in calculating the electron scattering probability.

2. ELECTRON RELAXATION TIME DUE TO SCATTERING BY MIXED-VALENCE IRON IONS IN HgSe : Fe CRYSTALS

In the model proposed in [6, 17, 18], the system of iron ions in HgSe : Fe is treated as a binary substitution alloy consisting of charged Fe^{3+} centers and of neutral (on the lattice) Fe^{2+} centers. The electron momentum relaxation at low temperatures is due to interaction of the electrons with these centers. The interaction with neutral centers is assumed to be a contact interaction, while the interaction with charged centers is described by the screened Coulomb potential characterized by the Fermi–Thomas screening length. In calculating the relaxation time $\tau(\varepsilon)$, the nonparabolic conduction band of HgSe is described in terms of the Kane two-band model [15]:

$$\varepsilon(k) = \frac{\hbar^2 k^2}{2m_0} + \frac{\varepsilon_g}{2}\left\{\left[1 + \frac{2\hbar^2 k^2}{m_n \varepsilon_g}\right]^{1/2} - 1\right\}, \qquad (1)$$

where m_n is the electron effective mass at the bottom of the band and $\varepsilon_g = \varepsilon(\Gamma_8) - \varepsilon(\Gamma_6)$. For HgSe, we have $\varepsilon_g = 0.22$ eV and $m_n \cong 0.02m_0$, where m_0 is the free-electron mass [1].

In contrast to [6, 17, 18], in calculating the electron transition probability from the state $|\mathbf{k}, \mathbf{j}\rangle$ to $|\mathbf{k}', \mathbf{j}'\rangle$ due to scattering by MV iron ions, we use Bloch wave functions for the Γ_8 conduction band ($j_\pm = \pm 3/2$) normalized to the crystal volume [13–15]:

$$\begin{gathered}
\psi_{kj} = V^{-1/2} u_{kj} \exp(i\mathbf{kr}), \\
u_{kj^+} = \left(iaS - d^- \frac{k_+}{k} R_- + d^+ \frac{k_-}{k} R_+ + c\frac{k_z}{k} z\right)\uparrow \\
- b\left(\frac{k_z}{k} R_+ - \frac{1}{\sqrt{2}}\frac{k_z}{k} z\right)\downarrow, \\
u_{kj^-} = \left(iaS + d^+ \frac{k_+}{k} R_- - d^- \frac{k_-}{k} R_+ + c\frac{k_z}{k} z\right)\downarrow \\
+ b\left(\frac{k_z}{k} R_- - \frac{1}{\sqrt{2}}\frac{k_z}{k} z\right)\uparrow,
\end{gathered} \qquad (2)$$

where $k_\pm = k_x \pm ik_y$; $R_\pm = (x \pm iy)/2^{1/2}$; arrows ↑ and ↓ indicate the spin direction (up and down); S and (X, Y, Z) are the s and p wave functions, respectively [15]; $d^\pm = (b \pm c*2^{1/2})/2$; and a, b, and c are coefficients defined as

$$\begin{gathered}
a^2 = (\Delta + 3/2*\varepsilon)(\Delta + \varepsilon)\varepsilon/D, \quad b^2 = \Delta^2(\varepsilon + \varepsilon_g)/3D, \\
c^2 = 2(\Delta + 3/2*\varepsilon)^2(\varepsilon + \varepsilon_g)/3D, \\
D = (\Delta + 3/2*\varepsilon)(\Delta + \varepsilon)\varepsilon \\
+ (\Delta + \varepsilon)^2(\varepsilon + \varepsilon_g) + 1/2(\varepsilon + \varepsilon_g)\varepsilon,
\end{gathered} \qquad (3)$$

with Δ being the spin–orbit splitting (for HgSe, $\Delta = 0.45$ eV). From the normalization condition for the Bloch amplitudes, it follows that

$$a^2 + b^2 + c^2 = 1. \qquad (4)$$

The inverse relaxation time of Γ_8-band electrons can be written as [6, 18]

$$\tau^{-1}(\varepsilon) = \frac{2\pi\hbar k}{m}\int_0^\pi [1 - \cos(\theta)]\sigma(\theta)\sin(\theta)d\theta. \qquad (5)$$

Here, θ is the angle between the momenta of the incident and scattered electrons and

$$\begin{gathered}
\sigma(\theta) = [m/(2\pi\hbar^2)]^2 \\
\times \sum_{\alpha, \beta = +;\, 0;\, j'} (N_\alpha N_\beta)^{1/2} |V_\alpha(q) V_\beta(q)|^2 I_{\alpha\beta}(\theta) S_{\alpha\beta}(q),
\end{gathered} \qquad (6)$$

where $q = 2k\sin(\theta/2)$; N_+ and N_0 are the concentrations of charged and neutral (on the lattice) iron ions, respectively; $V_+(q) = -(4\pi e^2/\chi)(q^2 + r_s^{-2})^{-1}$ is the Fourier transform of the screened Coulomb potential; χ is the dielectric constant; and r_s is the screening length. The interaction of Γ_8-band electrons with neutral centers is described by two parameters, $V_0(q) \equiv V_0$ and W_0; the parameter V_0 characterizes this interaction for the s-type Bloch amplitudes and W_0, for the p-type Bloch amplitudes [19]:

$$V_0 = \langle S|V_0(r)|S\rangle, \quad W_0 = \langle X|V_0(r)|X\rangle. \qquad (7)$$

In HgSe : Fe crystals, iron substitutes for divalent mercury at lattice sites; therefore, the interaction of an electron with neutral (on the lattice) Fe^{2+} ions is described by the potential $V_0(r) = V_{Fe^{2+}}(r) - V_{Hg^{2+}}(r)$ localized within a unit cell. Since the electronegativity of Fe^{2+} ions is less than that of Hg^{2+} ions [1], $V_0(r)$ and, hence, V_0 are negative. The functions $I_{\alpha\beta}(\theta)$ take into account the difference in scattering between a Bloch Γ_8-band electron and a free electron and are given by

$$\begin{gathered}
I_{\alpha\beta}(\theta) = \sum_{n=1}^{3} z^{(2n-1)} \varphi_{\alpha\beta}^{n}, \quad z = \sin(\theta/2), \\
\varphi_{++}^{(1)} = 1, \quad \varphi_{++}^{(2)} = -4[(1 - a^2) - b^2(b/2 - c\sqrt{2})^2], \\
\varphi_{++}^{(3)} = 4[(1 - a^2)^2 - b^2(b/2 - c\sqrt{2})^2], \\
\varphi_{+0}^{(1)} = a^2 + w(1 - a^2), \\
\varphi_{+0}^{(2)} = -[2(1 + w)a^2(1 - a^2) + 2\varphi_{++}^{(3)}], \quad \varphi_{+0}^{(3)} = 4w\varphi_{++}^{(3)}, \\
\varphi_{00}^{(1)} = a^4 + w[a^2(1 - a^2)], \\
\varphi_{00}^{(2)} = -4w[a^2(1 - a^2) + w\varphi_{++}^{(3)}], \\
\varphi_{00}^{(3)} = 4w^2[a^2(1 - a^2) + b^2(b/2 - c\sqrt{2})^2].
\end{gathered} \qquad (8)$$

Here, $w = W_0/V_0$ is the ratio between the constants characterizing the interaction of a Γ_8-band electron with neutral centers [19]. For $Hg_{1-x}Cd_xSe$ solid solutions, we have $V_0 = 3.6 \times 10^{-22}$ eV cm^3 and $w = -0.29$ [20]. According to the estimates made for HgSe : Fe in [21], $V_0 = 8.2 \times 10^{-22}$ eV cm^3 and $w \approx -0.1 \pm 0.1$.

The structure factors $S_{\alpha\beta}(q)$ depend on the relative positions of the ions [22],

$$S_{\alpha\beta}(q) = \frac{1}{(N_\alpha N_\beta)^{1/2}} \sum_{i,j} \exp[i\mathbf{q}(\mathbf{R}_i^\alpha - \mathbf{R}_j^\beta)], \quad (9)$$

and can be expressed in terms of the total correlation functions $h_{\alpha\beta}(r) = g_{\alpha\beta}(r) - 1$, where $g_{\alpha\beta}(r)$ are the partial pair correlation functions for the Fe^{3+}–Fe^{2+} ion system [22, 23]:

$$S_{\alpha\beta}(q) = \delta_{\alpha\beta} + 4\pi\sqrt{N_\alpha N_\beta}\int_0^\infty r^2 h_{\alpha\beta}(r)\frac{\sin(qr)}{qr}dr. \quad (10)$$

For the Fe^{3+}–Fe^{2+} iron impurity system, we have

$$S_{++}(q) = 1 + N_+ h_{++}(q), \quad S_{00}(q) = 1 + N_0 h_{00}(q),$$
$$S_{+0}(q) = S_{0+}(q) = \sqrt{N_+ N_0}\, h_{+0}(q). \quad (11)$$

Thus, in order to analyze electron momentum relaxation involving MV iron ions, one needs to find the four pair correlation functions $g_{\alpha\beta}(r)$ which describe the spatial distribution of Fe^{2+} and Fe^{3+} ions in HgSe : Fe crystals. In [18], an approximate scheme was proposed for calculating the partial pair correlation functions $g_{\alpha\beta}(r)$ and the corresponding structure factors $S_{\alpha\beta}(q)$. The scheme is based on a set of integral Ornstein–Zernike equations for MV iron ions treated within a penetrating hard sphere model [18] and on the following physical arguments. The Coulomb repulsion $V_{++}(r)$ of d holes localized at different sites is the strongest interaction in the MV (Fe^{2+}–Fe^{3+}) ion system and determines the rearrangement of d holes and neutral centers in space; the interactions $V_{0+}(r)$ and $V_{00}(r)$ are significantly weaker and can be ignored. For this reason, we solve the Ornstein–Zernike equation in the Percus–Yevick approximation for the d-hole subsystem using the hard-sphere model [6] and find $S_{++}(q)$. Then, we calculate the remaining structure factors $S_{\alpha\beta}(q)$ using exact relations between the partial correlation functions for binary substitution alloys [22]. The result is [18]

$$S_{++}(q) = [1 - N_+ c_{++}(q)]^{-1},$$
$$S_{+0}(q) = S_{0+}(q) = \sqrt{N_+/N_0}[1 - S_{++}(q)], \quad (12)$$
$$S_{00}(q) = 1 + (N_+/N_0)[S_{++}(q) - 1],$$

and the Fourier transform $c_{++}(q)$ of the direct-correlation function has the form

$$c_{++}(q) = -\frac{4\pi d^3}{u^3}\left\{\left[\alpha + 2\beta + 4\gamma - \frac{24\gamma}{u^2}\right]\sin u\right.$$
$$\left. + \left[\frac{2}{u}(\beta + 6\gamma) - (\alpha + \beta + \gamma)u - \frac{24\gamma}{u^3}\right]\cos u + \frac{24\gamma}{u^3} - \frac{2\beta}{u}\right\},$$
$$u = qd, \quad \alpha = \frac{(1 + 2\eta)^2}{(1 - \eta)^4}, \quad (13)$$
$$\beta = \frac{-6\eta(1 + 0.5\eta)^2}{(1 - \eta)^4}, \quad \gamma = \frac{1}{2}\eta\alpha,$$

where $\eta = \pi d^3 n/6$ is the packing fraction characterizing the degree of ordering of hard spheres (this quantity is equal to the ratio of the volume of the hard spheres to the total volume of the system). It is clear that Coulomb repulsion of d holes in the MV iron ion system results not only in spatial ordering of charged centers (Fe^{3+} ions) but also in correlation between the positions of neutral centers with respect to the charged centers [17, 18]. Therefore, the charge redistribution in the MV (Fe^{3+}–Fe^{2+}) iron ion system leads to coherent electron scattering, which can significantly affect the transport characteristics of HgSe : Fe crystals.

Performing integration in Eq. (5), the inverse relaxation time for Γ_8-band electrons scattered by MV iron ions is found to be

$$\tau^{-1}(k) = \frac{4\varepsilon_B(\varepsilon)}{3\pi\hbar}\left\{\frac{\Phi_{++}(k)}{y^3}\right.$$
$$\left. + \Lambda\left[2\left(\frac{N_0}{N_+}\right)^{1/2}\frac{\Phi_{+0}(k)}{y} + \Lambda y \Phi_{00}(k)\frac{N_0}{N_+}\right]\right\} \quad (14)$$
$$= \frac{4\varepsilon_B(\varepsilon)}{3\pi\hbar}\Phi(k) = \tau_{++}^{-1}(k) + \tau_{al}^{-1}(k),$$
$$\tau_{al}^{-1} = \tau_{+0}^{-1} + \tau_{00}^{-1}, \quad \varepsilon_B(\varepsilon) = \varepsilon_{Bn}(1 + 2\varepsilon/\varepsilon_g).$$

Here, $y = k/k_F$, ε_{Bn} is the Bohr energy for an electron at the bottom of the conduction band, $\Lambda = m_F a_B k_F^2 |V_0|/\pi\hbar^2$ is an alloy scattering parameter dependent on the ratio between the electron interaction constants with neutral and charged centers, $a_B = \chi\hbar^2/m_F e^2$ is the Bohr radius, ε_F is the Fermi energy, and the functions $\Phi_{\alpha\beta}(k)$ are given by

$$\Phi_{\alpha\beta} = \sum_{n=1}^{3}\varphi_{\alpha\beta}^{(n)} I_{\alpha\beta}^{(2n+1)}, \quad I_{\alpha\beta}^{(N)} = 2\int_0^1 \frac{x^N S_{\alpha\beta}(2kx)dx}{(x^2 + b_k^{-1})^\nu}, \quad (15)$$
$$b_k = (2kr_s)^2,$$

where $\nu = 0$, 1, and 2 for I_{00}, I_{0+}, and I_{++}, respectively. Thus, the electron momentum relaxation due to scattering by the correlated Fe^{2+}–Fe^{3+} ion system is determined by three contributions: one from scattering by correlated Fe^{3+} ions, one from scattering by neutral centers, and the interference contribution Φ_{0+}. It should be noted that in the case of randomly distributed iron ions, we have $S_{++}(q) = S_{00}(q) = 1$ and $S_{0+}(q) = S_{+0}(q) = 0$. In this case, there is no interference contribution and Matthiessen's rule holds for electron scattering on neutral- and charged-center systems.

In HgSe : Fe crystals with $N_{Fe} < N^* = 4.5 \times 10^{18}$ cm^{-3}, the Fermi level lies below the iron d level; therefore, $N_0 = 0$ and the Fe^{3+} ions are randomly distributed over the lattice sites. In this case, $S_{++}(q) = 1$, $\tau_{+0}^{-1} = \tau_{00}^{-1} = 0$, and the expression for the inverse relaxation time τ_{++}^{-1} reduces to that derived earlier for the case of scattering by randomly distributed donors [14, 15]:

$$\tau_{++}^{-1}(\varepsilon) = \frac{4\varepsilon_B(\varepsilon)}{3\pi\hbar y^3}\Phi_{\Gamma^8}, \quad \Phi_{\Gamma^8} = \sum_{n=1}^{3}\varphi_{++}^{(n)}I_{++}^{(2n+1)}, \qquad (16)$$

where $I_{++}^{(3)} = \ln(1+b_k) - (1+b_k^{-1})^{-1}$, $I_{++}^{(5)} = 1 + (1+b_k)^{-1} - 2b_k^{-1}\ln(1+b_k)$, and $I_{++}^{(7)} = \frac{1}{2}\{1 - 4b_k^{-1} - 2b_k^{-1}(1 + b_k^{-1})^{-1} + 6b_k^{-2}\ln(1+b_k)\}$.

In the case of scattering by randomly distributed neutral centers ($S_{00}(q) = 1$), Eq. (14) for $\tau_{00}^{-1}(\varepsilon)$ reduces to the expression derived in [15, 19]:

$$\tau_{00}^{-1}(\varepsilon) = \frac{4\varepsilon_B(\varepsilon)}{3\pi\hbar}\Lambda y\Phi_{00}(k)\frac{N_0}{N_+}, \quad \Phi_{00} = \sum_{n=1}^{3}\varphi_{00}^{(n)}I_{00}^{(2n+1)},$$
$$I_{00}^{(3)} = 1/2, \quad I_{00}^{(5)} = 1/3, \quad I_{00}^{(7)} = 1/4. \qquad (17)$$

Further, we analyze the dependence of the electron mobility on the impurity content in HgSe : Fe crystals and discuss the specific features of the coherent scattering of Γ_8-band electrons by MV iron ions.

3. INTERFERENCE IN ELECTRON SCATTERING BY MIXED-VALENCE IRON IONS AND THE MOBILITY OF CONDUCTION ELECTRONS IN HgSe : Fe CRYSTALS

The dependence of the mobility of electrons on the impurity concentration N_{Fe} in HgSe : Fe crystals was analyzed in [6, 17, 18]. Nonparabolicity of the conduction band was included only in the dispersion law of carriers. In contrast to those papers, we take into account the specific features of the Γ_8-band wave functions in calculating the probability of electron scattering by MV iron ions and analyze the dependence of the electron mobility $\mu_{++}(N_d) = e\tau_{++}/m_F$ limited by scattering by randomly distributed donors on the donor concentration N_d in HgSe crystals. By comparing the results of the calculations with the experimental data taken from [14, 24, 25], we determine the parameters characterizing Γ_8-band electron scattering by charged centers, namely, the dielectric constant χ, effective mass m_F^*, and electron mobility μ^* for $N_d = N^* = 4.8 \times 10^{18}$ cm^{-3}. Then, these parameters are used to calculate the electron mobility limited by scattering on MV iron ions in HgSe : Fe crystals. An analysis of the electron mobility in HgSe crystals on the basis of Eq. (16) for $\tau_{++}(\varepsilon_F)$ revealed that the calculated $\mu(N_d)$ dependence (curve *1* in Fig. 1) agrees with the experimental data [14, 24, 25] if the parameters are taken to be $\chi \approx 27$ and $m_F^* \approx 0.07m_0$ ($m_n \approx 0.023m_0$); in this case, $\mu^* \approx 2.23 \times 10^4$ cm^2/V s. As the iron content in HgSe : Fe is increased, the Fermi level reaches the d level at $N_{Fe} \approx 4.5 \times 10^{18}$ cm^{-3} and then, with a further increase in N_{Fe}, the electron concentration n_e ($n_e = N_+$) saturates and remains equal to $n_e = N^* \approx 4.8 \times 10^{18}$ cm^{-3} [1] virtually everywhere in the range $N_{Fe} \sim (5–500) \times 10^8$ cm^{-3} [1, Fig. 3b]. Therefore, in what follows, we use the parameters m_F^* and μ^* determined for this concentration.

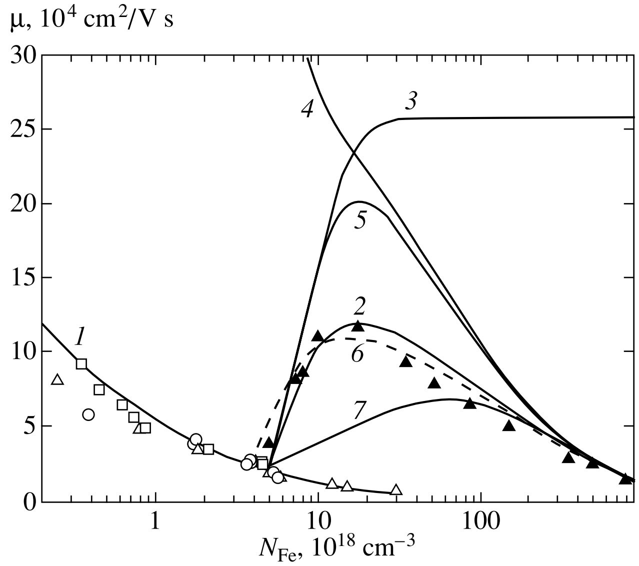

Fig. 1. Electron mobilities (*1*) $\mu(N_d)$ in HgSe crystals and (*2*) $\mu(N_{Fe})$ in HgSe : Fe crystals; (*3, 4*) contributions to mobility $\mu(N_{Fe})$ from electron scattering by correlated Fe^{3+} ions and from alloy scattering, respectively; (*5*) $\mu(N_{Fe})$ dependence not including the effect of coherent electron scattering; (*6*) $\mu(N_{Fe})$ dependence including the effect of intrinsic defects of concentration $N_d = 1 \times 10^{18}$ cm^{-3}; and (*7*) $\mu(N_{Fe})$ dependence calculated using "basic equation" (25) derived in [27]. Open and filled symbols are experimental data on $\mu(N_d)$ in HgSe crystals [14, 24, 25] and on $\mu(N_{Fe})$ in HgSe : Fe crystals [3, 30], respectively.

Let us consider the dependence of the electron mobility on the impurity content in HgSe : Fe crystals and analyze the role of coherent scattering of Γ_8-band electrons by MV iron ions. We express $\mu(N_{Fe})$, limited by electron scattering on MV iron ions, in terms of the quantity μ^*:

$$\begin{aligned}\mu(N_{\mathrm{Fe}}) &= \mu^*\Phi^*_{\Gamma_8}(k_{\mathrm{F}})/\Phi(k_{\mathrm{F}})\\ &= [\mu^{-1}_{++}(N_{\mathrm{Fe}}) + \mu^{-1}_{+0}(N_{\mathrm{Fe}}) + \mu^{-1}_{00}(N_{\mathrm{Fe}})]^{-1}\\ &= [\mu^{-1}_{++}(N_{\mathrm{Fe}}) + \mu^{-1}_{al}(N_{\mathrm{Fe}})]^{-1},\end{aligned} \tag{18}$$

$$\mu^*(0) = \frac{3\pi\hbar e}{m^*_{\mathrm{F}}4\varepsilon^*_{\mathrm{B}}\Phi^*_{\Gamma_8}(k_{\mathrm{F}})},\quad \Phi^*_{\Gamma_8} \approx 1.37,\quad \varepsilon^*_{\mathrm{B}} \approx 1.38\ \mathrm{meV}, \tag{19}$$

where the function $\Phi_{\alpha\beta}$ and structure factors $S_{\alpha\beta}(q)$ are given by Eqs. (15) and (12), respectively. It should be noted that the structure factor $S_{00}(q)$ is noticeably different from unity only in the range of low neutral-center concentrations $N_0 < N_+$, where the electron scattering by these centers is weak and can be neglected [18]. At higher iron impurity contents ($N_0 \gg N_+$), where the neutral-center scattering becomes significant, we have $S_{00}(q) \approx 1$. Therefore, for the sake of simplicity, we put $S_{00}(q) \approx 1$; in this case, the quantity Φ_{00} is given by Eq. (17).

When a correlated Fe^{3+} ion system is treated statistically within the hard-sphere model, the structure factor $S_{++}(q, \eta)$ depends on the packing fraction characterizing the degree of ion ordering. In order to calculate the electron mobility and other transport characteristics of HgSe : Fe crystals, we need to acquire the relation between the packing fraction and the iron impurity content. Several methods have been proposed for determining this relation [5, 6, 17, 18, 26–28]. The most reliable and physically substantiated is the method suggested in [6] and refined in [17, 18]. According to this method, the $\eta(N_{\mathrm{Fe}})$ dependence is found as follows. First, the alloy scattering parameter Λ is determined using the experimental values of the electron mobility $\mu^{\exp}(N_{\mathrm{Fe}})$ in the range of high iron concentrations $N_{\mathrm{Fe}} > 10^{20}$ cm^{-3} (where the alloy scattering is dominant). Then, the contribution $\mu^{\exp}_{++}(N_{\mathrm{Fe}})$ due to scattering by correlated Fe^{3+} ions is calculated:

$$\mu^{\exp}_{++} = (\mu^{-1}_{\exp} - \mu^{-1}_{al})^{-1}. \tag{20}$$

Then, using the expression for the structure factor $S_{++}(q, \eta)$, we calculate $\mu_{++}(\eta)$ as a function of η. Finally, by equating the experimental and calculated values of the mobility, $\mu^{\exp}_{++}(N_{\mathrm{Fe}}) = \mu_{++}(\eta)$, the $\eta(N_{\mathrm{Fe}})$ dependence is determined. It is found that the empirical $\eta(N_{\mathrm{Fe}})$ dependence can be closely approximated by the expression

$$\eta = \eta_\infty\{1 - \exp[-(\eta/\eta_\infty)(N_{\mathrm{Fe}}/N_+)]\}. \tag{21}$$

It is seen that $\eta(N_{\mathrm{Fe}})$ saturates as the iron content increases: $\eta(N_{\mathrm{Fe}} \longrightarrow \propto) = \eta_\propto$. The calculated $\mu(N_{\mathrm{Fe}})$ dependence with $\eta_\propto \approx \eta_L = 0.45$ agrees with the experimental data; therefore, the system of Fe^{3+} ions in an HgSe : Fe crystal at low temperatures can be considered as a strongly correlated Coulomb liquid in the case of $N_{\mathrm{Fe}} \gg N_+$ [6]. The empirical method used in [6] was substantiated in [18, 28, 29], where the dependence of the correlation sphere radius and, hence, of the packing fraction on the iron impurity content was calculated for $N_0 < N_+$ by using the balance equation for d holes and neutral centers in the short-range-order cluster of an Fe^{3+} ion:

$$\eta(N_{\mathrm{Fe}}) = \frac{1}{8}\Delta N_1\left(\frac{N_0}{N_{\mathrm{Fe}}}\right) \approx 0.74\left(\frac{N_0}{N_{\mathrm{Fe}}}\right),\quad \Delta N_1 = 5.92. \tag{22}$$

The empirical $\eta(N_{\mathrm{Fe}})$ dependence Eq. (21) for $N_0 < N_+$ correlates well with Eq. (22) (see [18, Fig. 3]). It was shown in [18] that Eq. (22) is an exact asymptotic expression in the limit of $N_0 \ll N_+$ (i.e., $N_0 \longrightarrow 0$). On the other hand, from empirical equation (21) for $N_0 \ll N_+$, it follows that $\eta(N_{\mathrm{Fe}}) \approx 2\eta_\propto N_0/N_{\mathrm{Fe}}$; a comparison with Eq. (21) gives $\eta_\propto \approx 0.37$. In what follows, we take into account this refinement and use this value of $\eta_\propto$ in calculating the electron mobility $\mu(N_{\mathrm{Fe}})$ and the contributions from alloy scattering and from scattering by correlated Fe^{3+} ions. The quantities V_0 and $w = W_0/V_0$ are adjustable parameters characterizing Γ_8-band electron scattering by iron ions that are neutral on the lattice. The values of these parameters are found by comparing the calculated $\mu(N_{\mathrm{Fe}})$ dependences with the experimental data from [3, 30].

The results of the analysis described above are shown in Fig. 1. It is seen that there is good agreement with the experimental data taken from [3, 30]. We succeeded in adequately describing both the $\mu(N_d)$ dependence in HgSe crystals (curve *1*) and the $\mu(N_{\mathrm{Fe}})$ dependence in HgSe : Fe crystals (curve *2*) in terms of the same set of parameters. First of all, it is to be noted that the weakened electron scattering by spatially ordered charged centers is further weakened (by a factor of approximately 1.5) in the case of Γ_8-band electrons: the mobility $\mu_{++}(N_{\mathrm{Fe}})$ reaches a saturation value of $\mu_S \approx 25.8 \times 10^4$ cm/V s for $N_{\mathrm{Fe}} \gg N^*$, while in the case of randomly distributed charged centers of the same concentration N^*, we have $\mu^* \approx 2.2 \times 10^4$ cm/V s; therefore, the ratio $\mu_S/\mu^* \approx 12$ is larger by a factor of 1.5 than in the case where the Bloch amplitudes are ignored in calculating the electron relaxation time due to scattering by correlated Fe^{3+} ions [6, 17, 18]. It is also seen from Fig. 1 that when $\mu_{++}(N_{\mathrm{Fe}})$ reaches saturation (curve *3*) for $N_{\mathrm{Fe}} > 2 \times 10^{19}$ cm^{-3}, the alloy scattering is dominant (curve *4*). For this reason, the total mobility in this impurity concentration range is insensitive to changes in the value of η_∞ within the range $\eta_\infty \approx (0.37$–$0.45)$. The alloy-scattering parameters are found to be

$V_0 \approx 7.9 \times 10^{-22}$ eV cm^3 and $w \approx 0.15$ ($\Lambda = 0.4$), which correlates well with the estimates made in [21] ($V_0 \approx 8.2 \times 10^{-22}$ eV cm^3, $w \approx -0.1 \pm 0.1$).

Allowance for the Bloch wave functions results not only in weakened electron scattering by charged centers but also in significantly suppressed scattering by neutral centers: for *s* wave functions, we have $\Phi_{00} \approx 0.5$ [17, 18], whereas for the Γ_8 band, $\Phi_{00} \approx 0.11$. Therefore, the alloy-scattering parameters V_0 and Λ become approximately twice as large as their values used in [17, 18] in calculating the $\mu(N_{\text{Fe}})$ dependence. In the range where the mobility is maximum, the electron scattering is dominated by scattering on correlated Fe^{3+} ions and by the interference contribution. It should be noted that the electron mobility $\mu(N_{\text{Fe}})$ calculated without regard for coherent scattering (curve *5*) is roughly twice as large. Obviously, the interference effects in electron scattering by neutral and charged centers in HgSe : Fe crystals are of importance and should be taken into account when analyzing electron transport phenomena. Curve *6* demonstrates the effect of intrinsic defects (shallow donors) of concentration $N_d = 1 \times 10^{18}$ cm^{-3} on the $\mu(N_{\text{Fe}})$ dependence in an HgSe : Fe crystal. The calculation of this dependence is performed using the same method as in [8].

Now, we discuss Matthiessen's rule, which is violated in the case of electron scattering by MV iron ions because of interference effects in electron scattering on neutral and charged centers. If there is no spatial correlation, we have $S_{0+}(q) = 0$ and Matthiessen's rule holds. In this case, the contributions from electron scattering by charged and neutral iron impurity centers to electron momentum relaxation are additive [31] and we have

$$\mu_{MR}(N_{\text{Fe}}) = [\mu_{++}^{-1}(N_{\text{Fe}}) + \mu_{00}^{-1}(N_{\text{Fe}})]^{-1}. \qquad (23)$$

The degree of violation of Matthiessen's rule for the electron mobility can be characterized by the quantity

$$\Delta\mu/\mu = (\mu - \mu_{MR})/\mu. \qquad (24)$$

Figure 2 shows the dependence of the deviation from Matthiessen's rule on the iron impurity content. It is seen that the deviation vanishes for both $N_0 \longrightarrow 0$ ($N_{\text{Fe}} \longrightarrow N^*$) and $N_0 \gg N_+$ and reaches a maximum value of 60% for $N_{\text{Fe}} \sim (1\text{–}2) \times 10^{19}$ cm^{-3} (when $N_0 \approx N_+$).

Thus, with allowance for the actual band structure of HgSe : Fe crystals, the model developed in [6, 18, 28] enables one to adequately describe all characteristic features of the $\mu(N_{\text{Fe}})$ dependence in a wide range of iron impurity contents, namely, the value and position of the maximum of the electron mobility at $N_{\text{Fe}} \sim (1\text{–}2) \times 10^{19}$ cm^{-3}, the sharp increase in $\mu(N_{\text{Fe}})$ for $N_0 < N_+$ associated with weakened electron scattering on correlated Fe^{3+} ions, and the decrease in the electron mobility for $N_{\text{Fe}} > 2 \times 10^{19}$ cm^{-3} due to alloy scattering.

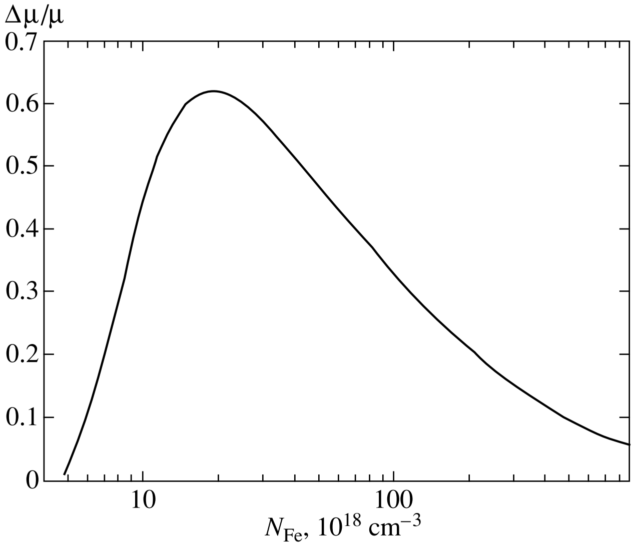

Fig. 2. Deviation from Matthiessen's rule as a function of iron impurity content, calculated with the same values of parameters as for the electron mobility.

Another model that takes into account spatial ordering of MV iron ions was proposed by Mikheev [26, 27]. Unfortunately, no equations were derived and solved to find the impurity-content dependence of the correlation-sphere radius $r_c(N_{\text{Fe}})$ in those papers; instead, some assumptions were made. Since Mikheev [26, 27] cast doubt on the correctness of the short-range correlation model (SRCM) developed in [6, 17, 18, 28] and used in this paper, we thoroughly analyzed the assumptions made in [26, 27] and can say the following to clarify the point. By assuming that the probability of a correlated particle arrangement $W(N_+, r_c, r_1)$ is equal to the probability W_0 that there will be no *d* hole in the volume Ω_c in the case of randomly distributed MV iron ions [i.e., when the Coulomb repulsion of Fe^{3+} ions (*d* holes) is turned off], the following basic equation was derived in [26]:

$$\eta(N_{\text{Fe}}) = \frac{N_+\Omega_c}{8} \cong 0.74\left[1 - (N_+/N_{\text{Fe}})^{\frac{1}{\Delta N_1}}\right]. \qquad (25)$$

This dependence of the packing fraction on the iron impurity content is significantly weaker than that given by Eq. (21) (Fig. 3a) and is not consistent with exact asymptotic expression (22) for $r_c(N_{\text{Fe}})$ for $N_0 < N_+$. In [27], in order to substantiate Eq. (25), the case of extremely low neutral-center concentrations was considered ($N_0/N_+ \ll 1$, $\Omega_c N_+ = 8\eta \ll 1$). Under the assumption that in this limit the Fe^{3+} ion correlation spheres do not overlap, Mikheev [27] derived the following relation (believing it to be an exact asymptotic expression):

$$N_+ = N_{\text{Fe}}(1 - N_+\Omega_c) \quad \text{or} \quad \eta(N_{\text{Fe}}) = N_0/(8N_+). \qquad (26)$$

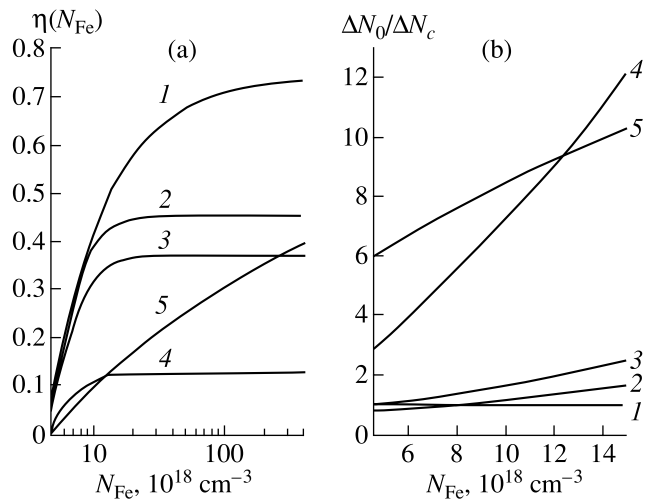

Fig. 3. Dependences of (a) the packing fraction $\eta(N_{\mathrm{Fe}})$ and (b) ratio $\Delta N_0/\Delta N_c$ on the iron impurity content as calculated on the basis of (*1*) balance equation (22) for particles; (*2*, *3*) empirical equation (21) with $\eta_\infty \approx 0.45$ and 0.37, respectively; (*4*) short-range correlation model (SRCM-I) [5]; and (*5*) the basic equation of [26, 27].

Equation (26) is consistent with Eq. (25), and the dependence on the impurity concentration in Eq. (26) is significantly weaker than that in Eqs. (21) and (22) (Fig. 3a). However, the Fe^{3+} ion correlation spheres always overlap, including the limiting case of $N_0/N_+ \ll 1$. By definition, the correlation sphere ($\Omega_c = 4\pi r_c^3/3$) constructed around each Fe^{3+} ion contains only neutral centers. If the correlated Fe^{3+} ions are approximated by hard spheres, the spacing between the centers of Fe^{3+} ions cannot be less than $r_c = d$ (d is the hard-sphere diameter): $g_{++}(r) = 0$ for $r < r_c$. Outside the correlation volume Ω_c (in the spherical layer $r_c < r < 2r_c$), the pair correlation function $g_{++}(r) \neq 0$ and the probability of finding an Fe^{3+} ion in this layer is nonzero for any nonvanishing value of the parameter η. Therefore, the correlation spheres of the Fe^{3+} ions located within the spherical layer $r_c < r < 2r_c$ will inevitably overlap. For the function $g_{++}^{(1)}(r)$ used in [26] (see also [23, Fig. 8.6.1b]), the average number of Fe^{3+} ions located within this layer is easily found to be $\Delta N = 56\eta + 34\eta^2$. For $\eta \sim 10^{-2}$, half of the short-range-order clusters in the $r_c < r < 2r_c$ spherical layer contain an Fe^{3+} ion and the correlation spheres of such Fe^{3+} ions overlap. Therefore, the assumption on which the derivation of Eq. (26) is based is incorrect.

The adequacy of the different methods can be verified by using them for calculating electron-transport effects in HgSe : Fe crystals (see below) or by analyzing the balance of d holes and neutral centers redistributed over the correlation sphere and the spherical layer in the extreme case of $N_0 \ll N_+$, where the correlation sphere radius is limited by the number of empty sites for d-hole redistribution (i.e., by the Fe^{2+} concentration N_0) in the spherical layer $r_c < r < r_1$. Allowance for this balance is the basic point of the SRCM [2, 28, 29]. Let us consider the influence of the iron content on the average number ΔN_c of d holes passing to the spherical layer and on the change ΔN_0 in the number of empty sites for their redistribution (i.e., in the number of Fe^{2+} ions) in the spherical layer as the Coulomb repulsion of d holes is turned on. In the extreme case of $N_0 \ll N_+$, d holes occupy all empty sites in the spherical layer; i.e., $\Delta N_0 \approx \Delta N_c$. Therefore, for $N_0 < N_+$, the following inequality should be satisfied:

$$|\Delta N_0/\Delta N_c - 1| \ll 1, \qquad (27)$$

where $\Delta \bar{N}_c = 8\eta$ and $\Delta \bar{N}_0 = (\Delta N_1 - 8\eta)N_0/N_+$. Inequality (27) is a criterion for the validity of different phenomenological methods used for describing the spatial ordering of MV iron ions. As seen from Fig. 3, inequality (27) holds, with a large margin for the $\eta(N_{\mathrm{Fe}})$ dependences following from Eqs. (21) and (22). For Eq. (22), following from the balance equation for d holes and neutral centers, the ratio $\Delta N_0/\Delta N_c = 1$ over the entire range of iron contents. The surprising thing is that, for empirical equation (21) with $\eta_\infty \approx 0.45$ (curve *2* in Fig. 3) and $\eta_\infty \approx 0.37$ (curve *3*), criterion (27) is satisfied with a large margin everywhere over the range $N_0 < N_+$. In contrast, strong inequality (27) does not hold for SRCM-I [5] (curve *4*) and especially not for the basic equation of the theory developed in [26, 27] (curve *5*) in the range of $N_0 < N_+$. Due to the unduly slow increase in the packing fraction in Eq. (25) [which is the result of the assumption that $W(N_+, r_c, r_1) = W_0$], the ratio $\Delta N_0/\Delta N_c \sim 6$ significantly exceeds unity for $N_0 \ll N_+$ (curve *5* in Fig. 3b). Obviously, Eq. (25) is not valid in the limit of $N_0/N_+ \ll 1$: in the spherical layer $r_c < r < r_1$, a large number of empty sites remain accessible for d-hole redistribution, but the equality $W(N_+, r_c, r_1) = W_0$, assumed in [26, 27] to hold, forbids the greater part of d holes from transferring to these sites.

Thus, empirical formula (21) satisfies criterion (27) everywhere over the $N_0 < N_+$ range and can be used to calculate electron transport effects in HgSe : Fe crystals. It is not surprising that the $\mu(N_{\mathrm{Fe}})$ dependence calculated on the basis of Eq. (21) adequately describes all specific features of this dependence observed experimentally over a wide range of iron contents (curve *2* in Fig. 1). In contrast, the $\mu(N_{\mathrm{Fe}})$ dependence calculated on the basis of Eq. (25) for $\eta(N_{\mathrm{Fe}})$ (curve *5* in Fig. 3a) with the same values of the parameters as for curve *2* leads to an unduly slow increase in $\mu_{++}(N_{\mathrm{Fe}})$ with increasing iron content (curve *7* in Fig. 1). There is a significant discordance between the calculations and experimental data in the range where the electron mobility increases and reaches a maximum $\mu(N_{\max})$: the calculated $\mu_{\max}$ is less than its experimental value by a factor of approximately 2.5, and the position of the mobility maximum [experimental value $N_{\max} \approx (1–2) \times 10^{19}$ cm^{-3}] is significantly shifted to higher iron contents ($N_{\max} \approx 6 \times 10^{19}$ cm^{-3}). In this method, the values of the adjustable parameters cannot be chosen in such a way as to adequately describe the $\mu(N_{\mathrm{Fe}})$ dependence in both the range of the mobility increase and the range of the mobility maximum. It should be noted that in [27], in calculating the mobility, the specific features of the conduction band were not taken into account, coherent electron scattering was ignored (which led to a twice as large value of the maximum mobility), and μ^* was taken to be an adjustable parameter.

In [27], in calculating the effect of intrinsic defects (shallow donors) on the electron mobility in HgSe : Fe crystals, Eq. (25) is used and the pair correlation function of iron ions and intrinsic defects is assumed to have the form of a step function, $g_{FD}(r) = \vartheta(r - r_c)$. Such a correlation function is adequate for use in the case of a low density ($\eta \ll 1$) or of weak spatial correlations of Fe^{3+} ions and intrinsic defects. To justify this approximation, Mikheev [27] does not analyze the set of equations for the pair correlation functions of MV iron ions and intrinsic defects but instead introduces the concept of a “perforated system.” When analyzing the temperature dependence of the electron mobility, Mikheev [32] also uses Eq. (25) and the weak spatial correlation approximation to calculate the structure factor.

In the weak-correlation model, as indicated in [18], the particle conservation law breaks down and the thermodynamic functions exhibit a nonphysical behavior. Therefore, the application of this model for calculating electron transport effects is ill founded. The inadequacy of this model also manifests itself in the fact that the structure factors and, hence, the electron-scattering probabilities become negative as the density of the system increases. For the step function $g^{(0)}(r) = \vartheta(r - r_c)$, the structure factor $S^{(0)}(q)$ for small wave vectors becomes negative even for $\eta > 0.125$. In the next orders in density, $S^{(1)}(q)$ and $S^{(2)}(q)$ become negative for $\eta > 0.235$ and 0.18, respectively. Therefore, the low-density or weak-spatial-correlation approximation gives physically reasonable results only for a weakly correlated gas, i.e., for $\eta < 0.125$, which corresponds to $N_{\mathrm{Fe}} < 6 \times 10^{18}$ cm^{-3}. In order to calculate the $\mu(N_{\mathrm{Fe}})$ dependence in the entire range of N_{Fe} values, one needs to use the pair correlation functions that are adequate for the case of a large particle number density for which particle correlations are strong. In this paper, we use structure factors (12) calculated within the Percus–Yevick approximation, which is not subject to the drawbacks indicated above. Our analysis of the basic assumptions and the physical consequences on which the results of [26, 27, 32] are based allows one to judge the reliability of those results.

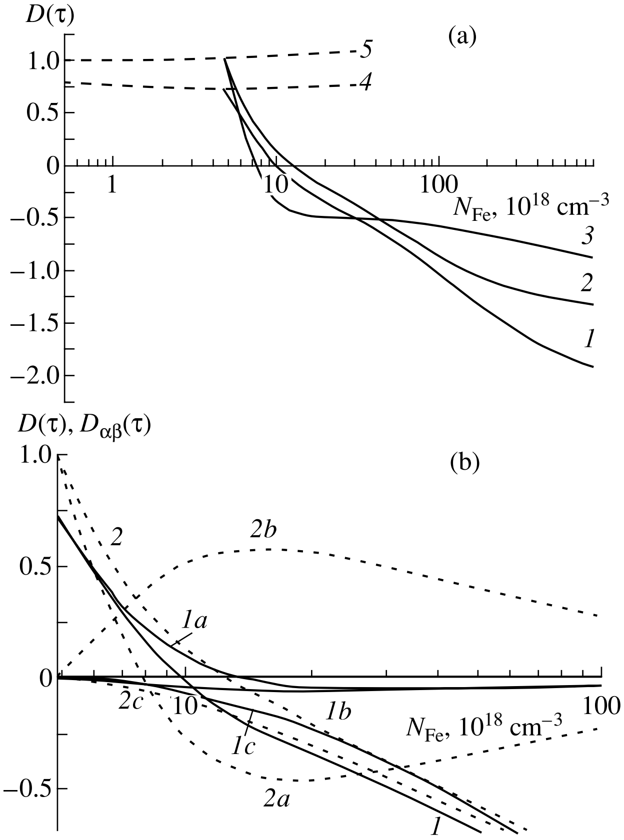

Fig. 4. Dependences of (a, b) dimensionless parameter $D(\tau)$ and (b) its partial contributions $D_{\alpha\beta}(\tau)$ on the iron impurity content as calculated (a) (*1*) for the Γ_8 band, (*2, 3*) for the Γ_6 band without regard for the Bloch amplitudes in the electron scattering probability, and (*4, 5*) from the Brooks–Herring formula and for Γ_8-band electrons, respectively, in the case of electron scattering by randomly distributed charged centers; (b) (*1, 1a–1c*) for Γ_8-band electrons, (*2, 2a–2c*) for Γ_6-band electrons, (*1a, 2a*) contribution $D_{++}(\tau)$, (*1b, 2b*) contribution $D_{+0}(\tau)$, and (*1c, 2c*) contribution $D_{00}(\tau)$.

The short-range correlation model proposed by us is based on the Ornstein–Zernike equations for the partial correlation functions and can be used in both cases of weak and strong Coulomb correlations of *d* holes in MV iron ions. This model is adequate for description of all specific features of the experimental dependence of the electron mobility on the iron content in HgSe : Fe crystals at low temperatures. It is shown that the coherent electron scattering plays an important part in electron momentum relaxation; this scattering results in a breakdown of Matthiessen’s rule and should undoubtedly be taken into account in analyzing electron transport effects.

4. ENERGY DEPENDENCE OF THE RELAXATION TIME OF Γ_8-BAND ELECTRONS

Let us consider the energy dependence of the relaxation time of Γ_8-band electrons and make a comparison with the calculations performed earlier without regard for the Bloch amplitudes in calculating the electron scattering probability [9, 10]. This dependence is of importance in studying the thermomagnetic effects [33]. The point is that, for example, the longitudinal and transverse Nernst–Ettingshausen effects are proportional to the energy derivative of the relaxation time. Therefore, a variation in the spatial ordering of MV iron ions can cause the Nernst– Ettingshausen effects to change sign, whereas the electron mobility is changed only in magnitude in this case. Experimental studies support this theoretical prediction [9, 10].

Figure 4a shows the dependence of the dimensionless parameter $D(\tau)$ on the iron impurity content:

$$D(\tau) = \varepsilon_F \frac{d}{d\varepsilon}[\ln(\tau(\varepsilon))]_{\varepsilon = \varepsilon_F}$$

$$= \frac{\varepsilon_F}{\tau(\varepsilon_F)}\left(\frac{d\tau(\varepsilon_F)}{d\varepsilon}\right)_{\varepsilon = \varepsilon_F} = D_{++} + D_{+0} + D_{00}. \quad (28)$$

In calculating $D(\tau)$ and the $\mu(N_{\mathrm{Fe}})$ dependence, we used the same values of the parameters. It is seen from Fig. 4 that the $\tau(\varepsilon)$ dependence changes in a qualitative manner: in both the cases of scattering by randomly distributed iron ions and by MV iron ions, $\tau(\varepsilon)$ increases with energy $[D(\tau) > 0]$ in the region of weak spatial correlations, whereas in the region of strong correlations ($N_{\mathrm{Fe}} > 10^{19}$ cm^{-3}), $\tau(\varepsilon)$ becomes a decreasing function of energy $[D(\tau) < 0]$. A comparison of curves *1* and *2* in Fig. 4a shows that the allowance for the Bloch amplitudes (curve *1*) results in $D(\tau)$ shifting to lower iron contents. The assumption of $S_{+0} = 1$, made in [9, 10] in studying the transverse Nernst–Ettingshausen effect, leads to a sharper change in $D(\tau)$ in the region of relatively low iron contents (curve *3*). This approximation is obviously inadequate for quantitative description of the thermomagnetic effects. In the case of scattering by randomly distributed charged centers, the parameter $D(\tau)$ calculated from the Brooks–Herring formula (curve *5*) and for Γ_8-band electrons (curve *4*) is positive throughout the entire N_d-concentration range. Therefore, an increased degree of spatial ordering of MV iron ions leads not only to weakened electron scattering and to an anomalously increased electron mobility in comparison with the case of electron scattering by randomly distributed iron ions but also to a qualitative change in the energy dependence of the electron relaxation time. The $D(\tau)$ sign reversal with increasing iron content will cause the Nernst–Ettingshausen effects to change sign.

The contributions to $D_{\alpha\beta}(\tau)$ coming from electron scattering by correlated Fe^{3+} ions, $D_{++}(\tau)$, and by neutral centers, $D_{00}(\tau)$, as well as from the interference effect in scattering by charged and neutral centers, $D_{+0}(\tau)$, are shown in Fig. 4b as functions of the iron content for Γ_8-band electrons (curves *1*, *1a–1c*) and for Γ_6-band electrons without *s–p* wave-function hybridization (curves *2*, *2a–2c*). It is seen from Fig. 4b that the allowance for the Bloch amplitudes in calculating the electron-scattering probability affects the interference contribution $D_{+0}(\tau)$ most significantly; for Γ_6-band electrons, this contribution is positive and fairly large (curve *2b*), whereas for Γ_8-band electrons, coherent scattering makes a small contribution to $D(\tau)$ throughout the entire iron-content range (curve *1b*). For a relatively low iron content $N_0 < N^*$, $D(\tau)$ is dominated by the contribution $D_{++}(\tau)$, while at high concentrations $N_{\mathrm{Fe}} \gg N^*$, $D(\tau)$ is dominated by the contribution $D_{00}(\tau)$ from neutral-center scattering. Although coherent scattering affects the energy dependence of the relaxation time [i.e., $D(\tau)$] only slightly in the case of Γ_8-band electrons, this scattering makes a significant contribution to the electron mobility, as demonstrated above.

5. CONCLUSIONS

Thus, we have analyzed the influence of the band nonparabolicity on the electron momentum relaxation in HgSe and HgSe : Fe crystals and determined the parameters characterizing electron scattering by MV iron ions. In terms of the same set of parameters, we succeeded in describing both the dependence of the electron mobility on the intrinsic-defect concentration in HgSe crystals and the $\mu(N_{\mathrm{Fe}})$ dependence in HgSe : Fe crystals. The good quantitative agreement of the calculated mobility with the experimental data for HgSe crystals [14, 24, 25] and of the calculated $\mu(N_{\mathrm{Fe}})$ with the data for HgSe : Fe [3, 30] indicates that the spatial ordering of MV iron ions and the main electron momentum relaxation mechanisms are correctly taken into account. An analysis of the energy dependence of the electron relaxation time revealed that in order to describe the thermomagnetic effects quantitatively, one needs to allow for the nonparabolicity of the dispersion law of carriers in HgSe and HgSe : Fe crystals and, in addition, include the *s–p* hybridization and the Bloch amplitudes of the electron wave functions in calculating the electron-scattering probability.

An analysis of the thermomagnetic effects in HgSe : Fe crystals with allowance for the band nonparabolicity and of the effect of hydrostatic pressure on the electrical conductivity at low temperatures is of considerable interest in itself and will be published elsewhere.

ACKNOWLEDGMENTS

The authors are grateful to A.P. Tankeev for his participation in discussions and helpful comments.

This study was supported by the Russian Foundation for Basic Research, project nos. 00-02-16299 and 01-02-06238.

REFERENCES

1. I. M. Tsidil’kovskiĭ, Usp. Fiz. Nauk **162** (2), 63 (1992) [Sov. Phys. Usp. **35**, 85 (1992)].

2. I. M. Tsidilkovskii and I. G. Kuleyev, Semicond. Sci. Technol. **11**, 625 (1996).
3. F. Pool, J. Kossut, U. Debska, and R. Reifenberger, Phys. Rev. B **35** (5), 3900 (1987).
4. R. Reifenberger and J. Kossut, J. Vac. Sci. Technol. **5** (5), 2995 (1987).
5. Z. Wilamowski, K. Swiatek, T. Dietl, and J. Kossut, Solid State Commun. **74** (8), 833 (1990); Z. Wilamowski, Acta Phys. Pol. A **77** (1), 133 (1990).
6. I. G. Kuleev, I. I. Lyapilin, and I. M. Tsidil'kovskiĭ, Zh. Éksp. Teor. Fiz. **102** (5), 1652 (1992) [Sov. Phys. JETP **75**, 893 (1992)].
7. I. G. Kuleev, A. T. Lonchakov, I. Yu. Arapova, and G. I. Kuleev, Zh. Éksp. Teor. Fiz. **114** (1), 191 (1998) [JETP **87**, 106 (1998)].
8. I. G. Kuleyev, N. K. Lerinman, L. D. Sabirzyanova, *et al.*, Semicond. Sci. Technol. **12**, 840 (1997).
9. I. G. Kuleev, I. I. Lyapilin, A. T. Lonchakov, and I. M. Tsidil'kovskiĭ, Zh. Éksp. Teor. Fiz. **103** (4), 1447 (1993) [JETP **76**, 707 (1993)].
10. I. G. Kuleev, I. I. Lyapilin, A. T. Lonchakov, and I. M. Tsidil'kovskiĭ, Fiz. Tekh. Poluprovodn. (St. Petersburg) **28** (6), 937 (1994) [Semiconductors **28**, 544 (1994)].
11. I. G. Kuleev, I. I. Lyapilin, A. T. Lonchakov, and I. M. Tsidil'kovskiĭ, Zh. Éksp. Teor. Fiz. **106** (4), 1205 (1994) [JETP **79**, 653 (1993)].
12. I. G. Kuleev, A. T. Lonchakov, G. L. Shtrapenin, and I. Yu. Arapova, Fiz. Tverd. Tela (St. Petersburg) **39** (10), 1767 (1997) [Phys. Solid State **39**, 1575 (1997)].
13. W. Szymanska, P. Boguslawki, and W. Zawadzki, Phys. Status Solidi B **65**, 641 (1974).
14. T. Dietl and W. Szymanska, J. Phys. Chem. Solids **39** (10), 1041 (1978).
15. V. M. Askerov, *Electron Transport Phenomena in Semiconductors* (Nauka, Moscow, 1985).
16. V. F. Gantmakher and I. B. Levinson, *Carrier Scattering in Metals and Semiconductors* (Nauka, Moscow, 1984; North-Holland, Amsterdam, 1987).
17. I. G. Kuleev and I. Yu. Arapova, Fiz. Met. Metalloved. **88** (3), 43 (1999).
18. I. G. Kuleev and I. Yu. Arapova, Fiz. Tverd. Tela **43** (3), 403 (2001) [Phys. Solid State **43**, 420 (2001)].
19. J. Kossut, Phys. Status Solidi B **86** (2), 593 (1978).
20. R. J. Iwanowski, T. Dietl, and W. Szymanska, J. Phys. Chem. Solids **39** (10), 1059 (1978).
21. C. Skrierbiszewski, Z. Wilamowski, and J. Kossut, Semicond. Sci. Technol. **8**, S22 (1993).
22. J. M. Ziman, *Models of Disorder: The Theoretical Physics of Homogeneously Disordered Systems* (Cambridge Univ. Press, Cambridge, 1979; Mir, Moscow, 1982).
23. R. Balescu, *Equilibrium and Nonequilibrium Statistical Mechanics* (Wiley, New York, 1975; Mir, Moscow, 1978), Vol. 1.
24. S. L. Lehoczky, J. G. Broerman, D. A. Nelson, and C. R. Whitsett, Phys. Rev. B **9** (4), 1598 (1974).
25. C. R. Whitsett, Phys. Rev. **138** (3A), 829 (1965).
26. V. M. Mikheev, Fiz. Tverd. Tela (St. Petersburg) **41** (11), 1994 (1999) [Phys. Solid State **41**, 1830 (1999)].
27. V. M. Mikheev, Fiz. Tverd. Tela (St. Petersburg) **43** (3), 414 (2001) [Phys. Solid State **43**, 430 (2001)].
28. I. G. Kuleev, Fiz. Tverd. Tela (St. Petersburg) **39** (2), 250 (1997) [Phys. Solid State **39**, 219 (1997)].
29. I. G. Kuleev, Fiz. Tverd. Tela (St. Petersburg) **40** (3), 425 (1998) [Phys. Solid State **40**, 389 (1998)].
30. N. G. Gluzman, L. D. Sabirzyanova, I. M. Tsidil'kovskiĭ, *et al.*, Fiz. Tekh. Poluprovodn. (Leningrad) **20** (11), 1994 (1986) [Sov. Phys. Semicond. **20**, 1251 (1986)].
31. I. M. Tsidil'kovskiĭ, I. G. Kuleev, and G. L. Shtrapenin, Dokl. Akad. Nauk **347** (4), 472 (1996) [Phys. Dokl. **41**, 145 (1996)].
32. V. M. Mikheev, Fiz. Tverd. Tela (St. Petersburg) **43** (10), 1785 (2001) [Phys. Solid State **43**, 1860 (2001)].
33. I. M. Tsidil'kovskiĭ, *Thermomagnetic Effects in Semiconductors* (Nauka, Moscow, 1960; Academic, New York, 1962).

Translated by Yu. Epifanov

Physics of the Solid State, Vol. 45, No. 2, 2003, pp. 224–230. Translated from Fizika Tverdogo Tela, Vol. 45, No. 2, 2003, pp. 215–221.

SEMICONDUCTORS
AND DIELECTRICS

Optical Dephasing in Solid Toluene Activated by Octaethylporphine Zinc

Yu. G. Vaĭner*, M. A. Kol'chenko*, A. V. Naumov*, R. I. Personov*, and S. J. Zilker**
** Institute of Spectroscopy, Russian Academy of Sciences, Troitsk, Moscow oblast, 142190 Russia*
*** University of Bayreuth, D-95440 Bayreuth, Germany*
Received March 13, 2002

Abstract—The optical dephasing in frozen amorphous toluene doped with octaethylporphine zinc is investigated using the photon echo technique over a wide range of temperatures (0.4–100 K) up to the Debye temperature of solid toluene (T_D = 100.7 K). The contributions of different mechanisms to the broadening of the zero-phonon line (ZPL) are reliably separated owing to the measurements performed over such a wide range of temperatures. Analysis of the experimental data demonstrates that, at low temperatures, the main contribution to the optical dephasing is determined by the interaction of impurities with fast tunneling transitions in two-level systems. The temperature dependence of the linewidth exhibits a quasi-linear behavior at temperatures below 3–4 K. At higher temperatures, the dominant contribution to the dephasing is made by the interaction of impurities with quasi-local phonons, which leads to a quasi-exponential temperature dependence of the linewidth. It is shown that the latter contribution can be described in the framework of the soft-potential model allowing for a broad spectrum of low-frequency phonon vibrations in the matrix. The temperature of the crossover between the aforementioned two mechanisms of line broadening is determined. *© 2003 MAIK "Nauka/Interperiodica".*

1. INTRODUCTION

As is known, the presence of spatial and energy microinhomogeneities in condensed disordered media (glasses, polymers, frozen solutions, amorphous semiconductors, etc.) leads to a considerable difference between the properties of these materials and crystals. For example, temperature dependences of the heat capacity and the thermal conductivity of disordered materials at temperatures below 1 K exhibit anomalous (linear or quadratic) behavior as compared to the cubic dependences of these parameters for crystalline materials [1]. Despite numerous experimental and theoretical investigations into the dynamic processes occurring in amorphous media at low temperatures, up to now, the nature of these processes has remained unclear and there has been no consistent theoretical description of the above phenomena. This circumstance and the wide practical applications of amorphous materials explain the urgency of the problems and the great interest expressed by researchers in this field.

Traditionally, dynamic processes in condensed media are investigated using optical spectroscopy of impurity centers (atoms, ions, or molecules). These impurity centers are specially introduced in low concentrations as spectral microprobes into the matrix under investigation. The matrix dynamics most clearly manifests itself in a broadening of zero-phonon lines (ZPLs) in optical spectra of impurity centers. Examination of the temperature dependence of the width of zero-phonon lines allows one to obtain important information on the mechanisms responsible for the dynamic properties of the studied system. However, the inhomogeneous line broadening effects inherent in amorphous media lead to a considerable smearing of the observed spectra. This appreciably restricts the possibility of extracting dynamic information on the properties of these materials with the use of traditional spectroscopic methods. The development of new selective spectroscopic techniques, such as the laser burning of stable spectral holes [2, 3], fluorescence and phosphorescence fine-structure spectroscopy under laser excitation [4, 5], and different variants of the photon echo technique [6, 7], made it possible to eliminate the influence of the inhomogeneous broadening on the spectra studied. These techniques have provided a considerable amount of valuable information on the glass dynamics. Over the period of the last ten to fifteen years, a large number of studies concerned with the problem of temperature broadening of zero-phonon lines have been performed using selective spectroscopic techniques. It has been found that, at low temperatures (T < 3–5 K), the homogeneous width of zero-phonon lines observed for amorphous materials is one or two orders of magnitude larger than that for crystals and exhibits a quite different temperature behavior [8]. According to the universally accepted concepts, this is explained by the fact that amorphous materials contain atomic or molecular groups which undergo tunneling transitions between two local minima on the potential energy surface of the material. These atomic or molecular groups form the so-called two-level systems [9, 10]. The transitions occurring in two-level systems bring about changes in the frequencies of electron transitions in impurity molecules and, thus, lead to a broadening of zero-phonon lines. Despite its simplicity, the model of tunneling two-level systems adequately describes the majority of experimental data on the broadening of the spectral lines of impurity centers in amorphous matrices at temperatures below 2–3 K (see, for example, monographs [11–13] and references therein). At higher temperatures, the temperature dependence of the linewidth changes drastically. In this case, experimental data are interpreted in terms of both the above mechanism of line broadening associated with two-level systems and the broadening caused by the interaction of impurity centers with one or two quasi-local low-frequency modes whose frequencies fall in the range 10–30 cm^{-1} [14, 15]. This approach was developed in analogy to the model used for crystals in which, beginning with temperatures higher than several degrees Kelvin, the dephasing is affected by the quasi-local low-frequency modes arising upon introduction of impurity centers into the solid matrix. However, these modes have never been observed in experiments with amorphous materials containing impurities. In recent years, dynamic phenomena in condensed disordered media at low temperatures have been described within the soft-potential model [16]. Within this model, low-frequency vibrational excitations in these media are treated as motions of atomic or molecular groups in local single-well minima of the potential surface. It is essential that, in the framework of this model, the low-frequency vibrational modes are the excitations inherent in the solid amorphous matrix and are characterized by a broad frequency distribution function $n(\omega) \sim \omega^4$. It was of interest to analyze experimental data on the optical dephasing not only in terms of the discrete spectrum of low-frequency modes, as has been often done in the literature, but also with the use of the concept of a broad frequency distribution of vibrational excitations in the amorphous matrix, as is predicted by the soft-potential model.

In the majority of experimental works performed thus far, the broadening of spectral lines of impurity molecules in organic glasses and polymers has been measured in a relatively narrow temperature range (the temperature varied by a factor of no more than 10–20). This circumstance substantially restricts the possibility of reliably interpreting experimental data, because the contributions of different mechanisms to the broadening of zero-phonon lines can superpose in the narrow temperature ranges studied. In this respect, extension of the temperature range of measurements is an important problem. The solution of this problem requires the development of new experimental approaches, since none of the existing techniques provides a way of measuring the zero-phonon line widths over a very wide range of temperatures.

In the present work, the optical dephasing in an organic amorphous system was experimentally investigated using the photon echo technique over a wide temperature range (from 0.4 to 100 K). An impurity organic glass, namely, a frozen solution of octaethylporphine zinc in toluene, served as the object of investigation. We succeeded in performing the measurements over such a wide range of temperatures owing to the use of two experimental photon echo setups adapted specially for two variants of the photon echo technique: the two-pulse picosecond photon echo and incoherent photon echo. The experiments at low temperatures were carried out on a two-pulse picosecond photon echo setup [17] equipped with a 3He cryostat. The use of this setup permitted us to perform measurements at temperatures down to 0.35 K. An insufficiently high time resolution of the setup made measurements at temperatures above 4 K impossible. For this reason, at higher temperatures, we used the incoherent photon echo setup [18], which has a considerably higher time resolution. The appropriate choice of impurity chromophore molecules is of importance in extending the temperature range of measurements toward high temperatures. As a chromophore molecule, we chose the octaethylporphine zinc molecule, which is characterized by a large Debye–Waller factor. This enabled us to raise substantially the upper boundary of the temperature range of measurements.

2. EXPERIMENTAL TECHNIQUE

The experiments were performed at $T < 4$ K on the two-pulse picosecond photon echo setup at the University of Bayreuth (Bayreuth, Germany) and at $T > 1.6$ K on the incoherent photon echo setup at the Institute of Spectroscopy, Russian Academy of Sciences (Troitsk, Russia). These setups were described in detail in [17, 18]. For this reason, only their basic parameters are given below. The two-pulse picosecond photon echo setup was based on a picosecond dye laser with a time resolution of 6 ps. The 3He cryostat of the setup provided a means of performing measurements in the temperature range 0.35–4 K. The temperature was controlled with an accuracy higher than 10 mK. The incoherent photon echo setup was based on a specially designed broadband dye noncavity laser. The spectral width of laser radiation was approximately equal to 100 cm^{-1} (λ = 573–576 nm), and the pulse width was 12–15 ns. The time resolution of this setup was determined by the lasing spectrum width and the accuracy of recording the time instrument function of the setup (the decay curve corresponding to the minimum time T_2) and was as high as 25–30 fs [18].

In the experiments, special care was taken to eliminate undesirable effects that could be caused either by high impurity concentrations or by high laser radiation power. For this purpose, a sample with a low concentration of octaethylporphine zinc impurity molecules (1×10^{-4} M) was prepared and the intensity of the radiation incident on the sample was chosen to be as low as possible. The radiation energy densities in the two-pulse picosecond photon echo and incoherent photon echo

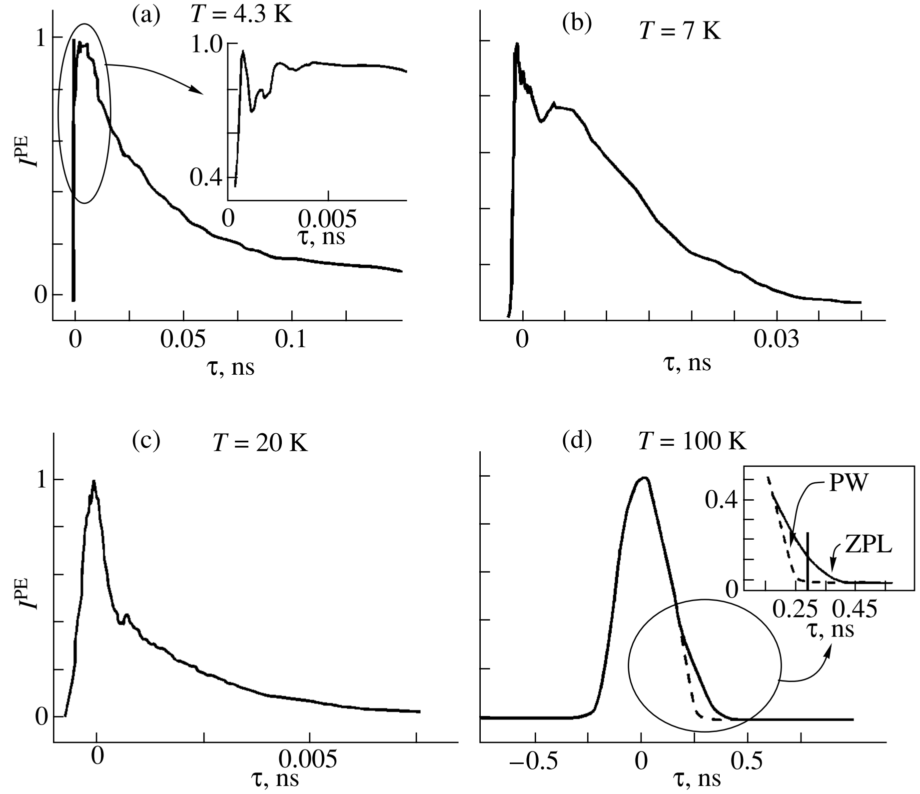

Fig. 1. Decay curves of incoherent photon echo signals for a solution of octaethylporphine zinc in toluene at different temperatures. The inset in panel (a) shows a portion of the decay curve at short delay times on an enlarged scale, and the inset in panel (d) represents a portion of the decay curve with contributions of the zero-phonon line and the phonon wing at long delay times.

measurements were lower than 10^{-5} and 5×10^{-4} J/cm^2, respectively. The special check showed that, at these intensities of laser radiation, the measured optical dephasing time T_2 is virtually independent of the laser pulse energy.

The samples were prepared from anhydrous toluene (Aldrich; the content of the main product was 99.8 wt %). The solution was placed in silica cells 1 mm thick. In order to prevent contact with atmospheric water vapor, which led to cracking of toluene upon freezing, the samples were prepared in a helium atmosphere. The optical density of the sample in the excitation range (at the long-wavelength wing of the purely electronic absorption band) at room temperature was equal to 0.8–1.0. This density is close to optimum from the viewpoint of compromising between the echo generation efficiency and the elimination of undesirable effects caused by the high optical density of the sample.

3. RESULTS AND DISCUSSION

The decay curves of incoherent photon echo signals at different temperatures are depicted in Fig. 1. The high time resolution of the setup makes it possible to separate clearly the portions corresponding to the zero-phonon line and the phonon wing (PW) in the decay curve. The sharp peak in the range of zero delay time (Fig. 1a) is associated with the contribution of the phonon wing to the echo signals. The decay curves measured at temperatures from 4 to 20 K (Figs. 1b, 1c) at delay times ~2 ps exhibit a well-defined feature caused by the interference of the contributions from the zero-phonon line and phonon wing. At delay times longer than 4–5 ps, the zero-phonon line makes the main contribution to the recorded curves at the above temperatures. As the temperature increases, the contribution of the zero-phonon line decreases owing to a decrease in the Debye–Waller factor and virtually disappears at $T \sim 100$ K. It is this decrease in the contribution of the zero-phonon line (as compared to the contribution of the phonon wing) with an increase in the temperature, rather than the time resolution of the setup, that is the main factor limiting the possibility of separating the contributions of the zero-phonon line and the phonon wing at $T > 100$ K. This situation is illustrated in Fig. 1d.

The computational algorithm is of considerable importance in determining the dephasing time T_2 from the experimental curves. At low temperatures (Figs. 1a, 1b), the time T_2 was determined from the portion of the decay curve at long delay times τ at which the contribution of the phonon wing to the echo signals could be ignored. At higher temperatures (Figs. 1c, 1d), this contribution increased sharply and the dephasing time was calculated by subtracting the contribution of the phonon wing from the resultant curve. Since the peak associated with the phonon wing at these temperatures was nearly symmetric and coincided with the left portion of the photon echo decay curve, this portion was used to approximate the phonon wing peak by a symmetric Voigt function (Fig. 1d). The function thus obtained was subtracted from the resultant decay curve, which permitted us to derive the contribution of the zero-phonon line. Note that, according to experimental and theoretical data, the decay curves of two-pulse picosecond photon echo signals and the decay curves of incoherent photon echo signals at $T > 10$ K are nearly exponential in shape. Therefore, the dephasing time T_2 in these cases was determined by approximating the curves with the use of the standard expression relating the photon echo signal intensity to the delay time, that is,

$$I^{\mathrm{PE}}(\tau) = I^{\mathrm{PE}}(0)\exp\left(-\frac{4\tau}{T_2}\right). \tag{1}$$

As follows from the theory, the decay curves of incoherent photon echo signals at low temperatures are not strictly exponential but are described by a more complicated function. Consequently, the experimental decay curves of incoherent photon echo signals at $T < 10$ K were approximated by the relationship [19]

$$I^{\mathrm{IPE}}(\tau) = B + C\left(u + \frac{32(1-u)^2\exp(-4\tau/T_2) + 32u(1-u)\exp[-(2+u)\tau/T_2]}{(2-u)^2} + \frac{8u^2\exp(-2u\tau/T_2)}{(2-u)^2}\right), \tag{2}$$

where $u = T_2/T_1$ and B is the delay-time-independent incoherent component of the incoherent photon echo signals. It is easy to see that, in the limit $T_2/T_1 \ll 1$, relationship (2) transforms into the standard exponential expression (1).

Figure 2 shows the temperature dependence of the reciprocal of the time T_2 : $\Gamma^{\mathrm{PE}}(T) = 1/\pi T_2(T) = 1/2\pi T_1 + 1/\pi T_2'(T)$. This quantity can be considered a homogeneous width of the zero-phonon line, which is calculated from the measured decay curves. Here, T_2' is the time of pure optical dephasing and T_1 is the excited-state lifetime of impurity molecules. This time was measured by the induced grating technique on a modified two-pulse picosecond photon echo setup and proved to be equal to 1.9 ns for the studied system. It can be seen from Fig. 2 that the measured dependence exhibits a temperature behavior characteristic of impurity amorphous systems: as the temperature increases, the zero-phonon line width insignificantly increases at $T < 3$ K and steeply increases at higher temperatures. The observed temperature dependence of the linewidth, as a rule, is explained by the contribution of at least two mechanisms of optical dephasing. These are the broadening due to the interaction of the impurity center with transitions in two-level systems at low temperatures and the broadening caused by the contribution from low-frequency vibrational modes of the matrix at higher temperatures. The data obtained with the two techniques somewhat differ in the range $T = 1.5$–3 K. In our opinion, this difference is associated with the fact that the spectral diffusion on the nanosecond time scale affects the results of incoherent photon echo measurements. The point is that the incoherent photon echo and two-pulse picosecond photon echo techniques are characterized by different measurement time scales t_x [18, 20] and, therefore, have different sensitivities to the spectral diffusion. The two-pulse picosecond photon echo technique is used to measure the homogeneous linewidth and is insensitive to this process. In the incoherent photon echo technique, the time scale is determined by the lifetime T_1 of chromophore molecules and the laser pulse duration [19], which can be longer than the dephasing time T_2. In particular, the time scale t_x in

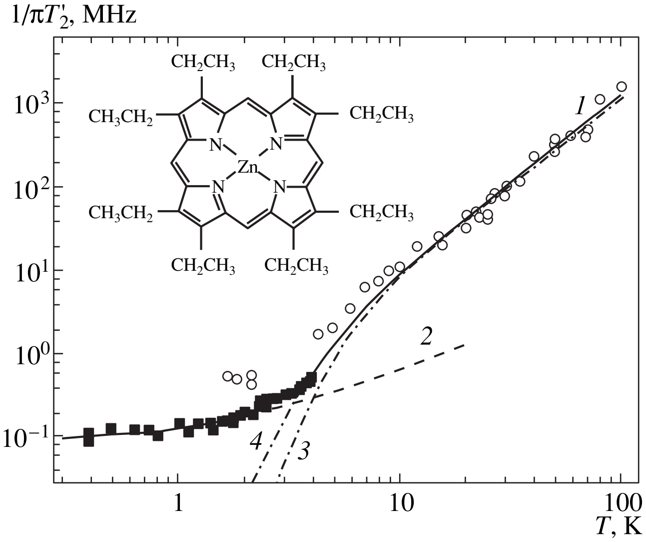

Fig. 2. Temperature dependences of the reciprocal of the optical dephasing time $1/\pi T_2' = 1/\pi T_2 - 1/2\pi T_1$ for a solution of octaethylporphine zinc in toluene according to the two-pulse picosecond photon echo (squares) and incoherent photon echo (circles) data: (*1*) the approximation of the experimental data by expression (3), (*2*) the contribution of two-level systems, (*3*) the contribution of one low-frequency mode with a frequency of 14.5 cm^{-1}, and (*4*) the contribution of the broad spectrum of low-frequency modes according to relationship (4). The inset shows the structural formula of the octaethylporphine zinc molecule.

Fitting parameters obtained by approximating the temperature dependence of the optical dephasing with the use of relationship (3) for a solution of octaethylporphine zinc in toluene

b, MHz/K$^{\alpha}$	α	c, GHz	ΔE, cm^{-1}
41.07	1.1 ± 0.1	50	14.5 ± 1.5

our experiments is determined by the time T_1, i.e., is equal to several nanoseconds.

The experimental temperature dependence was approximated using the relationship

$$\Gamma^{\mathrm{PE}}(T) = \Gamma_0 + bT^{\alpha} + c\frac{\exp(-\Delta E/kT)}{[1-\exp(-\Delta E/kT)]^2}, \quad (3)$$

which describes the two aforementioned mechanisms of broadening of the zero-phonon line in the case when the high-temperature dephasing is due to the interaction with only one low-frequency quasi-local vibration. In this relationship, the first term is defined by the formula $\Gamma_0 = 1/2\pi T_1$, the second term describes the line broadening caused by the interaction with tunneling two-level systems, and the third term accounts for the broadening attributed to the interaction with the low-frequency mode at the energy ΔE.

In order to separate more correctly the two contributions to the temperature broadening of the zero-phonon line, the approximation was carried out as follows. At the first stage, the low-temperature portion of the curve ($T < 1$–2 K), in which the contribution of the low-frequency mode to the dephasing could be obviously disregarded, was approximated by the power dependence $\Gamma^{\mathrm{PE}}(T) = \Gamma_0 + bT^{\alpha}$ and the parameters b and α were determined. Then, these parameters were fixed and the experimental points were approximated with the use of relationship (3), which allowed us to derive the parameters c and ΔE. As can be seen from Fig. 2, relationship (3) adequately describes the experimental data, except for the incoherent photon echo data in the range $T < 10$ K. As was noted above, this discrepancy is attributed to the effect of spectral diffusion. The parameters corresponding to the best fit are listed in the table.

The parameter α characterizes the dynamic properties of the amorphous system under investigation. This parameter has been determined in numerous experimental works dealing with hole burning and photon echo. As a rule, the obtained values of α fall in the range 1.2–1.9. In early works concerned with the conventional two-level system model (see, for example, [21]), it was stated that, under the assumption of a uniform energy distribution of two-level systems $P(E) \sim$ const, the parameter α should be equal to unity. The larger parameters α observed in many experiments have been explained by the fact that the energy distribution of two-level systems actually has the form $P(E) \sim E^{\mu}$, so that $\alpha = 1 + \mu$, where $\mu = 0.1$–0.7 [22]. Subsequent more rigorous theoretical investigations have demonstrated that the parameter α should exceed unity even at very low temperatures. In our recent work [23], we showed that the parameter α for different systems can vary from 1 to 2 depending on the constant of the two-level system–phonon interaction. Unfortunately, at present, the parameter α for the system under consideration cannot be calculated in terms of the existing theories, because the necessary data are unavailable in the literature.

Earlier [24], we carried out photon echo measurements for a number of impurity organic matrices, namely, two polymers [poly(methyl methacrylate) and poly(isobutylene)] and one glass (ethanol) in the temperature range 0.36– 50 K. In the case of polymers, the value of α appeared to be equal to 1.1, which almost coincides with the α parameter obtained for the toluene matrix in the present work. For the ethanol matrix, the exponent α was equal to 1.9. It remains unclear why this exponent is approximately identical for the above polymers and the toluene matrix and turns out to be considerably larger for the ethanol matrix. In our opinion, this difference can be associated with the fact that molecules of resorufin, which was used for doping the ethanol matrix, are ionic, whereas the impurity molecules introduced into the other matrices are electroneutral. The nearest environment of an ionic molecule can undergo a considerable transformation with the formation of a particular shell (the so-called shell effect [25]). This can lead to a change in the dynamics of the nearest environment and, hence, in the temperature dependence of the linewidth.

The frequency of the local mode in the solution of octaethylporphine zinc in toluene is determined to be $\Delta E \sim 14.5$ cm^{-1}, which is typical of impurity amorphous systems. For example, the values of ΔE obtained experimentally for several systems in [24] lie in the range 7–29 cm^{-1}.

Now, let us analyze the high-temperature portion of the temperature dependence of the zero-phonon linewidth in the framework of the soft-potential model [16], which includes a broad frequency distribution of quasi-local vibrations. For this purpose, the high-temperature portion was approximated by the expression

$$\Delta\Gamma^{\mathrm{HO}}(T) = aT^7 \int_0^{E_b/k_{\mathrm{B}}T} dx \frac{x^6 e^x}{(e^x - 1)^2}. \quad (4)$$

This equation was derived by Garcia and Fernandez [26] within the soft-potential model. The equation describes the broadening of a homogeneous line of an impurity center due to low-frequency phonon excitations (harmonic oscillators in terms of the model) in the matrix. Here, E_b is the energy of the boson peak, which is approximately equal to 20 cm^{-1} for toluene [27].

Figure 2 presents the results of this approximation (curve *4*) and also the data obtained on the basis of the model allowing for one vibrational mode. The interaction constant a determined within the model with a broad vibrational spectrum of the matrix is equal to 2×10^{-1} s^{-1} K^{-7}. It can be seen from this figure that both approximating curves are similar to each other. However, this does not mean that both approaches used to describe the optical dephasing caused by the phonon excitations are equivalent. In the first approach, the obtained frequency ΔE does not correspond to any actually existing vibrational mode (unlike the analogous case with impurity crystals). Therefore, the quantity ΔE should be treated as an effective frequency characterizing the broad distribution of low-frequency modes. The validity of the second approach is confirmed by the experimental data, which prove the occurrence of the broad spectrum of vibrational excitations.

In this work, we restricted our consideration to the specific case of the contribution made to the optical dephasing by the interaction of impurities with two-level systems and low-frequency vibrations of the phonon type in the matrix. However, it should be noted that, over the wide temperature range studied, other mechanisms of broadening can also manifest themselves: the interaction of impurities with two- and three-phonon tunneling transitions in two-level systems, the dephasing associated with the thermally activated over-barrier transitions in two-level systems, and the broadening caused by the acoustic phonons of the matrix. At present, the problem concerning the ratio between the contributions of the aforementioned mechanisms to the line broadening in impurity amorphous systems has not been studied. This problem is also unclear for the system under consideration. In our recent work [28], using the system of tetra-*tert*-butylterrylene in poly(methyl methacrylate) as an example, the contributions of two-phonon tunneling transitions and over-barrier transitions in two-level systems to the dephasing were calculated in terms of the soft-potential model for the first time in impurity amorphous materials. It was shown that, in the studied system, the contribution of over-barrier transitions in two-level systems to the optical dephasing over the entire temperature range is less than that of tunneling two-level systems. The contribution of two-phonon tunneling transitions in two-level systems exceeds the contribution of one-phonon transitions at high temperatures ($T > 15$ K) but is less than the contribution of low-frequency modes. Unfortunately, we could not evaluate the influence of these mechanisms of broadening on the parameters of the temperature dependence of the linewidth for the studied system of octaethylporphine zinc in toluene, because the data necessary for calculations are not available in the literature. We can only assume that the contributions of the two studied mechanism of dephasing are also dominant in the system under investigation.

We now dwell on the possible contribution of acoustic phonons to the temperature broadening of the zero-phonon line in our system. From numerous experiments, it follows that, at temperatures below 10–20 K, the density of states of acoustic phonons is substantially less than that of two-level systems and low-frequency modes. Consequently, acoustic phonons should not noticeably affect the dynamics of amorphous materials and, in particular, the line broadening at these temperatures. As regards higher temperatures, the conditions under which the contribution of acoustic phonons to the dephasing begins to manifest itself have not been revealed up to now. Note that, in our case, the entire temperature dependence of the linewidth can be explained without regard for the contribution of acoustic phonons, even though the measurements were performed up to the Debye temperature of solid toluene. The elucidation of the actual role played by acoustic phonons in the broadening of the homogeneous line of the impurity center in the amorphous matrix calls for further investigation.

4. CONCLUSIONS

Thus, the optical dephasing processes were investigated in an impurity organic system composed of solid amorphous toluene doped with octaethylporphine zinc. Owing to the use of two variants of the photon echo technique, the dephasing times T_2 were measured for the first time over a wide range of temperatures (0.35–100 K), which differ by more than two orders of magnitude and cover the range from millikelvins to the Debye temperature of solid toluene. The high time resolution achieved in the incoherent photon echo measurements made it possible to distinguish clearly the portions corresponding to the zero-phonon line and the phonon wing in the decay curves. The measurements performed over a wide range of temperatures allowed us to separate reliably two different mechanisms of broadening in the optical spectrum of impurity molecules in the system under investigation. These are the optical dephasing caused by the tunneling transitions in two-level systems at low temperatures and the dephasing associated with the quasi-local low-frequency phonons of the matrix at high-temperatures. It was demonstrated that the experimental data can be adequately described using the spectrum of low-frequency vibrations of the matrix, which was predicted by the soft-potential model.

ACKNOWLEDGMENTS

This work was supported by the US Civilian Research and Development Foundation for the Independent States of the Former Soviet Union (CRDF) (project no. RC1-2215) and the Russian Foundation for Basic Research (project nos. 01-02-16481 and 02-02-16739).

REFERENCES

1. R. C. Zeller and R. O. Pohl, Phys. Rev. B **4**, 2029 (1971).

2. B. M. Kharlamov, R. I. Personov, and L. A. Bykovskaya, Opt. Commun. **12** (12), 191 (1974).
3. A. A. Gorokhovskiĭ, R. K. Kaarli, and L. A. Rebane, Pis'ma Zh. Éksp. Teor. Fiz. **20** (7), 216 (1974) [JETP Lett. **20** (1974)].
4. R. I. Personov, E. I. Al'shchits, and L. A. Bykovskaya, Pis'ma Zh. Éksp. Teor. Fiz. **15** (10), 609 (1972) [JETP Lett. **15**, 431 (1972)].
5. R. I. Personov, E. I. Al'shits, and L. A. Bykovskaya, Opt. Commun. **6** (2), 169 (1972).
6. N. A. Kurnit, I. D. Abella, and S. R. Hartmann, Phys. Rev. Lett. **13** (19), 567 (1964).
7. J. Hegarty, J. Lumin. **36** (4–5), 273 (1987).
8. S. Voelker, Annu. Rev. Phys. Chem. **40**, 499 (1989).
9. P. W. Anderson, B. I. Halperin, and C. M. Varma, Philos. Mag. **2**, 1 (1972).
10. W. A. Phillips, J. Low Temp. Phys. **7**, 351 (1972).
11. *Amorphous Solids: Low Temperature Properties*, Ed. by W. A. Phillips (Springer-Verlag, Berlin, 1981).
12. S. Hunklinger and A. K. Raychaudhuri, in *Progress in Low Temperature Physics*, Ed. by D. F. Brewer (Elsevier, Amsterdam, 1986), Vol. 9.
13. *Tunneling Systems in Amorphous and Crystalline Solids*, Ed. by P. Esquinazi (Springer-Verlag, Berlin, 1998).
14. B. Jackson and R. Silbey, Chem. Phys. Lett. **99**, 331 (1983).
15. G. Schulte, W. Grond, D. Haarer, and R. Silbey, J. Phys. Chem. **88**, 679 (1988).
16. V. G. Karpov, M. I. Klinger, and F. N. Ignat'ev, Zh. Éksp. Teor. Fiz. **84**, 760 (1983) [Sov. Phys. JETP **57**, 439 (1983)].
17. S. J. Zilker, D. Haarer, and Yu. G. Vainer, Chem. Phys. Lett. **273**, 232 (1997).
18. N. V. Gruzdev and Yu. G. Vaĭner, Opt. Spektrosk. **76**, 252 (1994) [Opt. Spectrosc. **76**, 230 (1994)].
19. N. Morita and T. Yajima, Phys. Rev. A **30** (5), 2525 (1984).
20. L. R. Narasimhan, Y. S. Bai, M. A. Dugan, and M. D. Fayer, Chem. Phys. Lett. **176** (3–4), 335 (1991).
21. G. I. Small, in *Spectroscopy and Excitation Dynamics of Condensed Molecular Systems*, Ed. by V. M. Agranovich and R. M. Hochstrasser (North-Holland, Amsterdam, 1983).
22. D. L. Huber, M. M. Broer, and B. Golding, Phys. Rev. Lett. **52**, 2281 (1984).
23. A. V. Naumov, Yu. G. Vainer, and S. J. Zilker, J. Lumin. **86**, 273 (2000).
24. Yu. G. Vainer, M. A. Kol'chenko, A. V. Naumov, *et al.*, J. Lumin. **86**, 265 (2000).
25. D. W. Pack, L. R. Narasimhan, and M. D. Fayer, J. Chem. Phys. **92** (7), 4125 (1990).
26. A. J. García and J. Fernández, Phys. Rev. B **56**, 579 (1997).
27. J. Wiedersich, N. V. Surovtsev, and E. Rössler, J. Chem. Phys. **111** (3), 1143 (2000).
28. Yu. G. Vaĭner, M. A. Kol'chenko, and R. I. Personov, Zh. Éksp. Teor. Fiz. **119** (4), 738 (2001) [JETP **92**, 643 (2001)].

Translated by O. Borovik-Romanova

Physics of the Solid State, Vol. 45, No. 2, 2003, pp. 231–235. Translated from Fizika Tverdogo Tela, Vol. 45, No. 2, 2003, pp. 222–226.
Original Russian Text Copyright © 2003 by Alshits, Lyubimov.

SEMICONDUCTORS AND DIELECTRICS

Anomalies in the Spectrum of Electromagnetic Eigenwaves in Anisotropic Plates

V. I. Alshits and V. N. Lyubimov
Shubnikov Institute of Crystallography, Russian Academy of Sciences, Leninskiĭ pr. 59, Moscow, 117333 Russia
e-mail: alshits@ns.crys.ras.ru

Received April 5, 2002

Abstract—A radical transformation of the spectrum of electromagnetic eigenwaves in anisotropic plates of optically biaxial and uniaxial crystals is investigated for small deviations of the direction of wave propagation from crystallographic orientations. It is demonstrated that, in the case when the sagittal plane and plate faces are the symmetry planes of the permittivity tensor **ε**, there exist four independent families of bulk eigenwaves, each characterized by an infinite set of dispersion curves. Dispersion curves of the independent families intersect one another to form a network structure. Under the action of perturbations, the sagittal plane and the plate faces cease to be the symmetry planes. Moreover, these perturbations lead to interactions between waves belonging to different families, the generation of mixed polarization modes, and divergence of the dispersion curves, i.e., the disappearance of intersection points. In the vicinity of these points, the polarization of wave fields changes drastically even with insignificant variations in the frequency. *© 2003 MAIK “Nauka/Interperiodica”.*

1. INTRODUCTION

It is known that, as for a stretched string with characteristic natural sound frequencies, an anisotropic crystal plate can be characterized by an infinite set of electromagnetic eigenwaves. The properties of these waves depend on many factors, such as the components of the permittivity tensor **ε**, the orientations of the plate surfaces with respect to the crystallographic axes, specific boundary conditions on these surfaces, and the direction of wave propagation. In this work, we investigated eigenwaves in anisotropic plates of optically biaxial and uniaxial crystals within the standard concepts of crystal optics [1–3] and described possible situations where even very insignificant changes in the propagation conditions bring about radical transformations in the structure of wave fields and, consequently, in the dispersion curves.

If the sagittal plane (the plane of wave vectors) and plate faces are the symmetry planes of the permittivity tensor **ε**, there exist four independent families of bulk eigenwaves. In this case, each family is characterized by an infinite set of dispersion curves and for each curve there is a characteristic polarization of the wave field. Dispersion curves of the independent families intersect one another to form a network structure. Under the action of perturbations, the sagittal plane and the plate faces cease to coincide with the symmetry planes. These perturbations lead to interactions between waves belonging to different families, the generation of mixed polarization modes, and the divergence of the dispersion curves at the points of their intersection. In the vicinity of these points, even insignificant variations in the frequency drastically affect the polarization of wave fields. This phenomenon will be analytically described below.

2. FOUR INDEPENDENT FAMILIES OF BULK EIGENWAVES

Let us consider an anisotropic plate of thickness $2d$, which was cut from an optically biaxial crystal. The plate faces are aligned parallel to the planes of symmetry of the optical properties characterized by the permittivity tensor **ε** (Fig. 1a). The plate is bordered on both sides by an isotropic medium with the permittivity ε. All the properties of electromagnetic eigenwaves in this plate are determined using Maxwell equations with standard boundary conditions.

The electrical component of the electromagnetic wave field both in the plate and in the adjacent isotropic medium can be represented in the following form:

$$\mathbf{E}(x, y, z; t) = \mathbf{E}(z) \times \exp\left\{i\omega\left[\frac{1}{c}n(x\cos\varphi + y\sin\varphi)\right] - t\right\}. \tag{1}$$

Here, x, y, and z are the coordinates of the variable point (the coordinate axes are directed along the principal axes of the permittivity tensor **ε**; hence, we can write $\varepsilon_{ij} = \varepsilon_i\delta_{ij}$); t is the time; ω is the frequency; c is the velocity of light in free space; $n = c/v$; v is the velocity of propagation of the electromagnetic wave field; and φ is the angle specifying the direction of propagation of the wave field. The magnetic component of the electro-

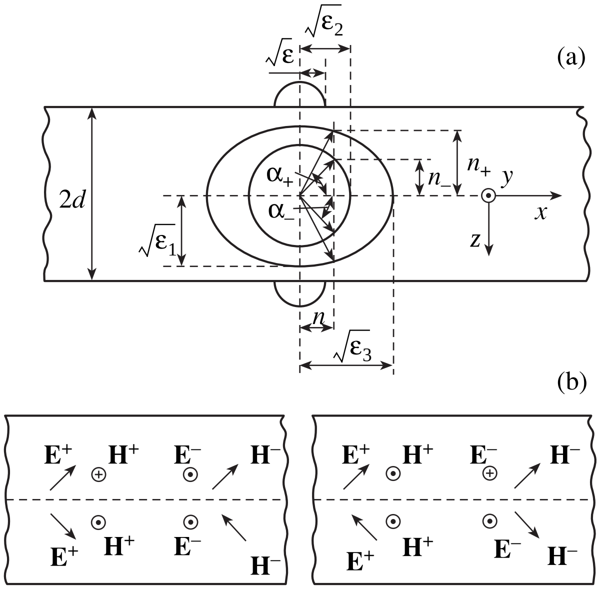

Fig. 1. Characteristics of the wave fields in the case when the sagittal plane and plate faces are the symmetry planes of the permittivity tensor $\boldsymbol{\varepsilon}$: (a) sections of the surfaces of the refractive indices by the sagittal plane and the refraction vectors of bulk waves in the plate, (b) orientations of the polarization vectors of electromagnetic fields for bulk eigenwaves of the families $(S_EA_H)_+$ and $(S_EA_H)_-$, and (c) orientations of the polarization vectors for bulk eigenwaves of the families $(A_ES_H)_+$ and $(A_ES_H)_-$.

magnetic wave field $\mathbf{H}(x, y, z; t)$ has a form similar to expression (1).

Under the conditions when the plate faces are aligned parallel to the symmetry planes, there exist two independent families of electromagnetic wave fields for any direction of wave propagation (at any angle φ). First, the wave fields are symmetric in the electrical components and antisymmetric in the magnetic components simultaneously (Fig. 1b):

$$\begin{aligned} &E_{x,y}(z) = E_{x,y}(-z), \quad E_z(z) = -E_z(-z); \\ &H_{x,y}(z) = -H_{x,y}(-z), \quad H_z(z) = H_z(-z). \end{aligned} \tag{2}$$

In what follows, these fields will be designated as S_EA_H. Relationships (2) describe the behavior of the wave fields with respect to reflection in the central plane of the plate when $z \longrightarrow -z$.

Second, the electromagnetic wave fields can be antisymmetric in the electrical components and symmetric in the magnetic components simultaneously (hereafter, these fields will be denoted by A_ES_H). In this case, the electrical and magnetic components in relationships (2) should change position (Fig. 1c).

In each family, the vector amplitude $\mathbf{E}(z)$ contains partial wave contributions from branches of two types, which are denoted by the plus and minus signs:

$$\mathbf{E}(z) = \mathbf{E}^+(z) + \mathbf{E}^-(z). \tag{3}$$

These branches correspond to two independent solutions of the Maxwell equations. The z dependence of the partial contributions involved in expression (3) has the form

$$\mathbf{E}^{\pm}(z) = \mathbf{E}_1^{\pm}\exp(i\omega n_{\pm}z/c) + \mathbf{E}_2^{\pm}\exp(-i\omega n_{\pm}z/c). \tag{4}$$

Here, the z coordinate varies within the range $-d \le z \le d$. Relationships for the vectors $\mathbf{E}^{\pm}$, which specify the polarization of the wave field, and for the parameters $n_{\pm} = n_{\pm}(n^2)$ will be derived below.

The wave field in the adjacent isotropic medium at $z \ge d$ can be adequately described by expression (1) under the conditions

$$\mathbf{E}(z) = \mathbf{E}_1\exp(-\omega pz/c), \quad p = p(n^2) = \sqrt{n^2 - \varepsilon}. \tag{5}$$

Here, $\mathbf{E}_1$ is the polarization vector and p is the parameter of the wave-field localization in the isotropic medium ($p > 0$). For $z \le -d$, it is necessary to perform the following replacements in relationships (5): $\mathbf{E}_1 \longrightarrow \mathbf{E}_2$ and $p \longrightarrow -p$. Therefore, the wave field outside the plate exponentially decays as the distance from the plate surfaces increases.

In the case when the wave fields in the plate are generated by bulk waves, the waves obey the inequality $n_{\pm}^2 \ge 0$ and the wave normals form the angles $\alpha_{\pm} = \arctan(n_{\pm}/n)$ with the plate faces (Fig. 1a).

For symmetric directions of wave propagation (when $\varphi = 0$ or $\pi/2$), the sagittal plane is the plane of symmetry and each of the aforementioned two independent families of eigenwaves, in turn, can be separated into two families, of which one family contains waves of branches with the plus sign and the other family includes waves of branches with the minus sign (Figs. 1b, 1c). In this case, the dispersion relationships for eigenwaves of all four families can be easily obtained in the explicit form. In particular, at $\varphi = 0$, we can write the following four expressions for the dimensionless frequencies $\Omega = \omega d/c$:

$$\Omega(n^2) = \begin{cases} [-\arctan(n_+\varepsilon/p\varepsilon_1) + \pi m]/n_+, \quad (S_EA_H)_+, & (6) \\ [\arctan(p/n_-) + \pi s]/n_-, \quad (S_EA_H)_-, & (7) \\ [\arctan(p\varepsilon_1/n_+\varepsilon) + \pi k]/n_+, \quad (A_ES_H)_+, & (8) \\ [-\arctan(n_-/p) + \pi l]/n_-, \quad (A_ES_H)_-. & (9) \end{cases}$$

Here,

$$\begin{aligned} n_+ &= n_+(n^2) = \sqrt{\varepsilon_1 - n^2\varepsilon_1/\varepsilon_3}, \\ n_- &= n_-(n^2) = \sqrt{\varepsilon_2 - n^2}, \end{aligned} \tag{10}$$

and m, s, k, and l are natural numbers corresponding to the numbers of the dispersion branches. The dispersion curves described by relationships (6)–(9) for four independent families of eigenwaves are depicted in Figs. 2a and 2b. These curves are conveniently constructed using the asymptotic expressions at small and large arguments of the trigonometric functions, i.e., when $p \longrightarrow 0$ (at $n^2 \longrightarrow \varepsilon$), $n_+ \longrightarrow 0$ (at $n^2 \longrightarrow \varepsilon_3$), and $n_- \longrightarrow 0$ (at $n^2 \longrightarrow \varepsilon_2$).

The vector amplitudes of the wave fields for the configurations $(S_EA_H)_\pm$ described by relationships (6) and (7) take the form

$$\mathbf{E}^+(z) = a^+\begin{bmatrix}(n_+/\varepsilon_1)\cos(\Omega n_+ z/d)\\ 0\\ -(n/\varepsilon_3)i\sin(\Omega n_+ z/d)\end{bmatrix},$$

$$\mathbf{H}^+(z) = a^+\begin{bmatrix}0\\ i\sin(\Omega n_+ z/d)\\ 0\end{bmatrix}, \tag{11}$$

$$\mathbf{E}^-(z) = a^-\begin{bmatrix}0\\ \cos(\Omega n_- z/d)\\ 0\end{bmatrix},$$

$$\mathbf{H}^-(z) = a^-\begin{bmatrix}-n_- i\sin(\Omega n_- z/d)\\ 0\\ n\cos(\Omega n_- z/d)\end{bmatrix}. \tag{12}$$

Here, $a^\pm$ are the amplitude multipliers. For the configurations $(A_ES_H)_\pm$ described by relationships (8) and (9), the vector amplitudes of the wave fields can be obtained from expressions (11) and (12) upon the replacement $\cos \rightleftarrows i\sin$ (Figs. 1b, 1c).

Considering the curves approaching different asymptotic levels, namely, $n^2 \longrightarrow \varepsilon_3$ and $n^2 \longrightarrow \varepsilon_2$ (Figs. 2a, 2b), it is easy to understand that superposition of Figs. 2a and 2b should result in a large number of intersections of the dispersion curves in the region defined by the inequality

$$\varepsilon < n^2 < \min(\varepsilon_2, \varepsilon_3). \tag{13}$$

For the second orientation of the sagittal plane, which also coincides with the plane of symmetry (at $\varphi = \pi/2$), the above results hold true provided the coordinate axes change their directions as follows: $x \longrightarrow y$ and $y \longrightarrow -x$. Note that, in the relationships thus obtained, it is necessary to perform the replacement $\varepsilon_1 \rightleftarrows \varepsilon_2$.

3. GENERATION OF HYBRID POLARIZATION MODES

Let us consider the case when the sagittal plane and the plate faces simultaneously cease to be symmetry planes and all four families of eigenwaves are no longer independent. This leads to the generation of hybrid polarization modes. As a result, all the points of intersection of the dispersion curves disappear and the divergence of these curves is observed (Figs. 3a–3c). For example, this situation can occur upon a small rotation of the plate faces about a common (nonsymmetric) axis aligned parallel to the xy plane. Consequently, the separation between the dispersion curves $\Delta\Omega$ proves to be proportional to the angle of this rotation. It should be noted that a similar effect of divergence for elastic waves in crystals was described in our earlier work [4].

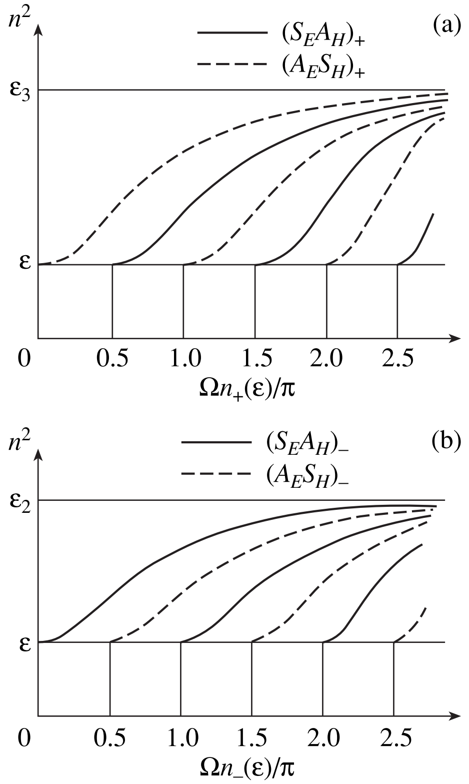

Fig. 2. Dispersion curves for four independent families of bulk eigenwaves.

Now, we analyze in more detail the special case when only the sagittal plane ceases to be the symmetry plane due to a perturbation, whereas the plate faces remain the planes of symmetry as before. Such a perturbation can manifest itself in an insignificant change in the direction of wave propagation, specifically in a deviation of the propagation direction from the x axis through a small angle $\Delta\varphi$. This leads to the hybridization of waves of the same parity that belong to branches with both the plus and minus signs. The aforementioned four series of solutions are joined into two independent families formed by linear combinations (3) of the previously independent configurations $(S_EA_H)_+$ and $(S_EA_H)_-$, on the one hand, and $(A_ES_H)_+$ and $(A_ES_H)_-$, on the other. Analysis of the dispersion curves for wave fields of the same parity in the vicinity of any point of their intersection demonstrates that, upon perturbation, the intersection of the branches disappears and the sep-

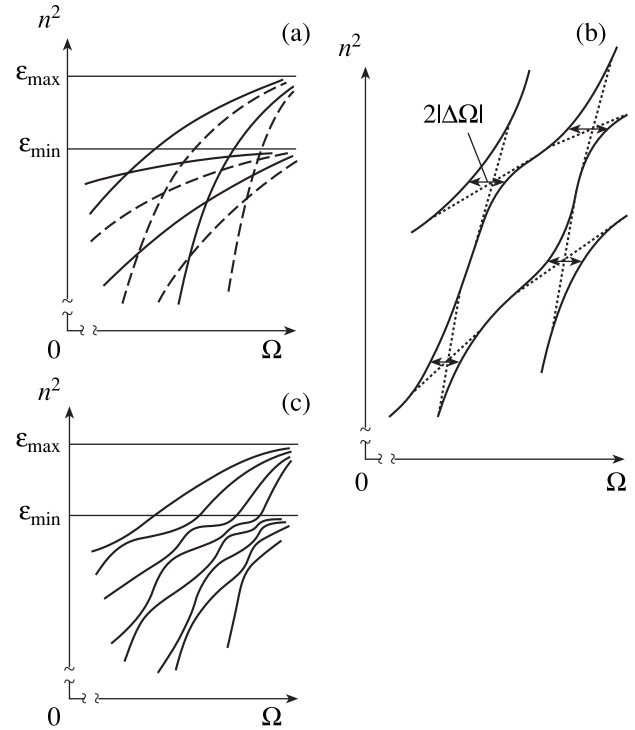

Fig. 3. Schematic diagrams illustrating the generation of mixed polarization modes: (a) intersections of the families of dispersion curves for eigenwaves of independent polarizations in the absence of perturbations, (b) divergence of the dispersion curves due to perturbations (dotted lines are the dispersion curves in the absence of perturbations), and (c) changes in the dispersion curves shown in Fig. 3a due to perturbations.

aration between the dispersion curves becomes proportional to the perturbation parameter ($\Delta\Omega \sim \Delta\varphi$). We leave aside the rather cumbersome calculations and write the final result

$$\Delta\Omega = \pm(\Delta\varphi)n^2 \times \sqrt{\frac{\varepsilon_3(f_+\varepsilon_1/\varepsilon_2 - 1)(f_- - 1)}{(\varepsilon_2 - \varepsilon)[(\varepsilon_1\varepsilon_3 - \varepsilon^2)n^2 - \varepsilon\varepsilon_3(\varepsilon_1 - \varepsilon)]}}. \tag{14}$$

Here, for brevity, we introduced the following designations:

$$f_\pm = f_\pm(n^2) = \frac{p^2(\delta_3 - \delta_1) + \delta_3\varepsilon\varepsilon_2/\varepsilon_1}{\delta_1 n_\pm^2 + \delta_3 n^2}, \tag{15}$$

$$= 1/\varepsilon_1 - 1/\varepsilon_2, \quad \delta_3 = 1\text{Œd-¥t}\varepsilon_3 - 1/\varepsilon$$

In these expressions, the values of n^2 can be determined from the positions of the points of intersection of the dispersion curves in the absence of perturbations. The appropriate conditions are obtained by equating the right-hand sides of Eqs. (6) and (7) or (8) and (9).

As a consequence, the polarization of wave fields becomes hybrid and changes drastically even with insignificant variations in the frequency Ω in the portions of the dispersion curves that are close to discontinuities. Although the perturbations are relatively small, they lead to radical changes in the dispersion curves. In particular, the smooth dispersion curves take on a clearly defined wavy shape. Moreover, there appears a new specific feature: the polarization sharply changes with a certain periodicity along the dispersion curve. In this case, the polarization vectors execute a motion between the mutually orthogonal limiting orientations (this can be seen from relationships (11), (12) and Figs. 1b, 1c). Thus, considerable effects are induced by small perturbations.

It should be noted that the above perturbations do not lead to the disappearance of the points of intersection of the branches attributed to wave fields of different parity. The wave fields remain independent until the plate surfaces are aligned parallel to the symmetry planes of the permittivity tensor $\boldsymbol{\varepsilon}$.

Expression (14) holds for optically biaxial crystals and can be substantially simplified in the case of optically uniaxial media. Specifically, if the optic axis in the initial unperturbed state is perpendicular to the sagittal plane, i.e., is aligned along the y axis, expression (14) takes the form

$$\Delta\Omega = \pm(\Delta\varphi)n^2\sqrt{\frac{\varepsilon_0 - \varepsilon}{\varepsilon_0(\varepsilon_e - \varepsilon)[(\varepsilon_0 + \varepsilon)n^2 - \varepsilon\varepsilon_0]}}. \tag{16}$$

Here, ε_0 and ε_e are the permittivities of optically uniaxial crystals [1–3]; in our case, the permittivities satisfy the conditions $\varepsilon_0 = \varepsilon_1 = \varepsilon_3$ and $\varepsilon_e = \varepsilon_2$.

When the optic axis in the initial unperturbed state is parallel to the sagittal plane and is aligned along the x axis, expression (14) takes the form

$$\Delta\Omega = \pm(\Delta\varphi)\frac{n^2}{\varepsilon_0 - n^2} \times \sqrt{\frac{\varepsilon_0(\varepsilon_0 - \varepsilon)}{(\varepsilon_0\varepsilon_e - \varepsilon^2)n^2 - \varepsilon\varepsilon_0(\varepsilon_e - \varepsilon)}}. \tag{17}$$

In this case, we have $\varepsilon_0 = \varepsilon_2 = \varepsilon_3$ and $\varepsilon_e = \varepsilon_1$. Note that expressions (14), (16), and (17) are derived in the linear approximation with respect to the perturbation $\Delta\varphi$ and hold only for the parameters at which the separation $\Delta\Omega$ remains small.

4. DISCUSSION

Let us now elucidate how perturbations of different types affect the dispersion curves. Upon rotation of the plate faces with respect the crystallographic axes through a small angle $\Delta\vartheta$ about the normal to the sagittal plane (i.e., about the y axis), the sagittal plane remains the plane of symmetry but the plate faces cease to coincide with the symmetry planes. As a result, the four initially independent families also become hybrid in pairs. However, these pairs are formed in another manner: one pair is formed only by waves of branches with the plus sign, whereas the other pair is formed only by waves of branches with the minus sign. The perturbation distorts the structure of the wave fields in such a way that the parity properties defined by relationships (2) disappear. However, no divergence of the intersecting dispersion curves is observed. Actually, the small perturbation under consideration only slightly distorts the dispersion curves shown in Figs. 2a and 2b and cannot eliminate the intersections of branches with the plus and minus signs. In the case when this perturbation is supplemented by a small change in the direction of wave propagation $\Delta\varphi$, the sagittal plane ceases to coincide with the symmetry plane and all the points of intersection of the branches should disappear. Consequently, the divergence of the branches associated with wave fields of the initially (prior to perturbation) equal parity can be approximately described by the above relationships in which $\Delta\Omega \sim \Delta\varphi$. At the same time, the divergence of the branches attributed to wave fields of different (prior to perturbation) parities appears to be less pronounced and is determined by the product of two small parameters: $\Delta\Omega \sim (\Delta\varphi)(\Delta\vartheta)$.

Upon perturbation when the plate faces are rotated through an angle $\Delta\vartheta$ about the direction of wave propagation parallel to the x axis, the sagittal plane and the plate faces simultaneously cease to be symmetry planes. As a result, all the points of intersection of the dispersion curves disappear. Analysis demonstrates that, in this case, the separation proportional to the perturbation parameter $\Delta\Omega \sim \Delta\vartheta$ is observed only for the branches corresponding to wave fields of initially different parities, whereas the separation between the branches attributed to wave fields of equal (prior to perturbation) parity has a higher order of smallness: $\Delta\Omega \sim (\Delta\vartheta)^2$.

The excitation of the wave fields under investigation can be achieved using attenuated total internal reflection, as is the case with the excitation of surface electromagnetic and elastic waves in solids. The appropriate techniques were described in our recent works [5, 6]. Note that, in actual practice, hybrid wave fields and the separation between the dispersion curves can be easily controlled by varying only the direction of wave propagation (i.e., the φ angle). It is important that even very insignificant variations in the direction of wave propagation lead to considerable changes in the structure of wave fields.

REFERENCES

1. A. F. Konstantinova, B. N. Grechushnikov, B. V. Bokut’, and E. G. Valyashko, *Optical Properties of Crystals* (Navuka i Tékhnika, Minsk, 1995).
2. Yu. I. Sirotin and M. P. Shaskolskaya, *Fundamentals of Crystal Physics* (Nauka, Moscow, 1975; Mir, Moscow, 1982).
3. V. M. Agranovich and V. L. Ginzburg, *Crystal Optics with Spatial Dispersion, and Excitons* (Nauka, Moscow, 1965; Springer, New York, 1984).
4. V. I. Alshits and V. N. Lyubimov, Kristallografiya **33** (2), 279 (1988) [Sov. Phys. Crystallogr. **12**, 163 (1988)].
5. V. I. Alshits, V. N. Lyubimov, and L. A. Shuvalov, Fiz. Tverd. Tela (St. Petersburg) **43** (7), 1322 (2001) [Phys. Solid State **43**, 1377 (2001)].
6. V. I. Alshits, A. S. Gorkunova, V. N. Lyubimov, *et al.*, in *Proceedings of the International Symposium on Trends in Continuum Physics* (World Scientific, Singapore, 1999), p. 28.

Translated by O. Borovik-Romanova

Physics of the Solid State, Vol. 45, No. 2, 2003, pp. 236–239. Translated from Fizika Tverdogo Tela, Vol. 45, No. 2, 2003, pp. 227–230.
Original Russian Text Copyright © 2003 by Mikheev.

SEMICONDUCTORS AND DIELECTRICS

Giant Low-Temperature Thermal Resistance of ZnSeNi

V. M. Mikheev
Institute of Metal Physics, Ural Division, ul. S. Kovalevskoĭ 18, Yekaterinburg, 620219 Russia
e-mail: mikheev@imp.uran.ru

Received April 5, 2002

Abstract—The 200-fold increase in the thermal resistance of ZnSe at 15 K caused by doping of these crystals with nickel is accounted for by suppression of the thermal phonon contribution to thermal conductivity. As follows from our calculations, in order to reach such high thermal resistances, one has to suppress the contribution from phonons with frequencies lying in an interval not narrower than 100 K. *© 2003 MAIK “Nauka/Interperiodica”.*

One of Slack’s older publications reported on measurement of the thermal conductivity of iron-doped ZnS crystals within a broad temperature range (from 3 to 300 K) [1]. The curves plotting the temperature dependence of the thermal-conductivity coefficient of $Zn_{1-x}Fe_xS$ revealed minima whose depth depended on iron concentration. For $x \approx 0.01$, the thermal conductivity at the minimum (T = 20 K) was found to be two orders of magnitude lower than that of pure ZnS at the same temperature. The corresponding value of the thermal resistance at T = 20 K may be called giant. Slack [1] proposed assigning these clearly pronounced features in thermal conductivity to resonant phonon scattering from iron atoms occurring when the phonon frequency coincides with the energy gaps between the electronic states of the iron atom in the ZnS matrix. This idea was not developed further, however, and no interpretation has been put forward for the experiment.

Interest in this problem was spurred by a recent paper reporting on a study of the temperature dependences of thermal conductivity of nickel-doped ZnSe crystals [2]. The crystals studied were high-electrical-resistivity samples, for which the electron contribution to thermal conductivity is negligible. The experimental results obtained in [2] are displayed in Fig. 1. One readily sees that the thermal conductivity of the crystal drops with increasing doping. Samples 3 and 4, with nickel concentrations of 3.6×10^{19} and 1×10^{20} cm^{-3}, respectively, exhibit a minimum in the thermal conductivity at T = 15 K. The thermal conductivity of sample 4 at this temperature is 200 times lower than that of pure ZnSe at the same temperature. These anomalies in the temperature dependence of thermal conductivity were assigned in [2] to resonant phonon scattering caused by a nickel impurity. In contrast to [1], where resonant phonon scattering was attributed to intracenter transitions in iron atoms, in [2], the resonant scattering was explained as being due to the phonon frequency coinciding with the frequency of the local lattice vibration induced by nickel atoms. It is believed [2] that the only reason for the unusually strong resonant change in thermal conductivity is the anomalously large cross section of the resonant scattering. It should be pointed out, however, that the effect of phonon scattering on thermal conductivity depends, generally speaking, on two factors, namely, the phonon scattering cross section and

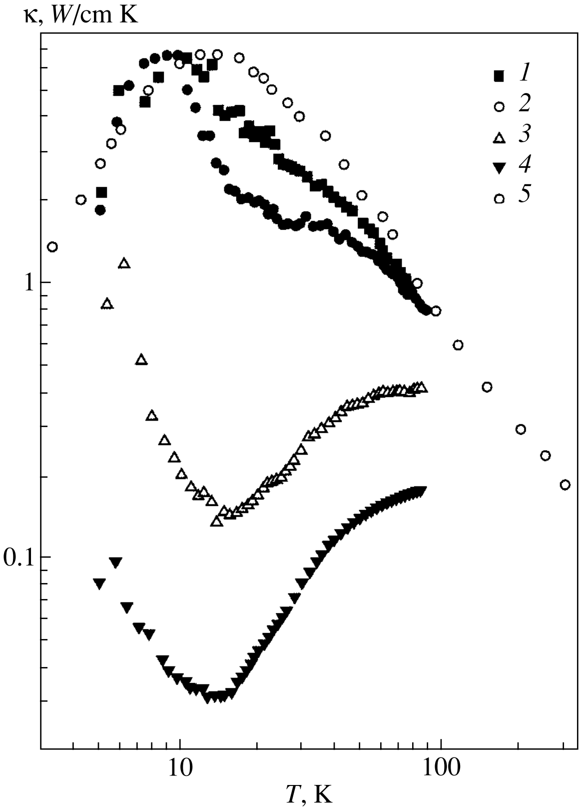

Fig. 1. Temperature dependences of thermal conductivity of zinc selenide crystals [2]. (*1*) Sample 1 (pure ZnSe); (*2–4*) ZnSeNi samples with different Ni concentrations, (*2*) sample 2 (4.3×10^{17}), (*3*) sample 3 (3.6×10^{19}), and (*4*) sample 4 (1×10^{20}) cm^{-3}; and (*5*) pure ZnSe [1].

1063-7834/03/4502-0236$24.00 © 2003 MAIK “Nauka/Interperiodica”

the phonon frequency interval within which this scattering mechanism is efficient. The fact that the thermal conductivity of sample 4 at the temperature of the minimum is 200 times lower than that of a pure sample at the same temperature implies that the vast majority of thermal phonons in sample 4 do not contribute to thermal conductivity. Therefore, in order for the resonant phonon scattering from local vibrations to lower the thermal conductivity of ZnSeNi by two orders of magnitude, the resonant frequencies have to be distributed over a fairly broad interval (this frequency interval must be equal, in order of magnitude, to that occupied by thermal phonons). We propose a simple phenomenological calculation scheme which permits one to perform a quantitative description of the experimental data and to estimate the frequency interval of thermal phonons whose contribution to thermal conductivity is negligible.

Our estimation is based on a phenomenological expression for the thermal conductivity of a phonon gas:

$$\kappa \sim C_V v_f^2 \tau, \tag{1}$$

where C_V is the phonon gas (lattice) specific heat, v_f is the phonon velocity, and $l = v_f\tau$ is the phonon mean free path. The specific heat of the phonon gas is calculated from the relation

$$C_V \sim \int_0^\infty d\omega\omega^2 g(\omega)\frac{e^{\hbar\omega/kT}}{(e^{\hbar\omega/kT}-1)^2}, \tag{2}$$

where $g(\omega)$ is the density of phonon states in pure ZnSe [3] (Fig. 2).

We assume that the doping of ZnSe crystals with nickel initiates a new powerful phonon scattering mechanism (for instance, resonant scattering from local modes), with the result that the phonon contribution from a finite frequency interval $\omega_0 - \Delta\omega < \omega < \omega_0 + \Delta\omega$ to thermal conductivity becomes negligible. In the model we accepted, only phonons with frequencies outside the above frequency interval contribute to the heat flux in ZnSeNi; it is these phonons that are only weakly involved in the new scattering mechanism. Therefore, the mean free path of these phonons differs little from that in pure ZnSe. Thus, we divide phonons in ZnSeNi into two groups. The first group includes the phonons for which the new scattering mechanism is efficient. Their contribution to the heat flux can be neglected. Phonons of the second group provide the major contribution to the heat flux. For these phonons, the mean free path is determined by the same scattering mechanisms that operate in pure ZnSe.

The scheme we propose for calculating $\kappa(T)$ in nickel-doped crystals is as follows.

First, we calculate the phonon relaxation time in pure ZnSe:

$$\tau_0(T) = \kappa_0(T)/C_V(T)v_f^2.$$

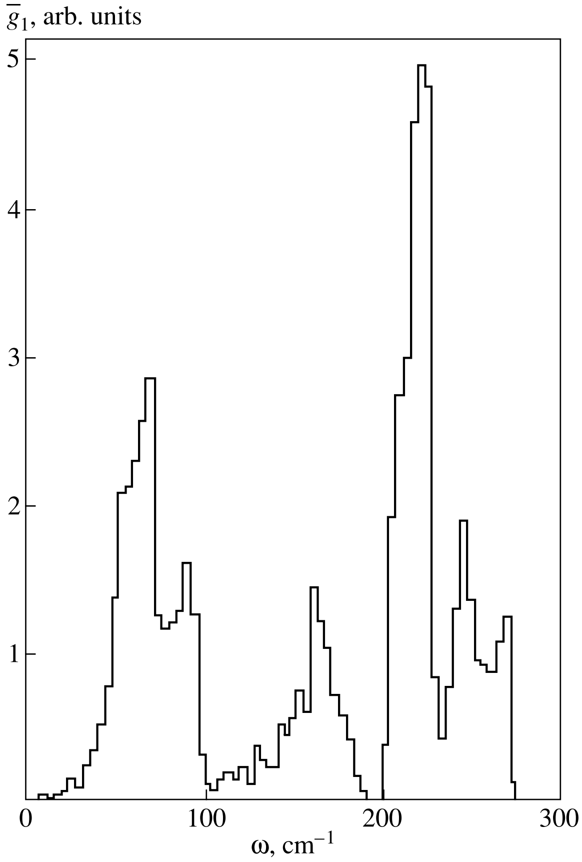

Fig. 2. Density of phonon states $\bar{g}_1$ in pure ZnSe [3].

Here, $\kappa_0(T)$ is the experimental value of thermal conductivity for pure ZnSe (curve *1* in Fig. 1) and the specific heat is calculated from Eq. (2). In calculating the thermal conductivity of ZnSeNi, we identify the phonon relaxation time with $\tau_0(T)$ and include into the heat flux only the contribution of the phonons for which the new scattering mechanism associated with the presence of nickel is inefficient. Therefore, our calculation of the specific heat will take into account only the contribution of the phonons whose frequencies lie outside the interval $\omega_0 - \Delta\omega < \omega < \omega_0 + \Delta\omega$. We finally come to a simple expression for estimating the thermal conductivity of ZnSeNi,

$$\begin{aligned}\kappa(T) &= \kappa_0(T)(1 - I(\omega_0 - \Delta\omega, \omega_0 + \Delta\omega)/I(0, \infty)),\\ I(a, b) &= \int_a^b d\omega\omega^2 g(\omega) v_f^2(\omega)\frac{e^{\hbar\omega/kT}}{(e^{\hbar\omega/kT}-1)^2}.\end{aligned} \tag{3}$$

Equation (3) takes into account the frequency dependence of the acoustic phonon velocity. We simulated this dependence using the relation for the spectrum of a one-dimensional chain: $\nu(q) \sim \sin qa(\omega_{\max}a = \pi/2)$. Therefore, we set $v_f(\omega) \sim \sqrt{1-(\omega/\omega_{\max})^2}$ in Eq. (3).

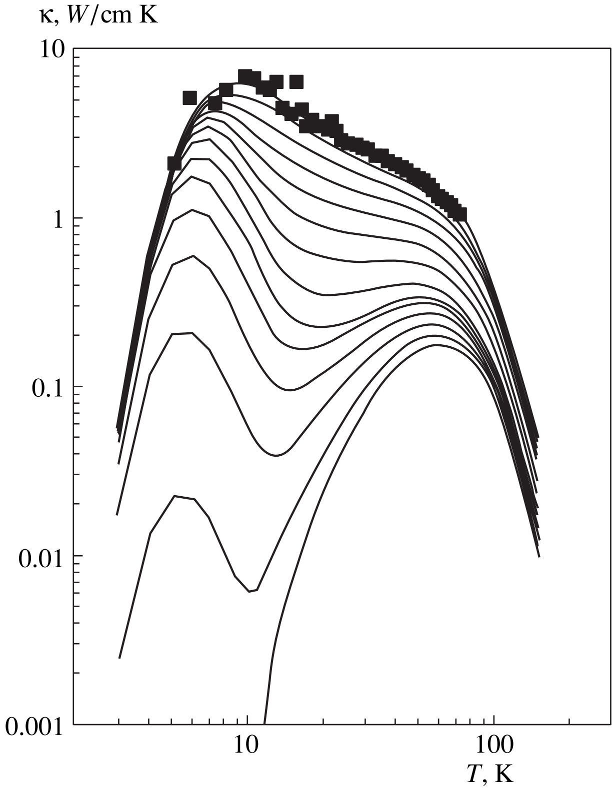

Fig. 3. Temperature dependences of thermal conductivity. Symbols are experimental points for pure ZnSe [2], and solid curves are model calculations. The center of the chosen phonon frequency interval lies at $\omega_0 \cong 68$ K, and the frequency interval halfwidth Δω varies from zero (top curve) to 65 K (bottom curve) in steps of 5 K.

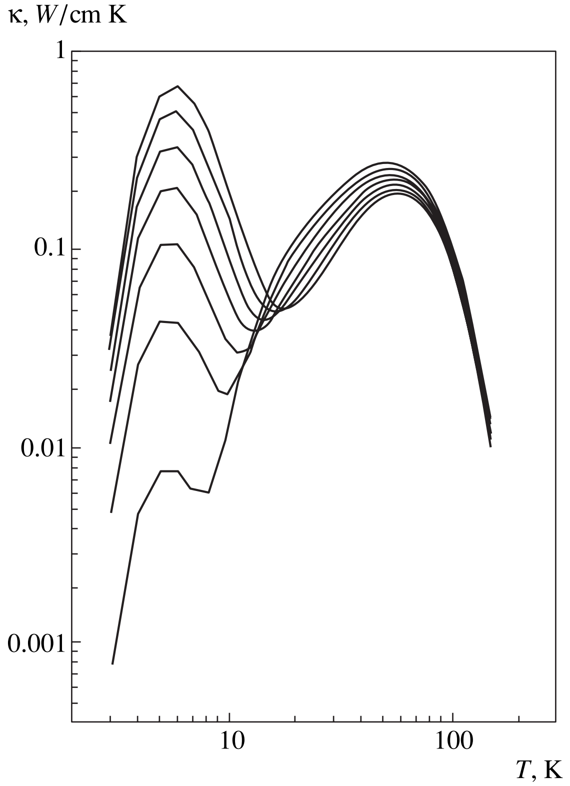

Fig. 4. Temperature dependences of thermal conductivity (calculation). Parameter $\Delta\omega = 55$ K. Parameter ω_0 is varied from 62 (bottom curve) to 74 K (top curve) in 2-K steps.

Equation (3) makes it possible to calculate the thermal conductivity of a phonon system with inclusion of the additional scattering mechanism, whose efficiency in a certain phonon frequency interval is so high as to justify neglect of the contribution from these phonons to the heat flux. Only the thermal conductivity and phonon spectrum of the original system and the frequency interval within which the new scattering mechanism operates need to be known. This frequency interval is determined by two parameters, ω_0 and Δω, which serve as fitting parameters in our phenomenological theory. It is assumed that all significant changes in the phonon spectrum occur in the frequency interval within which the new scattering mechanism is efficient.

We calculated the phonon gas thermal-conductivity by taking pure ZnSe as the starting system (sample 1 [2]). The experimental temperature dependence of thermal conductivity is shown by symbols (filled squares) in Fig. 1. The density of phonon states was taken from [3] (Fig. 2). Our calculations of the specific heat were confined to the low-temperature region and took into account only the acoustic branch of the phonon spectrum. Experiments have shown [2] that the doping of ZnSe with nickel initiates an additional scattering mechanism, which may give rise to a thermal conductivity that is decreased by two orders of magnitude. To describe this effect phenomenologically, we introduce the frequency interval within which phonons undergo anomalously strong scattering. We assume the width of this interval to increase monotonically with nickel concentration. Thus, our model contains two fitting parameters, namely, the position of the center of the interval ω_0 and the interval halfwidth Δω. The results of the model calculations are shown graphically in Figs. 3–5. Figure 3 plots a series of theoretical curves, with each corresponding to the parameter $\omega_0 = 68$ K and to a halfwidth varied from 0 to 65 K in 5-K steps. The calculated curve corresponding to $\Delta\omega = 0$ passes through the experimental points obtained on pure ZnSe. As the parameter Δω increases, a flattening appears in the temperature dependence of thermal conductivity, which then transforms to a clearly pronounced minimum. At $\Delta\omega = 55$ K, the magnitude of thermal conductivity at the minimum is two orders of magnitude lower than that of pure ZnSe. The presence of a characteristic minimum in thermal conductivity can be interpreted as follows. At very low temperatures, where scattering from a boundary is dominant, the phonon mean free path is temperature-independent and the thermal conductivity grows together with the specific heat. The fact is that the phonons excited with increasing temperature have frequencies $\omega < \omega_0 - \Delta\omega$, for which the new mechanism is inefficient. As the temperature increases still further, phonons from the frequency interval $\omega_0 - \Delta\omega < \omega < \omega_0 + \Delta\omega$, which do not contribute to thermal conductivity, will become excited. At the same time, the contribution of phonons with frequencies $\omega < \omega_0 - \Delta\omega$ decreases with increasing temperature because of increased scattering. As a result, thermal conductivity decreases. As the temperature continues to rise, phonons with frequencies $\omega > \omega_0 + \Delta\omega$, for which the new scattering mechanism is inefficient, undergo excitation. Therefore, in this temperature interval, the thermal conductivity passes through a minimum and starts to grow. The depth of the minimum grows with increasing parameter $\Delta\omega$.

Figure 4 presents a series of curves displaying the temperature dependence of thermal conductivity for various values of the parameter ω_0. The curves (from bottom up) were drawn for a halfwidth of the frequency interval $\Delta\omega = 55$ K and for the band center position varied from 62 to 74 K in 2-K steps. As follows from our calculations, as the frequency band center ω_0 moves toward higher frequencies, the position of the minimum in the curve also shifts toward higher temperatures. This is accompanied by an increase in the thermal conductivity at the temperature of the minimum by an order of magnitude.

Figure 5 compares the calculations with experimental data. The top curve (open triangles) is drawn for the frequency interval $22 < \omega < 109$ K. The experimental points [2] refer to sample 3, with a nickel concentration of 3.6×10^{19} cm^{-3}. The bottom curve (filled triangles) corresponds to frequencies $11 < \omega < 125$ K. The experimental data [2] are for sample 4, with a nickel concentration of 1×10^{20} cm^{-3}. In both cases, the center of the chosen frequency interval lies at $\omega_0 \cong 67$ K. Thus, our calculations show that in order to suppress the contribution of thermal phonons to thermal conductivity (and reduce the magnitude of thermal conductivity by two orders of magnitude) at 15 K, a new strong scattering mechanism efficient within a broad phonon frequency interval ($2\Delta\omega \cong 100$ K) has to be initiated. It is difficult to conceive of a reason for which resonant scattering peaks would appear within such a broad frequency interval. Whatmore, on assuming that there is an infinitely high phonon scattering cross section in the frequency interval in question, we obtained too small a width for this interval. Therefore, we believe the conjecture made in [2] as to the thermal conductivity minima in ZnSeNi being due to resonant phonon scattering from nickel-induced modes to be unrealistic. In our opinion, the reason for the suppression of the phonon contribution to thermal conductivity may lie either in the change to some new scattering mechanism that is efficient in the frequency interval in question or in a rearrangement of the phonon spectrum within this frequency interval. Because phonon spectrum rearrangement brings about a change in the density of phonon states, further study of this problem would benefit considerably from measurements of the temperature dependence of the specific heat of nickel-doped ZnSe crystals.

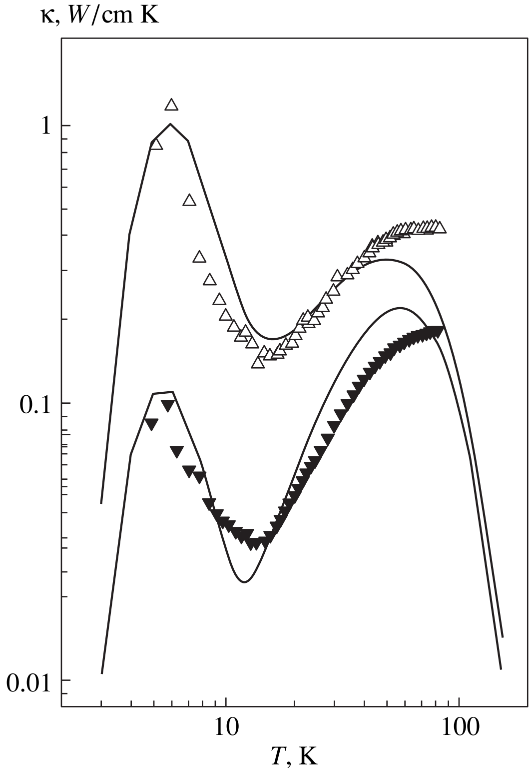

Fig. 5. Temperature dependences of thermal conductivity. Open triangles are experimental points for sample 3 [2] (Ni concentration, 3.6×10^{19} cm^{-3}); the calculated curve corresponds to the chosen phonon frequency interval $22 < \omega < 109$ K. Filled triangles are experimental points for sample 4 [2] (Ni concentration, 1×10^{20} cm^{-3}); the calculated curve corresponds to the chosen frequency interval $11 < \omega < 125$ K.

REFERENCES

1. G. A. Slack, Phys. Rev. B **6** (10), 3791 (1972).
2. V. I. Sokolov and A. T. Lonchakov, Pis'ma Zh. Éksp. Teor. Fiz. **73** (11), 708 (2001) [JETP Lett. **73**, 626 (2001)].
3. K. King, M. Balkonski, and M. A. Nusimovici, Phys. Status Solidi B **72** (1), 229 (1975).

Translated by G. Skrebtsov

Physics of the Solid State, Vol. 45, No. 2, 2003, pp. 240–243. Translated from Fizika Tverdogo Tela, Vol. 45, No. 2, 2003, pp. 231–234.
Original Russian Text Copyright © 2003 by Akimov, Virchenko, Golubev, Kaplyanskiĭ, Kurdyukov, Pevtsov, Shcherbakov.

SEMICONDUCTORS AND DIELECTRICS

Laser-Pulse-Induced Bragg Diffraction Spectrum Rearrangement in Opal–VO_2 Composites

A. V. Akimov, A. V. Virchenko, V. G. Golubev, A. A. Kaplyanskiĭ,
D. A. Kurdyukov, A. B. Pevtsov, and A. V. Shcherbakov
Ioffe Physicotechnical Institute, Russian Academy of Sciences,
Politekhnicheskaya ul. 26, St. Petersburg, 194021 Russia

Received May 16, 2002

Abstract—The Bragg diffraction spectrum of a synthetic opal with pores filled by the vanadium dioxide semiconductor (VO_2) was found to be strongly affected by 0.1-μs-long YAG:Nd laser first-harmonic pulses (1.06 μm). This effect is associated with a structural phase transition in the opal–VO_2 composite, which is accompanied by a strong change in the VO_2 permittivity. *© 2003 MAIK “Nauka/Interperiodica”.*

Optical properties of photonic crystals, i.e., objects with dielectric permittivity modulated with a period close to the light wavelength, are presently generating considerable interest [1]. A photonic band gap (PBG) forms in the spectrum of electromagnetic eigenstates of such crystals, which precludes propagation of photons with energies lying in the PBG through the photonic crystal. These energies depend on the direction of light propagation, and bands originating from Bragg diffraction from a periodic structure appear in the corresponding spectra of light transmission and reflection. Under certain conditions, the PBG may become complete; in this case, light of a photon energy lying within some interval cannot propagate in any direction. The interest in photonic crystals stems from their application potential in light-propagation control [2] and the development of zero-threshold lasers [3] and components of quantum computers [4].

Synthetic opal, representing a periodic ordered close-packed array of amorphous SiO_2 (a-SiO_2) spheres of a submicron diameter, may be currently considered the best studied example of three-dimensional photonic crystals for visible light [5, 6, and references therein]. The voids between the spheres add up to 26% of the total volume. By properly varying the a-SiO_2 sphere diameter (from 0.1 to 1 μm), one can tune the PBG position in energy (from ultraviolet to near infrared). Another possibility of adjusting the PBG position lies in filling the voids between spheres in a controlled manner with various materials, in particular, semiconductors [5, 7]. Filling the opal with semiconductors also results in an increased depth of permittivity modulation in the photonic crystal; this approach is particularly promising in developing a complete three-dimensional PBG [8].

Of particular interest for the purposes of application is possible external control of the PBG position and width in photonic crystals. PBG tuning with an electric field in liquid-crystal-based photonic materials was considered theoretically in [9] and recently tested experimentally in [10, 11]. The PBG position in periodically ordered structures based on monodisperse colloidal dye particles has also been controlled using laser pulses [12]. Recently, the same was reached by varying the temperature of an opal sample filled by nanocrystalline vanadium dioxide (opal–VO_2 composite) [13]. It is well known that VO_2 undergoes a dielectric–metal structural phase transition near $T_c \approx 70°C$ [14], which is accompanied by a strong variation of the dielectric permittivity of VO_2. The latter permits one, by properly changing the sample temperature, to vary the average value and modulation amplitude of the permittivity in the composite, thereby changing the position and width of the PBG. Reversible displacement of a peak in the Bragg reflectance spectrum by 25 nm to shorter wavelengths and back under multiple repetition of the heating–cooling cycles of the sample in the range from room temperature to $T > T_c$ [13] was observed.

This communication reports on the possibility of controlling the PBG position in an opal–VO_2 composite by means of laser pulses. The synthetic opal samples used had a polydomain structure. Single-crystal domains with a highly ordered array of a-SiO_2 spheres 230 ± 5 nm in diameter forming an fcc lattice measured 30 to 100 μm. The samples studied were plates $5 \times 5 \times 0.1$ mm in size cut along a plane close to the (111) opal growth face. The opal–VO_2 composite was prepared by filling the opal matrix pores with a solution of vanadium pentoxide in nitric acid, with V_2O_5 reduced subsequently to VO_2 by high-temperature annealing of the sample in vacuum. This technology made it possible to fill the pores to 80%. X-ray diffraction and Raman studies provided evidence supporting the formation of nanocrystalline vanadium dioxide in the pores of the opal matrix. Characterization of the samples by using

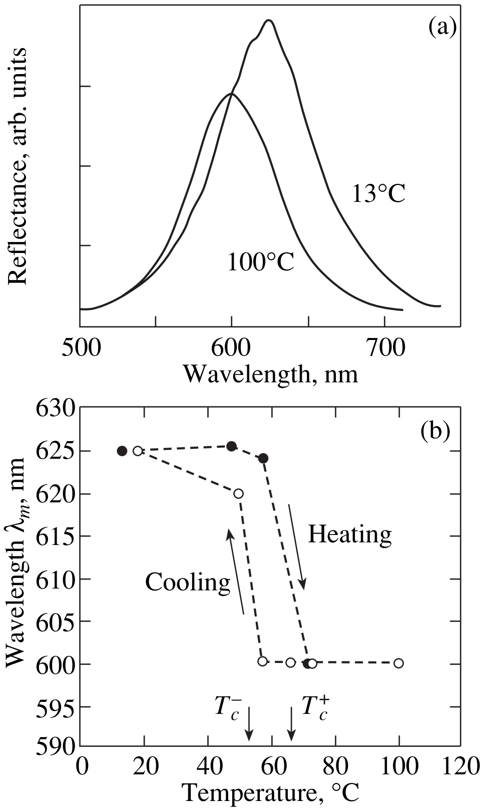

Fig. 1. (a) Stationary Bragg diffraction spectrum from the (111) plane of the opal–VO_2 composite measured at temperatures corresponding to the semiconducting (T = 13°C) and metallic (T = 100°C) VO_2 phases, and (b) temperature dependence of the position of the Bragg diffraction spectrum maximum under slow heating and cooling of a sample. Vertical arrows identify the phase transition temperatures observed in the heating (T_c^+) and cooling (T_c^-) runs.

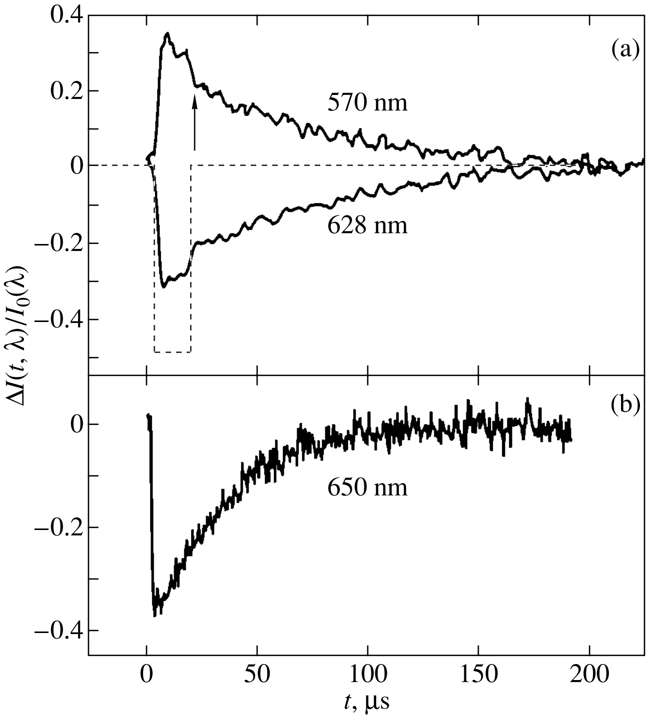

Fig. 2. Evolution of the relative change in Bragg diffraction intensity measured at different wavelengths under laser pulse pumping; (a, b) panels were obtained on different samples of the opal–VO_2 composite. The Bragg diffraction spectrum of the sample corresponding to the (a) panel is presented in Fig. 1a. The dashed line schematically shows the signal expected for an ideal composite structure (see text for explanation). The vertical arrow identifies the jump in intensity in the temporal dependence.

various techniques is described in considerable detail in [13]. Several samples of the opal–VO_2 composite prepared in the same conditions were studied.

Let us turn now to the results of our preliminary stationary studies of the temperature effects; the studies were aimed at characterization of the samples and checking the existence of a phase transition in the material. A collimated beam of light from a halogen lamp was focused on the surface of an opal–VO_2 composite plate at close-to-normal incidence. The reflected light included the mirror-reflected beam from the sample surface and the Bragg-diffracted light from the (111) plane, whose spectrum is a characteristic of the PBG of a photonic crystal. Due to defects present on the sample surface and to the sample face deviating slightly from the opal (111) plane, the mirror-reflected and the Bragg-diffracted beams propagate in slightly different directions, which permitted us to isolate the diffracted component of interest. By using optimal angles of incidence and collection of light and by projecting (by means of a microscope and an optical fiber) the image of a small (≤100 μm, within one domain) region of the sample surface onto the monochromator slit, one could suppress the mirror-reflected beam and measure the reflectance band in the [111] direction; this band related only to Bragg diffraction in the opal–VO_2 composite.

The Bragg diffraction spectra (Fig. 1a) clearly exhibit a 100-nm-wide band peaking at a wavelength λ_m whose position depends on temperature T. As is evident from Fig. 2b, the Bragg diffraction band shifts by $\Delta\lambda_m$ = 25 nm to shorter wavelengths with increasing T. The temperature dependence of the band shift reveals a distinct hysteresis. The observation of this relation in the vicinity of the phase transition and of a hysteresis in the opal–VO_2 composite is due to the nanocrystalline structure of the VO_2 material and correlates with earlier studies of the electrical properties of polycrystalline VO_2 films [15, 16] and of the opal–VO_2 composite [13]. The temperature T_c^+ = 67°C, at which λ_m changes sharply under heating, is shown by a vertical arrow in Fig. 1b. The temperature of the jump in $\lambda_m(T)$ measured in a cooling run is lower, $T_c^- = 53°C$. The $\lambda_m(T)$ hysteresis loop measured on other samples was also in the interval 50–75°C. The slight differences in T_c^+ and T_c^- between various samples can be assigned to uncontrollable variations in the conditions of VO_2 synthesis in the opal pores.

The shift of λ_m in the $T_c^+ - T_c^-$ temperature interval is due to a structural phase transition in VO_2 embedded in the opal pores. Indeed, the position of the Bragg diffraction peak observed in the [111] direction is given by the relation $\lambda_m = 2d\sqrt{\langle\varepsilon\rangle}$, where d is the distance between the sphere-close packing planes in opal and $\langle\varepsilon\rangle$ is the average permittivity of the opal–VO_2 composite. It is known that crystalline VO_2 undergoes a phase transition with increasing T, which is accompanied by a decrease in the real part of the dielectric permittivity from 8.4 to 5.3 [17]. In the opal–VO_2 composite, this effect should obviously reduce $\langle\varepsilon\rangle$ and, accordingly, λ_m. At the same time, the permittivity modulation depth in the opal–VO_2 composite also decreases, which brings about the theoretically predicted decrease in the PBG width and a narrowing of the Bragg diffraction band [18, 19].

We turn now to a discussion of the experiments with pulsed optical excitation, which were performed on the same samples at a fixed temperature. In these experiments, a sample was maintained at room temperature and additionally pumped by 0.1-μs-long YAG:Nd laser first-harmonic pulses ($\lambda = 1.06$ μm, pulse repetition frequency of 1 kHz). We measured the evolution of the change $\Delta I(t, \lambda)$ in the Bragg diffraction spectral intensity in the experimental arrangement employed in the stationary measurements of the temperature behavior. The maximum pulse energy density of the YAG:Nd laser beam on the sample was $J^{\max} \sim 7$ mJ/cm^2; at higher densities, the sample surface underwent damage. No changes in the Bragg diffraction spectrum were observed to occur at excitation densities $J < J^{\min} \approx 2$ mJ/cm^2. The Bragg diffraction spectrum did change when the excitation density increased above the threshold $J^{\min} < J < J^{\max}$. Figure 2a shows the typical behavior of the ratio $\Delta I(t, \lambda)/I_0(\lambda)$ in time, where $I_0(\lambda)$ is the stationary intensity of the reflected light at the wavelength λ in the absence of laser pulses for the sample whose spectrum is displayed in Fig. 1a. Near the maximum of the spectral band ($\lambda \approx \lambda_m$), laser pulses cause a decrease in intensity and, accordingly, $\Delta I(t, \lambda) < 0$, whereas on the short-wavelength wing of the band, we have $\Delta I(t, \lambda) > 0$. This behavior indicates a shortward shift of the Bragg diffraction band similar to that observed to occur with increasing temperature in stationary conditions. This observation, together with the experimentally established threshold in the appearance of the $\Delta I(t, \lambda)$ signal for $J > J^{\min}$, permits one to conclude that laser pulses initiate a phase transition in VO_2 which, similar to the case of sample heating in stationary experiments (Fig. 1), brings about a shift of the Bragg diffraction band to shorter wavelengths.

The $\Delta I(t, \lambda)$ pulses observed in all the samples studied have a steep leading edge whose duration is equal to that of the laser pulses (0.1 μs), followed by a long decay with an average time constant ~100 μs. In one of the samples, a reproducible drop in $|\Delta I(t, \lambda)|$ was observed at $t = 20$ μs on the trailing edge (vertical arrow in Fig. 2a). In the other samples, no such jump was observed at any pump intensity J, with $|\Delta I(t, \lambda)|$ falling off smoothly (Fig. 2b).

The pulsed-laser photon energy exceeds the bandgap width $E_g = 0.8$ eV in semiconducting VO_2. Thus, optical pulses of the YAG:Nd laser are absorbed strongly by the semiconductor filler of the opal and generate free carriers (electrons and holes). The fast relaxation of photoexcited carriers in VO_2 creates phonons; in other words, the local temperature T of the optically excited region near the sample surface increases. If the optical excitation density J is in excess of a certain threshold ($J > J^{\min}$), then $T > T_c^+$ and the material undergoes a phase transition, which brings about a shortward shift of the Bragg diffraction spectrum and, accordingly, the observation of a $\Delta I(t, \lambda)$ signal.

In the ideal uniform case, where the variation of temperature $T(t)$and the phase transition occur simultaneously at all points of the region pumped by laser pulses and involved in the formation of the Bragg spectrum, one should expect the $\Delta I(t, \lambda)$ signal to have a rectangular shape, as shown schematically in Fig. 2a. Indeed, the sharp leading edge of the $\Delta I(t, \lambda)$ signal appears under heating by a laser pulse to $T > T_c^+$; the duration of the constant $\Delta I(t, \lambda)$ signal should be equal to the time required to cool to T_c^-, and the amplitude of $\Delta I(t, \lambda)$ should be determined from the difference in intensity between stationary Bragg diffraction spectra measured in different phases at the corresponding wavelength λ.

The difference of the experimentally observed $\Delta I(t, \lambda)$ signals from the ideal case is accounted for by the fact that laser pulses nonuniformly heat VO_2 at different points of the spatial region producing the Bragg signal. The reason for this obviously lies in the small penetration depth of pulsed laser radiation into the sample. This brings about a nonuniform temperature distribution in depth from the pumped surface. Furthermore, the opal–VO_2 composite system is not uniform both due to the polydomain structure of the opal and in view of the nonuniform thermal contact of nanocrystalline VO_2 in the opal pores with a-SiO_2 spheres. Therefore, when comparatively long laser pulses (0.1 μs) are used, different microscopic regions in VO_2 will heat to different $T > T_c^+$ and cool to the transition temperature T_c^- for different times. As a result, the observed signal will exhibit an essentially smooth falloff with a certain characteristic mean time. As already mentioned, on one of the samples, we succeeded in observing a jump in $\Delta I(t, \lambda)$ at the trailing edge (Fig. 2a); however, this jump was not reproduced in the other opal–VO_2 composite samples (Fig. 2b). This suggests that the difference in the behavior of our samples is associated with the nonuniformity of the opal pore filling by VO_2 and with imperfection of the interfaces between the opal spheres and the nanocrystalline VO_2.

It is important that the observed average decay time of ~100 μs is substantially in excess of the times (shorter than 0.1 μs) seen in similar experiments on the laser-pulse-induced variation of optical characteristics of crystalline VO_2 films [20]. This is apparently connected with the heat removal in the opal–VO_2 composite being considerably slower than that in epitaxial VO_2 films deposited on glass substrates. Such a strong difference in the decay time is in accord with current concepts of the thermal conductivity in disordered and porous objects.

Thus, we have demonstrated laser-pulse-induced rearrangement of the Bragg diffraction spectrum in synthetic opals with pores filled by VO_2. The rearrangement is caused by the dynamic heating of the opal–VO_2 sample and is directly related to the structural phase transition in VO_2. The above results, combined with experiments on the effect of femtosecond-scale laser pulses on the optical constants of crystalline VO_2 films [17, 20], give one grounds to assume that the Bragg spectrum switching upon application of ultrashort laser pulses in photonic opal–VO_2 crystals may occur in times less than 1 ps.

ACKNOWLEDGMENTS

The authors are indebted to A.V. Baryshev, A.V. Il'inskiĭ, M.F. Limonov, A.V. Sel'kin, and E.B. Shadrin for valuable discussions.

This study was supported by the "Low-Dimensional Quantum Structures" program of the RAS; "Fundamental Studies in Physical Sciences" program of the Ministry of Industry, Science, and Technologies of the Russian Federation; and INTAS.

REFERENCES

1. *Photonic Band Gap Materials*, Ed. by C. M. Soukoulis (Kluwer Academic, Dordrecht, 1996), NATO ASI Ser. E, Vol. 315.
2. J. D. Joannopoulos, P. R. Villeneuve, and S. Fan, Nature **386**, 143 (1997).
3. Y. Yamamoto and R. E. Slusher, Phys. Today **46**, 66 (1993).
4. S. Ya. Kilin, Usp. Fiz. Nauk **169**, 507 (1999).
5. V. N. Astratov, V. N. Bogomolov, A. A. Kaplyanskii, *et al.*, Nuovo Cimento D **17**, 1349 (1995).
6. X. Xia, B. Gates, Y. Yin, and Y. Lu, Adv. Mater. **12**, 693 (2000).
7. V. N. Bogomolov, V. G. Golubev, N. F. Kartenko, *et al.*, Pis'ma Zh. Tekh. Fiz. **24** (8), 90 (1998) [Tech. Phys. Lett. **24**, 326 (1990)].
8. K. Busch and S. John, Phys. Rev. E **58**, 3896 (1998).
9. K. Busch and S. John, Phys. Rev. Lett. **83**, 967 (1999).
10. Q.-B. Meng, C.-H. Fu, S. Hayami, *et al.*, J. Appl. Phys. **89**, 5794 (2001).
11. Y. Shimoda, M. Ozaki, and K. Yoshino, Appl. Phys. Lett. **79**, 3627 (2001).
12. G. Pan, R. Kesavamoorthy, and S. A. Asher, Phys. Rev. Lett. **78**, 3860 (1997).
13. V. G. Golubev, V. Yu. Davydov, N. F. Kartenko, *et al.*, Appl. Phys. Lett. **79**, 2127 (2001).
14. N. F. Mott, *Metal–Insulator Transitions* (Taylor and Francis, London, 1974; Nauka, Moscow, 1979).
15. A. A. Bugaev, B. P. Zakharchenya, and F. A. Chudnovskiĭ, *Metal–Semiconductor Phase Transition and Its Application* (Nauka, Leningrad, 1979).
16. E. B. Shadrin and A. V. Il'inskiĭ, Fiz. Tverd. Tela (St. Petersburg) **42**, 1092 (2000) [Phys. Solid State **42**, 1126 (2000)].
17. A. Cavalleri, Cs. Toth, C. W. Siders, *et al.*, Phys. Rev. Lett. **87**, 237401 (2001).
18. H. S. Sözüer, J. W. Haus, and R. Inguva, Phys. Rev. B **45**, 13962 (1992).
19. V. G. Golubev, V. A. Kosobukin, D. A. Kurdyukov, *et al.*, Fiz. Tekh. Poluprovodn. (St. Petersburg) **35**, 710 (2001) [Semiconductors **35**, 680 (2001)].
20. M. F. Becker, A. B. Buckman, R. M. Walser, *et al.*, J. Appl. Phys. **79**, 2404 (1996).

Translated by G. Skrebtsov

Physics of the Solid State, Vol. 45, No. 2, 2003, pp. 244–247. Translated from Fizika Tverdogo Tela, Vol. 45, No. 2, 2003, pp. 235–237.
Original Russian Text Copyright © 2003 by Bochkova, M. Volnyanskiĭ, D. Volnyanskiĭ, Shchetinkin.

SEMICONDUCTORS AND DIELECTRICS

Color Centers in Lead Molybdate Crystals

T. M. Bochkova, M. D. Volnyanskiĭ, D. M. Volnyanskiĭ, and V. S. Shchetinkin

Dnepropetrovsk National University, Naukova ul. 13, Dnepropetrovsk, 49050 Ukraine

e-mail: mdvoln@ff.dsu.dp.ua

Received February 20, 2002; in final form, June 6, 2002

Abstract—Color center formation in $PbMoO_4$ crystals, originating from nonstoichiometric batch composition, BaO and Bi_2O_3 additions, high-temperature annealing of crystals, and UV illumination, is discussed. Additional optical absorption bands are identified. The photochromism of the crystals is shown to be due to charge exchange, $Pb^{2+} + Mo^{6+} \rightleftharpoons Pb^{3+} + Mo^{5+}$, of the centers. © *2003 MAIK “Nauka/Interperiodica”.*

1. INTRODUCTION

Lead molybdate ($PbMoO_4$) is a well-known acoustooptical material with scheelite structure. The yellowish color of crystals grown in air and the photochromic effect in crystals bleached by annealing at a low oxygen partial pressure prevent the application of $PbMoO_4$ in optical-instrument engineering. Suppression of these phenomena requires both refinement of crystal growth techniques [1–4] and elucidation of the nature of the defects responsible for the main bands in the optical absorption spectra of $PbMoO_4$. While the optical properties and carrier transfer in a lead molybdate have been discussed in the literature [5–10] and various conjectures bearing on the color center structure have been put forward, there is still no consensus on this point.

It is known that compounds with scheelite-like structure exhibit vacancy disorder because of off-stoichiometry and oxygen exchange with ambient air. It has been suggested that $PbMoO_4$ is deficient in molybdenum ions because of MoO_3 having a higher vapor pressure than PbO and of the mobility of molybdenum ions being higher than that of lead ions [5, 6]. By contrast, some properties of $PbMoO_4$ are accounted for by a deficiency of lead on the crystal lattice [7].

In this paper, we attempted to analyze, within a common framework, some experimental studies into the effect of dopants and of the off-stoichiometry of the main components, illumination by UV light, and high-temperature annealing in air on color center formation in $PbMoO_4$ single crystals.

2. EXPERIMENT

$PbMoO_4$ crystals were grown by the Czochralski method from platinum crucibles in air. The starting materials were OSCh-grade MoO_3 and PbO oxides taken both in the stoichiometric ratio and with deviations from stoichiometry toward a molybdenum excess of up to 1.5 mol %. BaO and Bi_2O_3 oxides were added as dopants in amounts of up to 1 wt %. The crystals were annealed in a muffle furnace at 1175 K in air. A 200-W mercury lamp with a water solution of $CuSO_4$ used as a filter served to illuminate the samples with UV light. The optical transmittance spectra were measured with a Specord M-40 spectrophotometer at room temperature.

3. RESULTS AND DISCUSSION

The $PbMoO_4$ crystals grown by us using the Czochralski technique from batches with different component ratios, from 50 mol % MoO_3 + 50 mol % PbO to 51.5 mol % MoO_3 + 48.5 mol % PbO, were yellowish and colored by UV light at room temperature (Fig. 1). After illumination, the optical visible absorption spectra exhibit three broad bands peaking at 25 100, 23 000, and 17 300 cm^{-1} (390, 435, 580 nm). We denote them by *A*, *B*, and *C*, respectively. The photochromic effect is reversible; annealing at 625 K indeed restores the crystals to their original state.

While no noticeable effect of excess molybdenum on photoinduced absorption was observed, the original spectra obtained on crystals with different contents of MoO_3 and PbO differ from one another. Figure 1 presents optical transmittance spectra of crystals grown from a batch with stoichiometric composition and from a batch with the maximum deviation from stoichiometry. As is evident from the difference spectra, the molybdenum excess brings about additional absorption of light in the region of bands *B* and *C*.

High-temperature annealing in air performed at 1175 K on all crystals with different MoO_3 and PbO contents results in a considerable increase in light

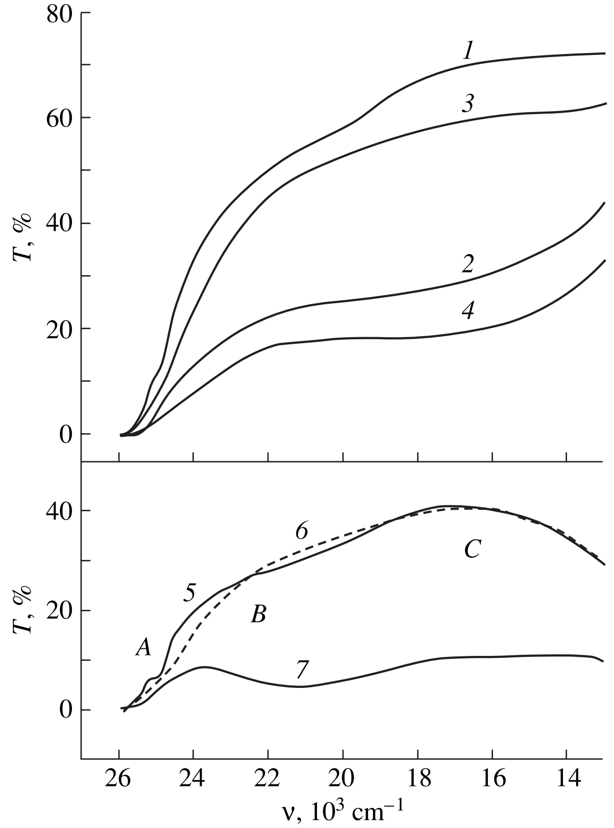

Fig. 1. Optical transmittance of $PbMoO_4$ crystals (*1, 3*) grown from a batch of stoichiometric composition and (*2, 4*) of a composition of 51.5 mol % MoO_3 + 48.5 mol % PbO (*1, 2*) after annealing at 950 K and (*3, 4*) after UV illumination. (*5–7*) Difference spectra: *5 = 1 – 3*, *6 = 2 – 4*, and *7 = 1 – 2*. Sample thickness, 10.2 mm.

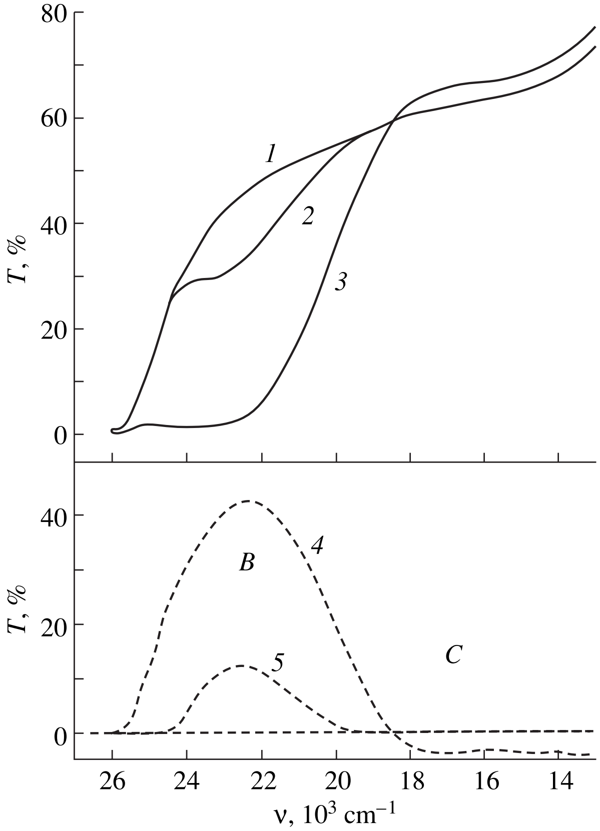

Fig. 2. Optical transmittance of $PbMoO_4$ crystals grown from a batch of stoichiometric composition: (*1*) starting crystal, (*2*) after 7 h of annealing at 1200 K, and (*3*) after 87 h of annealing at 1200 K. (*4, 5*) Difference spectra: *4 = 1 – 3* and *5 = 1 – 2*. Sample thickness, 10.8 mm.

absorption in the region of band *B* and a decrease in the intensity of band *C* (Fig. 2). Crystals with a small MoO_3 excess also exhibit a decrease in absorption in the region of band *A*.

Earlier studies [5, 8] reported on heat treatments of $PbMoO_4$ crystals in various media with the purpose of influencing the thermodynamic activity of Mo and Pb ions and producing samples with defects of various types originating from off-stoichiometric component ratios. Investigation of the electrical conductivity of annealed $PbMoO_4$ samples [5] has indicated that there is a Frenkel-type disorder on the Mo sublattice of original nominally stoichiometric crystals that is caused by an MoO_3 deficiency. The coloring of the crystals is due to holes associating with Mo (Pb) vacancies or with acceptor defects produced by substitution of Mo^{6+} by Pb^{2+} (Pb^{4+}) ions. A study of the charge and mass transport carried out in [6] provided supportive evidence for the interaction (association) of defects on the Mo sublattice with holes, for instance, the formation of complexes including two Mo vacancies and one hole or molybdenum and oxygen vacancies.

There are also other hypotheses on the nature of the centers responsible for the coloring of $PbMoO_4$. For instance, it was assumed in [9] that the absorption near 435 nm (band *B*) is due to the presence of Mn^{3+} ions. Ballmann [8] showed, however, that absorption band *B* is not related to iron group ions. Ballmann believes that the existence of this band is due rather to Pb^{3+} centers; an analysis of the optical absorption at 30, 80, and 300 K of $PbMoO_4$ crystals, which were annealed at 1025 K and an oxygen pressure of ≤1.3 Pa and subjected subsequently to x-ray irradiation, revealed two characteristic absorption bands in the visible range (390, 575 nm); Ballmann assigns these bands to Mo^{5+} ions.

A study of the luminescence of $PbMoO_4$ crystals led to the conclusion that the center responsible for the luminescence in these crystals is the Pb^{3+}–MoO_4^{3-} complex [10].

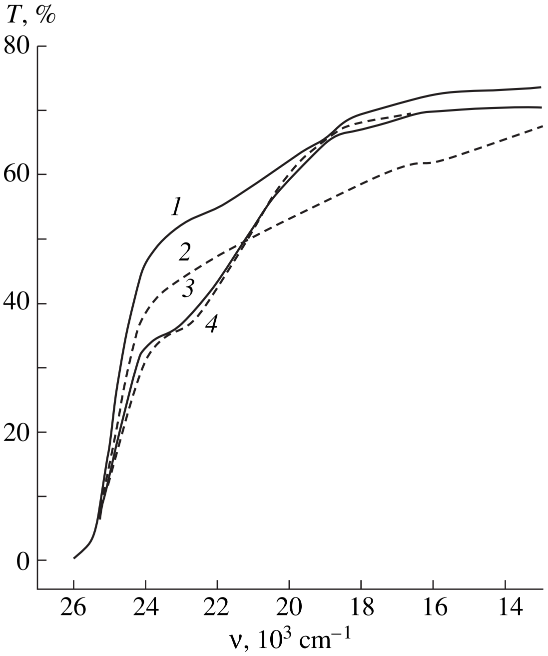

Fig. 3. Photochromic effect in (*1, 2*) $PbMoO^4$–1 wt % Ba and (*3, 4*) $PbMoO^4$–0.3 wt % Bi crystals (*1, 3*) before and (*2, 4*) after UV illumination. Sample thickness, 12.4 mm.

An analysis of our experiments on the influence of compositional nonstoichiometry, of high-temperature annealing in air, and of the photochromic effect corroborates the conjectures put forward in [8, 10] and, thus, permits us to take them as a basis for a model of local centers in $PbMoO_4$.

The Pb^{3+} hole paramagnetic center (ground state $^2S_{1/2}$) has been repeatedly observed using EPR in various compounds. For instance, Pb^{3+} centers produced by irradiation with x-rays were studied in KCl : Pb in and $CaWO_4$: Pb [11, 12]. The assignment of these centers is corroborated by the presence of hyperfine interaction of the unpaired 6*s* electron of the Pb^{3+} ion with the nuclear magnetic moment of the ^{207}Pb isotope (nuclear spin $I = 1/2$), and investigation of the superhyperfine interaction of Pb^{3+} with the ligands indicates a strong effect of covalent bonding.

Mo^{5+} centers in $PbMoO_4$ crystals have also been detected using EPR [13]. The absorption bands associated with Mo^{5+} centers may be related both to intracenter transition involving the unfilled *d* shell and to charge transfer [14].

Thus, we believe that a deviation from compositional stoichiometry toward an excess of MoO_3 decreases the charge of part of the Mo^{6+} ions in the course of the reaction taking place spontaneously in $PbMoO_4$ during crystal growth [13]:

$$Mo^{6+} + e^- \longrightarrow Mo^{5+}.$$

This becomes manifest in the appearance of absorption bands *A* and *C*. Furthermore, the MoO_3 excess is, at the same time, a deficiency of PbO, which accounts for the increase in charge on part of the lead ions to Pb^{3+} and brings about the formation of band *B*.

High-temperature annealing in air may initiate the formation of Pb^{3+} by the reaction

$$4Pb^{2+} + O_2 \rightleftarrows 4Pb^{3+} + 2O^{2-}.$$

In this case, absorption band *B* grows strongly in intensity. At the same time, the intensity of bands *A* and *C* decreases. An assumption was put forward in [15] that the presence of oxygen vacancies in the nearest environment of Mo^{6+} favors electron capture with the formation of Mo^{5+} centers in scheelite crystals. It is likely that annealing in air could decrease the concentration of oxygen vacancies and, hence, of the Mo^{5+} ions through interaction with oxygen in the environment:

$$4Mo^{5+} + O_2 \rightleftarrows 4Mo^{6+} + 2O^{2-}.$$

The photochromic effect can be described in terms of our model by the reaction

$$Mo^{6+} + Pb^{2+} \rightleftarrows Mo^{5+} + Pb^{3+},$$

which accounts for the appearance of all three absorption bands *A*, *B*, and *C* after sample illumination by UV light.

We also studied the optical transmittance of $PbMoO_4$ crystals with BaO and Bi_2O_3 additions. Judging from the close similarity of their ionic radii, we believe that Ba^{2+} and Bi^{3+} should isomorphically substitute for Pb^{2+} ions, with Bi^{3+} playing the part of the Pb^{3+} center. Figure 3 presents the spectral response of the optical transmittance of $PbMoO_4$–Ba^{2+} and $PbMoO_4$–Bi^{3+} crystals before and after UV illumination.

A comparison of the photochromic effect in the original and barium-doped crystals shows that the introduction of Ba^{2+} reduces photoinduced coloring. Doping with Ba^{2+} obviously exerts a stabilizing effect on the lead sublattice. The spectrum of bismuth-doped crystals exhibits a strong absorption band near 23 000 cm^{-1} (band *B*) but no photochromism. This supports our model for color centers in lead molybdate crystals.

REFERENCES

1. N. Senguttuvan, S. M. Babu, and R. Dhanasekaran, Mater. Chem. Phys. **49** (2), 120 (1997).
2. H. C. Zeng, L. C. Lim, H. Kumagai, and M. Hirano, J. Cryst. Growth **171** (3), 493 (1997).
3. L. C. Lim, L. K. Tan, and H. C. Zeng, J. Cryst. Growth **167** (3), 686 (1996).
4. H. C. Zeng, J. Cryst. Growth **171** (1), 136 (1997).
5. A. Ya. Neiman, A. A. Afanasiev, L. M. Fedorova, *et al.*, Phys. Status Solidi A **83**, 153 (1984).

6. A. Ya. Neĭman, L. M. Fedorova, and A. A. Afanas’ev, Izv. Akad. Nauk SSSR, Neorg. Mater. **23** (5), 811 (1986).
7. W. van Loo, J. Solid State Chem. **14** (2), 359 (1975).
8. W. Ballmann, Krist. Tech. **15**, 367 (1980).
9. H. Bernhardt, Phys. Status Solidi A **45**, 353 (1978).
10. W. van Loo, Phys. Status Solidi A **27**, 565 (1975); Phys. Status Solidi A **28**, 227 (1975).
11. D. Shoemaker and J. L. Kolopus, Solid State Commun. **8** (6), 435 (1970).
12. G. Born, A. Hofstaetter, and A. Schermann, Phys. Status Solidi **87** (1), 255 (1970).
13. E. G. Reut and A. I. Ryskin, Opt. Spektrosk. **35** (5), 862 (1973).
14. D. T. Sviridov, R. K. Sviridova, and Yu. F. Smirnov, *Optical Spectra of Transition Metal Ions in Crystals* (Nauka, Moscow, 1976).
15. G. H. Azerbayejani and A. Merlo, Phys. Rev. A **137**, 489 (1965).

Translated by G. Skrebtsov

Physics of the Solid State, Vol. 45, No. 2, 2003, pp. 248–252. Translated from Fizika Tverdogo Tela, Vol. 45, No. 2, 2003, pp. 238–241.
Original Russian Text Copyright © 2003 by Shelykh, Melekh.

SEMICONDUCTORS AND DIELECTRICS

$CeAlO_3$ Crystals: Preparation and Study of Their Electrical and Optical Characteristics

A. I. Shelykh and B. T. Melekh

Ioffe Physicotechnical Institute, Russian Academy of Sciences,
Politekhnicheskaya ul. 26, St. Petersburg, 194021 Russia

Received May 16, 2002; in final form, June 6, 2002

Abstract—Crystals of cerium aluminate with perovskite structure were obtained using the cold-crucible technique. The electrical and optical properties of cerium aluminate were studied in air in the range 300–1300 K. The main characteristics of $CeAlO_3$ at $T = 300$ K are a follows: electrical conductivity $\sigma = 10^{-7}$ S/cm, dielectric permittivity $\varepsilon = 3000–10000$ (both measured at a frequency of 1000 Hz), thermal band-gap width $\Delta E = 2.3 \pm 0.5$ eV, and optical width $\delta E = 2.65 \pm 0.25$ eV, which decreases at a rate of -0.62×10^{-3} eV/K with increasing temperature in the 300- to 1500-K interval. © *2003 MAIK "Nauka/Interperiodica".*

1. INTRODUCTION

Oxygen compounds of cerium of various valences were studied systematically in [1–5]. These publications describe the preparation of oxides using ceramic technology, the structural and physicochemical properties of a number of perovskite-type compounds, and original techniques employed in their investigation.

The interest in oxides with this type of structure stems primarily from their electrical characteristics; some of these oxides exhibit ferroelectric properties and offer promise as solid electrolytes with ionic conduction, sensors for gaseous media, and catalysts.

This communication reports on the preparation of cerium aluminate through cold-crucible melting and directional crystallization of this oxide. The optical and dielectric characteristics of the crystals obtained were studied. The possibility of using optical transmittance measurements to determine the temperature and deduce the phase transition kinetics in these oxides was investigated.

2. EXPERIMENTAL TECHNIQUE

The technology employed in melting high-melting-point oxides and growing their crystals using cold-crucible technology was described in [6, 7].

The electrical characteristics were derived from the capacity and electrical conductivity of plane-parallel plates of the oxide measured with an E 7-8 digital meter at 1000 Hz. The dielectric permittivity was derived, using the conventional method, from the capacity and geometric dimensions of the sample assuming the oxide to be homogeneous. If the conduction of a material is partially or completely ionic, the sample may become inhomogeneous in the course of measurements. This phenomenon for ionic conduction was analyzed in [8], where the magnitude and temperature dependence of the capacity were shown to correlate with the conductivity.

Optical measurements were carried out with a DMR-4 monochromator and an SF-16 spectrophotometer. The refractive index and its variation with temperature in the range 300–1500 K were determined from the deflection of a light beam with a wavelength 0.63 μm (LG-78 laser) by a prismatic sample. The phase transitions were detected by measuring the temperature dependence of light transmittance. The light flux was chopped with a frequency of 1000 Hz before passing through the sample under study. This removed the effect of radiation of the heated sample on the light detector and provided the possibility of lock-in measurement of electrical signals. The measurements were conducted in air in the temperature range from room temperature to 1300 K. Crossed-polarizer studies were also carried out. In this case, the signal from the light receiver arrived only if the sample under study was optically anisotropic. The signal was minimal if, for instance, the sample was driven by temperature to the optically isotropic cubic structure.

A heater was used for measurements conducted under temperature variation; it consisted of a hollow rod of SiC-based material with electrodes at the ends and was 18 cm long with outer and inner diameters of 1.4 and 0.5 cm, respectively. Two mutually perpendicular channels drilled in the central part of the rod increased its Ohmic resistance, and a local heating of up to 1500 K could be reached by passing a current through the rod. One of the channels housed the sample under study, and the other served to pass the light or supply electrical contact to the sample. The sample temperature was measured with a thermocouple mounted along the rod axis.

1063-7834/03/4502-0248$24.00 © 2003 MAIK "Nauka/Interperiodica"

The quantities to be measured (temperature and optical transmittance) were fed to an LKD-4 *X–Y* recorder.

3. RESULTS AND DISCUSSION

3.1. Crystal Characteristics

The $CeAlO_3$ samples obtained by directional crystallization from melt had a columnar structure form from intergrown crystals that was up to 0.5 cm in length and about 0.3 cm in diameter. The lattice parameters were $a = 3.772$ Å and $c = 3.804$ Å [9]. The ceramic samples are characterized by the values $a = 3.78$ Å [4] and 3.77 Å [10].

According to the chemical formula of the oxide, the cerium cation has a charge of +3 and is a paramagnetic ion in this state. As expected, cerium aluminate is paramagnetic and is attracted to a permanent magnet. This cerium valence is corroborated by optical measurements, which reveal a characteristic absorption peak at a wavelength of 4.55 μm [9]. X-ray line shift measurements yield a cerium valence of 2.98 ± 0.02 for the starting sample and 3.01 ± 0.02 after its thermal treatment (1100 K, 5 h) in ambient air [11].

Repeated heating and cooling of crystals within the range 300–1500 K does not change their properties markedly. The crystals differ in this respect from ceramic samples, which become oxidized in these conditions and decompose into CeO_2 and Al_2O_3 [5].

The crystals prepared from melt apparently contain, as do polycrystalline samples, an oxygen excess with respect to the stoichiometric composition [5]. This may be associated with a possible valence change of part of the cations from Ce^{3+} to Ce^{4+}. Annealing of a crystal in vacuum at 1900 K brings its composition closer to stoichiometric and reduces the Ce^{4+} concentration. After the annealing, the optical band-gap width of cerium aluminate increases slightly and the dark green color of its crystals grows paler. A similar effect of annealing on the color, albeit in an oxidizing medium, has been observed in studies of a partially reduced CeO_2 oxide single crystal [12]. Annealing in an oxidizing medium reduces the number of Ce^{3+} ions available in the partially reduced CeO_2 and, as a consequence, brings the oxide closer to stoichiometric composition and bleaches the crystals. These observations imply a connection between the color characteristics of the oxides containing cerium and off-stoichiometry in their composition, which originates from the mixed valence of cerium.

3.2. Electrical Conductivity

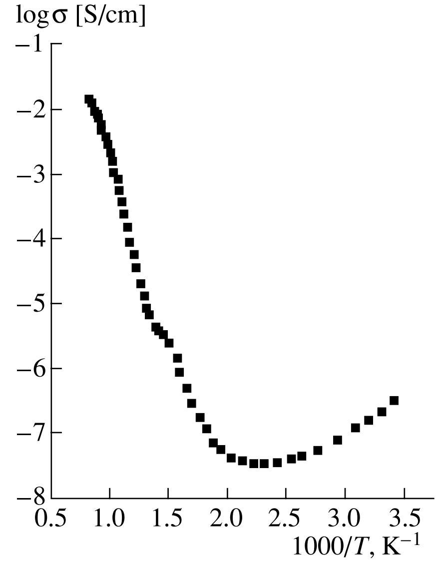

Fig. 1. Temperature dependence of the electrical conductivity of crystalline cerium aluminate.

Figure 1 plots the temperature dependence of the electrical conductivity of a cerium aluminate sample. Its slope in the region of intrinsic conduction yields $\Delta E(0) = 2.3 \pm 0.5$ eV (including the scatter between different samples) for the thermal band-gap width, which corresponds to a temperature $T = 0$ for a linear $\Delta E(T)$ relation [13]. This band gap decreases with increasing temperature as $\Delta E(T) = \Delta E(0) + \alpha T$, where the coefficient $\alpha = -0.62 \times 10^{-3}$ eV/K was derived from optical transmittance measurements carried out on the cerium aluminate within the range 300–1300 K. Knowing that $\Delta E(T)$, one can estimate the intrinsic carrier concentration and, if the electrical conductivity is available, determine the carrier mobility. For $T = 1000$ K, $m^* = m_e$, and $\Delta E(0) = 2.3$ eV, this estimation yields a value of about 1 cm^2/V s for the mobility in cerium aluminate.

In this analysis, the oxide conductivity was assumed to retain its electronic character throughout the temperature range covered. However, the existence of ionic conduction in $BaCeO_3$, $SrCeO_3$ [14–16], and CeO_2 [12] suggests that the ionic component can also appear in the electrical conductivity of $CeAlO_3$, particularly, at high temperatures (about 1000 K). This conclusion finds supportive evidence in our studies of the dielectric characteristics of cerium aluminate at high temperatures in comparison with the ionic-conductivity oxides $BaCe_{0.8}Y_{0.2}O_3$ and CeO_2.

3.3. Dielectric Characteristics

Figure 2 presents the dielectric permittivity of $CeAlO_3$ measured in the region 250–1000 K. At low temperatures (up to ~170 K), $\varepsilon = 16$ and grows slightly with temperature. In the 250- to 600-K interval, the dielectric permittivity reaches as high as a few thousands and is only weakly temperature dependent. Starting from 600 K up, ε exhibits an activated behavior,

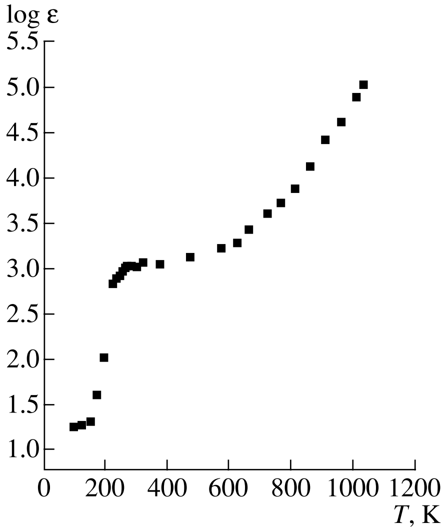

Fig. 2. Temperature dependence of the permittivity of crystalline cerium aluminate measured at 1000 Hz.

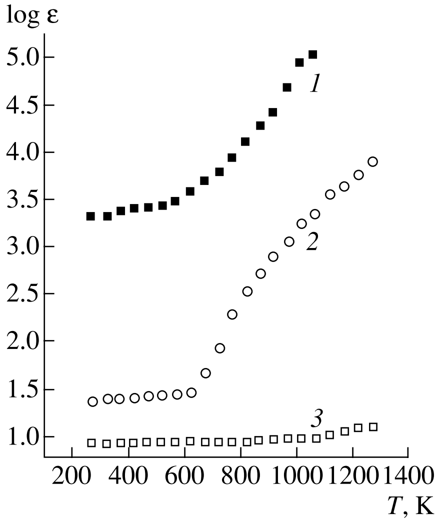

Fig. 3. Temperature dependence of the permittivity of (*1*) $CeAlO_3$, (*2*) CeO_2 oxide with ionic conductivity, and (*3*) Al_2O_3 oxide with electronic conductivity.

which is characterized by an activation energy close to that of electrical conductivity. As already mentioned, this feature is characteristic of ionic conduction.

It is of interest to compare the permittivity of cerium aluminate with those of Al_2O_3 and the ionic conductor CeO_2. Our measurements show that in the high-temperature domain, the permittivities of the CeO_2 and $CeAlO_3$ oxides behave in a similar way (Fig. 3).

Measurements carried out on ceramic samples show the permittivity of cerium aluminate to rise with temperature, reaching as high as 9, 209, and 1796 at temperatures of 93, 298, and 549 K, respectively [10]. In [4], the values ε = 14–300 were reported to be obtained and the thermal conditions maintained in the preparation of ceramic samples were shown to affect the permittivity of this oxide.

3.4. Optical Characteristics

The spectral response of transmittance $\tilde{T}$ in the energy interval 0.15–3 eV and that of the reflectance at 1–5 eV of cerium aluminate were studied in [9]. It was shown that the absorption band at 0.3 eV is due to the Ce^{3+} ion. The optical band-gap width δE and the refractive index n were estimated as 2.7 eV and 2.3, respectively.

In the present communication, the refractive index was determined for light with a wavelength of 0.63 μm on a prismatic sample in the 300- to 1500-K region to be $n = 2.13$, with $\Delta n/\Delta T = 5.5 \times 10^{-6}\ K^{-1}$.

The optical characteristics of the oxide depend on its stoichiometric composition. This factor, as well as light scattering, which varies with temperature, is responsible for a certain scatter in the corresponding experimental data.

The transmittance spectrum of a 0.03-cm-thick cerium aluminate plate and its variation following annealing of the oxide in vacuum at $T = 1900$ K are displayed in Fig. 4. The band gap increases as the sample approaches stoichiometric composition as a result of annealing in vacuum. The optical band gap for cerium aluminate with different deviations from stoichiometry was found to be $\delta E = 2.65 \pm 0.25$ eV. As follows from measurements of the transmittance spectrum performed at various temperatures, the optical band gap width

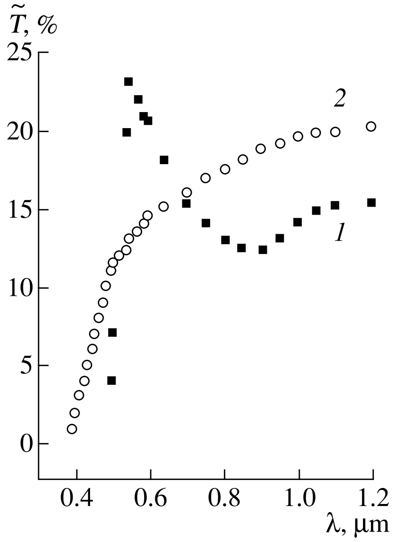

Fig. 4. Spectral response of the transmittance of a 0.03-cm-thick cerium aluminate crystal obtained after annealing (*1*) in air and (*2*) in vacuum.

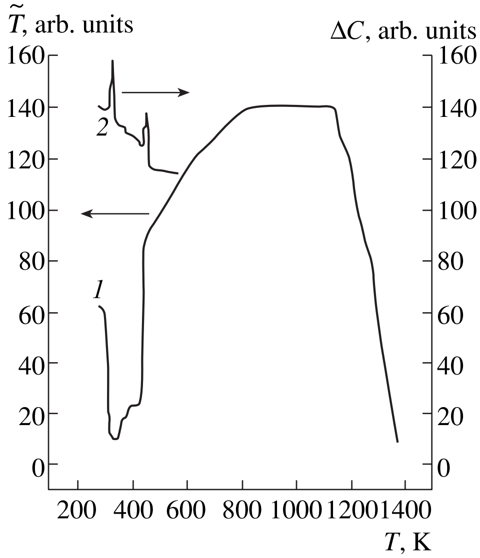

Fig. 5. (*1*) Temperature dependences of the optical transmittance of cerium aluminate. The measurements were conducted in the crossed-polarizer arrangement; λ = 0.77 μm. (*2*) Calorimetric measurements performed on a fused sample [17].

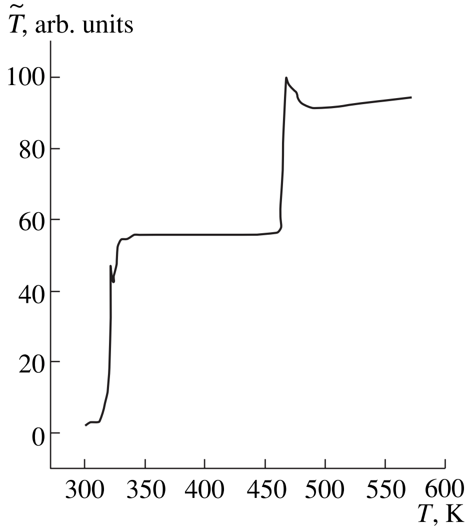

Fig. 6. Effect of phase transitions on the optical transmittance of cerium aluminate. The 0.03-cm-thick crystal was preliminarily annealed in vacuum at 2100 K. The measurements were conducted in the crossed-polarizer arrangement at the wavelength 0.63 μm.

decreases with increasing temperature in the 300- to 1300-K region, with $d(\delta E)/dT = -0.62 \times 10^{-3}$ eV/K.

3.5. Phase Transitions

Cerium aluminate was established to undergo several phase transformations. Observations made using an optical microscope revealed that one of the transformations occurs at 360 K and is associated with changes in the lattice symmetry, whereas another is a transition to an isotropic cubic phase at 1250 K [3]. Differential scanning calorimetry measurements carried out in the region 300–800 K indicate two phase transitions, taking place at 310 and 450 K, respectively [17].

In this study, the above phase transitions in the oxide were established by measuring its light transmittance at wavelengths of 0.63 and 0.77 μm in the region 300–1500 K. The results of the measurements are displayed in graphical form in Fig. 5, which also presents calorimetric measurements [17]. The temperature dependence of transmittance exhibits anomalies associated with phase transformations. The decrease in transmittance caused by the transition of the oxide to the optically isotropic cubic structure starts from 1170 K and comes to completion at 1400 K, with a hysteresis of about 100 K being seen. At 440 K, the transmittance is observed to change sharply with a slight (a few degrees) hysteresis. A change in optical transmittance is also observed to occur in a phase transition at about 310 K. To return the oxide to the starting state after this transition, the sample has to be maintained at room temperature for 1–2 h. This transition becomes progressively sharper as the oxide approaches the stoichiometric composition under annealing in vacuum (Fig. 6).

ACKNOWLEDGMENTS

This study was partially supported by the Russian Foundation for Basic Research (project no. 00-03-32476) and INTAS (grant no. 99-00636).

REFERENCES

1. A. I. Leonov and É. K. Keler, Izv. Akad. Nauk. SSSR, Ser. Khim., No. 11, 1905 (1962).
2. A. I. Leonov, *High-Temperature Chemistry of Oxygen Compounds of Cerium* (Nauka, Leningrad, 1970).
3. A. I. Leonov, *High-Temperature Microscope to Observe Melting, Polymorphous Transformations of Crystalline Materials and Other Processes* (Tsentr. Inst. Tekh.-Ékonom. Inform., Moscow, 1961), No. 17.
4. V. A. Ioffe, A. I. Leonov, and I. S. Yanchevskaya, Fiz. Tverd. Tela (Leningrad) **4** (7), 1788 (1962) [Sov. Phys. Solid State **4**, 1282 (1962)].
5. V. E. Shvaĭko-Shvaĭkovskiĭ, A. I. Leonov, and A. I. Shelykh, Neorg. Mater. **1** (5), 737 (1965).
6. M. A. Borik, E. E. Lomonova, V. V. Osiko, and A. M. Prokhorov, in *Problems of Crystallography* (Nauka, Moscow, 1987).
7. B. T. Melekh, Yu. N. Filin, I. V. Korkin, *et al.*, in *Proceedings of 5th International Conference on Crystals: Growth, Properties, Real Structure, and Application* (Aleksandrovsk, 2001), Vol. 1, p. 59.

8. A. B. Lidiard, in *Handbuch der Physik*, Ed. by S. Flugge (Springer, Berlin, 1957; Inostrannaya Literatura, Moscow, 1962), p. 246.
9. A. I. Shelykh, N. S. Zhdanovich, B. T. Melekh, *et al.*, Fiz. Tverd. Tela (St. Petersburg) **36** (3), 817 (1994) [Phys. Solid State **36**, 448 (1994)].
10. M. L. Keith and R. Roy, Am. Mineral. **39** (1–2), 1 (1954).
11. A. E. Sovestnov, V. A. Shaburov, I. A. Smirnov, *et al.*, Fiz. Tverd. Tela (St. Petersburg) **36** (4), 1140 (1994) [Phys. Solid State **36**, 620 (1994)].
12. I. V. Vinokurov, É. N. Zonn, and V. A. Ioffe, Neorg. Mater. **3** (6), 1012 (1967).
13. J. S. Blakemore, *Semiconductor Statistics* (Pergamon, Oxford, 1962; Mir, Moscow, 1964).
14. R. C. T. Slade and N. Singh, Solid State Ionics **46** (1–2), 111 (1991).
15. V. P. Gorelov and D. S. Zubankova, Elektrokhimiya **28** (6), 944 (1992).
16. A. L. Samgin, Neorg. Mater. **36** (8), 979 (2000).
17. V. M. Egorov, Yu. M. Baĭkov, N. F. Kartenko, *et al.*, Fiz. Tverd. Tela (St. Petersburg) **40** (11), 2109 (1998) [Phys. Solid State **40**, 1911 (1998)].

Translated by G. Skrebtsov

Physics of the Solid State, Vol. 45, No. 2, 2003, pp. 253–258. Translated from Fizika Tverdogo Tela, Vol. 45, No. 2, 2003, pp. 242–247.
Original Russian Text Copyright © 2003 by Randoshkin, Vasil'eva, Plotnichenko, Pyrkov, Saletskiĭ, Sysoev, Galkin, Dudorov.

Optical Absorption in Cobalt-Containing Single-Crystal Epitaxial Films of Gadolinium Gallium Garnets

V. V. Randoshkin*, N. V. Vasil'eva, V. G. Plotnichenko***, Yu. N. Pyrkov***, A. M. Saletskiĭ****, N. N. Sysoev****, A. M. Galkin****, and V. N. Dudorov***

** Joint Laboratory of Magnetooptoelectronics, Institute of General Physics, Russian Academy of Sciences, Mordovian State University, Bol'shevistkaya ul. 68, Saransk, 430000 Russia*

*** Institute of General Physics, Russian Academy of Sciences, ul. Vavilova 38, Moscow, 119991 Russia*

**** Research Center of Fiber Optics, Institute of General Physics, Russian Academy of Sciences, ul. Vavilova 38, Moscow, 119991 Russia*

***** Moscow State University, Vorob'evy gory, Moscow, 119899 Russia*

e-mail: antonv@aha.ru

Received June 10, 2002

Abstract—Cobalt-containing single-crystal garnet films are grown by liquid-phase epitaxy from supercooled $PbO–B_2O_3$- and $Bi_2O_3–B_2O_3$-based solution melts on $Gd_3Ga_5O_{12}$ substrates. It is shown that cobalt in the films is in a trivalent state. Upon introduction of GeO_2 into the initial solution melt, cobalt transforms into a bivalent state. It is revealed that the absorption spectrum of the grown films exhibits two broad bands in the wavelength ranges 450–800 and 900–1800 nm. Each of these bands contains three components. The spin–orbit splitting of the observed bands is determined. © *2003 MAIK "Nauka/Interperiodica".*

1. INTRODUCTION

In single-crystal garnet films synthesized by liquid-phase epitaxy from a supercooled solution melt, the valence of crystal-forming ions can be controlled by the introduction of different additives into the solution melt (see, for example, [1]). Specifically, the valence of cobalt ions in epitaxial single-crystal garnet films changes upon introducing GeO_2 into the solution melt [2]. Note that cobalt-containing single crystals are very promising for use as saturable filters in infrared (IR) lasers [3]. This is associated with the fact that the transmission spectra of these crystals exhibit a broad absorption band in the wavelength range $\lambda = 1.3–1.6$ μm.

The purpose of the present work was to analyze the possibility of varying the valence of cobalt ions in epitaxial single-crystal garnet films and to investigate optical absorption in the wavelength range from 0.2 to 2.5 μm.

This work is a continuation of our recent study [2] on the optical absorption of bivalent and trivalent cobalt ions in single-crystal films of gadolinium gallium garnet. These films were grown by liquid-phase epitaxy from supercooled $PbO–B_2O_3$- and $PbO–B_2O_3–GeO_2$-based solution melts.

2. THE GROWTH OF FILMS

Cobalt-containing films were grown on $Gd_3Ga_5O_{12}$ (GGG) substrates with the (111) orientation from $PbO–B_2O_3$- (**I**), $PbO–B_2O_3–GeO_2$- (**II**), $Bi_2O_3–B_2O_3$- (**III**), and $Bi_2O_3–B_2O_3–GeO_2$-based (**IV**) solution melts in a platinum crucible. In the absence of GeO_2 in the solution melt, cobalt occurs predominantly in a trivalent state in order to provide charge compensation [1]. Only a small amount of Co^{2+} ions can form to compensate for the charge of Pb^{4+} and Pt^{4+} impurity ions transferring from the solution melt into the film. Platinum passes into the solution melt due to dissolution of the crucible material. Upon introduction of GeO_2 into the solution, cobalt ions should transform into the bivalent state to compensate for the charge of Ge^{4+} ions incorporated mainly into the tetrahedral sublattice of the garnet structure.

The composition of solution melts **I**–**IV** was characterized by the following molar ratios.

For **I**,

$$R_1 = (Ga_2O_3 + Co_3O_4)/Gd_2O_3,$$

$$R_2 = PbO/B_2O_3,$$

$$R_3 = (Gd_2O_3 + Ga_2O_3 + Co_3O_4)/(Gd_2O_3 + Ga_2O_3 + Co_3O_4 + PbO + B_2O_3),$$

$$R_4 = Ga_2O_3/Co_3O_4.$$

For **II**,

$$R_1 = (Ga_2O_3 + GeO_2 + Co_3O_4)/Gd_2O_3,$$

$$R_2 = PbO/B_2O_3,$$

$$R_3 = (Gd_2O_3 + Ga_2O_3 + GeO_2 + Co_3O_4)/(Gd_2O_3 + Ga_2O_3 + GeO_2 + Co_3O_4 + PbO + B_2O_3),$$

Table 1. Molar ratios of the components in solution melts

Solution melt	R_1	R_2	R'_2	R_3	R'_3	R_4
I	14.42	16.03	–	0.08	–	9.00
II	30.77	16.03	–	0.15	–	20.35
III	1.11	–	15.92	–	0.14	9.00
IV	2.34	–	15.92	–	0.20	20.14
V	14.42	16.03	–	0.08	–	–
VI	1.11	–	15.92	–	0.14	–

Table 2. Growth parameters for epitaxial garnet films

Sample no.	T_g, °C	t_g, min	$2h$, μm	f_g, μm/min
I-1	985	5	5.8	0.58
I-2	956	5	10.3	1.03
I-3	931	5	6.2	0.63
I-4	904	5	4.3	0.43
I-5	877	5	2.3	0.23
I-6	937	60	92.3	0.77
II-1	906	5	1.98	0.20
II-2	889	5	2.6	0.26
II-3	859	5	3.3	0.33
II-4	822	5	2.3	0.23
II-5	874	120	44.6	0.19
III-1	1015	5	22.2	2.2
III-2	996	5	23.8	2.4
III-3	977	5	22.6	2.3
III-4	960	5	17.7	1.8
III-5	943	5	14.5	1.4
III-6	952	5	70.8	7.1
III-7	931	5	35.1	3.5
III-8	914	5	27.8	2.8
III-9	1003	15	29.3	0.98
III-10	952	15	87.5	2.9
IV-1	990	5	1.3	0.13
IV-2	963	5	9.1	0.91
IV-3	937	5	13.8	1.37
IV-4	953	15	27.6	0.92
IV-5	948	40	59.4	0.74
V-1	1017	10	28.4	1.42
V-2	1005	13	43.4	1.67
V-3	987	10	30.5	1.52
V-4	971	11	20.8	0.95
VI-1	925	15	16.2	0.54
VI-2	912	15	22.8	0.76
VI-3	902	15	32.8	1.1

$$R_4 = (Ga_2O_3 + GeO_2)/Co_3O_4.$$

For **III**,

$$R_1 = (Ga_2O_3 + Co_3O_4)/Gd_2O_3,$$

$$R'_2 = Bi_2O_3/B_2O_3,$$

$$R'_3 = (Gd_2O_3 + Ga_2O_3 + Co_3O_4)/(Gd_2O_3 + Ga_2O_3 + Co_3O_4 + Bi_2O_3 + B_2O_3),$$

$$R_4 = Ga_2O_3/Co_3O_4.$$

For **IV**,

$$R_1 = (Ga_2O_3 + GeO_2 + Co_3O_4)/Gd_2O_3,$$

$$R'_2 = Bi_2O_3/B_2O_3,$$

$$R'_3 = (Gd_2O_3 + Ga_2O_3 + GeO_2 + Co_3O_4)/(Gd_2O_3 + Ga_2O_3 + GeO_2 + Co_3O_4 + Bi_2O_3 + B_2O_3),$$

$$R_4 = (Ga_2O_3 + GeO_2)/Co_3O_4.$$

The films grown from solution melts **I**–**IV** were yellowish green, greenish blue, green, and blue colored, respectively. Table 1 lists the molar ratios for the solution melts used in growing the epitaxial films. The molar ratios for PbO–B_2O_3 (**V**) [4] and Bi_2O_3–B_2O_3 (**VI**) solution melts [5], from which the films of nominal composition $Gd_3Ga_5O_{12}$ were grown, are also given in Table 1 for comparison.

3. EXPERIMENTAL TECHNIQUE

The total thickness $2h$ of the studied films on both sides of the substrate was determined by weighing the substrate prior to and after the epitaxial growth [4–6]. We ignored the difference in the densities of the grown film and the substrate.

The transmission spectra of the films were measured on a Lambda 900 (Perkin-Elmer) spectrophotometer in the wavelength range 0.2–2.5 μm at room temperature. The absorption spectra of the films were calculated from the transmission spectra of the substrates with the grown films by subtracting the absorption by the substrate. The growth parameters for the studied films are presented in Table 2, where T_g, t_g, f_g, and $2h$ are the temperature, time, growth rate, and film thickness, respectively. Roman numerals refer to the solution melt, and Arabic numerals refer to the number for films sequentially grown from the relevant solution melt. Note that, for sample **III**-6, which was grown immediately after homogenization of the solution melt, the growth rate of the film was maximum and amounted to 7.1 μm/min.

4. RESULTS AND DISCUSSION

Figure 1 shows the absorption spectra of the GGG substrate (curve *0*) and films grown from solution melts **I**, **III**, **V**, and **VI** (curves *1–4*, respectively). These spectra exhibit absorption peaks that can be attributed to impurity and dopant ions. As follows from the comparison of curves *0, 1,* and *3,* the absorption peak at a wavelength of 280 nm is associated with Pb^{2+} ($6s^2$) impurity ions. This is in agreement with the results obtained by Scott and Page [7], who assigned this peak to the $^1S_0 \longrightarrow {}^3P_1$ electron transition.

The spectrum of the film grown from solution melt **I** contains two broad absorption bands in the wavelength ranges 540–800 and 900–1700 nm and a narrow absorption band with a maximum at approximately 390 nm (Table 3). Reasoning from the inferences drawn by Wood and Remeika [8], these bands can be assigned to Co^{3+} dopants.

Each of these broad bands consists of three components with maxima at 570, 625, 680 and 1100, 1265, 1630 nm, respectively.

A comparison of curves *0, 2,* and *4* (Fig. 1) shows that the absorption peak centered at a wavelength ~290 nm is associated with Bi^{3+} ($6s^2$) impurity ions (the $^1S_0 \longrightarrow {}^3P_1$ electron transition [1]).

A broad absorption band in the range 900–1700 nm and a narrow absorption band with a maximum at about 400 nm in the spectrum of the film grown from solution melt **III** are attributed to Co^{3+} dopants. The second absorption band in the wavelength range 520–740 nm is due to the $^4A_2 \longrightarrow {}^4T_1(^4P)$ electron transition in the tetrahedral Co^{2+} ion [8]. For films grown from solution melt **III**, the charge compensation is provided by Pt^{4+} impurity ions.

For films grown from solution melt **III**, each of the two broad bands (in the ranges 900–1700 nm for Co^{3+} and 520–740 nm for Co^{2+}) also contains three components, whose parameters are given in Table 3.

According to the data obtained in [8], the absorption peak centered at about 1100 nm can be assigned to the $^5E \longrightarrow {}^5T_2$ electron transition in the Co^{3+} ions incorporated into the tetrahedral sublattice of the garnet structure. The absorption peaks with maxima at 680 and 390 nm should be attributed to the electron transitions $^1A \longrightarrow {}^1T_1$ and $^1A_1 \longrightarrow {}^1T_2$, respectively, in the Co^{3+} ions involved in the octahedral sublattice. Finally, the absorption peak centered at about 625 nm should be assigned to the $^5E \longrightarrow {}^5T_2$ electron transition in the Co^{3+} ions contained in the dodecahedral sublattice (Table 3).

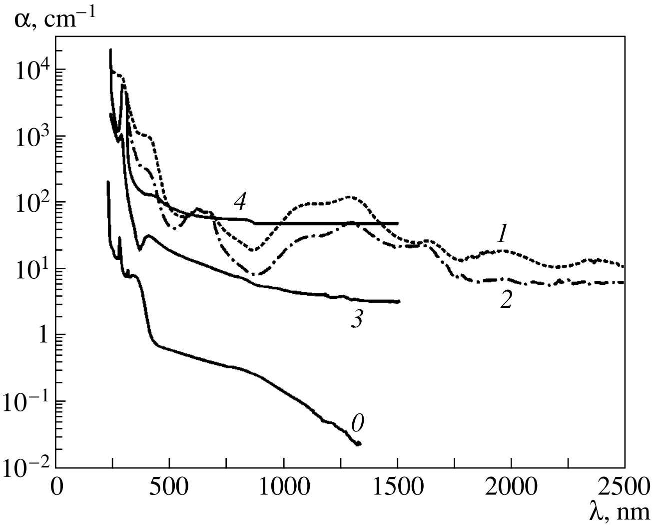

Fig. 1. Absorption spectra of (*1*) **I**-1, (*2*) **III**-3, (*3*) **V**-3, and (*4*) **VI**-2 samples and (*0*) the GGG substrate. The sample numbering corresponds to that in Table 2.

It can be seen from the comparison of curves *1* and *2* (Fig. 1) that, in the wavelength range from 0.7 to 1.5 μm, the absorption spectrum of the film grown from solution melt **I** lies above the absorption spectrum of the film grown from solution melt **III**. Therefore, we can optimize the growth parameters with the aim of preparing films with a specified optical absorption coefficient.

The absorption spectra of the films grown from solution melt **I** at different temperatures are shown in Fig. 2 (see also Table 2). It can be seen that, as the growth temperature decreases, the optical absorption coefficient α increases over the entire temperature range covered. This correlates with an increase in the cobalt distribution coefficient (which is less than unity) due to further supercooling of the solution melt. The dependences of the absorption coefficient α on the growth temperature T_g for characteristic absorption peaks of the Co^{3+} ions are depicted in Fig. 3. As is clearly seen, these dependences are almost linear and can be described by the linear functions given in Fig. 3. Consequently, the dependences obtained can be used to determine the temperatures required to grow films with specified absorption coefficients.

Figure 4 shows the absorption spectra of the films grown from solution melts **I**, **II**, and **V** (curves *1–3*, respectively) and the spectrum of the GGG substrate (curve *0*). It can be seen that, upon introduction of GeO_2 into the solution melt, both broad bands become all the more broadened, whereas a weak absorption band associated with Co^{3+} ions (λ = 390 nm) incorporated into the octahedral sublattice disappears. On this basis, we can conclude that cobalt transforms into the bivalent

Table 3. Positions of the maxima of the absorption bands and their assignment in the transmission spectra of cobalt-containing films and crystals

Solution melt	Range of absorption bands	Positions of the maxima of the optical bands	Spin–orbit splitting of the bands	Electron transition [8]
$PbO–B_2O_3$ (**I**)	540–800 nm	570, 625, 680 nm	2800 cm^{-1}	625 nm ($^5E \longrightarrow {}^5T_2$)
	(18500–12500 cm^{-1})	(17500, 16000, 14700 cm^{-1})		Dodecahedron Co^{3+}
				680 nm ($^1A_1 \longrightarrow {}^1T_1$)
				Octahedron Co^{3+}
	900–1700 nm	1100, 1265, 1630 nm	2970 cm^{-1}	1100 nm ($^5E \longrightarrow {}^5T_2$)
	(11100–5900 cm^{-1})	(9100, 7900, 6130 cm^{-1})		Tetrahedron Co^{3+}
	390 nm (25600 cm^{-1})			390 nm ($^1A_1 \longrightarrow {}^1T_2$)
				Octahedron Co^{3+}
	280 nm (35600 cm^{-1})			280 nm ($^1S_0 \longrightarrow {}^3P_1$)
				Pb^{2+} ($6s^2$)
$PbO–B_2O_3–GeO_2$ (**II**)	500–770 nm	573, 613, 657 nm	2300 cm^{-1}	613 nm ($^4A_2 \longrightarrow {}^4T_1(^4P)$)
	(20000–13000 cm^{-1})	(17500, 16300, 15200 cm^{-1})		Tetrahedron Co^{2+}
	1060–1760 nm	1295, 1425, 1625 nm	1570 cm^{-1}	1425 nm ($^4A_2 \longrightarrow {}^4T_1(^4F)$)
	(9400–5700 cm^{-1})	(7720, 7020, 6150 cm^{-1})		Tetrahedron Co^{2+}
	280 nm (35600 cm^{-1})			280 nm ($^1S_0 \longrightarrow {}^3P_1$)
				Pb^{2+} ($6s^2$)
$Bi_2O_3–B_2O_3$ (**III**)	520–740 nm	575, 613, 651 nm	2040 cm^{-1}	613 nm ($^4A_2 \longrightarrow {}^4T_1(^4P)$)
	(19200–13500 cm^{-1})	(17400, 16300, 15360 cm^{-1})		Tetrahedron Co^{2+}
	900–1700 nm	1100, 1290, 1630 nm	2970 cm^{-1}	1100 nm ($^5E \longrightarrow {}^5T_2$)
	(11100–5900 cm^{-1})	(9100, 7750, 6130 cm^{-1})		Tetrahedron Co^{3+}
	400 nm (25000 cm^{-1})			
				400 nm ($^1A_1 \longrightarrow {}^1T_2$)
				Octahedron Co^{3+}
	290 nm (34500 cm^{-1})			290 nm ($^1S_0 \longrightarrow {}^3P_1$)
				Bi^{3+} ($6s^2$)
$Bi_2O_3–B_2O_3–GeO_2$ (**IV**)	450–741 nm	573, 613, 657 nm	2300 cm^{-1}	613 nm ($^4A_2 \longrightarrow {}^4T_1(^4P)$)
	(22200–13500 cm^{-1})	(17500, 16300, 15200 cm^{-1})		Tetrahedron Co^{2+}
	1100–1800 nm	1295, 1425, 1625 nm	1570 cm^{-1}	1425 nm ($^4A_2 \longrightarrow {}^4T_1(^4F)$)
	(9100–5560 cm^{-1})	(7720, 7020, 6150 cm^{-1})		Tetrahedron Co^{2+}
	290 nm (34500 cm^{-1})			290 nm ($^1S_0 \longrightarrow {}^3P_1$)
				Bi^{3+} ($6s^2$)
Spinel crystal $MgAl_2O_4 : Co^{2+}$ (4×10^{19} ion/cm^3)	490–680 nm	549, 583, 624 nm	2180 cm^{-1}	
	(20400–14700 cm^{-1})	(18210, 17150, 16030 cm^{-1})		
	1050–1660 nm	1230, 1340, 1520 nm	1520 cm^{-1}	
	(9500–6000 cm^{-1})	(8100, 7460, 6580 cm^{-1})		
Silica glass: Co^{2+} [9]		19700, 16500, 14500 cm^{-1}	5200 cm^{-1}	
		8000, 6300, 5300 cm^{-1}	2700 cm^{-1}	
Crystalline quartz: Co^{2+} [9]		18500, 17100, 15600 cm^{-1}	2900 cm^{-1}	
		7700, 6700, 5700 cm^{-1}	2000 cm^{-1}	

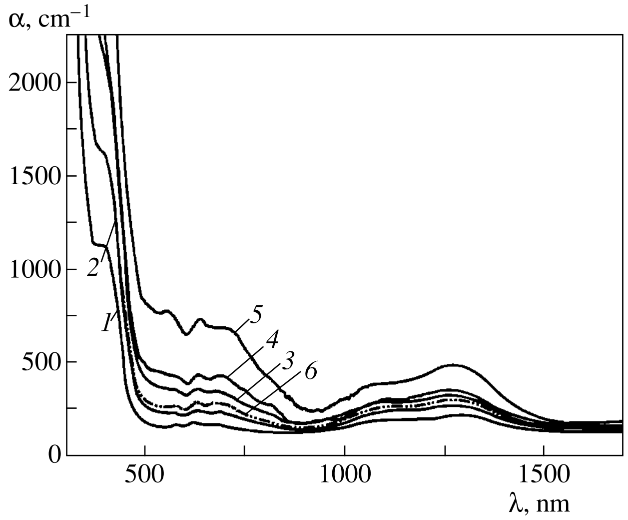

Fig. 2. Absorption spectra of (*1*) **I**-1, (*2*) **I**-2, (*3*) **I**-3, (*4*) **I**-4, (*5*) **I**-5, and (*6*) **I**-6 samples. The sample numbering corresponds to that in Table 2.

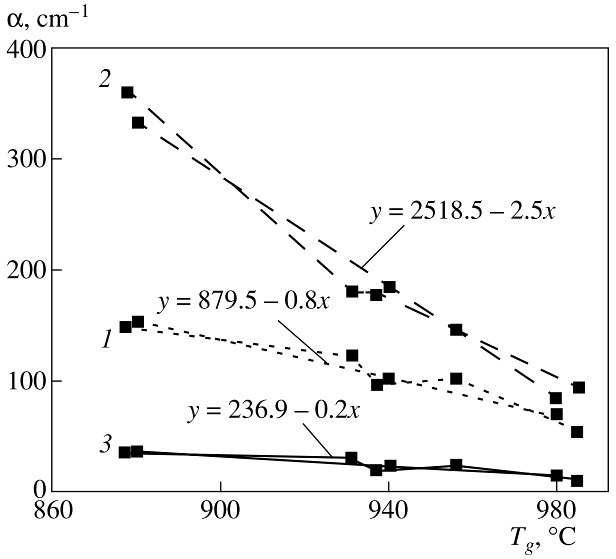

Fig. 3. Dependences of the absorption coefficient α for films grown from solution melt **I** at wavelengths λ = (*1*) 1071, (*2*) 1265, and (*3*) 1630 nm.

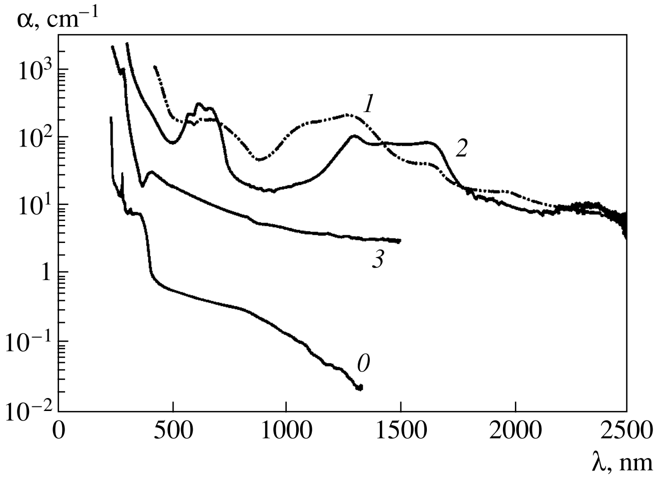

Fig. 4. Absorption spectra of (*1*) **I**-6, (*2*) **II**-5, and (*3*) **V**-3 samples and (*0*) the GGG substrate. The sample numbering corresponds to that in Table 2.

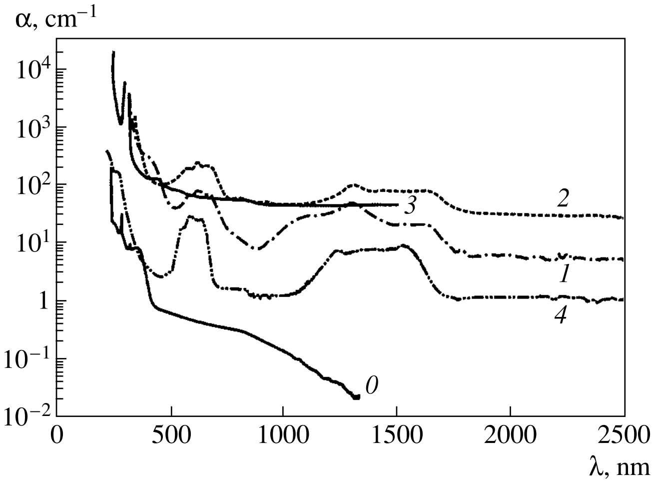

Fig. 5. Absorption spectra of (*0*) the GGG substrate, (*1*) **III**-3, (*2*) **IV**-5, and (*3*) **VI**-2 samples and (*4*) Co^{2+}-doped $MgAl_2O_4$ spinel. The sample numbering corresponds to that in Table 2.

state. Table 3 lists the positions of the maxima of the first triplet, which is broadened toward the short-wavelength range and, consequently, is located in the range 500–770 nm, and the maxima of the second triplet, which is shifted to the long-wavelength range (1060–1760 nm).

Figure 5 depicts the absorption spectra of the GGG substrate (curve *0*) and the films grown from solution melts **III**, **IV**, and **VI** (curves *1–3*, respectively), as well as the absorption spectrum of the Co^{2+}-doped $MgAl_2O_4$ spinel (curve *4*). It can be seen that, upon introduction of GeO_2 into the solution melt, the first triplet shifts to the short-wavelength range 450–741 nm, whereas the second triplet broadens toward the long-wavelength range 1100–1800 nm. Reasoning from the results obtained in [8], we assigned the absorption peaks with maxima at approximately 613 and 1425 nm to the electron transitions $^4A_2 \longrightarrow {}^4T_1(^4P)$ and $^4A_2 \longrightarrow {}^4T_1(^4F)$, respectively, in the Co^{2+} ions involved in the tetrahedral sublattice of the garnet structure.

The absorption spectrum of the Co^{2+}-doped $MgAl_2O_4$ spinel contains two absorption bands in the ranges 490–680 and 1050–1660 nm. Each of these two absorption bands is split into three components (Table 3). It is evident that the absorption bands of Co^{2+} ions in epitaxial films are broader than those of single-crystal spinel.

The spin–orbit splittings of the levels for films grown from solution melts **II** and **IV** are identical and equal to 2300 and 1570 cm^{-1}. Moreover, the spin–orbit splittings are equal to 2970 and 2800 cm^{-1} for films grown from solution melt **I**, 2970 and 2040 cm^{-1} for films grown from solution melt **III**, and 2180 and 1520 cm^{-1} for Co^{2+}-doped spinel. Note also that, according to [9], the spin–orbit splittings are 5200 and 2700 cm^{-1} for Co^{2+}-doped silica glass and 2900 and 2000 cm^{-1} for crystalline Co^{2+}-doped quartz.

5. CONCLUSIONS

Cobalt-containing garnet films of compositions $Gd_3Ga_5O_{12} : Co^{3+}$ and $Gd_3(Ga,Ge)_5O_{12} : Co^{2+}$ were grown for the first time by liquid-phase epitaxy from $PbO–B_2O_3$- and $Bi_2O_3–B_2O_3$-based solution melts.

The results obtained in this work can be summarized as follows.

(i) Upon incorporation of GeO_2 into the solution melt, cobalt in the grown films transforms into the bivalent state and occupies the tetrahedral sublattice of the garnet structure.

(ii) The absorption spectra of epitaxial films containing bivalent and trivalent cobalt ions exhibit two broad bands in the near-IR range. Each of these bands involves three components.

(iii) The absorption bands of tetrahedral Co^{2+} ions in epitaxial films are broader than those in single-crystal spinel.

ACKNOWLEDGMENTS

We would like to thank A.V. Vasil’ev, M.I. Belovolov, and V.A. Mikhaĭlov for their assistance in the experiments and for their participation in discussing the results.

REFERENCES

1. V. V. Randoshkin and A. Ya. Chervonenkis, *Applied Magnetooptics* (Énergoatomizdat, Moscow, 1990).
2. V. V. Randoshkin, N. V. Vasil’eva, V. G. Plotnichenko, and Yu. N. Pyrkov, Pis’ma Zh. Tekh. Fiz. **26** (23), 55 (2000) [Tech. Phys. Lett. **26**, 1053 (2000)].
3. B. I. Galagan, E. A. Godovikova, B. I. Denker, *et al.*, Kvantovaya Élektron. (Moscow) **26** (3), 189 (1999).
4. V. V. Randoshkin, N. V. Vasil’eva, A. V. Vasil’ev, *et al.*, Fiz. Tverd. Tela (St. Petersburg) **43** (9), 1594 (2001) [Phys. Solid State **43**, 1659 (2001)].
5. V. V. Randoshkin, N. V. Vasil’eva, V. G. Plotnichenko, *et al.*, Pis’ma Zh. Tekh. Fiz. **26** (10), 22 (2000) [Tech. Phys. Lett. **26**, 412 (2000)].
6. V. V. Randoshkin, A. M. Belovolov, M. I. Belovolov, *et al.*, Kvantovaya Élektron. **25** (3), 233 (1998).
7. G. B. Scott and J. L. Page, J. Appl. Phys. **48** (3), 1342 (1977).
8. D. L. Wood and J. P. Remeika, J. Chem. Phys. **46** (9), 3595 (1967).
9. M. A. El’yashevich, *Spectra of Rare-Earth Elements* (Gostekhizdat, Moscow, 1953).

Translated by N. Korovin

Physics of the Solid State, Vol. 45, No. 2, 2003, pp. 259–265. Translated from Fizika Tverdogo Tela, Vol. 45, No. 2, 2003, pp. 248–253.
Original Russian Text Copyright © 2003 by Shevchenko, Izotov.

DEFECTS, DISLOCATIONS, AND PHYSICS OF STRENGTH

Dislocation-Induced Photoluminescence in Silicon Crystals of Various Impurity Composition

S. A. Shevchenko and A. N. Izotov

Institute of Solid-State Physics, Russian Academy of Sciences,
Chernogolovka, Moscow oblast, 142432 Russia

Received May 14, 2002

Abstract—The effect of oxygen on the dislocation-induced photoluminescence (DPL) spectra at 4.2 K is studied in silicon crystals with different impurity compositions subjected to plastic deformation at temperatures above 1000°C. A strong effect of doping impurities on the DPL spectra is observed for concentrations above 10^{16} cm^{-3}. It is shown that the peculiarities of many DPL spectra in silicon can be explained by assuming that the *D*1 and *D*2 lines are associated with edge-type dislocation steps on glide dislocations. © *2003 MAIK "Nauka/Interperiodica".*

1. INTRODUCTION

Dislocation-induced photoluminescence (DPL) in silicon at 4.2 K is characterized by the lines *D*1 (0.807 eV), *D*2 (0.870 eV), *D*3 (0.935 eV), and *D*4 (1.00 eV) [1]. The *D*4 line and *D*3 line (TO phonon replica of the *D*4 line) are attributed to the emission of regular segments of split 60° dislocations [2–4]. The interest in the origin of the *D*1 and *D*2 lines, which has not been clarified completely, is due to the possible application of this radiation in optoelectronics, which was demonstrated in [4].

It is well known that *D*1 and *D*2 lines are observed in silicon crystals subjected to plastic deformation at temperatures $T < 900$°C and then annealed in the temperature range 400–1200°C. The analysis of the conditions for the emergence and disappearance of these lines carried out in [2, 5–10] indicates their possible relation to translational-symmetry violation at dislocations, i.e., to specific step-type defects and dislocation nodes.

On the other hand, *D*1 and *D*2 lines of appreciable intensity have been detected in initial Czochralski-grown silicon (Cz-Si) crystals after annealings facilitating the nucleation and growth of oxygen precipitates [11–13]. Oxygen precipitation is accompanied by the generation of interstitial Si_i atoms and the formation of interstitial dislocation loops, whose plane is perpendicular to the Burgers vector **b**: partial Frank dislocation loops ($\mathbf{b} = (a/3)\langle 111\rangle$, with a being the lattice constant) and perfect prismatic dislocation loops [$\mathbf{b} = (a/2)\langle 110\rangle$]. As a result of absorption of excess Si_i atoms, these dislocations climb through the formation and displacement of edge steps in the plane of the loop [14]. The *D*1 and *D*2 lines detected in the recrystallized (100) Si layers after annealing at 1100°C in a chlorine-containing atmosphere are attributed to a three-dimensional network of pure edge dislocations [15]. The occurrence of a change in the defect structure of these layers upon annealing is due to the expansion of perfect prismatic loops as a result of climbing and to the elastic interaction between large loops that approach one another.

Transmission electron-microscopic studies revealed that these dislocation loops in silicon are effective getters of transition metals [16–18]. In silicon crystals grown through crucibleless floating-zone melting (FZ-Si) intentionally contaminated with copper, colonies of copper precipitates were observed in the area swept by helicoidal dislocations [16, 17] formed from gliding screw dislocations with edge steps as a result of climbing of these steps [14]. This fact, as well as a discrete arrangement of copper precipitates on partial Frank dislocations [17], allows us to consider edge steps as defects that facilitate the nucleation of copper precipitates. According to [18–20], oxygen precipitates in the form of SiO_x polyhedrons ($1 < x < 2$) are formed at temperatures above 900°C in some regions on dislocations and at the nodes of a dislocation network.

The above arguments suggest that the *D*1 and *D*2 lines in plastically deformed crystals are associated with edge-type steps on gliding dislocations, as well as with dislocation nodes, i.e., with defects near which precipitates of various impurities nucleate. The maximum decrease in the concentration of interstitial oxygen atoms as a result of precipitation occurs at 1050°C [21]; therefore, the effect of oxygen on the DPL spectrum may be pronounced most strongly in this temperature region. In order to verify this hypothesis, we studied DPL spectra in silicon crystals with different concentrations of oxygen and doping impurities deformed at $T > 1000$°C.

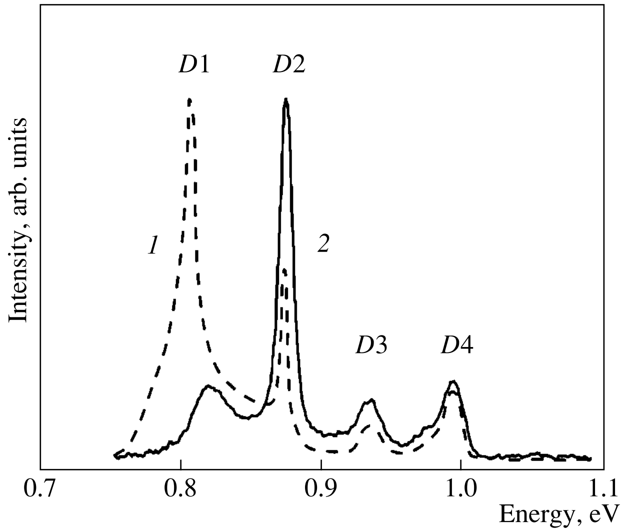

Fig. 1. DPL spectra recorded at 4.2 K in (*1*) *n*-type FZ-Si ($N_P = 6 \times 10^{13}$ cm^{-3}) and (*2*) *n*-type Cz-Si crystals ($N_P = 2 \times 10^{14}$ cm^{-3}. The dislocation density N_D is equal to (*1*) 4×10^6 and (*2*) 6×10^6 cm^{-2}; T_d = 1050°C.

2. EXPERIMENTAL TECHNIQUE

Experiments were carried out on silicon single crystals doped with boron (*p* type) or phosphorus (*n* type) with different oxygen contents and with a growth-dislocation density below 100 cm^{-2}. The boron concentration N_B and the phosphorus concentration N_P were varied in the intervals $10^{12} < N_B < 1.6 \times 10^{16}$ cm^{-3} and $6 \times 10^{13} < N_P < 8 \times 10^{16}$ cm^{-3}. In FZ- and Cz-Si crystals, the oxygen concentration was $\sim 1 \times 10^{17}$ and $\sim 1 \times 10^{18}$ cm^{-3}, respectively. In crystals with N_B, $N_P > 10^{16}$ cm^{-3}, the carbon concentration amounted to 10^{17} cm^{-3}. These data were obtained from the infrared absorption spectra. Chemically polished parallelepipeds with dimensions of 3.2 × 3.4 × 11 mm were deformed in a vacuum of ~7 Pa through compression along the longest edge ($\langle 123 \rangle$ direction) at various temperatures from the interval $1050 \le T_d \le 1200$°C up to strains $0.5\% < \delta < 30\%$ [6]. After deformation, the crystals were unloaded and cooled slowly (at a rate of less than 10 deg/min) to room temperature, which facilitated the formation of an equilibrium dislocation structure in the samples. The dislocation density was determined from etching pits on the {111} face.

The dislocation structure produced by high-temperature deformation was studied earlier in [6]. This structure is formed not only through the motion of dislocations in the slip plane but also through their leaving this plane due to cross glide of screw segments and climb of edge segments. In the crystals with the above-mentioned orientation, for moderate deforming stresses τ, only one glide system operates and part of the isolated dislocations takes the form of rectilinear (regular) segments of screw- or 60° dislocations separated by kinks and jogs. Activation of other glide systems at higher values of τ and the interaction of dislocations facilitate the formation of a cellular structure and the emergence of dislocation nodes. For $\delta > 20\%$, regular segments of screw- and 60° dislocations form a network whose connectivity increases with δ.

The PL spectra were measured at 4.2 K in the energy range 0.8–1.2 eV using a technique employed earlier in [5–7, 10]. The power density of excitation of nonequilibrium electrons and holes by Ar laser radiation at a wavelength of 488.8 nm was 2 mW/cm^2.

3. RESULTS

According to [7], the shapes of the DPL spectra in FZ- and Cz-Si crystals of type *p* with $N_B = 4 \times 10^{13}$ cm^{-3} deformed at 1050°C differ significantly for relatively small densities of introduced dislocations ($N_D < 2 \times 10^7$ cm^{-2}). The DPL spectra of FZ- and Cz-Si crystals (with different types and concentrations of doping impurities) deformed at $T \ge 1050$°C are presented below. It was found that an analogous difference is also observed in the DPL spectra of FZ- and Cz-Si crystals of type *n* with $N_P \le 2 \times 10^{14}$ cm^{-3}. An *n*-type FZ-Si sample (curve *1* in Fig. 1, $N_P = 6 \times 10^{13}$ cm^{-3}) is characterized by a typical DPL spectrum containing *D*1–*D*4 lines attributed to dislocations. In the spectrum of an *n*-type Cz -Si sample (curve *2*, $N_P = 2 \times 10^{14}$ cm^{-3}), instead of the *D*1 line, a broadened line with maximum energy E_m = 0.82 eV appears, which is displaced to E_m = 0.83 eV for $N_D \sim 1.5 \times 10^7$ cm^{-2}. A specific DPL spectrum is observed for Cz-Si samples of the *n* and *p* types, deformed in the temperature range $1050 \le T_d \le 1200$°C, with a donor concentration $N_P \le 2 \times 10^{15}$ and acceptor concentration $N_B \le 1.6 \times 10^{16}$ cm^{-3}, respectively.

The effect of dislocation density on the PL spectra is investigated in the *p*-type Cz-Si crystals with $N_B = 1.6 \times 10^{16}$ cm^{-3} (T_d = 1170°C; Fig. 2). As in [7], an increase in the dislocation density for $N_D < 2 \times 10^7$ cm^{-2} intensifies the PL in the vicinity of the *D*1 and *D*2 lines. However, for $N_D > 2 \times 10^7$ cm^{-2}, radiation appears with energy E_m = 0.807 eV, corresponding to the *D*1 line; the intensity of this radiation increases with N_D at a much higher rate than the intensity of the *D*2 line. Consequently, the broad *D*1 line (curve 3, $N_D \sim 10^9$ cm^{-2}) dominates in the PL spectra for $N_D \sim 10^8$–10^9 cm^{-2}. Samples *1–3* display an increase in the radiation intensity at energies 0.95–0.97 eV (inset to Fig. 2), which is often observed in the form of a small step on the long-wavelength wing of the *D*4 line (see, e.g., Fig. 1).

Figure 3 shows the DPL spectra in *n*-type Cz-Si crystals doped with phosphorus ($N_P = 2.6 \times 10^{16}$cm^{-3}, T_d = 1170°C). For samples with $N_D \sim 10^7$ cm^{-2}, quite

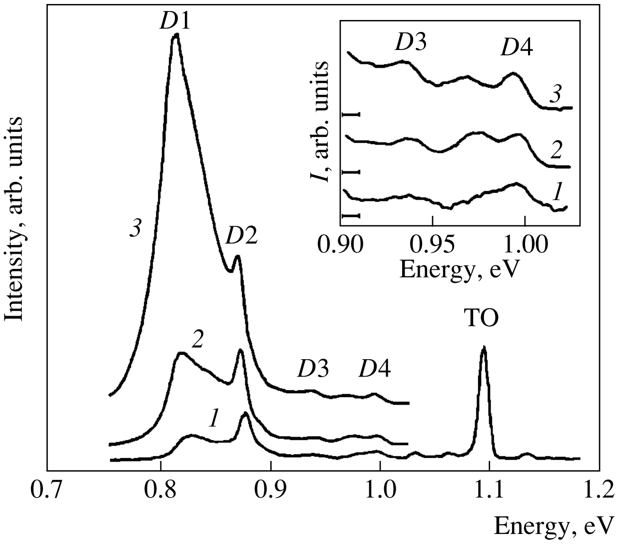

Fig. 2. DPL spectra recorded at 4.2 K in *p*-type Cz-Si crystals (N_B = 1.6 × 10^{16} cm^{-3}) for different dislocation densities N_D: (*1*) 8 × 10^6, (*2*) higher than 2 × 10^7, and (*3*) ~10^9 cm^{-2}. T_d = 1170°C.

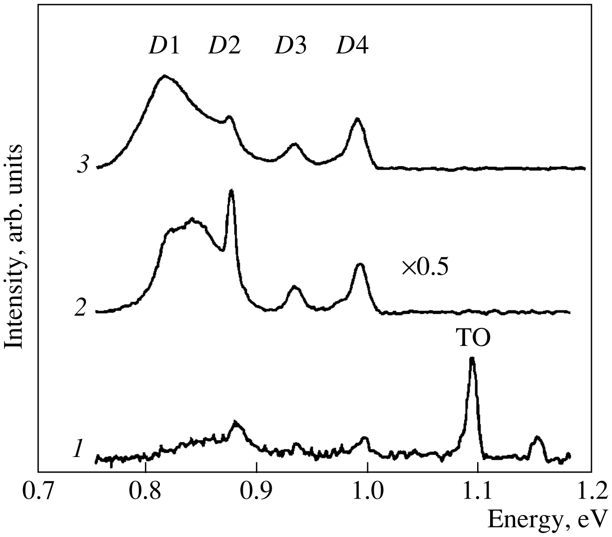

Fig. 3. DPL spectra recorded at 4.2 K in *n*-type Cz-Si crystals (N_P = 2.6 × 10^{16} cm^{-3}) for different dislocation densities N_D: (*1*) 1.2 × 10^7, (*2*) ~10^8, and (*3*) ~10^9 cm^{-2}. T_d = 1170°C.

small peaks are detected in place of the *D*2, *D*3, and *D*4 lines (curve *1*). A further increase in N_D facilitates a rise in the intensity of the *D*1–*D*4 lines. A wide emission band on the left of the *D*2 line (curve *2* in Fig. 3) indicates that samples with $N_D \sim 10^8$ cm^{-2} display emissions with E_m = 0.807 and 0.830 eV, which are of approximately equal intensities. In the sample with δ = 25% (curve *3* in Fig. 3), emission in the vicinity of the *D*1 line becomes dominant; its integrated intensity (I_{D1}), reduced to the same measurement conditions, turned out to be an order of magnitude lower than that in sample *3* (Fig. 2).

Since the concentrations of oxygen and carbon are virtually identical in the initial Cz-Si crystals of the *n* and *p* types with N_B, $N_P > 2 \times 10^{16}$ cm^{-3}, the considerable decrease in radiation intensity in the vicinity of the *D*1 and *D*2 lines observed in *n*-type Cz-Si samples could be due to the type of the doping impurity involved. For this reason, DPL spectra were also studied in *n*-type FZ-Si crystals with $N_P = 8 \times 10^{16}$ cm^{-3}. In the sample with $N_D = 3 \times 10^6$ cm^{-2}, the dislocation-induced PL is not detected. A very weak *D*2 line and quite intense *D*3 and *D*4 lines are observed for N_D = 1.5×10^7 cm^{-2} (curve *1* in Fig. 4). A 30-min annealing of the sample at T_0 = 700–800°C does not affect the spectrum. At higher values of N_D, emission in the vicinity of the *D*1 and *D*2 lines is detected (curve *2*), but the values of I_{D1} are also an order of magnitude smaller than those for sample *3* (Fig. 2).

It should be noted that in samples with different oxygen contents (Figs. 2–4), an increase in N_D from 10^7 to 10^9 cm^{-2} does not lead to a large difference in the values of I_{D4} (these quantities differ by only a factor of several units). Consequently, the comparable values of I_{D1} and I_{D4} in samples with $\delta > 20\%$ (Figs. 3, 4) reflect a decrease in the effectiveness of emission in the vicinity of the *D*1 line.

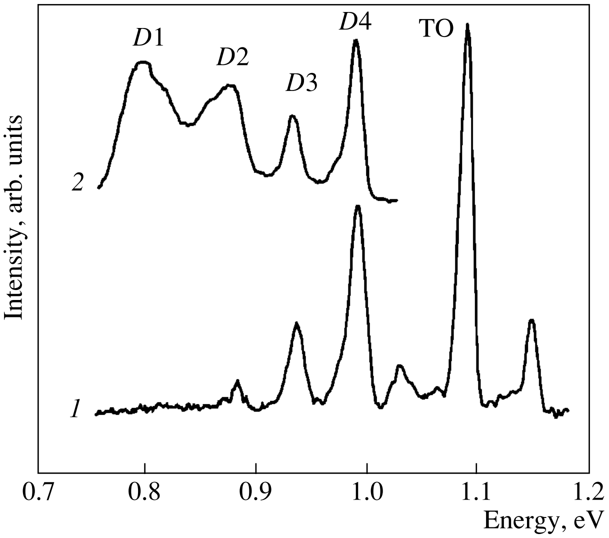

Fig. 4. DPL spectra recorded at 4.2 K in *n*-type FZ-Si crystals (N_P = 8 × 10^{16} cm^{-3}) for different dislocation densities N_D: (*1*) 1.5 × 10^7 and (*2*) ~10^9 cm^{-2}. T_d = 1050°C.

For FZ- and Cz-Si samples with N_B, $N_P > 10^{16}$ cm^{-3} and $N_D \le 1.5 \times 10^7$ cm^{-2} (Figs. 2–4), the emission of a TO exciton, its phonon replica, and the emission of a TA exciton were detected in [10] for $E > 1$ eV.

Thus, the above results indicate specific changes in the DPL spectra upon an increase in the oxygen, boron, and phosphorus concentrations.

4. DISCUSSION

4.1. DPL Spectra for Energies E < 0.9 eV

A comparative analysis of the DPL spectra in FZ- and Cz-Si crystals carried out by us earlier [7] and in this work made it apparent that the broadened line with $E_m = 0.82$–0.83 eV is a characteristic feature of deformed Cz-Si crystals with $N_D < 2 \times 10^7$ cm^{-2}. The $D1$ line appears in the DPL spectrum after annealing of these crystals at 1070°C for $t_0 = 30$ min, followed by slow cooling to room temperature [7], or after the introduction of a large number of dislocations ($N_D = 2 \times 10^7$ cm^{-2}, Fig. 2). These facts correlate with results obtained by other authors. The $D1$ line is shifted towards higher energies under uniaxial elastic deformation of samples with introduced dislocations [22] or after their annealing in oxygen at 750°C [23]. In *n*-type Cz-Si samples deformed at 900°C ($N_d = 2 \times 10^{14}$ cm^{-3}, $N_D \sim 10^9$ cm^{-2}), the emission in the vicinity of the $D1$ line depends on the cooling rate of the samples after annealing at 1200°C [24]. In the case of slow cooling, the $D1$ line is replaced by a broad step adjoining the long-wavelength wing of the $D2$ line and falling off steeply for $E < 0.82$ eV; after annealing, $D1$ and $D2$ lines of approximately equal intensities are detected. The broad band with a peak at $E \approx 0.82$ eV and the $D2$–$D4$ lines are observed after rapid ($t_d = 15$ min, $N_D = 5 \times 10^5$ cm^{-2}) deformation of Cz-Si samples at 700°C [9], while for $t_d = 14$ h, DPL disappears completely.

The sum of these factors indicates that oxygen precipitation in Cz-Si crystals is a possible reason for the strong effect of the conditions of sample preparation on radiation in the vicinity of the $D1$ line.

We assume that, in the case of slow cooling of *n*- and *p*-type Cz-Si samples (Figs. 1, 2) followed by deformation, interstitial oxygen atoms precipitate on the available growth precipitates and in the vicinity of dislocation steps. The mismatching of the molar volumes of the matrix and the precipitates gives rise to elastic stresses whose magnitude are maximal for the plane precipitate and decreases by an order of magnitude at a distance $\sim 10^{-5}$ cm [11]. The effect of elastic stresses on the position of the $D1$ line [22, 23] allows us to attribute the emergence of radiation with $E_m = 0.82$–0.83 eV (Figs. 1, 2; see also [9, 24]) to the presence of the steps responsible for the $D1$ line in the vicinity of precipitates.

The emergence of the $D1$ line in the spectra of deformed Cz-Si samples after annealing at 1070°C [7] is probably due to the removal of steps from precipitates as a result of dislocation climbing upon absorption of interstitial silicon atoms generated during precipitate growth. The detachment of 60° dislocations from oxygen precipitates through climbing was observed in Cz-Si crystals at 900°C [20]. The transformation of a line with $E_m = 0.818$ eV into a $D1$ line ($E_m = 0.807$ eV) after long-term annealing of Cz-Si crystals correlates with the removal of dislocation loops from precipitates [13], while the excitation of the $D1$ line (reported in [24]) after annealing at 1200°C followed by quenching correlates with precipitate dissolution [21].

The number of steps increases with N_D as a result of moving-dislocations overcoming obstacles in the form of impurity atoms, precipitates, and forest dislocations, as well as due to the generation of steps during the formation of dislocation nodes [14]. According to [6], the separation between the nodes in dislocation networks in samples subjected to strong plastic deformations ($\delta \sim 20$–30%) amounts to 50–500 nm. Assuming that the number of steps exceeds the number of nodes, we take a value of 50 nm for the mean distance between the steps. In this case, for the dislocation density $N_D \sim 10^9$ cm^{-2}, we obtain the step concentration $\sim 10^{14}$ cm^{-3}, which is an order of magnitude higher than the maximum possible concentration of precipitate nuclei in Cz-Si crystals with $N_O \sim 10^{18}$ cm^{-3} [25]. At a given temperature T_0, this concentration is determined by the annealing time for which the oxygen diffusion length becomes comparable with the mean distance between precipitates. In this case, the growth of existing precipitates is more probable than the nucleation of new precipitates; i.e., the number of steps near which no precipitates are formed increases with N_D. For this reason, the $D1$ line emerges in the DPL spectrum for $N_D > 10^7$ cm^{-2}, with its intensity increasing with δ (Fig. 2).

The sensitivity of the $D1$ line to oxygen, the minimal energy barrier for the formation of copper precipitates at perfect prismatic dislocations [17], and the formation of helicoidal dislocations during oxygen precipitation in silicon [20] indicate that the edge steps associated with the $D1$ line could be localized at screw dislocations. The $D2$ line can be attributed to edge-type steps at 60° dislocations. Regular segments of a screw dislocation are split into two 30° partial dislocations, while 60° dislocations are split into 30° and 90° partial dislocations. Ruptured bonds of both partial dislocations are reconstructed (pairwise closed) and do not create any deep states in the band gap of silicon. Two quasi-one-dimensional bands that are split off from the conduction band (empty E_{Dc} band) and from the valence band (filled E_{Dv} band) and that are located at a distance of ~ 0.07 eV from the edges of their parent bands are associated with the deformation potential of 90° partial dislocations. Consequently, deep states associated with edge steps or dislocation nodes and manifested in PL may be due to the presence of silicon atoms with unsaturated bonds.

A considerable decrease in the PL intensity in the vicinity of the *D*1 and *D*2 lines in deformed *n*-type Cz- and FZ-Si samples with $N_P > 10^{16}$ cm^{-3} (Figs. 3, 4) relative to *p*-type Cz-Si samples (Fig. 2) correlates with the suppression of oxygen precipitation in *n*-type Cz-Si samples as a result of strong doping by Group V impurities (in contrast to doping with boron) [26], as well as with the difference between the effects produced by boron and phosphorus on the mobility of dislocations in Si [27]. The problem of interaction of technological impurities (nitrogen, oxygen, carbon) and some other doping impurities from Groups III and V with cores of 90° partial dislocations in silicon was investigated theoretically in [28]. The decelerating effect of oxygen on the motion of dislocations was attributed to accelerated diffusion of interstitial oxygen atoms O_i along the cores of these dislocations and to the formation of a stable complex of two O_i atoms in the region of extension. The As, B, N, and P impurities, in contrast to oxygen, interact chemically with the core of a 90° partial dislocation, thus rupturing the reconstructed bonds, and with a reconstruction defect in this core (soliton). A soliton is a solitary Si atom with three saturated bonds and one unsaturated bond situated at the boundary between reconstructed regular segments of partial dislocations with different phases. Consequently, a phosphorus atom in the core of a partial dislocation can replace, for example, a Si atom with (a) four or (b) three saturated bonds (during its interaction with a soliton). In case (a), there is a shallow donor level of phosphorus and a deep level of the soliton in the band gap, while in case (b), we are left only with a shallow level (associated with a pair of valence electrons in phosphorus) near the top of the valence band or in the valence band; i.e., passivation of unsaturated bonds of the soliton takes place. According to [28], the soliton being pinned at these impurities (case b) is more advantageous from the energy point of view. As a result, dislocation-pinning centers with high binding energies are formed ($E^* = 2.3$–2.5 eV for As, B, and P and 3.4 eV for N). Such values of E^* are due to a change in the structure of chemical bonds in the core and to the necessity of their switching during the motion of dislocations (otherwise, an impurity atom would follow the dislocation).

The chemical interaction of phosphorus with edge steps may also lead to passivation of their electric activity, which explains the considerable decrease in the intensity of the *D*1 and *D*2 lines in *n*-Si with $N_P > 10^{16}$ cm^{-3} (Figs. 3, 4). The high intensity of the *D*1 line in *p*-type Cz-Si (Fig. 2) and the above-mentioned results [26, 27] indicate that the behavior of boron does not match the predictions made in [28]. In real crystals, the formation of impurity complexes depends, in particular, on the charge state of doping impurities and intrinsic point defects, the concentration of technological impurities, and the probability of formation and the thermal stability of clusters SiO_x, B_2O_3, P_2O_5, etc. [26]. Boron and phosphorus atoms differ in the value of the covalent radius (0.86, 1.10, and 1.18 Å for B, P, and Si, respectively) and in the sign of the ions at $T \sim 1000$°C in the samples under investigation (positive for P and negative for B). In the case of doping with boron, the nucleation of oxygen precipitates near edge steps is apparently more advantageous from the energy viewpoint, while in the case of doping with phosphorus, the chemical interaction of phosphorus with the steps dominates.

In the framework of this hypothesis, the reason for the emergence of the *D*1 and *D*2 lines in the presence of transition metals is associated in [29] with the formation of edge steps due to dislocation climb during diffusion or precipitation of these impurities.

4.2. DPL Spectra for Energies E > 0.9 eV

In deformed *p*-type Cz-Si samples (Fig. 2), the *D*4 line ($E_m = 0.998 \pm 0.001$ eV) is attributed to the emission of regular segments of 60° dislocations with an equilibrium value of the stacking fault width Δ_0. This radiation is the result of recombination of nonequilibrium electrons and holes trapped in quasi-one-dimensional bands E_{Dc} and E_{Dv}, respectively. The deformation potential of a 30° partial dislocation plays the role of a weak perturbation whose magnitude depends on the distance between partial dislocations, i.e., on the value of Δ. This parameter affects the depths of the bands E_{Dc} and E_{Dv} and, accordingly, the energy of radiation. The value of Δ can be changed, for example, by cooling a deformed sample to room temperature under a large load [2, 3]. Such a sample acquires regular segments of 60° dislocations with nonequilibrium values of Δ, while the DPL spectra of Si acquire a series of narrow lines (instead of the *D*4 line). For $\Delta > \Delta_0$, each value of Δ corresponds to a narrow line with a value of $E_m > 1.00$ eV, which increases discretely with Δ, while for $\Delta < \Delta_0$, the values of E_m decrease discretely in the interval 1.00–0.93 eV. Thus, radiation with $E_m = 0.95$–0.97 eV in *p*-type Cz-Si samples with an equilibrium dislocation structure (see the inset to Fig. 2) falls in the energy range corresponding to segments of 60° dislocations with nonequilibrium values of $\Delta < \Delta_0$. This could mean that, in addition to regular segments of 60° dislocations with equilibrium values of Δ_0, such samples also contain regular segments with $\Delta_{0e} < \Delta_0$.

An analysis of the DPL spectra of plastically deformed Ge crystals with an equilibrium dislocation structure [30] reveals that the value of $E_m = 0.513$ eV for band 1, associated with 60° dislocations, corresponds to regular segments of 60° dislocations with an equilibrium splitting Δ_0 in only one sample. For the remaining samples, lower values of $E_m = 0.497–0.508$ eV are observed.

The electron-microscopic images presented in [31] show that regular segments of glide dislocations in Ge samples with an equilibrium dislocation structure are characterized by different lengths and values of Δ. Regular segments with $L > L_c$ correspond to the value Δ_0, while those with $L < L_c$ correspond to the value $\Delta_{0e} < \Delta_0$. The critical length L_c amounts to ~100 nm; i.e., the relation $L > (20–30)\Delta_0$ holds for long segments ($L > L_c$), while the minimal values Δ_{0e} correspond to segments with $L \sim 30$ nm.

The above results lead to the conclusion that the spectral composition of PL in Si and Ge associated with an equilibrium ensemble of regular segments of 60° dislocations is determined by the distribution of these segments over the lengths and the values of Δ. A higher intensity of radiation with $E_m = 0.95–0.97$ eV (due to an increase in the number of 60° dislocations with lengths $L < L_c$) in p-type Cz-Si samples with $N_D > 10^7$ cm^{-2} correlates with the presence of oxygen precipitates.

In the spectra of deformed FZ- and Cz-Si samples doped with phosphorus with $N_P > 10^{16}$ cm^{-3}, the $D4$ line is characterized by the value $E_m = 0.988 \pm 0.001$ eV (Figs. 3, 4), which is 10 eV lower than the values of E_m for crystals with a different level of doping (Figs. 1, 2). In analogy with the above arguments, we assume that these values of E_m are due to a decrease in the lengths of the majority of regular segments of 60° dislocations to values $L < L_c$. This range of L values is apparently determined by the number of steps whose electrical activity is passivated by phosphorus.

5. CONCLUSIONS

Thus, the hypothesis on the relation between the $D1$ and $D2$ lines and the edge-type steps makes it possible to explain specific features of the DPL spectra in Si crystals with a large oxygen content. Oxygen precipitates formed in deformed p-type Cz-Si crystals with dislocations affect the number and the radiation energy of the steps separating regular segments, as well as the length of these segments. The quenching of the $D1$ and $D2$ lines in the case of an elevated phosphorus concentration is, in all probability, a manifestation of the chemical interaction of phosphorus with the steps. Low solubility of oxygen and transition metals at room temperature and their effective interaction with the steps facilitate concentration of these impurities in individual regions on dislocations, which causes carrier recombination to occur at quasi-one-dimensional dislocation segments and defects separating them.

ACKNOWLEDGMENTS

The authors are grateful to V.V. Kveder, V.P. Kisel’, and A.I. Kolyubakin for useful discussions; E.A. Steinman for his interest in this work and for discussions of the results; and to A.V. Bazhenov for determining the oxygen and carbon concentration in the initial crystals.

This study was supported by the Russian Foundation for Basic Research, project nos. 00-15-96703 and 02-02-17024.

REFERENCES

1. N. A. Drozdov, A. A. Patrin, and V. D. Tkachev, Pis’ma Zh. Éksp. Teor. Fiz. **23**, 651 (1976) [JETP Lett. **23**, 597 (1976)].
2. R. Sauer, C. Kisielowski-Kemmerich, and H. Alexander, Appl. Phys. A **36**, 1 (1985).
3. A. N. Izotov, A. I. Kolyubakin, S. A. Shevchenko, and E. A. Steinman, Phys. Status Solidi A **130**, 193 (1992).
4. V. V. Kveder, E. A. Steinman, S. A. Shevchenko, and H. G. Grimmeiss, Phys. Rev. B **51**, 10520 (1995).
5. A. N. Izotov and E. A. Stienman, Phys. Status Solidi A **104**, 777 (1987).
6. S. A. Shevchenko, Yu. A. Ossipyan, T. R. Mchedlidze, *et al.*, Phys. Status Solidi A **146**, 745 (1994).
7. S. A. Shevchenko and A. N. Izotov, Phys. Status Solidi A **138**, 665 (1993).
8. T. Sekiguchi and K. Sumino, J. Appl. Phys. **79**, 3253 (1996).
9. O. V. Feklisova, G. Mariani-Reguta, B. Pichaud, and E. B. Yakimov, Phys. Status Solidi A **171**, 341 (1998).
10. E. A. Steinman, V. I. Vdovin, T. G. Yugova, *et al.*, Semicond. Sci. Technol. **14**, 582 (1999).
11. W. Wijaranakula, J. Appl. Phys. **72**, 4026 (1992).
12. C. Clayes, E. Simoen, and J. Vanhellemont, J. Phys. III **7**, 1469 (1997).
13. S. Pizzini, M. Guzzi, E. Grilli, and G. Borionetti, J. Phys.: Condens. Matter **12**, 10131 (2000).
14. J. Friedel, *Dislocations* (Pergamon, Oxford, 1964; Mir, Moscow, 1967).
15. V. I. Vdovin, N. A. Sobolev, A. M. Emel’yanov, *et al.*, Izv. Ross. Akad. Nauk, Ser. Fiz. **66**, 279 (2002).
16. H. Gotschalk, Phys. Status Solidi A **137**, 447 (1993).
17. B. Shen, T. Sekiguchi, J. Jablonski, and K. Sumino, J. Appl. Phys. **76**, 4540 (1994).
18. K. Sumino, Phys. Status Solidi A **171**, 111 (1999).
19. A. Cavallini, M. Vandini, F. Cirticelli, and A. Armigliato, Inst. Phys. Conf. Ser. **134**, 115 (1993).
20. K. Minova, I. Yonenaga, and K. Sumino, Mater. Lett. **11**, 164 (1991).
21. H. Möller, L. Long, M. Werner, and D. Yang, Phys. Status Solidi A **171**, 175 (1999).

22. A. N. Drozdov, A. A. Patrin, and V. D. Tkachev, Phys. Status Solidi B **83**, K137 (1977).
23. A. N. Drozdov, A. A. Patrin, and V. D. Tkachev, Phys. Status Solidi A **64**, K63 (1981).
24. A. N. Izotov and E. A. Steinman, Fiz. Tverd. Tela (Leningrad) **28**, 1172 (1986) [Sov. Phys. Solid State **28**, 655 (1986)].
25. A. Borghesi, B. Pivac, A. Sassela, and A. Stella, J. Appl. Phys. **77**, 4169 (1995).
26. S. Hahn, F. A. Ponce, W. A. Tiler, *et al.*, J. Appl. Phys. **64**, 4454 (1988).
27. M. Imai and K. Sumino, Philos. Mag. A **47**, 599 (1983).
28. R. Jones, A. Umerski, P. Sitch, *et al.*, Phys. Status Solidi A **138**, 369 (1993).
29. E. C. Lightowlers and V. Higgs, Phys. Status Solidi A **138**, 665 (1993).
30. A. I. Kolyubakin, Yu. A. Osip'yan, S. A. Shevchenko, and E. A. Steinman, Fiz. Tverd. Tela (Leningrad) **26**, 677 (1984) [Sov. Phys. Solid State **26**, 407 (1984)].
31. G. Packeiser and P. Haasen, Philos. Mag. **35**, 821 (1977).

Translated by N. Wadhwa

Physics of the Solid State, Vol. 45, No. 2, 2003, pp. 266–269. Translated from Fizika Tverdogo Tela, Vol. 45, No. 2, 2003, pp. 254–256.
Original Russian Text Copyright © 2003 by Petrzhik, Darinskaya, Erofeeva, Raukhman.

DEFECTS, DISLOCATIONS, AND PHYSICS OF STRENGTH

Effects of Doping and Preliminary Processing on the Magnetically Stimulated Mobility of Dislocations in InSb Single Crystals

E. A. Petrzhik*, E. V. Darinskaya*, S. A. Erofeeva, and M. R. Raukhman*****

**Shubnikov Institute of Crystallography, Russian Academy of Sciences, Leninskiĭ pr. 59, Moscow, 117333 Russia*

e-mail:petrzhik@ns.crys.ras.ru

***Institute of Solid State Physics, Russian Academy of Sciences, Chernogolovka, Moscow oblast, 142432 Russia*

****Baikov Institute of Metallurgy and Materials Science, Russian Academy of Sciences,*
Leninskiĭ pr. 49, Moscow, 119991 Russia

Received February 27, 2002; in final form, June 20, 2002

Abstract—The effect of the type of conductivity and the doping level of InSb single crystals on the mobility of fast 60° dislocations in a magnetic field is discovered. It is found that doping of a pure InSb crystal with tellurium (n-type impurity) to 10^{18} cm^{-3} reduces the mobility of dislocations to the background level. At the same time, in p-type InSb crystals doped with Ge with the same carrier concentration (10^{18} cm^{-3}), the magnetoplastic effect is manifested clearly. It is shown that preliminary mechanical loading and, hence, internal stresses in the crystal affect not only the mean path length of dislocations in a magnetic field but also the magnitude of the threshold magnetic field below which the magnetoplastic effect is not observed. Possible reasons for these phenomena are discussed. © *2003 MAIK “Nauka/Interperiodica”.*

1. INTRODUCTION

The magnetoplastic effect (MPE), viz., the motion of dislocations in a dc magnetic field in the absence of mechanical loading, was discovered first in NaCl crystals [1]. The MPE is manifested macroscopically in the lowering of the yield stress of nonmagnetic crystals in a magnetic field [2], in a decrease in their microhardness [3] and in the coefficient of strengthening [4], and in a change in the internal friction [5, 6]. The MPE is observed in alkali-halide crystals [1–10], nonmagnetic metals [11, 12], polymers [13, 14], molecular crystals [15], semiconductors [16–19], and ferroelectrics [20, 21]. An analysis of the type of motion of dislocations in a weak magnetic field ($\mu B \ll kT$, where μ is the Bohr magneton, B is the magnetic induction, k is the Boltzmann constant, and T is the temperature) and its dependence on various physical parameters proved that the MPE is associated with depinning of dislocations from magnetically sensitive stoppers as a result of spin-dependent electron transitions occurring under the action of an external magnetic field in the dislocation-paramagnetic-center system [7–10]. A similar concept [22, 23] forms the basis of interpretation of a number of phenomena associated with the effect of weak magnetic fields on the physical and chemical properties of nonmagnetic materials.

This work is devoted to an analysis of the MPE effect in InSb semiconducting crystals with different types of conduction and doping levels and to investigation of the effect of internal stresses in a crystal on the mobility of fast 60° dislocations in a dc magnetic field.

2. EXPERIMENTAL TECHNIQUE

Experiments were carried out on InSb single crystals with different types of conduction and different doping levels: n type (1×10^{14}, 1×10^{18} cm^{-3}) and p type (5×10^{13}, 1.6×10^{14}, 1×10^{17}, 1×10^{18} cm^{-3}).

Samples were cut in the form of rectangular bars with dimensions of 3 × 1.5 × 40 mm in the directions [111], [112], and [110], respectively. Dislocations were introduced by scratching the sample observation surface (111) with a corundum needle along the [110] direction and were subsequently dispersed by four-point bending at elevated temperatures (over distances of 1000–2000 μm). The method of sample preparation is described in detail in [24, 25].

The prepared samples were placed in the uniform dc field of an electromagnet (B = 0.2–0.9 T) for a time t varying from a few seconds to 20 min. The experiments were made at an elevated temperature (T = 200°C) with preliminary slow heating for 40–60 min followed by analogous slow cooling.

The initial and final positions of dislocations (before and after “magnetic processing,” respectively) were revealed with the help of selective chemical etching (with etchant SR-4A) [16, 25]. The path lengths of fast 60° dislocations were measured.

3. RESULTS AND DISCUSSION

The MPE is manifested in semiconducting InSb crystals as a preferred motion of dislocations from a scratch (“diverging” half-loops) under the action of a dc magnetic field at elevated temperatures in the absence of mechanical loading [16]. The displacement of dislocations towards the scratch (“contracting” half-loops) is also observed. It was shown in [16], however, that the relative number of contracting dislocations in magnetic fields $B = 0.7$–0.9 T amounts to only ~10% of the total number of displaced dislocations, while the relative number of such dislocations in the case of control annealing in the absence of magnetic action is of the order of 90%. The mean path lengths of diverging dislocations are considerably larger in a magnetic field than for $B = 0$.

We observed the effect of the conduction type and the doping level of InSb single crystals on the MPE. It was found that doping of a pure *n*-InSb crystal (carrier concentration $C = 1 \times 10^{14}$ cm^{-3}; symbols *1* in Fig. 1) with tellurium to a concentration $C = 1 \times 10^{18}$ cm^{-3} (symbols *5* in Fig. 1) suppresses the MPE; i.e., the path lengths of dislocations diverging from the scratch decrease to the background level, while the relative number of dislocations contracting to the scratch increases to 80–90%, which is typical of annealing. However, the MPE in *p*-type InSb crystals doped with Ge is manifested clearly even for the Ge impurity concentration ($C = 1 \times 10^{18}$ cm^{-3}, symbols *3* in Fig. 1) equal to the Te impurity concentration in *n*-InSb: the path lengths of diverging dislocations coincide, to within the experimental error (~15%), with the path lengths in an undoped crystal (Fig. 1). As the concentration of the Ge doping impurity decreases ($C = 1 \times 10^{17}$ cm^{-3}), the path length of diverging dislocations in a magnetic field decreases (point *4* in Fig. 1, obtained from measurements on five samples). A further decrease in the Ge concentration to 1.6×10^{14} cm^{-3} suppresses the MPE effect completely. It should be noted that, in the same crystals subjected to mechanical tests in a zero magnetic field [24], the path lengths increased with Te concentration insignificantly, while an increase in the Ge concentration led to a considerable decrease in the path length. Thus, magnetic processing in the absence of mechanical loading leads to the opposite effect: the path lengths decrease to the background level upon an increase in the Te doping level, while doping with Ge to the same concentration virtually does not change the path length, which remains the same as that in pure samples. Consequently, the mobility of dislocations in semiconducting crystals in a magnetic field is determined not only by the type of conductivity but also by the magnetic state of the doping impurity. Probably, doping of InSb with tellurium strengthens the crystal in a magnetic field, as was observed in [9] for NaCl(Pb) crystals.

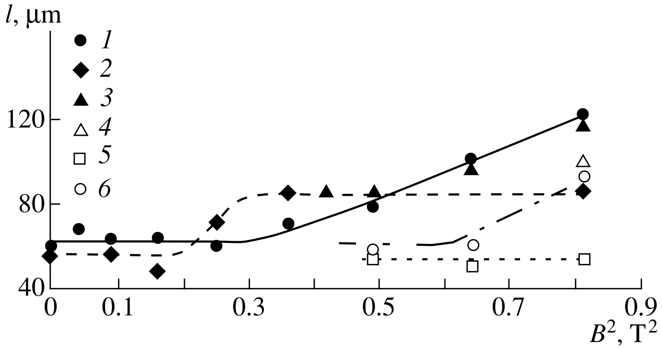

Fig. 1. Dependence of the mean path length *l* of diverging fast 60° dislocations on the magnetic induction *B* for InSb single crystals subjected to preliminary mechanical loading of (*1*–*5*) 15 and (*6*) 10 MPa. $T = 200$°C, and $t = 10$ min. Crystals of the *n* type: (*1, 6*) InSb-I (1×10^{14} cm^{-3}), (*2*) InSb-II (1×10^{14} cm^{-3}), and (*5*) InSb(Te) (1×10^{18} cm^{-3}); and of the *p* type: (*3*) InSb(Ge) (1×10^{18} cm^{-3}), and (*4*) InSb(Ge) (1×10^{17} cm^{-3}).

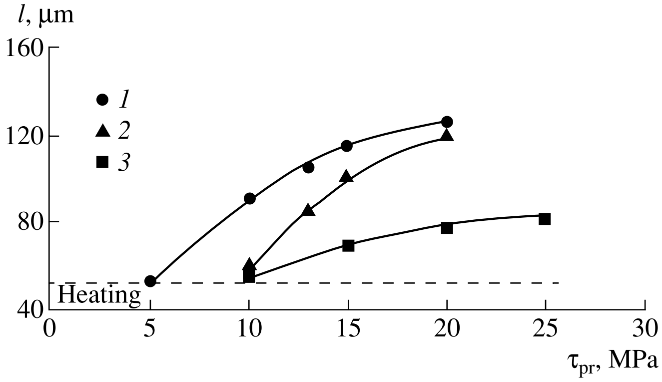

Fig. 2. Dependence of the mean path length *l* of diverging fast 60° dislocations in the InSb-I crystal (of the *n* type, with concentration 1×10^{14} cm^{-3}) on the preliminary mechanical loading τ_{pr} for various values of magnetic induction *B*: (*1*) 0.9, (*2*) 0.8, and (*3*) 0.7 T. $T = 200$°C and $t = 10$ min.

A comparative analysis was carried out for three *n*-type InSb crystals with the same carrier concentration ($C = 1 \times 10^{14}$ cm^{-3}) but taken from different boules. Special analysis of the temperature dependence of electrical conductivity, as well as chemical analysis, revealed no difference between the samples from the three boules. However, the mobilities of dislocations in these seemingly identical crystals in a magnetic field differ significantly.

The dependences of the mean path length of diverging dislocations for InSb-I crystals [16] (symbols *1*) and InSb-II (symbols *2*) are presented in Fig. 1. The observed saturation level for path lengths in InSb-II depends neither on the magnetic-processing time nor on the value of the preliminary mechanical loading. The saturation level is apparently determined by the presence of nonmagnetically sensitive stoppers that cannot be overcome by dislocations in a magnetic field. An analysis of the entire optical transmission band and (separately) the edge of the absorption band revealed small changes in the structure of the optical spectrum and a small shift in the edge of the absorption band in InSb-II relative to those in InSb-I. The reason for these changes is unclear. The InSb-III crystal subjected to mechanical tests behaved similarly to InSb-I (in which the MPE is manifested most clearly): under identical conditions, the activation energy for InSb-I crystals is $U_{\text{InSb-I}} = 0.8$ eV, while the activation energy for InSb-III crystals is $U_{\text{InSb-III}} = 0.88$ eV; however, under the action of a dc magnetic field in the absence of mechanical loading, fast 60° dislocations contract and diverging dislocations are not observed. The analysis of the mobility of dislocations in three types of InSb crystals with the same charge carrier concentration in a magnetic field suggests that the magnitude of the MPE is affected either by a small amount of a magnetically sensitive impurity (whose presence is not manifested in conductivity or in mechanical tests) or by different magnetic states of the same impurity in different crystals, which may facilitate strengthening of the crystal in analogy with [9].

The effect of preliminary mechanical loading during the “withdrawal” of dislocations from a scratch with the help of four-point bending on the dislocation mobility in a magnetic field was studied on InSb-I samples (n type, $C = 1 \times 10^{14}$ cm^{-3}). Preliminary magnetic loading sets the density of dislocations in an array originating at the scratch and, hence, the level of internal stress. Figure 2 shows the dependence of the mean path length l of dislocations on the preliminary mechanical loading stress τ_{pr} for various values of the magnetic field. We plotted the path length of diverging dislocations alone. It can be seen from Figs. 1 and 2 that the level of internal stress determines not only the dislocation path lengths in a magnetic field but also the threshold magnetic field starting from which diverging dislocations are predominantly observed. For example, $B_{\text{thr}} \approx 0.6$ T for $\tau_{\text{pr}} = 15$ MPa (symbols *1* in Fig. 1), while $B_{\text{thr}} \approx 0.8$ T for $\tau_{\text{pr}} = 10$ MPa (symbols *6* in Fig. 1).

Our experiments proved that, in semiconducting crystals, as in alkali-halide crystals and metals, the internal stresses of the crystal serve as the driving force for dislocations in the MPE. The role of the magnetic field lies in the creation of conditions for depinning of dislocations from stoppers.

ACKNOWLEDGMENTS

The authors are grateful to V.I. Al’shits for valuable discussions and to V.K. Karandashev, S.A. Shevchenko, É.A. Sheĭman, and A.F. Bazhenov for their help in carrying out this research.

This study was partly supported by the Russian Academy of Science (in the framework of the Sixth Competition of Research Projects of Young Scientists of the RAS).

REFERENCES

1. V. I. Al’shits, E. V. Darinskaya, T. M. Perekalina, and A. A. Urusovskaya, Fiz. Tverd. Tela (Leningrad) **29** (2), 467 (1987) [Sov. Phys. Solid State **29**, 265 (1987)].
2. V. I. Al’shits, A. A. Urusovskaya, A. E. Smirnov, and N. N. Bekkauer, Fiz. Tverd. Tela (St. Petersburg) **42** (2), 270 (2000) [Phys. Solid State **42**, 277 (2000)].
3. Yu. I. Golovin, R. B. Morgunov, D. V. Lopatin, and A. A. Baskakov, Phys. Status Solidi A **160**, R3 (1997).
4. Yu. I. Golovin and R. B. Morgunov, Pis’ma Zh. Éksp. Teor. Fiz. **61** (7), 583 (1995) [JETP Lett. **61**, 596 (1995)].
5. N. A. Tyapunina, V. L. Krasnikov, and É. P. Belozerova, Izv. Ross. Akad. Nauk, Ser. Fiz. **64** (9), 1776 (2000).
6. O. I. Datsko, Fiz. Tverd. Tela (St. Petersburg) **44** (2), 289 (2002) [Phys. Solid State **44**, 300 (2002)].
7. V. I. Alshits, E. V. Darinskaya, O. L. Kazakova, *et al.*, Mater. Sci. Eng. A **234–236**, 617 (1997).
8. V. I. Al’shits and E. V. Darinskaya, Pis’ma Zh. Éksp. Teor. Fiz. **70** (11), 749 (1999) [JETP Lett. **70**, 761 (1999)].
9. E. V. Darinskaya and M. V. Koldaeva, Pis’ma Zh. Éksp. Teor. Fiz. **70** (3), 226 (1999) [JETP Lett. **70**, 228 (1999)].
10. Yu. I. Golovin, R. B. Morgunov, V. E. Ivanov, and A. A. Dmitrievskiĭ, Zh. Éksp. Teor. Fiz. **117**, 1080 (2000) [JETP **90**, 939 (2000)].
11. V. I. Al’shits, E. V. Darinskaya, I. V. Gektina, and F. F. Lavrent’ev, Kristallografiya **35** (4), 1014 (1990) [Sov. Phys. Crystallogr. **35**, 597 (1990)].
12. V. I. Al’shits, E. V. Darinskaya, and E. A. Petrzhik, Fiz. Tverd. Tela (St. Petersburg) **34** (1), 155 (1992) [Sov. Phys. Solid State **34**, 81 (1992)].
13. N. N. Peschanskaya and P. N. Yakushev, Fiz. Tverd. Tela (St. Petersburg) **39** (9), 1690 (1997) [Phys. Solid State **39**, 1509 (1997)].
14. Yu. I. Golovin, R. B. Morgunov, and S. Yu. Liksutin, Vysokomol. Soedin., Ser. B **40**, 373 (1999).
15. Yu. A. Osip’yan, Yu. I. Golovin, R. B. Morgunov, *et al.*, Fiz. Tverd. Tela (St. Petersburg) **43** (7), 1333 (2001) [Phys. Solid State **43**, 1389 (2001)].
16. E. V. Darinskaya, E. A. Petrzhik, S. A. Erofeeva, and V. P. Kisel’, Pis’ma Zh. Éksp. Teor. Fiz. **70** (4), 298 (1999) [JETP Lett. **70**, 309 (1999)].
17. A. A. Skvortsov, A. M. Orlov, V. A. Frolov, *et al.*, Fiz. Tverd. Tela (St. Petersburg) **42** (10), 1814 (2000) [Phys. Solid State **42**, 1861 (2000)].

18. A. A. Skvortsov, A. M. Orlov, and L. I. Gonchar, Zh. Éksp. Teor. Fiz. **120** (1), 134 (2001) [JETP **93**, 117 (2001)].
19. V. A. Makara, L. P. Steblenko, N. Ya. Gorid’ko, *et al.*, Fiz. Tverd. Tela (St. Petersburg) **43** (3), 462 (2001) [Phys. Solid State **43**, 480 (2001)].
20. B. I. Smirnov, N. N. Peschanskaya, and V. I. Nikolaev, Fiz. Tverd. Tela (St. Petersburg) **43** (12), 2154 (2001) [Phys. Solid State **43**, 2250 (2001)].
21. S. A. Gridnev, K. S. Drozhdin, and V. V. Shmykov, Fiz. Tverd. Tela (St. Petersburg) **42** (2), 318 (2000) [Phys. Solid State **42**, 326 (2000)].
22. B. Ya. Zel’dovich, A. L. Buchachenko, and E. L. Frankevich, Usp. Fiz. Nauk **155** (1), 3 (1988) [Sov. Phys. Usp. **31**, 385 (1988)].
23. A. L. Buchachenko, R. Z. Sagdeev, and K. M. Salikhov, *Magnetic and Spin Effects in Chemical Reactions* (Nauka, Novosibirsk, 1978).
24. S. A. Erofeeva, Philos. Mag. A **70**, 943 (1994).
25. V. P. Kisel, S. A. Erofeeva, and M. Sh. Shikhsaidov, Philos. Mag. A **67**, 343 (1992).

Translated by N. Wadhwa

Physics of the Solid State, Vol. 45, No. 2, 2003, pp. 270–275. Translated from Fizika Tverdogo Tela, Vol. 45, No. 2, 2003, pp. 257–261.
Original Russian Text Copyright © 2003 by Morgunov, Baskakov, Trofimova, Yakunin.

The Role of Thermally Activated Processes in the Formation of Magnetosensitive Point-Defect Complexes in NaCl : Eu Single Crystals

R. B. Morgunov, A. A. Baskakov, I. N. Trofimova, and D. V. Yakunin
Institute of Solid-State Physics, Russian Academy of Sciences, Chernogolovka, Moscow oblast, 142432 Russia
e-mail: morgunov@issp.ac.ru

Received May 21, 2002

Abstract—The formation of magnetosensitive point-defect complexes in NaCl : Eu crystals is investigated. It is shown that the formation of intermediate metastable magnetosensitive point-defect complexes and their subsequent spontaneous transformation into relaxation products are thermally activated processes and do not depend on the diffusion mobility of impurity–vacancy dipoles. It is revealed that the magnetic field induces a transition of the magnetosensitive point-defect complexes to a new state that cannot occur in the absence of a magnetic field. A variation in the heat treatment temperature makes it possible to enhance the magnetoplastic effect significantly (by a factor of three) and to create the appropriate conditions for the existence of magnetosensitive complexes in the crystal over a long period of time. *© 2003 MAIK "Nauka/Interperiodica".*

1. INTRODUCTION

Recent investigations into the magnetoplastic effect in diamagnetic crystals [1–7] have demonstrated that spin-dependent reactions between structural defects are primarily responsible for the plastic properties of the crystals [5]. The hypothesis that the effect of a magnetic field on the plasticity of ionic crystals should be associated with the change in the kinetics of spin-dependent reactions was first put forward by Al'shits *et al.* [4] with respect to the interaction between point defects and dislocations. At present, it has been established that the aggregation of impurity–vacancy dipoles into composite complexes can be treated as a specific type of spin-dependent reactions affecting the dislocation mobility in magnetic fields [5–7]. These reactions are of great practical interest, because the effect of a magnetic field on the kinetics of relaxation of a point-defect subsystem brings about the transformation of dislocation stoppers and can manifest itself not only in ionic crystals but also in ionic–covalent (ZnS, InSb) [8, 9] and covalent (Si, Ge) crystals [10–15]. In the latter group of crystals, this effect can be revealed from the changes in the mechanical [10, 11], electrical, and optical properties [8, 9, 12–15].

Up to now, many aspects of the interaction between paramagnetic impurity–vacancy dipoles that migrate in the crystal and aggregate into complexes due to thermal fluctuations remain unknown. A large number of works and reviews [16–20] that were concerned with this problem long before the discovery of the magnetoplastic effect did not provide insight into the mechanisms of the most important, early stages of aggregation of impurity–vacancy dipoles and the evolution of already existing complexes. The main problem lies in the fact that the standard spectroscopic techniques used for measuring electron paramagnetic resonance (EPR), luminescence, and other properties of defect crystals possess an insufficient sensitivity to distinguish different impurity–vacancy dipole complexes formed at the earliest stages of aggregation and to identify numerous conformations of complexes of the same type [20]. However, as was shown in our earlier work [7], it is these initial stages of point-defect relaxation that are responsible for the formation of comparatively long-lived complexes (~1–10 h at room temperature) whose structure undergoes transformations in magnetic fields. In this respect, the investigation into the kinetics of formation and subsequent transformations of these complexes can provide better insight into the interrelation between the spin and molecular dynamics of defects in magnetic fields, which is essential to the understanding of the magnetoplastic effects in crystals.

One of the most efficient methods of determining the height of the barriers between different states of defects and investigating the kinetics of reactions in crystals involves thermoactivation analysis. In recent years, many attempts have been made to elucidate the role played by thermally activated processes in the magnetoplastic effect [1, 2, 5]. However, under the experimental conditions used in the aforementioned works, a change in temperature could affect several concurrent processes occurring prior to, during, and even after the spin-dependent stage. Among these processes are the formation of the atomic structure of magnetosensitive point-defect complexes, the thermofluctuation generation of the electronic magnetosensitive states, spin–lattice relaxation in a magnetosensitive state, etc. The aim of the present work was to examine magnetosensitive point-defect complexes under experimental conditions providing separation of the contributions from the concurrent processes to the thermoactivation of magnetic-field-induced reactions in a subsystem of paramagnetic point defects in NaCl : Eu crystals.

2. SAMPLE PREPARATION AND EXPERIMENTAL TECHNIQUE

The experiments were carried out with quenched crystals of NaCl : Eu (~0.1 wt % Eu). The choice of europium impurities was motivated by the possibility of forming magnetosensitive point-defect complexes based on Eu impurity ions [6, 7]. Moreover, there is strong evidence that the relaxation of a thermally excited subsystem of europium impurity–vacancy dipoles is a chemical reaction occurring through spin-dependent stages [20]. The quenching required to excite the subsystem of point defects was performed using crystals heat treated under the following conditions: (1) at $T = 920$ K for 2 h, (2) at 770 K for 1 h, and (3) at $T = 770$ K for 10 min. Then, in all three cases, the crystals were cooled in a copper vessel to a temperature of 293 K at a mean rate of ~5 K/s. These heat-treatment conditions were used to elucidate the role played by the possible dissociation of defect complexes in the studied processes and to separate their fragments at a high temperature. In order to prevent diffusion of oxygen and hydroxyl groups into the crystals, their heating in each experiment was performed in a helium or argon atmosphere.

It is evident that the possibility of promoting a magnetosensitive reaction offers considerable advantages for its separation from concurrent (or consecutive) processes. Therefore, the experimental conditions used in magnetic treatment of the crystals have to provide a rapid transformation of magnetosensitive point-defect complexes. Earlier [21], we established that treatment of NaCl : Eu crystals in crossed dc and microwave magnetic fields (under the EPR conditions) results in fast relaxation of magnetosensitive point-defect complexes and a change in the microhardness when the magnetic field induction falls in several discrete ranges. A set of magnetic field inductions that correspond to locations of the lines in the classical EPR spectrum is a unique characteristic of the studied complexes and makes it possible to identify them as defects containing Eu^{2+} paramagnetic ions [6]. Point defects in the crystal subjected to this treatment in a magnetic field more rapidly transform into new states (for ~5 min) as compared to point defects in the crystals exposed to a dc magnetic field with an induction of ~1 T in the absence of a microwave field (for 30–50 min at $T = 293$ K [3–5]). For this reason, in order to initiate transformations in the structure of magnetosensitive point-defect complexes, the sample was placed in a cylindrical cavity of an RÉ-1306 standard radiospectrometer, which was set to measure one of the lines of the electron paramagnetic resonance detected in [5, 6, 21] from the change in plasticity. The chosen line corresponded to transitions between the states with spin projections –1/2 and +1/2 onto the direction of the dc magnetic field under the conditions when the induction vector was directed along the [001] principal magnetic axis [16]. Another fast technique for magnetic-field initiation of transformations in a subsystem of point defects consists in increasing the magnetic field induction to 6 T. In this case, the use of four magnetic-field pulses, which have the shape of a half-cycle of a sinusoid and a pulse width of 10 ms, makes it possible to transform completely all the magnetosensitive point-defect complexes accumulated in the crystal at a given instant of time.

In order to reveal magnetosensitive point-defect complexes in a crystal, the microhardnesses H of the crystal under investigation was measured before and immediately after a 5-min treatment in crossed magnetic fields. The magnitude of the difference ΔH between these microhardnesses served as a quantitative measure of the magnetoplastic effect and indirectly characterized the concentration of magnetosensitive centers accumulated in the crystal. In all the experiments, the Vickers microhardness H of the crystals was measured under an indenter load of 0.2 N and the loading time was 10 s. The indentation diagonals were oriented along the [110] direction. Each point in the graphs was obtained by averaging over 20–30 measurements. As a result, the error in the microhardness measurement was reduced to 1–1.5%. This is a typical error in measurements of the microhardness in ionic crystals and other materials (see, for example, [22]). It should be noted that, in all the experiments, the microhardness measurements and magnetic treatment of the crystals were performed at $T = 293$ K and the total duration of these procedures was considerably shorter than that of the transient processes examined in this work. Under these conditions, any variations in the kinetics and magnitude of the magnetoplastic effect ΔH could be associated only with the influence of the thermal prehistory on the formation of magnetosensitive point-defect complexes and not with the change in the conditions of measuring the plastic properties or the magnetic treatment.

3. RESULTS AND DISCUSSION

The magnitude of the microhardness H of the crystals quenched upon isothermal treatment at 920 K for 1 h varies nonmonotonically with time t after the quenching (Fig. 1, curve *1*). Special experiments revealed similar changes in the microhardness H upon indentation of the crystals that were cleaved not immediately after quenching but directly before the indentation was performed on the as-prepared surface. This

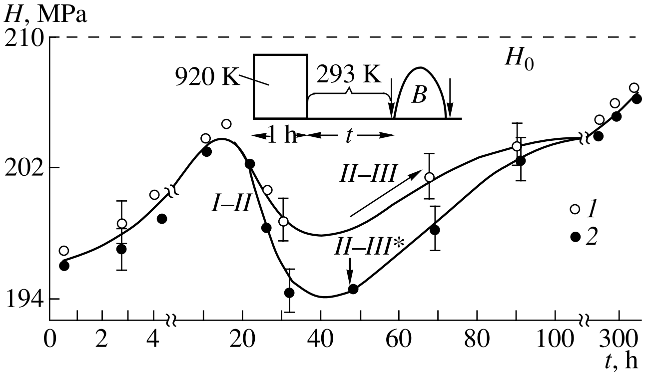

Fig. 1. Dependences of the microhardness H on the time t elapsed after quenching of the crystals from 920 K for (*1*) samples in the absence of a magnetic field and (*2*) the same samples exposed to a single magnetic-field pulse (B = 7 T; pulse width, 10 ms). H_0 is the microhardness of the crystals unquenched or held after quenching for several years at room temperature. Roman numerals denote the impurity relaxation stages corresponding to the occurrence of different-type complexes in the crystal: (*I*) point defects forming magnetosensitive point-defect complexes, (*II*) magnetosensitive point-defect complexes, (*III*) products of relaxation of magnetosensitive point-defect complexes in the absence of an external magnetic field, and (*III**) products of relaxation of magnetosensitive point-defect complexes formed in the presence of an external magnetic field. The inset illustrates the temperature–time schedule of measurements (T is the variable temperature), the instants of indentation (indicated by arrows), and the time interval of exposure to magnetic fields (designated as B).

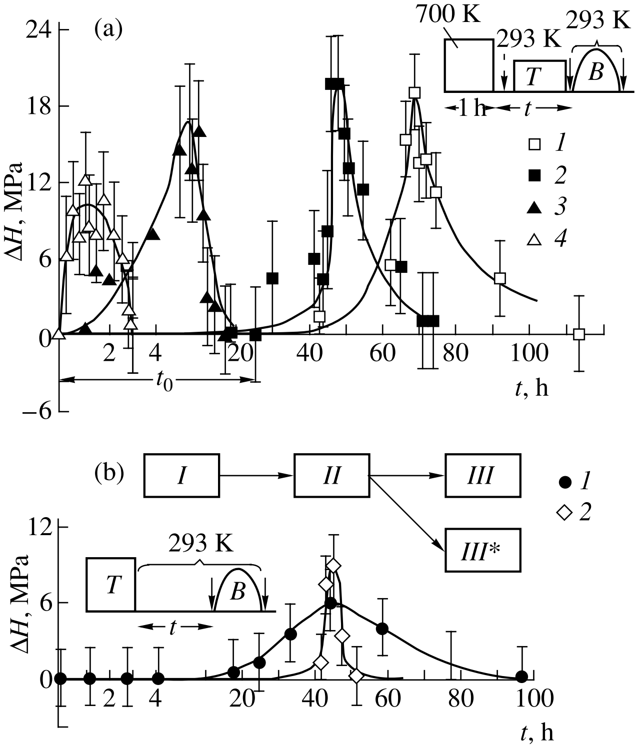

Fig. 2. (a) Dependences of the microhardness change ΔH induced by the crossed dc and microwave magnetic fields under EPR conditions on the time t elapsed after quenching of the crystals from 770 K (upon isothermal treatment for 1 h). After quenching, the samples were held at temperatures of (*1*) 77, (*2*) 293, (*3*) 393, and (*4*) 473 K. The inset illustrates the temperature–time schedule of measurements (T is the variable temperature), the instants of indentation (indicated by arrows), and the time interval of exposure to magnetic fields (designated as B). (b) Dependences of the microhardness change ΔH induced by the crossed dc and microwave magnetic fields under EPR conditions on the time t elapsed after quenching of the crystals from (*1*) 920 K (upon isothermal treatment for 1 h) and (*2*) 770 K (upon isothermal treatment for 10 min) and a schematic diagram of the stages of the evolution of point-defect complexes (designations are the same as in Fig. 1).

suggests that the nonmonotonic variations in the microhardness H are caused by changes in the state of impurities in the crystal bulk rather than by random variations in the atmosphere-sensitive surface properties of the samples. Similar variations in the microhardness after quenching have been observed earlier by other authors [23]. In our experiments, after measuring the microhardness H used in plotting curve *1* (Fig. 1), the crystal was exposed to a magnetic field and the microhardness H was measured once again. The instant of time at which the latter value of the microhardness was measured (Fig. 1, curve *2*) differed only slightly from that of the former value. As a result, we obtained two different values within a relatively narrow time interval. Thus, the same sample was used to obtain two points at identical (to within minutes) instants of time in curves *1* and *2* (Fig. 1). After measuring the two points, the sample was not used, because treatment in a magnetic field leads to irreversible changes in the crystal [21]. The reliability of the results obtained was checked by measuring the microhardness H for several samples prepared under the same conditions.

The change in the plasticity of the crystals ΔH due to exposure to magnetic fields is equal to zero immediately after quenching and in a long period of time after quenching (at $t > 100$ h) (Fig. 2a, curve *2*). Upon isothermal treatment of the crystals at $T = 293$ K for $t \sim 25$ h after quenching, the quantity ΔH becomes nonzero and reaches a maximum at $t \sim 50$ h. At $t > 50$ h, the change in the plastic properties of the crystals in response to external magnetic fields decreases and then becomes zero. Similar behavior is observed for other quenching conditions when the crystals are held at $T = 293$ K between quenching and indentation (Fig. 2a, curve *2*; Fig. 2b).

The presence of the maximum in the dependence $\Delta H(t)$ indicates that the accumulation of magnetosensitive point-defect complexes depends not only on the kinetics of their formation at stage *I–II* (Fig. 2b) but also on a subsequent relaxation of the subsystem of point defects at stage *II–III*, during which the magnetosensitive point-defect complexes spontaneously (in the absence of external magnetic fields) transform into new complexes insensitive to magnetic fields. With the aim of analyzing the role of these processes, we carried out a series of experiments in which the crystals were (i) quenched from 770 to 293 K; (ii) slowly cooled (for 1–3 min) to 77, 393, or 473 K; and (iii) subjected to isothermal treatment under the new conditions up to the measurement of the microhardness and softening of the sample in the magnetic field at 293 K. (Cooling to room temperature during quenching in all experiments is necessary to ensure the same rate of freezing of the metastable states of point defects and the same initial concentration of impurity–vacancy dipoles and their metastable complexes.) It was found that an increase in the temperature *T* of isothermal treatment of the crystals after quenching leads to a shift of the maximum in the time dependence of the microhardness change Δ*H* toward the short-time range (Fig. 2a). Moreover, we revealed a noticeable decrease in the lifetime of the magnetosensitive state of the crystal. All the above findings suggest that the formation of magnetosensitive complexes occurs more rapidly with an increase in the temperature. This assumption is quite consistent with universally accepted concepts of an increase in the rate of mutual transformation between different configurations of complexes. A decrease in the maximum value of Δ*H* with an increase in the temperature *T* can imply that the rate of transformation of defects from a magnetosensitive state into a new state (stage *II–III*) also increases with an increase in the temperature. In order to verify this assumption, the crystal was held at T = 293 K until the stage of accumulation of magnetosensitive defects (*I–II*) was attained (this corresponds to the maximum softening of the crystal in a magnetic field). After reaching the maximum microhardness change Δ*H* (at ~50 h), when the defect accumulation was assumed to be close to completion, the temperature was changed and the crystal was held at a different temperature (Fig. 3). It turned out that, upon cooling of the crystal, spontaneous weakening of the magnetoplastic effect becomes considerably less pronounced (Fig. 3). This means that thermal fluctuations favor not only the accumulation of magnetosensitive point-defect complexes but also their relaxation and transformation into reaction products that are insensitive to a magnetic field. Therefore, in the absence of a magnetic field, the accumulation of magnetosensitive point-defect complexes in the crystal depends on the rate of defect formation at stage *I–II* and the rate of transformation into products of relaxation at stage *II–III* (see scheme in Fig. 2b).

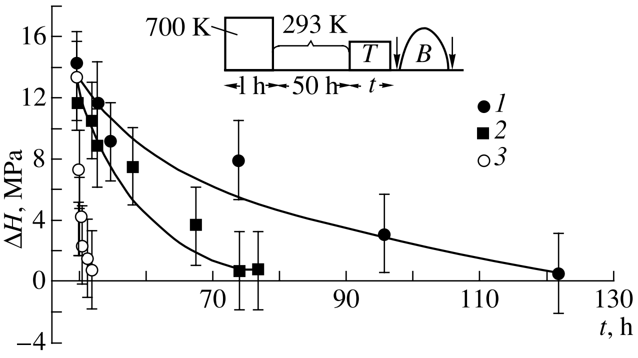

Fig. 3. Dependences of the microhardness change Δ*H* induced by the crossed dc and microwave magnetic fields under EPR conditions on the time *t* elapsed after quenching of the crystals (isothermal treatment at 770 K for 1 h). After quenching, the samples were held first at a temperature of 293 K for 50 h and then at temperatures *T* = (*1*) 77, (*2*) 293, and (*3*) 473 K. The inset illustrates the temperature–time schedule of measurements (*T* is the variable temperature), the instants of indentation (indicated by arrows), and the time interval of exposure to magnetic fields (designated as *B*).

Before proceeding to the discussion of the results, one additional essential remark needs to be made. The magnitude of the microhardness *H* of the crystals quenched from 770 K is smaller than that of the crystals quenched from 920 K and amounts to approximately 150 MPa. In contrast, the magnitude of the softening Δ*H* of the former crystals (18 MPa at a maximum) is larger than that of the latter crystals. By varying the quenching conditions and the temperature of isothermal treatment between quenching and exposure to a magnetic field, we succeeded in enhancing the effect of softening of the crystals to 12%, which is three times larger than the effect observed earlier in [6, 7, 21]. Furthermore, the revealed possibility of retarding the spontaneous transformation of magnetosensitive point-defect complexes through cooling of the crystals (Fig. 3) opens the way to the stabilization of magnetosensitive point-defect complexes.

At T = 770 K, the diffusion coefficient D is approximately equal to 10^{-20} m^2 s^{-1} [24] and the diffusion length L_1 of an impurity–vacancy dipole for time $t = 6 \times 10^2$ s amounts to $\sim(6Dt)^{1/2} \approx 6 \times 10^{-9}$ m, which is almost two orders of magnitude smaller than the mean distance between complexes (~10^{-7} m). Consequently, the heat treatment at 770 K for 10 min can result only in dipole displacements comparable in size to the complexes themselves. However, as was shown in [24], the diffusion activation energy is 0.7 eV. On this basis, we found that, upon isothermal treatment at a higher temperature (920 K) for 2 h, the mean distance L_2 (diffusion length) to which an impurity–vacancy dipole can move away from the dissociating complex turns out to be nearly 30 times larger than the diffusion length L_1. This implies that the dipole ceases to belong to a particular complex. Hence, if the diffusion significantly contributes to the formation of complexes, the change in the quenching conditions should substantially affect both the redistribution of dissolving impurities in the crystal and the time of their subsequent aggregation at the same temperature, T = 293 K. In particular, the times required to form a magnetosensitive point-defect complex under the above conditions should differ by

$\sim(L_2/L_1)^2 \sim 30^2$, i.e., by approximately three orders of magnitude. On the other hand, it can be seen from Fig. 2 that, if a difference between the positions of the maxima in the dependences $\Delta H(t)$ does actually occur, it is considerably less than the difference that would be observed if the diffusion processes were to be involved in the formation of magnetosensitive point-defect complexes. Most likely, this suggests that bimolecular processes and higher order reactions do not appreciably affect the kinetics of formation of magnetosensitive point-defect complexes. This inference is confirmed by the waiting time required for thermally activated detachment of the impurity–vacancy dipole from the complex during isothermal treatment of the crystals at a high temperature for any reasonable activation energy of detachment of the dipole from the complex (~0.1–1 eV [25]). Therefore, the processes occurring at stages *I–II* and *II–III* are most probably governed by the intracenter excitation and structural relaxation of the complexes existing in the crystal already prior to quenching. The possible intracenter process that can be favorable to the formation of magnetosensitive point-defect complexes is a thermostimulated transformation of the complex from one configuration into another with a change in the location of a constituent dipole. For example, upon thermoactivation of the four relatively stable trimer configurations, which were calculated and described in [25], a change in the orientation of one of the dipoles can result in a change in the configuration of the complex as a whole.

Analysis of the experimental results revealed that magnetosensitive point-defect complexes in crystals can nucleate in the absence of magnetic fields. The question arises as to the role played by the external magnetic field in the evolution of the point-defect subsystem: whether or not the magnetic field promotes the transformation of magnetosensitive point-defect complexes into state *III*, which can be achieved by these complexes for a longer time in the absence of the field, or the magnetic field initiates the formation of the complexes in new states. The branching of processes after the spin-dependent stage is a well-known phenomenon in the theory of spin-dependent reactions [26]. Since the formation of magnetosensitive point-defect complexes is attended by a decrease in the magnitude of the crystal microhardness and stage *II–III* is accompanied by an increase in the microhardness H (Fig. 1), the acceleration of stage *II–III* upon exposure to a magnetic field, all other factors being equal, should lead to a strengthening of the crystals rather than to their softening, as observed in our experiments. This allows us to assume that exposure of point defects to magnetic fields stimulates their relaxation from state *II* to a state *III** differing from state *III*; i.e., the magnetic field induces a new concurrent process of relaxation of metastable magnetosensitive point-defect complexes.

ACKNOWLEDGMENTS

This work was supported by the Russian Foundation for Basic Research (project nos. 02-02-99302 and 01-02-99115) and the Ministry of Education of the Russian Federation (project no. E00-3.4-552).

REFERENCES

1. Yu. I. Golovin and R. B. Morgunov, Fiz. Tverd. Tela (St. Petersburg) **37** (4), 1239 (1995) [Phys. Solid State **37**, 674 (1995)].
2. Yu. I. Golovin and R. B. Morgunov, Fiz. Tverd. Tela (St. Petersburg) **37** (5), 1352 (1995) [Phys. Solid State **37**, 734 (1995)].
3. V. I. Al’shits, E. V. Darinskaya, and E. A. Petrzhik, Izv. Vyssh. Uchebn. Zaved., Chern. Metall., No. 10, 85 (1990).
4. V. I. Al’shits, E. V. Darinskaya, and E. A. Petrzhik, Fiz. Tverd. Tela (Leningrad) **33** (10), 3001 (1991) [Sov. Phys. Solid State **33**, 1694 (1991)].
5. Yu. I. Golovin and R. B. Morgunov, Zh. Éksp. Teor. Fiz. **115** (2), 605 (1999) [JETP **88**, 332 (1999)].
6. Yu. I. Golovin, R. B. Morgunov, and A. A. Dmitrievskii, Mater. Sci. Eng. **288/2**, 261 (2000).
7. R. B. Morgunov and A. A. Baskakov, Fiz. Tverd. Tela (St. Petersburg) **43** (9), 1632 (2001) [Phys. Solid State **43**, 1700 (2001)].
8. Yu. I. Golovin, R. B. Morgunov, A. A. Baskakov, *et al.*, Pis’ma Zh. Éksp. Teor. Fiz. **69** (2), 114 (1999) [JETP Lett. **69**, 127 (1999)].
9. Yu. I. Golovin, R. B. Morgunov, A. A. Baskakov, and S. Z. Shmurak, Fiz. Tverd. Tela (St. Petersburg) **41** (11), 1944 (1999) [Phys. Solid State **41**, 1783 (1999)].
10. V. A. Makara, L. P. Steblenko, N. Ya. Gorid’ko, *et al.*, Fiz. Tverd. Tela (St. Petersburg) **43** (3), 462 (2001) [Phys. Solid State **43**, 480 (2001)].
11. A. M. Orlov, A. A. Skvortsov, and L. I. Gonchar, Fiz. Tverd. Tela (St. Petersburg) **43** (7), 1207 (2001) [Phys. Solid State **43**, 1252 (2001)].
12. V. M. Maslovskiĭ, Yu. A. Klimov, N. S. Samsonov, and E. V. Simanovich, Fiz. Tekh. Poluprovodn. (St. Petersburg) **28**, 772 (1994) [Semiconductors **28**, 453 (1994)].
13. V. P. Vlasov, F. A. Zaitov, V. M. Kanevskiĭ, *et al.*, Fiz. Tverd. Tela (St. Petersburg) **34** (10), 3264 (1992) [Sov. Phys. Solid State **34**, 1747 (1992)].
14. M. Levin and V. Maslowsky, Solid State Commun. **90** (12), 813 (1994).
15. V. N. Davydov, E. A. Loskutova, and E. P. Naĭden, Fiz. Tekh. Poluprovodn. (Leningrad) **23**, 1596 (1989) [Sov. Phys. Semicond. **23**, 989 (1989)].
16. A. Mutoz, E. Cabrera, H. Riveros, *et al.*, Phys. Rev. B **31** (12), 8196 (1985).
17. J. M. García, J. A. Hernández, E. H. Carillo, and J. O. Rubio, Phys. Rev. B **21** (11), 5012 (1980).

18. E. Orozco, J. Soullard, C. Zaldo, and F. Agully-Lypez, Philos. Mag. A **50** (3), 425 (1984).
19. C. Zaldo, E. Orozco, A. Mendoza, and J. Rubio, J. Phys. D: Appl. Phys. **18**, 247 (1985).
20. J. Rubio, J. Phys. Chem. Solids **52** (1), 101 (1991).
21. Yu. I. Golovin, R. B. Morgunov, V. E. Ivanov, and A. A. Dmitrievskiĭ, Zh. Éksp. Teor. Fiz. **117**, 1080 (2000) [JETP **90**, 939 (2000)].
22. Yu. S. Boyarskaya, D. Z. Grabko, and M. S. Kats, *Physics of Microindentation* (Shtiintsa, Kishinev, 1986), pp. 10–12.
23. Yu. S. Boyarskaya, R. P. Zhitaru, and M. A. Linte, Cryst. Res. Technol. **17** (10), 1283 (1982).
24. A. Hartmanova, Phys. Status Solidi A **7**, 303 (1971).
25. N. M. Bannon and J. Corish, Philos. Mag. A **51** (6), 797 (1985).
26. K. M. Salikhov, Yu. N. Molin, R. Z. Sagdeev, and A. L. Buchachenko, in *Spin Polarization and Magnetic Field Effects in Radical Reactions*, Ed. by Yu. N. Molin (Elsevier, Amsterdam, 1984).

Translated by O. Borovik-Romanova

Physics of the Solid State, Vol. 45, No. 2, 2003, pp. 276–282. Translated from Fizika Tverdogo Tela, Vol. 45, No. 2, 2003, pp. 262–268.
Original Russian Text Copyright © 2003 by Troyanchuk, Trukhanov, Chobot, Szymczak.

MAGNETISM AND FERROELECTRICITY

Preparation and Magnetic and Electrical Properties of $EuBaMn_2O_{6-\gamma}$ (γ = 0, 1)

I. O. Troyanchuk*, S. V. Trukhanov*, G. M. Chobot*, and H. Szymczak**
**Institute of Solid-State and Semiconductor Physics, National Academy of Sciences of Belarus, ul. Brovki 17, Minsk, 220072 Belarus*
e-mail: troyan@ifttp.bas-net.by
***Institute of Physics, Polish Academy of Sciences, Warsaw, PL-02-668 Poland*

Received February 26, 2002

Abstract—The $EuBaMn_2O_6$ composition prepared in air at T = 1500°C is shown to be a cubic perovskite exhibiting spin-glass properties below T_f = 40 K. The reduced composition, $EuBaMn_2O_5$, crystallizes in a perovskite-like, $YBaCuFeO_5$-type layered structure with a tetragonal unit cell. $EuBaMn_2O_5$ with crystallographically ordered Eu^{3+} and Ba^{2+} ions is a ferromagnet with T_N = 160 K. The anomalous behavior of the paramagnetic susceptibility is assumed to be due to a partial ordering of the Mn^{2+} and Mn^{3+} ions. $EuBaMn_2O_5$ oxidized in air at 900°C to $EuBaMn_2O_6$ has a magnetic ordering temperature T_M = 260 K, near which the magnetoresistance reaches a peak value. X-ray diffraction measurements show the long-range order in the Eu^{3+} and Ba^{2+} ion arrangement to persist in the oxidized $EuBaMn_2O_6$ sample. *© 2003 MAIK “Nauka/Interperiodica”.*

1. INTRODUCTION

The discovery of the colossal magnetoresistance phenomenon in the $Ln_{1-x}D_xMnO_3$-type manganites (Ln stands for the lanthanide, and D, for an alkaline-earth metal) [1–3] initiated intense study of their physicochemical properties aimed at establishing the nature of the relation connecting the magnetic and electrical characteristics of these systems. It is well known that the magnetic and electrical states of the manganites are determined to a great extent by the relative concentrations of the tri- and quadrivalent manganese. This relation is usually varied by properly doping the compound by an alkaline-earth metal. There is, however, another way in which the oxygen content can be varied in the sample. It was found, for instance, that oxidation of $LaMnO_3$ initiates a transition from the antiferromagnetic to a ferromagnetic state that exhibits a clearly pronounced relation between the magnetic and electrical properties [4, 5]. The formation of oxygen vacancies gives rise to a strong increase in ionic conductivity in the manganites, which has a certain potential application [6]. Oxygen vacancies can order, as occurs in $CaMnO_{3-\gamma}$ [7]. Interesting results were obtained in a study of the $Y_{1-x}Ba_xMnO_{3-\gamma}$ system. Attempts to synthesize the $YBa_2Mn_3O_7$ compound in this system, by analogy with the high-temperature superconductor $YBa_2Cu_3O_7$, failed, however. The compound that was obtained was $YBa(Mn^{2+}Mn^{3+})O_5$, which has the structure of $YBaCuFeO_5$ with crystallographically ordered Y and Ba ions, as well as oxygen vacancies [8]. All manganese ions are arranged in square pyramids. Magnetic measurements showed this compound to have a magnetic-ordering temperature T_M = 167 K and a spontaneous magnetic moment per formula unit of $0.5\mu_B$. According to neutron diffraction studies, the spontaneous magnetic moment is due to antiparallel ordering of the magnetic moments of the Mn^{2+} and Mn^{3+} ions [9]. It should be pointed out that the magnetic and electrical properties of the manganites depend strongly, for the same Mn^{3+}/Mn^{4+} ratio, on the radius of the rare-earth ion. For instance, $La_{0.7}Ca_{0.3}MnO_3$ is a ferromagnetic metal below T_C = 250 K [10], whereas $Tb_{0.7}Ca_{0.3}MnO_3$ is a spin glass with T_f = 40 K [11]. This stimulated our study of the properties of the $Eu_{0.50}Ba_{0.50}MnO_{3-\gamma}$ system as functions of the oxygen content. The europium ion was chosen because the Eu^{3+} ions reside, as a rule, in the ground diamagnetic state and do not contribute noticeably to the sample magnetization.

2. EXPERIMENT

Polycrystalline $Eu_{0.50}Ba_{0.50}MnO_3$ was prepared using the usual ceramic technology. The OSCh-grade Eu_2O_3 and Mn_2O_3 oxides and the $BaCO_3$ carbonate were weighed in the required molar ratio and mixed thoroughly in an agate mortar with addition of a small amount of ethyl alcohol. The mixture thus prepared was pressed into a pellet and calcined in air at 1150°C for 4 h with subsequent grinding. The final synthesis was carried out in air at 1560°C for 2 h. The sample was spread on a platinum substrate. To obtain a composition with a close-to-stoichiometric oxygen content, the samples were maintained at 900°C in air for 100 h and cooled afterwards to room temperature at a rate of 100°C/h.

X-ray diffraction measurements on the product of the chemical reaction were performed on a DRON-3 diffractometer in Cr-K_α radiation at room temperature within the angular interval $30° \le 2\theta \le 100°$. The oxygen content was deduced from thermal gravimetry data (TGA). Our studies suggest that the sample synthesized in air was stoichiometric in oxygen. According to [12], the oxygen content in manganites prepared in air and substituted strongly ($x \sim 0.50$) by calcium and strontium ions is close to its stoichiometric value.

A reduced $EuBaMn_2O_5$ sample was prepared using a topotactic reaction. The sample was placed in an evacuated quartz ampule containing a predetermined amount of metallic tantalum employed as an oxygen absorber. The quartz ampule was maintained at 900°C for 10 h, followed by cooling to room temperature at a rate of 100°C/h.

The oxygen content in the reduced sample was derived from the change in sample mass by weighing the sample before and after the reduction. The sample chosen for reduction had a mass of ~3 g. In this case, the error in the oxygen concentration measurements did not exceed 0.03%.

The reduced sample was reoxidized in air at 900°C for 5 h. The weighing made after the reoxidation showed that the oxygen content increased and corresponded to the chemical formula $EuBaMn_2O_6$.

The magnetization was studied on a commercial OI-3001 vibrating-sample magnetometer in the temperature range 4–300 K. The magnetic transition temperature was determined in a weak magnetic field of 100 Oe. Electrical-resistivity measurements were performed on samples 8 × 2 × 2 mm in size, following the standard four-probe technique at temperatures of 77–350 K. The magnetoresistance was calculated from the expression

$$MR(\%) = \{[\rho(H) - \rho(0)]/\rho(H)\} \times 100\%, \quad (1)$$

where $\rho(H)$ is the electrical resistivity in a magnetic field of 9 kOe and $\rho(0)$ is that in a zero magnetic field. The magnetic field was applied parallel to the electrical current flowing through the sample.

3. RESULTS AND DISCUSSION

X-ray diffraction measurements show the $Eu_{0.50}Ba_{0.50}MnO_3$ perovskite prepared in air to have cubic structure with the unit-cell parameter $a = 3.881$ Å ($V = 58.47$ Å^3) (Fig. 1a). The $EuBaMn_2O_5$ sample reduced in the quartz ampule produces the same reflections as $YBaCuFeO_5$; therefore, these two compounds are isostructural. The reduced compound $EuBaMn_2O_5$ has a tetragonal unit cell with the parameters $a = 3.945$ Å and $c = 7.712$ Å ($V = 120.03$ Å^3; Fig. 1b). The doubling of the unit-cell parameter along one direction is due to the Y and Ba ions ordering in alternate planes. A similar structure was observed in $HoBaCo_2O_5$ cobaltites in [13]. TGA data suggest that the oxidation of the $EuBaMn_2O_5$ sample in air starts at 250°C and comes to an end at approximately 500°C. The change in mass corresponds to an increased oxygen content and the chemical formula $EuBaMn_2O_6$. The samples annealed at 1300°C and prepared from reagents at 1560°C have identical diffractograms. In this case, both samples are cubic perovskites. However, if the annealing was performed at temperatures below 1200°C, strong deviations from cubic symmetry are observed. For instance, the unit cell of the $EuBaMn_2O_6$ sample annealed at 900°C for 5 h exhibits pronounced orthorhombic distortions (Fig. 1c). The unit-cell parameters are $a = 3.917$ Å, $b = 3.835$ Å, and $c = 7.764$ Å ($V = 116.63$ Å^3).

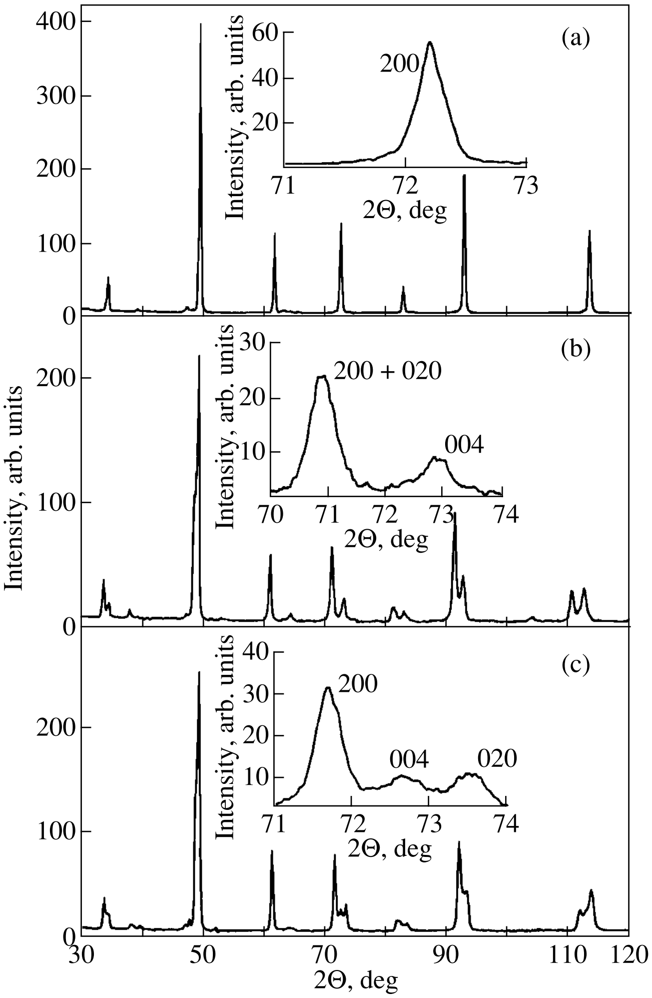

Fig. 1. X-ray powder diffractograms obtained at room temperature for the following compositions: (a) starting, crystallographically disordered $Eu_{0.50}Ba_{0.50}MnO_3$; (b) anion-deficient, crystallographically ordered $EuBaMn_2O_5$; and (c) crystallographically ordered $EuBaMn_2O_6$ annealed in air at 900°C and stoichiometric in oxygen. The reflections shown in the insets are (a) (200), (b) (200) + (020) and (004), and (c) (200), (020), and (004).

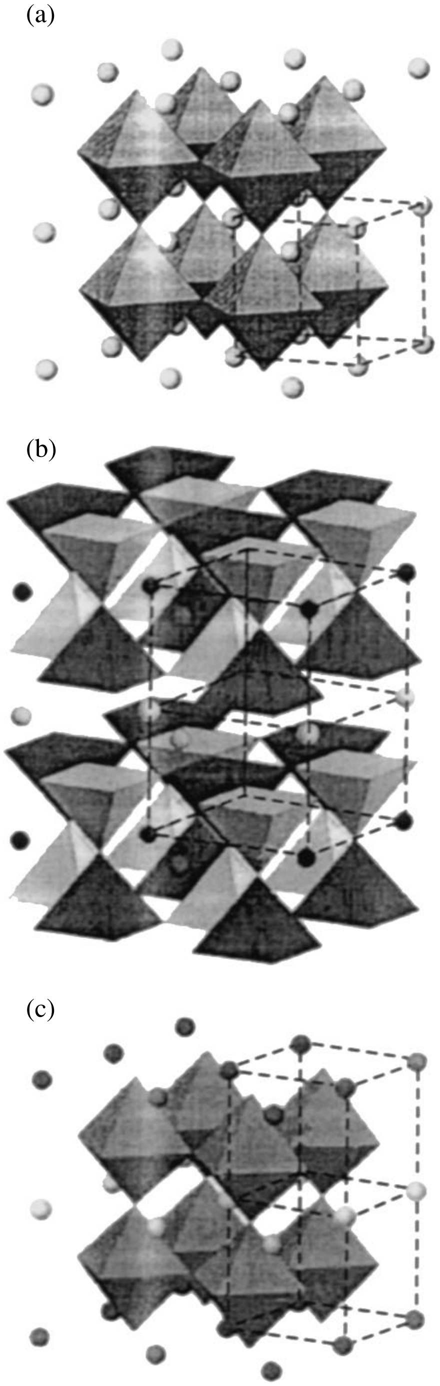

Fig. 2. A model of the crystal structure for (a) starting, crystallographically disordered $Eu_{0.50}Ba_{0.50}MnO_3$; (b) anion-deficient, crystallographically ordered $EuBaMn_2O_5$; and (c) crystallographically ordered $EuBaMn_2O_6$ annealed in air at 900°C and stoichiometric in oxygen. The light and dark circles in (b, c) denote the Eu^{3+} and Ba^{2+} ions, respectively. The dashed contour shows the unit cells of the compositions.

Remarkably, the reduced volumes of the samples prepared in air at 1560°C and annealed at 900°C for 5 h after the reduction are approximately equal, although in the second case the volume is slightly smaller. This implies that the annealed ordered composition $EuBaMn_2O_6$ has shorter Mn–O bond lengths than the disordered $Eu_{0.50}Ba_{0.50}MnO_3$ compound.

Our studies suggest that the structure of the starting disordered composition $Eu^{3+}_{0.50}Ba^{2+}_{0.50}Mn^{3+}_{0.50}Mn^{4+}_{0.50}O^{2-}_3$ prepared in air represents an array of MnO_6 oxygen octahedra which share corners and extend in all three spatial directions (Fig. 2a). The Mn^{3+} and Mn^{4+} ions are located in the MnO_6 oxygen octahedra. The cations are distributed randomly. The structure of the reduced composition is as follows. The Eu^{3+} and Ba^{2+} cations are located in different planes alternating along the *c* direction (Fig. 2b). The oxygen vacancies lie in the planes at the level of the Eu^{3+} ion. The Mn^{3+} and Mn^{2+} ions reside in the MnO_5 oxygen pentahedra, which likewise share corners and extend in all three spatial directions. The chain of the pentahedra breaks along the *c* axis. The ordering of the cations and oxygen vacancies makes the unit cell double. The ordering of the Eu^{3+} and Ba^{2+} cations and oxygen vacancies permits one to consider the anion-deficient compositions $Eu^{3+}_{0.50}Ba^{2+}_{0.50}Mn^{3+}_{0.50}Mn^{2+}_{0.50}O^{2-}_{2.50}$ as independent compounds with a doubled chemical formula $EuBaMn_2O_5$. The structure of the ordered composition $Eu^{3+}Ba^{2+}Mn^{3+}Mn^{4+}O^{2-}_6$, which is stoichiometric in oxygen, retains the ordered distribution of the Eu^{3+} and Ba^{2+} cations, as a result of which the unit cell also doubles. However, the symmetry of the unit cell changes from tetragonal to orthorhombic.

The temperature dependences of the magnetization were measured under heating in a field of 100 Oe following field cooling (FC) and zero-field cooling (ZFC). The ZFC magnetization curve of the $Eu_{0.50}Ba_{0.50}MnO_3$ sample prepared in air at 1560°C exhibits a sharp maximum near $T_f = 40$ K. Below this temperature, the ZFC and FC curves diverge (Fig. 3a). The dependence of magnetization on an external magnetic field does not reveal linear parts up to $H = 15$ kOe (Fig. 4). The magnetization in a field of 15 kOe is $0.36\mu_B$, which is a few times less than the value expected for the case of purely ferromagnetic ordering ($3.5\mu_B$). Note that the temperature $T_f = 40$ K is typical of a spin-glass-type state in manganites [14]. Figure 3b illustrates the measurements of the ZFC and FC magnetizations as functions of temperature made on the $EuBaMn_2O_5$ reduced composition. The FC magnetization begins to rise sharply below $T_N = 160$ K. Almost immediately below this temperature, the ZFC and FC curves diverge. The magnitude of the ZFC magnetization depends weakly on temperature below 140 K and is considerably lower than the FC magnetization. Near 145 K, a maximum in the temperature dependence of the FC magnetization appears. This type of behavior of the ZFC and FC magnetizations may be expected in strongly anisotropic ferro- or ferrimagnets. An interesting feature of the FC

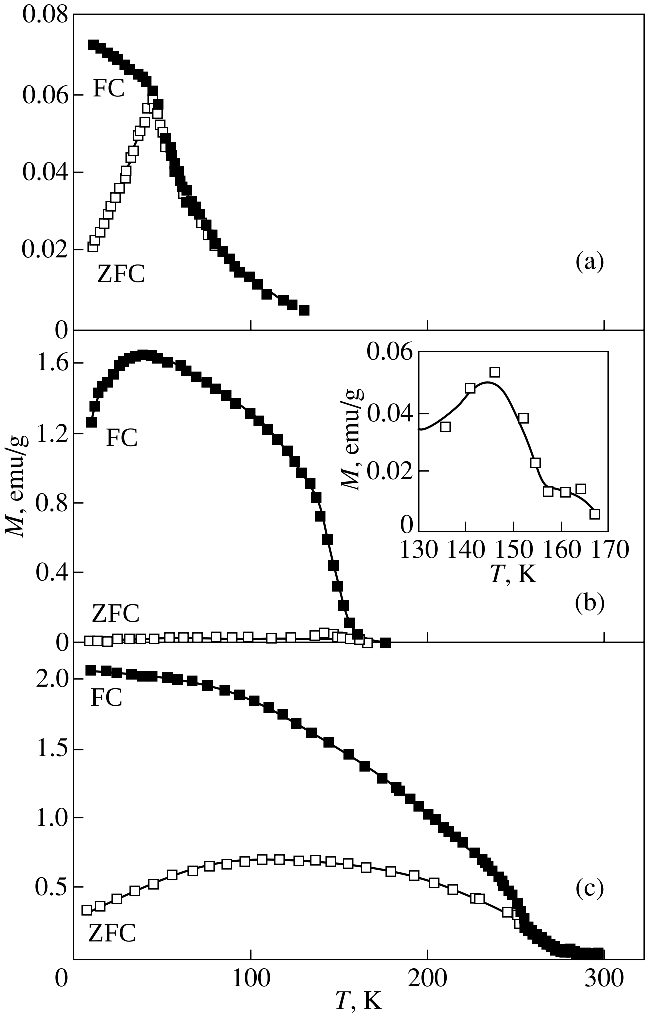

Fig. 3. Temperature dependence of magnetization in an external magnetic field $H = 100$ Oe after zero-field cooling (ZFC) (open symbols) and field cooling (FC) (filled symbols) for (a) starting, crystallographically disordered $Eu_{0.50}Ba_{0.50}MnO_3$; (b) anion-deficient, crystallographically ordered $EuBaMn_2O_5$, and (c) crystallographically ordered $EuBaMn_2O_6$ annealed in air at 900°C and stoichiometric in oxygen. The inset shows the ZFC magnetization peak for panel (b).

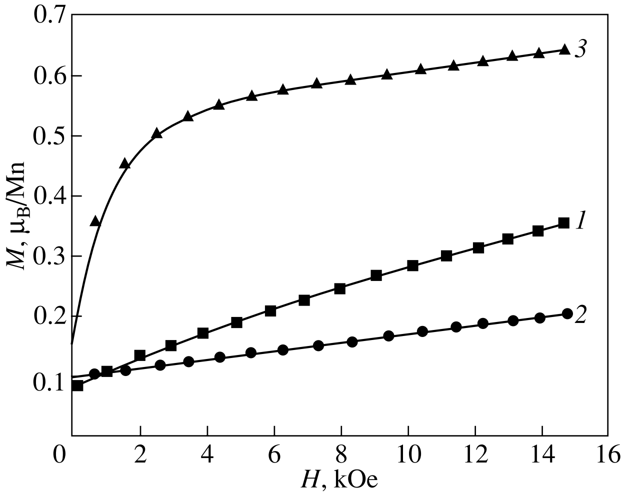

Fig. 4. Magnetization plotted vs. external magnetic field at 15 K for (*1*) starting, crystallographically disordered $Eu_{0.50}Ba_{0.50}MnO_3$; (*2*) anion-deficient, crystallographically ordered $EuBaMn_2O_5$; and (*3*) crystallographically ordered $EuBaMn_2O_6$ annealed in air at 900°C and stoichiometric in oxygen.

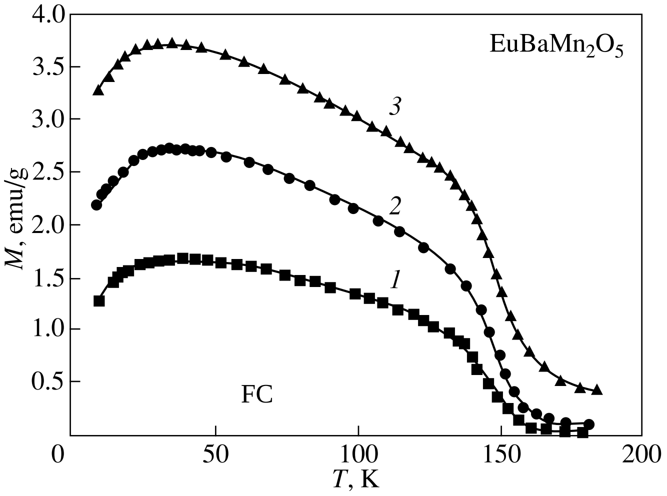

Fig. 5. Temperature dependence of magnetization measured in various magnetic fields H: (*1*) 0.1, (*2*) 2.5, and (*3*) 10 kOe for the anion-deficient, crystallographically ordered $EuBaMn_2O_5$.

curves is the drop in magnetization with decreasing temperature in the interval 40–50 K. This effect is also well pronounced in strong fields, which is not characteristic of phenomena dominated by the contribution from the rare-earth sublattice or spin reorientation (Fig. 5). This phenomenon is possibly caused by changes in the crystal structure or by the formation of a spin-glass component. Due to large magnetic anisotropy, estimation of the spontaneous magnetic moment from the dependence of the magnetization on an external magnetic field is difficult. It can, however, be conjectured that this moment does not exceed $0.3\mu_B$ per $EuBaMn_2O_5$ formula unit (Fig. 4). The measured temperature dependence of the paramagnetic susceptibility yielded additional information on the magnetic state (Fig. 6). It turned out that this dependence exhibits a hysteretic, temperature-broadened anomaly characteristic of first-order phase transformations.

Orthorhombic $EuBaMn_2O_6$ annealed in air revealed a strong increase in the critical temperature for magnetic ordering. While cubic $Eu_{0.50}Ba_{0.50}MnO_3$ has a critical temperature $T_f = 40$ K, the orthorhombic sample of the same composition becomes magnetically ordered at 260 K (Fig. 3c). However, the spontaneous magneti-

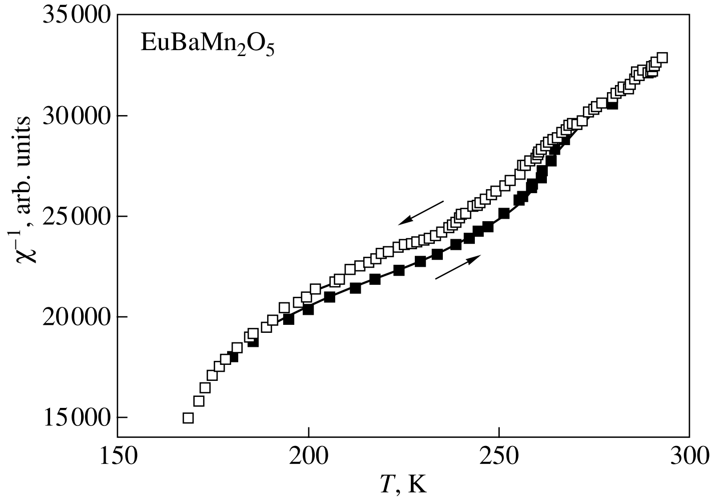

Fig. 6. Temperature dependence of inverse magnetic susceptibility in the paramagnetic region measured for the anion-deficient, crystallographically ordered $EuBaMn_2O_5$. Arrows identify the direction of measurement.

tion, which is close to 1 μ_B per formula unit of $EuBaMn_2O_6$, is considerably smaller than the value 7 μ_B/f.u. that could be expected in the case of purely ferromagnetic ordering.

An investigation of the electrical properties showed that all the compounds under study behave as semiconductors both above and below the magnetic-ordering temperature. The room-temperature electrical resistivity was found to be the highest in the reduced $EuBaMn_2O_5$ sample and the lowest in the orthorhombically distorted overoxidized $EuBaMn_2O_6$. The latter is the only sample exhibiting a clearly pronounced relation between the magnetic and electrical properties. Near the magnetic-ordering temperature, the temperature dependence of electrical conductivity reveals a break and the magnetoresistance reaches a maximum (Fig. 7). Note that this behavior is typical of weakly doped, ferromagnetic dielectric samples of manganites, such as $La_{1-x}Ca_xMnO_3$ $(0.10 \le x \le 0.20)$ [15].

It is well known that the magnetic state of the stoichiometric manganites $Ln_{1-x}D_xMnO_3$ is governed by the Mn^{3+}/Mn^{4+} ratio on the B sublattice of the ABO_3 perovskite, by the average ionic radii of the lanthanide and the alkaline-earth ion $\langle r_A \rangle$, and by the cation size misfit in the A sublattice:

$$\sigma^2 = \Sigma x_i r_i^2 - \langle r_A \rangle^2, \qquad (2)$$

where x_i is the filling of the A sublattice by the ith cation with the corresponding ionic radius r_i [16]. The smaller the average ionic radius on the A sublattice and the larger the difference between the Ln and D radii, the lower, as a rule, the magnetic ordering temperature [17, 18]. The variation in the magnetic properties of the $Ln_{0.50}Ba_{0.50}MnO_3$ system with decreasing Ln radius can be explained in terms of this model. The $Ln_{0.50}Ba_{0.50}MnO_3$ compounds (Ln = La, Pt, Nd) are ferromagnetic metals below T_C, with the magnetic-ordering temperature dropping sharply with decreasing radius of the rare-earth ion [19–21]. The spin-glass transition in the $Sm_{1-x}Ba_xMnO_3$ system occurs already for $x > 0.12$, with the ferromagnetic state failing to form within the concentration region $0 \le x \le 0.50$ [20]. This behavior is accounted for by the fact that the ionic radius of the barium ion in the 12-fold oxygen coordination, $R(Ba^{2+}) = 1.61$ Å, is much larger than $R(Sr^{2+}) = 1.44$ Å and $R(Ca^{2+}) = 1.34$ Å [22]. As a result, the misfit between the ionic radii of the rare-earth and barium ions is large. The spin-glass state sets in because of the large Mn–O–Mn bond-angle differences near the Ba^{2+} ions and of the breakdown of translational symmetry for the Mn–O bonds resulting from the Ba^{2+} ions being distributed statistically over the A sublattice. It is known that the closer the Mn–O–Mn bond angle is to 180°, the larger will be the positive exchange coupling [23]. As the Mn–O–Mn bond angle decreases, antiferromagnetic exchange interaction can become dominant [24]. Because of the barium ions being distributed at random over the A sublattice, the Mn–O–Mn bond angles that are opposite in exchange-interaction sign are also distributed statistically, which may give rise to the formation of a spin-glass-type state.

Reduction of $Eu_{0.50}Ba_{0.50}MnO_3$ to $EuBaMn_2O_5$ entails crystallographic ordering of the Eu^{3+} and Ba^{2+} ions and oxygen vacancies, as was established to occur in $YBaMn_2O_5$ [8]. The planes filled by the Eu^{3+} and Ba^{2+} ions alternate along the c direction in the tetragonal unit cell. Oxygen vacancies order in the plane containing the Eu^{3+} ions. The clearly pronounced transition to a paramagnetic state implies a well-formed long-range magnetic order. The magnetic structure of $YBaMn_2O_5$ is determined by the antiparallel orientation of the Mn^{2+} and Mn^{3+} magnetic moments [19]. If the magnetic moments of the Mn^{2+} and Mn^{3+} ions are oriented antiparallel to each other, the magnetic moment per formula unit ($EuBaMn_2O_5$) should be close to $2\mu_B$, whereas magnetic measurements indicate a smaller value, $0.5\mu_B$. As follows from neutron diffraction studies of $YBaMn_2O_5$, its magnetic structure is of the G type, in which the Mn^{2+} and Mn^{3+} ions are arranged in staggered order (with each Mn^{3+} ion surrounded by five Mn^{2+} ions, and vice versa). We believe that the arrangement of the Mn^{2+} and Mn^{3+} ions is not in complete order, thus reducing the average magnetic moment. This conjecture is buttressed by paramagnetic susceptibility measurements (Fig. 6). We assign the anomalous behavior of the paramagnetic susceptibility to the ordering of the Mn^{2+} and Mn^{3+} ions. The transition is strongly temperature-broadened, which may be due to the ions being ordered gradually; however, the ion order does not become complete.

Consider the nature of exchange interactions in $EuBaMn_2O_5$. A study of $YBaMn_2O_5$ [8] suggests that the Mn–O–Mn bond angles can be equal to 180° and 160°. The 180° bond is directed along the c axis of the unit cell, whereas the two 160° bonds lie in the a–c plane. The half-filled d_{z^2} orbitals of the Mn^{2+} and Mn^{3+} ions should overlap along the c axis, which corresponds, according to the Goodenough–Kanamori rule [23], to strong antiferromagnetic exchange. In the bases of the square pyramids, the half-filled (Mn^{2+}) and empty (Mn^{3+}) $d_{x^2-y^2}$ orbitals should overlap. In the case of 180° configuration, this corresponds to ferromagnetic exchange coupling and an overall A-type antiferromagnetic structure, whereas the structure revealed in actual fact is G type. Apparently, a decrease in the Mn–O–Mn angle to 160° results in a reversal of the sign of exchange interaction; one should also take into account the substantial antiferromagnetic contribution from the t_{2g} orbitals.

The results of the structural and magnetic studies suggest that the long-range order in the arrangement of the Eu^{3+} and Ba^{2+} ions breaks down after annealing in air at 1300°C. At lower temperatures, the long-range order persists, although the chemical formula $EuBaMn_2O_6$ corresponds to complete oxidation. The ordering of the Eu^{3+} and Ba^{2+} ions apparently entails an increase in the mean ⟨Mn–O–Mn⟩ bond angle and the onset of translational symmetry in the arrangement of these ions. These factors should stabilize the ferromagnetic component of exchange interaction. Indeed, the temperature of magnetic ordering rises sharply to 260 K; the magnitude of the spontaneous moment, however, is at odds with a purely ferromagnetic state. It may be suggested that the Mn^{3+} and Mn^{4+} ions are ordered and that the magnetic structure corresponds to antiparallel ordering of the magnetic moments of these ions. However, the magnetic moment is fairly high for such a structure (Fig. 4) and measurements show a very high electrical conductivity. The magnetoresistance peak is also characteristic of the ferromagnetic rather than ferrimagnetic state. The small magnetic moment can also be due to a noncollinear magnetic structure; the nature of this phenomenon remains, however, unclear. We believe that in this case we have a nonhomogeneous magnetic system characterized by the presence of ferromagnetic and antiferromagnetic regions of a fairly large size. Ordered $EuBaMn_2O_6$ can apparently support the coexistence of structural modifications characterized by different magnetic structures, as is the case, for instance, with $BiSrMn_2O_6$ [25]. Neutron diffraction measurements would be needed, however, to gain a better understanding of these features.

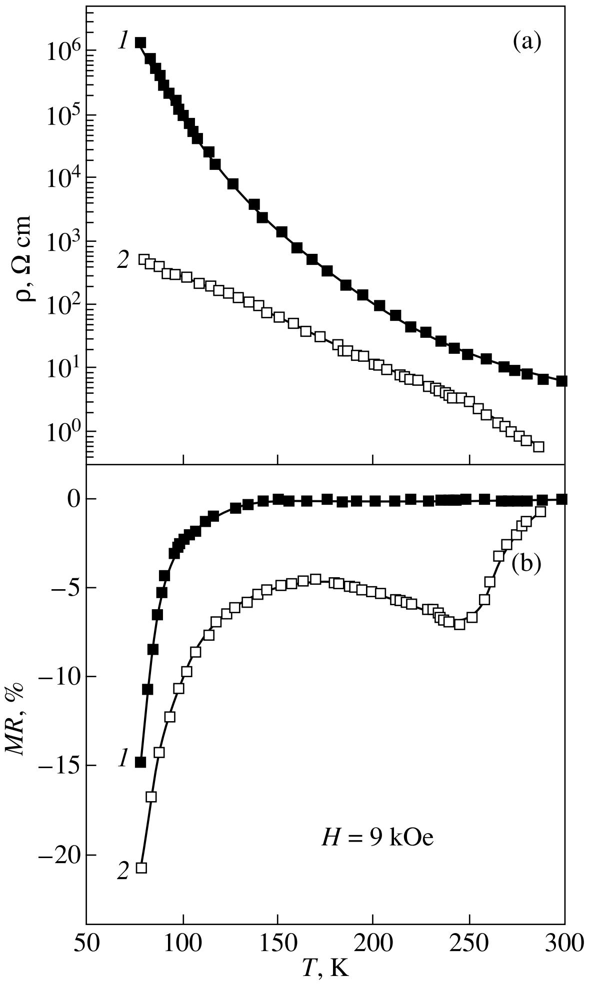

Fig. 7. Temperature dependence of (a) electrical resistivity and (b) magnetoresistance measured in a magnetic field of 9 kOe on the (*1*) starting, crystallographically disordered $Eu_{0.50}Ba_{0.50}MnO_3$ composition and (*2*) crystallographically ordered $EuBaMn_2O_6$ annealed in air at 900°C and stoichiometric in oxygen.

ACKNOWLEDGMENTS

This study was partially Supported by the Belarussian Foundation for Basic Research (grant no. F00-223) and the Committee for Science of Poland (KBN, grant no. 5 PO3B 016 20).

REFERENCES

1. K. Chahara, T. Ohno, M. Kasai, and Y. Kozono, Appl. Phys. Lett. **63**, 1990 (1993).
2. R. von Helmholt, J. Wecker, B. Holzapfel, *et al.*, Phys. Rev. Lett. **71**, 2331 (1993).
3. S. Jin, T. H. Tiefel, M. McCormack, *et al.*, Science **264**, 413 (1994).
4. M. Verelst, N. Rangavittal, C. N. R. Rao, and A. Rousset, J. Solid State Chem. **104**, 74 (1993).
5. J. Tëpfer and J. B. Goodenough, J. Solid State Chem. **130**, 117 (1997).
6. R. A. DeSouza, M. S. Islamb, and E. Ivers-Tiffée, J. Mater. Chem. **9**, 1621 (1999).
7. C. R. Wiebe, J. E. Greedan, J. S. Gardner, *et al.*, Phys. Rev. B **64**, 064421 (2001).
8. T. P. Beales, M. Mölgg, J. Jutson, and C. M. Friend, Phys. Status Solidi **161**, 271 (1997).
9. J. A. McAllister and J. P. Attfield, J. Mater. Chem. **8**, 1291 (1998).
10. J. W. Lynn, R. W. Erwin, J. A. Borchers, *et al.*, Phys. Rev. Lett. **76**, 4046 (1996).
11. J. M. De Teresa, M. R. Ibarra, J. García, *et al.*, Phys. Rev. Lett. **76**, 3392 (1996).
12. P. Schiffer, A. P. Ramírez, W. Bao, and S.-W. Cheong, Phys. Rev. Lett. **75**, 3336 (1995).
13. E. Suard, F. Fauth, V. Caignaert, *et al.*, Phys. Rev. B **61**, R11871 (2000).
14. J. Blasco, J. M. de Teresa, M. R. Ibarra, *et al.*, J. Phys.: Condens. Matter **8**, 7427 (1996).
15. I. O. Troyanchuk, Zh. Éksp. Teor. Fiz. **102**, 251 (1992) [Sov. Phys. JETP **75**, 132 (1992)].
16. P. V. Vanitha, P. N. Santoch, R. S. Sing, *et al.*, Phys. Rev. B **59**, 13539 (1999).
17. Y. Moritomo, Phys. Rev. B **60**, 10374 (1999).
18. L. M. Rodríguez-Martínez and J. P. Attfield, Phys. Rev. B **58**, 2426 (1998).
19. A. Barnabé, F. Millange, A. Maignan, *et al.*, Chem. Mater. **10**, 252 (1998).
20. I. O. Troyanchuk, D. D. Khalyavin, S. V. Trukhanov, and H. Szymczak, J. Phys.: Condens. Matter **11**, 8707 (1999).
21. I. O. Troyanchuk, S. V. Trukhanov, H. Szymczak, and K. Bärner, J. Phys.: Condens. Matter **12**, L155 (2000).
22. R. D. Shannon, Acta Crystallogr. A **32**, 751 (1976).
23. J. B. Goodenough, A. Wold, R. J. Arnott, and N. Menyuk, Phys. Rev. **124**, 373 (1961).
24. R. von Helmholt, L. Haupt, R. Bärner, and U. Sondermann, Solid State Commun. **82**, 693 (1992).
25. C. Frontera, J. L. García-Múñoz, A. Llobet, *et al.*, J. Phys.: Condens. Matter **13**, 1071 (2001).

Translated by G. Skrebtsov

Physics of the Solid State, Vol. 45, No. 2, 2003, pp. 283–286. Translated from Fizika Tverdogo Tela, Vol. 45, No. 2, 2003, pp. 269–272.
Original Russian Text Copyright © 2003 by Kimel', Pisarev, Rzhevskiĭ, Kalinin, Sitnikov, Stogneĭ, Bentivegna, Rasing.

Magnetooptical Study of Granular Silicon Oxide Films with Embedded CoNbTa Ferromagnetic Particles

A. V. Kimel'*, R. V. Pisarev*, A. A. Rzhevskiĭ*, Yu. E. Kalinin,
A. V. Sitnikov**, O. V. Stogneĭ**, F. Bentivegna***, and Th. Rasing*****

**Ioffe Physicotechnical Institute, Russian Academy of Sciences,
Politekhnicheskaya ul. 26, St. Petersburg, 194021 Russia*
e-mail: pisarev@pop.ioffe.rssi.ru
***Voronezh State Technical University, Moskovskiĭ pr. 14, Voronezh, 394026 Russia*
****Research Institute for Materials, University of Nijmegen, Toernooiveld 1, 6525 ED Nijmegen, The Netherlands*

Received April 2, 2002

Abstract—Granular silicon oxide films with embedded CoNbTa ferromagnetic particles and different relative contents of the metal and dielectric phases were studied using both steady-state and dynamic magnetooptical techniques with subpicosecond time resolution. Measurements were conducted in the spectral interval from 1.45 to 1.70 eV. The concentration dependences of the linear and photoinduced Kerr effects were found to behave similarly. Both relations are nonmonotonic with a maximum lying near the percolation threshold. *© 2003 MAIK "Nauka/Interperiodica".*

1. INTRODUCTION

Granular Fe-, Co-, and Ni-based nanocomposites containing ions of other transition metals have been recently attracting considerable interest. This interest can be attributed primarily to the giant magnetoresistance (GMR) effect observed in these materials [1]. In addition, nanocomposites exhibit a number of other unusual magnetic, electrical, optical, and magnetooptical properties, among which one can place the possibility of varying the electrical resistivity within a broad range, enhancement of optical nonlinearities [2], a correlation between the magnetic transport and nonlinear optical properties [3], the high magnetorefractive effect [4], and high electromagnetic-radiation absorption in the rf and microwave regions [5]. Although some physical mechanisms responsible for these phenomena still remain unclear, granular nanocomposites can be confidently classed among materials promising for use in developing reading heads and magnetooptical storage components [6, 7]. Thus, investigation of the magnetic, optical, and magnetooptical properties of granular structures is interesting from the standpoint of both fundamental and applied research. It should be pointed out that present-day requirements for the recording of information and readout speed impose stringent constraints not only on the magnitude of magnetoresistance or of nonlinear optical susceptibility but also on the response time of a material to magnetic or light excitation.

In this communication, we report on a study of the magnetic, optical, and magnetooptical properties of granular structures of amorphous silicon oxide containing cobalt-based ferromagnetic nanoclusters with various metallic phase contents. This investigation made use of both stationary and dynamic magnetooptical techniques, the latter providing the possibility of studying the magnetic and optical properties of a medium with subpicosecond time resolution.

2. SAMPLE GROWTH AND STRUCTURE

Granular films consisting of a silicon oxide dielectric matrix with ferromagnetic inclusions of a cobalt-, niobium-, and tantalum-based amorphous alloy with different contents of the metal phase represent typical percolation systems. Such films were prepared using ion beam sputtering on fixed glass ceramic substrates [8]. The metal grains were 2–5 nm in size, depending on the actual content of the metal phase. The metal nanoparticles made up a granular, electrically unconnected structure below the percolation threshold and a conducting cluster structure above this threshold. We studied three composites based on silicon oxide with embedded CoNbTa particles and an amorphous metal-alloy film which did not contain the oxide. The targets employed to prepare films of the metal alloy and of amorphous granular nanocomposites were of two types, namely, monolithic and composite. The monolithic targets of $Co_{86}Nb_{12}Ta_2$ composition were obtained from metals in the corresponding proportion through rf alloying in vacuum. To prepare the alloys, we employed 99.98%-pure cobalt and technical-grade tantalum and niobium, using the component weight content relative to the alloy composition required. After mechanical stirring, the melt of the corresponding composition was poured into a special ceramic mould. The

Film parameters

Sample	Number of SiO_2 plates in target	Composition	Silicon oxide content	Thickness, μm
A	0	$Co_{86.1}Nb_{12.2}Ta_{1.7}$	–	5.0
B	9	$Co_{53.4}Nb_{8.3}Ta_{1.1}$	$Si_{20.2}O_{17}$	4.6
C	11	$Co_{47.3}Nb_{7.0}Ta_{1.4}$	$Si_{23.6}O_{20.7}$	4.7
D	15	$Co_{27.7}Nb_{3.0}Ta_{0.7}$	$Si_{26.7}O_{41.9}$	4.6

melting and casting operations were performed in vacuum. Two targets measuring 270 × 70 × 14 mm were melted from one charge of the alloy. The targets were ground on both sides and soldered to the water-cooled base; one of them was mounted in the vacuum chamber for subsequent sputtering. The composite target of composition Co–Nb–Ta + SiO_2 was a $Co_{86}Nb_{12}Ta_2$ alloy target with quartz single-crystal plates, ~2 mm thick and ~9 mm wide, fixed to the surface of the alloy target perpendicular to its longitudinal axis. By properly varying the number of quartz plates (9, 11, and 15 plates were used in our case) and the distance between them, one could change the relative volumes of the deposited magnetic and dielectric phases and, thus, control the composition of the composite. The choice of the number of quartz plates for the composite target was dictated by the need for obtaining granular composites with a unconnected and a conducting-cluster structure, as well as with a structure close to the percolation threshold [8]. The samples prepared by sputtering were films 4.6–5 μm thick. The film thickness was measured with a MII-4 Linnik interferometer. The composition of the composites thus obtained was monitored using electron microprobe x-ray spectral analysis. The parameters of the films grown are specified in the table.

3. EXPERIMENTAL SETUP

The steady-state magnetic properties of the films were studied by measuring the meridional magnetooptical Kerr effect following the technique described in [9]. We used the radiation of a femtosecond titanium–sapphire laser with photon energy $\hbar\omega = 1.45–1.70$ eV and of a cw helium–neon laser with $\hbar\omega = 1.96$ eV. The sensitivity of determining the Kerr rotation angle of the light polarization was 10 seconds of arc. The light struck the sample at 45°. The strength of the dc magnetic field applied to the sample could be varied within the interval ±15 kOe.

Theoretical [10, 11] and, later, experimental [12] studies carried out as far back as the 1960s showed that magnetization in a medium can be produced not only by an external magnetic field but also by the electric field of a light wave. This approach, however, was earlier employed to study only diamagnetic and paramagnetic materials [13]; the investigation of magnetically ordered crystals was started only very recently [14]. Such studies make use of the completely optical technique of probing fast magnetic phenomena, in which a stronger (pump) beam transfers the medium to an excited state and a weaker beam (probe) interacts with the medium to reveal its new state. If a pulsed radiation source is available, this technique of optical pumping and probing can be employed to study the dynamic phenomena occurring in a solid with the time resolution limited by the pulse duration.

Consider a double-beam method in which a circularly polarized pump beam induces a magnetic moment in a medium as a result of the inverse Faraday effect [10, 11]. In this case, due to the Kerr magnetooptical effect, the polarization plane of the probe beam will be rotated by an angle θ_K:

$$\theta_K = \mathrm{Im}\left(\frac{1}{n(n^2-1)\int\limits_{-\infty}^{+\infty}|E|^2dt}\int\limits_{-\infty}^{+\infty}(p^{(+)}-p^{(-)})E^*dt\right), \quad (1)$$

where n is the refractive index of the medium, E is the pump pulse electric field, and $p^{(+)}$ and $p^{(-)}$ are the third-order nonlinear polarizations induced by the right-handed circularly polarized pump pulse and the right- and left-handed circularly polarized components of the probe pulse, respectively [15]. We will call this phenomenon the Kerr dynamic magnetooptical effect in what follows.

Dynamic measurements were carried out using the technique described in [15]. When using a femtosecond Ti-doped sapphire laser ($\hbar\omega = 1.45–1.60$ eV) operating with a pulse duration of 100 fs and a repetition frequency of 82 MHz, the pump and probe beams were focused on a sample at a 10 : 1 intensity ratio to a spot 100 μm in diameter for the pump beam and a slightly smaller spot for the probe beam. The spatial energy exposure per pump pulse was 10 μJ cm^{-2} in most measurements. The angles of incidence of the pump and probe beams were 20° and 30°, respectively. The Kerr rotation was measured as a function of the delay time between the pulses and of the photon energy. To exclude possible spurious signals, photoinduced rotation was measured as a function of the pump polarization ellipticity. In complete agreement with the theory of the dynamic magnetooptical Kerr effect, the

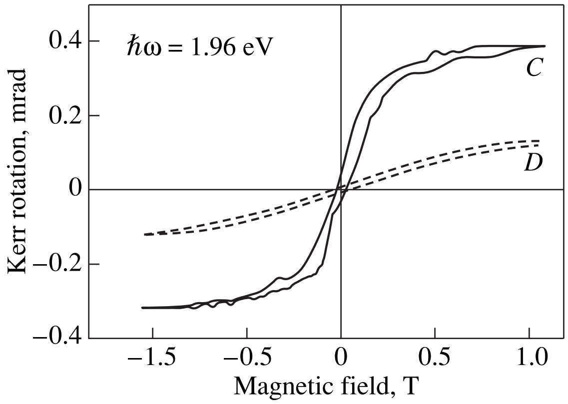

Fig. 1. Field dependences of the steady-state meridional Kerr effect in films *C* and *D*.

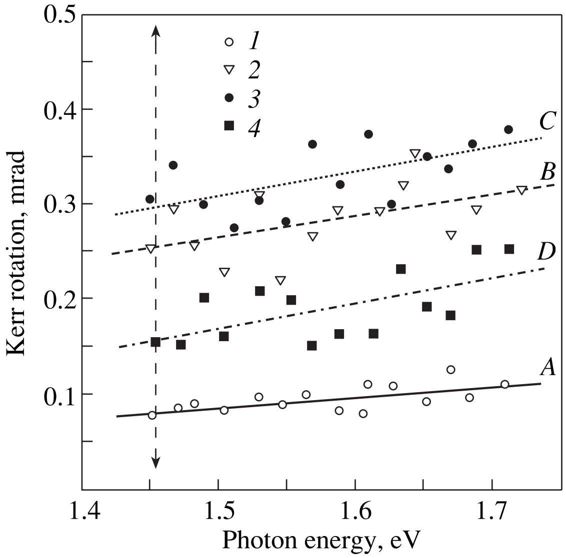

Fig. 2. Spectral response of the steady-state meridional Kerr effect in films (*1*) *A*, (*2*) *B*, (*3*) *C*, and (*4*) *D* measured in a field of 3 kOe. The lines plot linear fits to experimental data.

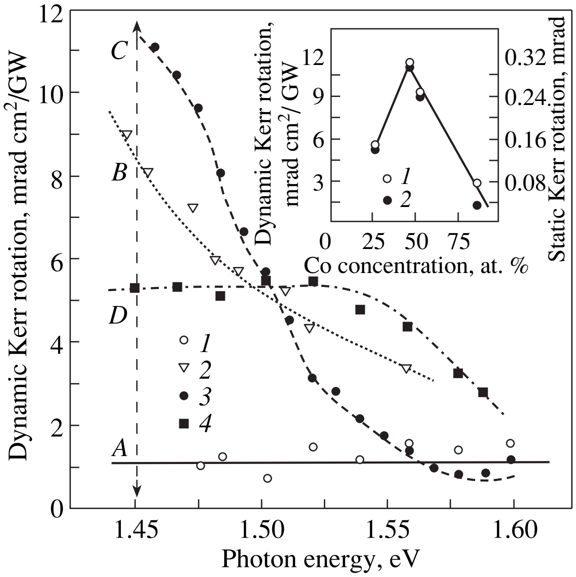

Fig. 3. Spectral response of the dynamic Kerr effect in films (*1*) *A*, (*2*) *B*, (*3*) *C*, and (*4*) *D*. The lines plot linear fits to experimental data. The inset shows (*1*) the steady-state and (*2*) dynamic Kerr effects as functions of cobalt content.

response was maximal under circularly polarized pumping.

4. EXPERIMENTAL RESULTS AND DISCUSSION

Figure 1 displays field dependences of the Kerr effect for films *C* and *D*. The field dependences exhibit a narrow hysteresis and reach practically complete saturation in fields ±15 kOe. The weak saturation fields imply that the CoNbTa particles embedded in the SiO_2 matrix are ferromagnetic. No noticeable dispersion was observed in the spectral responses within the photon energy range covered (Fig. 2). At the same time, one clearly sees a nonmonotonic dependence of the magnitude of the effect on the Co content, which passes through a maximum at a cobalt concentration of 45 at. %. Note that in granular films, the magnitude of the magnetooptical Kerr effect is two to three times larger than that in a metal alloy.

Investigation of the behavior of the Kerr effect with time showed the signal to be observed only in the region where the pump and probe pulses overlap. Note that in granular structures, local-field enhancement effects occurring during the pulse overlap may contribute considerably to the magnitude of nonlinear optical phenomena, in particular, of the dynamic magnetooptical Kerr effect. After termination of the pumping, the local-field effects decay rapidly as the optical coherence is lost. This may account for the dynamic Kerr effect being observed only during the pump and probe pulse overlap. Another factor that may explain this behavior of the Kerr effect is the short nonequilibrium spin polarization lifetime, which is associated with the short lifetimes of electrons in the excited state [16] and of spin excitations [5].

The spectral response of the dynamic magnetooptical Kerr effect is shown graphically in Fig. 3. In contrast to the static effect, the dynamic one reveals strong dispersion in all granular structures. The spectral response exhibits the presence of electron transitions near 1.45 eV or at a lower energy beyond the operating range of the Ti-doped sapphire laser. It should be pointed out that the dynamic Kerr effect in a monolithic CoNbTa film is practically independent of photon energy. Thus, the electron transition near 1.45 eV (or at a lower energy) is obviously induced by processes occurring in CoNbTa nanoparticles and manifestations of this transition can be revealed only by using a method based on measuring the dynamic magnetooptical Kerr effect. In our opinion, the resonant behavior of the nonlinear magnetooptical signal near 1.45 eV is due to local-field enhancement effects in the vicinity of plasmon transitions in CoNbTa nanoparticles.

The inset to Fig. 3 plots the dynamic and steady-state magnetooptical Kerr effects vs. cobalt content in granular films observed at a photon energy $\hbar\omega$ = 1.45 eV. The identical behavior of the concentration dependences of these phenomena appears remarkable. This implies a correlation between the steady-state and dynamic Kerr effects. Note that a correlation between the magnetic transport and nonlinear optical properties in granular nanocomposites was earlier observed experimentally in [3]. Revealing the mechanisms responsible for the interrelation of these phenomena appears to be an interesting task for further studies.

5. CONCLUSIONS

Thus, we have obtained and studied granular nanocomposites of a CoNbTa ferromagnetic alloy embedded in a silicon oxide matrix with different cobalt contents by using the steady-state and dynamic magnetooptical methods. The spectral response and concentration dependences of the steady-state and dynamic magnetooptical Kerr effects were investigated and compared. The spectral response of the linear Kerr effect exhibits a weak and monotonic dependence on photon energy. By contrast, the spectral studies of the dynamic Kerr effect provide evidence of electron transitions occurring in granular films at photon energies below 1.45 eV. The difference between the steady-state and dynamic spectral responses can be accounted for by local-field enhancement effects near the plasmon resonance in metal grains. The concentration dependences of the steady-state and dynamic Kerr effects reveal a nonmonotonic behavior and exhibit a maximum near the percolation threshold, where the cobalt concentration is about 45 at. %.

ACKNOWLEDGMENTS

This study was supported by the Russian Foundation for Basic Research and programs of the Ministry of Industry and Science of the Russian Federation.

REFERENCES

1. A. E. Berkovitz, J. R. Mitchell, M. J. Carey, *et al.*, Phys. Rev. Lett. **68**, 3745 (1992).
2. V. M. Shalaev and A. K. Sarychev, Phys. Rev. B **57**, 13265 (1998).
3. T. V. Murzina, T. V. Misuryaev, A. F. Kravets, *et al.*, Surf. Sci. **482–485**, 1101 (2001).
4. E. A. Gan'shina, A. B. Granovskiĭ, B. Dieny, *et al.*, Fiz. Tverd. Tela (St. Petersburg) **42**, 1860 (2000) [Phys. Solid State **42**, 1911 (2000)].
5. L. V. Lutsev, Fiz. Tverd. Tela (St. Petersburg) **44** (1), 97 (2002) [Phys. Solid State **44**, 102 (2002)].
6. A. Inoue, T. Zhang, H. Koshida, and A. Makino, J. Appl. Phys. **83**, 6326 (1998).
7. R. J. Gambino and T. R. McGuire, J. Appl. Phys. **57**, 3906 (1985).
8. Yu. E. Kalinin, A. T. Ponomarenko, A. V. Sitnikov, and O. V. Stogneĭ, Fiz. Khim. Obrab. Mater., No. 5, 14 (2001).
9. A. G. Banshchikov, A. V. Kimel', V. V. Pavlov, *et al.*, Fiz. Tverd. Tela (St. Petersburg) **42**, 884 (2000) [Phys. Solid State **42**, 909 (2000)].
10. L. P. Pitaevskiĭ, Zh. Éksp. Teor. Fiz. **39**, 1450 (1960) [Sov. Phys. JETP **12**, 1008 (1960/1961)].
11. L. D. Landau and E. M. Lifshitz, *Course of Theoretical Physics*, Vol. 8: *Electrodynamics of Continuous Media*, 3rd ed. (Nauka, Moscow, 1992; Pergamon, New York, 1984).
12. P. van der Ziel, P. S. Pershan, and L. D. Malmstrom, Phys. Rev. Lett. **15**, 190 (1965).
13. *Optical Orientation*, *Modern Problems in Condensed Matter Science*, Ed. by F. Meier and B. P. Zacharchenya (North-Holland, Amsterdam, 1984; Nauka, Leningrad, 1989), Vol. 8.
14. Ganping Ju, A. Vertikov, A. V. Nurmikko, *et al.*, Phys. Rev. B **57**, R700 (1998).
15. A. V. Kimel, V. V. Pavlov, R. V. Pisarev, *et al.*, Phys. Rev. B **62**, R10610 (2000).
16. A. V. Kimel, R. V. Pisarev, F. Bentivegna, and Th. Rasing, Phys. Rev. B **64**, 201103 (2001).

Translated by G. Skrebtsov

Physics of the Solid State, Vol. 45, No. 2, 2003, pp. 287–291. Translated from Fizika Tverdogo Tela, Vol. 45, No. 2, 2003, pp. 273–277.
Original Russian Text Copyright © 2003 by Balaev, Ivanova, Kazak, Ovchinnikov, Rudenko, Sosnin.

MAGNETISM AND FERROELECTRICITY

Magnetic Anisotropy of the VBO_3 and $CrBO_3$ Transition-Metal Borates

A. D. Balaev[1], N. B. Ivanova[2], N. V. Kazak[1], S. G. Ovchinnikov[1, 2],
V. V. Rudenko[1], and V. M. Sosnin[1]
[1]*Kirenskiĭ Institute of Physics, Siberian Division, Russian Academy of Sciences,*
Akademgorodok, Krasnoyarsk, 660036 Russia
e-mail: nat@iph.krasn.ru
[2]*Krasnoyarsk State Technical University, Krasnoyarsk, 660074 Russia*

Received April 5, 2002

Abstract—Temperature and field dependences of the magnetization of VBO_3 and $CrBO_3$ single crystals with the magnetic field applied parallel and perpendicular to the (111) basal plane were measured. VBO_3 was found to have a considerable uniaxial anisotropy with a field $H_a \approx 6.25$ T. $CrBO_3$ was shown to exhibit not only uniaxial but also hexagonal anisotropy. The experimental anisotropy constants were estimated, and their temperature dependences are presented. © *2003 MAIK "Nauka/Interperiodica".*

1. INTRODUCTION

Transition metal borates with the chemical formula ABO_3 (A = Fe, V, Cr, Ti) are attracting interest in connection with the rich variety of physical properties exhibited in this isostructural series [1]. Although the Mott–Hubbard strongly correlated dielectric oxides of the 3*d* metals have been investigated intensely due to their nontrivial physical properties, such as the high-temperature superconductivity of cuprates and the colossal magnetoresistance of manganese oxides, a number of the ABO_3 3*d*-metal borates, except $FeBO_3$, remain very poorly studied. As for the VBO_3 and $CrBO_3$ compounds, considered in this study, the literature does contain sufficient information to draw well-grounded conclusions concerning their magnetic structure [2–4], but there are practically no available data on their magnetic anisotropy. Knowledge of the magnitude and character of the anisotropic interactions are essential both to the understanding of the nature of the static and dynamic properties and to searching for possible applications of these materials.

The crystal lattices of the ABO_3 compounds belong to the rhombohedral symmetry group. A number of magnetic structures can exist in these compounds, depending on the actual filling of the *d* shell. For instance, VBO_3 is a collinear ferromagnet with a Curie temperature $T_C \approx 32$ K, $FeBO_3$ is a weak ferromagnet with the Néel temperature $T_N = 348$ K, and $CrBO_3$ is tentatively identified [2] as a collinear two-sublattice antiferromagnet with $T_N = 15$ K and magnetic moments aligned with the (111) threefold symmetry axis. The electron configurations of the magnetic ions V^{3+}, Fe^{3+}, and Cr^{3+} are d^2, d^5, and d^3, respectively. The main mechanism responsible for magnetic order in these compounds is believed to be indirect 90° exchange mediated by the O^{2-} anions.

Of the whole series of the 3*d*-metal borates, experimental studies of the magnetic anisotropy have thus far been performed on $FeBO_3$ only. This compound is known to be an easy-plane weak ferromagnet. A review of experimental data on the magnetic anisotropy of $FeBO_3$ single crystals can be found in [5]. As justly pointed out in [5], there is unfortunately some disagreement between the experimental data on the anisotropy of $FeBO_3$. For instance, the value of the uniaxial-anisotropy field H_a quoted in early studies [6, 7] is approximately 6.25–6.30 T, while in [8] this value is believed to be the sum of the contributions due to both the anisotropy and the Dzyaloshinski fields. In later studies [9, 10], the uniaxial-anisotropy field H_a, as derived from the data on the antiferromagnetic resonance, is reported to be 0.31–0.33 T, whereas the hexagonal anisotropy is considerably weaker and the corresponding field does not exceed 10^{-4} T.

The present communication reports on an experimental study of the temperature and field dependences of magnetization of VBO_3 and $CrBO_3$ single crystals.

2. SAMPLES AND EXPERIMENTAL TECHNIQUES

VBO_3 and $CrBO_3$ single crystals were grown by spontaneous crystallization from melt solutions of the systems M_2O_3–B_2O_3–(70 wt % PbO + 30 wt % PbF_2), where M = V, Cr. The single crystals obtained were thin plates up to 4 × 4 mm in size and about 0.1 mm thick, with a smooth lustrous surface. Unfortunately, the VBO_3 plates had an irregular shape, thus making in-plane anisotropy measurements impossible; the $CrBO_3$ single crystals were shaped as regular hexagonal plates.

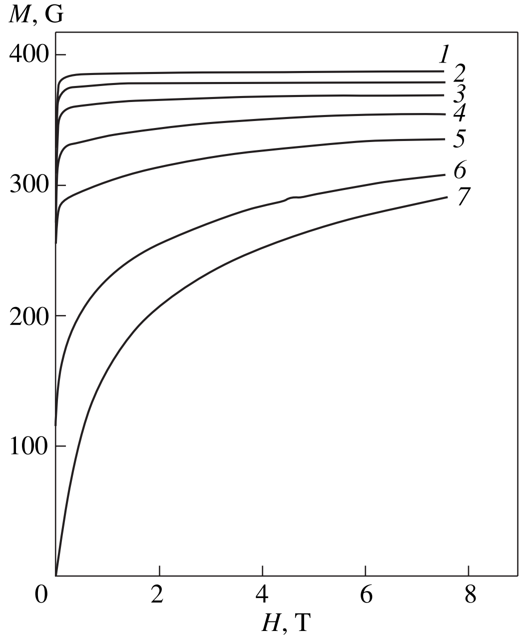

Fig. 1. Magnetic-field dependences of the magnetization of a VBO_3 single crystal measured in a magnetic field parallel to the (111) basal plane at different temperatures *T*: (*1*) 4.2, (*2*) 10, (*3*) 15, (*4*) 20, (*5*) 25, (*6*) 30, and (*7*) 32 K.

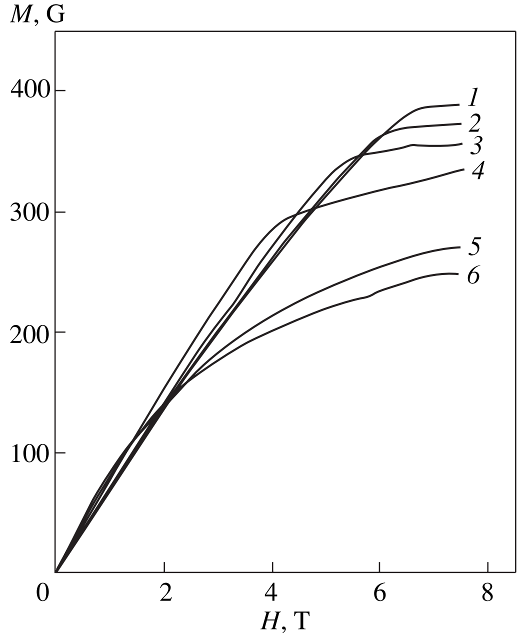

Fig. 2. Magnetic-field dependences of the magnetization of a VBO_3 single crystal measured in a magnetic field perpendicular to the (111) basal plane at different temperatures *T*: (*1*) 4.2, (*2*) 10, (*3*) 15, (*4*) 20, (*5*) 30, and (*6*) 32 K.

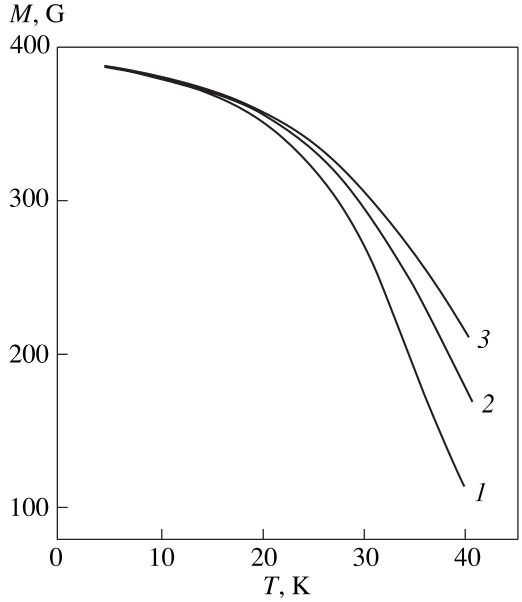

Fig. 3. Temperature dependences of the magnetization of a VBO_3 single crystal measured in a magnetic field parallel to the (111) basal plane for different values of the magnetic-field *H*: (*1*) 2, (*2*) 4, and (*3*) 6 T.

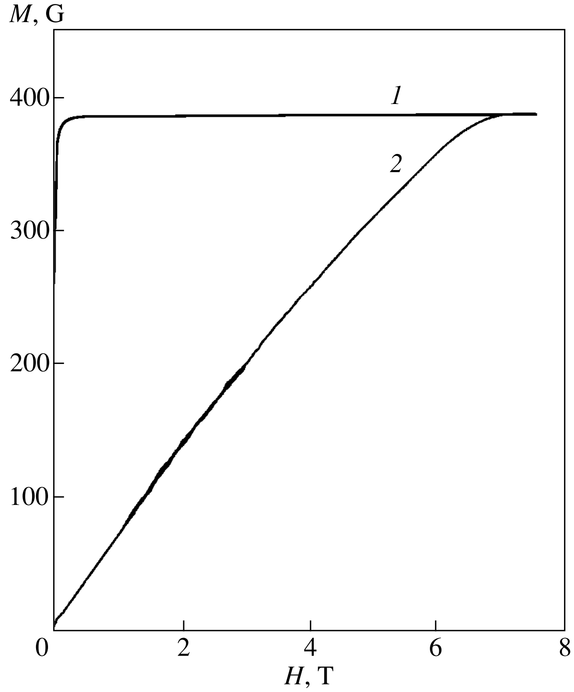

Fig. 4. Magnetization curves of VBO_3 in a magnetic field (*1*) parallel and (*2*) perpendicular to the (111) plane obtained at *T* = 4.2 K.

The temperature and magnetic field dependences of magnetization were performed using a vibrating-sample magnetometer with a superconducting solenoid within the temperature range 4.2–350 K and in magnetic fields of up to 7.5 T [11].

3. EXPERIMENTAL RESULTS

The magnetic-field dependences of the magnetization *M*(*H*) measured at various temperatures on VBO_3 single crystals in fields parallel and perpendicular to the

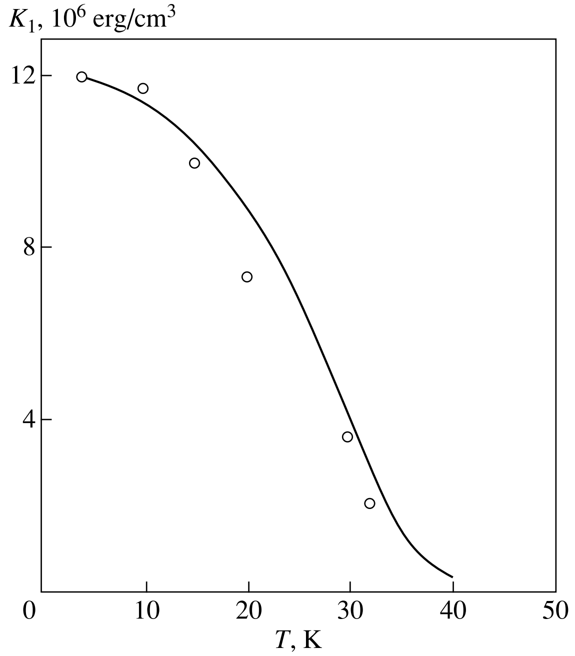

Fig. 5. Experimental (circles) and calculated (solid line) temperature dependences of the uniaxial-anisotropy constant of VBO_3.

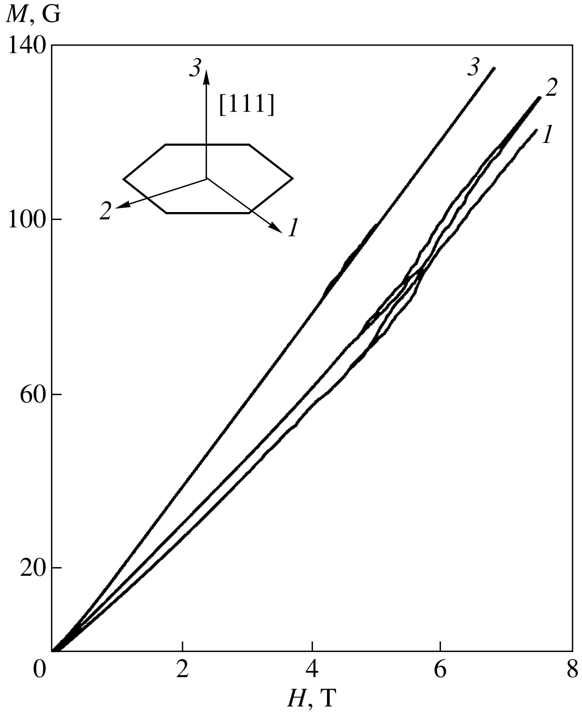

Fig. 6. Magnetization curves of a $CrBO_3$ single crystal obtained at T = 7.6 K.

(111) basal plane, which coincided with the plane of the plate, are displayed in Figs. 1 and 2, respectively, with due account of the demagnetization factor. The field orientation in the plane was chosen arbitrarily, because preliminary measurements showed the in-plane anisotropy to be negligible compared with the uniaxial one. Figure 3 displays temperature dependences of the magnetization $M(T)$ measured in various fields parallel to the plane of the crystal plate. As seen from Figs. 1–4, the behavior of the VBO_3 magnetization is characteristic of easy-plane ferromagnets [12]. The first uniaxial-anisotropy constant K_1, as calculated using the area method, was found to be approximately 1.2×10^7 erg/cm^3 (T = 4.2 K), which corresponds to a magnetic-anisotropy field H_a = 6.25 T. This is the largest value among the anisotropy fields of known rhombohedral antiferromagnets [13].

Figure 5 compares the experimental temperature dependence of the uniaxial-anisotropy constant for VBO_3 (symbols) with a theoretical curve calculated from the relation [14]

$$K_1(T) = K_{10}\left(\frac{M(T)}{M_S}\right)^3,$$

where K_{10} is the value of K_1 at T = 4.2 K, $M(T)$ is the VBO_3 magnetization in a field of 2 T, and M_S is the saturation magnetization. The experimental dependence is seen to be in good agreement with the calculated curve.

Using the paramagnetic Curie temperature Θ = 34 K determined in [2] and the magnetic moment $M = 1.8\mu_B$ measured by us earlier [1], we estimated the exchange field in VBO_3 as $H_E \approx 78.2$ T; this figure is lower by an order of magnitude than that for $FeBO_3$.

The magnetization curves for $CrBO_3$ are displayed in Fig. 6 for three magnetic field directions. Curves *1* and *2* correspond to two directions in the basal plane; namely, direction *1* points to the corner of the hexagonal plate, and direction *2* is perpendicular to a side of the plate. Curve *3* corresponds to the magnetic field aligned with the [111] axis. The magnetic field orientations are shown in the inset to Fig. 6. Figure 7 plots temperature dependences of the magnetization in a field of 0.5 T oriented in directions *1* and *3*.

As seen from Fig. 6, the $M(H)$ curve for $CrBO_3$ measured in the [111] direction is a straight line without any features, which apparently corresponds to the sublattice magnetization vectors canting toward the magnetic field direction. At the same time, the magnetization curves measured in an in-plane field exhibit a break in the interval 5–6 T; this break is accompanied by hysteresis and noise, which indicate instability of the magnetic state occurring in this field interval. According to [12], this instability may reflect that the exchange and anisotropic interactions compete with the effect of the external magnetic field. Thus, application of an in-plane magnetic field apparently initiates a spin-reorientation transition. This conjecture is buttressed by the hysteresis observed in the temperature dependences of magnetization (Fig. 8). A similar spin-reorientation phase transition was also observed to occur in the Cr_2O_3

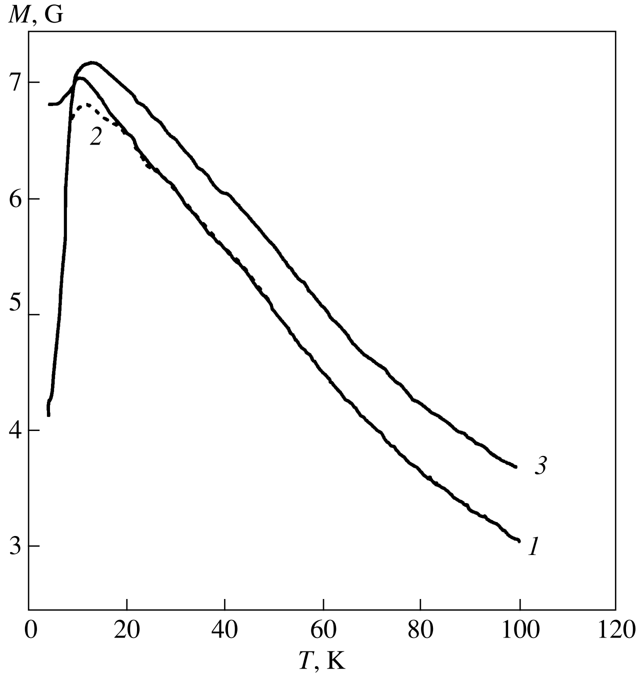

Fig. 7. Temperature dependences of the magnetization of a $CrBO_3$ single crystal measured in a magnetic field of 0.5 T.

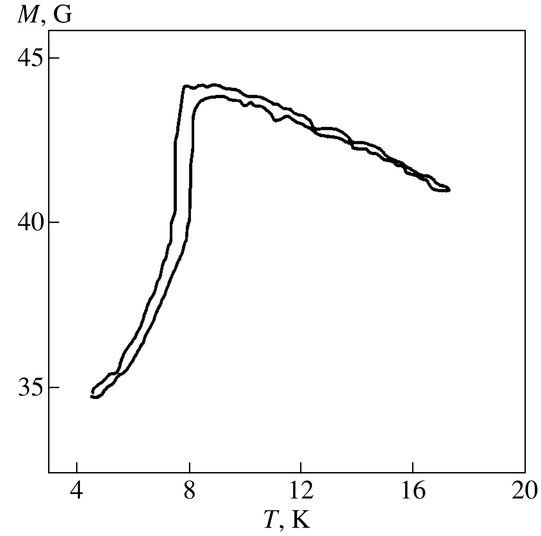

Fig. 8. Temperature dependence of the magnetization of $CrBO_3$ measured in a magnetic field of 7.5 T in direction *1*.

isostructural compound in the same critical-field interval [15]. The ratio of the magnetic susceptibilities corresponding to the directions parallel and perpendicular to the basal plane is approximately 1.24 in the low-field region. In the high-field region, curves *1–3* in Fig. 6 have similar slopes, which possibly corresponds to a magnetic susceptibility $\chi_\perp \approx 2 \times 10^{-3}$ in a magnetic field perpendicular to the antiferromagnetism vector.

Our set of experimental data does not permit us to fit the magnetic properties of $CrBO_3$, as was done in [2], to a simple model of a collinear two-sublattice antiferromagnet with magnetic moments aligned with the [111] axis. It appears more likely that the antiferromagnetism vector of $CrBO_3$ makes a small angle with the basal plane, because when the crystal is magnetized perpendicular to (111), the *M*(*H*) relation has a simple shape characteristic of the sublattice magnetic moments being canted toward the magnetic field. At the same time, the existence of hysteresis and of a region of magnetic-state instability with magnetization produced along mutually perpendicular crystallographic directions *1* and *2* in the basal plane apparently implies that neither of these two directions is the easiest magnetization axis. Otherwise, one of the two magnetization curves would be a straight line, whereas the other would exhibit a more or less pronounced jump or break corresponding to a spin flop. Thus, the magnetic structure of $CrBO_3$ is apparently more complex than was assumed in [2] and magnetization experiments alone cannot determine this structure reliably. Our experimental data should be correlated with studies of neutron scattering, AFMR, measurements of magnetostriction or ultrasound propagation through the sample, etc.

By extrapolating the *M*(*H*) dependence to high fields using the $\chi_\perp$ value found above, we estimated the exchange field *E* in $CrBO_3$ to be 38.2 T. The totality of our results is presented in the table together with known data for $FeBO_3$.

4. DISCUSSION OF RESULTS

As is evident from the experimental data presented above, the anisotropic properties of the $FeBO_3$, VBO_3, and $CrBO_3$ borates exhibit both common features and substantial differences. A common feature is that the dominant component of the magnetic moment in all three compounds apparently lies in the (111) plane. The anisotropies of these compounds are naturally different

Magnetic properties of $FeBO_3$, VBO_3, and $CrBO_3$

Compound	$T_{C,N}$, K	μ_S, μ_B	H_a, T	K_1, erg/cm^3	H_E, T
$FeBO_3$	348	5.9	0.3 [10]		580 [5]
VBO_3	32 [2]	1.81	6.25	12×10^6	78.2
$CrBO_3$	15 [2]	3.73 [2]			38.2

in magnitude due to the types of magnetic ordering in these compounds being completely different.

The problem of the nature of magnetic anisotropy cannot be considered solved at present even for the well-known compound $FeBO_3$. Although the *S* state with zero orbital magnetic moment is the ground state of the Fe^{3+} ion, it is believed [16] that, in addition to the magnetic dipole interaction, the single-ion mechanism contributes noticeably to the anisotropy and that the orbital magnetic moment is induced by the field created by the trigonally distorted rhombohedral crystal lattice. The same distortions can bring about partial unfreezing of the Cr^{3+} orbital angular momentum.

The *F* state is the ground state of the V^{3+} ion. Although the magnetic moment of V^{3+} ($1.63\mu_B$) is believed to be the sum of the spin and orbital moments, its experimental value ($1.81\mu_B$), derived by us from measurements of the static magnetization [1], suggests that part of the orbital angular momentum is quenched by the crystal field. One cannot exclude the possibility that the high uniaxial anisotropy in VBO_3 originates from a stronger spin–orbit coupling.

As for the third known source of magnetic anisotropy (anisotropic exchange), this mechanism, together with the spin–orbit coupling, may play a substantial role in generating anisotropy in cases where the orbital angular momentum is not quenched. Furthermore, although its contribution to the anisotropy of rhombohedral antiferromagnets is believed to be small [13], it is possibly that this contribution accounts for the small discrepancy between the critical temperatures observed when magnetizing $CrBO_3$ in different directions (Fig. 8). At any rate, in order to estimate the effect of various microscopic sources of magnetic anisotropy, one has to carry out theoretical calculations, which could be subsequently compared with data obtained from a series of different experiments.

ACKNOWLEDGMENTS

This study was supported by the federal program "Integration" (grant no. B0017) and the Krasnoyarsk Krai Science Foundation.

REFERENCES

1. N. B. Ivanova, V. V. Rudenko, A. D. Balaev, *et al.*, Zh. Éksp. Teor. Fiz. **121** (2), 1 (2002) [JETP **94**, 299 (2002)].
2. T. A. Bither, C. G. Frederick, T. E. Gier, *et al.*, Solid State Commun. **8**, 109 (1970).
3. H. Schmid, Acta Crystallogr. **17**, 1080 (1964).
4. B. Andlauer, J. Schneider, and W. Wetting, Appl. Phys. **10**, 189 (1976).
5. E. A. Turov, A. V. Kolchanov, V. V. Men'shenin, I. F. Mirsaev, and V. V. Nikolaev, *Symmetry and Physical Properties of Antiferromagnetics* (Fizmatlit, Moscow, 2001).
6. R. Wolfe, A. J. Kurtzing, and R. C. LeCraw, J. Appl. Phys. **41**, 1218 (1970).
7. M. Eibschutz and M. E. Lines, Phys. Rev. B **7**, 4907 (1973).
8. A. M. Kadomtseva, R. Z. Levitin, Yu. F. Popov, *et al.*, Fiz. Tverd. Tela (Leningrad) **14** (1), 214 (1972) [Sov. Phys. Solid State **14**, 172 (1972)].
9. V. N. Seleznev, Doctoral Dissertation (Khar'kov State Univ., Khar'kov, 1989).
10. L. V. Velikov, A. S. Prokhorov, E. G. Rudashevskiĭ, and V. N. Seleznev, Zh. Éksp. Teor. Fiz. **66** (5), 1847 (1974) [Sov. Phys. JETP **39**, 909 (1974)].
11. A. D. Balaev, Yu. B. Boyarshinov, M. M. Karpenko, and B. P. Khrustalev, Prib. Tekh. Éksp. **3**, 167 (1985).
12. G. S. Krinchik, *Physics of Magnetic Phenomena* (Mosk. Gos. Univ., Moscow, 1976).
13. V. V. Rudenko, Candidate's Dissertation (Simferopol State Univ., Simferopol, 1983).
14. S. Chikasumi, *Physics of Ferromagnetism: Magnetic Characteristics and Engineering Application* (Syokabo, Tokyo, 1984; Mir, Moscow, 1987), Vol. 2.
15. S. Foner, Phys. Rev. **130** (1), 183 (1963).
16. S. N. Lukin, V. V. Rudenko, V. N. Seleznev, and G. A. Tsintsadze, Fiz. Tverd. Tela (Leningrad) **22** (1), 51 (1980) [Sov. Phys. Solid State **22**, 29 (1980)].

Translated by G. Skrebtsov

Physics of the Solid State, Vol. 45, No. 2, 2003, pp. 292–297. Translated from Fizika Tverdogo Tela, Vol. 45, No. 2, 2003, pp. 278–283.
Original Russian Text Copyright © 2003 by Mishchenko, Zvezdin, Barbara.

Field-Swept Magnetization Hysteresis of Magnetic V_{15} Nanoclusters

A. S. Mishchenko*, A. K. Zvezdin, and B. Barbara*****
**Moscow State University, Vorob’evy gory, Moscow, 119899 Russia*
e-mail: smischenko@yahoo.com
***General Physics Institute, Russian Academy of Sciences, ul. Vavilova 38, Moscow, 119991 Russia*
e-mail: zvezdin@nnet.org
****Laboratoire de Magnetisme Louis Néel, CNRS, BP 166, 38042 Grenoble, France*
e-mail: barbara@labs.polycnrs-gre.fr

Received December 19, 20001; in final form, April 9, 2002

Abstract—The mechanism of hysteresis of magnetization in superparamagnetic systems under a time-increasing (decreasing) magnetic field is studied. The model used involves the nonequilibrium thermodynamic properties of superparamagnetic systems, such as the difference in temperature between the spin subsystem and the lattice caused by a sweeping magnetic field. It is shown that the temperature of the spin system and, hence, the magnitude of the magnetization always lag behind a variable magnetic field, which might be the cause of the observed hystertesis of magnetization. The results of calculations are compared with the experimental data for V_{15} nanoclusters. © *2003 MAIK “Nauka/Interperiodica”.*

1. INTRODUCTION

High-spin magnetic molecules, or magnetic nanoclusters, attract much attention [1– 3]. Objects of this type include nanoclusters containing *d* or *f* ions ($Mn_{12}Ac$, Fe_6, Fe_8, Fe_{10}, V_{15}, and others) [3–21]. Such objects are of interest for studying the fundamental problems of magnetism and for physical applications, such as quantum calculations or magnetic recording of information. In this study, we suggest a model that explains the hysteresis observed in a superparamagnet consisting of magnetic nanoclusters. Such hysteresis has recently been observed in V_{15} nanoclusters [4, 5]. The characteristic feature of this hysteresis is that it occurs in nonequilibrium conditions: during cyclic measurements, the magnetic field is first increased in proportion with time, $B(t) = \dot{B}t$, from $-B_{\max}$ to $B_{\max}$ and then the field is decreased according to the law $B(t) = -\dot{B}t$ to $-B_{\max}$. The characteristics of hysteresis essentially depend on the rate $\dot{B}$ of the magnetic-field sweep (Figs. 1, 2). In recent years, other interesting effects have been revealed in nanoclusters. These effects are determined by the rate $\dot{B}$ or, what is the same, by the steady-state vortex electric field existing in the object under study during a sweep of the magnetic field. The dependence of magnetic hysteresis of nanoclusters on the rate $\dot{B}$ was observed in Mn_{12} and Fe_8 in [6–8] when studying the effect of macroscopic quantum tunneling of magnetization [9] in these clusters and was theoretically explained in [10, 11]. New quantum effects in nanoclusters and nanostructures determined by the rate $\dot{B}$ were predicted in [12–14].

As mentioned above, interesting experimental results were obtained in [4, 5] from measurements of the dynamic magnetic characteristics of a single crystal formed by V_{15} molecules. In particular, the magnetization of a sample as a function of magnetic field showed hysteretic behavior at temperatures $T \sim 0.1$ K. At first glance, the existence of such a hysteresis seems strange, because the system of magnetic molecules under study was a superparamagnet. The observed

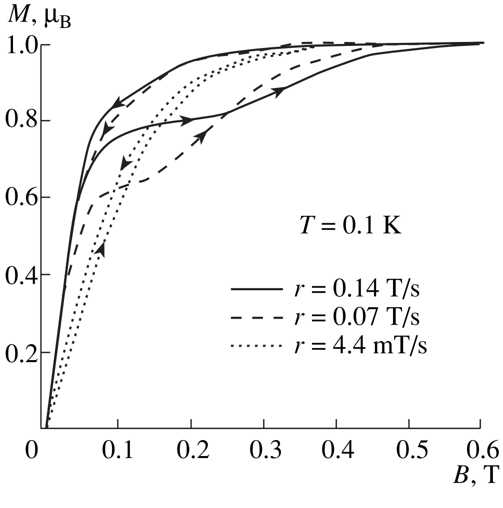

Fig. 1. Experimental magnetization curves at $T = 0.1$ K for various rates r of the magnetic field sweep.

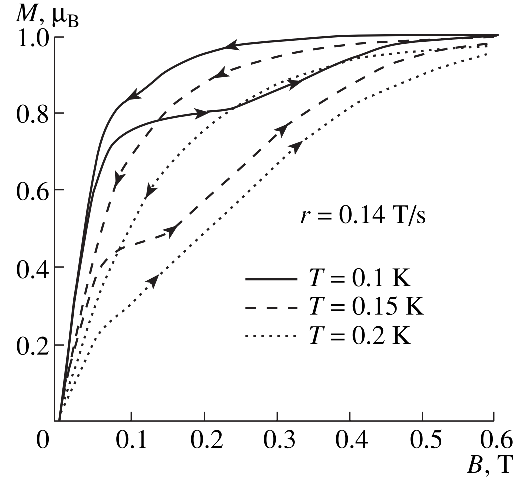

Fig. 2. Experimental magnetization curves at various temperatures and a constant rate of the magnetic field sweep, $r = 0.14$ T/s.

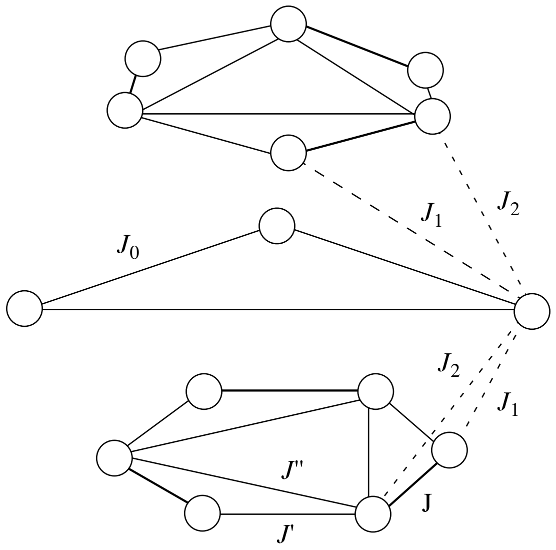

Fig. 3. Structure of the mesoscopic V_{15} complex.

behavior of magnetization was explained in terms of the model of a narrow phonon bottleneck [4, 5]. The main idea of this model consists in the following. A spin subsystem placed in a magnetic field can exchange energy only with resonance phonons having energy Δ_H (the Zeeman splitting of the ground state of the V_{15} molecule in a magnetic field). The phonon heat capacity of a sample in the course of the experiment is far less than the heat capacity of the spin subsystem; therefore, the temperature of the subsystem of resonance phonons sufficiently quickly becomes equal to the temperature of the spin subsystem; however, because the number of resonance phonons is small as compared to the number of spins in the sample, the energy transfer through the chain "spin subsystem–resonance phonon subsystem–sample holder" is hampered. Such an approach requires detailed knowledge of the characteristics of the phonon system and of the spin–phonon interaction in a sample. In [4, 5], this model is described by two first-order differential equations with respect to time for the mean occupation numbers of both spin and resonance phonon subsystems. In this study, we suggest a qualitative and a quantitative explanation of this effect in terms of a different model; it is assumed that in an ac magnetic field, the temperature of the spin subsystem becomes unequal to the lattice temperature. Our model does not detail the mechanism of energy transfer from the spin subsystem to a sample holder; it only assumes the existence of such a mechanism, which allows one to draw on only one equation for energy transfer. The advantage of this model is a smaller number of unknown microscopic parameters in comparison to other models, such as the above-mentioned model of a narrow phonon bottleneck.

2. MODEL

The crystals formed by molecules of polyoxivanadate ($K_6[V^{IV}_{15}As_6O_{42}(H_2O)] \cdot 8H_2O$) are trigonal (space group $R3$, $a = 14.029$ Å, $\alpha = 79.26°$, $V = 2632$ Å^3). The V_{15} complex consists of 15 V^{IV} anions, each having the spin $S = 1/2$ in the ground state. Vanadium atoms in the V_{15} molecule form a quasi-spherical three-layered structure [20]. Three vanadium atoms, forming an equilateral triangle, are located in the central layer, and six vanadium atoms, forming a regular hexagon, are in the adjacent layers (Fig. 3). Each hexagon consists of three pairs of strongly interacting spins ($J \approx -800$ K), and each spin at a vertex of the triangle interacts with two pairs of spins (one pair from each hexagon, $J' \approx J_1 \approx -150$ K, $J'' \approx J_2 \approx -300$ K).[1] Exchange interaction between the spins located at the vertices of the triangle is rather weak ($J_1 \approx -2.5$ K). The total spin of the molecule in magnetic fields up to 2.8 T is equal to $S = 1/2$; in higher fields, the spin system is rearranged and the total spin becomes equal to $S = 3/2$ [4, 5]. In the megagauss range of magnetic fields, the ferrimagnetic structure of the molecule changes into a ferromagnetic one [19]. The unit cell consists of two V_{15} molecules, which, however, are located far apart from each other; magnetic dipole interaction between their spins can be neglected. In the absence of a magnetic field, the ground state of a molecule is split into two energy doublets separated by an energy $\Delta_0 \sim 0.01$ K.

The experimental dependence of magnetization of the V_{15} single crystal on a dc magnetic field up to 5 T

---

[1] In recent publications [V. M. Platonov, O. M. Tatsenko, V. I. Plis, and B. Barbara, Fiz. Tverd. Tela (St. Petersburg) **44**, 2010 (2002); V. V. Kostyuchenko and A. K. Zvezdin, Fiz. Tverd. Tela (St. Petersburg), in press], a different set of exchange parameters was chosen, with lower magnitudes of the exchange integrals.

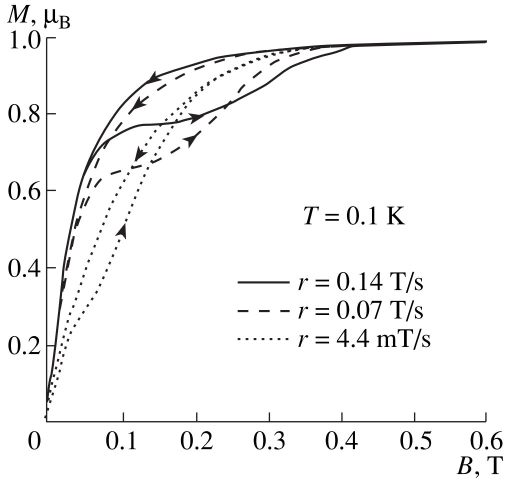

Fig. 4. Theoretical magnetization curves at T = 0.1 K and various rates r of the magnetic field sweep.

can be described in terms of the Heisenberg Hamiltonian for three spins $S = 1/2$ [4, 5]:

$$H = -J(\mathbf{S}_1\mathbf{S}_2 + \mathbf{S}_2\mathbf{S}_3 + \mathbf{S}_3\mathbf{S}_1) - g\mu_B B(\mathbf{S}_1 + \mathbf{S}_2 + \mathbf{S}_3), \tag{1}$$

where $S_1 = S_2 = S_3 = 1/2$, $g = 2$ is the spectroscopic splitting factor, $J = -2.5$ K is the exchange integral of the antiferromagnetic interaction in the central layer, and B is an external magnetic field.

One of the specific features of the mesoscopic system under discussion is that the particles have intrinsic spin degrees of freedom independent of their translation. If the equilibrium between the spin and translation degrees of freedom is established sufficiently slowly, then, in order to describe the magnetic properties of the whole system, one can introduce the concept of the temperature of the spin system, which differs generally from the temperature associated with a translation of particles. Thus, we consider two different thermodynamic subsystems: the subsystem associated with the spin degree of freedom (henceforth spin system) and the subsystem associated with the translation of molecules, the temperature of which is maintained constant by a thermostat (henceforth environment).

The concept of the spin system temperature can be cleared up by considering a simple two-level system. Let the spacing between the energy levels of the spin system be $\hbar\omega$; the temperature of the spin system T_S in this case is defined by the ratio $n_a/n_b = \exp(\hbar\omega/kT_S)$, where n_a and n_b are the mean occupation numbers of the lower and upper levels, respectively. For two-level systems, to which V_{15} belongs, this definition of the spin temperature is quite natural.

If the spin system temperature is not equal to the temperature of the environment, the process of leveling of temperatures should occur. The rate of this process is determined by the heat capacities of the spin system and its environment, as well as by the rate of energy transfer from the spin system to its environment. If the heat capacity of the environment is much higher than that of the spin system, the temperature of the spin system reaches the temperature of the environment in a time determined only by the rate of energy transfer between the systems; this process is characterized by the spin–lattice relaxation time τ_b [22].

3. THE BASIC EQUATIONS

We assume that the temperature of the spin system differs from the temperature of the environment, which is quite justified because the characteristic spin–lattice relaxation time $\tau_b \sim 0.01$ s at temperatures of the order of 0.1 K [23] is long in comparison to the time scales of the magnetic-field sweep in the experiment. The temperature of the environment is kept constant by a thermostat. The equation of energy transfer from the spin system to the environment can be written as

$$\frac{\delta Q}{dt} = -C\frac{T - T_0}{\tau_b}, \tag{2}$$

where $\delta Q/dt$ is the amount of energy transferred from the spin system to the environment per unit time; T and C are the temperature and heat capacity of the spin system, respectively; T_0 = const is the temperature of the environment; and τ_b is the spin–lattice relaxation time. According to the second law of thermodynamics, we have

$$\frac{\delta Q}{dt} = T\left[\left(\frac{\partial S}{\partial T}\right)_B\frac{dT}{dt} + \left(\frac{\partial S}{\partial B}\right)_T\frac{dS}{dt}\right], \tag{3}$$

where S is the entropy of the spin subsystem. Substituting Eq. (3) with $\left(\frac{\partial S}{\partial B}\right)_T = \left(\frac{\partial M}{\partial T}\right)_B$ into Eq. (2), after simple calculations, the following first-order differential equation with respect to time is obtained for the temperature of spin system:

$$\frac{dT}{dt} = \left\{-\frac{(\partial M/\partial T)_B}{(\partial S/\partial T)_B}\frac{dB}{dt}\right\} - \left\{\frac{T - T_0}{\tau_b}\right\}, \tag{4}$$

where M is the magnetization of the spin system and dB/dt is a given function of time. The thermodynamic functions $M(B, T)$ and $S(B, T)$ can be calculated from the energy spectrum of particles of the system in the magnetic field; for V_{15}, this spectrum can be found from the Hamiltonian (1). Within the range of magnetic fields of interest (from 0 to 0.7 T), the total spin of a molecule is $S = S_1 + S_2 + S_3 = 1/2$ and the energy spectrum, according to the experimental data [4, 5], consists of two doubly degenerate levels with a gap between them (inset to Fig. 7), the nature of which is not clear. Equation (4) may be interpreted in a different way: the change in the temperature of the spin subsystem with

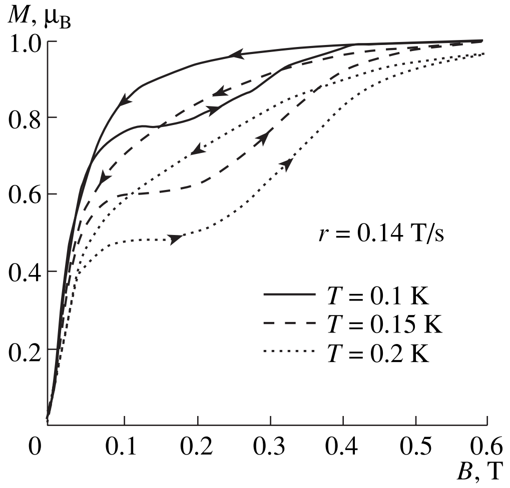

Fig. 5. Theoretical magnetization curves at various temperatures and constant rate of the magnetic field sweep, r = 0.14 T/s.

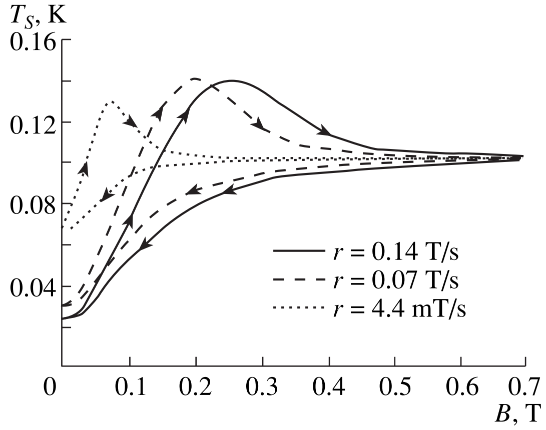

Fig. 6. Theoretical dependence of the spin subsystem temperature on magnetic field for various rates r of the magnetic field sweep.

time is caused by the magnetocaloric effect in the spin system (the first term in the right-hand side of Eq. (4)) and by the relaxation of temperature to its equilibrium value T_0 (the second term in the right-hand side). In contrast to the standard magnetocaloric effect, we deal here with heating (or cooling) of the spin system alone rather than of the whole sample. Substituting a solution to Eq. (4) with the initial condition $T(0) = T_0$ into the expression for magnetization $M(T(t), B(t))$, we obtain the time dependence of the magnetization of the system.

For the results to be adequate, it is necessary to take into account the dependence of the spin–lattice relaxation time τ_b on magnetic field and temperature. In [22], it is shown that the relaxation time for a two-level system can be represented as

$$\tau_b = \alpha\frac{\tanh^2(\Delta_B/2k_BT)}{\Delta_B^2}, \tag{5}$$

where $\Delta_B = 2\sqrt{(g\mu B_zS_z)^2 + \Delta_0^2}$ is the energy difference between the two levels and α is a constant. The system is considered to be close to equilibrium; i.e., the temperature of the spin subsystem differs only slightly from the temperature of the environment.

4. SOLUTION OF THE EQUATION AND COMPARISON WITH EXPERIMENT

Now, we shall calculate the magnetization of a V_{15} sample as a function of magnetic field B within the model proposed above.

Using the data given in Section 2 on the energy spectrum of the V_{15} molecule in a magnetic field, one can calculate the magnetization $M(B, T)$ and the entropy $\tilde{S}(B, T)$ of the system of V_{15} molecules from the standard formulas

$$M(B, T) = -\left(\frac{\partial F}{\partial B}\right)_T, \quad \tilde{S}(B, T) = -\left(\frac{\partial F}{\partial T}\right)_B,$$
$$F = -k_BT\ln(Z(B, T))^N, \tag{6}$$
$$Z(B, T) = 4\cosh\left(\frac{\sqrt{(g\mu_BS_zB_z)^2 + \Delta_0^2}}{kT}\right),$$

where $Z(B, T)$ is the partition function for a V_{15} particle, N is the number of V_{15} particles in the system, and

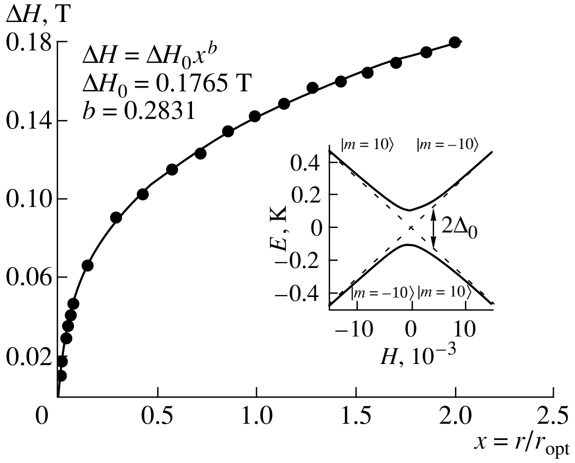

Fig. 7. Characteristic width of the hysteresis loop as a function of the relative rate of increase in the magnetic field r/r_{opt} (r_{opt} = 0.14 T/s). The calculated points are approximated by the curve $\Delta H = \Delta H_0x^b$.The inset shows splitting of the ground state of the V_{15} molecule in a magnetic field (including the repulsion of the energy levels).

$F(B, T)$ is the free energy of the system.[2] Substituting the results of the calculations into Eq. (4), we obtain a first-order differential equation with respect to time for the temperature of the spin subsystem. In dimensionless variables, this equation has the form

$$\frac{da}{df} = \frac{ab}{(b^2 + (\Delta_0/J)^2)}\frac{db}{df} - \frac{a - a_0}{\tau}. \tag{7}$$

Here, $a = k_BT/J$, $a_0 = k_BT_0/J$, $b = \mu_BB/J$, $f = t/\tau_{\text{field}}$, and $\tau = \tau_b/\tau_{\text{field}}$, where J is the exchange integral involved in the effective Heisengerg Hamiltonian that approximately describes the behavior of the V_{15} complex in a magnetic field ($J \cong -2.5$ K [4, 5]) and $2\tau_{\text{field}}$ is the time required for the magnetic field to change from $-B_{\max}$ to $B_{\max}$. The time dependence of the magnetic field in terms of the dimensionless variables introduced above has the form $b(f) = b_0(f - 1)$, where $b_0 = \mu_BB_0/J$. For the dimensionless magnetization of the spin system under study ($m = M/\mu_BN$, with N being the number of V_{15} molecules in a sample), we have

$$m(a, b) = \frac{b}{\sqrt{b^2 + (\Delta_0/J)^2}}\tanh\left(\frac{\sqrt{b^2 + (\Delta_0/J)^2}}{a}\right). \tag{8}$$

The field dependence of the spin–lattice relaxation time in Eq. (5) at sufficiently low temperatures can be approximated as

$$\tau = \frac{\tau_0}{b^2 + (\Delta_0/J)^2}, \tag{9}$$

where τ_0 is independent of T and B. Numerical calculations show that the use of a more cumbersome formula (5) instead of Eq. (9) gives similar results; however, a solution to differential equation (7) in this case cannot be written in an explicit form.

A solution to differential equation (7) with the initial condition $a|_{f=0} = a_0$ has the form

$$a(f) = a_0\exp\left(-\frac{1}{3}\frac{\rho(f)}{\tau}\right)$$
$$\times\left\{1 + \frac{1}{\tau}\int_0^f \sqrt{[(b(u))^2 + (\Delta_0/J)^2][b_0^2 + (\Delta_0/J)^2]} \right. \tag{10}$$
$$\left. \times\exp\left(\frac{1}{3}\frac{\rho(u)}{\tau}\right)du\right\}\frac{\sqrt{(b(f))^2 + (\Delta_0/J)^2}}{\sqrt{b_0^2 + (\Delta_0/J)^2}},$$

where

$$\rho(x) = x(b_0^2x^2 - 3b_0^2x + 3b_0^2 + 3(\Delta_0/J)^2).$$

Substituting Eq. (10) into Eq. (8) for $m(a, b)$, we obtain the magnetization $m(a(f), b(f))$ of a sample as a function of time (or, what is the same, as a function of magnetic field, $m(a(b), b)$, since the magnetic field and time are related linearly). The results of calculations according to this scheme are presented in Figs. 4 and 5. The spin–lattice relaxation time τ_b and zero-field splitting Δ_0 are chosen in such a way as to minimize the deviations of theoretical curves from the experimental data. The best-fit values $\tau_0 = 0.016$ s and $\Delta_0 = 0.028$ K are obtained by finding the minimum of the root-mean-square deviation of the theoretical $m(a(b), b)$ curve from the experimental one as a function of two variables, τ_0 and Δ_0. These values of the parameters are in good agreement with the parameters fitted in [4, 5] to account for an experimental hysteresis loop in terms of the model of a narrow phonon bottleneck ($\tau_0 = 0.01$ s, $\Delta_0 = 0.05$ K). The time dependence of the temperature of the spin subsystem is shown in Fig. 6. Since the curves are symmetrical with respect to the axis of ordinates, Fig. 6 shows only their parts for $B > 0$.

The model suggested was used to calculate the dependence of the characteristic width of a hysteresis loop for the V_{15} sample on the rate $\dot{B}$ of increase in the magnetic field (Fig. 7). The width of the loop was calculated at the inflection point of the function $M(B)$ corresponding to the field increasing. The obtained dependence is well approximated by the function $\Delta B = \Delta B_0x^b$, where $\Delta B_0 = 0.1765$ T, $b = 0.2831$, and $x = r/r_{\text{opt}}$, with $r_{\text{opt}} = 0.14$ T/s being the rate of increase in the magnetic field corresponding to the optimal fit of the experimental and theoretical curves.

Now, let us analyze possible ways of improving our model. First, substitution of a more precise formula (or, possibly, experimental data) for $\tau_0(B, T)$ in expression (9) will improve the final results, but the complexity of the expression will not allow one to solve Eq. (7) explicitly and obtain a formula similar to Eq. (10). Second, it is possible to take into account the mechanism of spin–phonon relaxation by introducing (in addition to the temperature T_S of the spin subsystem) the temperature T_{ph} of the subsystem of resonance phonons. However, instead of a single equation of energy conservation, Eq. (1), this approach requires consideration of a system of two coupled equations (see [23]).

5. CONCLUSIONS

Thus, the results obtained within the model proposed in this paper well describe the experimental data for the V_{15} complex. An explicit quadrature formula is derived, Eq. (10), describing the dependence of the spin subsystem temperature on the external magnetic field for a V_{15} single crystal. Our model requires the use of less information for the description of this phenomenon than the model of a narrow photon bottleneck; however, the results obtained within both models describe the

---

[2] This form of the spectrum is taken from [4], where it was proposed that it be used as an optimal parametrization of the experimental data. The authors of [4] believe that the energy gap is due to the hyperfine interaction; however, as indicated above, the question as to the origin of the gap remains open.

experimental data equally well. The model suggested in this paper should not be considered an alternative to that proposed in [4, 5]. On the contrary, these models complement each other and, when combined, give a deeper insight into the possible mechanisms of formation of hysteresis in mesoscopic nanomagnets in a sweeping magnetic field.

Because of the sufficiently general character of the assumptions as to the structure of the material studied and the interactions in it, the model can be generalized to a wider spectrum of systems of mesoscopic magnets. Preliminary estimations confirm this prediction.

ACKNOWLEDGMENTS

This study was supported by the Russian Foundation for Basic Research (projects nos. 01-02-17703, 99-02-17830), the Ministry of Industry, Science, and Technology (project no. 97-471), and INTAS, (grant no. 99-01839).

REFERENCES

1. R. Sessoli, D. Gattecshi, A. Canecshi, and H. A. Novak, Nature **356**, 1054 (1993).
2. D. Gattecshi, A. Canecshi, L. Pardi, and R. Sessoli, Science **265**, 1054 (1994).
3. A. K. Zvezdin, Priroda **12**, 11 (2000).
4. I. Chiorescu, W. Wernsdorfer, A. Mueller, *et al.*, Phys. Rev. Lett. **84**, 3454 (2000).
5. I. Chiorescu, W. Wernsdorfer, A. Mueller, *et al.*, J. Magn. Magn. Mater. **221**, 103 (2000).
6. J. R. Friedman, M. P. Sarachik, J. Tejada, and R. Ziolo, Phys. Rev. Lett. **76**, 3830 (1996).
7. L. Thomas, F. Lionti, R. Ballou, *et al.*, Nature **383**, 145 (1996).
8. R. Grössinger, A. Caneschi, M. Dörr, *et al.*, J. Magn. Magn. Mater. **294–295**, 307 (2001).
9. E. M. Chudnovsky and J. Tijada, *Macroscopic Quantum Tunneling of the Magnetic Moment* (Cambridge Univ. Press, Cambridge, 1998).
10. V. V. Dobrovitski and A. K. Zvezdin, Europhys. Lett. **38**, 377 (1997).
11. L. Gunther, Europhys. Lett. **39**, 1 (1997).
12. A. K. Zvezdin, cond-mat/0004074; Kratk. Soobshch. Fiz., No. 12, 13 (1999).
13. A. K. Zvezdin, Kratk. Soobshch. Fiz., No. 11, 3 (2000).
14. A. K. Zvezdin, cond-mat/0102198; Kratk. Soobshch. Fiz., No. 3, 37 (2001).
15. A. Canecshi, D. Gattecshi, and R. Sessoli, J. Am. Chem. Soc. **113**, 5872 (1991).
16. R. Sessoli, Hin-Lien Tsai, A. R. Shake, *et al.*, J. Am. Chem. Soc. **115**, 1804 (1993).
17. A. K. Zvezdin and A. I. Popov, Zh. Éksp. Teor. Fiz. **109**, 2115 (1996) [JETP **82**, 1140 (1996)].
18. A. L. Barra, P. Debrunner, G. Gattecshi, *et al.*, Europhys. Lett. **35**, 133 (1996).
19. A. K. Zvezdin, V. I. Plis, A. I. Popov, and B. Barbara, Fiz. Tverd. Tela (St. Petersburg) **43** (1), 177 (2001) [Phys. Solid State **43**, 185 (2001)].
20. D. Gatteschi, L. Pardi, A. L. Barra, *et al.*, Nature **354**, 465 (1991).
21. B. Barbara, L. Thomas, F. Lionti, *et al.*, J. Magn. Magn. Mater. **200**, 167 (1999).
22. S. A. Al'tshuler and B. M. Kozyrev, *Electron Paramagnetic Resonance in Compounds of Transition Elements* (Nauka, Moscow, 1972; Halsted, New York, 1975).
23. A. Abragam and B. Bleaney, *Electronic Paramagnetic Resonance of Transition Ions* (Clarendon, Oxford, 1970), Chap. 10.

Translated by A. Zalesskiĭ

Physics of the Solid State, Vol. 45, No. 2, 2003, pp. 298–303. Translated from Fizika Tverdogo Tela, Vol. 45, No. 2, 2003, pp. 284–289.

MAGNETISM AND FERROELECTRICITY

Acoustic and Magnetic Properties of $La_{0.825}Sr_{0.175}MnO_3$ Lanthanum Manganites

Kh. G. Bogdanova*, A. R. Bulatov*, V. A. Golenishchev-Kutuzov*, L. V. Elokhina, A. V. Kapralov*, A. V. Korolev**, É. A. Neĭfel'd**, and M. M. Shakirzyanov***

**Zavoĭskiĭ Kazan Physicotechnical Institute, Russian Academy of Sciences,*
Sibirskiĭ trakt 10/7, Kazan, 420029 Russia

e-mail: acustica@dionis.kfti.knc.ru

***Institute of Metal Physics, Ural Division, Russian Academy of Sciences,*
ul. S. Kovalevskoĭ 18, Yekaterinburg, 620219 Russia

Received April 9, 2002

Abstract—This paper reports on measurements of the acoustic, magnetic, and electrical properties and on an x-ray microprobe analysis of a $La_{0.825}Sr_{0.175}MnO_3$ single-crystal sample. The acoustic studies were made with a pulsed acoustic spectrometer operating on a 770-MHz carrier. The studies revealed anomalies in the damping coefficients and sound velocity near 300, 200 K, and the Curie temperature T_C (283 K) where the colossal magnetoresistance occurs. The effect of a magnetic field on the magnetic texture of lanthanum manganites cooled below T_C, observed earlier in samples of other composition, is confirmed. In addition, a region was found wherein the magnetic susceptibility of an unclamped sample behaves anomalously. The electrical resistivity was observed to decrease substantially below T_C; this effect exhibits a hysteretic pattern in the interval 200–180 K. *© 2003 MAIK "Nauka/Interperiodica".*

1. INTRODUCTION

The interest expressed in lanthanum manganites was initiated primarily by the discovery of colossal magnetoresistance (CMR) in them at room temperature [1]. It soon became clear that the CMR in these materials is accompanied by specific features not only in the electrical and magnetic but also in the structural properties. This stimulated investigation of lanthanum manganites using various experimental techniques [1–4], including acoustic measurements [5–9]. Major attention was focused on manganites of the $La_xSr_{1-x}MnO_3$ composition ($0.16 \le x \le 0.18$), which exhibit the largest values of CMR. However, despite the large number of relevant publications, the nature of the CMR and the character of the temperature anomalies in the electrical, magnetic, and elastic characteristics of these materials remain unclear. In particular, the temperatures and compositions favoring magnetic and structural transitions known from the literature differ markedly, which may be traced to either the techniques of sample preparation employed or the method used being based on measuring one or two characteristics of these materials.

Our previous studies showed the crystal with $x = 0.175$ to possess a number of acoustic anomalies near 305, 290, and 220 K [9]. We refined the method of acoustic measurements at 700–800 MHz, which made it possible to more reliably identify the anomalies discovered earlier and investigate their behavior in an applied magnetic field.

Prior to looking for an interpretation of these features, it had to be established whether they are related to any anomalies in other (structural, magnetic, electrical) properties of the samples studied in relation to the available literature data. With this purpose in mind, we carried out an x-ray microprobe analysis of the chemical composition and magnetic and electrical measurements, whose results were subsequently compared with the literature data quoted for manganite samples of the same composition.

The x-ray microprobe analysis was employed to detect inhomogeneities with dimensions of 1 μm or larger whose presence could account for the observed acoustic anomalies. The negative result obtained means that the anomalies are associated with the properties of the manganite material rather than with specific features of the sample under study. The fact that the electrical and magnetic measurements coincide with the literature data also shows that our sample differs little in its individual characteristics from those used by other researchers.

2. X-RAY STRUCTURAL AND MICROPROBE ANALYSIS OF THE SAMPLE

An $La_{0.825}Sr_{0.175}MnO_3$ lanthanum manganite single crystal was grown by laser-beam zone melting at the

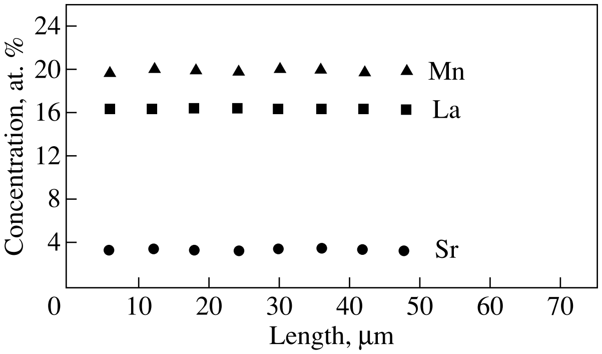

Fig. 1. Local concentration profiles of La, Sr, and Mn (in at. %) obtained by electron beam scanning of the sample surface.

Moscow Power Institute (group of A.M. Balbashov). The phase diagram [10] shows that the crystal structure of lanthanum–strontium manganites differs only slightly from cubic. It was earlier assumed that below $T = 200$ K, these distortions correspond to orthorhombic symmetry and above it, to rhombohedral. Some publications (see, e.g., [10]) suggest that both phases consist of small twins, with the above distortions oriented in different directions. Due to this twinning, the sample as a whole recovers its cubic symmetry, and it is this symmetry that is revealed in standard x-ray structural analysis.

The x-ray microprobe analysis of chemical composition for La, Sr, and Mn was performed on a JEOL Superprobe-733 microanalyzer. This instrument is capable of detecting inhomogeneities in chemical compositions with sizes above 1 μm, which is considerably smaller than the ultrasound wavelength ($\lambda = 5$ μm) at a frequency of 770 MHz. No such inhomogeneities in any of the elements indicated above were revealed. Figure 1 illustrates concentration profiles obtained by scanning the sample surface. To improve the accuracy, the scanning was done by translating the sample relative to the electron beam exciting the characteristic x-ray lines. Numerous scans of this type were obtained on different parts of the surface, and none detected a deviation from the pattern shown in Fig. 1.

These data show that the response of our sample to the 770-MHz ultrasound should be similar to that of a homogeneous cubic single crystal.

3. RESULTS OF MAGNETIC AND ELECTRICAL STUDIES

The magnetic studies were performed on a SQUID magnetometer (Quantum Design) capable of measuring magnetic moments to within 1%. The measurements were made on a free $La_{0.825}Sr_{0.175}MnO_3$ sample 6.06 mg in weight. Figure 2 displays magnetization curves obtained at $T = 2$ K after cooling in a zero magnetic field (ZFC) and in a field $H = 2$ kOe. These curves are shown in expanded scale in Fig. 2b. They differ in the following features: (i) the magnetization rate is maximal in fields $H \approx 1$ kOe; (ii) the magnetization noticeably exceeds the remanent magnetization, which is not seen in the scale of Fig. 2b; (iii) the character of magnetization does not affect the saturation magnetization M_S (the magnitude of M_S is the same, to within experimental error, for both curves); and (iv) the difference between the ZFC and FC magnetization curves does not change under remagnetization (the remagnetization hysteresis is not discernible in the scale of Fig. 2b).

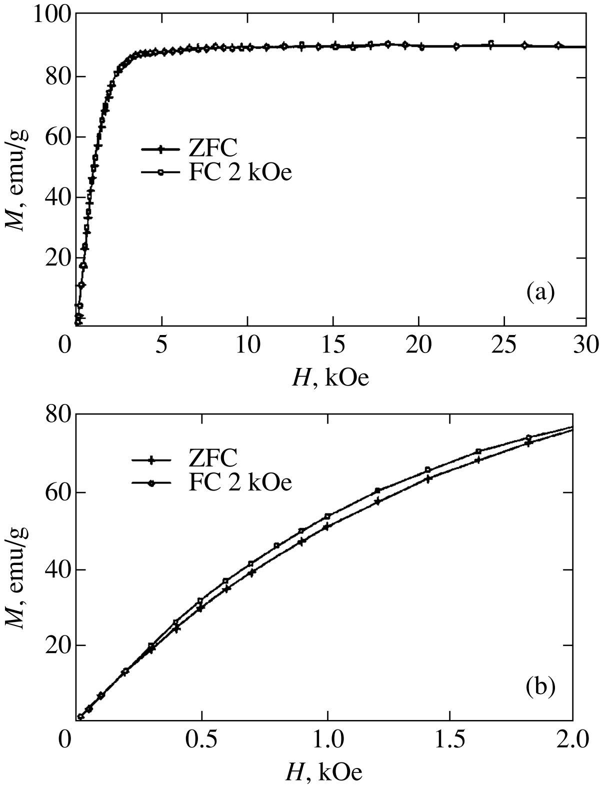

Fig. 2. (a) Magnetization curve of a free $La_{0.825}Sr_{0.175}MnO_3$ single-crystal sample measured at T = 2 K, and (b) its part in the field $H \simeq 2$ kOe shown in expanded scale.

The difference seen between the $M(T)$ curves of samples cooled in a field $H = 2$ kOe and $H = 0$ implies that a magnetic texture appears in the latter case; this texture, as follows from property (iii), is due to scatter in the easy magnetization axes rather than in the T_C temperature. Application of a field $H = 2$ kOe at temperatures $T > T_0$ suppresses (apparently, completely) the formation of such a texture. We show subsequently that $T_0 = 140$ K.

The value of M_S (Fig. 2a) was used to calculate the average magnetic moment per Mn atom:

$$\mu_{\mathrm{Mn}} = (3.80 \pm 0.04)\mu_{\mathrm{B}}, \tag{1}$$

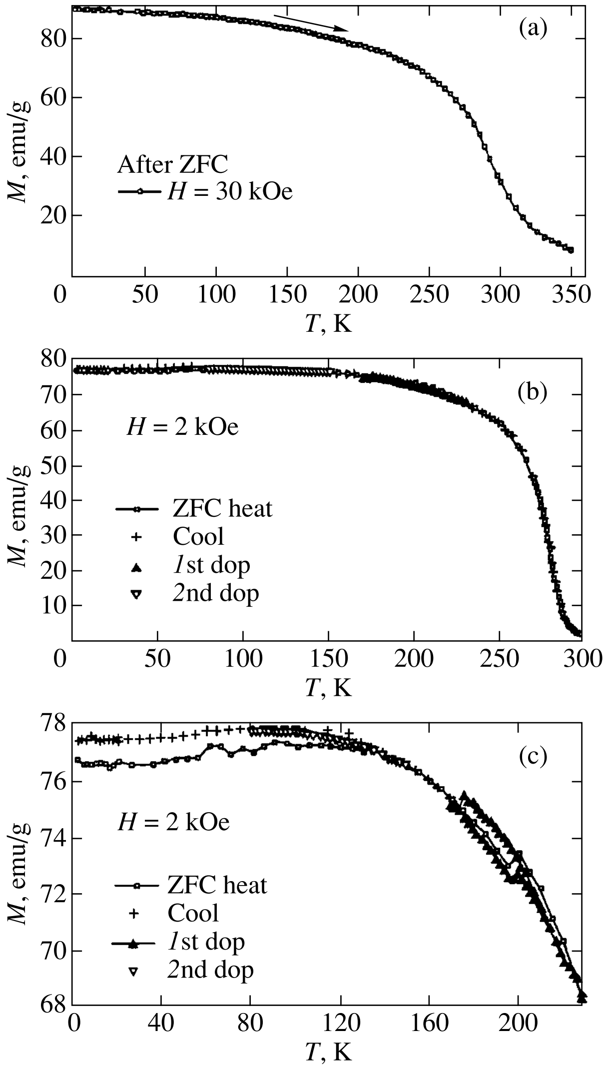

Fig. 3. Temperature dependences of magnetization of the sample under study measured in a field H of (a) 30 and (b) 2 kOe and (c) curve $M(T)$ obtained in the field H = 2 kOe and shown in expanded scale.

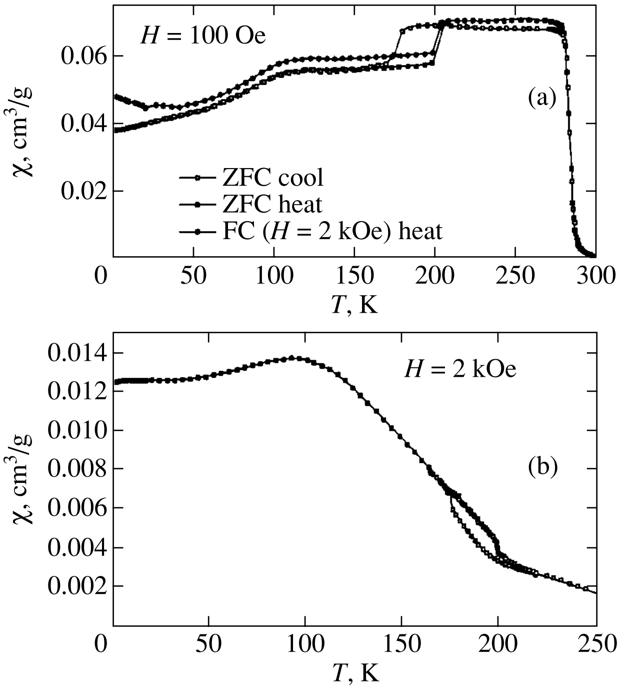

Fig. 4. Temperature dependence of the real part of magnetic susceptibility measured in a magnetic field H of (a) 0.1 and (b) 2 kOe.

where μ_B is the Bohr magneton. This figure agrees, to within experimental error, with the value $\mu_{Mn} = 3.825\mu_B$, which follows from the assumption that 82.5% of Mn atoms with valence 3+ should bear a moment $\mu_{Mn} = 4\mu_B$, while for the remaining 17.5%, having a valence 4+, $\mu_{Mn} = 3\mu_B$. This agreement indicates that the sample is of very high quality (absence of magnetic impurities, no oxygen off-stoichiometry, etc.).

The temperature dependences of magnetization $M(H, T)$ measured at H = 30 and 2 kOe are presented in Fig. 3. Because the saturation field for the sample under study is in excess of 5 kOe (Fig. 2a), the low-field $M(H, T)$ curve (Fig. 3b) corresponds to a nonuniformly magnetized state. Below the temperature T = 140 K, this curve splits, as shown in expanded scale in Figs. 3b and 3c. The top branch (crosses) of the curve corresponds to $M(H, T)$ of a sample cooled in a field H = 2 kOe (Fig. 3c), while the bottom branch (squares) relates to a ZFC sample; in other words, this splitting is due to the above-mentioned magnetic texture forming as a result of scatter of the easy magnetization axes. Displacement over the lower branch of the $M(H, T)$ curve (squares) is reversible if the heating is replaced by cooling, provided the heating was done to temperatures T < 140 K. Heating above 140 K brings about a switch to the top curve (crosses). This means that T_0 = 140 K is indeed the temperature above which a field H = 2 kOe suppresses the formation of a magnetic texture.

The low-field $M(H, T)$ curve (H = 2 kOe) has a region with hysteresis within the temperature interval 175 < T < 215 K. According to the phase diagram presented in [10], this region corresponds to coexistence of the orthorhombic and rhombohedral phases. The suppression of the hysteresis by a magnetic field H = 30 kOe (Fig. 3a) implies that these phases differ in magnetic-anisotropy constants rather than in the saturation magnetization and T_C temperatures.

Application of an 80-Hz ac magnetic field 4 Oe in amplitude made it possible to measure the magnetic susceptibility $\chi = \partial M/\partial H$ of the sample under study for various values of the dc magnetic field H. Figure 4a presents the temperature dependence $\chi(H, T)$ for H = 100 Oe. One readily sees a difference in the $\chi(T)$ behavior between a ZFC sample and a sample cooled in H =

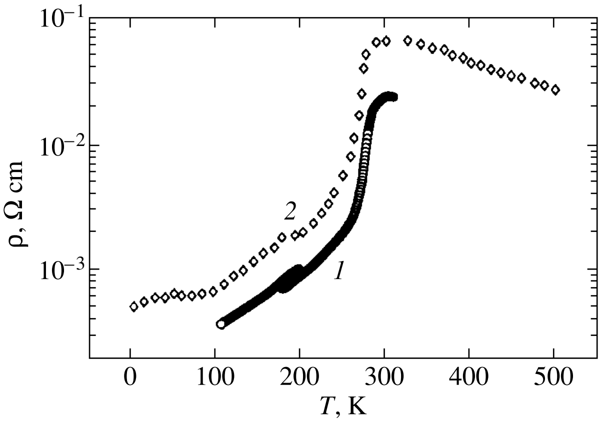

Fig. 5. Temperature dependence of the electrical resistivity of the $La_{0.825}Sr_{0.175}MnO_3$ sample. (*1*) Our data and (*2*) data from [2].

2 kOe, as well as a temperature hysteresis corresponding to the transition between the orthorhombic and rhombohedral phases. While the difference in $\chi(T)$ between samples cooled in zero and 2-kOe fields is no longer seen already in a magnetic field H = 2 kOe (Fig. 4b), the temperature hysteresis still persists. The most significant feature of this curve is the drop in $\chi(T)$ with increasing T in the region from 100 to 250 K. This behavior is considered anomalous for a ferromagnet, because when magnetized along the easy axis, $\chi(T)$ should grow and, along the hard magnetization axis, be independent of T. Additional studies would be required to establish the nature of the observed anomaly.

The $\chi(T)$ curve is usually employed to determine the Curie temperature T_C from the position of the maxima. Such maxima appear in the sample under study for $H >$ 0.5 kOe. In weaker fields, their formation is precluded by the domain structure. Extrapolating the positions of these maxima to zero field yielded T_C = 282 K, which is in accord with the phase diagram presented in [10].

The electrical resistivity and magnetoresistance are among the best studied properties of the lanthanum manganites, including the $La_{0.825}Sr_{0.175}MnO_3$ composition investigated here [2]. We measured the electrical resistivity $\rho(T)$ of our sample in order to make sure the latter did not differ significantly in its electrical properties from the samples studied by other authors. Figure 5 shows $\rho(T)$ curves obtained in the temperature range from 100 to 300 K. Our curve exhibits a clearly defined temperature hysteresis near the transition from the orthorhombic to rhombohedral phases, which is seen in the $M(T)$ (Fig. 3c) and $\chi(T)$ (Fig. 4) curves.

4. ACOUSTIC STUDIES

We measured the velocity and amplitude of longitudinal and transverse ultrasound waves in an $La_{0.825}Sr_{0.175}MnO_3$ lanthanum manganite sample in the shape of a rectangular parallelepiped with dimensions 4.85 × 8.2 × 7.9 mm whose end faces were plane-parallel to within a few seconds of arc. The sample faces were perpendicular to the [100], [010], and [001] axes to within 0.5°. Short ($\tau \sim 0.5$ μs) ultrasonic pulses were propagated along the [100] axis of the sample. By stabilizing the temperature to within 0.5 K and reducing the step in the temperature variation in the 350- to 150-K region, we succeeded in detecting a number of additional changes in the acoustic parameters v and A (v is the velocity and A is the amplitude of the ultrasonic wave) as compared with the data from [9]. The velocity and damping were determined in external fields H = 0 and 10 kOe by measuring the time of arrival of the first pulse that had passed through the piezoelectric transducer–sample-piezoelectric transducer system to the detector and the intensity of the pulse. As seen from the character of the curves in Figs. 6 and 7, plotting the temperature dependences of the velocity of the longitudinal, v_l, and transverse, v_t, waves, their amplitude starts to increase in the interval 320–308 K. In the 305- to 297-K interval, the first minimum in v_l and v_t was observed. The values of the amplitudes A_l and A_t in this region correlate with the variation in the velocity; more specifically, the amplitudes grow with increasing velocity and vice versa. Application of a magnetic field (H = 10 kOe) had no noticeable affect on the velocity and amplitude of the acoustic pulses.

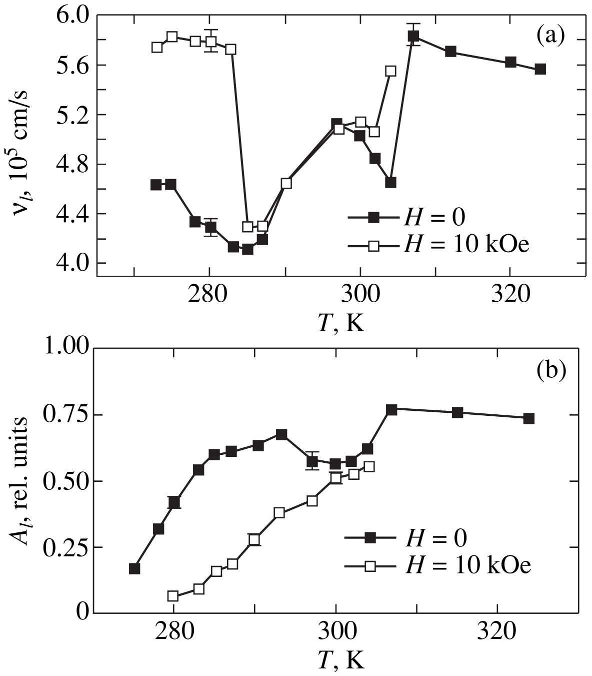

Fig. 6. Temperature dependences of (a) the velocity and (b) amplitude of longitudinal acoustic pulses.

The second minimum in the velocities v_l and v_t was observed in the interval 297–275 K and was centered at about 283 K. Application of a magnetic field in this

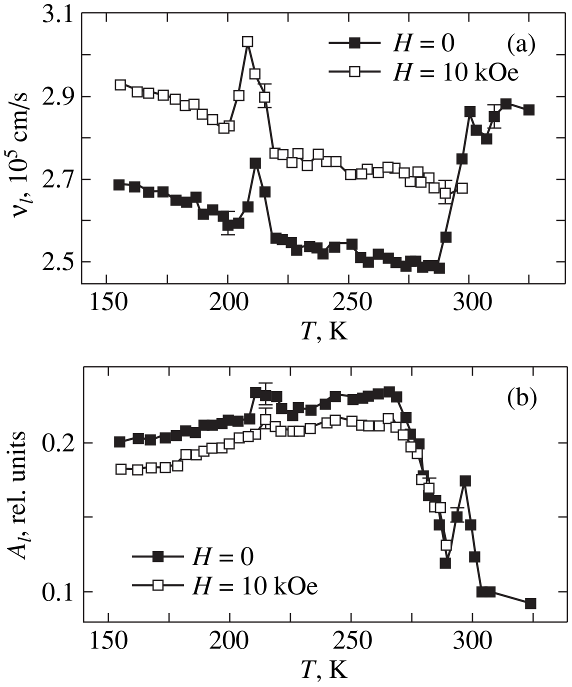

Fig. 7. Temperature dependences of (a) the velocity and (b) amplitude of transverse acoustic pulses.

interval increased the acoustic stiffness of the sample. Simultaneously, starting from 310 K, the pulse of the longitudinal wave began to split into two. The first of them, with amplitude A_l, was associated with the longitudinal wave, and the second, A_t, with the transverse one. The value of A_t increased and that of A_l decreased when the temperature was lowered to 270 K. The application of a magnetic field resulted in a noticeable decrease in A_l and a slight increase in A_t.

As the temperature was lowered still more to 220 K, the velocity and amplitude of the transverse wave were observed to grow smoothly. Some anomalies in v_t and A_t were also found in the interval 220–200 K. The effect of a magnetic field on the velocity and damping in the intervals 305–297 and 220–190 K was weak. Note that the variations of velocity and damping in the ranges 305–297 and 220–190 K had a hysteretic temperature pattern. At the same time, no hysteresis in v_l and v_t was observed within the 295- to 275-K interval.

A combined analysis of temperature-induced acoustic anomalies and of the results of magnetic and electrical measurements led us to the unambiguous conclusion that in the sample with $x = 0.175$, a first-order structural phase transition occurs near 305 and 210 K. The identification of these transitions with a first-order phase transformation is supported by the temperature hysteresis in the velocities and damping of the ultrasonic waves (near 305 and 210 K) and magnetization ($175 \le T \le 215$ K). It is in these temperature regions of structural phase transitions that the CMR reaches its peak values [2]. These transitions differ in character in that the first of them (at 305 K) sets in above T_C in the paramagnetic phase; the second (at 210 K), in the ferromagnetic state.

It is the transition in the vicinity of 220 K that is identified in most studies with a structural transformation from rhombohedral to orthorhombic symmetry. Our results show, however, that noticeable changes in structure also occur near 305 K. They are most likely related to the closeness in temperature to the magnetic transition (T_C = 283 K). In any case, this problem requires further study performed with additional experimental techniques.

The onset of ferromagnetic ordering below T_C accounts for the transformation of the longitudinal acoustic mode to the magnetoelastic one. The strong damping of the longitudinal mode below T_C finds explanation in the magnon–phonon mechanism of absorption [11], which results in damping that is proportional to the frequency squared for longitudinal waves only. The difference between the magnetic field effects on the longitudinal and magnetoelastic modes suggests that their transformation takes place at the front face of the sample rather than in its bulk, which is in full agreement with the mechanism of acoustic wave transformation in ferromagnets proposed earlier [12].

5. CONCLUSIONS

Thus, our integrated studies provide support for the model proposed in [13], which assumes that strong electron–lattice coupling mediated by orbital ordering of the 3*d* electrons of Mn^{3+} ions exists above T_C. It is this coupling that accounts for the decrease in the velocity and amplitude of acoustic waves. Below T_C, the electron–lattice coupling is suppressed by the ordering in the spin system. This spin–lattice coupling is the reason for the anomalous damping and softening of acoustic modes near T_C.

ACKNOWLEDGMENTS

This study was supported by the Russian Foundation for Basic Research, project no. 02-02-16440.

REFERENCES

1. R. M. Kusters, D. A. Singleton, D. A. Keen, *et al.*, Physica **155**, 362 (1989).
2. A. Urushibara, Y. Morimoto, T. Arima, *et al.*, Phys. Rev. B **51** (20), 14103 (1995).
3. B. Dabrowski, X. Xiong, Z. Bukowski, *et al.*, Phys. Rev. B **60** (10), 7006 (1999).
4. N. N. Loshkareva, Yu. P. Sukhorukov, É. A. Neĭfel'd, *et al.*, Zh. Éksp. Teor. Fiz. **117** (2), 440 (2000) [JETP **90**, 389 (2000)].

5. Yu. P. Gaĭdukov, N. P. Danilova, A. A. Mukhin, and A. M. Balbashov, Pis'ma Zh. Éksp. Teor. Fiz. **68** (2), 141 (1998) [JETP Lett. **68**, 153 (1998)].
6. T. W. Darling, A. Migliori, E. G. Moshopoulon, *et al.*, Phys. Rev. B **57** (9), 5093 (1998).
7. H. Fujishiro, M. Ikebe, Y. Konno, and T. Fukase, J. Phys. Soc. Jpn. **66** (12), 3703 (1997).
8. Ch. Zhu and R. Zheng, Phys. Rev. B **59** (17), 11169 (1999).
9. Kh. G. Bogdanova, A. R. Bulatov, V. A. Golenishchev-Kutuzov, and M. M. Shakirzyanov, Fiz. Tverd. Tela (St. Petersburg) **43**, 1512 (2001) [Phys. Solid State **43**, 1572 (2001)].
10. M. Parashevopolos, F. Magz, J. Hunberger, *et al.*, J. Phys.: Condens. Matter **12**, 3993 (2000).
11. J. W. Tucker and V. W. Rampton, *Microwave Ultrasonics in Solid State Physics* (North-Holland, Amsterdam, 1972; Mir, Moscow, 1975).
12. E. A. Turov and A. A. Lugovoĭ, Zh. Éksp. Teor. Fiz. **50**, 903 (1980).
13. J. D. Lee and B. I. Min, Phys. Rev. B **55** (18), 12454 (1997).

Translated by G. Skrebtsov

Physics of the Solid State, Vol. 45, No. 2, 2003, pp. 304–310. Translated from Fizika Tverdogo Tela, Vol. 45, No. 2, 2003, pp. 290–295.
Original Russian Text Copyright © 2003 by Arbuzova, Naumov, Arbuzov, Shal'nov, Ermakov, Mysik.

MAGNETISM AND FERROELECTRICITY

Surface Magnetism of Nanocrystalline Copper Monoxide

T. I. Arbuzova, S. V. Naumov, V. L. Arbuzov, K. V. Shal'nov,
A. E. Ermakov, and A. A. Mysik

Institute of Metal Physics, Ural Division, Russian Academy of Sciences,
ul. S. Kovalevskoĭ 18, Yekaterinburg, 620219 Russia

e-mail: viglin@imp.uran.ru

Received January 25, 2002; in final form, May 14, 2002

Abstract—The effect of the surface on the magnetic susceptibility of nanopowders of the CuO semiconducting antiferromagnet was studied. Single-phase nanopowders with nanoparticles 15, 45, and 60 nm in size were prepared through copper vapor condensation in an argon environment, with subsequent oxidation of the copper. The temperature dependences of the magnetic susceptibility of the nanopowders differ qualitatively from the $\chi(T)$ relations for bulk samples. In the region $80 \le T \le 600$ K, the magnetic susceptibility of nanopowders is inversely proportional to temperature and is described by the sum of contributions due to the bulk part of CuO and to the Cu^{2+} paramagnetic ions localized in surface layers. The paramagnetic contribution to the total susceptibility is shown to increase with decreasing particle size and sample density. A comparison of the $\chi(T)$ relations is made for nanopowders and for a dense CuO nanoceramic with grain size $5 \le d \le 100$ nm prepared using the shock wave technique. © *2003 MAIK "Nauka/Interperiodica".*

1. INTRODUCTION

Studies of the properties of nanoparticles may both contribute to our knowledge in the fundamental areas of the physics of surface phenomena and be of interest for practical applications of nanocrystalline materials. Decreasing the size of particles changes their properties as compared to those of bulk materials. The exchange coupling parameters of magnetic ions on the surface of nanoparticles and the direction of their magnetic moments can change due to a loss of three-dimensional lattice periodicity and to breaking of a large number of surface ion exchange bonds. Large perturbations in crystal symmetry entail a change in the surface anisotropy energy as compared to that in the bulk. The best studied effects caused by a decrease in particle size are the superparamagnetism and weak ferromagnetism observed in 3*d* metals and their alloys. Size effects manifest themselves in a strong increase in the coercive force and in the magnetic moment, a shift of the hysteresis loops, and in irreversibility of the magnetization curves.

Magnetic order in 3*d*-metal oxides is governed by the superexchange interaction with second-to-nearest neighbors and depends on bond length and bond angle. A decrease in particle size in ionic compounds may produce a stronger effect than in metallic compounds. The influence of a decrease in the coordination and of surface anisotropy on the magnetic properties of oxide compounds was considered by Kodama and Bercowitz in [1, 2]. They believe that pair exchange interactions in the bulk and on the surface are identical, but the total exchange coupling is weaker for surface ions because of their lower coordination and, hence, of the smaller number of neighbors. They also postulated the existence of broken exchange bonds due to the presence of oxygen vacancies or ligands. The main effect induced in ferrimagnets by a decrease in particle size is frustration of the exchange bonds and spin disorder in surface layers. At low temperatures, the disordered spins are frozen, which results in the hysteresis loops becoming irreversible. As the temperature is raised to $T > 50$ K, the spin-glass phase transforms to a canted spin structure.

The magnetic properties of nanoparticles of ionic antiferromagnets have been insufficiently studied. Only information on NiO is available at present. The nickel monoxide is a two-sublattice collinear antiferromagnet with $T_N = 523$ K. At $T = 5$ K, NiO nanoparticles ($d =$ 53–315 Å) exhibit large magnetic moments, coercive force, and hysteresis loop shifts, which cannot be accounted for within the two-sublattice model. It may be conjectured that the microscale surface structure gives rise to a change in the ground state and to a breakup into a larger number of magnetic sublattices. Modeling of the spin configuration in NiO nanoparticles shows the four-, six-, and eight-sublattice states to be preferable for the two-sublattice structure [1, 2]. The reason for the multiple breakup of the magnetic lattice lies in the closeness of the energies (degeneracy) between the two- and many-sublattice states.

Copper monoxide occupies a particular place among the transition-metal oxides. This compound has a low-symmetry monoclinic lattice and is a quasi-one-dimensional antiferromagnet with a high Néel temperature, $T_N = 230$ K. Intense investigation of CuO properties was spurred by the discovery of high-temperature superconductivity [3, 4]. CuO is the basis of HTSC cuprates and exhibits properties similar to those of semiconducting HTSC phases. Copper monoxide and the related structures enjoy application in photosensitive transducers, catalysts, and gas sensors. Ishihara *et al.* [5] found that an equimolar powder mixture of $BaTiO_3$ with 3*d*-metal oxides can be used to develop semiconductor sensors for CO_2 detection. CuO–$BaTiO_3$-based sensors possess a giant capacitive effect [6].

In an earlier publication [7], we reported on the effect of grain size on the magnetic susceptibility of a dense CuO nanoceramic produced from polycrystalline CuO subjected to isentropic shock waves. The present study deals with the effect of the surface on the magnetic properties of copper monoxide nanopowders with different particle dimensions. We carried out temperature measurements of the magnetic susceptibility of loose nanopowders with an average particle size varying from 100 to 1000 Å over a broad temperature range ($80 < T < 600$ K) both above and below T_N.

2. SAMPLES AND MEASUREMENT TECHNIQUE

Single-phase CuO nanopowders were prepared through condensation of metallic copper in a gas medium. In this method, a drop of molten metal blown with an inert gas flow (Ar) is suspended and heated in this state to 2000°C by a high-frequency magnetic field of a specially designed inductor. Maintaining a drop in the suspended state permits one to prevent the molten metal from capturing uncontrollable impurities. The metal vaporizing from the drop surface cools together with the inert gas and condenses into particles of nanocrystal size, which deposit on a filter. The average particle size is controlled by the inert-gas pressure in the setup and by the velocity of gas flow near the metal drop. By properly varying these parameters, copper nanopowders with an average particle size of 15 to 100 nm could be produced. The size of the Cu particles was monitored using transmission electron microscopy. The particle size distribution was relatively narrow and close to normal logarithmic. The Cu nanopowders were oxidized to CuO in air at temperatures of 90–240°C for 0.5–2.0 h. The choice of the annealing temperature and annealing time was dictated by the following considerations. The powders needed to be oxidized completely but with CuO crystallization avoided and the absence of the Cu and Cu_2O phases ensured. Increasing the oxidation temperature above 300°C resulted in a strong increase in the CuO particles in size.

The size of the CuO nanoparticles thus prepared was monitored by means of an STM-U1 scanning tunneling microscope. The powder was spread in a thin layer on a polished silicon plate. Because of the low electrical conductivity of CuO, a fairly high voltage had to be applied to the tip to obtain a tunneling current; therefore, an additional instability arose in the operation of the tip–sample system. Computer image processing made it possible to partially eliminate noise. To amass more complete information on the state of a sample, ten or more images of each region of interest were obtained and used to determine the average nanoparticle size. The error in nanoparticle size determination from STM images was 30–50%, depending on the scan extent, tip translation step, and subsequent image processing regime.

The phase and structural analysis was made with a DRON-2.0 diffractometer using CrK_α radiation. The magnetic susceptibility of CuO nanopowders was measured with a magnetic balance over a broad temperature range (80–600 K). The sensitivity of the balance permitted susceptibility measurements of down to 10^{-8} cm^3/g. The measurement error of χ did not exceed 5%.

We succeeded in preparing single-phase CuO nanopowders with an average grain size of 15, 45, and 60 nm. Figure 1 presents the microstructure of these samples obtained with the STM. It is seen that in the samples with small particles, $d = 15$ and 45 nm in size, the grains were spherical, whereas for $d = 60$ nm, part of the grains had an elongated shape. The grains in the sample in Fig. 1c are substantially larger in size than those in Fig. 1a. The grains in Fig. 1c are spread in size; i.e., there are both particles with $d = 60$ nm and larger ones with $d \geq 100$ nm. However, to understand the role of surface magnetism in CuO, it is essential that the fraction of surface layers in the sample with $d = 15$ nm (Fig. 1a) be substantially larger than that in the sample shown in Fig. 1c.

3. MAGNETIC SUSCEPTIBILITY OF CuO NANOPOWDERS

Among all the copper oxides, only the compounds containing divalent copper ions ($3d^9$, $S = 1/2$) can be magnetically ordered. Univalent copper ions have a filled 3*d* shell ($3d^{10}$, $S = 0$) and are nonmagnetic. There is presently no experimental evidence supporting the presence of Cu^{3+} ions ($3d^8$, $S = 1$) in ionic copper-containing oxides. The Cu^{2+}-containing compounds are characterized by the formation of low-dimensional magnetic systems, more specifically, linear (1D) chains and two-dimensional (2D) planes, which may be a consequence of the Jahn–Teller effect. A specific feature of low-dimensional systems is a flat maximum in the susceptibility and heat capacity at temperatures comparable with the exchange interaction parameters in a chain or plane [8].

CuO is a quasi-one-dimensional antiferromagnet with a high Néel temperature ($T_N = 230$ K) as compared with those for other known low-dimensional compounds ($T_N < 50$ K). Below $T = 213$ K, a collinear anti-

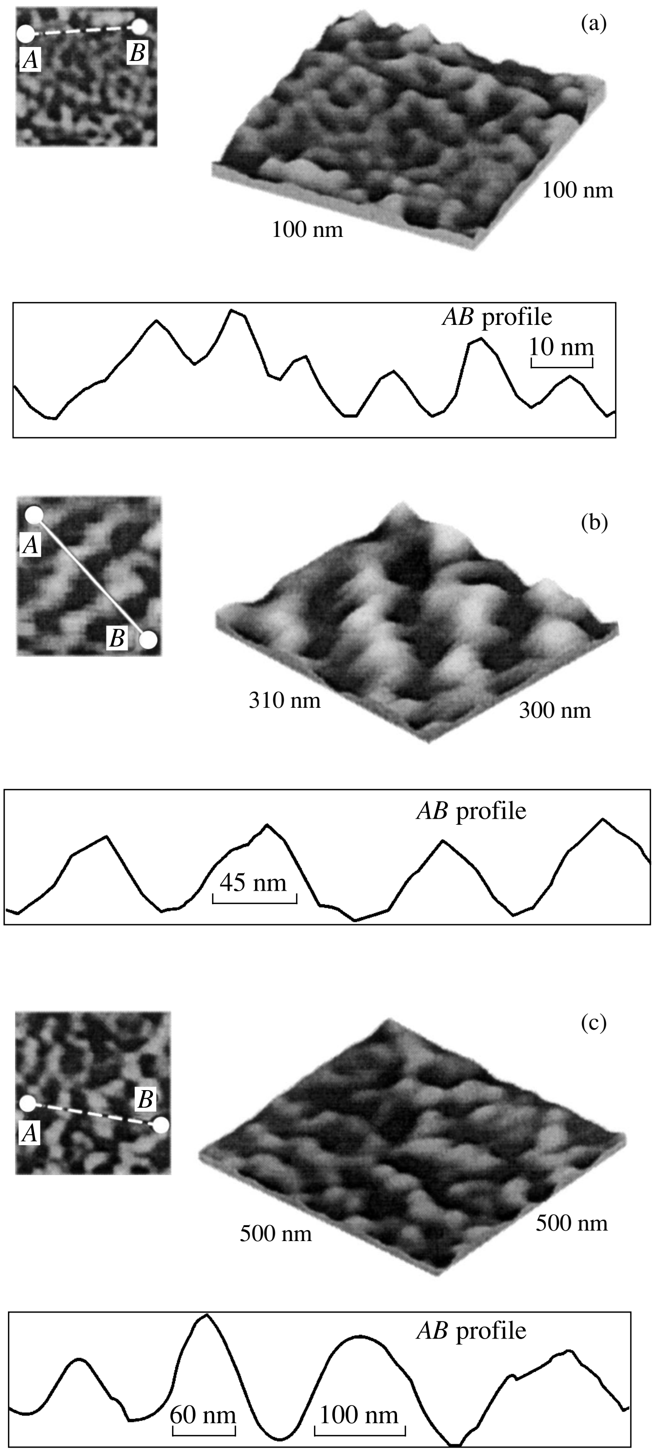

Fig. 1. Microstructure of CuO nanopowders with grains of different sizes obtained with scanning tunneling microscopy. *d*: (a) 15, (b) 45, and (c) 60 nm.

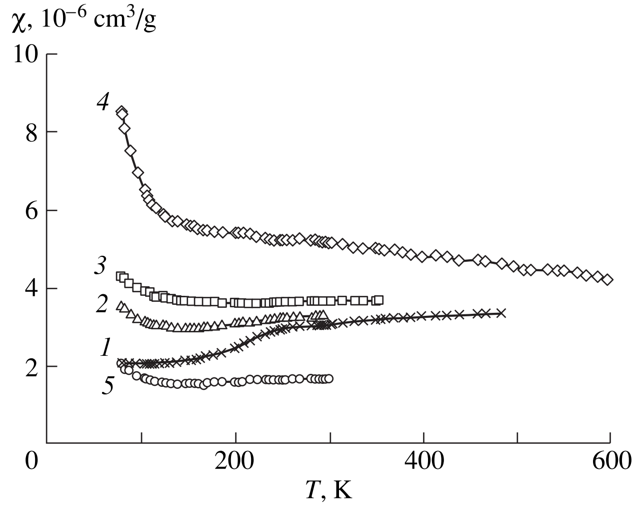

Fig. 2. Temperature dependences of magnetic susceptibility (*1*) for polycrystals; (*2–4*) for CuO nanopowders with particles of different size d = (*2*) 60, (*3*) 45, and (*4*) 15 nm; and (*5*) for heterophase powder with $d \lesssim 100$ nm.

ferromagnetic structure forms in CuO, and within the 213 K < $T < T_N$ region, a noncollinear (chiral) configuration forms. Strong spin correlations among the Cu^{2+} ions along the $[10\bar{1}]$ direction persist considerably above the Néel temperature. The temperature dependence of magnetic susceptibility of bulk CuO samples follows a pattern typical of low-dimensional antiferromagnetic systems, which undergo a transition to a 3D state with decreasing temperature. Above T_N, the susceptibility, rather than decreasing with increasing temperature, grows and passes through a broad maximum near 550 K. In the vicinity of T_N, there is no susceptibility peak characteristic of 3D antiferromagnets; only the slope of $\chi(T)$ changes. The absence of a χ peak near T_N indicates a smooth transition from the 3D state with a long-range antiferromagnetic order to a low-dimensional state with strong spin correlations. Intrinsic defects (oxygen vacancies) and Li^+, Zn^{2+}, and Ni^{2+} ions substituting for a part of the Cu^{2+} ions (<3%) do not affect the pattern of the $\chi(T)$ relations qualitatively [9].

Figure 2 displays temperature dependences of the magnetic susceptibility in a dc magnetic field H = 9 kOe obtained on CuO nanopowders with different average grain sizes. Also shown for comparison is the $\chi(T)$ plot for a polycrystal with $d > 1000$ nm (curve *1*). The susceptibility of nanopowders with grains of $d = 45$ and 60 nm, unlike the $\chi(T)$ relation for the polycrystal, decreases with increasing temperature for $T < 140$ K. In nanopowders with d = 15 nm, the susceptibility is inversely proportional to temperature throughout the temperature range covered. This is well illustrated in Fig. 3, which presents the temperature dependences of inverse susceptibility. The Curie–Weiss law $\chi = C/T - \Theta$ (where $C = N\mu_{\text{eff}}^2/3k$ is the Curie–Weiss constant and Θ is the paramagnetic Curie temperature) is met only for the sample with the smallest grain size within a broad temperature range T = 150–600 K. The effective magnetic moment $\mu_{\text{eff}} = 2.12\mu_B$ is, however, higher than

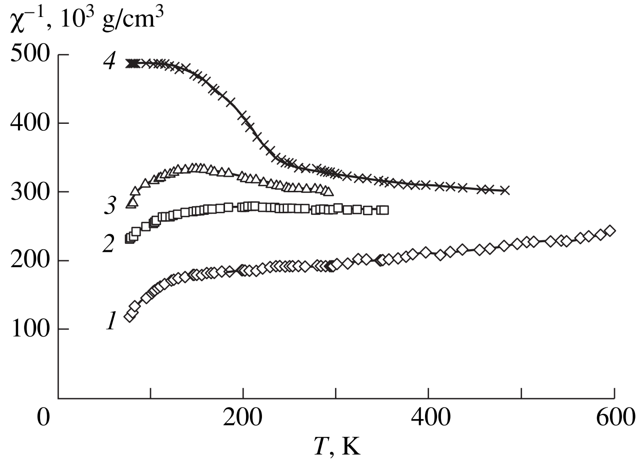

Fig. 3. Temperature dependences of inverse susceptibility in a magnetic field $H = 9$ kOe obtained for CuO nanopowders with particles of different size d = (*1*) 15, (*2*) 45, and (*3*) 60 nm; and (*4*) for polycrystal.

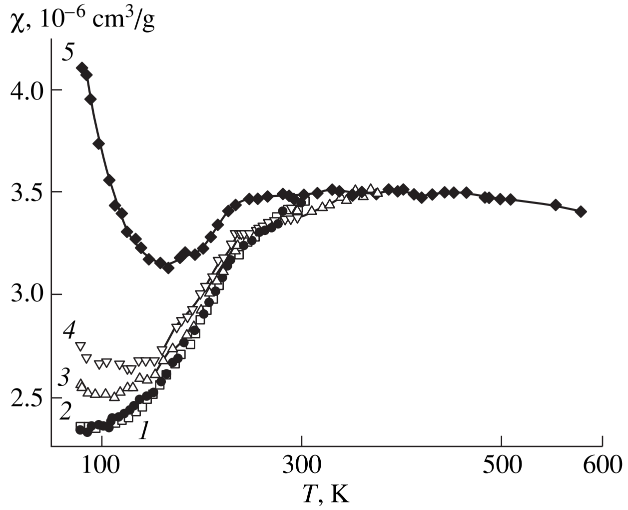

Fig. 4. Temperature dependences of magnetic susceptibility measured in a dc magnetic field $H = 9$ kOe on polycrystalline CuO samples with different grain size d subjected to a spherical shock wave. d: (*1*) 110, (*2*) 70, (*3*) 30, (*4*) 15, and (*5*) 5 nm.

the theoretical value $\mu_{\text{eff}} = 1.73\mu_B$ for single Cu^{2+} ions, which implies the presence of exchange coupling between Cu^{2+} ions in this temperature region. The value of the susceptibility is observed to correlate with particle size for CuO nanopowders for all temperatures; namely, the smaller the d dimension, the higher the value of χ.

An important factor affecting the pattern of the $\chi(T)$ relation is not only the particle size but also the sample density. Figure 4 presents temperature dependences of the susceptibility in a magnetic field $H = 9$ kOe obtained on dense (98%) nanoceramic CuO samples with different grain dimensions acted upon by a shock wave. The temperature dependence of susceptibility of the large-grain sample ($d = 110$ nm) coincides with $\chi(T)$ measured for polycrystals. While the grain size in this series of samples varies in the same range as that of the particles prepared through gas condensation, the pattern of the $\chi(T)$ curve is somewhat different. As seen from Fig. 4, the susceptibility of loaded samples is independent of grain size in the region where short-range magnetic order dominates ($T_N < T < 550$ K). In the region of long-range magnetic order ($T < T_N$), the so-called "paramagnetic" contribution $\chi \sim 1/T$ appears and grows with decreasing d. Note that the $\chi(T)$ relations obtained on the samples of the two series with the same grain size do not coincide. Loose samples, in which the fraction of surface layers in the total mass is considerably larger, have higher values of χ.

To study the effect of nonmagnetic phases Cu_2O and Cu on the magnetic susceptibility of CuO, we measured $\chi(T)$ for heterophase samples containing a mixture of these phases (50 wt %). The magnetic susceptibility of a finely dispersed powder ($d \le 100$ nm) prepared by sputtering copper in vacuum with high-power current pulses remained practically constant, $\chi = (1.55–1.65) \times 10^{-6}$ cm^3/g, in the region $T = 100–300$ K (curve *5* in Fig. 2). At $T = 80$ K, the susceptibility increased slightly to $\chi = 2.08 \times 10^{-6}$ cm^3/g. Both the absolute values of the susceptibility and the pattern of the $\chi(T)$ relation for the heterophase sample can be described for $T > 100$ K by the sum of contributions due to all the phases:

$$\chi_\Sigma = a\chi(\mathrm{CuO}) + b\chi(\mathrm{Cu_2O}) + c\chi(\mathrm{Cu}), \qquad (1)$$

where a, b, and c are the concentrations of the CuO, Cu_2O, and Cu phases, respectively. We measured the temperature dependences for the single-phase Cu_2O and Cu samples. The susceptibility of Cu_2O is small and decreases with increasing temperature from $\chi = 0.81 \times 10^{-6}$ ($T = 80$ K) to 0.23×10^{-6} cm^3/g ($T = 290$ K). Metallic copper exhibits a diamagnetic (negative), weakly temperature-dependent susceptibility ($\chi = -0.1 \times 10^{-6}$ cm^3/g at $T = 300$ K). The susceptibility of CuO usually increases from $\chi_{\min} = 2 \times 10^{-6}$ to 3.6×10^{-6} cm^3/g [10, 11]. The lower values of χ of the heterophase sample as compared with the single-phase CuO (Fig. 2) are due to the contribution of the Cu_2O and Cu phases to the total susceptibility. Hence, the observed behavior of $\chi(T)$ of CuO nanopowders, rather than being due to the presence of the Cu_2O and Cu phases, is a manifestation of the nanocrystalline state of the copper monoxide. Note that magnetic-susceptibility measurements are a convenient tool to reveal the presence of uncontrollable magnetic impurities in weakly magnetic materials.

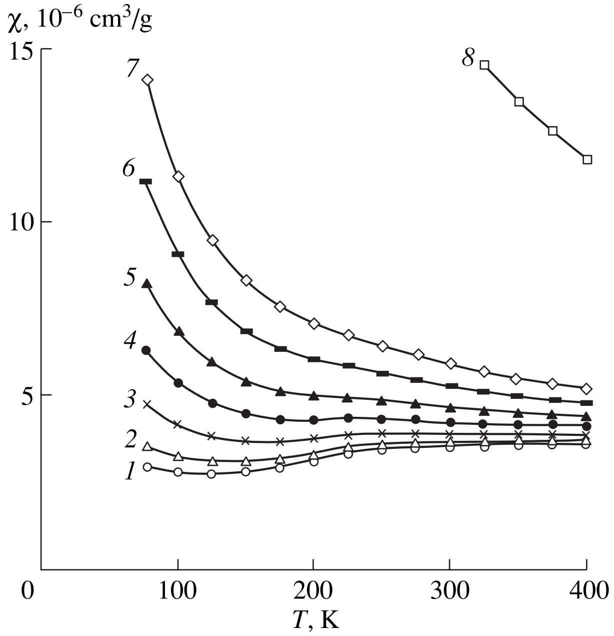

Fig. 5. Temperature dependences of magnetic susceptibility calculated for various concentrations (x) of paramagnetic Cu^{2+} ions in nanocrystalline CuO samples. x: (*1*) 1, (*2*) 2, (*3*) 4, (*4*) 6.7, (*5*) 10, (*6*) 15, (*7*) 20, and (*8*) 100%.

4. DISCUSSION

The antiferromagnetic ordering in CuO is mediated by superexchange interaction of Cu^{2+} ions with second-to-nearest neighbors through the O^{2-} ions along the $[10\bar{1}]$ axis. The Cu–O–Cu bond angle along this direction is the closest to 180°. In all the other directions, the Cu–O–Cu angle is close to 90° and provides ferromagnetic coupling. The CuO magnetic structure can be represented in the form of Cu–O–Cu zigzag antiferromagnetic chains aligned with $[10\bar{1}]$. The interchain exchange coupling is weaker and ferromagnetic in character. At high temperatures, i.e., under the conditions where thermal energy kT becomes comparable with the interchain exchange parameter, this interaction breaks down, with CuO transferring to the quasi-one-dimensional antiferromagnetic state. Above $T = 550$ K, copper monoxide resides in the paramagnetic state.

As the size of particles in nanocrystalline samples decreases, the $\chi(T)$ relation acquires a complex shape apparently connected with the paramagnetic contribution, which is inversely proportional to temperature. It appears reasonable to relate the paramagnetic contribution to the measured χ with surface layers. The fraction of surface layers in the total mass in a loose nanopowder is larger than that in a dense nanoceramic; therefore, this contribution operates in the whole temperature range.

We consider the possible reasons for the influence of the surface on the magnetic properties of CuO. The breakdown of three-dimensional periodicity in surface layers ruptures exchange bonds between the Cu^{2+} ions. In 1D antiferromagnets, alternating chains with a limited number of spins form [12]. It is unlikely that the larger part of alternating chains in CuO consists of an odd number of spins; this is the case in which a rise in χ should be observed. For alternating antiferromagnetic chains with an even number of spins, the susceptibility decreases smoothly with decreasing temperature. As a result of the rupture of exchange bonds in the surface layers, CuO becomes, most likely, a strongly frustrated antiferromagnet. In such antiferromagnets, the perpendicular and parallel susceptibilities (with $\chi = 2/3\chi_{\perp} + 1/3\chi_{\parallel}$) may grow with decreasing temperature. The exchange bond frustration should manifest itself only in the magnetically ordered region. In the high-temperature region $T > T_N$, a decrease in particle size should not affect the absolute values of the susceptibility $\chi(T)$. Such a behavior of $\chi(T)$ is observed in samples of dense nanoceramic. Their magnetic properties can be accounted for by strongly frustrated antiferromagnetism. In the case of loose nanopowders, however, the absolute values of susceptibility grow with decreasing d throughout the temperature range covered.

As already mentioned, the breakdown of a large number of exchange bonds of surface ions in nanoparticles may produce a spin-glass state. As is evident from Figs. 2 and 4, the spin-glass state in CuO can set in only below 80 K. Above the freezing temperature T_f, at which the susceptibility should reach a maximum, nanoparticles should reside in the paramagnetic state and their susceptibility should follow the Curie–Weiss law. Our studies show that the Curie–Weiss law is met only for nanopowders with $d = 15$ nm (Fig. 3). The large value of μ_{eff} indicates, however, that the spin-glass state in small CuO particles cannot set in for $T > 80$ K.

In our opinion, the appearance of the paramagnetic component of susceptibility in nanocrystalline CuO is initiated primarily by paramagnetic Cu^{2+} ions localized in surface layers. We calculated the total susceptibility under the assumption that the variation of the temperature dependences of susceptibility for nanocrystalline samples with particles of different size is accounted for by the variation of the relative contributions from the antiferromagnetic matrix and the Cu^{2+} paramagnetic ions to χ:

$$\chi = (1-x)\chi(\mathrm{CuO}) + x[Ng^2S(S+1)\mu_{\mathrm{B}}^2/3kT], \qquad (2)$$

where x is the concentration of Cu^{2+} paramagnetic ions, $S = 1/2$, and $g = 2$.

The first term in Eq. (2) was derived from the temperature dependence of susceptibility for a CuO polycrystal with a close-to-stoichiometric composition [9]. The second term in Eq. (2) is actually the Curie law, because Cu^{2+} ions in surface layers of a nanoparticle do not order magnetically at any temperature (the paramagnetic Curie temperature $\Theta = 0$).

Figure 5 plots calculated $\chi(T)$ curves for various concentrations, $x = 0.01–0.20$. The $\chi(T)$ relations calculated for nanocrystals with $d > 70$ nm and polycrystals follow the same pattern, because, for small $x \leq 0.01$, the total susceptibility is dominated by the first term in Eq. (2). As the Cu^{2+} concentration increases, the second term grows in magnitude, particularly at low temperatures. The temperature dependences of susceptibility have the same pattern as those in Fig. 4 for nanoceramics, with a minimum within the temperature interval 150–200 K. For higher Cu^{2+} ion concentrations ($x > 0.10$), the second term in Eq. (2) is dominant. These relations are similar in pattern to the $\chi(T)$ curves in Fig. 2 measured on CuO nanopowders. If all Cu^{2+} ions were to be isolated, the susceptibility would reach the value $\chi = 61.2 \times 10^{-6}$ cm^{-3}/g at 77 K. The experimental values of χ obtained for nanocrystalline samples are an order of magnitude smaller. Hence, a larger part of the Cu^{2+} ions in nanoparticles remain antiferromagnetically ordered.

The appearance of paramagnetic Cu^{2+} ions in CuO multilayers below T_N was observed in [13]. Polycrystalline and epitaxial CuO films of a thickness varying within $d = 2–200$ nm were deposited on substrates of the MgO and Al_2O_3 nonmagnetic phases. Within the range $4.2 < T < 300$ K, the susceptibility of all film samples was inversely proportional to temperature, $\chi \sim 1/T$. For the same total thickness of the multilayers, the susceptibility of thinner films is higher. The susceptibility at 4.2 K was established to grow linearly with increasing number of interfaces. The $\chi(T)$ relations are plotted in [13] in arbitrary units, thus precluding a comparison of the absolute values of susceptibility for films and nanopowders. From the magnetic and Mössbauer measurements, the conclusion was drawn that, in addition to the main antiferromagnetic CuO phase, the films contain paramagnetic Cu^{2+} ions localized in sheets of effective thickness 2–4 Å adjoining the interface layers. The concentration of Cu^{2+} paramagnetic ions in thin polycrystalline (CuO 20 Å)/(Al_2O_3 30 Å) 100-layer films was estimated from magnetic susceptibility data to be 6.7% of the total number of copper ions. The Mössbauer spectra obtained at 4.2 K on the same films consisting of 50 CuO layers can be well fitted by assuming the concentration x to be 0.10. Increasing the film thickness (CuO 100 Å/Al_2O_3 150 Å, ten layers) reduces the paramagnetic contribution intensity to 4%.

A comparison of the experimental with calculated $\chi(T)$ relations leads to the conclusion that the model proposed adequately describes the behavior of susceptibility in nanocrystalline CuO samples prepared using various techniques. An increase in the fraction of free surface layers in the total sample mass should bring about an increase in the concentration of the Cu^{2+} paramagnetic ions. Estimates show that the concentration of Cu^{2+} paramagnetic ions in nanopowders with particle size $d = 60$ nm is $x = 0.02$; for $d = 15$ nm, $x = 0.082$. As for the dense nanoceramics, the sample with the minimum grain size $d = 5$ nm revealed the maximum value $x = 0.03$. Our values of the Cu^{2+} paramagnetic ion concentration in CuO nanocrystals are in agreement with the data obtained for multilayered films.

In addition to the size of nanoparticles, the density of a sample is an important factor that influences the magnitude of the paramagnetic contribution to χ. In loose nanopowders, particles are separated by large distances; therefore, the susceptibility characterizes the magnetic properties of the nanoparticles themselves. The spins of the Cu^{2+} ions on the surface are not exchange-coupled with those in the bulk of the nanoparticles. Due to the small distances between nanoparticles in a dense ceramic, the spins of surface Cu^{2+} ions are correlated. In this case, one should take into account the interaction between nanoparticles [14]. The difference in the $\chi(T)$ relations between nanopowders and a dense CuO nanoceramic for the same size of particles is due to the fact that the paramagnetic Cu^{2+} ion concentration in the latter decreases because of the interaction between nanoparticles and a change in the surface spin structure.

5. CONCLUSIONS

Thus, the surface of a nanocrystalline sample noticeably affects the magnetic properties of CuO. On the surface of nanoparticles, breakdown of three-dimensional periodicity disrupts antiferromagnetic bonds between Cu^{2+} ions. As a result, part of the copper ions in the surface layers resides in the paramagnetic state at $T < T_N$ and behaves like a paramagnetic impurity. The magnetic susceptibility of CuO nanoparticles is the sum of the contribution due to the antiferromagnetic matrix and the contribution of isolated paramagnetic Cu^{2+} ions. The paramagnetic contribution grows with increasing fraction of surface layers in the total sample mass, in particular, with decreasing nanoparticle size and sample density.

ACKNOWLEDGMENTS

This study was supported by the Russian Foundation for Basic Research (project no. Ural-01-02-96403) and the Ministry of Science (project no. 26).

REFERENCES

1. R. H. Kodama, J. Magn. Magn. Mater. **200**, 359 (1999).
2. R. H. Kodama and A. E. Bercowitz, Phys. Rev. B **59** (9), 6321 (1999).
3. E. Gmelin, Indian J. Pure Appl. Phys. **30**, 596 (1992).

4. A. A. Samokhvalov, T. I. Arbuzova, N. A. Viglin, *et al.*, Fiz. Tverd. Tela (St. Petersburg) **40** (2), 295 (1998) [Phys. Solid State **40**, 268 (1998)].
5. T. Ishihara, K. Kometanis, M. Hashida, and Y. Yakita, Chem. Lett. **223**, 1163 (1990).
6. Q. Wei, W. D. Luo, B. Liao, *et al.*, J. Appl. Phys. **88** (8), 4818 (2000).
7. T. I. Arbuzova, S. V. Naumov, A. A. Samokhvalov, *et al.*, Fiz. Tverd. Tela (St. Petersburg) **43** (5), 846 (2001) [Phys. Solid State **43**, 878 (2001)].
8. R. Carlin, *Magnetochemistry* (Springer, Heidelberg, 1986; Mir, Moscow, 1989).
9. T. I. Arbuzova, I. B. Smolyak, S. V. Naumov, and A. A. Samokhvalov, Fiz. Tverd. Tela (St. Petersburg) **40** (10), 1876 (1998) [Phys. Solid State **40**, 1702 (1998)].
10. T. I. Arbuzova, A. A. Samokhvalov, I. B. Smolyak, and S. V. Naumov, J. Magn. Magn. Mater. **168**, 95 (1991).
11. M. O'Keeffe and F. S. Stone, J. Phys. Chem. Solids **23**, 261 (1962).
12. J. C. Bonner and M. E. Fisher, Phys. Rev. A **135**, 640 (1964).
13. M. Sohma, K. Kawaguchi, and Y. Fujii, J. Appl. Phys. **77** (3), 1189 (1995).
14. M. F. Hansen and S. Morup, J. Magn. Magn. Mater. **184**, 262 (1998).

Translated by G. Skrebtsov

Physics of the Solid State, Vol. 45, No. 2, 2003, pp. 311–318. Translated from Fizika Tverdogo Tela, Vol. 45, No. 2, 2003, pp. 296–303.
Original Russian Text Copyright © 2003 by Bespyatykh, Dikshteĭn, Mal'tsev, Wasilewski.

MAGNETISM AND FERROELECTRICITY

Magnetostriction Domain Structure in a Periodic System of Magnetoelastic and Elastic Nonmagnetic Layers

Yu. I. Bespyatykh*, I. E. Dikshteĭn*, V. P. Mal'tsev*, and W. Wasilewski**

**Institute of Radio Engineering and Electronics, Russian Academy of Sciences,*
Fryazino, Moscow oblast, 141120 Russia

***Technical University, Radom, Poland*

Received February 27, 2002; in final form, June 20, 2002

Abstract—The spectrum of magnetoelastic waves in a periodic structure of alternating ferromagnetic and nonmagnetic layers was studied. In the case of ferromagnetic layers with easy magnetization axes parallel to the layer surfaces, an orientational phase transition induced by an external tangential magnetic field $\mathbf{H}_e$ was considered. The formation of an inhomogeneous phase with a spatially modulated order parameter, which is caused by the magnetization being coupled through magnetostriction to lattice strains near the interfaces separating the magnetoelastic from elastic media, is predicted. It is shown that at a certain critical field in excess of the orientational phase transition field in the system without magnetostriction, a magnetoelastic wave propagating in a direction parallel to the in-plane magnetization vector $\mathbf{M}$ becomes unstable at finite values of the wave vector and condenses into a magnetostriction domain structure. A phase diagram in the (L, T, H_e) coordinates is constructed, and the regions of existence of thermodynamically equilibrium collinear, canted, and domain phases are established (L and T are the thicknesses of the ferromagnetic and nonmagnetic layers, respectively). *© 2003 MAIK "Nauka/Interperiodica".*

1. INTRODUCTION

Magnetostriction noticeably affects the dynamic and static properties of ferromagnets near a spin-orientational phase transition. In unbounded samples, a magnetoelastic gap appears in the spin wave spectrum near the orientational phase transition and the velocity of one of the transverse acoustic mode branches decreases to zero for wave vector $k \longrightarrow 0$ [1–4]. In bounded magnets, Néel-type domain structures are frequently observed, whose existence is assigned to magnetoelastic interaction [5–9]. By analyzing the spectrum of magnetoelastic waves in magnetic materials, one can determine the type of soft mode driving the second-order phase transition [10].

The magnetoelastic-wave spectrum and the distribution of magnetization and elastic strains in a uniaxial ferromagnetic plate with the easy axis normal to its plane were studied in [8, 9]. It was established that near a magnetic-field-induced orientational phase transition, the frequency and group velocity of a magnetoelastic wave vanish for finite values of the wave vector $k = k_c \neq 0$, with the sample breaking down into domains. As a result of domain structure formation, the energy of the long-range demagnetization fields in vacuum decreases. Competition between the magnetoelastic and dipole energies brings about a substantial dependence of the direction of propagation and of polarization of the soft magnetoelastic mode on the plate thickness L. In the case of thick plates ($L > L_N$), the soft mode is a transverse wave polarized perpendicular to the plane of the plate and propagating along the magnetization direction ($\mathbf{k} \parallel \mathbf{M}$). This mode condenses into a Néel-type domain structure. In thin films ($L < L_B$), the transverse wave polarized in the plate plane and propagating perpendicular to $\mathbf{M}$ is soft, which signals nucleation of a Bloch-type domain structure.

An alternative case of domain structure nucleation, in a ferromagnetic film with the easy magnetization axis parallel to a surface clamped to an elastic substrate, was studied recently in [11–13]. It was shown that in the vicinity of an orientational phase transition induced by a tangential external magnetic field, a horizontally polarized critical Love wave becomes unstable and transforms into a magnetostriction domain structure localized near the film–substrate interface. In these conditions, transition to the domain state reduces the energy of the long-range elastic-strain fields in the nonmagnetic substrate.

This study deals with nucleation of a domain structure in a periodic system in which ferromagnetic layers with the easy magnetization axis parallel to the surface alternate with elastic nonmagnetic layers. Inhomogeneous magnetic states (domain structures) of multilayered systems have been a recent subject of intense investigation [14, 15]. The fairly large dispersion, combined with a high sensitivity to an external magnetic field, makes such systems promising for applications in signal processing devices. The formation of a domain structure is usually associated with the effect of magnetic charges on the surface of magnetic layers. We will show that a phase transition involving in-plane spin reorientation may give rise to the formation of a magnetostriction domain structure whose existence is fully determined by the possibility of reducing the energy of the long-range elastic-strain fields, which penetrate into a nonmagnetic material to a depth of the order of the domain structure period.

2. FORMULATION OF THE PROBLEM AND BASIC EQUATIONS

We write the energy of the system as

$$F = F_m + F_e + F_{me} = \int dv(f_m + f_e + f_{me}), \qquad (1)$$

where F_m is the magnetic energy, F_e is the elastic energy of the lattice, and F_{me} is the magnetoelastic interaction energy. If the magnetoelastic interaction constants are small, the elastic strains and displacements in the system may be considered small under certain conditions. The elastic energy density f_e is a positively definite quadratic form of the strain tensor u_{ik},

$$F_e > 0, \qquad (2)$$

and the magnetoelastic energy density f_{me} is linear in strains u_{ik}.

The ground and metastable states correspond to the minimum of the energy of the system F; therefore, the distributions of the magnetization **M** and of elastic displacements **u** satisfy the equations of state

$$[\mathbf{M} \times \mathbf{H}_{\text{eff}}] = 0, \quad \delta F/\delta \mathbf{u} = 0, \qquad (3)$$

where $\mathbf{H}_{\text{eff}}$ is the effective magnetic field

$$\mathbf{H}_{\text{eff}} = -\delta F/\delta \mathbf{M}. \qquad (4)$$

Using the second equation in Eqs. (3) and in view of the uniformity of f_e and f_{me} in elastic displacements, one readily obtains the relation

$$F_e + F_{me} = F_{me}/2 \le 0. \qquad (5)$$

The equality sign in Eqs. (2) and (5) takes place only in the absence of elastic strains in the system. Whence it follows that for a given magnetization distribution in the absence of external elastic stresses, interaction between the magnetic and elastic subsystems can reduce the total energy of the system. The second of equations of state (3) permits one to uniquely express the displacements through magnetization and to transfer to the effective magnetic energy, which depends on the magnetization alone. The total contribution of the elastic and magnetoelastic energies turns out to be negative and nonlocal. If there are no deformations and dipole fields in a homogeneous magnetic state (for instance, in a layered film–substrate system, in which a massive substrate precludes the development of strains in the film plane), magnetoelastic interaction may initiate instability of the homogeneous phase and nucleation of a domain structure. This may occur even in conditions where domains in a purely magnetic system do not exist at all [11–13].

Consider an orientational phase transition and the spectrum of magnetoelastic excitations in a periodic structure consisting of alternating ferromagnetic layers of thickness L and nonmagnetic layers of thickness T with no gap between them. All layers are assumed to be dielectric. Let the normal to the surfaces of each layer be directed along the $\mathbf{n}_y$ axis. The magnetic layers possess uniaxial magnetic anisotropy, with the symmetry axis $\mathbf{n}_a$ being the easy magnetization axis. This axis is oriented identically in the magnetic layers and is parallel to the layer planes, $\mathbf{n}_a \parallel \mathbf{n}_z$. The system is placed in a tangential external magnetic field $\mathbf{H}_e \parallel \mathbf{n}_x$ perpendicular to the anisotropy axis.

The energy of the periodic system F can be conveniently divided into two terms,

$$F = F_{fm} + F_{nm}. \qquad (6)$$

In Eq. (6), $F_{fm} = F_m + F_{me} + F_e$ is the energy of the ferromagnetic layers, where

$$F_m = \int\limits_{V_{fm}} dv\left(-\mathbf{H}_e\mathbf{M} - \frac{1}{2}\mathbf{H}_D\mathbf{M} - \frac{\beta}{2}M_z^2 + \frac{\alpha}{2}\frac{\partial\mathbf{M}}{\partial x_i}\frac{\partial\mathbf{M}}{\partial x_i}\right), \qquad (7)$$

$$F_e = \frac{1}{2}\int\limits_{V_f} dv C_{ijkl}^{(fm)} u_{ij}^{(fm)} u_{kl}^{(fm)}, \qquad (8)$$

$$\begin{aligned} F_{me} = B\int\limits_{V_f} dv[&-(M_0^2/3)(u_{xx}^{(fm)} + u_{yy}^{(fm)} + u_{zz}^{(fm)}) \\ &+ M_x^2 u_{xx}^{(fm)} + M_y^2 u_{yy}^{(fm)} + M_z^2 u_{zz}^{(fm)} \\ &+ 2(M_x M_y u_{xy}^{(fm)} + M_y M_z u_{yz}^{(fm)} + M_x M_z u_{xz}^{(fm)})], \end{aligned} \qquad (9)$$

and the energy of the nonmagnetic layers F_{nm} is purely elastic,

$$F_{nm} = \frac{1}{2}\int\limits_{V_{nm}} dv C_{ijkl}^{(nm)} u_{ij}^{(nm)} u_{kl}^{(nm)}. \qquad (10)$$

Here, $\mathbf{H}_D = \nabla\Phi$ is the dipole field, **M** is the magnetization, $\beta > 0$ is the uniaxial anisotropy constant, α is the nonuniform exchange constant, B is the magnetostriction constant of the ferromagnetic material, $C_{ijkl}^{(fm)}$ and $C_{ijkl}^{(nm)}$ are the elastic moduli, $u_{ik}^{(fm,\,nm)} = (\partial u_i^{(fm,\,nm)}/\partial x_k + \partial u_k^{(fm,\,nm)}/\partial x_i)/2$ are the strain tensors, and V_{fm} and V_{nm} are the total volumes of the magnetic and nonmagnetic media, respectively. The elastic anharmonicities and the nonlinearity of the strain tensor are neglected, because their influence reduces to an insignificant renormalization of the elastic and magnetoelastic moduli [2]. We restrict ourselves to an isotropic approximation for the magnetostriction energy and the elastic energy of the system. We assume also that the effect of lattice misfit between the magnetic and elastic layers and of the volume magnetostriction reduces to renormalization of the magnetic anisotropy constant and of the external field.

The dependence of the magnetization **M** and elastic strains $\mathbf{u}^{(fm,\,nm)}$ on time t is described by the equations

$$\frac{\partial \mathbf{M}}{\partial t} = -g[\mathbf{M}\times\mathbf{H}_{\text{eff}}],$$
$$\rho^{(fm,\,nm)}\frac{\partial^2 u_i^{(fm,\,nm)}}{\partial t^2} = \frac{\partial}{\partial x_k}\left(\frac{\delta F}{\delta u_{ik}^{(fm,\,nm)}}\right), \tag{11}$$

where $g > 0$ is the gyromagnetic ratio and $\rho^{(fm)}$ and $\rho^{(nm)}$ are the densities of the magnetic and nonmagnetic layers, respectively.

At the interfaces between the media, the dipole field potential $\Phi = \varphi M_0$ and the normal component of magnetic induction $\mathbf{B} = \mathbf{H}_e + \mathbf{H}_D + 4\pi\mathbf{M} = \mathbf{b}M_0 = (\mathbf{h} + \mathbf{h}_D + 4\pi\mathbf{m})M_0$ are continuous and the derivative of the magnetization vanishes:

$$\partial\mathbf{M}/\partial y = (\partial\mathbf{m}/\partial y)M_0 = 0. \tag{12}$$

The displacements **u** and the components of the magnetoelastic stress tensor σ_{yi} are also continuous at the interfaces:

$$\mathbf{u}^{(fm)} = \mathbf{u}^{(nm)},$$
$$\sigma_{xy}^{(fm)} = 2C_{44}^{(fm)}u_{xy}^{(fm)} + BM_0^2 m_x m_y = \sigma_{xy}^{(nm)} = 2C_{44}^{(nm)}u_{xy}^{(nm)},$$
$$\sigma_{yy}^{(fm)} = (C_{11}^{(fm)} - 2C_{44}^{(fm)})(u_{xx}^{(fm)} + u_{yy}^{(fm)} + u_{zz}^{(fm)})$$
$$+ 2C_{44}^{(fm)}u_{yy}^{(fm)} + BM_0^2 m_y^2 = \sigma_{yy}^{(nm)} \tag{13}$$
$$= (C_{11}^{(nm)} - 2C_{44}^{(nm)})(u_{xx}^{(nm)} + u_{yy}^{(nm)} + u_{zz}^{(nm)}) + 2C_{44}^{(nm)}u_{yy}^{(nm)},$$
$$\sigma_{yz}^{(fm)} = 2C_{44}^{(fm)}u_{yz}^{(fm)} + BM_0^2 m_y m_z = \sigma_{yz}^{(nm)} = 2C_{44}^{(nm)}u_{yz}^{(nm)}.$$

Let us analyze the character of variation of the low-frequency region in the magnetoelastic wave spectrum and of the ground state of the system with variation of the external magnetic field.

3. UNIFORM SPONTANEOUS STRAINS IN MAGNETOELASTIC AND ELASTIC LAYERS

If the external magnetic field $\mathbf{H}_e \parallel \mathbf{n}_x$ is strong, the magnetization in the magnetoelastic layers is parallel to the external field, $\mathbf{M} \parallel \mathbf{n}_x$. Although the magnetization is uniform, in contrast to the case of a magnetoelastic film on a massive elastic substrate [11–13], the spontaneous strains $\hat{u}_{ik0}$ and stresses $\hat{\sigma}_{ik0}$ in the system are nonzero.

If the elastic moduli of the magnetic and nonmagnetic layers are equal, $C_{ijkl}^{(fm)} = C_{ijkl}^{(nm)} = C_{ijkl}$, the nonvanishing components of the spontaneous strain tensor are

$$u_{xx0}^{(fm)} = u_{xx0}^{(nm)} = -2u_{zz0}^{(fm)} = -2u_{zz0}^{(nm)} = -\frac{BM_0^2 L}{3C_{44}(L+T)},$$
$$u_{yy0}^{(fm)} = \frac{BM_0^2}{6C_{44}}\left[1 - \frac{(C_{11} - 2C_{44})T}{C_{11}(L+T)}\right], \tag{14}$$
$$u_{yy0}^{(nm)} = \frac{BM_0^2(C_{11} - 2C_{44})L}{6C_{11}C_{44}(L+T)}.$$

The change in energy $\delta F/V$ per unit volume of the system due to the presence of spontaneous strains can be written as

$$\frac{\delta F}{V} = \frac{B^2 M_0^4}{2C_{44}}$$
$$\times\left\{\left[1 - \frac{(3C_{11} - 2C_{44})T}{3C_{11}(L+T)}\right]m_y^2 + \frac{L}{(L+T)}m_z^2\right\}. \tag{15}$$

As seen from Eq. (15), spontaneous strains and stresses give rise to renormalization of the magnetic anisotropy energy. Their existence makes the anisotropy of the ferromagnetic layers biaxial. The increment of the effective magnetic energy (15) is not negative. In the case where the anisotropy field in the magnetic layers is sufficiently strong and the magnetization is parallel to the layer boundaries, the term proportional to m_y^2 in Eq. (15) is of no interest to us. The remaining part of Eq. (15) can be included into the uniaxial anisotropy energy.

If the elastic moduli of the magnetic and nonmagnetic layers are not equal, the part of δF of importance to us is

$$\delta F = B^2 M_0^4 \frac{L m_z^2}{2(C_{44}^{(fm)}L + C_{44}^{(nm)}T)}. \tag{16}$$

We shall assume in what follows that the anisotropy constant β is renormalized. This will permit us to disregard the existence of spontaneous strains in studying the magnetoelastic-wave spectrum and the stability of the collinear state with $\mathbf{M} \parallel \mathbf{n}_x$. The correction to energy due to spontaneous strains in the canted phase with uniform magnetization parallel to the magnetic layer plane and canted at an angle to the bias field can also be written in the form of Eq. (16). In this case, by m_z one should understand the magnetization component m_z' in the reference frame $x'y'$ with the axis $\mathbf{n}_x'$ parallel to the direction of uniform magnetization.

4. SPECTRUM OF LOW-FREQUENCY MAGNETOELASTIC EXCITATIONS AND THE COLLINEAR-PHASE STABILITY LOSS LINE

We shall first analyze the variation of the state of the system that is homogeneous in the x and z coordinates in relation to an external magnetic field. Because the magnetization in each ferromagnetic layer is uniform and lies in the plane parallel to the interfaces separating the media, there are no elastic strains in the system (the contribution due to the spontaneous strains and stresses has already been taken into account by renormalizing of the constant β). We express the components of the normalized magnetization **m** through the polar angle ϑ and azimuthal angle φ:

$$m_x = \cos\vartheta, \quad m_y = \sin\vartheta\sin\varphi, \quad m_z = \sin\vartheta\cos\varphi. \tag{17}$$

Minimizing the energy (6) with respect to ϑ and φ yields the following homogeneous phases: a collinear phase with

$$\mathbf{m} \parallel \mathbf{H}_e \tag{18}$$

and two canted phases with magnetization parallel to the interfaces,

$$\varphi = 0, \quad \vartheta = \vartheta_0 = \begin{cases} 0 \ \text{ for } \ h > \beta, \\ \pm\arccos(h/\beta) \ \text{ for } \ 0 < h < \beta. \end{cases} \tag{19}$$

To determine the regions of stability of the collinear phase against small magnetoelastic perturbations, we find the spectrum of low-frequency excitations in the system. Consider the propagation of magnetoelastic waves in the direction parallel to the external field ($k_x \equiv k \neq 0$, $k_z = 0$). Such excitations possess the strongest magnetoelastic coupling and the highest threshold for instability against the field H_e, because the domain walls forming in this case have no magnetic charges and the dipole field in the system is zero [11, 12].

Let small nonuniform components of magnetization **m** and of displacements **u** depend on coordinates x and z and time t as $\exp[i(kx - \omega t)]$. In what follows, we will drop this exponential factor and consider $\mathbf{m}(y)$ and $\mathbf{u}(y)$ to be Fourier amplitudes of nonuniform magnetization and displacements. We look for a solution to the equations of motion of magnetization and the elastic medium in the form of Bloch functions:

$$\mathbf{m} = \mathbf{V}(y)\exp(i\kappa y), \quad \mathbf{u}(y) = \mathbf{U}(y)\exp(i\kappa y), \tag{20}$$

where $\mathbf{V}(y)$ and $\mathbf{U}(y)$ are periodic functions; κ is the wave number, varying within the first Brillouin zone $-\pi/D \le \kappa \le \pi/D$; and $D = T + L$ is the period of the structure.

If the anisotropy constant of the magnetic layers is sufficiently large, the dipole field and all components of the nonuniform magnetization and displacements, except $\tilde{m}_z$ and $\tilde{u}_z$, can be disregarded in the vicinity of the orientational phase transition. The distribution of nonuniform magnetization and displacements in a ferromagnetic layer I ($-L/2 < y < L/2$) can be cast in a general form as

$$\begin{aligned} \tilde{m}_z &= a_1\cosh(q_1 y) + a_2\cosh(q_2 y) + b_1\sinh(q_1 y) + b_2\sinh(q_2 y), \\ \tilde{u}_z^{(fm)} &= -\frac{i}{khB}\{[\Omega^2 - h(h - \beta + \alpha k^2 - \alpha q_1^2)] \\ &\quad \times [a_1\cosh(q_1 y) + b_1\sinh(q_1 y)] \\ &\quad + [\Omega^2 - h(h - \beta + \alpha k^2 - \alpha q_2^2)] \\ &\quad \times [a_1\cosh(q_2 y) + b_2\sinh(q_2 y)]\}, \end{aligned} \tag{21}$$

where $\Omega = \omega/\omega_M$, with $\omega_M = gM_0$.

Substituting solution (21) into equations of motion (11) yields a biquadratic characteristic equation for determining the quantities q_1 and q_2:

$$\begin{aligned} &[(k^2 - q_{1,2}^2) - \Omega^2 k_{fm}^2] \\ &\times [\Omega^2 - h(h - \beta + \alpha k^2 - \alpha q_{1,2}^2)] + k^2 h_{me} h = 0, \end{aligned} \tag{22}$$

where $k_{fm} = \omega_M/S_t^{(fm)}$, $S_t^{(fm)} = \sqrt{C_{44}^{(fm)}/\rho^{(fm)}}$ is the transverse sound velocity, and $h_{me} = B^2 M_0^4/C_{44}^{(fm)}$.

We conveniently write the general solution to equations of motion (11) of the elastic medium for the lower adjacent nonmagnetic layer II ($-L/2 - T < y < -L/2$) as

$$\tilde{u}_z^{(nm)} = \{a_3\cosh[q_3(y + D/2)] + b_3\sinh[q_3(y + D/2)]\} \times \exp(-i\kappa D/2) \tag{23}$$

and that for the upper adjacent nonmagnetic layer III ($L/2 < y < L/2 + T$) as

$$\tilde{u}_z^{(nm)} = \{a_3'\cosh[q_3(y - D/2)] + b_3'\sinh[q_3(y - D/2)]\} \times \exp(i\kappa D/2). \tag{24}$$

Here, $q_3^2 = k^2 - \Omega^2 k_{nm}^2$ and $k_{nm} = \omega_M/S_t^{(nm)}$. Equations (20) imply that the coefficients of Eqs. (23) and (24) are related as $a_3' = a_3$ and $b_3' = b_3$. The coefficients $a_{1,2,3}$ and $b_{1,2,3}$ and the dispersion relation for the Love magnetoelastic waves in a periodic structure are found from boundary conditions at the $y = \pm L/2$ surfaces:

$$\begin{aligned} d\tilde{m}_z/d_y = 0, \quad \tilde{u}_z^{(fm)} = \tilde{u}_z^{(nm)}, \\ C_{44}^{(fm)} d\tilde{u}_z^{(fm)}/dy = C_{44}^{(nm)} d\tilde{u}_z^{(nm)}/dy. \end{aligned} \tag{25}$$

We do not present here the dispersion relation in a general form, because the case of $\kappa = 0$, where excitations in layers of the same material vary in phase, is of most interest.

For $\kappa = 0$, the system supports independent symmetric ($a_{1,2,3} \neq 0$, $b_{1,2,3} = 0$) and antisymmetric ($a_{1,2,3} = 0$, $b_{1,2,3} \neq 0$) modes for each layer. The dispersion relation for the symmetric modes is

$$\begin{aligned} F_s(\Omega, k) = {} & [q_2(\Omega^2/h - h + \beta - \alpha k^2 + \alpha q_1^2)\tanh(q_2 L/2) \\ & - q_1(\Omega^2/h - h + \beta - \alpha k^2 + \alpha q_2^2)\tanh(q_1 L/2)]q_3 \\ & \times \tanh(q_3 T/2) + \alpha(q_1^2 - q_2^2)q_1 q_2 \varepsilon \\ & \times \tanh(q_1 L/2)\tanh(q_2 L/2) = 0, \end{aligned} \quad (26)$$

and that for the antisymmetric modes is

$$\begin{aligned} F_a(\Omega, k) = {} & [q_2(\Omega^2/h - h + \beta - \alpha k^2 + \alpha q_1^2)\tanh(q_1 L/2) \\ & - q_1(\Omega^2/h - h + \beta - \alpha k^2 + \alpha q_2^2)\tanh(q_2 L/2)]q_3 \\ & + \alpha(q_1^2 - q_2^2)q_1 q_2 \varepsilon \tanh(q_3 T/2) = 0, \end{aligned} \quad (27)$$

where $\varepsilon = C_{44}^{(fm)}/C_{44}^{(nm)}$. On expanding the nonuniform components of magnetization and of elastic strains in powers of the order parameter and carrying out manipulations similar to those made in [12, 13], one can show that the transformation from the collinear to canted or domain phase is a second-order phase transition. In what follows, we will not be interested in the antisymmetric modes, because the soft mode for the field-driven orientational phase transition in the system under study is the lowest symmetric mode.

The stability loss field for the collinear state h_c and the magnitude of the critical-mode wave vector k_c are found from Eq. (26) and the conditions

$$\Omega = 0, \quad \partial F_s(\Omega, k)/\partial k = 0. \quad (28)$$

If the layers in a periodic structure are very thin ($|q_{1,2}|L \ll 1$, $|q_3|T \ll 1$), Eq. (26) reduces to the equation

$$h - \beta + \alpha k^2 \cong h_{me} C_{44}^{(fm)} L/(C_{44}^{(fm)} L + C_{44}^{(nm)} T). \quad (29)$$

Variation of Eq. (29) with respect to k yields

$$k_c = 0, \quad h_c \cong \beta + h_{me} C_{44}^{(fm)} L/(C_{44}^{(fm)} L + C_{44}^{(nm)} T), \quad (30)$$

which means that magnetostriction domains do not form in a periodic system of ultrathin films.

For a small thickness of the ferromagnetic layer ($|q_{1,2}|L \ll 1$) and a large thickness of the nonmagnetic layer ($|q_3|T \gg 1$), Eq. (26) transforms to

$$\begin{aligned} & (h - \beta + \alpha k^2)(1 + k\Lambda/2) - h_{me} k\Lambda/2 \cong 0, \\ & \Lambda = (C_{44}^{(fm)}/C_{44}^{(nm)})L. \end{aligned} \quad (31)$$

From this equation, we derive approximate values of the critical field and reciprocal domain structure period:

$$h_c \cong \beta + h_{me}^2 \Lambda^2/(16\alpha), \quad k_c \cong h_{me}\Lambda/(4\alpha). \quad (32)$$

We readily see that the critical domain structure period grows with increasing stiffness $C_{44}^{(nm)}$ of the nonmagnetic layers.

In the case of thick nonmagnetic layers ($|q_3|T \gg 1$) and magnetoelastic layers of intermediate thicknesses ($|q_1|L \gg 1$, $|q_2|L \propto 1$), the critical parameters of the domain structure for $C_{44}^{(fm)} = C_{44}^{(nm)}$ can be written as

$$h_c \cong \beta + h_{me} - 2\alpha k_c^2, \quad k_c^2 \cong (\pi/L)(h_{me}/\alpha)^{1/2}. \quad (33)$$

Equations (32) and (33) coincide with the corresponding expressions presented in [11, 12] if the replacement $L \longrightarrow L/2$ is made in the latter.

An analysis of the roots of dispersion relation (26) shows that there is no domain structure in the system with absolutely soft or rigid nonmagnetic layers.

Equations (26) and (28) can be conveniently analyzed numerically by introducing dimensionless quantities $\xi = (h - \beta)/h_{me}$, $k' = k(\alpha/h_{me})^{1/2}$, $\kappa' = \kappa(\alpha/h_{me})^{1/2}$, $q' = q(\alpha/h_{me})^{1/2}$, $L' = L(h_{me}/\alpha)^{1/2}$, and $T' = T(h_{me}/\alpha)^{1/2}$. Only three parameters (L', T', ε) are left independent. The primes on the quantities k', κ', q', L', and T' will be subsequently dropped.

Figures 1 and 2 display (in normalized variables) the calculated nucleation field and the critical domain structure period plotted vs. the thicknesses of the magnetoelastic and elastic nonmagnetic layers. For a fixed thickness of nonmagnetic spacers, the critical field $h_c = \beta + h_{me}\xi_c$ grows monotonically with increasing magnetic-layer thickness (Fig. 1a). The reciprocal critical period (Fig. 1b) is maximal at a certain thickness of the magnetoelastic layer and tends to zero as $L \longrightarrow 0$ and $L \longrightarrow \infty$. As the thickness of the nonmagnetic spacers grows with the magnetic-layer thickness kept fixed, the critical field decreases monotonically (Fig. 2a) and the reciprocal critical period of the domain structure increases monotonically (Fig. 2b).

The domain size grows with decreasing thickness of the nonmagnetic layers (Fig. 2b); the magnetostriction domains disappear when the period of the domain structure becomes of the order of the nonmagnetic-spacer thickness. Therefore, as the external magnetic field decreases, the system undergoes a second-order phase transition from the collinear to either a homogeneous canted or domain phase, depending on the actual material parameters of the magnetoelastic and nonmagnetic layers. The stability loss field of the collinear phase against transition to the canted phase h_{c0} is described by the expression

$$h_{c0} = \beta + h_{me} C_{44}^{(fm)} L/(C_{44}^{(fm)} L + C_{44}^{(nm)} T), \quad (34)$$

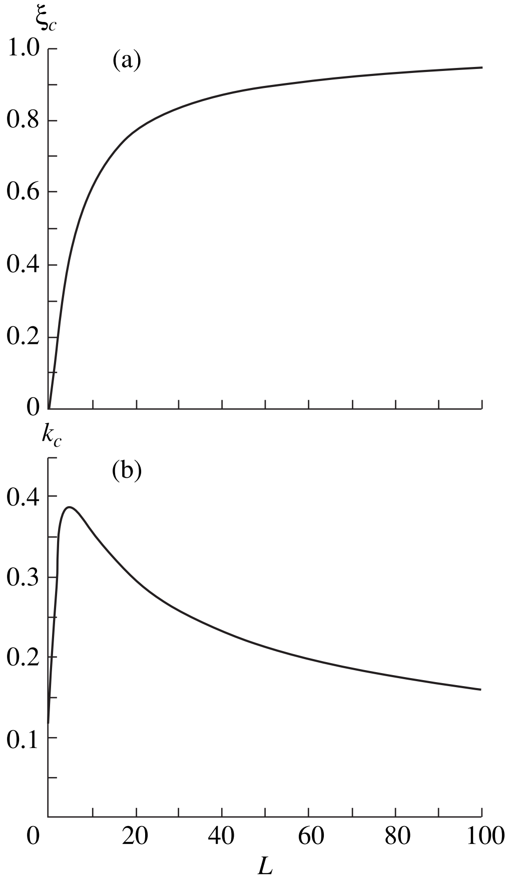

Fig. 1. (a) Critical field and (b) reciprocal period of the critical magnetostriction domain structure plotted vs. magnetic-layer thickness for ε = 1 and a fixed thickness of nonmagnetic spacers $T = 2000$.

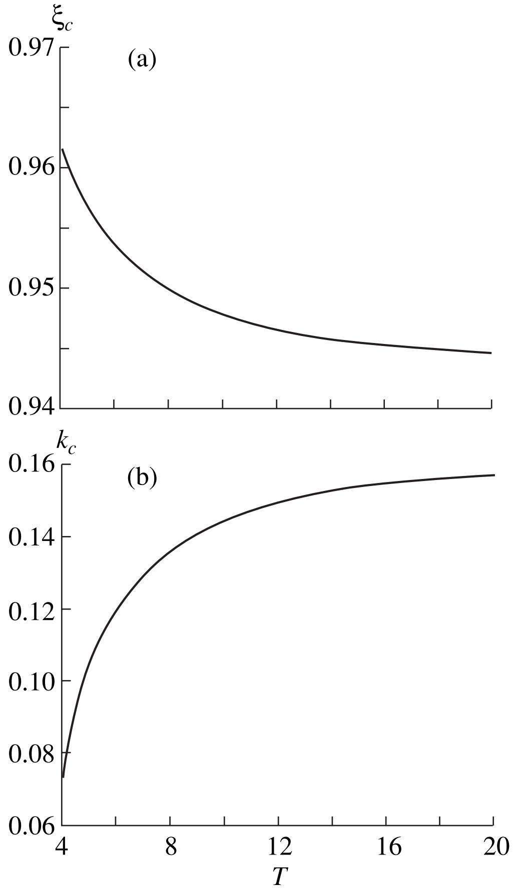

Fig. 2. (a) Critical field and (b) reciprocal period of the critical magnetostriction domain structure plotted vs. nonmagnetic-layer thickness for ε = 1 and a fixed thickness of magnetic layers $L = 100$.

which coincides with Eq. (30). For $h_c > h_{c0}$, the system transfers to the domain phase at the field h_c; in the case where the reverse inequality is met ($h_c < h_{c0}$), to the canted phase. The condition $h_c = h_{c0}$ is the equation of the $T^*(L)$ curve on the L–T plane separating the regions of transition from the collinear phase to the domain ($T > T^*$) and to the canted ($T < T^*$) phase. Since this phase transition is second-order, magnetostriction domains can form only for nonmagnetic spacer thicknesses $T > T^*$. Figure 3 shows the pattern of the $T^*(L)$ relation drawn in reduced variables. As the nonmagnetic-spacer thickness approaches $T^*(L)$ in the region of small magnetoelastic layer thicknesses, the reciprocal critical period of the domain structure tends monotonically to zero; therefore, Eq. (26) for the lowest static mode transforms to

$$\xi + k^2 \cong \varepsilon(kL/2)\coth(kT/2). \qquad (35)$$

The derivatives of the left- and right-hand parts of Eq. (35) with respect to k are monotonically growing functions of k, and the derivative of the right-hand side is maximal at $k = 0$. By expanding the right-hand part of Eq. (35) in powers of k, we can determine the $T^*(L)$ relation and the critical domain-structure parameters near the $T^*(L)$ curve:

$$T^* \cong 12(\alpha C_{44}^{(nm)})/(h_{me} L C_{44}^{(fm)}), \qquad (36)$$

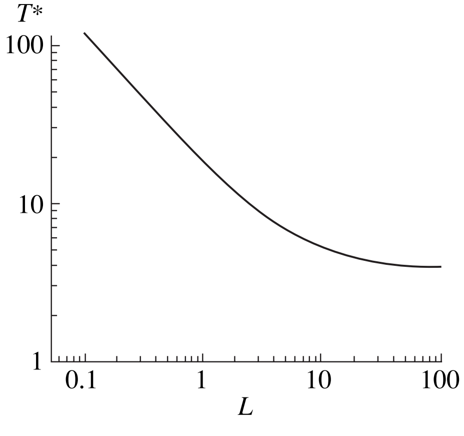

Fig. 3. $T^*(L)$ relation plotted on the L–T plane for ε = 1.

$$\begin{aligned} h_c &\cong \beta + h_{me}(C_{44}^{(fm)}/C_{44}^{(nm)})(L/T) \\ &\times [1 + 5(h_{me}/\alpha)^{1/2}(T - T^*)^2/T^*], \\ k_c^2 &\cong 60(h_{me}/\alpha)^{1/2}(T - T^*)/T^{*2}. \end{aligned} \tag{37}$$

We readily see from Fig. 3 that relation (36) fits quite well to the e $T^*(L)$ curve in the region of small L up to values $L \propto 1$. We did not succeed in deriving an analytical expression for $T^*(L)$ in the region of large values of L, because the values of k_c on this line are finite.

We will not discuss here specific features of the dispersion relation for magnetoelastic waves in the vicinity of the orientational phase transition, because, qualitatively, this relation has the same character as in a bilayer system of a magnetoelastic film and a nonmagnetic elastic substrate [11–13].

5. CONCLUSIONS

Thus, we have studied the spectrum of magnetoelastic waves in a periodic structure of alternating dielectric ferromagnetic and nonmagnetic layers. We considered an orientational phase transition driven by a tangential external magnetic field H_e for the case of uniaxial ferromagnetic layers with easy magnetization axes parallel to the layer surfaces. The formation of an inhomogeneous phase with a spatially modulated order parameter, which originates from magnetostriction-mediated coupling between the magnetization and lattice deformations, was predicted. The phase diagram in (L, T, H_e) space was constructed, and the regions of existence of the collinear, canted, and domain phases in thermodynamic equilibrium was determined.

The analysis of the transition of a multilayer system from the homogeneous to an inhomogeneous phase did not take into account the effect of exchange coupling between magnetic layers. For a system of dielectric layers, this is justified as long as the thickness of nonmagnetic layers exceeds a few lattice constants.

Consider briefly the effect of lattice misfit between the magnetic and elastic materials on the state of the system. The order parameter for the phase transition under study is the amplitude of the magnetization component m_z (or of the strain tensor component u_{xz}). If the misfit-stress symmetry does not coincide with the symmetry of the order parameter, the misfit stresses should not affect the final results as long as the difference between the parameters periods of the magnetic and nonmagnetic materials is small (i.e., as before, these stresses reduce to a renormalization of the external field and of the anisotropy constant). If, however, the lattice misfit between the magnetic and nonmagnetic layers is large, the ground state of the system may become inhomogeneous, i.e., in nucleation of a domain structure. In these conditions, magnetostriction domains will be observed against the background of the inhomogeneous phase if the period of those domains is small as compared to that of the domain structure, which is governed by the lattice misfit. Otherwise, the inhomogeneous state will have a more complex character.

Structures containing conducting components are of particular interest. If the nonmagnetic layers are conducting, the exchange coupling between the magnetic layers may acquire either ferromagnetic or antiferromagnetic character, depending on the nonmagnetic-layer thickness. Therefore, the results obtained here are applicable only if the thickness of the nonmagnetic layers is large enough to justify neglect of the exchange coupling between ferromagnetic layers. In the case where all layers are conducting, giant magnetoresistance may appear in the structure [16]. If only the magnetic layers are conducting, the presence of a domain structure in them can also give rise to giant magnetoresistance; if an in-plane current flows through the structure, the resistivity of each layer may vary, because the electron reflection coefficient depends on the spin polarization and the orientation of the magnetization in the domains. Finally, in ferromagnet–antiferromagnet multilayer systems, the phase transition from the homogeneous state to a magnetostriction domain structure may occur in a substantially different manner than in the system considered above, even if the components of the system are insulators. A comprehensive analysis showed that condition (12) fails at the ferromagnet–antiferromagnet interface [17]. Furthermore, exchange coupling between the ferro- and antiferromagnetic layers strongly affects the domain wall structure near the surface of the ferromagnet. Additional studies are needed to establish the character of the orientational phase transition in the structures indicated above.

ACKNOWLEDGMENTS

This study was supported by the Russian Foundation for Basic Research (project no. 02-02-16794), Polish Scientific Research Committee, and the ISTC Foundation (grant no. 1522).

REFERENCES

1. I. E. Dikshteĭn, E. A. Turov, and V. G. Shavrov, in *Dynamic and Kinetic Properties of Magnetic Systems*, Ed. by S. V. Vonsovskiĭ and E. A. Turov (Nauka, Moscow, 1986), Chap. 3.
2. V. I. Ozhogin and V. L. Preobrazhenskiĭ, Usp. Fiz. Nauk **155**, 593 (1988) [Sov. Phys. Usp. **31**, 713 (1988)].
3. V. G. Bar'yakhtar and E. A. Turov, in *Spin Waves and Magnetic Excitations*, Ed. by A. S. Borovik-Romanov and S. K. Sinha (North-Holland, Amsterdam, 1988), Vol. 2, Chap. 7.
4. Yu. V. Gulyaev, I. E. Dikshteĭn, and V. G. Shavrov, Usp. Fiz. Nauk **167**, 735 (1997) [Phys. Usp. **40**, 701 (1997)].
5. A. Hubert, *Theorie der Domanenwande in Geordneten Medien* (Springer, Berlin, 1974; Mir, Moscow, 1977).
6. R. W. Patterson and M. W. Muller, Int. J. Magn. **3**, 293 (1972).

7. M. H. Yang and M. W. Muller, J. Magn. Magn. Mater. **3**, 251 (1976).
8. Yu. I. Bespyatykh, I. E. Dikshteĭn, and V. V. Tarasenko, Fiz. Tverd. Tela (Leningrad) **23**, 3013 (1981) [Sov. Phys. Solid State **23**, 1757 (1981)].
9. I. E. Dikshteĭn, Fiz. Tverd. Tela (Leningrad) **32**, 1286 (1990) [Sov. Phys. Solid State **32**, 754 (1990)].
10. I. E. Dikshteĭn, Fiz. Tverd. Tela (Leningrad) **31** (3), 175 (1989) [Sov. Phys. Solid State **31**, 447 (1989)].
11. Yu. I. Bespyatykh and I. E. Dikshteĭn, Fiz. Tverd. Tela (St. Petersburg) **41**, 665 (1999) [Phys. Solid State **41**, 599 (1999)].
12. Yu. I. Bespyatykh, I. E. Dikshtein, Zhen-ya Li, and W. Wasilewski, Phys. Rev. B **62**, 3322 (2000).
13. Yu. I. Bespyatykh and I. E. Dikshtein, J. Magn. Magn. Mater. **220**, 214 (2000).
14. *Magnetic Ultrathin Films: Multilayers and Surface/Interface and Characterization*, Ed. by B. T. Janker (Material Res. Soc., Pittsburg, PA, 1993).
15. *Ultrathin Magnetic Structures*, Ed. by B. Heinrich and J. A. C. Bland (Springer, Berlin, 1994), Vols. 1 and 2.
16. M. N. Baibich, J. M. Broto, A. Fert, *et al.*, Phys. Rev. Lett. **61**, 2472 (1988).
17. V. D. Levchenko, A. I. Morozov, A. S. Sigov, and Yu. S. Sigov, Zh. Éksp. Teor. Fiz. **114**, 1817 (1998) [JETP **87**, 985 (1998)].

Translated by G. Skrebtsov

Physics of the Solid State, Vol. 45, No. 2, 2003, pp. 319–325. Translated from Fizika Tverdogo Tela, Vol. 45, No. 2, 2003, pp. 303–308.
Original Russian Text Copyright © 2003 by Nesterov, Sazonov.

Self-Induced Transparency of Hydrogen-Containing Ferroelectrics for Extremely Short Pulses in the Vicinity of the Curie Temperature

S. V. Nesterov and S. V. Sazonov
Kaliningrad State University, Kaliningrad, 236041 Russia
e-mail: nst@alg.kaliningrad.ru

Received March 4, 2002; in final form, June 10, 2002

Abstract—Nonlinear propagation of extremely short (carrierless) electromagnetic pulses in a KDP-type ferroelectric is investigated at temperatures close to the phase transition point. It is demonstrated that, although weak monochromatic signals undegro a sharp attenuation at these temperatures, an extremely short high-power pulse can propagate in the self-induced transparency regime and the associated soliton is stable to transverse perturbations. *© 2003 MAIK "Nauka/Interperiodica".*

1. INTRODUCTION

The self-induced transparency phenomenon involves a nonlinear bleaching of a resonant medium under the action of a laser pulse whose intensity exceeds a threshold [1]. Over the last decade, laser engineering has progressed to the stage where pulses of duration as short as one period of an electromagnetic oscillation (extremely short pulses) can be generated under experimental conditions [1–3]. The spectrum of these pulses is so broad that the carrier frequency cannot be separated. Consequently, the slowly varying amplitude approximation [4], which is traditionally used for quasi-monochromatic pulses with a carrier frequency, becomes inapplicable to theoretical investigations into the interaction of extremely short pulses with materials. The same is also true for the specific features observed in self-induced transparency for extremely short pulses as compared to quasi-monochromatic pulses [5]. However, in both cases, the mechanisms of propagation of self-induced transparency solitons are virtually identical and involve periodic energy exchange between the pulse and the medium.

In recent years, considerable interest has been expressed by researchers in laser actions on media undergoing structural phase transitions. A softening of vibrational modes in the vicinity of the phase transitions increases the role played by nonlinear effects. This opens up new possibilities for observing the specific features of nonlinear phenomena that cannot manifest themselves far from phase transitions. In particular, Belonenko [6] studied the self-induced transparency for quasi-monochromatic pulses propagating in a KDP-type ferroelectric and resonantly interacting with impurity two-level atoms. It was demonstrated that the soliton velocity can sharply decrease as the temperature T of the ferroelectric in polar and nonpolar phases approaches the Curie temperature T_C.

Note also that self-induced transparency solitons whose spectrum does not embrace frequencies of resonance transitions can propagate in a KDP-type ferroelectric at temperatures far from the Curie point T_C [7].

As the Curie temperature T_C is approached, the relaxation processes resulting in severe overdamping of the soft mode play an increasingly important role. As a result, the frequency dependence of the susceptibility of the ferroelectric is described by the Debye curve rather than by the Lorentzian curve [8, 9]. In this case, the softening of the vibrational mode manifests itself as a critical slowing down: the quasi-oscillation dynamics of polarization gives way to the relaxation dynamics, and the relaxation time tends to infinity at $T \longrightarrow T_C$. It should be noted that this relaxation is collective in nature and stems from a strong dipole–dipole interaction of polarization centers [10]. In a KDP-type ferroelectric, the function of the polarization centers is fulfilled by hydrogen ions whose vibrational mode is associated with tunneling these ions between minima of double-well potentials [8, 9].

In the vicinity of the Curie temperature, the self-induced transparency effect for quasi-monochromatic pulses (resonant with the soft mode) becomes impossible owing to a strong overdamping of the vibrational mode. Actually, the phase relaxation time for hydrogen ions tunneling in KH_2PO_4 is estimated as $T_2 \sim 10^{-12}$ s [8] and the frequency of the quantum tunneling is determined to be $\omega_0 \sim 10^{13}$ s^{-1}. At $|T - T_C| \sim 1$ K and $T_C \approx 222$ K, the frequency of the soft mode is estimated as $\omega_c \sim \omega_0\sqrt{|T - T_C|/T_C} \sim 10^{12}$ s^{-1} $\sim 1/T_2$. Since the pulse is resonant, its frequency is determined as $\omega = \omega_c \sim 1/T_2$. Observation of the self-induced transparency requires the fulfillment of the condition $\tau_p \ll T_2$ for the pulse duration τ_p. From this condition and the above relationships, we obtain $\omega\tau_p \ll 1$, which contradicts the condition $\omega\tau_p \gg 1$ for the quasi-monochromatic pulse and more likely corresponds to extremely short pulses. The spectrum of these pulses, in addition to resonance frequencies, contains other frequencies, including higher frequencies. As a result, the interaction of extremely short pulses with a medium can differ considerably from the interaction of quasi-monochromatic pulses and the medium. As the power of extremely short pulses increases, the interaction between the polarization centers (hydrogen ions) and the field of pulses becomes stronger than that between the polarization centers themselves. Consequently, the collective relaxation responsible for the overdamping of the soft mode makes a smaller contribution and, hence, the specific features of the polarization centers can show themselves more clearly. Therefore, the situation becomes similar to that observed for isolated atoms.

In the present work, we theoretically investigated the incoherent nonlinear propagation of extremely short high-power broadband pulses in hydrogen-containing ferroelectrics of the order–disorder type.

2. THE SELF-CONSISTENT SYSTEM OF CONSTITUTIVE AND WAVE EQUATIONS

In the right–left representation and the molecular-field approximation, the Hamiltonian of an active proton interacting with the electric field E of a pulse can be written in the form [8, 9, 11]

$$\hat{H}_1 = -\hbar\omega_0\hat{S}_x - \hbar(\Omega + JS_z)\hat{S}_z, \tag{1}$$

where $\hbar$ is the Planck constant, ω_0 is the frequency of quantum tunneling of the proton in an isolated double-well potential, J is the mean constant of the dipole–dipole coupling between quantum tunneling transitions of protons, $\Omega = \mathbf{d}\mathbf{E}/\hbar$, $\mathbf{d}$ is the dipole moment of the tunneling transition, and $\hat{S}_\rho^j$ ($\rho = x, y, z$) are the Pauli pseudospin operators for the ith center. In this case, the operator $\hat{S}_x^j$ determines the population inversion of two quantum levels of the jth center with the energy separation $\hbar\omega_0$. At the same time, the operator S_z^j is proportional to the dipole moment operator of the ith center. The role of the operator S_y^j reduces to the closure of the pseudospin operator algebra (note that $S_\rho = \langle\hat{S}_\rho\rangle$, where $\langle\ldots\rangle$ is the quantum averaging operation).

After quantum averaging of the Heisenberg equations written for the Pauli operators $\hat{S}_\rho^j$ ($\rho = x, y, z$), we obtain

$$\begin{gathered}\frac{\partial S_x}{\partial t} = (\Omega + JS_z)S_y,\\ \frac{\partial S_y}{\partial t} = \omega_0 S_z - (\Omega + JS_z)S_x, \quad \frac{\partial S_z}{\partial t} = -\omega_0 S_y.\end{gathered} \tag{2}$$

Relaxation is disregarded in these equations. Since this effect is very important in the vicinity of the Curie temperature T_C, according to [11], we take into account the relaxation by adding phenomenological relaxation terms to formulas (2). Owing to the critical slowing-down, the molecular field varies very slowly in the neighborhood of T_C. Therefore, the pseudospin components relax to the time-dependent quasi-equilibrium, which is determined by the instantaneous molecular field, rather than to the thermodynamic equilibrium [11].

First, we rewrite formulas (2) in the following form [11]:

$$\frac{\partial \mathbf{S}}{\partial t} = \mathbf{S} \times \boldsymbol{\Omega}^{\text{eff}}, \tag{3}$$

where $\mathbf{S} = (S_x, S_y, S_z)$ and $\boldsymbol{\Omega}^{\text{eff}} = \boldsymbol{\Omega}^m + \boldsymbol{\Omega}$. The components of the molecular field $\boldsymbol{\Omega}^m$ (with the frequency dimension) are represented in the form $\Omega_x^m = \omega_0$, $\Omega_y^m = 0$, and $\Omega_z^m = JS_z$.

It can be seen from relationship (3) that the vector $\mathbf{S}$ precesses about an instantaneous direction of the vector $\boldsymbol{\Omega}^{\text{eff}}$.

Let us introduce the effective susceptibility χ^{eff} as follows:

$$\mathbf{S}^q = \chi^{\text{eff}}\boldsymbol{\Omega}^{\text{eff}}, \tag{4}$$

where $\mathbf{S}^q$ is the quasi-equilibrium value of the vector $\mathbf{S}$, which is determined by the instantaneous value of $\boldsymbol{\Omega}^{\text{eff}}$.

In the state of thermodynamic equilibrium, we have [8, 9, 11]

$$S_x = S_x^e = \begin{cases}\tanh(\hbar\omega_0/k_B T), & T \ge T_C\\ \omega_0/J, & T \le T_C\end{cases} \tag{5}$$

and the Curie temperature T_C can be found from the expression

$$\frac{\omega_0}{J} = \tanh\left(\frac{\hbar\omega_0}{k_B T_C}\right), \tag{6}$$

where k_B is the Boltzmann constant.

From relationships (4) and (5), we obtain

$$\chi^{\text{eff}} = \frac{S_x^e}{\omega_0} = \frac{1}{\omega_0}\tanh\frac{\hbar\omega_0}{k_B T_C}. \tag{7}$$

The true static susceptibility $\chi(0)$ is deduced from the formula $S_{z0} = \chi(0)\Omega$ and, as follows from relationships (4) and (7), is related to χ^{eff} by the expression

$$\chi(0) = \frac{2\chi^{\text{eff}}}{1-2J\chi^{\text{eff}}} = \left(\omega_0\coth\frac{\hbar\omega_0}{k_{\text{B}}T_{\text{C}}} - J\right)^{-1}. \qquad (8)$$

This expression coincides with the corresponding expression derived for $\chi(0)$ in the framework of the thermodynamic theory [8] and, according to formula (6), has a singularity at $T = T_{\text{C}}$.

Taking into consideration that the vector **S** at temperatures close to T_{C} relaxes to its quasi-equilibrium value $\mathbf{S}^q$ [see formula (4)], relaxation terms in the form $-\gamma_\perp(\mathbf{S} - \mathbf{S}_\perp)$ and $\gamma_\parallel(\dot{S}_x - S_x^q)$ should be added to the right-hand side of formula (3). Then, we obtain

$$\frac{\partial\mathbf{S}}{\partial t} = \mathbf{S}\times\mathbf{\Omega}^{\text{eff}} - \gamma_\perp(\mathbf{S}_\perp - \chi^{\text{eff}}\mathbf{\Omega}_\perp^m) - \gamma_\parallel(S_x - \chi^{\text{eff}}\mathbf{\Omega}_x^m)\mathbf{e}_x, \qquad (9)$$

where $\mathbf{S}_\perp = (S_y, S_z)$, $\mathbf{\Omega}_\perp^m = (\Omega_y^m, \Omega_z^m)$, $\mathbf{e}_x$ is the unit vector aligned along the direction S_x (in the pseudospin space), and $\gamma_\perp$ and $\gamma_\parallel$ are the phase and energy relaxation rates, respectively. Note that the inequality $\omega_0^2 \gg \gamma_\perp^2$ is valid for hydrogen-containing ferroelectrics, in which the quantum tunneling through the barrier of the double-well potential has a high probability. Among ferroelectrics of this type are perovskites, SnTe, KDP, and other materials [8]. As a rule, the inequality $\gamma_\perp \ll \gamma_\parallel$ is satisfied [12]; hence, the relaxation rate $\gamma_\parallel$ will be ignored thereafter.

For the *z*th component, Eq. (9) takes the form

$$\frac{\partial S_z}{\partial t} = -\omega_0 S_y - \gamma_\perp(1 - JS_x^e/\Omega_0)S_z. \qquad (10)$$

At $T = T_{\text{C}}$, we have $JS_x^e/\omega_0 = 1$. Consequently, the relaxation terms in the last equation can be disregarded in the vicinity of the transition temperature. Taking into account the aforesaid and eliminating the physically meaningless *y*th component of the vector of the pseudopotential *S*, Eq. (10) can be rewritten in the form of a set of equations for the components of the vector **S**; that is,

$$\frac{\partial S_x}{\partial t} = -\frac{\Omega + JS_z}{\omega_0}\frac{\partial S_z}{\partial t}, \qquad (11)$$

$$\frac{\partial^2 S_z}{\partial t^2} + \gamma_\perp\frac{\partial S_z}{\partial t} + \omega_0^2 S_z = \omega_0(\Omega + JS_z)S_x. \qquad (12)$$

Below, it will be shown that the results obtained with the proposed technique of introducing the relaxation are in reasonable agreement with the experimental data on the dynamic properties of ferroelectrics in the vicinity of the Curie temperature.

Now, we supplement the constitutive equations (11) and (12) with the Maxwell equation for the external field Ω:

$$\Delta\Omega - \frac{1}{c^2}\frac{\partial^2\Omega}{\partial t^2} = \frac{4\pi d^2 n}{\hbar c^2}\frac{\partial S_z}{\partial t^2}, \qquad (13)$$

where *c* is the velocity of light in free space, *n* is the concentration of active centers, and Δ is the Laplacian. Further analysis is based on examination of the self-consistent system of equations (11)–(13), which describes the dynamics of the electromagnetic pulse in hydrogen-containing ferroelectrics of the order–disorder type at temperatures close to the Curie point.

3. ATTENUATION OF WEAK MONOCHROMATIC WAVES

Let us linearize the system of equations (11) and (12). For this purpose, we write $S_x = S_x^e + \xi$ and $S_z = S_{z0} + \zeta$ ($S_{z0} \neq 0$ at $T < T_{\text{C}}$), where ξ and $\zeta \ll S_x^e$, and S_{z0}. Then, from Eqs. (12) and (13), we find

$$\frac{\partial^2\zeta}{\partial t^2} + 2\gamma_\perp\frac{\partial\zeta}{\partial t} + \omega_c^2\zeta = \omega_0 S_x^e\Omega, \qquad (14)$$

where $\omega_c^2 = \omega_+^2 \equiv \omega_0^2(1 - JS_x^e/\omega_0)$ at $T > T_{\text{C}}$ and $\omega_c^2 = \omega_-^2 \equiv (JS_{z0})^2$ at $T < T_{\text{C}}$.

The dynamic susceptibility of the ferroelectric can be defined by the relationship

$$P - P_0 = dh\zeta = \chi(\omega)E, \qquad (15)$$

where $P_0 = dhS_{z0}$ is the equilibrium polarization (spontaneous at $T < T_{\text{C}}$), $P = dhS_z$ is the total polarization in the presence of the external electric field *E*, and ω is the field frequency.

By assuming that ζ and $\Omega = dE/\hbar \sim e^{i\omega t}$, from formulas (14) and (15), we have

$$\chi(\omega) = \chi(0)\frac{\omega_c^2}{\omega_c^2 - \omega^2 + 2i\gamma_\perp\omega}, \qquad (16)$$

where $\chi(0) = d^2 n\omega_0^2/(\hbar J\omega_c^2)$.

Expression (16) adequately describes the experimental data for hydrogen-containing ferroelectrics [8]. Moreover, it is easy to see that this expression is the limiting case of the more general relationship [11] at $\omega_0^2 \gg \gamma_\perp^2$. If the phase relaxation rate were to symmetrically enter into the equations for S_y and S_z (as is often the case in media at temperatures far from phase transitions), ω_c in expression (16) would not become zero at $T = T_{\text{C}}$. Therefore, we can draw the inference that the inclusion of the relaxation in the simplest manner (as in the preceding section) leads to agreement with the experiment and does not contradict the thermodynamic theory. The quantity $\chi(0)$ in expression (16) is the static and, simultaneously, thermodynamic equilibrium susceptibility. Indeed, for example, at $T > T_{\mathrm{C}}$, we obtain

$$\chi(0) = \frac{d^2 n}{\hbar J(1 - J S_x^e/\omega_0)}.$$

This relationship coincides with the theoretical expression derived within the molecular-field approximation in the vicinity of T_{C} [9]. The situation at $T < T_{\mathrm{C}}$ can be considered in a similar way.

By expanding expression (5) into a series in terms of the small parameter $(T - T_{\mathrm{C}})/T_{\mathrm{C}}$ at $T > T_{\mathrm{C}}$ with due regard for formula (6), we obtain $\omega_c^2 = \omega_+^2 = \Omega_+^2(T - T_{\mathrm{C}})/T_{\mathrm{C}}$, where $\Omega_+^2 = \omega_0^2(\hbar J/k_{\mathrm{B}}T_{\mathrm{C}})(1 - \omega_0^2/J^2)$. Similarly, in the ferroelectric phase, we have $\omega_c^2 = \omega_-^2 = \Omega_-^2(T_{\mathrm{C}} - T)/T_{\mathrm{C}}$, but the formula for Ω_-^2 is more cumbersome than that for Ω_+^2. This representation of ω_c in expression (16) results in the best agreement with the experimental data [8].

As the Curie temperature T_{C} is approached in the paraphase ($T > T_{\mathrm{C}}$) and the ferroelectric phase ($T < T_{\mathrm{C}}$), we obtain $\omega_c^2 \sim |T - T_{\mathrm{C}}|$. Therefore, in the immediate vicinity of the transition temperature, the free oscillator ($\Omega = 0$) described by formula (14) becomes overdamped (i.e., $\gamma_\perp > \omega_c$), because the rate $\gamma_\perp$ is virtually independent of the temperature [11]. At $\gamma_\perp^2 \gg \omega_c^2$, the first term on the left-hand side of expression (14) can be disregarded. As a result, the order parameter exhibits a purely relaxation dynamics with the characteristic relaxation time $\tau = 2\gamma_\perp/\omega_c^2 = \Omega_\pm^{-2} T_{\mathrm{C}}/|T - T_{\mathrm{C}}|$. In this case, there is direct evidence of a critical slowing down at $T \longrightarrow T_{\mathrm{C}}$. However, unlike hydrogen-free ferroelectrics, the relaxation in our case is caused by tunneling effects to a greater extent than by thermal over-barrier transitions in double-well potentials. Neglect of the term $\partial^2\zeta/\partial t^2$ in formula (14) at temperatures close to T_{C} corresponds to neglect of ω^2 in the denominator of expression (16). Consequently, the susceptibility of the ferroelectric exhibits Debye behavior [8, 9, 11].

The relaxation dynamics of the order parameter (polarization) indicates that, at temperatures close to the Curie point, electromagnetic waves incident on the ferroelectric should undegro a severe attenuation over a wide range of frequencies. According to the Beer law, the intensity of the wave propagating along the z axis is represented as $I \sim E^2 \sim \exp(-\kappa z)$, where $\kappa = 2\omega N_I/c$ is the attenuation coefficient and N_I is the imaginary part of the refractive index $N = \sqrt{1 + 4\pi\chi(\omega)} = N_R - iN_I$ [here, N_R is the real part of the refractive index and $\chi(\omega)$ is defined by relationship (15)].

Let us estimate the attenuation coefficient κ at different frequencies ω.

(1) **Low-frequency waves ($\omega \ll \omega_c$).** In this case, we can disregard ω^2 in expression (16). Setting $d \sim 10^{-18}$, $n \sim 10^{22}$ cm^{-3}, and $J \sim 10^{13}$ s^{-1}, we obtain $d^2n/\hbar J \sim 1$. Moreover, under the assumption that $\omega_0 \sim 10^{13}$ s^{-1} and $(T - T_{\mathrm{C}})/T_{\mathrm{C}} \sim 10^{-2}$, we find that $\omega_c \sim \omega_0\sqrt{(T - T_{\mathrm{C}})/T_{\mathrm{C}}} \sim 10^{12}$ s^{-1}. As a result, we have $\chi(0) \sim 10^2$. At $\gamma_\perp \sim 10^{12}$ s^{-1}, we obtain $\chi(\omega) \sim 10^2$ and $N \approx \sqrt{4\pi\chi(\omega)}$. By separating the imaginary part, we find

$$\kappa = 4\frac{\gamma_\perp}{c}\sqrt{\frac{\pi d^2 n}{\hbar J}}\frac{\omega_0\omega^2}{\omega_c^3}.$$

Therefore, at low frequencies, we have $\kappa \sim \omega^2$. At $\omega \sim 10^{11}$ s^{-1} (wavelength $\lambda \sim 1$ cm), from the last expression and with the aforementioned parameters, we obtain ~10 cm^{-1}, which corresponds to the penetration depth $l = \kappa^{-1} \sim 0.1$ cm. Since $l < \lambda$, the wave does not propagate in the medium.

(2) **Waves of resonance frequencies ($\omega = \omega_c$).** Estimates analogous to those made in the preceding case demonstrate that $4\pi|\chi(\omega)| \gg 1$. Therefore, we have $N^2 \sim 4\pi\chi(\omega)$ and

$$\kappa = 2\frac{\omega_0}{c}\sqrt{\frac{\pi d^2 n}{\hbar J}\frac{\omega}{\gamma_\perp}}.$$

At $\omega = \omega_c \sim 10^{12}$ s^{-1} ($\lambda = 0.1$ cm), we find $\kappa = l^{-1} \sim 10^3$ cm^{-1}. In this case, we obtain $l \ll \lambda$ and, hence, the wave attenuates even more rapidly than at low frequencies. Since $\kappa \sim \sqrt{\omega}$ and $\lambda \sim \omega^{-1}$, an increase in the frequency can result in an increase in the ratio l/λ. In this respect, we also examine the high-frequency range.

(3) **High-frequency waves ($\omega \gg \omega_c$).** The upper limit of the frequencies under investigation lies at $\omega \sim 10^{14}$ s^{-1}, because higher frequencies ω correspond to optical electron transitions and transitions of protons to higher lying levels in the double-well potential [8], whose contribution is disregarded in the present work. Consequently, setting $\omega_c/\omega \sim 10^{-2}$ in expression (16), we obtain $|\chi(\omega)| \sim \chi(0)(\omega_c/\omega)^2 \sim 10^{-2}$ and $4\pi|\chi(\omega)| \ll 1$. Hence, the refractive index is determined to be $N = N_R - iN_I \approx 1 + 2\pi\chi(\omega)$.

By separating the imaginary part in expression (16) and ignoring ω_c^2 in the denominator, we obtain

$$\kappa = \frac{8\pi d^2 n}{\hbar J}\frac{\gamma_\perp}{c}\frac{\omega_0^2}{\omega^2}.$$

Thus, in the high-frequency limit, we have $\kappa \sim \omega^{-2}$.

At $\omega \sim 10^{14}$ s^{-1} ($\lambda \sim 10^{-3}$ cm) and with the aforementioned parameters, we obtain $\kappa \sim 10$ cm^{-1}, which corresponds to $l \sim 10^2\lambda$.

Therefore, only in the case of very high frequencies in the IR range can the penetration depth be of the order of 10–100 wavelengths (or ~1 mm). In the other range ($\omega < 10^{14}$ s^{-1}), the weak electromagnetic field with the IR frequency spectrum virtually does not penetrate into the ferroelectric when its temperature is close to the Curie point.

4. NONLINEAR PROPAGATION OF PULSES UNDER THE CONDITIONS OF SPECTRAL OVERLAP

Now, let us consider the propagation of the extremely short high-power pulse in the ferroelectric along the polar axis perpendicular to the plane of tunneling oscillations of protons [9]. We assume that the pulse is so short that the following condition of spectral overlap is met [5, 13, 14]:

$$\omega_0\tau_p \ll 1. \tag{17}$$

Since the pulse has a spectral width $\delta\omega \sim \tau_p^{-1}$, condition (17) can be rewritten in the form $(\delta\omega/\omega_0)^2 \gg 1$. Therefore, the spectrum of the extremely short pulse involves the Fourier components that are resonant with even–odd quantum transitions between tunneling states of protons. This circumstance should lead to a substantial change in the difference between the populations of these states. As a consequence, condition (17) corresponds to a strongly nonlinear interaction of the pulse with the ferroelectric. Furthermore, it is also assumed that the following condition is satisfied:

$$\tau_p \ll \gamma_\perp^{-1}, \tag{18}$$

which allows us to ignore the relaxation term in Eq. (12). Setting $\omega_0 \sim 10^{13}$ s^{-1} and $\gamma_\perp \sim 10^{12}$ s^{-1} [8], we find that conditions (17) and (18) can be satisfied at $\tau_p \sim 10^{-14}$ s. In this case, the interaction of the extremely short pulse with high-lying quantum levels of protons in the double-well potential can be disregarded. In view of condition (17), the last term on the left-hand side of Eq. (12) can also be ignored.

On this basis, the system of equations (11) and (12) can be rewritten in the form

$$\frac{\partial X}{\partial t} = -\Psi Z, \quad \frac{\partial Z}{\partial t} = \Psi Z, \tag{19}$$

where

$$X = S_x, \quad Z = \frac{1}{\omega_0}\frac{\partial S_z}{\partial t}, \quad \Psi = \Omega + JS_z.$$

Making allowance for the initial conditions, we obtain $X(-\infty) = S_x^e$ and $Z(-\infty) = 0$ [see relationship (10) at $T > T_C$ and $T < T_C$]. After regaining the initial designations, the solution to system (19) can be represented in the following form:

$$S_x = S_x^e\cos\theta, \quad \frac{\partial S_z}{\partial t} = \omega_0 S_x^e \sin\theta, \tag{20}$$

where the “area” is given by the formula

$$\theta = \int_{-\infty}^{t}(\Omega + JS_z)dt'. \tag{21}$$

Since we have $JS_z \approx \omega_0$ and the Rabi frequency $\Omega \sim \tau_p^{-1}$ [5] in the vicinity of the transition temperature, condition (17) is equivalent to the inequality $\Omega \gg JS_z$.

This inequality corresponds to neglect of the dipole–dipole interaction between protons in different double-well potentials. Consequently, when condition (17) is met, the interaction of each proton with the field of the pulse is stronger than that with protons of the environment. The pulse as though suppresses interactions between the protons responsible for the phase transition. As a result, individual properties of the proton system rather than its collective properties manifest themselves in the field of the high-power pulse. Therefore, a number of effects, such as the softening of the vibrational mode and its overdamping, are not of considerable importance. Hence, the expression for θ can be written as follows:

$$\theta = \int_{-\infty}^{t}\Omega dt'. \tag{22}$$

Substitution of the second equation of system (20) into the right-hand side of Eq. (13) gives the three-dimensional sine-Gordon equation

$$\Delta\theta - \frac{1}{c^2}\frac{\partial^2\theta}{\partial t^2} = \beta\sin\theta, \tag{23}$$

where $\beta = 4\pi d^2 n\omega_0 S_x^e/\hbar c^2 \approx 4\pi d^2 n\omega_0^2/(\hbar Jc^2)$.

In the one-dimensional case, at $\theta = \theta(z, t)$ (where z is the polar axis), Eq. (23) becomes integrable [15]. The one-soliton solution of this equation has the form

$$\theta = 4\arctan\left[\exp\left(\frac{t - z/V}{\tau_p}\right)\right], \tag{24}$$

where V is the soliton velocity related to the soliton width τ_p by the expression

$$\frac{1}{V^2} = \frac{1}{c^2}\left(1 + \frac{4\pi d^2 n}{\hbar J}(\omega_0\tau_p^2)\right). \tag{25}$$

Since $d^2n/\hbar J \sim 1$ (see the preceding section), at $\omega_0\tau_p \sim 0.1$, the soliton velocity differs from c by 1–10%.

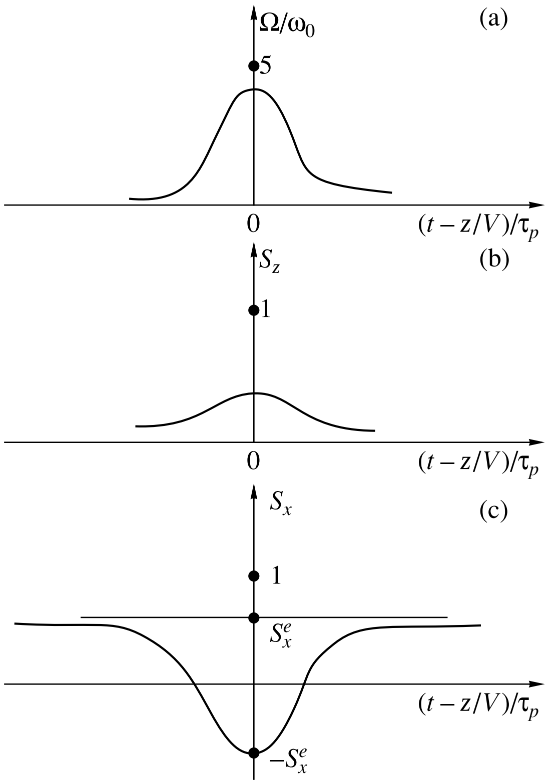

Fig. 1. An extremely short soliton of self-induced transparency in a ferroelectric: (a) soliton profile in a comoving frame of reference, (b) polarization dynamics during soliton propagation, and (c) evolution of the difference in the populations of the tunneling transition during soliton propagation.

With the use of relationships (20), (22), and (24), we find

$$\Omega = \frac{2}{\tau_p}\operatorname{sech}\left(\frac{t - z/V}{\tau_p}\right), \qquad (26)$$

$$S_z = S_{z0} + 2(\omega_0\tau_p)S_x^e\operatorname{sech}\left(\frac{t - z/V}{\tau_p}\right), \qquad (27)$$

$$S_x = S_x^e\left[1 - 2\operatorname{sech}^2\left(\frac{t - z/V}{\tau_p}\right)\right]. \qquad (28)$$

In this situation, we have $S_{z0} = 0$ in the paraphase and $S_{z0} \approx \sqrt{3(T_C - T)/T_C} \sim 0.1$ (at $|T_C - T|/T_C \sim 0.01$) in the ferroelectric phase. At the same time, we can write $S_x^e \approx \omega_0/J < 1$ and $\omega_0\tau_p \sim 0.1$. Consequently, the quantity S_{z0} and the multiplier $2(\omega_0\tau_p)S_x^e$ in expression (27) are of the same order of magnitude ($\sim 0.1 \ll 1$). Therefore, the displacement of protons from equilibrium positions in the double-well potentials appears to be insignificant when condition (17) is satisfied. As a result, the propagation of soliton (26) through the ferroelectric is accompanied by very weak changes in the ferroelectric polarization. On the other hand, according to relationship (28), the difference between the populations of the tunneling sublevels considerably changes from $S_x^e \approx \omega_0/J$ at $t - z/V \longrightarrow \pm\infty$ to $-S_x^e \approx -\omega_0/J$ at $t - z/V = 0$ (see Fig. 1).

Now, we analyze the stability of soliton (26) against self-focusing. For this purpose, it is necessary to return to the three-dimensional sine-Gordon equation (23) and to allow for the perturbation of the one-dimensional solution (26), provided that it weakly depends on the transverse coordinates $\mathbf{r}_\perp$. To accomplish this, we invoke the averaged variational principle [16].

Equation (23) can be derived from the Euler–Lagrange equations with the use of the Lagrangian density

$$\mathcal{L} = \frac{1}{2}(\nabla\theta)^2 - \frac{1}{2c^2}\left(\frac{\partial\theta}{\partial t}\right)^2 + \beta(1 - \cos\theta). \qquad (29)$$

The trial solution, which includes a weak dependence on the initial coordinates, can be written in the form

$$\theta = 4\arctan\{\exp[\rho(t - \varphi(r))]\}. \qquad (30)$$

In the one-dimensional case [see relationship (24)], we have $\rho(r) = \tau_p^{-1} = \text{const}$ and $\varphi(r) = z/V$.

Since the dependence on $r_\perp$ is weak, $\rho(r)$ is a slowly varying function of arguments and $\varphi(r)$ is a rapidly varying function in expression (30). Substituting expression (30) into formula (29) and ignoring the derivatives of the slowly varying function $\rho(r)$ [16], we find that the mean Lagrangian

$$L \equiv \frac{1}{4}\int_{-\infty}^{+\infty}\mathcal{L}\,dt$$

can be expressed by the formula

$$L = \rho(\nabla\varphi)^2 - \frac{\rho}{c^2} + \frac{\beta}{\rho}. \qquad (31)$$

The Euler–Lagrange equation for the variables φ and ρ can be represented in the following form:

$$\frac{\mathbf{V}^2}{2} + \int\frac{dP}{\rho} = \frac{1}{2c^2} = \text{const}, \qquad (32)$$

$$\nabla(\rho\mathbf{V}) = 0, \qquad (33)$$

where $\mathbf{V} = \nabla\varphi$ and P and ρ are related by the expression

$$\frac{dP}{d\rho} = \frac{\beta}{\rho^2} > 0. \qquad (34)$$

Note that equations (32) and (33) coincide with the well-known equations describing a steady potential flow of ideal fluid. In this case, Eq. (32) is the Bernoulli integral and Eq. (33) is the continuity equation. Therefore, the quantity P plays the role of an internal pressure and the quantity ρ fulfills the function of the density of this fluid, for which the equation of state coincides with Eq. (34). It is evident that the condition for the steady flow of this hypothetical fluid $dP/d\rho > 0$ corresponds to the condition for the stability of soliton (26) [see also expression (24)] against transverse perturbations.

According to relationship (34), the extremely short soliton of self-induced transparency does not undergo a self-focusing in the hydrogen-containing ferroelectric at temperatures close to the transition point. On the other hand, it is well known that self-induced transparency resonant quasi-monochromatic solitons are unstable with respect to transverse perturbations [17].

5. CONCLUSIONS

Thus, the results of the above investigation demonstrated that, unlike weak monochromatic signals, the high-power short ($\tau_p \sim 10^{-14}$ s) electromagnetic video pulse can propagate virtually without attenuation in the ferroelectric at temperatures close to the Curie point. It was revealed that the mechanism of this propagation is associated with the suppression of the dipole–dipole interactions between active centers under the action of a strong field induced by an electromagnetic pulse. As a result, the active centers (protons in the double-well potentials) behave like isolated atoms in the field of the pulse. Therefore, collective effects, such as the soft mode and the critical slowing down, are also suppressed in the region of propagation of extremely short pulses.

In the strict sense, at the pulse duration $\tau_p \sim 10^{-14}$ s, the pulse dynamics can be affected (even if insignificantly) by transitions to proton quantum levels that lie above the tunneling sublevels of the ground state. For these transitions, the condition of the wave transparency is satisfied: $(\omega_p\tau_p)^2 \gg 1$, where ω_p is the frequency of transition from one of the tunneling sublevels to the nearest high-lying proton level in the double-well potential. A technique taking account of these transitions for isolated atoms was proposed in [18]. With minor improvements, this technique can be applied to the solution of problems concerning the interaction of extremely short pulses with ferroelectrics.

ACKNOWLEDGMENTS

This work was supported by the Russian Foundation for Basic Research (project nos. 00-02-17436a and 02-02-17710a) and the Civilian Research and Development Foundation of the United States (CRDF, grant no. 6104).

REFERENCES

1. J. T. Darrow, B. B. Hu, X. C. Chang, and D. H. Auston, Opt. Lett. **15**, 323 (1990).
2. P. C. Becker, H. L. Fragnito, J. Y. Bigot, *et al.*, Phys. Rev. Lett. **63** (5), 505 (1989).
3. K. Tamura and M. Nakazawa, Opt. Lett. **21**, 68 (1996).
4. S. A. Akhmanov, V. A. Vysloukh, and A. S. Chirkin, *Optics of Femtosecond Laser Pulses* (Nauka, Moscow, 1988).
5. A. Yu. Parkhomenko and S. V. Sazonov, Zh. Éksp. Teor. Fiz. **114**, 1595 (1998) [JETP **87**, 864 (1998)].
6. M. B. Belonenko, Author’s Abstract of Doctoral Dissertation (Volgograd, 1998).
7. S. V. Sazonov, Fiz. Tverd. Tela (St. Petersburg) **37**, 1612 (1995) [Phys. Solid State **37**, 875 (1995)].
8. V. G. Vaks, *Introduction to the Microscopic Theory of Ferroelectrics* (Nauka, Moscow, 1973).
9. B. A. Strukov and A. P. Levanyuk, *Physical Principles of Ferroelectric Phenomena* (Nauka, Moscow, 1983).
10. S. V. Sazonov, Pis’ma Zh. Tekh. Fiz. **22** (21), 52 (1996) [Tech. Phys. Lett. **22**, 887 (1996)].
11. R. Blinc and B. Zeks, *Soft Modes in Ferroelectrics and Antiferroelectrics* (North-Holland, Amsterdam, 1974; Mir, Moscow, 1975).
12. R. H. Pantell and H. E. Puthoff, *Fundamentals of Quantum Electronics* (Wiley, New York, 1969; Mir, Moscow, 1972).
13. É. M. Belenov and A. V. Nazarkin, Pis’ma Zh. Éksp. Teor. Fiz. **51**, 252 (1990) [JETP Lett. **51**, 288 (1990)].
14. É. M. Belenov, A. V. Nazarkin, and V. A. Ushchanovskiĭ, Zh. Éksp. Teor. Fiz. **100**, 762 (1991) [Sov. Phys. JETP **73**, 422 (1991)].
15. G. L. Lamb, Jr., *Elements of Soliton Theory* (Wiley, New York, 1980; Mir, Moscow, 1983).
16. S. K. Zhdanov and B. A. Trubnikov, *Quasi-Gaseous Unstable Media* (Nauka, Moscow, 1991).
17. R. K. Dodd, J. C. Eilbeck, J. Gibbon, and H. C. Morris, *Solitons and Nonlinear Wave Equations* (Academic, New York, 1982; Mir, Moscow, 1988).
18. S. V. Sazonov and A. F. Sobolevskiĭ, Opt. Spektrosk. **90** (3), 449 (2001) [Opt. Spectrosc. **90**, 390 (2001)].

Translated by O. Borovik-Romanova

Physics of the Solid State, Vol. 45, No. 2, 2003, pp. 326–334. Translated from Fizika Tverdogo Tela, Vol. 45, No. 2, 2003, pp. 309–316.
Original Russian Text Copyright © 2003 by Dubovskiĭ, Orlov, Semenov.

LATTICE DYNAMICS AND PHASE TRANSITIONS

Vibrational Spectra of Fe_3P and Fe_2P Metal–Metalloid Compound Crystallites: Phonon and Breather Excitations

O. A. Dubovskiĭ, A. V. Orlov, and V. A. Semenov
State Scientific-Center Institute of Physics and Power Engineering,
pl. Bondarenko 1, Obninsk, Kaluga oblast, 249020 Russia
e-mail: dubov@ippe.obninsk.ru

Received June 20, 2002

Abstract—The spectra of small-amplitude single-phonon vibrations and large-amplitude nonlinear multiphonon vibrations of Fe_3P and Fe_2P metal–metalloid compound crystallites are investigated. The vibrational spectra of 3D crystallites of gradually increasing volumes are calculated within a microscopic approach using previously tested interatomic interaction potentials. The calculated energy of the main low-frequency peak is closer to its experimental value in comparison with previous calculations, which reduces the significant discordance between the experimental and theoretical spectra. The fine structure of the high-frequency part of the vibrational spectrum is discussed. A study of large-amplitude nonlinear vibrations (which determine the diffusion of atoms and dispersive processes in materials) showed that a specific nonlinear breather mode of vibration can be generated in the crystallites in question, which is a genetic precursor of nonlinear self-localized vibrations. *© 2003 MAIK "Nauka/Interperiodica".*

1. INTRODUCTION

Experimental studies of the vibrational spectra of crystalline and amorphous Fe–P metal–metalloid compounds (which are of interest in nuclear-reactor materials science) are presently performed on an FÉI DIN neutron spectrometer at the Joint Institute of Nuclear Research (Dubna) by using inelastic slow-neutron scattering. In solving practical radiation-materials science problems, one should use very accurately determined values of the parameters of the interatomic interaction potentials, which control the transport characteristics of the diffusion of atoms in materials. Among these characteristics are, first, the activation energy (the barrier height) for diffusive motion of atoms, which determines the exponential factor of the phenomenological diffusion coefficient, and, second, the spectrum of vibrations that precede the activation process and determine the preexponential factor of the diffusion coefficient. However, roughly estimated, heuristic values of these basic characteristics are generally used in radiation-materials science. In a number of papers, these characteristics were calculated using the molecular-dynamics method. In this case, however, the initial conditions are chosen heuristically, which does not allow one to establish the essential features (see below) of nonlinear subthreshold vibrations that determine the preexponential factor.

The parameters of the atom–atom interaction potentials in condensed materials can be determined most accurately by experimentally and theoretically analyzing the spectra of both single-phonon (small-amplitude) vibrations and nonlinear multiphonon (large-amplitude) vibrations of a subthreshold energy. The parameters of interatomic potentials and their effect on the single-phonon spectra of small-amplitude vibrations for a wide range of technological materials have been studied intensively at many scientific centers [1–5]. Some theoretical studies involve the tridiagonalization procedure, which significantly reduces the reliability of their results. Nonlinear, large-amplitude vibrations of high energy are difficult to investigate both experimentally and theoretically, and they have been considered only in a few papers [6–11]. These vibrations are of interest, because they are immediately followed by diffusive jumps of atoms, disruptive processes, and disintegration of materials. It is of most interest to study bound multiphonon complexes, such as biphonons, triphonons, solitons, breathers [12–15], self-localized vibrations [8–11], and microshock waves.

In this paper, the vibrational spectra of Fe_3P and Fe_2P crystallites are calculated without involving the tridiagonalization procedure [1], since this procedure reduces the reliability of the results of calculations performed for a large number of atoms ($N \cong 10^5$). We apply an alternative method for studying the vibrational spectrum of a 3D crystallite whose size is small and progressively increased until the asymptotic spectrum is obtained for $N \cong 0.5 \times 10^3$; the interaction of all atoms is fully taken into account and described by previously tested interatomic potentials. It is shown that in the Fe_3P crystal, the calculated energy corresponding to the main low-frequency peak is lower than that found in [1] and is closer to the experimentally measured energy [2]; this result explains the previously found discordance. Then, we discuss the fine structure of the spectrum. In the future, one will be able to fit the parameters of the interatomic potentials to the experimental data obtained using a DIN neutron spectrometer and to determine the values of these parameters more accurately.

Nonlinear vibrations are investigated in elementary Fe_2P and Fe_3P crystallites. The self-localized vibrations have not yet been observed experimentally, and it is of interest to discuss the possible detection of such multiphonon complexes. It should be noted that the studies reported in [8–11] dealt either with unbounded model crystals or with crystalline chains of 100 and 128 atoms for which numerical calculations were performed. In those studies, in order to solve the problem analytically, simplifying assumptions were made: the envelopes were assumed to be smooth, a cutoff of the spectrum was introduced, etc.

In this paper, we investigate the dynamics of nonlinear vibrations of closed crystallites, such as chains of small lengths or, what is the same, of unbounded crystallites with the Born–von Karman boundary conditions. This approach allows us to find exact analytical solutions which virtually cannot be found for crystals of large sizes or within the framework of the molecular-dynamics method. We note that the Fermi resonance interface modes (FRIMs, band-gap modes at Fermi resonance), which are solitons of a fundamentally new type, have been discovered using this approach [16, 17]. We find exact analytical solutions to the dynamic nonlinear equations for large-amplitude vibrations of crystallites of the smallest size possessing the symmetry elements of Fe_2P and Fe_3P. It is shown that in such crystallites, a new type of nonlinear periodic breather (NPB) vibrations can be generated. These NPB vibrations are similar, in part, to breather vibrations of the FRIM type [16, 17] and are likely a genetic precursor of self-localized vibrations. In these NPB excitations, the "modulus" of the system (see below) oscillates in time and the phase of the system has an oscillatory time dependence (which is characteristic of these excitations), so that the Fourier expansion contains an infinite set of frequencies. It is shown that the NPB vibrations follow closed multiturn trajectories only if the change in phase over a modulus oscillation period is a rational multiple of π (such a change in phase corresponds to a certain, fixed number of turns in the closed trajectory). The trajectories of the NPB vibrations correspond to strictly definite initial conditions, which practically cannot be determined using the molecular-dynamics method, where general initial conditions bring about nonresonant nonperiodic vibrations.

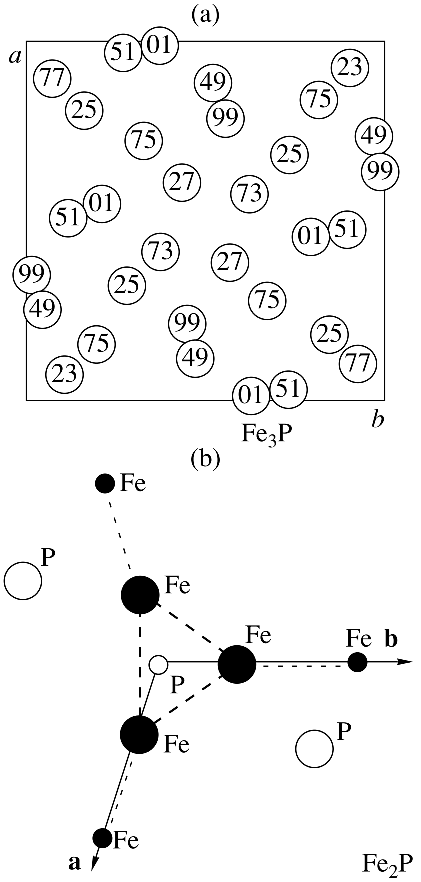

Fig. 1. Projection of the (a) Fe_3P and (b) Fe_2P unit-cell atoms onto the $c = 0$ plane.

2. PHONON EXCITATIONS

The Fe_3P crystal belongs to the tetragonal system, and its symmetry is described by the space group $S_4^2(I\bar{4})$. The unit cell consists of 32 atoms forming eight Fe_3P quasimolecules. The lattice parameters determining the unit-cell position vectors $a_0n\mathbf{i} + b_0m\mathbf{j} + c_0p\mathbf{k}$ (n, m, p are integers) are $a_0 = b_0 = 9.107$ Å and $c_0 = 4.460$ Å [18, 19]. All atoms of the body-centered tetragonal unit cell occupy the positions xyz, $\bar{x}\bar{y}z$, $y\bar{x}\bar{z}$, and $\bar{y}x\bar{z}$. The coordinates of the atoms of one of the eight quasimolecules (in units of a_0, b_0, c_0) are 0.106, 0.079, 0.234 for Fe(1); 0.031, 0.361, 0.986 for Fe(2); 0.219, 0.172, 0.755 for Fe(3); and 0.045, 0.292, 0.49 for P. The coordinates of the other atoms of the unit cell can be found using the rotation and reflection symmetry of the unit cell. The projections of the 32 atoms of the unit cell onto the xy plane are shown in Fig. 1a. The phosphorus atoms are represented by thick circles. The numbers in the circles indicate the height of the atom (in percentage of c_0) above the xy plane.

The Fe_2P crystal belongs to the hexagonal system, and its symmetry is described by the space group $P\bar{6}2m$. The unit cell consists of nine atoms forming three Fe_2P quasimolecules. The lattice parameters are $a_0 = b_0 = 5.865$ Å and $c_0 = 3.456$ Å [19]. The coordinates of the atoms in the unit cell are $(x, 0, 0)$, $(0, x, 0)$, and ($\bar{x}$, $\bar{x}$, 0) with $x = 0.256$ for Fe(*f*); (x, 0, 1/2), (0, x, 1/2), and ($\bar{x}$, $\bar{x}$, 1/2) with $x = 0.594$ for Fe(*g*); ±(1.3, 2/3, 0) for P(*c*); and (0, 0, 1/2) for P(*b*). Figure 1b shows the projection of the unit cell onto the *ab* basal plane ($r_c = 0$). It is worth noting that the three strongly interacting Fe atoms lying in the *ab* basal plane (large filled circles) form a closed trimerlike system.

The Hamiltonian H of the dynamic system of atoms oscillating about their equilibrium positions on the crystal lattice is the sum of the kinetic energy H_k and the interaction energy Φ of the atoms (which are assumed to interact via a pairwise potential):

$$\begin{gathered} H = H_k + \Phi, \quad H_k = \sum_{\alpha i} \frac{p_{\alpha i}^2}{2M_\alpha}, \\ \Phi = \frac{1}{2}\sum_{\alpha \neq \beta} u_{\alpha\beta}(R_{\alpha\beta}). \end{gathered} \tag{1}$$

Here, $p_{\alpha i}$ is the ith momentum component of an atom α of mass M_α. The interaction energy $u_{\alpha\beta}(R_{\alpha\beta})$ between atoms α and β depends on the spacing $R_{\alpha\beta}$ between them, which is determined by the equilibrium positions $r_{\alpha i}$ and small displacements $x_{\alpha i}$:

$$R_{\alpha\beta} = \sqrt{\sum_i (r_{\alpha i} + x_{\alpha i} - r_{\beta i} - x_{\beta i})^2}. \tag{2}$$

If the total energy of the system in the equilibrium state is taken as zero, the interaction energy for small-amplitude (single-phonon) vibrations can be written in the quadratic form as

$$\Phi = \frac{1}{2}\sum_{\alpha\beta ij} \Phi^{ij}_{\alpha\beta} x_{\alpha i} x_{\beta j}, \quad \Phi^{ij}_{\alpha\beta} \equiv \frac{\partial^2 \Phi}{\partial x_{\alpha i}\partial x_{\beta j}}, \tag{3}$$

where $\Phi^{ij}_{\alpha\beta}$ are the force constants. Within the harmonic approximation, the dynamic equations of motion for the displacements of atoms and their solutions are written in the conventional form as

$$M_\alpha \frac{\partial^2 x_{\alpha i}}{\partial t^2} = -\sum_{\beta j} \Phi^{ij}_{\alpha\beta} x_{\beta j}, \quad x_{\alpha i} = \frac{B_{\alpha i}}{\sqrt{M_\alpha}} e^{-i\omega t}. \tag{4}$$

The frequencies ω and amplitudes B of vibrational excitations in Eq. (4) can be found as eigenvalues and eigenvectors of the corresponding dynamic matrix D:

$$\omega^2 B_{\alpha i} = \sum_{\beta j} D^{ij}_{\alpha\beta} B_{\beta j}, \quad D^{ij}_{\alpha\beta} = \frac{1}{\sqrt{M_\alpha M_\beta}} \Phi^{ij}_{\alpha\beta}. \tag{5}$$

Taking into account that $u_{\alpha\beta}$ depend on $R_{\alpha\beta}$, which, in turn, are functions of the displacements of atoms in Eqs. (1)–(3), the harmonic force constants can be written as

$$\begin{aligned} \Phi^{ij}_{\alpha\beta} = {} & (1 - \delta_{\alpha\beta})\left[\frac{d^2 u_{\alpha\beta}}{dR^2_{\alpha\beta}} \frac{\partial R_{\alpha\beta}}{\partial x_{\alpha i}} \frac{\partial R_{\alpha\beta}}{\partial x_{\beta j}} + \frac{du_{\alpha\beta}}{dR_{\alpha\beta}} \frac{\partial^2 R_{\alpha\beta}}{\partial x_{\alpha i}\partial x_{\beta j}}\right] \\ & + \delta_{\alpha\beta}\left\{\sum_{\gamma \neq \alpha}\left[\frac{d^2 u_{\alpha\gamma}}{dR^2_{\alpha\gamma}} \frac{\partial R_{\alpha\gamma}}{\partial x_{\alpha i}} \frac{\partial R_{\alpha\gamma}}{\partial x_{\alpha j}} + \frac{du_{\alpha\gamma}}{dR_{\alpha\gamma}} \frac{\partial^2 R_{\alpha\gamma}}{\partial x_{\alpha i}\partial x_{\alpha j}}\right]\right\}. \end{aligned} \tag{6}$$

The first and second derivatives of $R_{\alpha\beta}$ ($\alpha \neq \beta$) are

$$\begin{gathered} \frac{\partial R_{\alpha\beta}}{\partial x_{\alpha i}} = \frac{r_{\alpha i} - r_{\beta i}}{R_{\alpha\beta}}, \quad \frac{\partial^2 R_{\alpha\beta}}{\partial x_{\alpha i}\partial x_{\beta j}} = \frac{g^{ij}_{\alpha\beta} - \delta_{ij}}{R_{\alpha\beta}}, \\ g^{ij}_{\alpha\beta} \equiv \frac{(r_{\alpha i} - r_{\beta i})(r_{\alpha j} - r_{\beta j})}{R^2_{\alpha\beta}}. \end{gathered} \tag{7}$$

Upon substitution of Eqs. (6) and (7) into Eq. (4), the matrix D takes the form

$$\begin{aligned} D^{ij}_{\alpha\beta} = {} & \frac{1}{\sqrt{M_\alpha M_\beta}} \\ & \times\left\{(\delta_{\alpha\beta} - 1)\left[g^{ij}_{\alpha\beta}\left(\frac{d^2 u_{\alpha\beta}}{dR^2_{\alpha\beta}} - \frac{1}{R_{\alpha\beta}}\frac{du_{\alpha\beta}}{dR_{\alpha\beta}}\right) + \frac{\delta_{ij}}{R_{\alpha\beta}}\frac{du_{\alpha\beta}}{dR_{\alpha\beta}}\right]\right. \\ & \left. + \delta_{\alpha\beta}\left[\sum_{\gamma}\left[g^{ij}_{\alpha\gamma}\left(\frac{d^2 u_{\alpha\gamma}}{dR^2_{\alpha\gamma}} - \frac{1}{R_{\alpha\gamma}}\frac{du_{\alpha\gamma}}{dR_{\alpha\gamma}}\right) + \frac{\delta_{ij}}{R_{\alpha\gamma}}\frac{du_{\alpha\gamma}}{dR_{\alpha\gamma}}\right]\right]\right\}. \end{aligned} \tag{8}$$

When theoretically analyzing the experimental vibrational spectra of metals and metal–metalloid compounds, various pairwise potentials, such as the Morse and Lennard-Jones potentials, were used [1]. The agreement with the experimental data was good only when an effective cutoff was introduced to account for the interaction between the electron and phonon subsystems. In this paper, we describe the interatomic interaction $u_{\alpha\beta}$ using the Morse potential (which was tested in [1] for compounds of iron with phosphorus) with a cutoff function $f(y)$:

$$u_{\alpha\beta}(y) = u_0(y) f(y), \tag{9a}$$

$$u_0(y) = \varepsilon[\exp(-2\alpha(y-1)) - 2\exp(-\alpha(y-1))], \tag{9b}$$

$$f(y) = \begin{cases} 1, & y < 1 \\ 3z^4 - 8z^3 + 6z^2, & 1 < y < y_c \\ 0, & y_c < y, \end{cases} \tag{9c}$$

$$y = \frac{R_{\alpha\beta}}{R_0}, \quad y_c = \frac{R_c}{R_0}, \quad z = \frac{y - y_c}{1 - y_c},$$

where R_c is the cutoff radius, taken equal to $1.4R_0$. The cutoff function $f(y)$ does not affect the potential and its derivatives at $R = R_0$. As $R \longrightarrow R_c$, we have $f(y) \longrightarrow 0$. The parameters R_0 and ε of the interatomic interaction potential for the Fe–Fe, Fe–P, and P–P pairs are taken to be (2.6, 2.2, 3.8 Å) and (0.51, 0.85, 0.19 eV), respectively, and $\alpha = 3.76$ for all pairs [1]. For crystallites of finite size, the boundaries are assumed (as is usually done) to be free.

The vibrational spectra of Fe_3P crystallites of progressively increasing size are calculated numerically by solving the set of secular equations (5) on a Pentium PC using the MATHCAD software. We note that, in recent years, a set of secular equations for finite crystallites has often been solved directly in the coordinate space, because the Fourier transform method is inadequate for use in solving this problem. The results of calculations are presented in Fig. 2a. The solid curve is the density of states ρ for a crystallite in the form of a parallelepiped consisting of 16 ($2 \times 2 \times 4$) Fe_3P unit cells (512 atoms), which is the maximum crystallite size for which the computer can handle the corresponding set of equations. The dashed curve is the Fe_3P vibration spectrum determined from inelastic slow-neutron scattering experiments [2]. For comparison, the dot-and-dash curve shows the spectrum calculated numerically in [1] by using the tridiagonalization procedure. All three curves are normalized to the unit integrated density of states. It can be seen from Fig. 2a that in the calculated spectra, the low-frequency maxima associated with the Fe–Fe interaction are shifted to higher energies relative to the low-frequency peak of the experimental spectrum; however, the position of the maximum in the spectrum calculated by us is closer to that in the experimental spectrum. The significant shift of the peak in our spectrum toward lower energies relative to the corresponding peak in the spectrum calculated in [1] is due to the larger shift in the position of the centroid of this peak, whereas the shift of the maximum of the peak is relatively small. We also note that in both calculated spectra, there are shoulders near the energy $\varepsilon \sim 10$–15 meV. In the high-frequency range of the spectrum in Fig. 2a, where the Fe–P and P–P interactions dominate, there is a fine structure consisting of four additional resonance peaks. The positions of the first (~40 meV) and third (~50 meV) peaks coincide with those observed in the experimental spectrum [2]. We note that, in the calculated spectra, the ratio of the average intensity of the high-frequency peaks to the low-frequency peak intensity is ~0.5, whereas in the experimental spectrum, this ratio is significantly smaller, ~0.2. The calculations are performed for crystallites of progressively increasing size, starting with the simplest case of one unit cell and finishing with the largest crystallite (mentioned above) computable with the computer at our disposal. An analysis shows that the calculated spectrum reaches its asymptotic form as the crystallite size is increased in the last steps of the calculation. In the future, it will be necessary to adjust the parameters of the interatomic interaction potentials in order to bring the calculated and experimental spectra into better agreement and find the optimum values of these parameters.

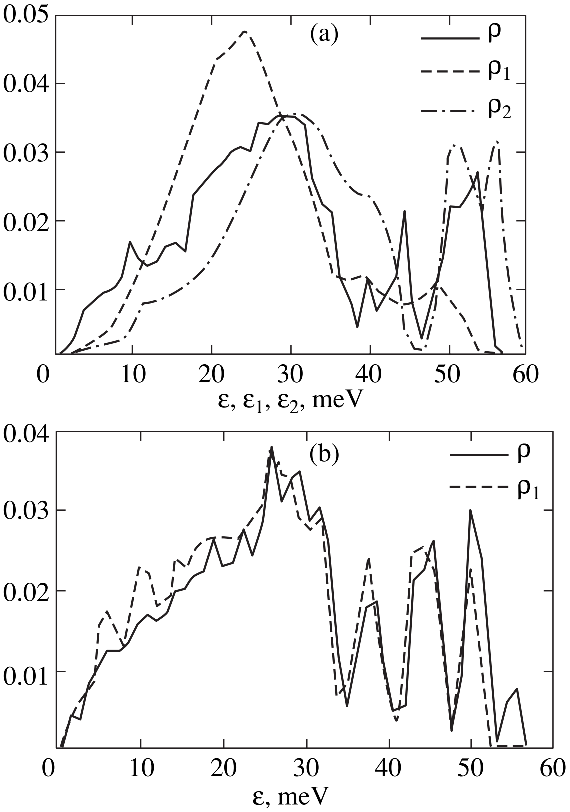

Fig. 2. Vibrational phonon spectra of (a) Fe_3P and (b) Fe_2P crystallites.

Figure 2b shows the calculated density of vibrational states of Fe_2P crystallites. The solid curve is the density of states of the largest crystallite, consisting of $3 \times 4 \times 5$ unit cells (540 atoms), and the dashed curve is the density of states of a smaller crystallite, consisting of 36 ($3 \times 3 \times 4$) unit cells (324 atoms). Through comparison with Fig. 2a for Fe_3P, it can be seen that the general structure of the spectrum is the same: there is a low-frequency broad resonance peak and a fine resonance structure in the high-frequency range. However, the low-frequency resonance peak in the Fe_2P spectrum is narrower and the high-frequency fine structure covers a wider energy range than in the spectrum in Fig. 2a. The maximum of the low-frequency peak is shifted toward lower frequencies by ~5 meV relative to that for Fe_3P (located at 30 meV), which is due to the smaller proportion of the heavier component in the former case. For the same reason, the lower frequency part of the high-frequency fine structure is more pronounced in Fe_2P in comparison with that in Fe_3P. The results obtained here can be useful in the preliminary stage of the experimental investigations of Fe_2P and Fe_3P with the help of the DIN neutron spectrometer.

3. BREATHER EXCITATIONS

Now, we consider large-amplitude nonlinear vibrations of Fe_2P crystallites. As in [8–11], the interaction energy of oscillating atoms of the crystallite system is assumed to consist of a harmonic and an anharmonic (fourth-order) component. As seen from Fig. 1b, the three nearest neighboring Fe atoms form a trimer, which can be considered as a closed crystalline chain of three atoms. We consider nonlinear vibrations of this trimer with allowance for the Fe–Fe interaction alone, because the spectrum of harmonic vibrations in the main-resonance region is determined by this interaction. (The effect of the Fe–P and P–P interactions will be allowed for in another paper.) Note that considerations of both closed crystalline systems and unbound crystalline systems subject to the Born–von Karman boundary conditions lead to absolutely identical results; we use the terminology of the former approach only for the sake of convenience. The trimer can be considered as the smallest element in the hierarchy of closed crystalline chains, and the exact solution found for the trimer in what follows can be used as a basis for the investigation of nonlinear vibrations of a system and of their possible localization [8, 11]. In the Fe–P compounds, the trimer or the tetrahedron (see below) is repeated as a motif in each unit cell of a crystal; therefore, the solutions obtained below can be used as basis intracell solutions, which will then be modified by the inclusion of intercell interactions. However, even at this initial stage, the exact solution is fairly intricate (see below). The Hamiltonian of this crystalline system with quartic anharmonicity in the scalar theory has the form

$$H = \sum_i \frac{P_i^2}{2M_{\mathrm{Fe}}} + \frac{K_2}{2}\sum_{ij}(X_i - X_j)^2 + \frac{K_4}{3}\sum_{ij}(X_i - X_j)^4, \tag{10}$$
$$i, j = 1, 2, 3; \quad K_2, K_4 > 0.$$

By introducing the normalized quantities

$$X_i \equiv \left(\frac{K_2}{K_4}\right)^{1/2} x_i, \quad t \equiv \left(\frac{M}{K_2}\right)^{1/2}\tau, \tag{11}$$

the dynamic equations can be simplified to

$$\frac{d^2 x_i}{d\tau^2} = -(2x_i - x_j - x_k) + (x_i - x_j)^3 - (x_i - x_k)^3, \tag{12}$$

where *i*, *j*, and *k* are equal to any cyclical permutation of subscripts 1, 2, and 3. If the center of gravity is fixed, we have $x_1 + x_2 + x_3 = 0$ and Eqs. (12) reduce to a set of two dynamic equations for $r_1 = x_1 - x_2$ and $r_2 = x_2 - x_3$:

$$\begin{aligned} \frac{d^2 r_1}{d\tau^2} &= -3r_1 - 3r_1(r_1^2 + r_1 r_2 + r_2^2), \\ \frac{d^2 r_2}{d\tau^2} &= -3r_2 - 3r_2(r_1^2 + r_1 r_2 + r_2^2). \end{aligned} \tag{13}$$

If the nonlinear terms are neglected, we have harmonic oscillations of frequency $\sqrt{3}$ in reduced units. Let us introduce polar coordinates for the variables $R_1 = (r_1 - r_2)/\sqrt{2}$ and $R_2 = \sqrt{3}(r_1 + r_2)/\sqrt{2}$: $R_1(\tau) = \rho(\tau)\cos\varphi(\tau)$ and $R_2(\tau) = \rho(\tau)\sin\varphi(\tau)$, where $\rho(\tau)$ and $\varphi(\tau)$ are the time-dependent modulus and polar angle (phase [15]), respectively. From Eqs. (13), it follows that $\rho(\tau)$ and $\varphi(\tau)$ obey two equations, which can be written in the form

$$\frac{d^2\rho}{d\tau^2} = \frac{C^2}{\rho^3} - 3\rho - \frac{3}{2}\rho^3, \quad \varphi(\tau) = C\int_{\tau_0}^{\tau}\frac{d\tau'}{\rho^2(\tau')}. \tag{14}$$

Here, *C* is a constant of integration involved in the expression for $\varphi(\tau)$ that is an integral function of $\rho(\tau')$ over the range $\tau_0 < \tau' < \tau$, where τ_0 can be chosen arbitrarily. It follows from Eq. (14) that $\rho(\tau)$ oscillates within the range $\rho_0 < \rho(\tau) < \rho_m$, whose limits determine the constant *C* in Eqs. (14) as

$$C = \frac{\sqrt{3}}{2}\rho_0\rho_m\sqrt{\rho_m^2 + \rho_0^2 + 4}. \tag{15}$$

From Eqs. (14), we obtain

$$\frac{d\rho}{d\tau} = \pm\frac{\sqrt{3}}{2\rho}\sqrt{(\rho^2 - \rho_0^2)(\rho_m^2 - \rho^2)(\rho_m^2 + \rho_0^2 + 4 + \rho^2)}. \tag{16}$$

It follows immediately from Eq. (16) that the inverse function $\tau(\rho)$, defined in the ρ range from ρ_0 (at $\tau = 0$) to ρ_m, has the form (which is the exact analytical solution found by us)

$$\tau(\rho) = \frac{2}{\sqrt{3}}\frac{1}{\sqrt{2\rho_m^2 + \rho_0^2 + 4}} \times F(\psi(\rho, \rho_0, \rho_m), k(\rho_0, \rho_m)), \tag{17a}$$

$$\psi(\rho, \rho_0, \rho_m) = \arcsin\left(\frac{1}{k}\sqrt{\frac{\rho^2 - \rho_0^2}{\rho^2 + \rho_m^2 + \rho_0^2 + 4}}\right), \tag{17b}$$

$$k(\rho_0, \rho_m) = \sqrt{\frac{\rho_m^2 - \rho_0^2}{2\rho_m^2 + \rho_0^2 + 4}}, \tag{17c}$$

where $F(\psi, k)$ is an elliptic integral of the first kind, with ψ being the argument and with parameter *k* defined by Eq. (17c). From Eqs. (14), it can be found

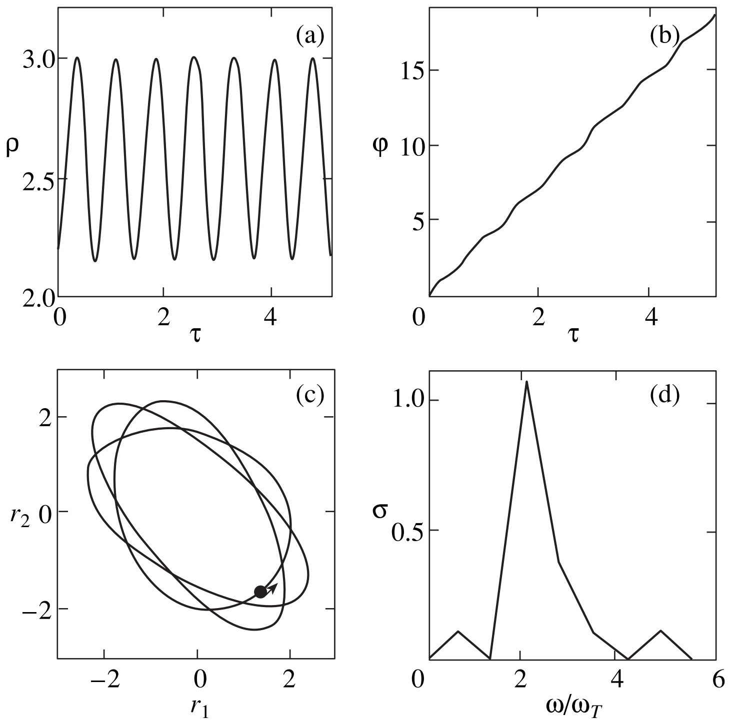

Fig. 3. Nonlinear periodic breather mode of vibration of Fe_2P crystallites. (a, b) Time dependences of modulus ρ and phase φ, respectively; (c) a trajectory of the dynamic system; and (d) vibration spectral density σ.

that the phase $\varphi(\rho)$ is given by the expression (which is also an exact analytical result obtained by us)

$$\varphi(\rho) = \frac{1}{\sqrt{2\rho_m^2 + \rho_0^2 + 4}}$$

$$\times\left[\frac{\rho_m^2 + 2\rho_0^2 + 4}{\rho_0^2(\rho_m^2 + \rho_0^2 + 4)}\Pi(\psi, n, k) - \frac{1}{\rho_m^2 + \rho_0^2 + 4}F(\psi, k)\right],$$

$$n = \frac{k^2}{\rho_0^2}(\rho_m^2 + \rho_0^2 + 4), \qquad (18)$$

where $\Pi(\psi, n, k)$ is a known tabulated special function, namely, an elliptic integral of the third kind with argument ψ, parameter k, and additional parameter n. In Eq. (18), the phase is defined such that $\varphi = 0$ for $\tau = 0$ and $\rho = \rho_0$.

An analysis of Eqs. (17) and (18) revealed that these equations describe nonlinear breather-type (NPB) vibrations with temporal oscillations in the modulus and (what is important) in the phase, which is an integral function of ρ. Such a time dependence of the phase, $\varphi(t) = \Omega t + \beta\sin\omega t$ with a small parameter β, was found for breather-type FRIM solitons in [15]. In this dependence, the first term is characteristic of harmonic oscillations, while the second term is due to anharmonicity and leads to a frequency spectrum when the quantity $\exp[i\varphi(t)]$ is expanded into a Fourier series.

The exact analytical dependences given by Eqs. (17) and (18) describe the dynamics of nonlinear vibrations over the range $0 < \tau < T_0/2$, where T_0 is the period of ρ oscillation from ρ_0 to ρ_m and vice versa:

$$T_0 = \frac{4}{\sqrt{3}}\frac{1}{\sqrt{2\rho_m^2 + \rho_0^2 + 4}}F\left(\frac{\pi}{2}, k\right). \qquad (19)$$

In the first half-period $T_0/2$, the change in phase $\varphi(\rho)$ is equal not to $\pi/2$ but rather to $\varphi(\rho_m) < \pi/2$. For consecutive half-periods, we must continue the functions. For instance, over the half-period $T_0/2 < \tau < T_0$, the continuations $\tau = \tau_1(\rho)$ and $\varphi = \varphi_1(\rho)$ are $\tau_1(\rho) = T_0 - \tau(\rho)$ and $\varphi_1(\rho) = 2\varphi(\rho_m) - \varphi(\rho)$, where $\tau(\rho)$ and $\varphi(\rho)$ are given by Eqs. (17) and (18). As a result, in the length of time $2T_0$, the change in phase is $\varphi(\tau = 2T_0) < 2\pi$ and the trajectory of the system in the (r_1, r_2) plane does not close. As the time increases further, for general values of ρ_0 and ρ_m, the trajectory intersects itself (with a different slope) rather than being tangent to itself; that is, NPB vibrations, characterized by a closed trajectory with smoothly varying slope, do not occur. Such vibrations arise only if the change in phase in a half-period $T_0/2$ is a rational multiple of $\pi/2$, i.e., when $\varphi(\rho_m) = 2\pi p/q$, where p and q are integers. In this case, the trajectory will close smoothly with the same slope after $2p$ modulus oscillation periods when the change in phase is equal to $q\varphi(\rho_m)$. In a sense, this condition for nonlinear vibrations can be interpreted as quantization of the trajectories, by analogy with the quantization of orbits in quantum mechanics. The integers p and q are by no means arbitrary because of the restriction $\rho_m > \rho_0$, and it would be of interest to establish their systematics.

Using the analytical expressions presented above, we calculated the corresponding curves on a Pentium PC. For this purpose, we chose a fixed sequence of values ρ_i lying in the range between ρ_0 and ρ_m and calculated the corresponding sequences of τ_i and φ_i from Eqs. (17) and (18) and from their continuations. Then, we found the inverse functions $\rho_i = \rho_i(\tau_i)$ and $\varphi_i = \varphi_i(\tau_i)$. The $\rho(\tau)$ and $\varphi(\tau)$ dependences for $\rho_m = 3$ and $\rho_0 = 2.153$ are shown in Figs. 3a and 3b for $p = 3$ and $q = 14$. The corresponding trajectory in the (r_1, r_2) plane is shown in Fig. 3c. The initial point of the arrow corresponds to the moment $\tau = 0$ and, simultaneously, is the point at which the trajectory becomes closed without a discontinuous change in slope. Figure 3d shows the frequency spectrum of NPB vibrations in units of $\omega_T = 2\pi/T$, where T is the total rotation period along the closed trajectory shown in Fig. 3c. It can be seen from Fig. 3d that, in addition to the fundamental frequency ω_T, there is a second harmonic ($2\omega_T$) of high intensity and also higher harmonics showing a progressive general decrease in intensity with a peak at $\sim 5\omega_T$ (there are also still higher harmonics not presented in Fig. 3d).

Next, we investigate nonlinear breather excitations in the Fe_3P crystal. Since this crystal belongs to the symmetry group $S_4^2(I\bar{4})$, we consider a three-dimensional elementary crystallite of this type in the form of a regular tetrahedron with four atoms at its vertices, constituting a quasimolecule (Fig. 1a). Note that the tetrahedron, as well as the Fe_3P crystal, possesses a fourfold rotation–inversion axis (Fig. 1a).

We assume that, in addition to expression (10) with the corresponding generalization of scalar displacements X_i ($i = 1, 2, 3, 4$) to the three-dimensional case, the Hamiltonian contains the interaction

$$H_4^{(a)} = \frac{K_4}{4} \times [(X_1 - X_3)^4 + (X_2 - X_4)^4 + 6(X_1 - X_3)^2(X_2 - X_4)^2]. \quad (20)$$

This interaction meets all symmetry requirements for the Hamiltonian and is quite realistic in the presence of the corresponding anisotropy. Physically, the inclusion of this interaction can be justified by the fact that, for large-amplitude nonlinear vibrations, as the atoms lying on opposite mutually perpendicular edges approach each other, the repulsion energies of all four atoms increase, whereas in the case where the atoms lying on two edges with a common point approach each other, the repulsion of only three atoms increases. The choice of the coefficients in expression (20) for H_4 is dictated by the fact that only with such coefficients is the analytical treatment of the problem significantly simplified and can at least the azimuth angle be calculated analytically (see below). The theory developed above, after the corresponding generalization, allows one to reduce the set of four dynamic equations for x_i ($i = 1, 2, 3, 4$) to a set of two equations for functions $\rho(\tau)$ and $\theta(\tau)$ which determine the displacements $(x_1 - x_3)/\sqrt{2} = \rho\sin\theta\cos\varphi$, $(x_2 - x_4)/\sqrt{2} = \rho\sin\theta\sin\varphi$, and $\sqrt{3}(x_1 + x_3)/\sqrt{2} = \rho\cos\theta$ in spherical coordinates, with $\varphi(\tau)$ being an integral function of ρ and θ. These two equations and the $\varphi = \varphi(\rho, \theta)$ dependence have the form

$$\frac{d^2\rho}{d\tau^2} - \rho\left(\frac{d\theta}{d\tau}\right)^2 = \frac{C^2}{\rho^3\sin^2\theta} - 3\rho^3\sin^2\theta - 2\rho(2 + 3\rho^2), \quad (21a)$$

$$\frac{d^2\theta}{d\tau^2} + \frac{2}{\rho}\frac{d\rho}{d\tau}\frac{d\theta}{d\tau} = \frac{C^2\cos^2\theta}{\rho^4\sin^3\theta} - 3\rho^2\sin\theta\cos\theta, \quad (21b)$$

$$\varphi(\tau) = C\int_0^{\tau}\frac{d\tau'}{\rho^2(\tau')\sin^2[\theta(\tau')]}, \quad (21c)$$

where, as before, $C > 0$ is a constant which determines the initial azimuthal velocity of an effective particle at the starting point with spherical coordinates (ρ_0, $\pi/2$, 0). It seems very difficult to solve the set of equations (21a) and (21b) analytically. Therefore, in order to investigate the problem of existence of breathers in more complicated systems than the trimer considered above, we solved the set of equations (21a) and (21b) numerically. However, it should be remembered that breather modes of vibrations occur only at certain values of the modulus and phase related to each other. In the case considered above, we determined these values analytically. Now, the analytical relation between these quantities is unknown and it is difficult to guess the exact initial values ρ_0, θ_0, and φ_0 at which breather vibrations can be simulated numerically. We determined these values by scanning the total energy of vibrations E (which is conserved) as a known function of the initial modulus ρ_0 and initial angle θ_0 at a fixed value of the constant C and $\varphi_0 = (d\rho/d\tau)_0 = (d\theta/d\tau)_0 = 0$. This dependence of the total energy (in dimensionless units) has the form

$$E = 2\rho^2\sin^2\theta_0 + 3\rho^2\cos^2\theta_0 + \frac{9}{4}\rho_0^4 + \frac{C^2}{2\rho_0^2\sin^2\theta_0}. \quad (22)$$

Equation (22) for fixed values of E, C, and ρ is quadratic in $\cos\theta_0$. By varying ρ_0, one can determine (through numerical calculations) the value of θ_0 at which the multiturn trajectory returns to the starting point with the same slope. Only in this case do periodic nonlinear breather modes of vibration arise. For other initial values, the trajectory intersects itself only at nonzero angles and nonlinear vibrations are nonperiodic and chaotic in nature.

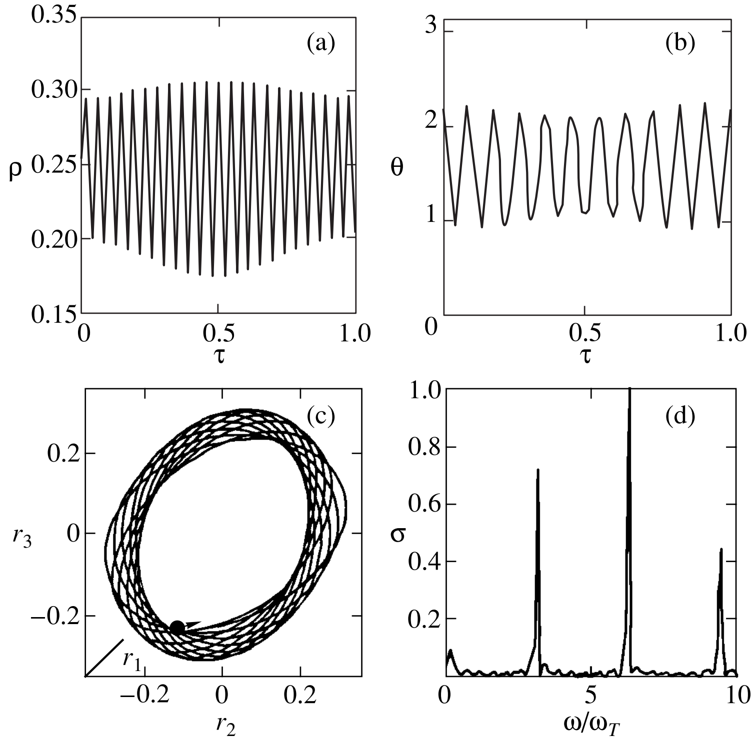

Fig. 4. Nonlinear periodic breather mode of vibration of Fe_3P crystallites. (a, b) Time dependences of modulus ρ and polar angle θ, respectively; (c) a trajectory of the dynamic system; and (d) vibration spectral density σ.

Figures 4a and 4b show the $\rho(t)$ and $\theta(t)$ dependences calculated for the Fe_3P crystallite using the parameters $E = 0.3$, $C = 0.1$, $\rho_0 = 0.2$, and $\theta_0 = 2.234$ found by scanning Eq. (22). The modulus $\rho(\tau)$ and the polar angle $\theta(\tau)$ are seen to exhibit periodic oscillations characteristic of a breather, the period being equal to $T = 32.96$. As in Fig. 3b, the time dependence of the azimuth angle is of the type $\varphi(t) \sim c(t + \alpha\sin\omega t)$, which is characteristic of a breather; the frequency spectrum of $\sin[c(t + \alpha\sin\omega t)]$ contains all frequencies $n \times 2\pi/T$ ($n = 1, 2, 3, \ldots$) with the characteristic frequency dependence of the Fourier amplitudes. Figure 4c shows the axonometric projection of the trajectory in the (r_1, r_2, r_3) space corresponding to the calculated $\rho(t)$, $\theta(t)$, and $\varphi(t)$ dependences. The dot marks the starting (and finishing) point of the trajectory, and the arrow indicates the direction along which the trajectory was calculated numerically. Figure 4d shows the Fourier spectrum of NPB vibration frequencies ω in units of ω_T. It can be seen that, in addition to the fundamental frequency ω_T, there are intense harmonics at $\sim 3\omega_T$ and $\sim 6\omega_T$ and a less intense harmonic at $\sim 9\omega_T$; there are also still higher harmonics of progressively decreasing intensity, which are not shown in Fig. 4d. In further investigations, the theoretical spectra (such as those shown in Figs. 3d, 4d) can be used to interpret the fine structure of the experimental spectra in the higher harmonic frequency range [20, 21]. It is also of interest to investigate the spectra for trajectories of different types in the case of $K_4 < 0$ and in the case of the total energy E being close to the threshold for disintegration of crystals caused by large-amplitude nonlinear vibrations [22, 23].

ACKNOWLEDGMENTS

The authors are grateful to V.M. Agranovich, Yu.V. Konobeev, and A.M. Minashin for discussions and encouragement.

This study was supported by the Russian State Research and Development Program "Topical Problems in the Physics of Condensed Matter" (subprogram "Neutron-Scattering Studies of Materials"), the Russian Foundation for Basic Research (project no. 01-02-96018), and the Kaluga oblast authority.

REFERENCES

1. Y. Ishii and T. Fujiwara, J. Phys. F: Met. Phys. **10**, 2125 (1980).
2. N. Lustig, J. S. Lannin, J. M. Carpenter, and R. Hasegawa, Phys. Rev. B **32** (5), 2778 (1985).
3. M. S. Daw, Phys. Rev. B **39** (11), 7441 (1989).
4. A. M. Guellil and J. B. Adams, J. Mater. Res. **7** (3), 639 (1992).
5. S. Chantasiriwan and F. Milstein, Phys. Rev. B **53** (21), 14080 (1996).
6. A. M. Kosevich and A. S. Kovalev, Zh. Éksp. Teor. Fiz. **67** (5), 1717 (1974) [Sov. Phys. JETP **40**, 855 (1975)].

7. A. J. Sievers and S. Takeno, Phys. Rev. Lett. **61** (8), 970 (1988).
8. V. M. Burlakov and S. A. Kiselev, Zh. Éksp. Teor. Fiz. **99** (5), 1526 (1991) [Sov. Phys. JETP **72**, 854 (1991)].
9. A. S. Kovalev, O. V. Usatenko, and O. A. Chubykalo, Fiz. Tverd. Tela (St. Petersburg) **35** (3), 693 (1993) [Phys. Solid State **35**, 356 (1993)].
10. S. Takeno, K. Kisoda, and A. J. Sievers, Prog. Theor. Phys. Suppl. **94**, 242 (1988).
11. V. M. Burlakov, S. A. Kiselev, and V. N. Pyrkov, Phys. Rev. B **42** (8), 4921 (1990).
12. V. M. Agranovich, O. A. Dubovsky, and A. V. Orlov, Phys. Lett. A **119** (2), 283 (1986).
13. O. A. Dubovskiĭ and A. V. Orlov, Fiz. Tverd. Tela (St. Petersburg) **36** (10), 3131 (1994) [Phys. Solid State **36**, 1663 (1994)].
14. V. M. Agranovich and O. A. Dubovsky, *Optical Properties of Mixed Crystals* (North-Holland, Amsterdam, 1988), p. 97.
15. O. A. Dubovskiĭ, Fiz. Tverd. Tela (St. Petersburg) **42** (4), 665 (2000) [Phys. Solid State **42**, 683 (2000)].
16. O. A. Dubovskiĭ and A. V. Orlov, Fiz. Tverd. Tela (St. Petersburg) **38** (4), 1221 (1996) [Phys. Solid State **38**, 675 (1996)].
17. V. M. Agranovich, S. A. Darmanyan, K. I. Grigorishin, *et al.*, Phys. Rev. B **57** (26), 2461 (1998).
18. B. G. Hyde and S. Andersen, *Inorganic Crystal Structure* (Wiley, New York, 1989).
19. R. W. G. Wyckoff, *Crystal Structures* (Wiley, New York, 1964), Vol. 2, p. 103.
20. S. Ikeda and N. Watanabe, KEK Preprint No. 66 (1986).
21. A. I. Kolesnikov, M. Prager, J. Tomkinson, *et al.*, J. Phys.: Condens. Matter **3** (6), 5297 (1991).
22. O. A. Dubovskiĭ, A. V. Orlov, and V. A. Semenov, Preprint No. 2870, FÉI (Institute of Physics and Power Engineering, Obninsk, 2001).
23. O. A. Dubovskiĭ, A. V. Orlov, and V. A. Semenov, Preprint No. 2909, FÉI (Institute of Physics and Power Engineering, Obninsk, 2001).

Translated by Yu. Epifanov

Physics of the Solid State, Vol. 45, No. 2, 2003, pp. 335–338. Translated from Fizika Tverdogo Tela, Vol. 45, No. 2, 2003, pp. 317–320.
Original Russian Text Copyright © 2003 by Slezov.

LATTICE DYNAMICS AND PHASE TRANSITIONS

Phase Transitions in Condensed Media at a Finite Rate of Formation of a Metastable State

V. V. Slezov

Kharkov Institute of Physics and Technology, National Scientific Center,
ul. Akademicheskaya 1, Kharkov, 61108 Ukraine

e-mail: abyzov@univer.kharkov.ua

Received March 13, 2002

Abstract—The influence of the finite rate of formation of a metastable state on the kinetics of the first-order phase transition is analyzed. The conditions determined by the thermodynamic parameters and the cooling rate of the system under consideration are derived. Under these conditions, the formation of the metastable state can be treated either as an instantaneous process, when nucleation occurs at the end of the cooling stage, or as a slow process, when intensive nucleation of a new phase proceeds within the cooling stage. An equation describing the time and temperature that correspond to intensive nucleation of new-phase particles is obtained. The nucleation stage of the new phase takes place in the immediate vicinity of the temperature determined from this equation. All the other parameters, which determine the kinetics of the initial and transient stages of the phase transition, are calculated with respect to this temperature. As an example, all the relationships for a weak solid solution are presented. © *2003 MAIK "Nauka/Interperiodica".*

1. INTRODUCTION

The formation of a metastable state is assumed to be instantaneous in virtually all the works dealing with the initial stage of nucleation of new-phase particles [1–15]. In the present paper, we consider the actual conditions of formation of a metastable state of the studied system during cooling. It is demonstrated that, depending on the thermodynamic parameters and the cooling rate of the system, the nucleation of a new phase and its evolution with time can be determined by the metastability either at the end of the cooling stage or within this stage. The former case can be considered instantaneous formation of metastability at the end of the cooling stage. The latter can be treated as a case of slow cooling.

As an example, let us consider the transition of a sufficiently weak solid solution from an equilibrium state to a metastable state with a decrease in the initial temperature T_0 to a final value T_f for the time t_f. Under these conditions, intensive nucleation of new-phase particles can occur either after the completion of cooling or at an instant of time $t^* < t_f$ within the cooling stage, at which point the conditions are most favorable (the smallest barrier) for the transition of the system to a disperse state. The occurrence of either of these two cases is determined by the parameters of the system and the rate of formation of the metastable state. In the former case ($t_f < t^*$), a decrease in the temperature leads to the formation of the metastable state at a final temperature, after which the metastable phase undergoes decomposition. This process corresponds to an instantaneous formation of the metastable phase. When the decrease in the temperature is sufficiently slow, it is necessary to determine the instant t^* of the onset of intensive nucleation of new-phase particles and the corresponding degree of metastability. Under these conditions, all the characteristics of the stage of nucleation of new-phase particles should be determined by parameters other than those describing the instantaneous transition to the metastable state.

Earlier [13], we showed that all the formulas derived for instantaneous formation of a metastable state are applicable provided the characteristic times obey the following hierarchy (which holds almost without exception):

$$t_{\mathrm{rel}} = \frac{5}{3}\frac{a^2}{D\alpha c_0}\frac{n_c^{2/3}}{\beta} \ll t_N = \sqrt{2}\frac{a^2}{D\alpha}c_0^{1/4}I_0^{-1/4}. \qquad (1)$$

Here, t_N is the time interval of intensive nucleation of new-phase particles; t_{rel} is the time interval of attaining a quasi-stationary state in the size range $1 \le n \le n_c$; n is the number of impurity atoms in a new-phase particle; n_c is the number of impurity atoms in a particle of critical size, i.e., in a new-phase particle in equilibrium with the solid solution at a given instant of time; a is the distance between the lattice sites of the matrix; D is the impurity diffusion coefficient in the lattice; α is the parameter accounting for the difference between the last jump of the impurity atom from the matrix onto a new-phase particle and the jump in the bulk of the

1063-7834/03/4502-0335$24.00 © 2003 MAIK "Nauka/Interperiodica"

matrix ($0 \le \alpha \le 1$); c_0 is the initial concentration of impurities in the matrix; $\beta = \frac{8\pi\sigma a^3}{3}\frac{}{T_f}$; σ is the interfacial tension; $n_c = \beta^3\left(\ln\frac{c_0}{c_\infty}\right)^{-3}$; c_∞ is the equilibrium concentration of impurities at a finite temperature [13]; $c_0 = e^{-Q/T_0}$ is the initial concentration of impurities in the solid solution; and T_0 is the temperature at which the solid solution with a given initial concentration becomes saturated with a decrease in the temperature. The temperature T_0 corresponds to the formation of a metastable (supersaturated) state of the solid solution, $c_\infty = e^{-Q/T_f}$ is the equilibrium concentration of impurities in the solid solution after cooling to a temperature T_f, I_0 is the flux of new-phase particles in the size space through the critical point in a unit of nondimensional time $\tau = \frac{Dt}{a^2}$ per lattice site of the matrix (formula (19) in [13]), and

$$I_0 = \sqrt{\frac{3}{2\pi}}\sqrt{\beta}\alpha c_0^2 \exp\left[-\frac{\beta^3}{2}\frac{1}{\left(\ln\frac{c_0}{c_\infty}\right)^2}\right], \qquad (2)$$

where $\frac{\beta^3}{2}\left(\ln\frac{c_0}{c_\infty}\right)^{-2} = \Delta\Phi(n_c)$ is the change in the thermodynamic potential of a weak solution due to the formation of a new-phase particle of critical size. The condition of instantaneous formation of the metastable state can be written in the form

$$t_{\mathrm{rel}} \ll t_N \ll t_f. \qquad (3)$$

2. SLOW COOLING

Let us consider the case of sufficiently slow cooling when the following condition is satisfied:

$$t_{\mathrm{rel}} \ll t_N \ll t^* \ll t_f, \qquad (4)$$

where t^* is the instant of the onset of intensive nucleation of new-phase particles. The flux of new-phase particles per lattice site in a unit time can be represented by the relationship [13]

$$I = \frac{D}{a^2}I_0 \sim \exp\left(-\frac{Q_D}{T}\right)\exp\left(-\frac{\beta^3(T)}{2}\frac{1}{\left(\ln\frac{c(t)}{c_\infty(T)}\right)^2}\right). \qquad (5)$$

For instantaneous supersaturation under condition (4), the initial concentration of impurities in the solid solution in relationship (2) needs to be replaced by the current concentration. This is caused by the fact that, under the given conditions, the flux of new-phase particles in the size space adjusts itself not only to the current temperature but also to the impurity concentration, which also varies with time due to the transfer of part of the impurity atoms to new-phase particles. Therefore, two processes, namely, the change in the impurity concentration with time $c(t)$ and the change in the equilibrium concentration with temperature $c_\infty = c_\infty(T(t))$, should be taken into account simultaneously. Their variation with time leads to the appearance of a time interval $t^* \gg t_N$ in which the nucleation rate of the new phase is maximum.

As follows from expression (5), the onset of intensive nucleation of the new phase is determined to an exponential accuracy by the smallest exponent in expression (5), which, in turn, is determined by the relationship

$$\frac{d}{dt}\left[\frac{Q_D}{T(t)} + \frac{\beta^3(T(t))}{2}\left(\ln\frac{c(t)}{c_\infty(T(t))}\right)^{-2}\right]\Bigg|_{t = t^*} = 0. \qquad (6)$$

Next, we perform the differentiation and obtain the following equation for t^* and, correspondingly, for $T^* = T(t^*)$:

$$\frac{d\varphi}{dt}\bigg|_{t = t^*} = \left[n_c^{*-1}\frac{Q_D}{(T^*)^2} + \frac{3}{2}\left(\ln\frac{c^*}{c_\infty^*}\right)\frac{1}{T^*} - \frac{Q}{(T^*)^2}\right]\frac{dT}{dt}\bigg|_{t = t^*}. \qquad (7)$$

After the differentiation, we set $c^*(t^*) = c_0 = \exp\left(-\frac{Q}{T_0}\right)$ in Eq. (6), which, as was shown in [13], can be done by virtue of the very strong exponential dependence of the nucleation rate on the supersaturation and, hence, the small change in the concentration during intensive nucleation. In relationship (7), we used the following designations: $n_c^* = \beta^3(T^*)\left(\ln\frac{c^*}{c_\infty(T^*)}\right)^{-3}$, $c_\infty(T^*) = \exp\left(-\frac{Q}{T^*}\right)$, $c^* \cong c_0 = \exp\left(-\frac{Q}{T_0}\right)$, and $\frac{d\varphi}{dt}\Big|_{t = t^*} = -\frac{1}{c^*}\frac{dc}{dt}\Big|_{t = t^*}$. According to [13], we have

$$\frac{d\varphi}{dt}\bigg|_{t = t^*} = \frac{8n_c^*}{c^*}I = \sqrt{\frac{3\beta^*}{2\pi}}\alpha c_0 8 n_c^*\frac{D(T^*)}{a^2} \times \exp\left[-\frac{\beta^{*3}}{2}\left(\ln\frac{c_0}{c_\infty^*}\right)^{-2}\right]. \qquad (8)$$

Substituting expression (8) into relationship (7), we obtain the following equation for $x = \frac{T^*}{T_0}$:

$$\sqrt{\frac{3\beta}{2\pi}}\alpha c_0 8\beta_0^3\left(\frac{T_0}{Q}\right)^3\frac{1}{(1-x)^2}\frac{1}{\sqrt{x}}\frac{D_0}{a^2}$$

$$\times\exp\left[-\frac{Q_D}{T_0}\frac{1}{x}\right]\exp\left[-\frac{\beta_0^3}{2}\left(\frac{T_0}{Q}\right)^2\frac{1}{x(1-x)}\right] \qquad (9)$$

$$= \frac{Q}{T_0}\frac{1}{x^2}\left(x-\frac{1}{3}-\frac{2}{3}\frac{Q_D}{Q}\frac{1}{n_c^*}\right)\left(-\frac{1}{T_0}\frac{dT}{dt}\right)\Bigg|_{t = t^*}.$$

Here, $\beta_0 = \frac{8\pi\sigma a^2}{3}\frac{}{T_0}$ and $D = D_0\exp\left(-\frac{Q}{T^*}\right) = D_0\exp\left(-\frac{Q}{T_0}\frac{1}{x}\right)$. As a rule, we have $\frac{Q_D}{Q} < 1$ and $n_c^* \gg 1$. Hence, expression (9) can be represented in the form

$$\frac{x^{3/2}}{(1-x)^3(x-1/3)}$$

$$\times\exp\left[-\frac{\beta_0^3}{2}\left(\frac{T_0}{Q}\right)\frac{1}{x(1-x)^2}-\frac{Q_D}{T_0}\left(\frac{1}{x}-1\right)\right] = \frac{\tilde{t}}{t_d}, \qquad (10)$$

where $\tilde{t} = \frac{3}{16}\frac{a^2}{D(T_0)}\frac{1}{\alpha c_0}\sqrt{\frac{2\pi}{3}}\beta_0^{-7/2}\left(\frac{Q}{T_0}\right)^4$ and $t_d = -\left(\frac{1}{T}\frac{dT}{dt}\right)^{-1}$ is the characteristic time of temperature decrease. Now, we will seek the solution to Eq. (10). It is evident that the roots of this equation at any value of its right-hand side lie in the range

$$1/3 < x < 1. \qquad (11)$$

Considering conditions (3) and (4), the cooling is instantaneous in the case when the following condition is satisfied:

$$x_f > x > 1/3. \qquad (12)$$

Condition (12) means that the smallest exponent in expression (5), which is determined by the temperature $T^* = T_0x$ from relationship (10), is not reached, whereas intensive nucleation occurs at the end of the cooling stage at a temperature $T_f = T_0x_f$ when the exponent in expression (5) is minimum in the range $T_f \le T \le T_0$. Consequently, the initial metastability is determined by the final temperature T_f; i.e., it coincides with the maximum possible metastability under the given conditions.

Slow cooling implies that intensive nucleation occurs within the cooling stage. This corresponds to the condition

$$1/3 \le x_f \le x. \qquad (13)$$

Therefore, from the comparison of the root x of Eq. (10) with conditions (12) and (13), we can determine the instant of time at which the nucleation of new-phase particles occurs, particularly, either at the end of the cooling stage or within this stage. In the latter case, the parameters of the nucleation and transient stages should be radically different. These parameters are determined by x rather than by x_f. It should be noted that the degree of metastability arising at the end of the cooling stage is identical in both cases. Therefore, the precipitation of new-phase particles in equal excess amounts becomes possible for sufficiently long times. Consequently, the kinetics of the nucleation and transient stages will be governed by the cooling rate and can differ significantly from the kinetics of instantaneous cooling. The later stage (Ostwald ripening) will also be identical. However, as was shown earlier in [18], the onset of this stage depends on the prehistory of the process and, correspondingly, can change with time. In [18], it was demonstrated that, at the later stage, the system forgets its prehistory and the kinetics of transition to this stage.

In general, the particular values of the roots of Eq. (10) can be obtained in the limiting cases. The maximum value with respect to x on the right-hand side is determined by the factor $\left(x-\frac{1}{3}\right)^{-1}$. The second factor

$$\frac{x^{3/2}}{(1-x)^3}\exp\left[-\frac{\beta_0^3}{2}\left(\frac{T_0}{Q}\right)^2\frac{1}{x(1-x)^2}-\frac{Q_D}{T_0}\left(\frac{1}{x}-1\right)\right] = \alpha \text{ is}$$

maximum and, to sufficient accuracy, is considerably less than unity at the point $x = 1/3$:

$$\alpha = \frac{3\sqrt{3}}{8}\exp\left[-\frac{27}{8}\beta_0^3\left(\frac{T_0}{Q}\right)^2-2\frac{Q_D}{T_0}\right] \ll 1. \qquad (14)$$

Hence, it follows that the root of Eq. (10) is close to 1/3 at $\frac{\tilde{t}}{t_d} \gg \alpha$. In this case, Eq. (10) takes the form

$$\frac{\alpha}{x-1/3} = \frac{t}{t_D}; \quad x = 1/3+\alpha\left(\frac{\tilde{t}}{t_D}\right)^{-1}. \qquad (15)$$

In the other limiting case $\left(\frac{\tilde{t}}{t_d} \ll \alpha\right)$, we first take the logarithm of Eq. (10) and then retain the principal terms. As a result, we obtain

$$(1-x)^2 = \frac{\beta_0^3}{2}\left(\frac{T_0}{Q}\right)^2\left(\ln\frac{t_d}{\tilde{t}}\right)^{-1};$$

$$x = 1-\left[\frac{\beta_0^3}{2}\left(\frac{T_0}{Q}\right)^2\left(\ln\frac{t_d}{\tilde{t}}\right)^{-1}\right]^{1/2}. \qquad (16)$$

The solution of the approximate equation gives a root in the tolerance range when

$$\frac{\tilde{t}}{t_d} < \exp\left[-\frac{9}{8}\frac{\beta_0^3}{2}\left(\frac{T_0}{Q}\right)^2\right] \approx \alpha. \qquad (17)$$

Therefore, knowing the parameters of the system (β_0, T_0, Q, Q_D, $\tilde{t}$) and the cooling rate, from relationship (10), we can determine parameters characterizing the nucleation stage of new-phase particles, such as $\beta(x)$ and $n_c(x)$ $\left(x = \frac{T^*}{T_0} < x_f = \frac{T_f}{T_0}\right)$, and, correspondingly, the transient stage. After the determination of the above parameters, all the characteristics of the kinetics of the nucleation and transient stages can be obtained by substituting these parameters into the formulas derived for instantaneous cooling in [13, 15]. As a consequence, we found that the slower the cooling $\left(\frac{\tilde{t}}{t_d} \longrightarrow 0\right)$, the smaller the number of nucleated particles of the new phase and the slower the decomposition of the metastable phase. Thus, the cooling rate can substantially affect the kinetics of the first-order phase transformation when the later stage of the decomposition (Ostwald ripening) is not reached [16, 17].

In conclusion, we should note that the above approach can also be applied to more complex systems in the case when the interaction of impurities in solid solutions is taken into account or multicomponent systems are examined [19, 20]. Some of these cases will be considered in a separate paper.

ACKNOWLEDGMENTS

The author would like to thank L.A. Maksimov for his participation in discussions of the results and helpful remarks.

REFERENCES

1. Yu. V. Mikhaĭlova and L. A. Maksimov, Zh. Éksp. Teor. Fiz. **59**, 1368 (1970) [Sov. Phys. JETP **32**, 747 (1971)].
2. M. Volmer, *Kinetik der Phasenbildung* (Th. Steinkorf, Dresden, 1933; Nauka, Moscow, 1986).
3. R. Becker and W. Döring, Ann. Phys. (Leipzig) **24**, 719 (1935).
4. K. Binder and D. Strauffer, Adv. Phys. **25**, 343 (1976).
5. H. Trinkaus and H. Yoo, Philos. Mag. A **55**, 269 (1987).
6. H. Wiedersich and J. Katz, Adv. Colloid Interface Sci. **10**, 33 (1979).
7. F. M. Kuni and A. P. Grinin, Kolloidn. Zh. **46** (3), 460 (1984).
8. F. M. Kuni and A. P. Grinin, Teor. Mat. Fiz. **80** (3), 4181 (1979).
9. J. Katz and M. Donohul, Adv. Chem. Phys. **40**, 137 (1979).
10. V. V. Slezov, *Theory of Diffusive Decomposition of Solids Solution* (Moscow, 1995); Sov. Sci. Rev., Sect. A **17** (1995).
11. V. V. Slezov and J. P. Schmelzer, Fiz. Tverd. Tela (St. Petersburg) **36** (2), 353 (1994) [Phys. Solid State **36**, 193 (1994)].
12. V. V. Slezov and J. P. Schmelzer, J. Phys. Chem. Solids **55**, 243 (1994).
13. V. V. Slezov and J. P. Schmelzer, Fiz. Tverd. Tela (St. Petersburg) **39** (12), 2210 (1997) [Phys. Solid State **39**, 1971 (1997)].
14. V. V. Slezov, Metallofiz. Noveĭshie Tekhnol. **22** (7), 31 (2000).
15. V. V. Slezov and J. P. Schmelzer, Fiz. Tverd. Tela (St. Petersburg) **43** (6), 1101 (2001) [Phys. Solid State **43**, 1141 (2001)].
16. I. M. Lifshits and V. V. Slezov, Zh. Éksp. Teor. Fiz. **35**, 475 (1958) [Sov. Phys. JETP **8**, 327 (1959)].
17. I. M. Lifshitz and V. V. Slezov, J. Phys. Chem. Solids **19**, 35 (1961).
18. V. V. Slezov, J. Phys. Chem. Solids **39**, 367 (1978).
19. V. V. Slezov, Ya. Yu. Tkach, and J. P. Schmelzer, Fiz. Tverd. Tela (St. Petersburg) **37** (10), 3212 (1995) [Phys. Solid State **37**, 1767 (1995)].
20. V. V. Slezov, Ya. J. Tkach, and J. Schmelzer, J. Phys. Chem. Solids **105** (18), 8340 (1996).

Translated by O. Moskalev

Physics of the Solid State, Vol. 45, No. 2, 2003, pp. 339–344. Translated from Fizika Tverdogo Tela, Vol. 45, No. 2, 2003, pp. 321–326.
Original Russian Text Copyright © 2003 by Belyaev, Volkov, Konopleva, Nazarkin, Pul'nev, Soloveĭ, Chekanov.

Martensitic Transformation in a Copper–Aluminum–Nickel Alloy Single Crystal after Short-Term Neutron Irradiation

S. P. Belyaev*, A. E. Volkov*, R. F. Konopleva, I. V. Nazarkin**,
S. A. Pul'nev***, V. L. Soloveĭ**, and V. A. Chekanov****

** Smirnov Research Institute of Mathematics and Mechanics, St. Petersburg State University,
St. Petersburg, 198504 Russia*

*** St. Petersburg Institute of Nuclear Physics, Russian Academy of Sciences,
Gatchina, Leningradskaya oblast, 198300 Russia*

**** Ioffe Physicotechnical Institute, Russian Academy of Sciences,
Politekhnicheskaya ul. 26, St. Petersburg, 194021 Russia*

e-mail: spb@smel.math.spbu.ru

Received May 16, 2002

Abstract—The influence of neutron irradiation on the temperature kinetics of thermoelastic martensitic transformation in a Cu–Al(13.4%)–Ni(5%) alloy single crystal is investigated by measuring the electrical resistivity directly under irradiation of the sample in a nuclear reactor channel. It is revealed that, after irradiation of the crystal in a martensitic or two-phase state, the temperature of the phase transition upon heating becomes 25–30 K higher than that prior to irradiation. This shift in the transition temperature is observed only upon the first heating, and the kinetics of martensitic transformation is restored in subsequent thermocycles. The shift in the transformation temperatures after irradiation increases with an increase in the fluence. The experimental results are explained by a disturbance of coherence at the interfaces in the irradiated crystals. *© 2003 MAIK "Nauka/Interperiodica".*

1. INTRODUCTION

Radiation-induced changes in the crystal structure of alloys substantially affect the martensitic transformations. These processes have been investigated most extensively in an TiNi equiatomic alloy, which exhibits a pronounced shape-memory effect and, consequently, holds considerable promise for practical applications [1–3]. Under irradiation of the TiNi alloy with fast neutrons, an increase in the fluence leads to a shift in the martensitic transformation temperature toward the low-temperature range [4–7]. In our earlier works [8, 9], it was demonstrated that, upon exposure of the alloys to low-temperature irradiation, an increase in the fluence is accompanied by an exponential decrease in the critical temperatures and a linear increase in the electrical resistivity. According to the experimental data, the decrease in the characteristic temperatures of the phase transformations in the TiNi alloy occurs at different rates. As a result, the temperature hysteresis of the phase transitions under reactor irradiation increases significantly. It is worth noting that, despite considerable variations in the temperature kinetics of martensitic transformation, the alloy completely retains the ability to change its shape reversibly after low-temperature irradiation with a fluence of 7×10^{18} cm^{-2} [8].

It is believed that radiation-induced disordering of a solid solution plays a decisive role in the aforementioned phenomena [10, 11]. However, it is not improbable that the martensitic transformation can also be affected either by elastic stresses arising in the region of cascades of atomic collisions or by radiation-induced ageing, which can cause the emergence of inhomogeneities in the chemical composition of the alloy under investigation [12]. All the above structural changes are observed in the TiNi alloy. Other materials with martensitic transformations have been poorly investigated. Very little information is available in the literature on the Fe–Mn–Si, Mn–Cu [13], V_3Si [14], Fe–Ni [15], and TiPd(Cr) [16] alloys and pure cobalt undergoing a transition from the face-centered cubic phase to the hexagonal close-packed phase [17]. For this reason, it has hitherto remained impossible to reveal regularities in the behavior of alloys with martensitic transformations of different types or to elucidate the physical nature of the effect of reactor irradiation on martensitic phase transitions in crystals.

The necessity of studying a wide variety of materials in detail is also dictated by the fact that metals undergoing martensitic transformations can be quite competitive with TiNi alloys in the manifestation of mechanical effects associated with the reversibility of severe deformations. Among these materials are primarily copper-based alloys (such as Cu–Al–Ni, Cu–Al–Mn, and Cu–Zn–Al), especially, in the form of single crystals, because they are not subject to intercrystalline brittleness—the chief drawback of copper-based shape-memory alloys [18]. Owing to a unique combination of

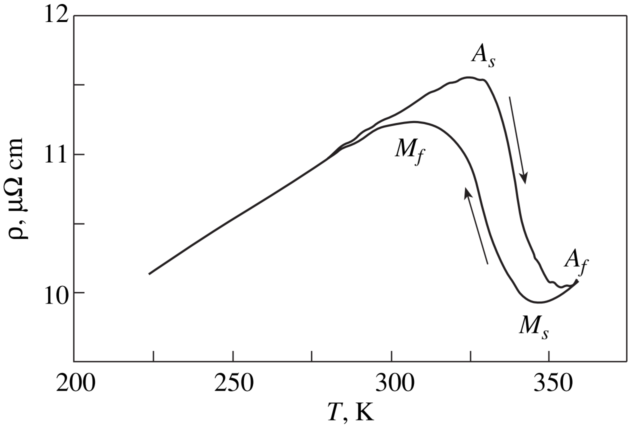

Fig. 1. Temperature dependence of the electrical resistivity in the range of the martensitic transformation in the Cu–Al(13.4%)–Ni(5%) alloy before irradiation.

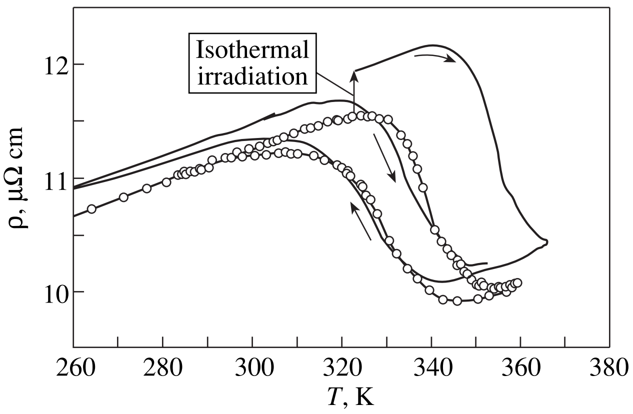

Fig. 2. Temperature dependences of the electrical resistivity measured under isothermal irradiation of the Cu–Al–Ni alloy in the martensitic phase at 322 K (indicated by the vertical arrow) and upon subsequent heating and thermocycling. Points represent the temperature dependence of the electrical resistivity of the unirradiated alloy.

their properties, single-crystal alloys in the Cu–Al–Ni system are very promising in technical applications, specifically in nuclear power plants [19, 20].

This paper reports on the results of investigations into the effect of neutron irradiation on the martensitic transformation in the Cu–Al–Ni alloy, which differs from titanium nickelide in both the crystal structures of the phases involved in the transformation and the temperature kinetics of the phase transition.

2. EXPERIMENTAL TECHNIQUE

A single crystal of the Cu–Al(13.4%)–Ni(5%) alloy (wt %) was chosen as the object of investigation. A cylindrical sample 30 mm long and 1 mm in diameter was irradiated in a low-temperature helium loop channel of a WWR-M reactor (St. Petersburg Institute of Nuclear Physics, Russian Academy of Sciences). In the course of irradiation, experimental instrumentation made it possible to vary the temperature of the studied samples in the range 100–400 K in an arbitrary manner. During the experiments, isothermal irradiation alternated with thermocycling in the temperature range of martensitic transformations. The temperature was varied in the following way: irradiation at a constant temperature ⟶ thermocycling (one or several thermocycles) ⟶ irradiation at a different temperature or at the same temperature ⟶ thermocycling and so on. The temperature was maintained constant to within ±3 K. The time of isothermal irradiation was 10–40 h. In the course of thermocycling, the temperature varied at a rate of 1–3 K/min. The temperature in the gas-filled channel was measured using a copper–constantan thermocouple located in the immediate vicinity of the sample.

In the experiments, the electrical resistivity of the studied alloy was continuously measured by the four-point probe method. The temperature kinetics of the martensitic transformation after isothermal neutron irradiation was judged from the temperature dependences of the electrical resistivity measured in the course of thermocycling. The irradiation temperatures corresponded to different structural states of the material (austenitic, martensitic, and two-phase states).

In the helium loop channel, the flux density of fast neutrons with an energy ≥1 MeV at a height corresponding to the irradiated sample was equal to 6×10^{12} cm^{-2} s^{-1}. In each experiment of isothermal irradiation, the fluence of fast neutrons did not exceed 9×10^{17} cm^{-2}. The integral dose for two weeks of the experiments was 5×10^{18} cm^{-2} (3×10^{-3} dpa).

3. RESULTS AND DISCUSSION

It is found that the studied alloy at room temperature undergoes a martensitic transformation from the high-temperature β_1 phase with a DO_3 structure to the γ'_1 martensitic phase (2H). Figure 1 depicts the temperature dependence of the electrical resistivity ρ of the unirradiated alloy. As can be seen, this dependence exhibits a linear behavior outside the transition temperature range. A drastic increase and a decrease in the electrical resistivity correspond to direct and reverse martensitic transformations with a temperature hysteresis of 12–13 K. The characteristic temperatures of the phase transformation are as follows: $M_s = 346$ K, $M_f = 297$ K, $A_s = 325$ K, and $A_t = 354$ K. In order to exclude the influence of repeated thermocycles on the transformation characteristics, the sample was cooled and heated repeatedly prior to the experiments. Consequently, the dependence shown in Fig. 1 is stable and is well reproduced with varying the temperature.

Figures 2 and 3 display typical temperature dependences measured under isothermal irradiation of the sample in the martensitic state at irradiation temperatures $T_{ir} = 322$ and 123 K, respectively. Note that the

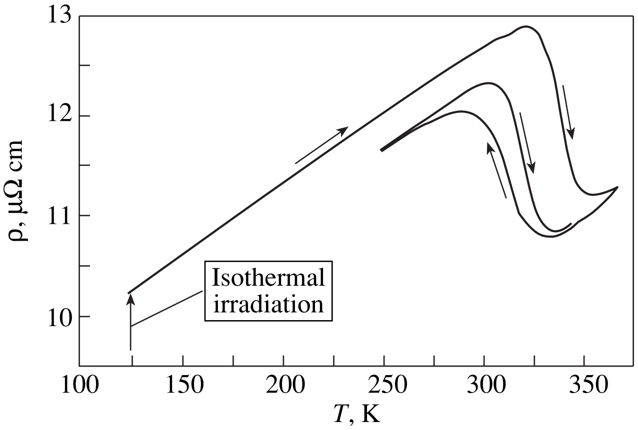

Fig. 3. Temperature dependences of the electrical resistivity measured under isothermal irradiation of the Cu–Al–Ni alloy at 123 K (indicated by the vertical arrow) and upon subsequent heating and thermocycling.

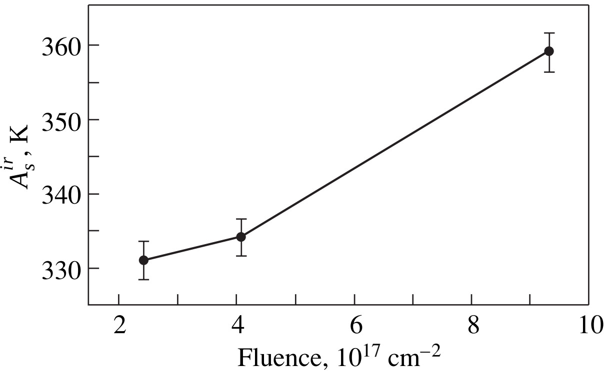

Fig. 4. Temperature of the onset of the reverse martensitic transformation during the first heating after irradiation at 123 K as a function of the neutron fluence for the irradiation time.

alloy has a martensitic structure at an irradiation temperature of 322 K in the temperature range of the martensitic transformation only in the case when this temperature is reached by heating from lower temperatures. The vertical arrows in Figs. 2 and 3 (and in all the other figures given below) show the increment of the electrical resistivity upon isothermal irradiation. After irradiation, the sample was heated in the temperature range involving the reverse transition temperature and additional thermocycling was performed in order to determine the kinetics of the phase transition in the irradiated alloy. For comparison, Fig. 2 shows the dependence $\rho = f(T)$ for the unirradiated alloy measured in the thermocycle immediately before irradiation.

It can be seen from Fig. 2 that the martensitic transformation upon heating immediately after irradiation at 322 K occurs at temperatures 20–25 K higher than those for the unirradiated alloy. Earlier, Abramov *et al.* [20] noted that the temperatures of the reverse martensitic transformation in Cu–Al–Mn and Cu–Al–Ni alloys increase by more than 100 K after fast-neutron irradiation with a fluence of approximately 1.5×10^{20} cm^{-2} at a temperature of 330 K. However, our experimental data demonstrate that a similar increase in the transformation temperatures is observed only once. Even in the next thermocycle, the temperature kinetics of the transformation becomes rather common for martensitic transitions and differs only slightly from the kinetics observed for the unirradiated alloy. For the most part, the difference resides in a small shift of the hysteresis loop toward the low-temperature range without a noticeable change in the temperature hysteresis (Fig. 2). A similar single increase in the temperatures of the martensite $\longrightarrow$ austenite transformation in the course of the first heating is observed after irradiation at the temperature T_{ir} = 123 K (Fig. 3).

Since the aforementioned single increase in the temperatures of the reverse transformation is caused by irradiation, it is reasonable to assume that the temperature shift depends on the integral neutron dose absorbed by the sample in the course of isothermal irradiation. In order to reveal this dependence, the alloy was irradiated at a temperature of 123 K with different fluences. Then, the temperature A_s^{ir} of the onset of the reverse martensitic transformation was measured upon heating performed immediately after isothermal irradiation. The results presented in Fig. 4 indicate that the shift of the martensitic transformation temperature increases with an increase in the neutron fluence.

Owing to the specific features in the temperature kinetics of the martensitic transformation, the crystal under investigation can occur in different structural states at the same absolute temperature. Analysis of the dependence depicted in Fig. 1 shows that, as was noted above, the crystal at a temperature of 322 K occurs in the martensitic state upon heating from low temperatures and in the two-phase state (a mixture of martensitic and austenitic phases in the temperature range of the direct transition, i.e., between M_s and M_f) upon cooling from high temperatures. This temperature was chosen for irradiation of the alloy in the two-phase state. It can be seen from Fig. 5 that, in this case, irradiation leads to the same effects as those observed upon irradiation of the sample in the single-phase martensitic state, i.e., to a single increase in the temperatures of the reverse transformation upon the first heating.

After neutron irradiation of the alloy in the austenitic state at T_{ir} = 340 K, no low-temperature anomalous changes are observed in the temperature kinetics of the martensitic transformation. Upon isothermal irradiation, the hysteresis dependence $\rho = f(T)$, as a whole, only slightly shifts toward the low-temperature range. The increase in the electrical resistivity of the alloy under irradiation at 340 K unexpectedly turns out to be considerably less than that under irradiation at other temperatures. The dependences of the relative change

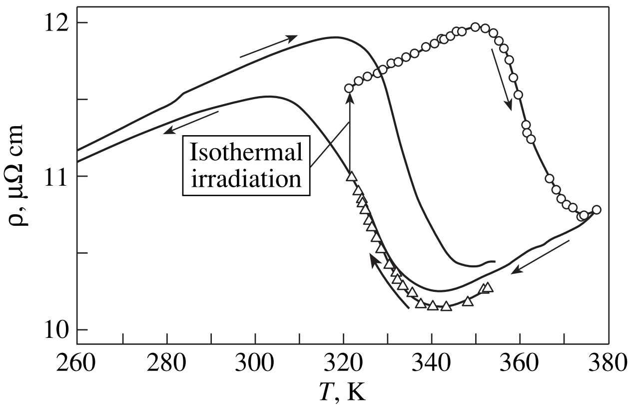

Fig. 5. Temperature dependences of the electrical resistivity measured upon cooling to the irradiation temperature (open triangles), under isothermal irradiation of the sample in the two-phase state at 322 K (indicated by the vertical arrow), upon heating after irradiation (open circles), and subsequent thermocycling (solid lines).

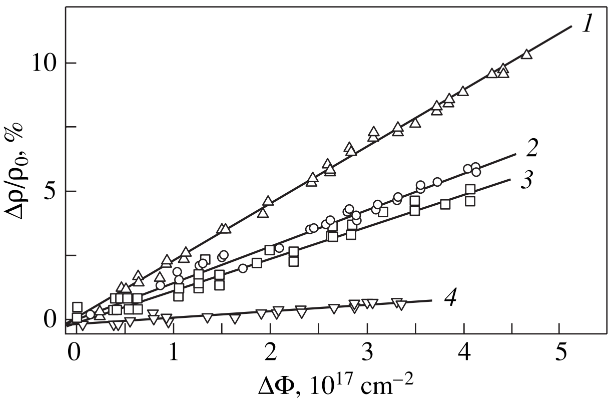

Fig. 6. Dependences of the electrical resistivity of the Cu–Al–Ni alloy on the fast-neutron fluence under isothermal irradiation at temperatures of (*1*) 120, (*2*) 302, (*3*) 322, and (*4*) 340 K.

in the electrical resistivity $\Delta\rho/\rho_0$ on the neutron fluence at different temperatures are shown in Fig. 6. The dependences exhibit a linear behavior. Their slopes $d\rho/(\rho_0 d\Phi)$, which characterize the rate of increase in the electrical resistivity, are as follows: 2.1×10^{-19} cm^2 at T_{ir} = 120 K (the martensitic state, curve *1* in Fig. 6), 1.4×10^{-19} cm^2 at T_{ir} = 302 K (the martensitic state, curve *2* in Fig. 6), 1.2×10^{-19} cm^2 at T_{ir} = 322 K (the two-phase state, curve *3* in Fig. 6), and 2.3×10^{-20} cm^2 at T_{ir} = 340 K (the austenitic state, curve *4* in Fig. 6).

The difference between the first three slopes can be explained by the change in the irradiation temperature (it is known that the lower the irradiation temperature, the higher the rate of accumulation of radiation damages in the crystal lattice). However, this simple explanation is inapplicable to the fourth case. Actually, an increase in the temperature by 18 K (from 322 to 340 K) is accompanied by more than a fivefold decrease in the rate of increase in the electrical resistivity. Therefore, the sharp change in the slope $d\rho/(\rho_0 d\Phi)$ can be attributed only to a change in the structural state of the crystal. It becomes clear that the considerable increase observed in the electrical resistivity during irradiation of the sample in the martensitic and two-phase states is associated not only with the formation of radiation-induced defects, such as vacancies, interstices, and their clusters, which are also formed during irradiation of the sample in the austenitic state. Consequently, the above findings and regularities should be explained in terms of structural features of the material in different states.

The two-phase state of the alloy upon cooling can be represented as an austenitic matrix with embedded martensitic crystals. The transformation is attended by a small volume effect (~0.3%) and an appreciable change in the shape of the newly formed regions, which results in the appearance of elastic stresses at the interfaces. The interfaces themselves are coherent and easily sliding, and the transformation upon cooling occurs through both the growth of the existing martensitic crystals and the formation and growth of new crystals. As a consequence, the crystal in the martensitic state consists of a set of martensitic structural domains with different crystallographic orientations. Therefore, the main distinctive feature of the martensitic and two-phase states, as opposite to the austenitic state, is the presence of a large number of phase boundaries (interfacial and interdomain). The transformation upon heating proceeds through the boundary motion in the reverse direction with complete recovery of the original austenitic structure. The reverse boundary motion is caused by the chemical driving force due to the difference between the free energies of the austenitic and martensitic states $G_{ch} = G_A - G_M$ and the mechanical force G_m associated with the elastic stresses.

There are strong grounds to believe that neutron irradiation causes the disturbance of coherence at the interfaces in the martensitic and two-phase states. This assumption is in complete agreement with the experimental data. Indeed, the disturbance of coherence leads to a decrease in the mobility of the interfaces and, hence, their motion in the course of the reverse transformation requires an additional thermodynamic contribution ΔG^{ir}, i.e., a substantial superheating, which is observed in the experiments. The interfaces disappear after transformation of the crystal into the austenitic state. This results in virtually complete disappearance of the irradiation memory in the metal structure and in the recovery of the temperature kinetics of the transformation. Note that incoherent or semicoherent planar lattice defects efficiently scatter charge carriers; as a consequence, the electrical resistivity of the material involving interfaces under irradiation increases considerably more steeply as compared to that of the material in the austenitic state.

The radiation-induced disturbance of coherence at the interfaces can be associated with the directed migration of radiation-induced point defects in the field of elastic stresses arising in the course of the transformation. Moreover, motion of point defects initiates motion of lattice dislocations. The emergence of dislocations at the inner interfaces or their intersection by dislocations also leads to a disturbance of the interface structure. A number of these mechanisms were discussed in [21, 22]. It should be emphasized that motion of lattice defects is attended by the plastic deformation, which leads to a decrease in G_m. In turn, this also favors an increase in the temperatures of the reverse martensitic transformation after irradiation.

It is of interest to consider the situation when the crystal irradiated in the two-phase state is cooled (rather than heated) to the completion of the austenite ⟶ martensite direct transition. In this case, first, the kinetics of the direct transformation should change owing to the disturbance of coherence at the interfaces of the martensitic crystals and, second, a specific kinetics of the reverse transformation should be expected, because, after cooling, a number of martensitic crystals have a usual structure and the interfaces of the other crystals are damaged by irradiation. The results of the experiment on these transformations are presented in Fig. 7. A small decrease in the temperature of the direct transformation is observed upon cooling after irradiation of the crystal in the two-phase state. It seems likely that, for the above reasons, the irradiated martensitic crystals cease to grow upon cooling and the transformation occurs only through the nucleation of new crystals, which requires an additional supercooling. According to the known property of thermoelastic martensitic transitions, the martensitic crystals disappear upon heating in inverse order to their sequence of formation; i.e., the crystals arising late in cooling disappear early in heating. In the experiment under consideration, heating is accompanied by the initial disappearance of the unirradiated crystals and then the crystals with damaged incoherent interfaces. This is why the first and second stages of the reverse transformation are characterized by small and large temperature hystereses, respectively (Fig. 7). In general, the experimental data presented in Fig. 7 indirectly confirm the proposed structural mechanisms of the influence of short-term neutron irradiation on the martensitic transformation in the Cu–Al–Ni alloy.

It turned out that the response of the Cu–Al–Ni alloy single crystal to neutron irradiation differed from that observed for TiNi alloy polycrystals in our earlier works [8, 9], even though the martensitic transformations in both materials follow the same thermodynamic and kinetic regularities. Elucidation of the origin of this difference calls for further investigation.

In conclusion, we should also note that the results obtained in this work can be used in practice. The drastic change revealed in the kinetics of the reverse martensitic transformation after irradiation can serve as a basis for the design of neutron radiation indicators. The simplest indicator, for example, in the form of a rod fabricated from the Cu–Al–Ni alloy, is sensitive to low radiation doses and can provide information on both the neutron irradiation in the course of exposure and the neutron fluence.

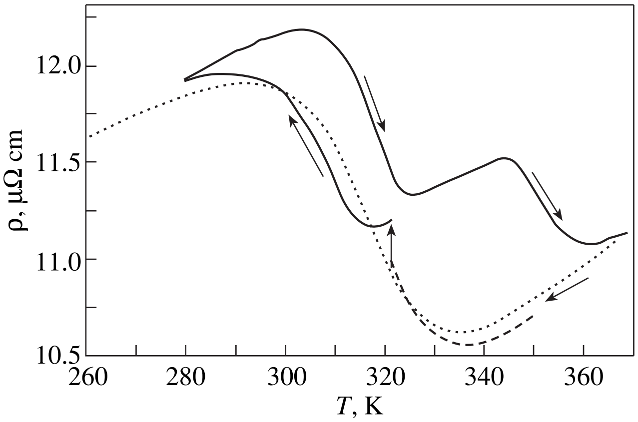

Fig. 7. Temperature dependences of the electrical resistivity measured upon cooling to the irradiation temperature (dashed line), under isothermal irradiation of the sample in the two-phase state at 322 K (indicated by the vertical arrow), upon subsequent cooling and heating in the temperature range of the martensitic transformation (solid lines), and upon repeated cooling (dotted line).

ACKNOWLEDGMENTS

We are grateful to G.V. Kolobanov (St. Petersburg Institute of Nuclear Physics, Russian Academy of Sciences) for his participation in the preparation and performance of the experiments and also to the service team at the cryogenic plant of the WWR-M reactor for technical support of the work.

This work was supported by the State Scientific and Technical Program “Topical Directions in the Physics of Condensed Matter: Neutron Investigations of Condensed Matter” of the Ministry of Science of the Russian Federation and the Russian Foundation for Basic Research, the State Program of Support for Leading Scientific Schools of the Russian Federation (project nos. 00-15-96023 and 00-15-96027).

REFERENCES

1. F. M. Mitenkov, O. B. Samoĭlov, and I. M. Shchukin, Tyazh. Mashinostr. **7**, 16 (1991).
2. M. Nishikawa, S. Toda, E. Tachibana, *et al.*, Fusion Eng. Des. **10**, 509 (1989).
3. M. Nishikawa, E. Tachibana, K. Watanabe, *et al.*, Fusion Eng. Des. **5**, 401 (1988).
4. A. Kimura, S. Myazaki, H. Horikawa, and K. Yamauchi, in *Proceedings of International Conference on Marten-*

sitic Transformation (ICOMAT'92) (Montrey, CA, 1992), p. 935.

5. T. Hoshiya, S. Shimakawa, Y. Ichihashi, *et al.*, J. Nucl. Mater. **179–181**, 1119 (1991).
6. S. F. Dubinin, S. T. Teploukhov, and V. D. Parkhomenko, Fiz. Met. Metallogr. **78** (2), 84 (1994).
7. T. Hoshiya, F. Takada, and Y. Ichihashi, Mater. Sci. Eng. A **130** (2), 185 (1990).
8. S. P. Belyaev, A. E. Volkov, R. F. Konopleva, *et al.*, Fiz. Tverd. Tela (St. Petersburg) **40** (9), 1705 (1998) [Phys. Solid State **40**, 1550 (1998)].
9. S. P. Belyaev, A. E. Volkov, R. F. Konopleva, *et al.*, Fiz. Tverd. Tela (St. Petersburg) **43** (11), 2070 (2001) [Phys. Solid State **43**, 2158 (2001)].
10. S. F. Dubinin, S. T. Teploukhov, and V. D. Parkhomenko, Fiz. Met. Metallogr. **82** (3), 136 (1996).
11. S. F. Dubinin, V. D. Parkhomenko, and S. T. Teploukhov, Fiz. Met. Metallogr. **85** (3), 119 (1998).
12. S. F. Dubinin, S. T. Teploukhov, and V. D. Parkhomenko, Fiz. Met. Metallogr. **87** (1), 75 (1999).
13. L. P. Sinel'nikov, E. N. Loguntsev, A. V. Kozlov, *et al.*, Radiats. Materialoved., Tr. Mezhdunar. Konf. **7**, 19 (1990).
14. I. G. Mikhaĭlov, V. M. Pan, A. V. Skripov, *et al.*, in *Radiation-Induced Defects in Metals* (Nauka, Alma-Ata, 1981), p. 224.
15. V. A. Bychkov, P. L. Gruzin, and Yu. V. Petrikin, *Radiation-Induced Defects in Metals* (Nauka, Alma-Ata, 1981), p. 214.
16. T. Hoshiya, I. Goto, M. Omi, *et al.*, Trans. Mater. Res. Soc. Jpn. B **18**, 1025 (1993).
17. Sh. Sh. Ibragimov, S. P. Pivovarov, O. V. Stakhov, and D. A. Aksenov, in *Radiation-Induced Defects in Metals* (Nauka, Alma-Ata, 1981), p. 253.
18. S. Myazaki, K. Otsuka, H. Sakamoto, and K. Shimizu, Trans. Jpn. Inst. Met. **4**, 224 (1981).
19. I. E. Viahhi, A. I. Priadko, S. A. Pulnev, and V. I. Yudin, in *Proceedings of the 2nd International Conference on Shape Memory and Superelastic Technologies* (Pacific Grove, USA, 1997), p. 263.
20. V. Ya. Abramov, V. P. Ushakov, R. R. Ionaĭtis, *et al.*, in *Shape Memory Materials* (St. Petersburg, 1995), Part 3, p. 26.
21. G. C. Weatherly, Philos. Mag. **17** (148), 761 (1968).
22. L. M. Brown, G. R. Woolhouse, and U. Valdre, Philos. Mag. **17** (148), 781 (1968).

Translated by O. Borovik-Romanova

Physics of the Solid State, Vol. 45, No. 2, 2003, pp. 345–351. Translated from Fizika Tverdogo Tela, Vol. 45, No. 2, 2003, pp. 327–333.
Original Russian Text Copyright © 2003 by Malygin.

Heterogeneous Nucleation of Martensite at Dislocations and the Martensitic-Transformation Kinetics in Shape Memory Alloys

G. A. Malygin
Ioffe Physicotechnical Institute, Russian Academy of Sciences,
Politekhnicheskaya ul. 26, St. Petersburg, 194021 Russia
e-mail: malygin.ga@mail.ioffe.ru

Received May 23, 2002

Abstract—The martensite phase formation in elastic fields of isolated screw and edge dislocations, as well as in planar clusters of like-sign dislocations and in a two-dimensional network of opposite-sign edge dislocations, is quantitatively analyzed within the theory of smeared martensitic transitions. The heterogeneous nucleation of martensite at dislocations is shown to increase the characteristic temperature of the martensitic transition and its temperature smearing. *© 2003 MAIK "Nauka/Interperiodica".*

1. INTRODUCTION

Currently, the mechanism of the influence of lattice defects on martensitic phase transformations is poorly studied both experimentally and theoretically. The available data allow the conclusion that plastic deformation and, hence, dislocations significantly affect martensitic transformations in shape memory alloys [1]. Quenching defects [2] and disperse particles [3, 4] also appreciably change the martensitic-transition parameters. Transmission-electron-microscopy studies of crystals show that dislocations [5–9] and coherent precipitates [3, 6] are centers of martensite heterogeneous nucleation.

Defects have an effect on all parameters of the transformation: the temperature width, temperature hysteresis, and characteristic temperature. There are only qualitative considerations for the mechanism of this effect because of the absence of a quantitative theory of first-order phase transitions, including the structural martensitic transitions in shape memory alloys. In this paper, we study the influence of dislocations on the martensitic-transition parameters in the framework of the phenomenological theory of smeared martensitic transitions (SMTs), recently developed in [10, 11], on the basis of the theory of smeared first-order phase transitions [11].

The theory defines the phase equilibrium between the high- and low-temperature phases (the equilibrium between the martensite and austenite volume fractions in the crystal) depending on a change occurring in the crystal internal energy during structural rearrangement of the crystal lattice. Since defects, e.g., dislocations, disturb this equilibrium due to the elastic fields produced by them, the kinetics and parameters of a martensitic transition will be affected by defects if their density is sufficiently high. The SMT theory allows one to make a quantitative calculation of this effect.

In this paper, we theoretically analyze the influence of dislocations and their clusters on the martensitic-transition kinetics in shape memory alloys within the SMT theory. In Section 2, we present the basic relations of the theory, which are then used in Section 3 to consider the formation of equilibrium martensite nuclei at isolated dislocations. Sections 4 and 5 are dedicated to the martensite formation near planar dislocation clusters and in a two-dimensional ensemble of uniform-density dislocations, respectively. In Section 6, we quantitatively analyze the influence of the dislocation density on the kinetics and parameters of an SMT.

2. BASIC RELATIONS OF THE SMEARED MARTENSITIC TRANSFORMATION THEORY

According to the theory, the relative volume fraction φ_M of martensite in a material at a given temperature T, stress τ, and pressure P is given by [10, 11]

$$\varphi_M(T, \tau) = \left[1 + \exp\left(\frac{\Delta U}{kT}\right)\right]^{-1}, \tag{1a}$$

where $\Delta U = \omega\Delta u$ is the internal-energy change in the crystal as its elementary volume ω undergoes the austenite-to-martensite transition;

$$\Delta u = q\frac{T - T_{c0}}{T_{c0}} - \xi_{ik}\tau_{ik} - \xi_0 P - [u_d]n_d \tag{1b}$$

is the change in the internal energy per unit volume of the material due to the phase transition; q is the transition heat; T_{c0} is the critical (characteristic) transition temperature in the absence of stress τ_{ik} and pressure P;

ξ_{ik} and ξ_0 are the spontaneous shear strain and dilatation of the lattice, respectively, during its structural rearrangement; $[u_d]$ is the change in the intrinsic energy of the lattice defects upon structural transition; and n_d is the defect concentration. Since the contribution of the last term in Eq. (1b) to the energy change is small in comparison with the others, we hereafter neglect it.

As is evident from Eq. (1), the amount of martensite in the crystal depends on the magnitude and sign of the energy Δu. Austenite and martensite prevail in the crystal at $\Delta u > 0$ and $\Delta u < 0$, respectively. The condition $\Delta u = 0$, under which the amounts of austenite and martensite in the crystal are equal, defines the characteristic transition temperature

$$T_c = T_{c0} + \frac{T_{c0}}{q}(\xi_{ik}\tau_{ik} + \xi_0 P). \qquad (2)$$

Equation (2) is a generalized Clausius–Clapeyron relation, according to which external stresses applied to the crystal or the internal stresses should cause a change in the critical temperature of the transformation. The crystal defects that are accompanied by long-range elastic fields should also affect the critical temperature.

Another SMT parameter is the temperature range of the phase transformation, i.e., the transition temperature smearing (width) ΔT_M. This quantity depends on the derivative $d\varphi_M/dT$ at the characteristic transition temperature T_{c0} and is equal to $\Delta T_M = (4/B)T_{c0}$, where $B = \omega q/kT \approx \omega q/kT_{c0}$. Thus, the smearing is determined by the transformation elementary volume and transformation heat. As for the transformation temperature hysteresis ΔT_f, this quantity depends on the force (stress) of interphase boundary locking by defects.

3. SCREW AND EDGE DISLOCATIONS

Isolated dislocations can affect the martensitic transformation parameters only locally, i.e., within the range of their elastic shear field. For a straight screw dislocation line oriented along the z axis, the shear stresses are given by

$$\begin{aligned} \tau_{zx} &= \tau_{xz} = -\frac{\mu b}{2\pi}\frac{x}{x^2+y^2}, \\ \tau_{zy} &= \tau_{yz} = -\frac{\mu b}{2\pi}\frac{y}{x^2+y^2}, \end{aligned} \qquad (3)$$

where μ is the shear modulus and b is the Burgers vector. Within the SMT theory, the martensite formation in elastic fields given by Eq. (3) can be correctly described on the scales $r > r_\omega$, where r_ω is the largest size of the elementary transformation volume ω. For example, in the case of a disk-shaped elementary transformation volume with a thickness of the order of the lattice parameter a, we have $r_\omega = (4\omega/\pi a)^{1/2}$, which corresponds to 3–6 nm for the characteristic values $\omega \approx$ 2–10 nm^3 in shape memory alloys and $a = 0.3$ nm.

For a general orientation of the screw dislocation with respect to the habit plane and in the presence of spontaneous shear strains $\xi_{z'x'}$ and $\xi_{z'y'}$, the energy of the martensitic relaxation of the local stress field of the dislocation is given by

$$\xi_{ik}\tau_{ik} = \frac{\mu b \xi}{2\pi}S_1(x, y), \quad S_1(x, y) = \frac{m_{zx}x + m_{zy}y}{x^2 + y^2}, \qquad (4)$$

where $\xi = (\xi_{z'x'}^2 + \xi_{z'y'}^2)^{1/2}$ and m_{zx} and m_{zy} are the direction cosines defining the dislocation orientation with respect to the habit plane and spontaneous-strain direction. Substituting Eq. (4) into Eq. (1b), we arrive at the martensite distribution near the screw dislocation:

$$\begin{aligned} &\varphi_M(t, X, Y) \\ &= \{1 + \exp[B(t - 1 - A_1|S_1(X, Y)|)]\}^{-1}, \end{aligned} \qquad (5)$$

where $t = T/T_{c0}$, $X = x/b$, and $Y = y/b$ are the dimensionless temperature and coordinates respectively, and $A_1 = \mu\xi/2\pi q \approx$ 1–10 is the parameter characterizing the relaxation intensity.

Figures 1a–1c show the martensite distribution near the screw dislocation according to Eq. (5) for $A_1 = 8$, $B = 50$, and $t = 1.25$ and for three different orientations of the dislocation line. Contours *1–3* bound the regions where $\varphi_M = 1$, 2/3, and 1/3, respectively, at a given temperature. One can see that the martensite distribution near the dislocation depends on the dislocation orientation with respect to the habit plane. Martensite arises in the region near the dislocation where, according to Eq. (3), positive and negative shear stresses are strongest. To eliminate the divergences as $x, y \longrightarrow 0$, the constant term $0.1b^2$ was introduced into the denominator of formula (4) in order to limit the dislocation stress field at distances $r < 0.3b$ from the dislocation.

Curve *2* in Fig. 1d shows the martensite concentration at the point $x = 5b$, $y = 0$ near the dislocation (Fig. 1a) as a function of temperature. For comparison, curve *1* shows the martensite concentration at this point in the absence of dislocations. One can see that, for the parameters indicated above, the martensite nucleation in the crystal is initiated at a significantly higher temperature ($T_c \approx 1.5T_{c0}$) than in the absence of dislocations. If the martensite concentration $\varphi_M = 0.99$ is taken as that defining the size of the martensite formation region in Figs. 1a–1c, then, according to Eq. (5), the region size can be estimated as

$$R_M = \frac{2mA_1 b}{T/T_{c0} - 1 + 4.6/B}, \qquad (6)$$

where $m = 0.5$ is the maximum value of the orientational factor. For the parameters indicated above and $T = 1.2T_{c0}$, we have $R_M \approx 24b$. This value appreciably exceeds $R_M \approx 4b$ for contour *1* in Figs. 1a–1c, since a higher φ_M value was taken as critical in the numerical calculation. As the temperature decreases, the martensite region near the dislocation grows and becomes infinitely large at the temperature $T_M = \left(1 - \frac{4.6}{B}\right)T_{c0}$. This means that the martensitic transformation occurs in the whole crystal at this and lower temperatures regardless of the dislocation.

In addition to shear stresses τ_{xy}, the edge dislocation in the crystal also produces a hydrostatic component $P = (\sigma_x + \sigma_y + \sigma_z)/3$:

$$\tau_{xy} = \tau_{yx} = \frac{\mu b}{2\pi(1-\nu)}\frac{x(x^2-y^2)}{(x^2+y^2)^2},$$
$$P = \frac{\mu b}{3\pi}\left(\frac{1+\nu}{1-\nu}\right)\frac{y}{x^2+y^2}. \tag{7}$$

The energy of the martensitic relaxation of the elastic field of the edge dislocation consists of two components: the energy of the shear-stress relaxation

$$\xi_{ik}\tau_{ik} = \frac{\mu b \xi}{2\pi(1-\nu)}S_2(x, y),$$
$$S_2(x, y) = m_{xy}\frac{x(x^2-y^2)}{(x^2+y^2)^2} \tag{8a}$$

(where m_{xy} is the orientational factor and $\xi = |\xi_{xy}|$) and the pressure relaxation energy

$$\xi_0 P = \frac{\mu b \xi_0}{3\pi}\left(\frac{1+\nu}{1-\nu}\right)S_3(x, y), \quad S_3(x, y) = \frac{y}{x^2+y^2}. \tag{8b}$$

Substituting these energies into Eq. (1b), we arrive at the martensite distribution near the straight edge dislocation line:

$$\varphi_M(t, X, Y) = \{1 + \exp[B(t - 1 - A_2|S_2(X, Y)| - A_3|S_3(X, Y)|)]\}^{-1}, \tag{9a}$$

$$A_2 = \frac{\mu\xi}{2\pi(1-\nu)q}, \quad A_3 = \frac{\mu\xi_0}{3\pi q}\left(\frac{1+\nu}{1-\nu}\right). \tag{9b}$$

The other designations are the same as those in formula (5). Figures 2a and 2b show the martensite regions near the edge dislocation calculated from Eq. (9) for pure shear ($A_2 = 8$, $m_{xy} = 0.5$) and pure dilatation ($A_3 = 2$) relaxation of the dislocation elastic field at the temperature $T = 1.25T_{c0}$. Figure 2c displays the calculated martensitic relaxation including both stress field components of the edge dislocation.

The electron microscopy observations [5–7] showed the size of martensite regions near dislocations to be approximately 10–20 nm, which corresponds to the estimates made from formula (6). Martensite structures near dislocations consist of a set of several-nanometer-thick martensite plates alternating with austenite phase regions [5]. The SMT theory ignores the plate shape

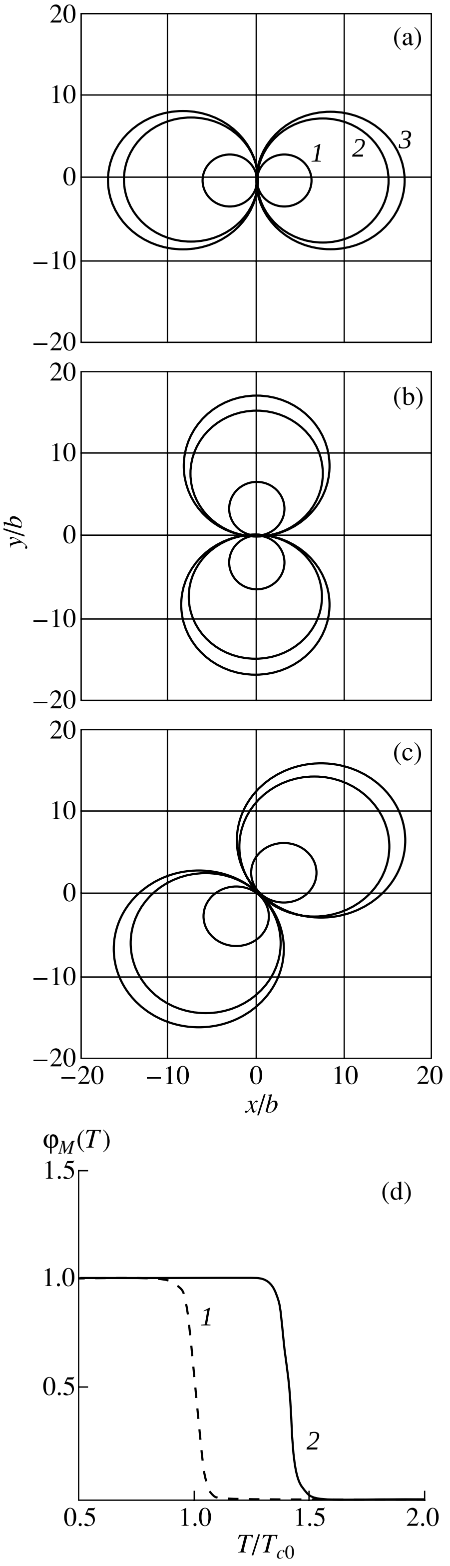

Fig. 1. Martensite formation near a screw dislocation at various orientations of the dislocation line with respect to the habit plane: (a) $m_{zx} = 0.5$, $m_{zy} = 0$; (b) $m_{zx} = 0$, $m_{zy} = 0.5$; (c) $m_{zx} = m_{zy} = 0.4$; and (d) temperature dependences of the amount of martensite at the point $x = 5b$, $y = 0$ [in case (a)] (*1*) without and (*2*) with dislocations. Contours *1–3* in (a–c) correspond to the martensite concentrations $\varphi_M = 1$, 2/3, and 1/3, respectively.

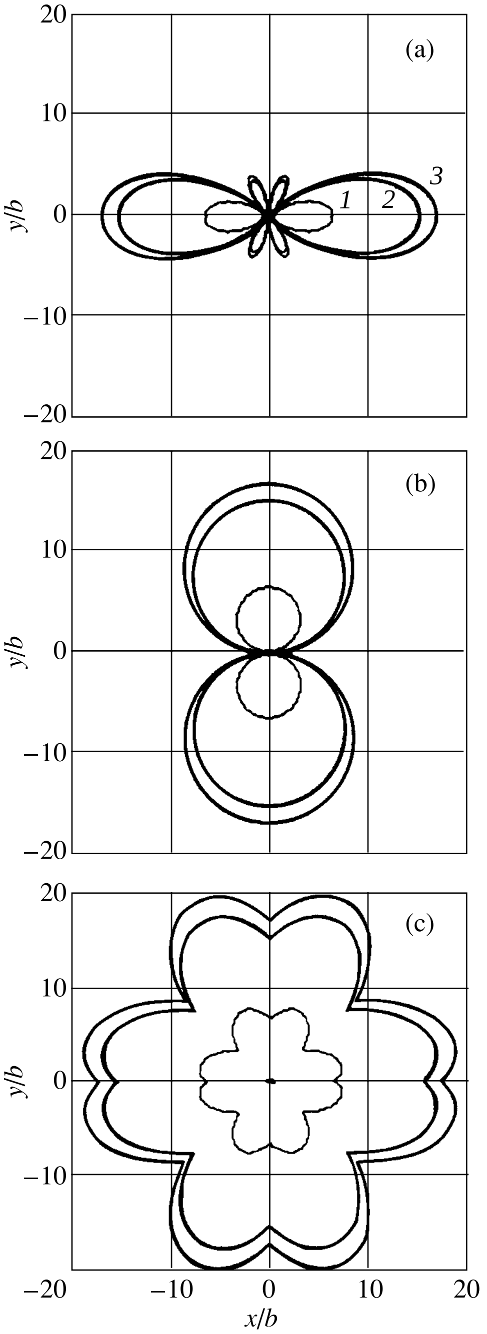

Fig. 2. Martensite phase distribution near an edge dislocation in the case of (a) a shear, (b) pure dilatation, and (c) total stress fields.

and sizes; however, this theory defines their number near dislocations at given plate sizes [11].

4. PLANAR DISLOCATION CLUSTERS

Dislocations in the crystal can comprise various clusters and dislocational structures. The long-range stress field of dislocations in such structures strengthen or compensate for each other depending on the region; therefore, the magnitude of local stresses depends on the sign and relative positions of dislocations. Below, we consider the martensite formation near clusters of like-sign edge dislocations in the glide plane, as well as near an edge dislocation cluster in the form of a vertical wall of finite height.

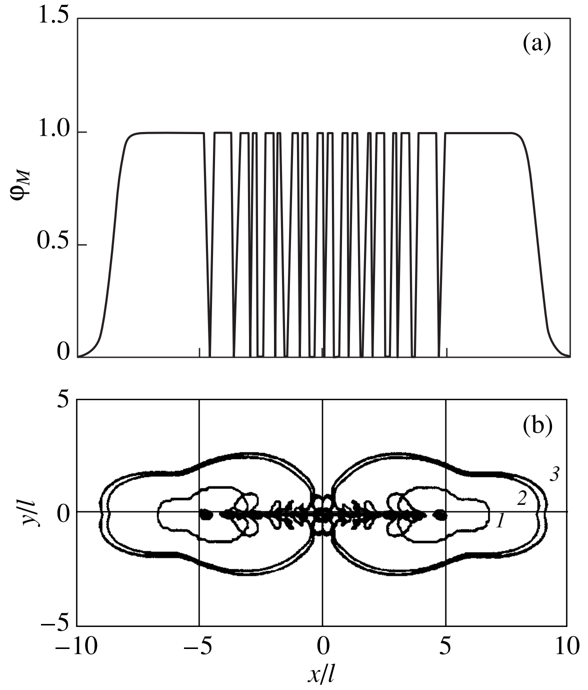

Fig. 3. Martensite phase distribution near a planar cluster of edge dislocations (a) over the glide plane at $y = 0$ and (b) over the plane normal to the dislocation lines.

In the former case, by summing up the shear and dilatation stresses from separate dislocations, we obtain

$$\begin{aligned}\tau_{xy} &= \frac{\mu b}{2\pi(1-\nu)}\sum_{-N}^{N}\frac{(x+nl)[(x+nl)^2-y^2]}{[(x+nl)^2+y^2]^2},\\ P &= \frac{\mu b}{3\pi}\left(\frac{1+\nu}{1-\nu}\right)\sum_{-N}^{N}\frac{y}{(x+nl)^2+y^2},\end{aligned}\tag{10}$$

where l is the distance between dislocations in the cluster, $2N + 1$ is their total number, and n specifies the dislocation position in the cluster. By substituting Eq. (10) into Eqs. (1), we calculated the martensite phase distribution near the plane cluster of edge dislocations.

Figure 3a shows the martensite distribution over the glide plane ($y = 0$) at the temperature $T = 1.6T_{c0}$, the distance $l = 10b$ between neighboring dislocations, and the total number $2N + 1 = 11$ of cluster dislocations. The other parameters are the same as above. One can see that the martensite region size is approximately $5l$ near the cluster edges where the opposite-sign stress fields do not compensate each other. Smaller martensite regions (of the order of l) arise near internal disloca-

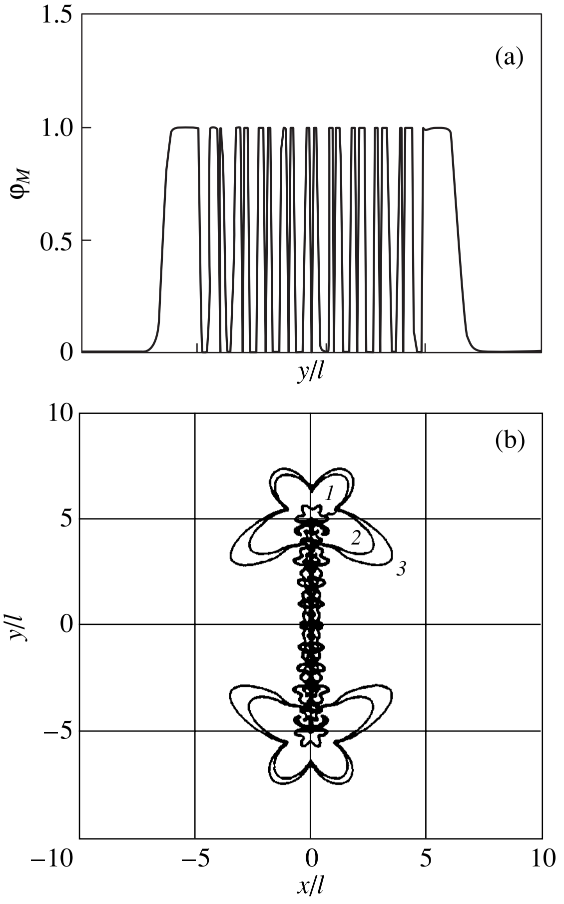

Fig. 4. Martensite phase distribution near a vertical wall of edge dislocations (a) over the wall at $x = 0$ and (b) over a plane normal to the dislocation lines.

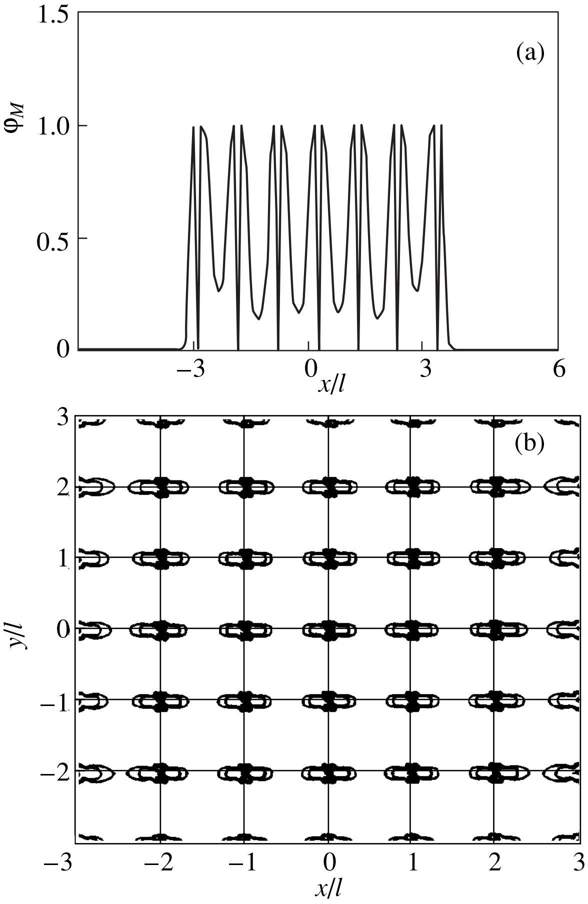

Fig. 5. Martensite distribution near a two-dimensional network of opposite-sign edge dislocations (a) over the dislocation glide plane $y = 0$ and (b) over the plane normal to the dislocation lines.

tions, since the fields compensate each other. The martensite phase distribution over a plane normal to the glide plane is shown in Fig. 3b. Contour *2* corresponds to the martensite phase concentration $\varphi_M = 2/3$. In the cluster center, the martensite region narrows, since dislocation stress fields compensate each other. Small martensite regions located near the glide plane in Fig. 3b correspond to martensite formed near separate dislocations. It is also evident that, in the case of a cluster of like-sign dislocations, large martensite regions arise at a higher temperature than in the case of isolated dislocations.

The martensite formation near a vertical wall of like-sign edge dislocations with the average distance l between dislocations [the wall height is $H = (2N + 1)l$] can be calculated in a similar way. Figures 4a and 4b display the calculated distribution for the parameters indicated above and the temperature $T = 1.5T_{c0}$. Figures 4a and 4b show the martensite phase distributions over the wall at $x = 0$ and over the plane normal to dislocations, respectively. One can see that significant martensite regions arise at the dislocation wall edges in the strongest stress regions. A dislocation wall of finite height can be considered to be a disclination dipole; therefore, Figs. 4a and 4b show the martensite phase distribution near such a dipole.

5. TWO-DIMENSIONAL NETWORK OF EDGE DISLOCATIONS

Heterogeneous martensite nucleation on a two-dimensional network of opposite-sign edge dislocations can be calculated similarly to the preceding case. The shear stresses in the network of opposite-sign dislocations arranged in staggered rows are described by the double sum

$$\tau_{xy} = \frac{\mu b}{2\pi(1-\nu)}$$
$$\times\sum_{-N}^{N}\sum_{-N}^{N}\frac{(-1)^{n+m}(x+nl)[(x+nl)^2-(y+ml)^2]}{[(x+nl)^2+(y+ml)^2]^2}. \quad (11a)$$

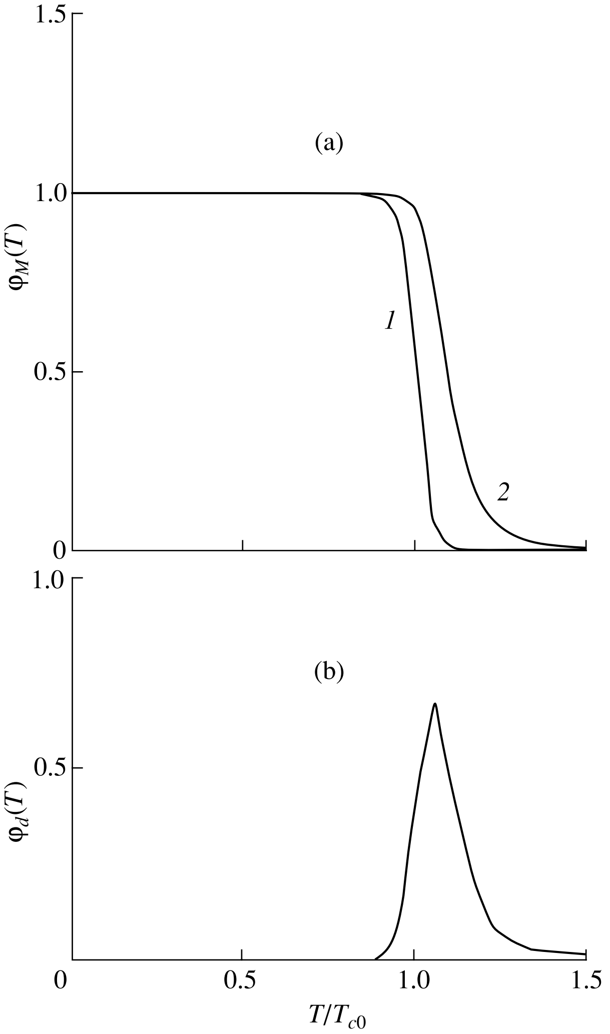

Fig. 6. Temperature dependences (a) of the martensite volume fraction in the crystal (*1*) without and (*2*) with dislocations and (b) of the martensite fraction caused by dislocations.

The hydrostatic stress is written as

$$P = \frac{\mu b}{3\pi}\left(\frac{1+\nu}{1-\nu}\right)\sum_{-N}^{N}\sum_{-N}^{N}\frac{(-1)^{n+m}(y+ml)}{(x+nl)^2+(y+ml)^2}. \quad (11b)$$

Figure 5a displays the martensite distribution over the dislocation glide plane $y = 0$ for the average distance $l = 100b$ between network dislocations; their total number is $(2N + 1)^2 = 49$, and the temperature is $T = 1.2T_{c0}$. The values of the other parameters are the same as those indicated above. It is evident that martensite exists at this temperature not only near dislocations but also between them. Figure 5b displays the martensite distribution over a plane normal to dislocation lines of the two-dimensional dislocation network.

6. INFLUENCE OF DISLOCATIONS ON THE MARTENSITIC-TRANSITION PARAMETERS

The temperature dependence of the amount of martensite in the crystal changes due to heterogeneous martensite nucleation at defects. Curve *2* in Fig. 6a displays this dependence in the case of the two-dimensional dislocation network shown in Fig. 5b. The dependence was calculated by integrating the local martensite distribution for the two-dimensional dislocation network:

$$\varphi_M(T) = \frac{1}{4L^2}\int_{-L}^{L}dx\int_{-L}^{L}\varphi_M(x, y, T)dy, \quad (12)$$

where $4L^2$ is the integration domain size. For comparison, Fig. 6a also shows the temperature dependence of φ_M in the absence of dislocations in the crystal (curve *1*). One can see that dislocations shift the temperature dependence to higher temperatures and extend the transformation temperature range, i.e., increase the transition temperature smearing. Figure 6b displays the temperature dependence of the amount of deformational martensite resulting from the dislocation network in the crystal. The dependence was constructed as the difference between curves *1* and *2* in Fig. 6a.

If the temperature at which half the crystal is in the martensite state is taken as a characteristic transition temperature in the crystal containing dislocations and the size of martensite regions near dislocations becomes close to [(1/2)l, where $l = \rho^{-1/2}$ and ρ is the dislocation density], then the characteristic temperature is estimated to be

$$T_c = [1 + 2(mA_2 + A_3)b\rho^{1/2}]T_{c0}, \quad (13)$$

where m is the orientational factor. At the values of the parameters $A_2 = 8$, $A_3 = 2$, $m = 0.5$, and $b = 0.25$ nm, the temperature T_c is $1.03T_{c0}$ for the dislocation density $\rho = 10^{10}$ cm^{-2}. Experience shows that plastic deformation [1] or quenching [2] of a crystal often decreases the characteristic transition temperature in shape memory alloys rather than increasing it, as well as increases the transformation temperature hysteresis. The latter increase is caused by the interaction between interphase boundaries and defects. The decrease in temperature T_c due to plastic deformation can also be caused by this factor.

7. CONCLUSIONS

In this paper, we restricted ourselves to the analysis of the martensite formation near dislocations and their clusters in the case of only one martensite variant present in the crystal. However, the SMT theory also allows one to analyze the case of a few martensite variants, as well as the case where the martensite formation is caused by the application of an external mechanical stress to the crystal, rather than by a temperature decrease.

REFERENCES

1. V. G. Pushin, V. V. Kondrat'ev, and V. N. Khachin, *Titanium Nickelide* (Nauka, Moscow, 1992).
2. A. Amengual, F. C. Lovey, G. Segui, and V. Torra, Mater. Sci. Forum **56/58**, 523 (1989).
3. N. Nishida and T. Honma, Scr. Metall. **18** (6), 1293 (1984).
4. V. I. Zeldovich, G. A. Sobyanina, and V. G. Pushin, Scr. Mater. **37** (1), 79 (1997).
5. T. Fukuda, T. Saburi, and K. Doi, Mater. Trans. JIM **33** (3), 271 (1992).
6. V. I. Zel'dovich, I. V. Khomskaya, N. Yu. Frolova, and G. A. Sbitneva, *Shape Memory Alloys and Other Perspective Materials* (St. Petersburg, 2001), Part 1, p. 63.
7. G. Guenin and P. F. Gobin, Metall. Trans. A **13** (7), 1127 (1982).
8. T. Saburi and S. Nenno, in *Proceedings of ICOMAT-86* (Japanese Inst. Metals, 1986), p. 671.
9. Yu. N. Gornostyrev, M. N. Katsnel'son, A. R. Kuznetsov, and A. V. Trefilov, Fiz. Met. Metalloved. **91** (3), 32 (2001).
10. G. A. Malygin, Fiz. Tverd. Tela (St. Petersburg) **36** (5), 1489 (1994) [Phys. Solid State **36**, 815 (1994)].
11. G. A. Malygin, Usp. Fiz. Nauk **171** (2), 187 (2001).

Translated by A. Kazantsev

Physics of the Solid State, Vol. 45, No. 2, 2003, pp. 352–357. Translated from Fizika Tverdogo Tela, Vol. 45, No. 2, 2003, pp. 334–338.
Original Russian Text Copyright © 2003 by Dmitriev.

Mechanism of the Transition between 1*q* and 3*q* Phases in a Two-Dimensional Crystal Model

S. V. Dmitriev
Department of Applied Physics and Chemistry, University of Electro-Communications,
Chofu-shi, Tokyo, 182-8585 Japan
e-mail: sergey-d@fedu.uec.ac.jp

Received December 17, 2001; in final form, May 29, 2002

Abstract—The previously proposed model of a crystal with rotational degrees of freedom is extended to the two-dimensional case. The model contains two nonlinear terms that allow for the stability of 1*q*, 2*q*, or 3*q* modulated phases, depending on the ratio between the model parameters. A numerical treatment is performed for the transition between the 1*q* and 3*q* phases that is characteristic of crystals with hexagonal symmetry. This model makes it possible to reconstruct the sequence of phase transitions occurring in quartz crystals upon cooling and offers a satisfactory explanation of the experimentally observed increase in the temperature range of existence of the 1*q* phase under external uniaxial loading. *© 2003 MAIK “Nauka/Interperiodica”.*

1. INTRODUCTION

In recent years, the formation of modulated phases in crystals has attracted considerable attention both in terms of the theory of phase transitions and as an example of a more general physical phenomenon, namely, spatial localization of energy under external homogeneous actions. Great interest expressed by researchers in the formation of modulated phases is associated with the aforementioned and other intriguing phenomena [1–7]. In a dielectric crystal, the modulated phase arises from the high-symmetry commensurate (normal) phase due to a second-order phase transition, which, in turn, is caused by the disappearance of the acoustic mode with a wave vector lying within the first Brillouin zone. A similar phase transition can be experimentally observed with a decrease in the temperature. In modulated phases, the atoms are slightly displaced from their lattice positions following a periodic law. It should be noted that, in the vicinity of the phase transition point, the modulation is nearly sinusoidal. Moreover, there exist modulations in the form of a superposition of two or three sinusoidal waves. In this case, modulated phases are referred to as the 2*q* and 3*q* phases, respectively, unlike the 1*q* phase, in which the modulation has the form of a single wave. When the ratio of the lattice parameter of the modulated phase to the modulation wavelength is an irrational number, this phase is termed incommensurate. However, since the exact value of the actual ratio is unknown, it is usually represented in the form of an irreducible fraction. Therefore, it is physically correct to characterize the incommensurate phase by such a ratio of the lattice parameter to the modulation wavelength that can be expressed by an irreducible fraction with a sufficiently large denominator [8].

During further cooling, the modulated phase undergoes a number of transitions and, as a rule, ultimately transforms into the low-symmetry commensurate phase. For example, the following sequences of phase transformations are observed upon cooling: (i) normal phase ⟶ 1*q* ⟶ 3*q* ⟶ commensurate phase for SiO_2 quartz [9, 10] and (ii) normal phase ⟶ 2*q* ⟶ 1*q* ⟶ commensurate phase for $Ba_2NaNb_5O_{15}$ crystals [11, 12].

It is conventional to describe the incommensurate phases in terms of microscopic models. In particular, the so-called ANNNI model, which was modified by Yamada and Hamaya [13], provides a qualitative description of a sequence of phase transformations from the incommensurate phase to the commensurate higher-order phase and, then, to the low-symmetry commensurate phase in crystals belonging to the structural family A_2BX_4. Parlinski and Chapuis [14] performed a molecular dynamics simulation of the transition between 3*q* and 3*q*′ phases with different modulation periods in the framework of a three-dimensional hexagonal model. These authors also applied the molecular dynamics method to an analysis of the kinetics of the 1*q* ⟶ 3*q* and 3*q* ⟶ 1*q* phase transitions [14, 15]. It was proved that, in order to obtain stable 2*q* and 3*q* phases, the Hamiltonian of the system has to contain specific nonlinear terms [14–17]. The aforementioned works elucidated the conditions of the existence of stable 2*q* and 3*q* phases in terms of two-dimensional and three-dimensional models. However, the origin and mechanisms of the 1*q* ⟶ 2*q* and 1*q* ⟶ 3*q* phase transitions are still not clearly understood. The former transition was thoroughly investigated in our previous work [18]. The latter transition will be considered in the present paper (see below). Our treatment is based on a microscopic model dealing with the so-called elastically hinged molecules of finite size, i.e., on the elastically hinged molecule (EHM) model [19, 20]. In this work, the one-dimensional variant of the EHM model proposed in [19, 20] is extended to the two-dimensional case. It should be noted that the one-dimensional models constructed under the physical assumptions made by Slot and Janssen [21] and Ishibashi [22] are described by equations of motion that are mathematically equivalent to the equation derived in the one-dimensional EHM model. The Hamiltonian of the two-dimensional EHM model is almost identical to the Hamiltonian treated earlier by Parlinski *et al.* [17]. The only difference between them is that the linear part of the Hamiltonian in the EHM model corresponds to the case of an arbitrary external pressure, whereas the Hamiltonian considered in [17] describes the case of hydrostatic pressure. As a consequence, the frequency of the soft mode in the EHM model can vanish at any point of the Brillouin zone. By contrast, in [17], the frequency of the soft mode becomes zero simultaneously at three points lying along the high-symmetry directions [1 0], which, as will be shown below, makes numerical treatment of the transition between the 1q and 3q phases impossible.

2. DESCRIPTION OF THE MODEL

A continuum analog of the one-dimensional EHM model can be represented in the form [19]

$$u_{tt} + Fu_{xxxx} + Pu_{xx} + u + u^3 = 0, \tag{1}$$

where $u(x, t)$ is an unknown field of displacements, F is the parameter describing the elastic properties of the medium, and P is the external pressure.

Now, we write an obvious two-dimensional generalization of Eq. (1) in the following form:

$$\begin{aligned} &u_{tt} + F_x u_{xxxx} + 2F_{xy} u_{xxyy} + F_y u_{yyyy} \\ &+ P_x u_{xx} + P_y u_{yy} + u + Hu^2 + u^3 = 0, \end{aligned} \tag{2}$$

where $u(x, y, t)$ is an unknown function of displacements; F_x, F_{xy}, and F_y are the elastic constants of the anisotropic medium; P_x and P_y are the external pressure components; and H is the parameter of the nonlinear part of the equation. By analogy with the calculations performed in [17], the nonlinear part of the equation in our case is chosen in a more general form than in Eq. (1).

Before proceeding further, one additional remark needs to be made. The coefficient of the term u^3 in Eq. (1) can be normalized to unity. However, this normalization is inapplicable in the case of Eq. (2). Nonetheless, the consideration of the aforementioned special case will suffice for our purposes. Note also that equations similar to Eqs. (1) and (2) are widely used in the theory of beams and thin plates.

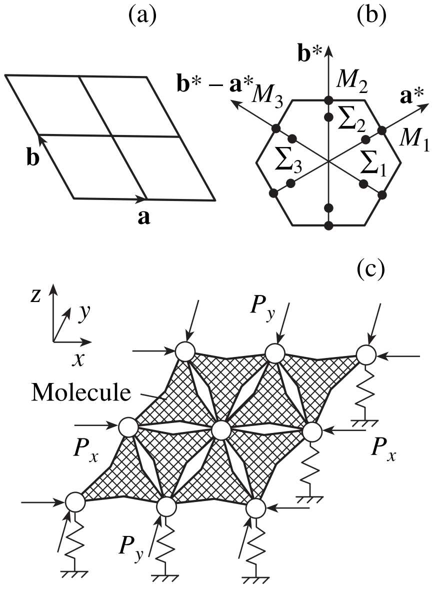

Fig. 1. (a) Hexagonal lattice, (b) reciprocal lattice and the first Brillouin zone, and (c) the two-dimensional EHM model. Rigid molecules are linked together by elastic hinges. The model is exposed to an external pressure with components P_x and P_y.

Let us now assume that the vectors $\mathbf{a} = (1, 0)$ and $\mathbf{b} = (-1/2, \sqrt{3/2})$ generate a hexagonal lattice with points $m\mathbf{a} + n\mathbf{b}$, where m and n are integral numbers (Fig. 1a). The reciprocal lattice is generated by the vectors $\mathbf{a}^*$ and $\mathbf{b}^*$. Figure 1b shows the reciprocal lattice specified by these vectors and the first Brillouin zone.

A discrete analog of Eq. (2), which is deduced for the hexagonal lattice, can be represented in the form

$$\begin{aligned} &\ddot{u}_{m,n} + (3P_x - P_y - 48F)(u_{m+1,n} + u_{m-1,n}) \\ &+ 2(P_y - 24F)(u_{m+1,n+1} + u_{m,n+1} + u_{m-1,n-1} + u_{m,n-1}) \\ &+ 16F(u_{m+2,n+1} + u_{m+1,n+2} + u_{m-1,n+1} \\ &+ u_{m-2,n-1} + u_{m-1,n-2} + u_{m+1,n-1}) \\ &+ (1 - 6P_x - 6P_y + 192F)u_{m,n} + Hu^2_{m,n} + u^3_{m,n} = 0. \end{aligned} \tag{3}$$

When deriving relationship (3), we restricted our consideration to the special case of an isotropic medium, that is, $F_x = F_{xy} = F_y = F$.

The Hamiltonian of the two-dimensional EHM model based on the hexagonal lattice has the following form:

$$\begin{aligned} H = &\frac{1}{2}\sum_{m,n}(\dot{u}_{m,n})^2 + \frac{1}{2}(3P_x - P_y - 48F) \\ &\times \sum_{m,n} u_{m,n}(u_{m+1,n} + u_{m-1,n}) + (P_y - 24F) \end{aligned}$$

$$\times\sum_{m,n}u_{m,n}(u_{m+1,n+1}+u_{m,n+1}+u_{m-1,n-1}+u_{m,n-1})$$

$$+8F\sum_{m,n}u_{m,n}(u_{m+2,n+1}+u_{m+1,n+2}+u_{m-1,n+1}\qquad(4)$$

$$+u_{m-2,n-1}+u_{m-1,n-2}+u_{m+1,n-1})$$

$$+\frac{1}{2}(1-6P_x-6P_y+192F)\sum_{m,n}u^2_{m,n}$$

$$+\frac{H}{3}\sum_{m,n}u^3_{m,n}+\frac{1}{4}\sum_{m,n}u^4_{m,n}.$$

Physically, relationships (3) and (4) can be interpreted in different ways. In particular, Parlinski *et al.* [17] proceeded from analyzing the interaction between point particles that had neither size nor shape. The EHM model proposed in our earlier work [19] offers another interpretation. Recall that the majority of dielectric crystals are composed of very rigid, virtually undistorted atomic groups. For example, quartz crystals consist of SiO_4 tetrahedral clusters. In this structure, the tetrahedra are linked together at vertices occupied by oxygen atoms, which play the role of hinges. Phase transitions in quartz crystals occur through mutual rotations of hinged tetrahedra in such a way that their distortions are negligible. Quartz crystals have hexagonal symmetry. Since modulations in the quartz incommensurate phase propagate in the (x, y) plane, they can be treated in the framework of a two-dimensional model. On this basis, we can consider the two-dimensional case of rigid triangle particles (molecules) joined through elastic hinges (Fig. 1c). Let us assume that the angle between the axes of the two neighboring, elastically hinged molecules is nonzero. In this situation, the elastic hinge is characterized by a force moment that tends to decrease the magnitude of this angle. The rigidity of the hinge is designated by F. Each hinge exhibits one degree of freedom, namely, displacement in the direction perpendicular to the (x, y) plane. The elastically hinged molecules interact through a potential with anharmonic third- and fourth-order terms. This potential describes how the molecular layer under consideration is affected by the rest of the crystal structure. An external pressure with components P_x and P_y is applied along the (x, y) plane.

The harmonic part of Eq. (1) leads to the following dispersion relationship:

$$\begin{aligned}\omega^2(\kappa_x,\kappa_y) &= 32F[C_xC_y(1+2C_x+2C_y)\\ &+S_xS_y(1-2C_x-2C_y)-C_x-C_y]\\ &+2(3P_x-P_y-48F)C_x+2(2P_y-48F)\\ &\times(C_xC_y-S_xS_y+C_y)+1-6P_x-6P_y+192F,\end{aligned}\qquad(5)$$

where

$$C_x = \cos(2\pi\kappa_x),\quad C_y = \cos(2\pi\kappa_y),$$

$$S_x = \sin(2\pi\kappa_x),\quad S_y = \sin(2\pi\kappa_y),$$

$$\kappa = \kappa_x a^* + \kappa_y b^*.$$

We assume that the elastic constant F and the parameter H depend on the temperature. A change in the temperature and (or) the external pressure components P_x and P_y causes a point particle to move in the four-dimensional phase space of the model; as a consequence, there can occur phase transitions.

Equation (3) has an obvious trivial solution, that is, $u_{m,n} = 0$ (normal phase). This solution is stable provided the function $\omega^2(\kappa_x, \kappa_y)$ defined by relationship (5) is strictly positive. A change in the parameters of the model results in variations in function (5). This function can vanish at a point with coordinates (κ_x, κ_y), which gives rise to a soft mode represented by the expression

$$\begin{aligned}u_{m,n} &= Q_1\cos[2\pi(m\kappa_x+n\kappa_y)+\varphi_1]\\ &+Q_2\cos[2\pi(m\kappa_x-n\kappa_y)+\varphi_2].\end{aligned}\qquad(6)$$

In expression (6), at least one coefficient (Q_1 or Q_2) is nonzero. If the (κ_x, κ_y) point lies on one of the three high-symmetry axes $\mathbf{a}^*$, $\mathbf{b}^*$, or $\mathbf{b}^* - \mathbf{a}^*$ (Fig. 1b), expression (6) corresponds to the $1q$ modulated phase; otherwise, this expression can describe either the $1q$ phase or the $2q$ phase (depending on the coefficients Q_1 and Q_2). In the case where the structure described by expression (6) has the lowest energy at both nonzero coefficients Q_1 and Q_2, we deal with the $2q$ phase; however, the situation where one of these coefficients appears to be zero corresponds to the $1q$ modulated phase. If function (5) reduces to zero simultaneously at several points of the Brillouin zone, the displacements in the modulated phase are represented by a linear superposition of all the soft modes described by expression (6). For this superposition, the coefficients should be determined from the minimum condition of the potential energy.

Now, we specify the conditions at which function (5) becomes zero. It is evident that, when $\omega^2(\kappa_x, \kappa_y) = 0$, we have $\omega^2(-\kappa_x, -\kappa_y) = 0$. In the subsequent discussion, we will use only one of these points. Within this model, function (5) can vanish at any point of the Brillouin zone. However, we restrict our consideration to the following two special cases.

(i) $P_x = P_y = P$. This case was analyzed earlier by Parlinski *et al.* [17]. Note that the dispersion surface defined by function (5) has a sixfold symmetry. Hence, this surface can vanish simultaneously either at the points M_1, M_2, and M_3 or at the points Σ_1, Σ_2, and Σ_3 (Fig. 1b). More specifically, the surface vanishes at the points M_1, M_2, and M_3 under the conditions

$$F \le P/8,\quad 1-16P+256F = 0\qquad(7)$$

and at the points Σ_1, Σ_2, and Σ_3 under the conditions

$$F > P/8, \quad F = P^2/4. \tag{8}$$

(ii) $P_y > P_x$. The dispersion surface described by function (5) exhibits a twofold symmetry. Therefore, the dispersion surface vanishes either at the M_2 point when we have

$$F \le P_y/8, \quad 1 - 16P_y + 256F = 0 \tag{9}$$

or at the Σ_2 point when

$$F > P_y/8, \quad F = P_y^2/4. \tag{10}$$

The possible scenario of the $1q \longleftrightarrow 3q$ phase transition implies that function (5) becomes zero simultaneously at three points of the Brillouin zone. In this situation, the $3q$ phase represents a superposition of three $1q$ modes expressed in terms of Eq. (6). Let us now assume that the symmetry of the dispersion surface is lowered, for example, under a low applied uniaxial pressure. Consequently, function (5) first vanishes at one of the three points and there arises the $1q$ phase. However, upon subsequent changes in the external parameters, function (5) can reduce to zero at other points of the Brillouin zone; as a result, the $1q \longrightarrow 3q$ phase transition becomes possible.

3. DISCUSSION

First, we analyze the case where $P_x = P_y = P$. By setting $H = -0.01$, we ensure the fulfillment of the stability conditions of the $3q$ phase [17]. It is assumed that a point particle in the phase parameter space moves from the stability region of a trivial solution and intersects the parabola $F = P^2/4$ [see relationships (8)] at a point with coordinates defined by the expressions

$$P(\kappa) = \frac{1}{8}[\sin(\pi\kappa)]^{-2}, \quad F(\kappa) = \frac{P^2(\kappa)}{4}. \tag{11}$$

Then, function (5) reduces to zero simultaneously at three points, namely, $\kappa\mathbf{a}^*$, $\kappa\mathbf{b}^*$, and $\kappa(\mathbf{b}^* - \mathbf{a}^*)$ (points Σ_1, Σ_2, and Σ_3 in Fig. 1b), where $\kappa = M/N$ and $N > 2M$ (M and N are relatively prime positive integral numbers).

As an example, we consider the motion of a point particle in the phase space (P, F) along the line defined by the equality

$$P = \text{const} = P(\kappa). \tag{12}$$

Here, $P(\kappa)$ is determined from expression (11). We examine the case where κ is close to 1/2 or, more precisely, where κ is 20/41. This value of κ implies that the modulation wavelength is equal to 41 points. In our numerical simulation, we dealt with an 82 × 82-point network.

The trivial solution (normal phase) remains stable until the inequality $F > F(20/41)$ holds. At $F = F(20/41)$, the frequencies of vibrations become zero simultaneously at three points (namely, Σ_1, Σ_2, and Σ_3) of the Brillouin zone and a transition to the incommensurate phase takes place. The numerical analysis demonstrated that the $3q$ phase is formed in this case.

Let us now examine the $1q \longrightarrow 3q$ phase transition by assuming there to be a small deviation from the condition $P_x = P_y = P$; more precisely, we suppose that $P_x = P$ and $P_y = P + \varepsilon$, where ε is small compared to P and (for definiteness) positive. Physically, ε is a low uniaxial pressure applied together with hydrostatic pressure P. The symmetry of the dispersion surface is lowered under a low uniaxial pressure. Consequently, according to relationships (10), the dispersion surface reduces to zero at the Σ_2 point with the formation of the $1q$ incommensurate phase. Upon a further decrease in the elastic constant F, the frequencies of vibrations become zero at the Σ_1 and Σ_3 points of the Brillouin zone and there occurs a transition to the $3q$ incommensurate phase. Figure 2 illustrates the simulation of phase transitions in the framework of the EHM model with a decrease in the elastic constant F along the line defined by formula (12) and the kinetics of the $1q \longrightarrow 3q$ phase transition at $H = -0.01$ and $\varepsilon = 2 \times 10^{-5}$. We introduced the dissipative term into the equation of motion (3) in order to determine the equilibrium states of the model at different external parameters. The interval $[-u_{\max}, u_{\max}]$ (where $u_{\max}$ is the maximum magnitude of the displacement of point particles) was divided into five equal intervals, and each displacement of point particles was indicated by a particular symbol (large open circle, small open circle, closed circle, small cross, or large cross), depending on the interval in which the displacement of a given point particle takes place. The normal phase (trivial solution) and one period of the supercooled $1q$ incommensurate phase are presented in Figs. 2a and 2b, respectively. Then, the parameter F was instantaneously changed to the value $F = F(20/41) - 10^{-4}$. As a result, the $1q$ incommensurate phase became unstable and the $1q \longrightarrow 3q$ phase transition was initiated. Figures 2c and 2d display intermediate stages of the phase transition. Figure 2e shows one period of the stable $3q$ incommensurate phase with $\kappa = 20/41$, which was formed as a result of relaxation. A further decrease in the elastic constant F was attended by a transition from the $3q$ incommensurate phase to the $3q$ low-symmetry commensurate phase with $\kappa = 1/2$ (Fig. 2f). The possible mechanism of the last transition was discussed in our recent work [23].

The aforementioned results can shed light on the origin of the phenomenon observed experimentally by Abe *et al.* [10]. These authors demonstrated that, for quartz crystals, the temperature range of existence of the $1q$ incommensurate phase increases under external uniaxial pressure. In the framework of the two-dimensional EHM model, this finding can be explained by the fact that an increase in the external uniaxial pressure brings about an increase in the degree of distortion of the dispersion surface. In turn, this leads to an increase

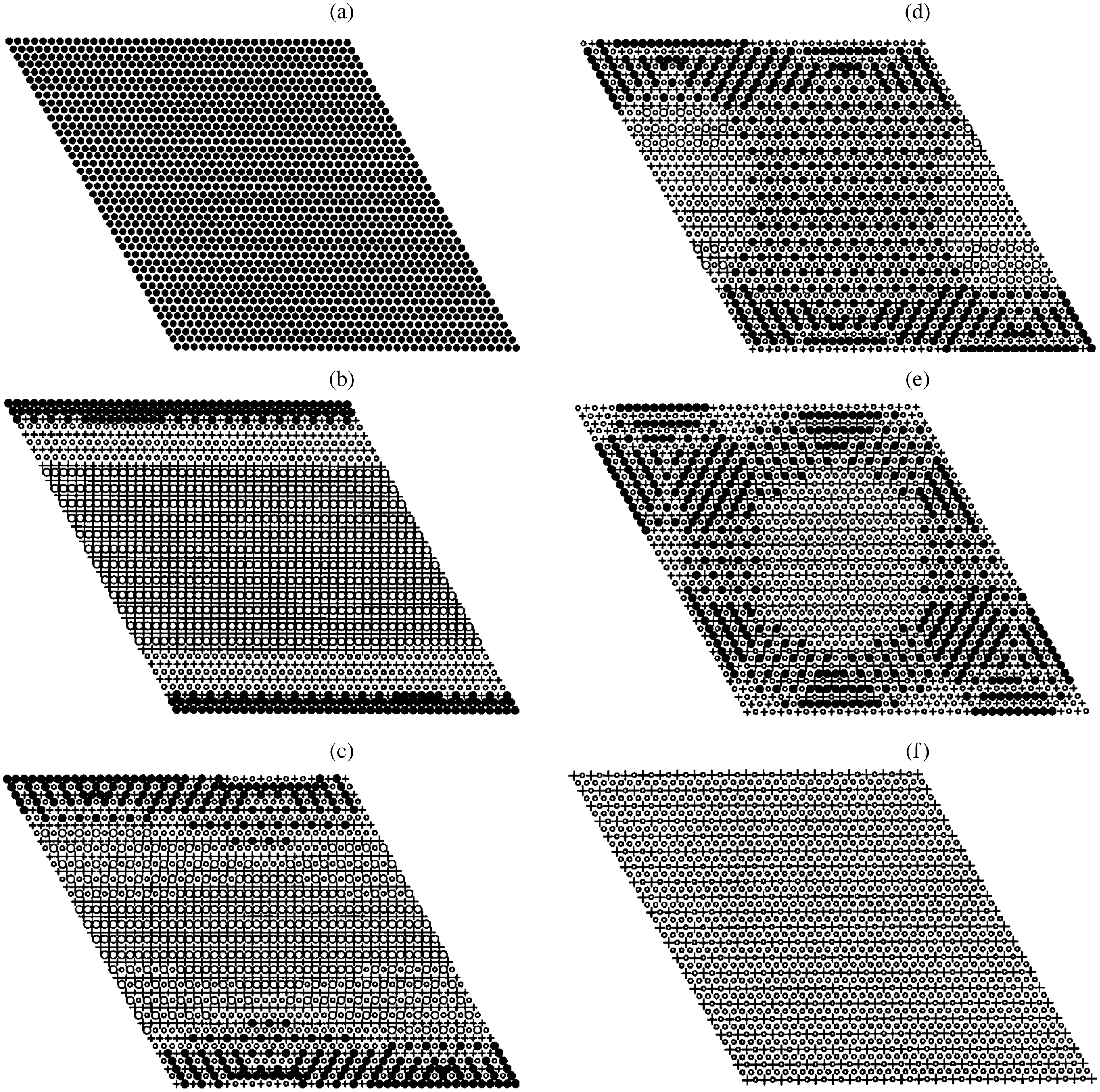

Fig. 2. Sequence of phase transformations observed in the framework of the EHM model with a decrease in the elastic constant F: (a) the normal phase (trivial solution), (b) the supercooled $1q$ incommensurate phase with $\kappa = 20/41$, (c, d) intermediate stages of the transition to the $3q$ phase, (e) the $3q$ incommensurate phase with $\kappa = 20/41$, and (f) the $3q$ low-symmetry commensurate phase with $\kappa = 1/2$.

in the phase path length at which the frequencies of vibrations become zero first at the Σ_2 point and then at the Σ_1 and Σ_3 points.

The case considered above corresponds to the condition $P_y > P_x$. Note that, in the case when $P_x > P_y$, the frequencies of vibrations reduce to zero first at the Σ_1 and Σ_3 points and then at the Σ_2 point. This means that our model can be applied to the simulation of the $2q \longrightarrow 3q$ phase transition.

4. CONCLUSIONS

Thus, the one-dimensional EHM model was extended to the two-dimensional case with hexagonal symmetry. This made it possible to elucidate the mechanism of the transition between the 1*q* and 3*q* incommensurate phases and to simulate its kinetics. Within the proposed model, the dispersion surface, under external hydrostatic pressure, can reduce to zero only at three points of the Brillouin zone simultaneously, which results in a transition from the normal phase to the 3*q* incommensurate phase. Under a low uniaxial pressure applied together with hydrostatic pressure, the symmetry of the dispersion surface is lowered. The frequencies of vibrations become zero first at one point and then at the other two points of the Brillouin zone due to slow variations in the external parameters. This behavior corresponds to a transition first from the normal phase to the 1*q* incommensurate phase and then from the 1*q* phase to the 3*q* incommensurate phase. Therefore, our model describes the sequence of phase transitions observed in quartz. Furthermore, this model offers an explanation of the increase in the temperature range of existence of the 1*q* phase in quartz with an increase in the applied uniaxial pressure.

ACKNOWLEDGMENTS

The author is grateful to A.A. Vasiliev (Tver State University, Russia) for his participation in discussions of the results and helpful remarks.

REFERENCES

1. *Incommensurate Phases in Dielectrics*, Ed. by R. Blinc and A. P. Levanyuk (North-Holland, Amsterdam, 1986), Vols. 14.1 and 14.2.
2. H. Z. Cummins, Phys. Rep. **185** (5–6), 211 (1990).
3. D. G. Sannikov and A. P. Levanyuk, Fiz. Tverd. Tela (Leningrad) **20** (4), 948 (1978) [Sov. Phys. Solid State **20**, 580 (1978)].
4. D. G. Sannikov and V. A. Golovko, Fiz. Tverd. Tela (Leningrad) **26** (4), 1117 (1984) [Sov. Phys. Solid State **26**, 678 (1984)].
5. J. M. Yeomans, in *Solid State Physics* (Academic, Orlando, 1988), Vol. 41.
6. W. Selke, in *Phase Transitions and Critical Phenomena*, Ed. by C. Domb and J. L. Lebowitz (Academic, New York, 1992), Vol. 15.
7. R. Currat and T. Janssen, in *Solid State Physics* (Academic, Orlando, 1988), Vol. 41.
8. T. Janssen and J. A. Tjon, Phys. Rev. B **25** (6), 3767 (1982).
9. G. Dolino, in *Incommensurate Phases in Dielectrics*, Ed. by R. Blinc and A. P. Levanyuk (North-Holland, Amsterdam, 1986), Vol. 14.2.
10. K. Abe, K. Kawasaki, K. Kowada, and T. Shigenari, J. Phys. Soc. Jpn. **60** (2), 404 (1991).
11. S. Barre, H. Mutka, C. Roucau, *et al.*, Phys. Rev. B **43** (13), 11154 (1991).
12. J. C. Toledano, J. Schneck, and G. Errandonea, in *Incommensurate Phases in Dielectrics*, Ed. by R. Blinc and A. P. Levanyuk (North-Holland, Amsterdam, 1986), Vol. 14.2.
13. Y. Yamada and N. Hamaya, J. Phys. Soc. Jpn. **52**, 3466 (1983).
14. K. Parlinski and G. Chapuis, Phys. Rev. B **47** (21), 13983 (1993).
15. K. Parlinski and G. Chapuis, Phys. Rev. B **49** (17), 11643 (1994).
16. K. Parlinski, Phys. Rev. B **48** (5), 3016 (1993).
17. K. Parlinski, S. Kwiecinski, and A. Urbanski, Phys. Rev. B **46** (9), 5110 (1992).
18. S. V. Dmitriev, T. Shigenari, and K. Abe, Phys. Rev. B **58** (5), 2513 (1998).
19. S. V. Dmitriev, K. Abe, and T. Shigenari, J. Phys. Soc. Jpn. **65** (12), 3938 (1996).
20. S. V. Dmitriev, T. Shigenari, A. A. Vasiliev, and K. Abe, Phys. Rev. B **55** (13), 8155 (1997); S. V. Dmitriev, T. Shigenari, and K. Abe, J. Phys. Soc. Jpn. **66** (9), 2732 (1997); T. Shigenari, A. A. Vasiliev, S. V. Dmitriev, and K. Abe, Ferroelectrics **203** (1/4), 335 (1997); S. V. Dmitriev, K. Abe, and T. Shigenari, Physica D (Amsterdam) **147** (1–2), 122 (2000).
21. J. J. M. Slot and T. Janssen, Physica D (Amsterdam) **32** (1), 27 (1988).
22. Y. Ishibashi, J. Phys. Soc. Jpn. **60** (1), 212 (1991).
23. S. V. Dmitriev, H. Jimbo, K. Abe, and T. Shigenari, Phys. Rev. E **64** (3), 036202 (2001).

Translated by O. Borovik-Romanova

Physics of the Solid State, Vol. 45, No. 2, 2003, pp. 358–363. Translated from Fizika Tverdogo Tela, Vol. 45, No. 2, 2003, pp. 339–344.
Original Russian Text Copyright © 2003 by Lyapilin, Bikkin.

LOW-DIMENSIONAL SYSTEMS AND SURFACE PHYSICS

Coulomb Drag of Conduction Electrons in Spatially Separated Two-Dimensional Layers: An Effective-Parameter Approximation

I. I. Lyapilin and Kh. M. Bikkin
Institute of Metal Physics, Ural Division, Russian Academy of Sciences,
ul. S. Kovalevskoĭ 18, Yekaterinburg, 620219 Russia
e-mail: Lyapilin@imp.uran.ru

Received February 12, 2002

Abstract—The Coulomb drag of electrons in spatially separated two-dimensional layers is considered under conditions of electron heating when the nonequilibrium distribution of electrons in the first layer can be described by macroparameters, such as the effective temperature. The nonequilibrium response is calculated using a projection operator that is an obvious generalization of the Mori operator to the case of nonequilibrium systems. *© 2003 MAIK "Nauka/Interperiodica".*

1. INTRODUCTION

Pogrebinskiĭ [1] and Price [2] showed that the electron–electron interaction between band charge carriers located in spatially separated two-dimensional layers should give rise to a response in the second system when the electric current I_1 is passed through the first system. The voltage V_2 induced in the second layer is proportional to the electric current I_1 and can be represented in the form

$$V_2 = \frac{R_d I_1 L}{W}. \tag{1}$$

Here, W and L are the parameters characterizing the width and length of the sample, respectively, and R_d is the transresistivity due to interlayer Coulomb interaction of charge carriers.

The experimental observation of the above phenomenon, which was called the Coulomb drag effect, became possible due to the considerable progress achieved in nanostructural technology. The Coulomb drag effect was investigated using both purely electron and electron–hole samples. It was demonstrated that, in the absence of a magnetic field, the transresistivity at low temperatures satisfies the relationship $R_d \sim T^2$. As is known, the Coulomb interaction is primarily responsible for the elastic properties and effects observed in two-dimensional systems. Moreover, this interaction immediately manifests itself in the Coulomb drag effect. Consequently, experimental investigations into the Coulomb drag effect have stimulated a large number of theoretical works dealing with different aspects of this effect (see review [3]).

In this paper, we consider the Coulomb drag effect under conditions of electron heating (in the hot electron approximation) when the nonequilibrium distribution of electrons in the first layer can be described by macroparameters, such as the effective temperature and drift velocity [4]. The nonequilibrium response is calculated with averaging over the quasi-equilibrium distribution with the effective electron temperature T_e. For this reason, even in the Born approximation of the scattering theory, the standard approach (within the formalism of Mori projection operators [5] or the Green's function method) has offered incorrect results [6]. In this respect, we will calculate the nonequilibrium response in terms of a projection operator that is an obvious generalization of the Mori operator [5] to the case of nonequilibrium systems.

2. GENERAL FORMALISM

Let us briefly formulate the theory of linear response of a nonequilibrium system to a weak measuring field. We assume that the nonequilibrium system described by the Hamiltonian H is affected by an additional weak field,

$$H_1(t) = -AF(t), \tag{2}$$

where A is an operator and $F(t)$ is the c-particle amplitude of the external field. In the nonequilibrium system, this perturbation gives rise to a new nonequilibrium state, which obviously cannot be described in terms of the initial set of basis operators.

The new nonequilibrium distribution $\rho(t)$ satisfies the Liouville equation, which can be represented in the following form:

$$\frac{\partial\rho(t,0)}{\partial t} + (iL + iL_1(t))\rho(t,0) = -\varepsilon(\rho(t,0) - \rho^0(t,0)),$$
$$\varepsilon \longrightarrow +0, \quad iLA = \frac{1}{i\hbar}[A, H], \tag{3}$$
$$iL_1(t)A = \frac{1}{i\hbar}[A, H_1(t)].$$

Here, $\rho^0(t)$ is the statistical operator specifying the initial nonequilibrium distribution of the system with the Hamiltonian H.

It is assumed that the initial condition for the distribution $\rho(t)$ is its coincidence with the initial nonequilibrium distribution $\rho^0(t)$ at an instant of time $t \longrightarrow -\infty$.

According to the Kubo theory, the nonequilibrium admittance corresponding to an arbitrary operator B can be written in the form

$$\chi_{BA}(t,\omega) = -\int_{-\infty}^{0} dt_1 e^{(\varepsilon - i\omega)t_1}$$
$$\times \frac{1}{i\hbar} SP\{B, e^{it_1L}[A, \rho^0(t + t_1, 0)]\}. \tag{4}$$

Using the identity

$$\varepsilon\int_{-\infty}^{0} dt_1 e^{\varepsilon t_1} e^{it_1L}[A, \rho^0(t + t_1, 0)]$$
$$= \int_{-\infty}^{0} dt_1 e^{\varepsilon t_1} e^{it_1L}[\dot{A}, \rho^0(t + t_1, 0)] - [A, \rho^0(t)] \tag{5}$$

($\dot{A} = (i\hbar)^{-1}[A, H]$) and introducing the definition of the correlation functions

$$\langle B, A\rangle = -\frac{1}{i\hbar}\int_{-\infty}^{0} dt_1 e^{\varepsilon t_1} SP\{Be^{it_1L}[A, \rho^0(t + t_1, 0)]\}, \tag{6}$$

$$\langle B, A\rangle^{\omega} = -\frac{1}{i\hbar}\int_{-\infty}^{0} dt_1 e^{(\varepsilon - i\omega)t_1}$$
$$\times \int_{-\infty}^{0} dt_2 e^{\varepsilon t_2} SP\{Be^{i(t_1 + t_2)L}[A, \rho^0(t + t_1 + t_2, 0)]\}, \tag{7}$$

we transform the expression for the admittance. After simple calculations, we obtain

$$\chi_{BA}(t,\omega) = \chi_{BA}(t,0)\frac{T_{BA}(t,\omega) + \varepsilon}{T_{BA}(t,\omega) + \varepsilon - i\omega}, \tag{8}$$

$$\chi_{BA}(t,0) = \langle B, A\rangle, \quad T_{BA} = \frac{1}{\langle B, A\rangle^{\omega}}\langle B, \dot{A}\rangle^{\omega}. \tag{9}$$

The transport matrix $T_{BA}(t, \omega)$ in the nonequilibrium case plays the same role as in the case of the response of an equilibrium system. The Green's function $G_{BA}(t, \omega)$ and the transport matrix $T_{BA}(t, \omega)$ are related by the expressions

$$G_{BA}(t,\omega)\{T_{BA}(t,\omega) + \varepsilon - i\omega\}^{-1}, \tag{10}$$

$$G_{BA}(t,\omega) = \frac{1}{\langle BA\rangle}\langle BA\rangle^{\omega}. \tag{11}$$

Within this approach, the problem involved in calculating the nonequilibrium admittance is reduced to the determination of the transport matrix or the Green's function, which, in turn, requires the use of the projection operators.

Let us introduce the operator Π projecting an arbitrary operator B on the basis set of operators P^+:

$$\Pi B^+ = P^+\frac{1}{\langle P, P^+\rangle}\langle P, B^+\rangle, \quad \Pi B = \langle B, P^+\rangle\frac{1}{\langle P, P^+\rangle}P,$$
$$\Pi P^+ = P^+, \quad Q = (1 - \Pi), \quad \Pi QP^+ = 0. \tag{12}$$

Next, we consider the identity

$$i(L - E)P^+(E) = P^+, \quad iE = i\omega - \varepsilon. \tag{13}$$

By alternating action on the left-hand and right-hand sides of this identity through the operators Π and Q, by making allowance for the identity $P^+(E) = \Pi P^+(E) + QP^+(E)$, and by taking into account that

$$\Pi P^+(E) = P^+G(t,\omega),$$
$$\Pi(-iE + QiL)^{-1}QiLP^+(E) = 0,$$

after simple transformations, we obtain the following equation for the Green's function:

$$G(t,\omega) = [R(t,\omega) + i\Omega(t,\omega) - iE]^{-1}, \tag{14}$$

where

$$i\Omega(t,\omega) = \frac{1}{\langle P, P^+\rangle}\langle P, \dot{P}^+\rangle, \tag{15}$$

$$R(t,\omega) = \frac{1}{\langle P, P^+\rangle}\langle Q\dot{P}, (-iE + QiL)^{-1}Q\dot{P}^+\rangle,$$
$$T(t,\omega) = R(t,\omega) + i\Omega(t,\omega). \tag{16}$$

Earlier, Kalashnikov [7] used a similar technique of projection with the Mori projection operator in order to prove the equivalence of the Mori method [5] and the linear version of the nonequilibrium statistical operator method.

Formulas (15) and (16) allow one to calculate the frequency matrix $T(t, \omega)$ and the memory function $R(t, \omega)$ in the case when the system is in a stationary nonequilibrium state and the statistical operator $\rho^0(t)$ is time independent or in the case of a periodic time dependence of the statistical operator.

3. CALCULATION OF THE COULOMB DRAG EFFECT

Let us now apply the above approach to the calculation of the Coulomb drag effect. We consider a two-dimensional system consisting of two spatially separated layers. In this system, the tunneling of carriers (electrons) between the layers is disregarded and the carrier concentrations are taken to be identical in both layers. Generalization to the case of different-type carriers with different concentrations does not present any problems.

The Hamiltonian of the system under consideration can be represented in the form

$$\begin{gathered} H = H_0 + H_{1F} + H_{12} + H_{eL}, \\ H_0 = H_1 + H_2 + H_L, \\ H_\lambda = \sum_j \frac{P_{\lambda j}^2}{2m}, \quad \lambda = 1, 2. \end{gathered} \tag{17}$$

Here, λ is the index of the layer, H_{1F} is the interaction of electrons of the first layer with the electric field,

$$H_{1F} = -e\sum X_{1j}^{\alpha} E^{\alpha}(t), \quad X_\lambda^\alpha = \sum_j X_{j\lambda}^\alpha,$$

e is the elementary charge, m is the electron mass, P_λ is the operator column vector composed of the components of the total electron momentum, X_j^α is the α projection of the coordinate of the jth electron, H_L is the Hamiltonian of the lattice, H_{eL} is the Hamiltonian of the interaction between electrons and the lattice, and H_{12} is the Hamiltonian of the interlayer Coulomb interaction of electrons,

$$H_{12} = \frac{1}{2}\sum_{\mathbf{k}, \mathbf{k}', \mathbf{q}} V(q) a^{+}_{\lambda, \mathbf{k}+\mathbf{q}} a^{+}_{\lambda', \mathbf{k}'-\mathbf{q}} a_{\lambda', \mathbf{k}} a_{\lambda, \mathbf{k}'}. \tag{18}$$

Here, $V(q)$ is the Fourier component of the interaction potential and $a^{+}_{\lambda, \mathbf{k}}$ and $a_{\lambda, \mathbf{k}}$ are the operators of production and annihilation of electrons, respectively, with the wave vector $\mathbf{k}$ in the band λ.

By assuming that the initial nonequilibrium state is stationary and by repeating the calculations performed in Section 2, we obtain

$$\rho_{12} = \frac{R_{12}}{\langle P_1 P_1\rangle \langle P_2 P_2\rangle}, \tag{19}$$

where

$$\begin{aligned} R_{12} &= \operatorname{Re}\int_{-\infty}^{0} dt_1 e^{\varepsilon t_1} \int_{-\infty}^{0} dt_2 e^{\varepsilon t_2} SP \\ &\times \left\{ Q\dot{P}_1 e^{i(t_1+t_2)L} \frac{1}{i\hbar}[Q\dot{P}_2 \rho^0] \right\}. \end{aligned} \tag{20}$$

Here, ρ^0 is the nonequilibrium statistical operator and iL is the Liouville evolution operator.

The above relationships have a general form and hold for any stationary nonequilibrium distribution.

Now, we specify a particular initial nonequilibrium distribution. This distribution is characterized by the following temperatures of the crystal subsystems: $\beta_1 = T_1^{-1}$ is the reciprocal temperature (expressed in energy units) of the kinetic degrees of freedom of conduction electrons in the first layer and $\beta = T^{-1}$ is the reciprocal (equilibrium) temperature of electrons in the second layer and lattice phonons. The nonequilibrium distribution can be specified by the quasi-equilibrium distribution

$$\begin{aligned} \rho_q &= \exp\{-S_0(t, 0)\} \\ &= \exp\{-\Phi - \beta_1 H_1 - \beta H_2 - \beta H_L\}, \\ \Phi &= \ln SP\{\exp(-\beta_1 H_1 - \beta H_2 - \beta H_L)\}. \end{aligned} \tag{21}$$

The Coulomb drag effect will be treated in the Born approximation. In this case, it will suffice to calculate the memory function in the second order with respect to the interlayer electron–electron interaction. Consequently, the nonequilibrium statistical operator $\rho^0(0)$ can be replaced by the quasi-equilibrium distribution (21), in which we disregarded the Hamiltonians describing the interaction of electrons with the scatterers. It is evident that the evolution operator should also be replaced by the evolution operator of noninteracting subsystems, $iL \longrightarrow iL_0$. Then, we take into account that

$$Q\dot{P}_\lambda = \dot{P}_{\lambda, V} + O(\dot{P}_{\lambda, V}), \quad \dot{P}_{\lambda, V} = \frac{1}{i\hbar}[P_\lambda, H_V].$$

With consideration taken of the aforementioned remarks, the expression for ρ_{12} can be written in the form

$$\rho_{12} = \frac{1}{n_1 n_2 m^2}\mathrm{Re}\int_{-\infty}^{0} dt_1 \int_{-\infty}^{0} dt_2 e^{\varepsilon(t_1+t_2)} SP$$

$$\times\left\{\dot{P}_1 e^{i(t_1+t_2)L_0}\frac{1}{i\hbar}[\dot{P}_2\rho_q]\right\}, \tag{22}$$

$$\dot{P}_\lambda = \frac{1}{i\hbar}[P_\lambda, H_{12}],$$

$$iL_0 A = \frac{1}{i\hbar}[A, H_1 + H_2 + H_L].$$

Here, we took into account that

$$\langle P_\lambda, P_\lambda^+\rangle = -n_\lambda m.$$

We now proceed to a step-by-step calculation of ρ_{12}. By using the explicit form of the interaction Hamiltonian H_{12}, we obtain the relationship

$$\dot{P}_{1,\,v} = i\frac{1}{2}\sum_{\mathbf{qk},\,\mathbf{k}'} V(q) q a^+_{1,\,\mathbf{k}-\mathbf{q}} a_{1,\,\mathbf{k}} a^+_{2,\,\mathbf{k}'+\mathbf{q}} a_{2,\,\mathbf{k}'}. \tag{23}$$

Next, we use the Kubo identity and obtain the equation

$$[\dot{P}_{2,\,v}, \rho_q]$$

$$= -\int_0^1 d\tau e^{-\tau S_0(t,\,0)}[\dot{P}_{2,\,v}, S_0(t,\,0)] e^{(\tau-1)S_0(t,\,0)}. \tag{24}$$

For the commutator under the integral, we derive the expression

$$[\dot{P}_{2,\,v}, S_0] = \frac{i}{2}\sum_{\mathbf{qk},\,\mathbf{k}'} V(q) q\{\beta_1(t)(\varepsilon_{1,\,\mathbf{k}-\mathbf{q}} - \varepsilon_{1,\,\mathbf{k}}) \tag{25}$$

$$+ \beta(\varepsilon_{2,\,\mathbf{k}'+\mathbf{q}} - \varepsilon_{2,\,\mathbf{k}'})\} a^+_{1,\,\mathbf{k}-\mathbf{q}} a_{1,\,\mathbf{k}} a^+_{2,\,\mathbf{k}'+\mathbf{q}} a_{2,\,\mathbf{k}'}.$$

After substituting expressions (23) and (25) into relationship (22) and averaging the Fermi operators according to the Wick theorem, we obtain the following relationship:

$$\rho_{12} = \frac{1}{4n_1 n_2 m^2}\mathrm{Re}\int_{-\infty}^{0} dt_1 e^{\varepsilon t_1}\int_{-\infty}^{0} dt_2 e^{\varepsilon t_2}$$

$$\times\sum_{\mathbf{k}',\,\mathbf{k},\,\mathbf{q}} q^2 V(q)^2 f(\varepsilon_{1,\,\mathbf{k}})(1 - f(\varepsilon_{1,\,\mathbf{k}-\mathbf{q}})) f(\varepsilon_{2,\,\mathbf{k}'}) \tag{26}$$

$$\times(1 - f(\varepsilon_{2,\,\mathbf{k}'+\mathbf{q}}))(e^{\beta_1(\varepsilon_{1,\,\mathbf{k}} - \varepsilon_{1,\,\mathbf{k}-\mathbf{q}}) + \beta(\varepsilon_{2,\,\mathbf{k}'} - \varepsilon_{2,\,\mathbf{k}'+\mathbf{q}})} - 1)$$

$$\times e^{i(t_1+t_2)(\varepsilon_{2,\,\mathbf{k}'+\mathbf{q}} - \varepsilon_{2,\,\mathbf{k}'} + \varepsilon_{1,\,\mathbf{k}-\mathbf{q}} - \varepsilon_{1,\,\mathbf{k}})}.$$

Here, $f(\varepsilon_{1,\,\mathbf{k}})$ and $f(\varepsilon_{2,\,\mathbf{k}})$ are the distribution functions of electrons in the first and second layers with the temperatures β_1^{-1} and β^{-1}, respectively.

By introducing the designations

$$f(\varepsilon_{1,\,\mathbf{k}}) \equiv f(\varepsilon_{\mathbf{k}}), \quad f(\varepsilon_{2,\,\mathbf{k}}) \equiv F(E_{\mathbf{k}})$$

and taking into account the result of integration with respect to time, we have

$$\rho_{12} = \frac{\pi\hbar}{4n_1 n_2 m^2}$$

$$\times\sum_{\mathbf{k}',\,\mathbf{k},\,\mathbf{q}} q^2 V(q)^2 f(\varepsilon_{\mathbf{k}})(1 - f(\varepsilon_{\mathbf{k}-\mathbf{q}}))F(E_{\mathbf{k}'}) \tag{27}$$

$$\times(1 - F(E_{\mathbf{k}'+\mathbf{q}}))\frac{\partial}{\partial\varepsilon_{\mathbf{k}}}\delta(\varepsilon_{\mathbf{k}'+\mathbf{q}} - \varepsilon_{\mathbf{k}'} + E_{\mathbf{k}-\mathbf{q}} - E_{\mathbf{k}}).$$

After integration by parts, we obtain the relationship

$$\rho_{12} = \frac{\pi\hbar}{4n_1 n_2 m^2}\sum_{\mathbf{k}',\,\mathbf{k},\,\mathbf{q}} q^2 V(q)^2 f'(\varepsilon_{\mathbf{k}})$$

$$\times[f(\varepsilon_{\mathbf{k}-\mathbf{q}})F(E_{\mathbf{k}'+\mathbf{q}})(1 - F(E_{\mathbf{k}'})) \tag{28}$$

$$+ (1 - f(\varepsilon_{\mathbf{k}-\mathbf{q}}))F(E_{\mathbf{k}})(1 - F(E_{\mathbf{k}'+\mathbf{q}}))]$$

$$\times\delta(\varepsilon_{\mathbf{k}'+\mathbf{q}} - \varepsilon_{\mathbf{k}'} + E_{\mathbf{k}-\mathbf{q}} - E_{\mathbf{k}}).$$

Here, $f'(\varepsilon_{\mathbf{k}})$ is the derivative of the nonequilibrium electron distribution function with respect to energy.

With due regard for the equalities

$$\delta(\varepsilon_1 + \varepsilon_2 - \varepsilon_{1'} - \varepsilon_{2'})$$

$$= \hbar\int_{-\infty}^{\infty} d\omega\,\delta(\varepsilon_1 + \varepsilon_{1'} - \hbar\omega)\delta(\varepsilon_2 - \varepsilon_{2'} + \hbar\omega), \tag{29}$$

$$f(\varepsilon)[1 - f(\varepsilon - \hbar\omega)]$$

$$= f(\varepsilon) - f(\varepsilon - \hbar\omega)(1 - e^{\beta\hbar\omega})^{-1}, \tag{30}$$

we rewrite the expression for β_{12} in the following form:

$$\rho_{12} = \frac{\pi\hbar^2}{4n_1 n_2 m^2}\sum_{\mathbf{k}',\,\mathbf{k},\,\mathbf{q}}\int_{-\infty}^{\infty} d\omega q^2 V(q)^2 f'(\varepsilon_{\mathbf{k}})$$

$$\times(F(E_{\mathbf{k}}) - F(E_{\mathbf{k}'+\mathbf{q}}))\left[\frac{f(\varepsilon_{\mathbf{k}-\mathbf{q}})}{e^{\Delta} - 1} - \frac{1 - f(\varepsilon_{\mathbf{k}-\mathbf{q}})}{1 - e^{-\Delta}}\right] \tag{31}$$

$$\times\delta(\varepsilon_{\mathbf{k}'-\mathbf{q}} - \varepsilon_{\mathbf{k}} + \hbar\omega)\delta(E_{\mathbf{k}'+\mathbf{q}} - E_{\mathbf{k}'} - \hbar\omega),$$

where $\Delta = \beta\hbar\omega$. Note that, in the equilibrium case ($\beta_1 = \beta$), expression (31) transforms into the corresponding formulas derived in [8].

Further calculations of ρ_{12} are reduced to calculation of the integrals. By changing over from the summation over **k**' to integration, we obtain

$$\sum_{\mathbf{k}'}[F(E_{\mathbf{k}'+\mathbf{q}}) - F(E_{\mathbf{k}'} + \hbar\omega)]\delta(E_{\mathbf{k}'+\mathbf{q}} - E_{\mathbf{k}'} - \hbar\omega)$$

$$= \frac{m^2\hbar\omega}{\hbar^4(2\pi)^2 q k_{\mathrm{F}}}\left[1 - \left(\frac{\omega}{q v_{\mathrm{F}}} - \frac{q}{2k_{\mathrm{F}}}\right)^2\right]^{-1/2}, \tag{32}$$

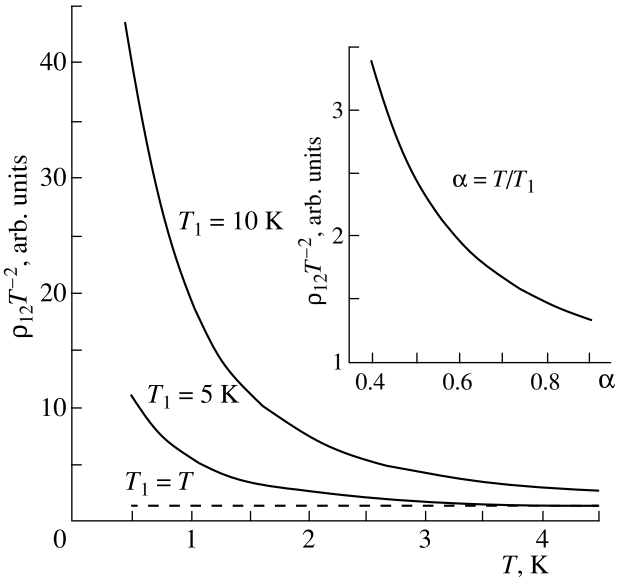

Temperature dependences of $\rho_{12}T^{-2}$ at different T_1. The inset shows the dependence of $\rho_{12}T^{-2}$ on the parameter α.

where k_F is the wave vector corresponding to the Fermi energy $\varepsilon_F = (\hbar k_F)^2/2m$.

After similar calculations for the first term in square brackets in relationship (31), we obtain the expression

$$\sum_{\mathbf{k}'} f'(\varepsilon_{\mathbf{k}}) f(\varepsilon_{\mathbf{k}-\mathbf{q}})\delta(\varepsilon_{\mathbf{k}-\mathbf{q}}-\varepsilon_{\mathbf{k}}+\hbar\omega) = \frac{m^2}{(2\pi)^2\hbar^3 q}\int_0^\infty d\varepsilon \frac{f'(\varepsilon)f(\varepsilon-\hbar\omega)}{(2m\varepsilon)^{1/2}} \quad (33)$$

$$\times\left\{1-\left[\frac{(2m\varepsilon)^{1/2}}{2\hbar q}+\frac{\hbar q}{2(2m\varepsilon)^{1/2}}-\frac{(\varepsilon+\hbar\omega)m}{\hbar q(2m\varepsilon)^{1/2}}\right]^2\right\}^{-1/2}.$$

Upon calculating the integral with respect to the energy for the degenerate electron statistics, we have

$$\sum_{\mathbf{k}'} f'(\varepsilon_{\mathbf{k}}) f(\varepsilon_{\mathbf{k}-\mathbf{q}})\delta(\varepsilon_{\mathbf{k}'-\mathbf{q}}-\varepsilon_{\mathbf{k}}+\hbar\omega)$$

$$= \frac{m^2 e^{\Delta_1}}{2\hbar^4 q(2\pi)^2 k_F\cosh(\Delta_1)}\left\{1-\left(\frac{\omega}{q v_F}-\frac{q}{2k_F}\right)^2\right\}^{-1/2}, \quad (34)$$

$$\Delta_1 = \frac{\beta_1\hbar\omega}{2}.$$

The integral with respect to the energy $\hbar\omega$ can be represented in the form

$$\int_0^\infty d\omega\,\omega\frac{\cosh((\beta_1-\beta)\hbar\omega/2)}{\cosh(\beta_1\hbar\omega/2)\sinh(\beta\hbar\omega/2)}. \quad (35)$$

By combining the intermediate results of calculations for ρ_{12}, we obtain

$$\rho_{12} = \frac{\pi T^2}{4\hbar(2\pi)^2 k_F^2\varepsilon_F^2}\int_0^\infty dq V^2(q)\left[1-\left(\frac{\omega}{q v_F}-\frac{q}{2k_F}\right)^2\right]^{-1}$$

$$\times\int_0^\infty dx x\frac{\cosh((\alpha-1)x)}{\cosh(\alpha x)\sinh(x)}, \quad \alpha = \beta_1/\beta. \quad (36)$$

In this expression, we took into account that $k_F^2 = 2\pi n_1$.

In order to calculate the other integral with respect to q, it is necessary to know the matrix element $V(q)$, which determines the interlayer Coulomb interaction of electrons. In the case when two-dimensional layers are treated as identical planes, we have the following expression [8]:

$$V(q) = \frac{2\pi e^2}{\kappa}$$

$$\times\frac{q}{2q_{TF}^2\sinh(qd)+(2qq_{TF}+q^2)\exp(qd)}, \quad (37)$$

where $q_{TF}^{-1} = \kappa\hbar/(2me^2)$ is the Thomas–Fermi screening length in the two-dimensional case, κ is the permittivity, and d is the interlayer distance.

The main contribution to the integral with respect to q is made by the region where $q \le d^{-1}$; however, since $d^{-1} \ll k_F$ and q_{TF}, the second term in the denominator of relationship (37) can be disregarded. In this case, the integration with respect to q is reduced to the integral

$$\int_0^\infty dx\frac{x^p}{4\sinh^2(x/2)} = p!\zeta(p). \quad (38)$$

Consequently, the expression for ρ_{12} can be represented in the form

$$\rho_{12} = \frac{\zeta(3)mT^2}{8\hbar\pi e^2(k_F d)^2(q_{TF}d)^2\varepsilon_F n_1}$$

$$\times\int_0^\infty x\frac{\cosh((\alpha-1)x)}{\cosh(\alpha x)\sinh(x)}dx. \quad (39)$$

In the absence of heating ($\beta_1 = \beta$), we obtain the same result as in [8].

Now, we determine the effective temperature β_1 responsible for the nonequilibrium distribution of electrons of the first layer. An expression for this temperature can be derived from the equations for the momentum and energy of electrons. Following the standard procedure [4, 9], the balance equations in the stationary case can be represented in the form

$$en_1\mathbf{E}\mathbf{V}_1 + \frac{\beta_1 - \beta}{\beta^2}C_e\tau_{1L}^{-1} = 0, \qquad (40)$$

$$en_1E^i - mn_1V_1^i\omega_{1L} = 0, \qquad (41)$$

where

$$\tau_{1L}^{-1} = \frac{\beta^2}{C_e}\int_{-\infty}^{0} dte^{\varepsilon t}(\dot{H}_{1(L)}; \dot{H}_{1(L)}(t))$$

is the reciprocal time of relaxation of the electron energy, C_e is the heat capacity, and

$$\omega_{1L} = \frac{\beta}{3mn_1}\int_{-\infty}^{0} dte^{\varepsilon t}(\dot{P}_{1(L)}; \dot{P}_{1(L)}^k(t))$$

is the frequency of relaxation of the momentum. In this case, we have

$$\dot{A}_{1(L)} = \frac{1}{i\hbar}[A_{1(L)}, H_{eL}],$$

$$(P^i; P^k) = \int_0^1 d\tau\langle P^i; \Delta P^k(i\tau)\rangle,$$

$$P_i(i\tau) = e^{-\tau H_0}P_ie^{\tau H_0}, \quad \langle\ldots\rangle = \mathrm{Sp}(\ldots\rho_0).$$

From expressions (40) and (41), we can determine the effective temperature

$$\beta_1^{-1} = \beta^{-1}\left(1 + \frac{\beta n_1e^2E^2}{mC_e}\tau_{1L}\omega_{1L}^{-1}\right). \qquad (42)$$

It follows from relationship (42) that the relative shift in the electron temperature is determined by both the momentum relaxation time and the energy relaxation time. Expressions (39) and (42) adequately describe the Coulomb electron drag in the case of carrier heating by an electric field in the first layer.

The dependence of ρ_{12} on the effective temperature T_1 is shown in the figure. As follows from the above calculations, the carrier heating leads to a considerable increase in the Coulomb electron drag at low temperatures.

REFERENCES

1. M. V. Pogrebinskiĭ, Fiz. Tekh. Poluprovodn. (Leningrad) **11**, 637 (1977) [Sov. Phys. Semicond. **11**, 372 (1977)].
2. P. J. Price, Physica B (Amsterdam) **117**, 750 (1983).
3. A. G. Rojo, J. Phys.: Condens. Matter **11**, R31 (1999).
4. V. P. Kalashnikov, Physica (Amsterdam) **48**, 93 (1970).
5. H. Mori, Prog. Theor. Phys. **33**, 423 (1965); Prog. Theor. Phys. **34**, 399 (1965).
6. L. L. Licea, Physica (Amsterdam) **63**, 172 (1973).
7. V. P. Kalashnikov, Teor. Mat. Fiz. **34**, 412 (1978).
8. Antti-Pekka Jauho and H. Smith, Phys. Rev. B **47**, 4420 (1993).
9. D. Y. Xing, P. Hu, and C. S. Ting, Phys. Rev. B **35**, 6379 (1987).

Translated by O. Moskalev

Physics of the Solid State, Vol. 45, No. 2, 2003, pp. 364–368. Translated from Fizika Tverdogo Tela, Vol. 45, No. 2, 2003, pp. 345–348.
Original Russian Text Copyright © 2003 by Lozovik, Volkov.

LOW-DIMENSIONAL SYSTEMS AND SURFACE PHYSICS

Control of Electron Correlations in a Spherical Quantum Dot

Yu. E. Lozovik and S. Yu. Volkov
Institute of Spectroscopy, Russian Academy of Sciences, Troitsk, Moscow oblast, 142092 Russia
e-mail: lozovik@isan.msk.su

Received February 7, 2002

Abstract—Spherical quantum dots containing several electrons are considered for different values of the total spin. Numerical calculations are carried out using the quantum path-integral Monte Carlo method. The dependence of the electron correlations on the dimensionless control quantum parameter q associated with the steepness of the confinement potential is studied. The quantum transition from a Wigner crystal-like state (i.e., from the regime of strongly correlated electrons) to a Fermi-liquid state (“cold” melting) driven by the parameter q is studied in detail. The behavior of the radial and pair correlation functions, which characterize quantum delocalization of the electrons, is considered. *© 2003 MAIK “Nauka/Interperiodica”.*

1. INTRODUCTION

The properties of electron systems in quantum dots are of great interest, especially in the regime of strong electron correlations [1–5]. This regime takes place at low densities of the electron system, which can be achieved by changing the steepness of the potential, for example, with the use of a controlling gate [6] or by means of a perpendicular magnetic field [7, 8]. This feature distinguishes quantum dots (giant artificial atoms) from natural atoms with rather weakly correlated electrons (in all natural atoms, the correlation energy is always smaller than the Hartree–Fock energy). For this reason, a detailed study of the characteristics of quantum dots in a wide range of values of the quantum parameter controlling the electron correlation is of great importance. In particular, it is very important to investigate the electron crystallization and quantum “cold” melting.

The behavior of an extended electron system in a random potential caused by impurities or interface roughness is also an interesting aspect of this problem. In this case, a sufficiently rarefied electron system is broken up into clusters located in the vicinity of the minima of the random potential. Thus, an analysis of the behavior of the electron system in an isolated quantum dot gives an idea of the short-range order in the disordered electron system and of changes in this order with an increase in the quantum parameter.[1]

In this paper, a system of several electrons in a spherical quantum dot with the parabolic confinement potential $\alpha \mathbf{r}^2$ is studied in detail. At low temperatures, all properties of the system depend only on the dimensionless quantum parameter q related to the steepness of the confinement potential. We study the dependence of the properties of a spherical quantum dot containing several electrons on q and the total spin of the system. We use the *ab initio* quantum path-integral Monte Carlo method for fermions.

If the parameter q is small, the characteristic quantum kinetic energy is also small; the electron system becomes strongly correlated and, in the limit of small q, forms a crystal-like, nearly classical electron cluster [1–4]. At larger values of q, the crystal structure is smeared due to quantum zero-point oscillations and the cluster undergoes a quantum (cold) transition into a Fermi-liquid phase. Finally, at large values of the quantum parameter, the dynamic correlations in the electron system become as small as those in natural atoms.

We study a number of characteristics of a system of several electrons in a quantum dot (such as radial and pair correlation functions, total and exchange energies, average distance between the particles) and analyze the effect of the Fermi statistics on these characteristics.

2. MODEL OF A QUANTUM DOT

Let us consider a system of Coulomb particles in a three-dimensional parabolic confinement potential as a model of a spherical quantum dot. Such a potential adequately describes real quantum dots with a small number of electrons. The Hamiltonian of the system is

$$H = -\sum_{i=1}^{N}\frac{\hbar^2}{2m}\nabla_i^2 + \sum_{i=1}^{N}\frac{m\omega^2}{2}r_i^2 + \sum_{i<j}^{N}\frac{\varepsilon^2}{\varepsilon|r_i - r_j|}.$$

---

[1] For extended systems, the quantum parameter q is related to the dimensionless parameter r_s characterizing the average distance between the electrons in units of the electron Bohr radius: $(4\pi/3)r_s^3 a_0^3 = 1/n$, where $a_0 = \hbar^2\varepsilon/(m^*e^2)$ is the effective Bohr radius and n is the electron density.

1063-7834/03/4502-0364$24.00 © 2003 MAIK “Nauka/Interperiodica”

In what follows, we use the dimensionless length, energy, and temperature: $r' = r/r_0$, $E' = E/E_0$, and $T' = T/E_0$, where $r_0 = (2e^2\varepsilon/m\omega^2)^{1/3}$ and $E_0 = e^2/\varepsilon r_0 = m\omega^2 r_0^2/2$. In terms of these dimensionless variables, the Hamiltonian takes the form

$$H = -\sum_i^N q\nabla_i^2 + \sum_i^N r_i^2 + \sum_{i<j}^N \frac{1}{r_{ij}},$$

where $q = (\hbar^2/2m)(m\omega^2\varepsilon^4/2e^8)^{1/3}$ is the dimensionless quantum parameter of the system. This parameter can be expressed as the ratio of the effective Bohr radius a_0^* associated with the effective interaction between the charges to the single-particle length $l = (\hbar/m^*\omega)^{1/2}$ (the characteristic size of the wave function of one electron in the parabolic confinement potential): $q = (a_B^*/2l)^{4/3}$.

Below, we study the behavior of the system in relation to the dimensionless parameter q. Experimentally, this parameter can be controlled by varying the value of the confinement potential with the help of a controlling gate.

3. CALCULATED QUANTITIES

We calculated the following characteristics of the system under consideration: the radial distribution of the particles

$$\rho(r) = \sum_i^N \frac{\delta(r_i - r)}{4\pi r^2 \Delta r};$$

the pair correlation function

$$f(r) = \sum_{i<j}^N \frac{\delta(r_{ij} - r)}{4\pi r^2 \Delta r};$$

the total energy of the system

$$E = \frac{3}{2}NMT + \frac{1}{M}\sum_{i,m}\left(-\frac{(r_i^m - r_i^{m-1})^2}{4q\tau^2} + \frac{1}{2}(r_i^m)^2\right) + \frac{1}{M}\sum_{i<j,m}\frac{1}{|r_i^m - r_j^m|},$$

where $\tau = 1/MT$ is the step of integration with respect to the reciprocal temperature; the widths at half-maximum for all distributions; the average number of particles $\langle N\rangle$ involved in permutation (see below); and the average interparticle distance $\langle a\rangle$.

We studied the dependence of these quantities on the quantum parameter q at a low temperature kept constant in oscillator units and equal to $T = 0.3\hbar\omega$.

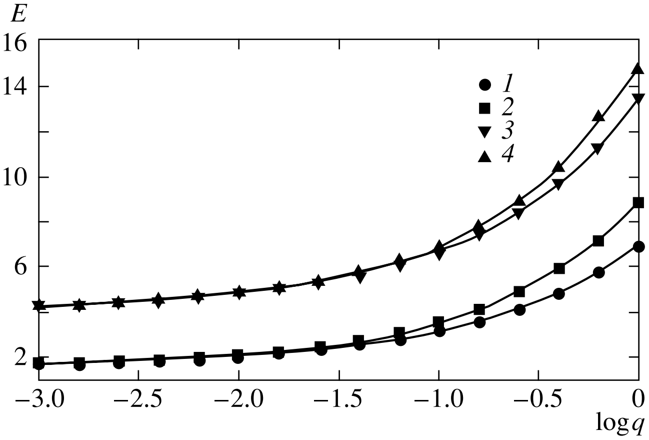

Fig. 1. Total energy of the system as a function of the quantum parameter q. (*1*, *2*) $N = 2$ and (*3*, *4*) 3; (*1*) $S = 0$, (*2*) 1, (*3*) 1/2, and (*4*) 3/2.

Averaging over the Monte Carlo steps was carried out in the following way:

$$\langle A\rangle = (1/N_{\text{eff}})\sum p_i A_i$$

$$A_i = \int\ldots\int dR_0 dR_1 \ldots dR_{M-1}\langle R_0|A|R_M\rangle \exp\left(-\sum_{m=1}^M S^m\right),$$

where p_i is the permutation parity, $p_0 = 1$, and $N_{\text{eff}} = \sum p_i$ is the effective length of a Markov chain. Each permutation of a pair of Fermi particles with the same spin changes the sign of p_i.

4. DISCUSSION

The dependences of the total and exchange energies on the quantum parameter q, as well as the q dependences of the radial distributions and the positions and widths of the maxima of the radial and pair correlation functions characterizing the electron correlation (and, in particular, electron crystallization) in the quantum dot, are shown in the figures. We also illustrate the electron localization in the quantum dot by projecting a bunch of Feynman paths (in imaginary time) in three-dimensional space onto the plane in which the electrons are localized in the classical limit $q = 0$.

We use the following notation: the state with $N = 3$ and $S = 1/2$ corresponds to a three-electron system with the total spin 1/2, etc. Since we neglect the spin–orbit interaction, the total spin of the system defines only the symmetry of the coordinate wave function. In the absence of an external magnetic field, the system is degenerate due to spin. Thus, the states corresponding to different spin components are described by the same coordinate wave functions. In the limit $q \longrightarrow 0$, the system under consideration is equivalent to a classical three-dimensional Thomson atom [1, 4]. For a classical two-electron system in an equilibrium state, the average

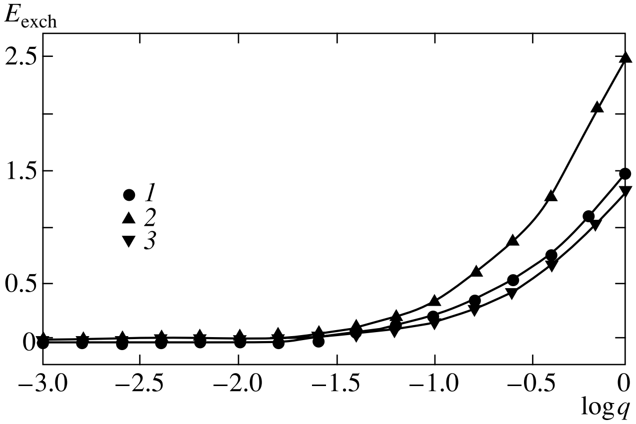

Fig. 2. Exchange energy E_{exch} as a function of the quantum parameter q. (*1*) $N = 2$ and (*2*, *3*) 3; (*1*) $S = 1$, (*2*) 1/2, and (*3*) 3/2.

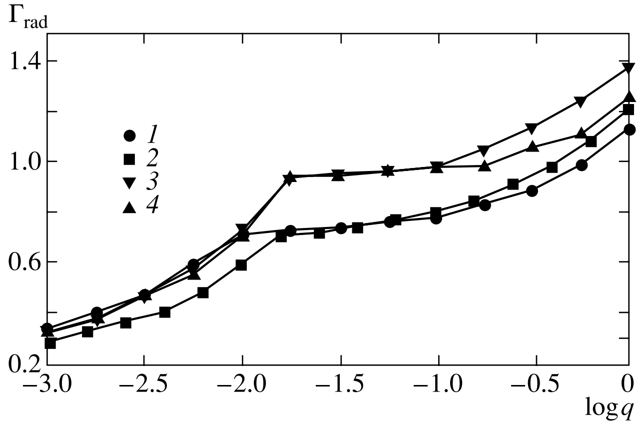

Fig. 3. Width of the radial distribution Γ_{rad} as a function of q. (*1*, *2*) $N = 2$ and (*3*, *4*) 3; (*1*) $S = 0$, (*2*) 1, (*3*) 1/2, and (*4*) 3/2.

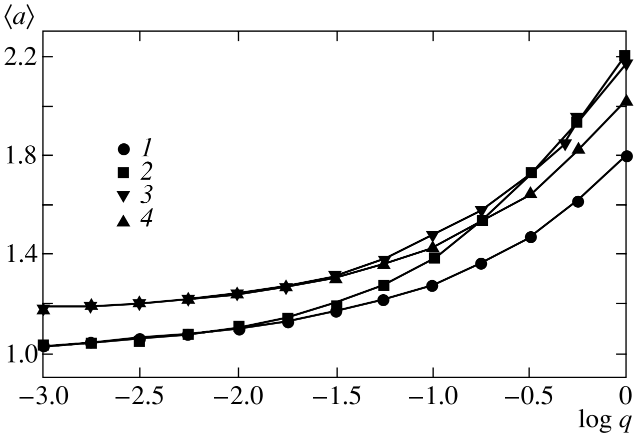

Fig. 4. Average interparticle distance ⟨a⟩ as a function of log$q$. (*1*, *2*) $N = 2$ and (*3*, *4*) 3; (*1*) $S = 0$, (*2*) 1, (*3*) 1/2, and (*4*) 3/2.

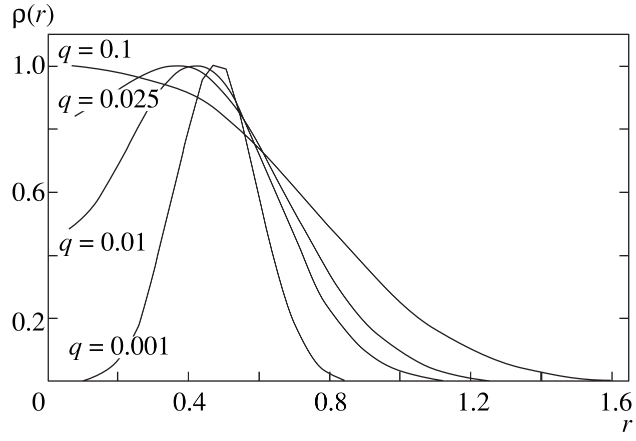

Fig. 5. Evolution of the radial distribution with increasing quantum parameter q. $S = 1$ and $N = 2$.

distance between the particles is ⟨a⟩ = 1 and the total potential is $V = 3/2$; a classical three-electron system forms an equilateral triangle with ⟨a⟩ $= (3/2)^{1/3} \approx 1.445$ and $V \approx 3.93$ in an equilibrium state. At sufficiently small values of q, the results of our calculations are in good agreement with these classical values.

We investigated the system for the values of the quantum parameter q lying in the range 10^{-3} to 1.

The total energy of the two- or three-electron system monotonically increases with the quantum parameter. The states with $S = 0$ and 1/2 are energetically favorable in the investigated range of values of the quantum parameter for two and three electrons to within the limits of error (Fig. 1). The exchange energy, determined as the difference between the total energies of the Fermi system and of the “Boltzmann” system of nonidentical particles in the same confinement potential, monotonically increases with q (Fig. 2).

It turned out that the Fermi statistics begins to affect the behavior of two particles at log$q \approx -1.25$. At this value of q, the exchange energy, which is closely related to the statistics, starts to increase significantly as a function of q (Fig. 2). The influence of the Fermi statistics can also be seen from the q dependence of the average number of particles ⟨N⟩ involved in permutations. This quantity starts to rise sharply at almost the same value of q as the exchange energy. For three electrons, the Fermi statistics becomes significant at $q \approx$ 1.75.

As the quantum parameter q increases, the system undergoes a quantum transition (crossover) from the crystal structure to a delocalized Fermi-liquid state. The position of the transition range is determined by the

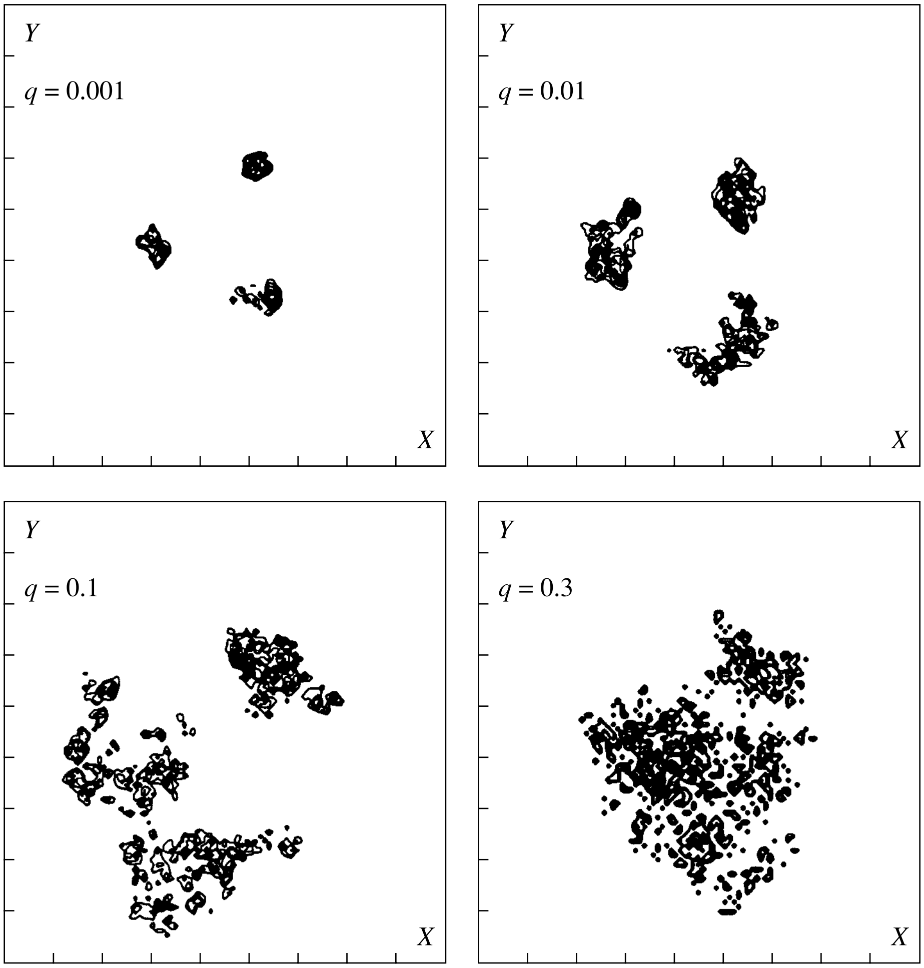

Fig. 6. Projections of the trajectories traced out by electrons with increasing imaginary time for different values of q.

condition $\langle a \rangle \approx 2\Gamma_{\rm rad}$, where a is the average distance between the particles and $\Gamma_{\rm rad}$ is the width of the electron distribution (Fig. 3). The average distance between the particles starts to increase monotonically (from its classical value) as the quantum parameter q increases. The additional statistical repulsion (due to the exclusion principle) results in the following regularity: the larger the total spin of the state, the more rapidly the average distance between electrons increases with q (Fig. 4).

It is of interest to analyze the evolution of the radial distribution for the case when the system undergoes the crossover from strong to weak correlations (Fig. 5). For convenience, we normalized the radial distribution such that its maximum was equal to unity. At small values of q, this distribution is narrow and its value is zero at $r = 0$. Thus, the electrons are strongly localized at small values of q and form a crystal-like structure. With increasing q, the width of the distribution increases. At $\log q = -1.0$, this distribution becomes sufficiently wide in comparison with the initial distribution; the maximum is at $r = 0$. Thus, as q increases, quantum melting occurs and the electrons are smeared over the quantum dot (Fig. 6). The quantum delocalization of the electrons also manifests itself in the widths of the pair correlation functions increasing monotonically for the two- and three-electron systems.

5. CONCLUSIONS

Thus, the main results of the work are the following.

(1) The states with $S = 0$ and 1/2 are energetically favorable for three-dimensional quantum dots with two and three electrons, respectively.

(2) It has been found that with increasing control quantum parameter, the electron system in a spherical quantum dot undergoes a transition from a crystal state (of strongly correlated electrons) to a disordered delocalized state (Fermi liquid); i.e., so-called quantum (cold) melting occurs.

ACKNOWLEDGMENTS

This work was supported by the Russian Foundation for Basic Research, INTAS, and the program “Physics of Solid-State Nanostructures.”

REFERENCES

1. A. V. Filinov, Yu. E. Lozovik, and M. Bonitz, Phys. Rev. Lett. **87** (21), 216804 (2001); Yu. E. Lozovik, Usp. Fiz. Nauk **153**, 356 (1987) [Sov. Phys.–Usp. **30**, 912 (1987)].
2. B. Reusch, W. Hausler, and H. Grabert, Phys. Rev. B **63** (11), 113313 (2001); R. Egger, W. Hausler, C. H. Mak, and H. Grabert, Phys. Rev. Lett. **82** (16), 3320 (1998).
3. C. Yannouleas and U. Landman, Phys. Rev. Lett. **85** (8), 1726 (2000); C. Yannouleas, Phys. Rev. B **61** (23), 15895 (2000).
4. Yu. E. Lozovik and V. A. Mandelshtam, Phys. Lett. A **145**, 269 (1991); Yu. E. Lozovik and E. A. Rakoch, Phys. Lett. A **235**, 55 (1997).
5. N. A. Bruce and P. A. Maksym, Phys. Rev. B **61** (7), 4718 (2000).
6. R. C. Ashoori, Nature **379**, 413 (1996).
7. Yu. E. Lozovik and V. I. Yudson, Pis’ma Zh. Éksp. Teor. Fiz. **22**, 551 (1975) [JETP Lett. **22**, 274 (1975)].
8. D. M. Ceperley, Rev. Mod. Phys. **67** (2), 279 (1995).

Translated by A. Poushnov

Physics of the Solid State, Vol. 45, No. 2, 2003, pp. 369–380. Translated from Fizika Tverdogo Tela, Vol. 45, No. 2, 2003, pp. 349–358.
Original Russian Text Copyright © 2003 by Bulaev, Margulis.

LOW-DIMENSIONAL SYSTEMS AND SURFACE PHYSICS

Electrodynamic Response of a Nanosphere Placed in a Magnetic Field

D. V. Bulaev and V. A. Margulis

Mordovian State University, ul. Bol'shevistskaya 68, Saransk, 430000 Russia
e-mail: theorphysics@mrsu.ru

Received May 22, 2002

Abstract—Absorption of electromagnetic radiation by 2D electrons at the surface of a quantum sphere placed in a weak magnetic field is studied. It is shown that at low temperatures, the absorption curve exhibits four resonance peaks observed in the Faraday geometry (photon wave vector parallel to the magnetic field) and six peaks in the Voigt geometry (photon wave vector perpendicular to the magnetic field). In the particular case of the Voigt geometry, where the photon polarization vector is parallel to the magnetic field, the absorption curve exhibits only two resonance peaks. The shape, position, and intensity of the peaks are examined. It is shown that at temperatures close to zero, steps of two types appear in the absorption curve. One type of steps is associated with crossing of the $\mu - \hbar\omega$ level by the electron energy levels, while steps of the other type arise when electron energy levels cross the chemical potential μ. © *2003 MAIK "Nauka/Interperiodica".*

1. INTRODUCTION

Considerable attention has been given recently to the production and study of spherical nanostructures [1–3], which is primarily due to the fact that optical and electronic devices of a new generation can be developed on their basis. Spherical nanostructures exhibit interesting spectral [4] and optical properties [5–7]. It has been shown [5–8] that the optical absorption of such structures can be adequately described in terms of the classical theory. It is worth noting that the spectral and other properties of a nanostructure essentially depend on its shape and size [9]. On the basis of spherical nanostructures, photonic crystals can be fabricated to possess a photonic band gap [10–12].

Quite recent advances in nanotechnology have provided a way of producing a dielectric nanosphere covered with a thin metallic or semiconducting layer. There are a few original techniques for fabricating such nanostructures. For example, Hines and Guyot-Sionnest [13] prepared crystals from nanospheres, each of which consisted of a CdSe core covered with a ZnS shell. Spherical nanoshell structures can also be produced by mixing $HAuCl_4$ and Na_2S aqueous solutions, with the resulting formation of spherical dielectric Au_2S cores covered with Au shells [14–17]. The sizes of spheres thus obtained are a few tens of nanometers. The electromagnetic-radiation absorption spectra of media containing such nanoshell structures were measured experimentally, and it was found that, in the optical range of these spectra, there was a resonance peak corresponding to nanoshell structures [14, 15]. In terms of the classical theory, it was shown in [8] that this peak is due to electron plasma resonance in the system. The position and intensity of this absorption peak were found to depend on the thickness of the metallic shell and on the diameter of the dielectric core [14, 15]. The shell can significantly enhance the nonlinear optical response of the nanostructure [18–20]. The study of optical properties of nanoshell structures provides important information on the growth kinetics of these nanostructures [15] and allows one to determine such parameters as the electron relaxation time and the electron–phonon coupling constant [14]. It should be noted that if the metallic or semiconducting shell is a few atomic-layers thick, quantum effects in the properties of the system become significant. In this case, the classical theory is inadequate to describe the properties of such nanostructures [14].

The objective of this paper is to investigate optical transitions of 2D electrons at the surface of a nanosphere placed in a weak uniform magnetic field. We note that the study of optical transitions is a powerful method for determining the parameters of the energy spectrum and the Fermi surface of electrons [21–25]. The model of an electron gas at a spherical surface is widely used to investigate the spectral [26, 27], magnetic [28–31], and transport [32] properties of spherical and spheroidal nanostructures and the effect of the electron–electron [33] and spin–orbit interactions [34] on the spectral properties of electrons in spherical systems. This model has been used, in particular, to study the electromagnetic-radiation absorption by a nanosphere in the absence of a magnetic field [35]. The model of an electron gas at a spherical surface is applicable for investigating a nanoshell structure in the case where the shell thickness is much smaller than the dimensions of the structure.

1063-7834/03/4502-0369$24.00 © 2003 MAIK "Nauka/Interperiodica"

2. ELECTRON TRANSITIONS INDUCED BY ELECTROMAGNETIC RADIATION

We consider a system of noninteracting electrons at the surface of a nanosphere placed in a weak uniform magnetic field. The Schrödinger equation for this system can be reduced to the differential equation

$$(1-\eta^2)f''(\eta) - 2\eta f'(\eta)$$
$$+\left[A - C^2(1-\eta^2) - \frac{m^2}{1-\eta^2}\right]f(\eta) = 0,$$
$$\eta \in [-1, 1],$$

where $A = (2m^*R^2/\hbar^2)(E - \hbar\omega_c m/2)$, $C = m^*\omega_c R^2/2\hbar$, m is the magnetic quantum number, E is the electron energy, R is the nanosphere radius, and m^* is the effective mass of an electron. The electron wave function is represented in the form $\psi(\varphi, \vartheta) = e^{im\varphi}f(\cos\vartheta)$. Solutions to this differential equation are the angular prolate-spheroidal functions $S_{ml}(C, \eta)$ [36]. In the case of a weak magnetic field, the term quadratic in a magnetic field can be dropped in the Hamiltonian. The spectral problem for the Hamiltonian in this approximation can easily be solved [28]:

$$\psi_{l,m}(\vartheta, \varphi) = Y_{l,m}(\vartheta, \varphi),$$
$$E_{l,m} = \frac{\hbar\Omega}{2}l(l+1) + \frac{\hbar\omega_c}{2}m, \quad (1)$$

where l is the orbital quantum number, $\Omega = \hbar/m^*R^2$, and $Y_{l,m}(\vartheta, \varphi)$ are the spherical harmonics. Note that the energy level splitting for electrons at the nanosphere in a magnetic field is similar to the Zeeman effect for an atom. Equations (1) are valid if the following inequality is satisfied:

$$B \ll 4c\hbar/|e|R^2. \quad (2)$$

By treating the interaction of electrons with a high-frequency electromagnetic field as a perturbation and using a conventional method [37], we can calculate the electromagnetic-radiation absorption of the nanosphere. For a degenerate electron gas, the absorption is found to be

$$\Gamma = \frac{\sqrt{\varepsilon(\omega)}}{2c\hbar R^2 N_{\mathbf{k}}}(1 - e^{-\hbar\omega/T})$$
$$\times \sum_{l,m}\sum_{l',m'} f_0(E_{l,m})[1 - f_0(E_{l,m} + \hbar\omega)] \quad (3)$$
$$\times |\langle l', m', -\mathbf{k}|H_R|l, m, 0\rangle|^2 \delta(E_{l,m} - E_{l',m'} + \hbar\omega),$$

where $\varepsilon(\omega)$ is the real part of the dielectric constant (there is assumed to be no dispersion in the frequency range in question), $N_{\mathbf{k}}$ is the concentration of incident photons of frequency ω, $\mathbf{k}$ is the wave vector of a photon incident on the nanosphere, $f_0(E_{l,m})$ is the electron distribution function, and the factor $[1 - \exp(-\hbar\omega/T)]$ accounts for the induced photon emission. The electron–photon interaction operator has the form

$$H_R = \frac{|e|}{m^*}\sqrt{\frac{2\pi\hbar N_{\mathbf{k}}}{\varepsilon(\omega)\omega}}\mathbf{e_k}\left(\mathbf{p} + \frac{|e|}{c}\mathbf{A}\right),$$

where $\mathbf{A}$ is the vector potential of the uniform magnetic field and $\mathbf{e_k}$ is the photon polarization vector.

In calculating the matrix elements of the operator H_R, the electromagnetic field is considered to be uniform, since the photon wavelength is much larger than the nanosphere radius.

We restrict our consideration to the case of a linearly polarized electromagnetic wave. The z axis is taken to be along the direction of the uniform magnetic field $\mathbf{B}$, and the x axis is chosen such that the photon polarization vector lies in the xz plane: $\mathbf{e_k} = (\sin\alpha, 0, \cos\alpha)$, where α is the angle between the photon polarization vector and the magnetic field. We consider two configurations that differ in symmetry: the Faraday geometry, in which the photon wave vector is parallel to the uniform magnetic field ($\mathbf{k} \parallel \mathbf{B}$) and, hence, $\mathbf{e_k} = (1, 0, 0)$, and the Voigt geometry, in which the photon wave vector is perpendicular to the magnetic field ($\mathbf{k} \perp \mathbf{B}$). In the latter case, the photon polarization vector can be arbitrarily oriented relative to the magnetic field, $\mathbf{e_k} = (\sin\alpha, 0, \cos\alpha)$.

In the Faraday geometry and in the symmetric gauge chosen for the vector potential of the magnetic field, we have $\mathbf{e_k}(\mathbf{p} + |e|\mathbf{A}/c) = p_x - m^*\omega_c y/2$. In this case, the transition matrix elements in the dipole approximation can be written as

$$\langle l', m', -\mathbf{k}|H_R|l, m, 0\rangle$$
$$= \frac{|e|}{m^*}\sqrt{\frac{2\pi\hbar N_{\mathbf{k}}}{\varepsilon(\omega)\omega}}\left\langle l', m'\middle|p_x - \frac{m^*\omega_c}{2}y\middle|l, m\right\rangle.$$

Using the recurrent formulas for the associated Legendre polynomials, one can calculate these matrix elements, from which it follows that, in the Faraday geometry, transitions in the dipole approximation are allowed only between energy levels of neighboring electron shells ($l' = l \pm 1$) with magnetic quantum numbers differing by unity ($m' = m \pm 1$). Note that the selection rules for electron transitions in this case are identical to those for the Zeeman effect. The resonance absorption peaks are split in a magnetic field into a few components, the number of these components being dependent on the orientation of the photon wave vector relative to the magnetic field (i.e., on the direction of observation). By analogy with the Zeeman effect, the resonance peaks due to transitions $m \longrightarrow m \pm 1$ will be referred to as σ components and the resonance peaks due to transitions $m \longrightarrow m$, as π components.

After simple algebra, the absorption can be written as the sum of four terms:

$$\Gamma_\sigma = \Gamma_1 + \Gamma_2 + \Gamma_3 + \Gamma_4, \tag{4}$$

where

$$\frac{\Gamma_{1,2}}{\Gamma_0} = \frac{\Omega}{\omega}(1 - e^{-\hbar\omega/T}) \times \sum_{l=0}^{\infty}\sum_{m=-l}^{l} f_0(E_{l,m})[1 - f_0(E_{l,m} + \hbar\omega)]$$
$$\times \frac{(l \pm m + 1)(l \pm m + 2)}{(2l+1)(2l+3)} \frac{(l \pm \omega_c/2\Omega)^2}{1 + \tau^2[\omega - \Omega(l+1) \mp \omega_c/2]^2},$$

$$\frac{\Gamma_{3,4}}{\Gamma_0} = \frac{\Omega}{\omega}(1 - e^{-\hbar\omega/T}) \times \sum_{l=0}^{\infty}\sum_{m=-l}^{l} f_0(E_{l,m})[1 - f_0(E_{l,m} + \hbar\omega)]$$
$$\times \frac{(l \mp m)(l \mp m - 1)}{(2l-1)(2l+1)} \frac{(l + 1 \mp \omega_c/2\Omega)^2}{1 + \tau^2[\omega + \Omega l \mp \omega_c/2]^2}$$

($\Gamma_0 = e^2\tau/4cm^*R^2\sqrt{\varepsilon(\omega)}$). Here, the resonance peak broadening due to scattering is described by the Lorentzian

$$\delta_\tau(\omega) = \frac{(\pi\tau)^{-1}}{\tau^{-2} + x^2}, \tag{5}$$

where τ is the phenomenological relaxation time.

First, we consider the particular case of the Voigt geometry where $\mathbf{e_k} \parallel \mathbf{B}$ and, hence, $\mathbf{e_k}(\mathbf{p} + |e|\mathbf{A}/c) = p_z$. In this case, the transition matrix elements in the dipole approximation have the form

$$\langle l', m', -\mathbf{k}|H_R|l, m, 0\rangle$$
$$= \frac{|e|}{m^*}\sqrt{\frac{2\pi\hbar N_\mathbf{k}}{\varepsilon(\omega)\omega}}\langle l', m'|p_z|l, m\rangle = \frac{|e|\hbar}{m^*R}\sqrt{\frac{2\pi\hbar N_\mathbf{k}}{\varepsilon(\omega)\omega}}\delta_{m',m} \tag{6}$$
$$\times\left[(l+1)\sqrt{\frac{l^2 - m^2}{4l^2 - 1}}\delta_{l',l-1} + l\sqrt{\frac{(l+1)^2 - m^2}{4(l+1)^2 - 1}}\delta_{l',l+1}\right].$$

It follows from Eq. (6) that, in the dipole approximation, the transitions are allowed only between energy levels of neighboring electron shells ($l' = l \pm 1$) with identical magnetic quantum numbers ($m' = m$). Therefore, only the π components of the resonance peaks will be observed in the absorption.

Substituting Eq. (6) into Eq. (3) yields

$$\Gamma_\pi = \frac{\pi e^2}{cm^*R^2\sqrt{\varepsilon(\omega)}}\frac{\Omega}{\omega}(1 - e^{-\hbar\omega/T})$$
$$\times \sum_{l=0}^{\infty}\sum_{m=-l}^{l} f_0(E_{l,m})[1 - f_0(E_{l,m} + \hbar\omega)]$$
$$\times\left[\delta(\omega + \Omega l)(l+1)^2\frac{l^2 - m^2}{4l^2 - 1} \right. \tag{7}$$
$$\left. + \delta[\omega - \Omega(l+1)]l^2\frac{(l+1)^2 - m^2}{4(l+1)^2 - 1}\right].$$

It is seen from Eq. (7) that the $\Gamma_\pi(\omega)$ dependence exhibits resonances at electromagnetic-radiation frequencies $\omega = \Omega(l + 1)$ for the values of l satisfying the condition $f_0(E_l) \gg f_0[E_l + \hbar\Omega(l + 1)]$.

If the resonance broadening due to scattering is described by Eq. (5), the absorption can be written as the sum of two terms, $\Gamma_\pi = \Gamma_1 + \Gamma_2$, where

$$\frac{\Gamma_1}{\Gamma_0} = 4\frac{\Omega}{\omega}(1 - e^{-\hbar\omega/T})\sum_{l=0}^{\infty}\sum_{m=-l}^{l}\frac{(l+1)^2(l^2 - m^2)}{4l^2 - 1}$$
$$\times \frac{f_0(E_{l,m})[1 - f_0(E_{l,m} + \hbar\omega)]}{1 + \tau^2(\omega + \Omega l)^2},$$

$$\frac{\Gamma_2}{\Gamma_0} = 4\frac{\Omega}{\omega}(1 - e^{-\hbar\omega/T})\sum_{l=0}^{\infty}\sum_{m=-l}^{l}\frac{l^2[(l+1)^2 - m^2]}{4(l+1)^2 - 1}$$
$$\times \frac{f_0(E_{l,m})[1 - f_0(E_{l,m} + \hbar\omega)]}{1 + \tau^2(\omega - \Omega(l+1))^2}.$$

The nonresonant term Γ_1 corresponds to photon emission. Near resonance, we have $\Gamma_1/\Gamma_2 = O[1/(\tau\omega)^2]$; therefore, the contribution from Γ_1 to the absorption of the high-frequency field can be neglected. Dropping this nonresonant term and the exponentially small term proportional to $\sim\exp(-\hbar\omega/T)$, we obtain

$$\frac{\Gamma_\pi}{\Gamma_0} = 4\frac{\Omega}{\omega}\sum_{l=0}^{\infty}\sum_{m=-l}^{l}\frac{l^2[(l+1)^2 - m^2]}{4(l+1)^2 - 1}$$
$$\times \frac{f_0(E_{l,m})[1 - f_0(E_{l,m} + \hbar\omega)]}{1 + \tau^2[\omega - \Omega(l+1)]^2}. \tag{8}$$

In the case of the Voigt geometry and an arbitrary orientation of the photon polarization vector relative to the magnetic field, i.e., $\mathbf{e_k} = (\sin\alpha, 0, \cos\alpha)$, the electromagnetic-radiation absorption of the nanosphere can be written as

$$\Gamma = \cos^2\alpha\Gamma_\pi + \sin^2\alpha\Gamma_\sigma, \tag{9}$$

where Γ_π is given by Eq. (8) and Γ_σ, by Eq. (4).

Thus, the absorption curve exhibits only σ components of the resonance peaks in the Faraday geometry and both σ and π components in the Voigt geometry. In the particular case of $\mathbf{e_k} \parallel \mathbf{B}$, the σ components disappear and only the π components survive; that is, only transitions $m \longrightarrow m$ are allowed.

3. ANALYSIS OF THE ABSORPTION CURVE

The formulas derived above for the absorption are valid both for an isolated sphere (N = const) and for a sphere exchanging electrons with a reservoir (μ = const). However, the behavior of absorption in these two cases is radically different. Let us first consider the case of a sphere placed in a thermostat characterized by chemical potential μ and temperature T.

Let l_0 be the value of the orbital quantum number satisfying the conditions $E_{l_0, -l_0} \le \mu < E_{l_0+1, -l_0-1}$. We also introduce the value m_0 of the magnetic quantum number equal to l_0 if the inequalities $E_{l_0, l_0} \le \mu < E_{l_0+1, -l_0-1}$ are satisfied; otherwise, the value m_0 is such that the two inequalities $E_{l_0, m_0} \le \mu < E_{l_0, m_0+1}$ are true. At zero temperature, l_0 and m_0 are the quantum numbers of the highest occupied level. From the normalization condition, it follows that at zero temperature, we have $N = 2(l_0^2 + l_0 + m_0 + 1)$.

In the Faraday geometry, the contribution from the nonresonant terms Γ_3 and Γ_4 to the high-frequency field absorption can be neglected near resonance. Resonance absorption is associated with transitions $(l_0, m) \longrightarrow (l_0 + 1, m \pm 1)$ and $(l_0 - 1, m) \longrightarrow (l_0, m \pm 1)$ and occurs at frequencies $\omega_{1,2} = \Omega l_0 \mp \omega_c/2$ and $\omega_{3,4} = \Omega(l_0 + 1) \mp \omega_c/2$.

Let us calculate the absorption at zero temperature. Keeping only the terms with $l = l_0 - 1$ and $l = l_0$ in Eq. (4), we obtain $\Gamma_\sigma(T = 0) \approx \Gamma_1 + \Gamma_2$, where

$$\frac{\Gamma_1}{\Gamma_0} = \frac{\Omega}{\omega}\left[\frac{(l_0 + m_0 + 1)(l_0 + m_0 + 2)(l_0 + m_0 + 3)(l_0 + \omega_c/2\Omega)^2}{3(2l_0 + 1)(2l_0 + 3)\{1 + \tau^2[\omega - \Omega(l_0 + 1) - \omega_c/2]^2\}}\right.$$
$$\left.+ \frac{(l_0 - 1 + \omega_c/2\Omega)^2}{(2l_0 - 1)(2l_0 + 1)[1 + \tau^2(\omega - \Omega l_0 - \omega_c/2)^2]} \sum_{m = -l_0 + 1}^{l_0 - 1} (l_0 + m)(l_0 + m + 1)\theta(E_{l_0 - 1, m} + \hbar\omega - \mu)\right], \tag{10}$$

$$\frac{\Gamma_2}{\Gamma_0} = \frac{\Omega}{\omega}\left[\frac{(l_0 + m_0 + 1)(7l_0^2 + m_0^2 - 4l_0 m_0 + 14l_0 - 4m_0 + 6)(l_0 - \omega_c/2\Omega)^2}{3(2l_0 + 1)(2l_0 + 3)\{1 + \tau^2[\omega - \Omega(l_0 + 1) - \omega_c/2]^2\}}\right.$$
$$\left.+ \frac{(l_0 - 1 - \omega_c/2\Omega)^2}{(2l_0 - 1)(2l_0 + 1)[1 + \tau^2(\omega - \Omega l_0 - \omega_c/2)^2]} \sum_{m = -l_0 + 1}^{l_0 - 1} (l_0 - m)(l_0 - m + 1)\theta(E_{l_0 - 1, m} + \hbar\omega - \mu)\right]. \tag{11}$$

Here, $\theta(x)$ is the step function

$$\theta(x) = \begin{cases} 0, & x \le 0 \\ 1, & x > 0. \end{cases}$$

We will make estimates for the case of zero temperature under the assumption that the resonance peaks are well resolved ($\tau\Omega \gg 1$, $\tau\omega_c \gg 1$, $\omega_c \ll \Omega$). Let $I_\sigma^{(i)}$ be the relative intensities of the σ components (Γ_σ/Γ_0) of the resonance peaks at frequencies ω_i (i = 1, 2, 3, 4). From Eqs. (10) and (11), we have

$$I_\sigma^{(1)}(T = 0) \approx \frac{(l_0 - 1 - \omega_c/2\Omega)^2 (l_0 - m_0 - 2)(l_0 - m_0 - 1)(l_0 - m_0)}{3(2l_0 - 1)(2l_0 + 1)(l_0 - \omega_c/2\Omega)}, \tag{12}$$

$$I_\sigma^{(2)}(T = 0) \approx \frac{(l_0 - 1 + \omega_c/2\Omega)^2 (l_0 - m_0)(7l_0^2 + m_0^2 + 4l_0 m_0 - 1)}{3(2l_0 - 1)(2l_0 + 1)(l_0 + \omega_c/2\Omega)}, \tag{13}$$

$$I_\sigma^{(3)}(T = 0) \approx \frac{(l_0 - \omega_c/2\Omega)^2 (l_0 + m_0 + 1)(7l_0^2 + m_0^2 - 4l_0 m_0 + 14l_0 - 4m_0 + 6)}{3(2l_0 + 1)(2l_0 + 3)(l_0 + 1 - \omega_c/2\Omega)}, \tag{14}$$

$$I_\sigma^{(4)}(T=0) \approx \frac{(l_0+\omega_c/2\Omega)^2(l_0+m_0+1)(l_0+m_0+2)(l_0+m_0+3)}{3(2l_0+1)(2l_0+3)(l_0+1+\omega_c/2\Omega)}. \quad (15)$$

It can be seen from Eqs. (12)–(15) that the intensities of the first and third peaks ($I_\sigma^{(1)}$, $I_\sigma^{(3)}$) decrease, while the intensities of the second and fourth peaks ($I_\sigma^{(2)}$, $I_\sigma^{(4)}$) increase, with increasing magnetic field.

Now, we consider the effect of temperature on the intensities $I_\sigma^{(1)}$ and $I_\sigma^{(2)}$. The first and second resonance peaks are associated with transitions $(l_0-1) \longrightarrow l_0$. At $T = 0$, transitions can occur only to unoccupied states of the l_0th electron shell ($m > m_0$). An increase in temperature causes the contributions due to transitions to the levels $m > m_0$ to decrease and the contributions due to transitions to the levels $m \le m_0$ to increase. Therefore, $I_\sigma^{(1)}$ increases, while $I_\sigma^{(2)}$ decreases, with increasing temperature (for $\hbar\omega_c/2T > 1$); that is, (since $I_\sigma^{(2)} > I_\sigma^{(1)}$) the lower of the two resonance peaks grows and the higher peak diminishes (Fig. 1). This difference in behavior is due to the fact that the contributions to $I_\sigma^{(1)}$ coming from transitions to levels with smaller values of m are larger, whereas in the case of $I_\sigma^{(2)}$, the opposite is true.

Next, we investigate the effect of temperature on $I_\sigma^{(3)}$ and $I_\sigma^{(4)}$. The third and fourth resonance peaks are associated with electron transitions from the l_0th to the (l_0+1)th shell. At $T = 0$, transitions can occur only from the occupied levels of the l_0th electron shell ($m \le m_0$). As the temperature is increased, the contributions due to transitions from the levels with $m \le m_0$ become smaller, whereas the contributions due to transitions from the levels with $m > m_0$ become larger. Therefore, $I_\sigma^{(3)}$ decreases, while $I_\sigma^{(4)}$ increases, with increasing temperature (for $\hbar\omega_c/2T > 1$), because the contributions to $I_\sigma^{(3)}$ due to transitions from levels with smaller values of m are larger, whereas in the case of $I_\sigma^{(4)}$, the situation is reversed. Since $I_\sigma^{(3)} > I_\sigma^{(4)}$ (for $m_0 < l_0$), an increase in temperature causes the smaller peak to increase and the larger peak to decrease (Fig. 1). A numerical analysis revealed that if the upper electron shell is filled, the intensities of both peaks decrease with increasing temperature.

Now, let us discuss the shape and position of the peaks. In the Faraday geometry, the peak position varies linearly with the magnetic field strength: $\omega_{1,2} = \Omega l_0 \mp \omega_c/2$ and $\omega_{3,4} = \Omega(l_0+1) \mp \omega_c/2$. In low fields ($\omega_c \ll \Omega$), the absorption peaks exhibit a doublet structure. The spacing between the first and second peaks, as well as the spacing between the third and fourth peaks, is equal to the cyclotron frequency. An increase in the magnetic field causes these spacings to increase and the second-to-third peak distance to decrease. At $\omega_c = \Omega$, the second and third absorption peaks merge into one peak.

It follows from Eq. (3) that at a sufficiently low temperature, the electromagnetic-radiation absorption involves only electrons whose energy lies within the

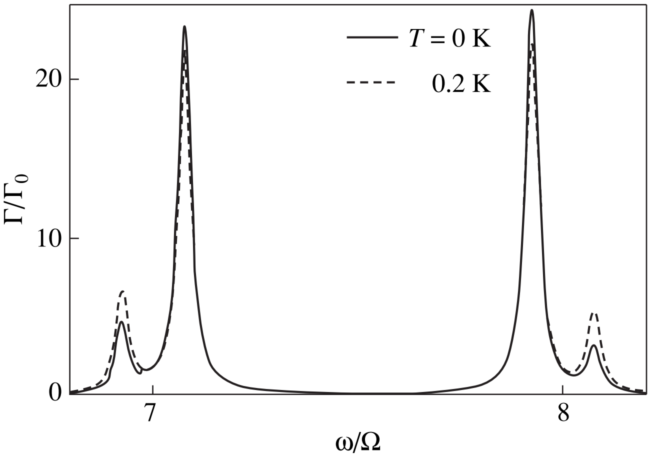

Fig. 1. Effect of temperature on the absorption peak intensities in the Faraday geometry. $R = 10^{-5}$ cm, $\tau = 3 \times 10^{-10}$ s, $\mu = 5.1 \times 10^{-15}$ erg, $\omega_c/\Omega = 0.15$, and $l_0 = 7$.

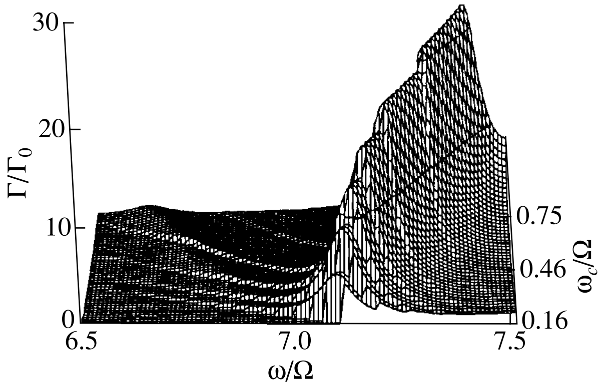

Fig. 2. Dependence of radiation absorption by a nanosphere on the frequency of radiation and magnetic field strength in the Faraday geometry. $R = 10^{-5}$ cm, $T = 0$, $\tau = 10^{-10}$ s, $\mu = 5.22 \times 10^{-15}$ erg, and $l_0 = 7$. The second peak, as well as the first peak forming with increasing magnetic field, is shown. Jumps of the first type are seen.

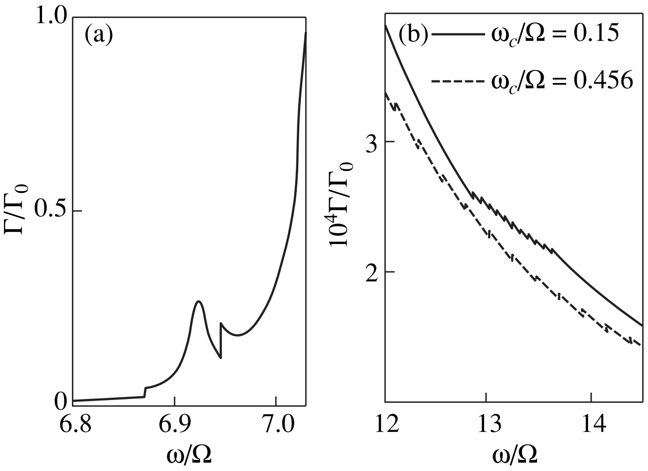

Fig. 3. (a) Jumps of the first type in the region of the first resonance peak ($\omega_c/\Omega = 0.15$) and (b) effect of a magnetic field on the position and magnitude of first-type jumps in the Faraday geometry. $R = 10^{-5}$ cm, $T = 0$, $\tau = 5 \times 10^{-10}$ s, $\mu = 5.165 \times 10^{-15}$ erg, and $l_0 = 7$.

range $[\mu - \hbar\omega, \mu]$. As the radiation frequency or the magnetic-field strength is varied, the number of electronic energy levels lying within this range changes. Therefore, the number of electrons involved in the radiation absorption is also varied and the absorption Γ undergoes discontinuous changes with increasing frequency ω and magnetic field B.

The changes in absorption that arise when electronic energy levels cross the level $\mu - \hbar\omega$ and the chemical potential μ will be referred to as jumps of the first and second types, respectively.

First, we consider jumps of the first type. Since in a weak field the distances between energy levels of neighboring electron shells are much larger than the distances between adjacent levels of the same shell, these jumps appear in series. Each series appears when the energy levels of an electron shell cross the level $\mu - \hbar\omega$; the number of jumps within each series is equal to the number of levels belonging to the corresponding shell. For instance, for the lth shell, the number of jumps is $2l + 1$. From the condition $\mu - \hbar\omega = E_{l,m}$ for a jump to appear, we find that the absorption curve will show jumps at electromagnetic-radiation frequencies:

$$\omega_{\text{jump}}(l, m) = \frac{\mu}{\hbar} - \frac{\Omega}{2}l(l+1) - \frac{\omega_c}{2}m. \quad (16)$$

It follows from Eq. (16) that the $(l_0 - 1)$th series of jumps occurs in the region of the first and second resonance peaks, while the other series of jumps arise on the higher frequency slope of the fourth peak.

Let us consider the $(l_0 - 1)$th series of jumps. At point $E_{l_0, m_0} = \mu$ for $m_0 > 0$ (the point at which second-type jumps arise in the region of the third and fourth peaks), we have, according to Eq. (16), $\omega_{\text{jump}}(l_0 - 1, m) = \Omega l_0 + \omega_c(m_0 - m)/2$. From this formula, it follows that the $(l_0 - 1, m_0)$ jump occurs at frequency $\omega_{\text{jump}}(l_0 - 1, m_0) = \Omega l_0$ (this jump lies midway between the first and second peaks), the $(l_0 + 1, m_0 + 1)$ jump arises at the first resonance frequency, and the $(l_0 - 1, m_0 - 1)$ jump occurs at the second resonance frequency (Fig. 2). Hence, the positions of the jumps at the maxima of the resonance absorption peaks remain unchanged with varying the magnetic field and are found from the equation $E_{l_0, m_0} = \mu$ (for $m_0 < -1$, the replacement $m_0 \longrightarrow m_0 + 1$ should be made in the last equation).

Note that the spacing between the first resonance peak and the jump $(l_0 - 1, 1)$, as well as the spacing between the second resonance peak and the jump $(l_0 - 1, -1)$, remains unchanged with increasing magnetic field.

If $m_0 = 0$ or -1, the position of the $(l_0 - 1, m_0)$ jump does not change with varying the magnetic field. The positions of the jumps with $m > 0$ shift to lower frequencies and those of the jumps with $m < 0$ shift to higher frequencies relative to Ωl_0 with increasing magnetic field.

Figure 3a shows the absorption curve in which jumps in absorption occur in the region of the first resonance peak when the energy levels of the sixth electron shell cross the $\mu - \hbar\omega$ level. The jumps occurring when the levels of the fifth shell cross the $\mu - \hbar\omega$ level are shown in Fig. 3b.

At temperatures close to zero, the relative magnitude of a first-type jump $\Delta^{(1)}_{l,m}$ is given by the approximate formula

$$\Delta^{(1)}_{l,m} \approx \frac{1}{[\mu/\hbar\Omega - l(l+1)/2 - \omega_c m/2\Omega](2l+1)(2l+3)} \quad (17)$$
$$\times \left[\frac{(l+m+1)(l+m+2)(l+\omega_c/2\Omega)^2}{1+\tau^2[\mu/\hbar - \Omega(l+1)(l+2)/2 - \omega_c(m+1)/2]^2} + \frac{(l-m+1)(l-m+2)(l-\omega_c/2\Omega)^2}{1+\tau^2[\mu/\hbar - \Omega(l+1)(l+2)/2 - \omega_c(m-1)/2]^2}\right].$$

It is seen from Eq. (17) that the magnitude of a jump is the larger, the closer the position of a jump of the $(l_0 - 1)$ series to the first or second resonance frequency. Therefore, the closer m to $m_0 \pm 1$, the larger $\Delta^{(1)}_{l_0 - 1, m}$. If the positions of jumps approach the resonance frequency as the magnetic field increases, the magnitude of such jumps increases with field; the magnitude of the other jumps decreases (Fig. 2).

The positions of jumps of the $(l_0 - 1)$th series can cross the first and second resonance frequencies with increasing field; in this case, for $m_0 > 0$, the absorption at these frequencies ($\omega_{1,2} = \Omega l_0 \mp \omega_c/2$) undergoes jumps

$$\Delta^{(1)}_{l_0-1,\, m_0\mp1} \approx \frac{(l_0 - 1 \mp \omega_c/2\Omega)^2)(l_0 \mp m_0 - 1)(l_0 \mp m_0)}{(2l_0-1)(2l_0+1)(l_0 \mp \omega_c/2\Omega)} \qquad (18)$$

(the upper sign corresponds to jumps at the first frequency; the lower, at the second frequency).

If $m_0 < -1$, the jumps at these frequencies are equal to $-\Delta^{(1)}_{l_0-1,\, m_0\mp1+1}$.

Now, we consider the other series of jumps. At $\Omega \gg \omega_c$, Eq. (17) can be rewritten as

$$\Delta^{(1)}_{l,m} \approx F(l,m)\{[l^2 + (\omega_c/2\Omega)^2] \times (l^2 + 3l + 2 + m^2) + 2lm(2l+3)\omega_c/\Omega\},$$

where

$$F(l,m) = \frac{[\mu/\hbar\Omega - l(l+1)/2 - \omega_c m/2\Omega](2l+1)(2l+3)}{1 + \tau^2[\mu/\hbar - \Omega(l+1)(l+2)/2 - \omega_c m/2]^2}.$$

It follows that $\Delta^{(1)}_{l,m}$ increases with increasing $|m|$ and the magnitude of a jump for positive m is larger than that for negative m (with the same $|m|$). It also follows that as the magnetic field increases, a jump increases in magnitude if $m > 0$ and decreases if $m < 0$ (Fig. 3b).

Next, we consider jumps of the second type, which occur only when the magnetic field is varied and the electronic energy levels cross the chemical-potential value. This value can be crossed only by the levels of the l_0th and ($l_0 + 1$)th shells. For example, the positions of the jumps corresponding to the l_0th-shell levels crossing the chemical potential are determined by the condition $\mu = E_{l_0, m_0}$. At these crossings, the quantum number m_0 changes by unity. Note that, in Eqs. (10) and (11), only the first terms (responsible for the formation of the third and fourth absorption peaks) are dependent on the quantum number m_0, whereas the second terms, describing the first and second peaks, do not depend on this quantum number. Therefore, the second-type jumps are significant only in the region of the third and fourth resonance peaks.

Let us calculate the changes in the intensity of the absorption peaks. If $m_0 > 0$, the value of m_0 decreases by unity when an energy level of the l_0th shell crosses the chemical potential. From Eqs. (14) and (15), it follows that, at zero temperature, the changes in the intensity of the third and fourth peaks are

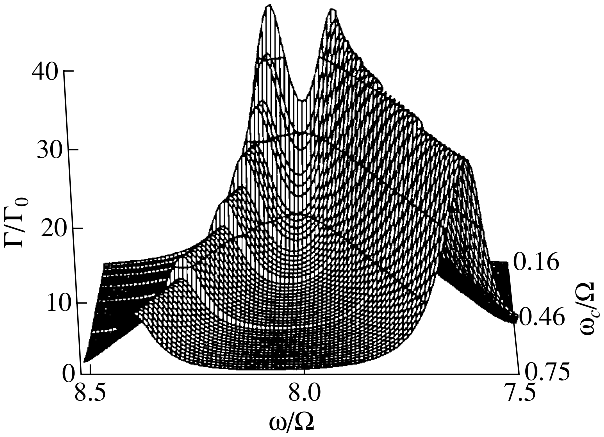

Fig. 4. Dependence of radiation absorption by a nanosphere on the frequency of radiation and magnetic field strength in the Faraday geometry. $R = 10^{-5}$ cm, $T = 0$, $\tau = 10^{-10}$ s, $\mu = 5.22 \times 10^{-15}$ erg, and $l_0 = 7$. The third and fourth resonance peaks are shown. Jumps of the second type are seen.

$$\Delta^{(2)}_{l_0, m_0} \approx -\frac{(l_0 \mp \omega_c/2\Omega)^2(l_0 \mp m_0 + 1)(l_0 \mp m_0 + 2)}{(2l_0+1)(2l_0+3)(l_0 + 1 \mp \omega_c/2\Omega)} \qquad (19)$$

(the upper sign corresponds to the jump in the intensity of the third peak). It follows from Eqs. (18) and (19) that, in this case, the first and second peaks increase in a jump, whereas the third and fourth peaks decrease (Figs. 2, 4).

If $m_0 < -1$, the value of m_0 increases by unity when an energy level of the l_0th shell crosses the chemical potential. The intensities of the third and fourth peaks are changed by $-\Delta^{(2)}_{l,\, m_0+1}$. Thus, according to Eqs. (18) and (19), the first and second peaks decrease and the third and fourth peaks increase in this case.

In the particular case of the Voigt geometry, where the photon polarization vector is parallel to the magnetic field, the absorption curve exhibits only π components of resonance peaks. At low temperatures, the resonance absorption peaks are associated with transitions $(l_0, m) \longrightarrow (l_0 + 1, m)$ and $(l_0 - 1, m) \longrightarrow (l_0, m)$. Therefore, the resonance frequencies are $\omega_1 = \Omega l_0$ and $\omega_2 = \Omega(l_0 + 1)$.

Let us calculate the absorption at zero temperature in this case. Near resonance, only the terms with $l = l_0 - 1$ and $l = l_0$ are significant in Eq. (8). Therefore, we can write

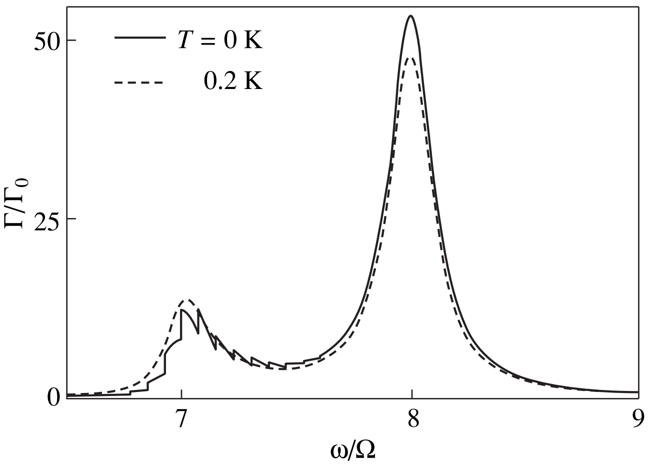

Fig. 5. Effect of temperature on the absorption peak intensities in the Voigt geometry. $R = 10^{-5}$ cm, $\tau = 5 \times 10^{-11}$ s, $\mu = 5.161 \times 10^{-15}$ erg, $\omega_c/\Omega = 0.15$, and $l_0 = 7$.

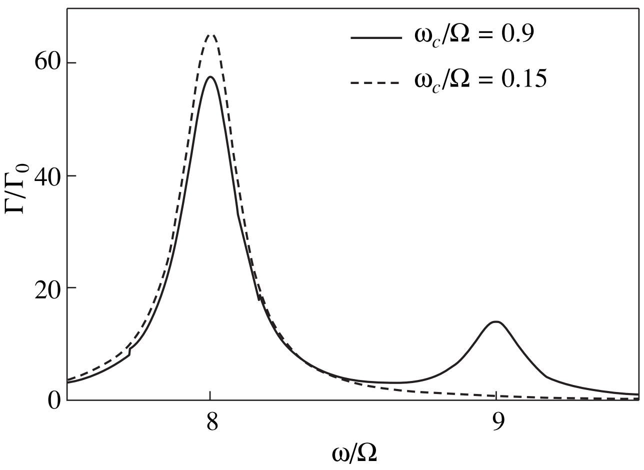

Fig. 6. Formation of a new resonance peak with increasing magnetic field in the Voigt geometry. $R = 10^{-5}$ cm, $T = 0$, $\tau = 5 \times 10^{-11}$ s, $\mu = 6.2 \times 10^{-15}$ erg, and $l_0 = 7$.

$$\frac{\Gamma_\pi(T=0)}{\Gamma_0} \approx 4\frac{\Omega}{\omega}\left\{\frac{l_0^2(l_0+m_0+1)(l_0+m_0+2)(4l_0-2m_0+3)}{6(2l_0+1)(2l_0+3)1+\tau^2[\omega-\Omega(l_0+1)]^2} + \frac{(l_0-1)^2}{(2l_0-1)(2l_0+1)[1+\tau^2(\omega-\Omega l_0)^2]} \times \sum_{m=-l_0+1}^{l_0-1}(l_0^2-m^2)\theta(E_{l_0-1,m}+\hbar\omega-\mu)\right\}. \quad (20)$$

Let $I_\pi^{(1)}$ and $I_\pi^{(2)}$ be the relative intensities of the peaks in the absorption Γ_π/Γ_0 at frequencies $\omega_1 = \Omega l_0$ and $\omega_2 = \Omega(l_0 + 1)$, respectively. Dropping the terms of the order of $(\tau\Omega)^{-2}$, these intensities can be found to be

$$I_\pi^{(1)}(T=0) \approx \frac{2(l_0-1)^2(l_0-m_0-1)(l_0-m_0)(4l_0+2m_0+1)}{3l_0(2l_0-1)(2l_0+1)}, \quad (21)$$

$$I_\pi^{(2)}(T=0) \approx \frac{2l_0^2(l_0+m_0+1)(l_0+m_0+2)(4l_0-2m_0+3)}{3(l_0+1)(2l_0+1)(2l_0+3)}. \quad (22)$$

A numerical analysis revealed that the second peak is higher than the first if $m_0 \geq -1$ and the situation is reversed if $m_0 < -1$. Note that the number of transitions $l_0 \longrightarrow (l_0 + 1)$ is larger than that of transitions $(l_0 - 1) \longrightarrow l_0$ for $m_0 \geq 0$.

For $m_0 = -1$, an increase in temperature causes an increase in the intensity of the larger peak and a decrease in the intensity of the smaller peak. For the other values of m_0, the situation is reversed (the larger peak decreases and the smaller peak increases; Fig. 5).

Now, we examine the shape and position of the absorption peaks. The values of the resonance frequencies are entirely determined by the chemical potential and the radius of the nanosphere; indeed, according to Eq. (20), the resonance absorption occurs at frequencies $\omega_1 = \Omega l_0$ and $\omega_2 = \Omega(l_0 + 1)$, which depend only on R and l_0, with l_0, in turn, determined by the chemical potential. As the magnetic field is increased, the electronic energy levels may cross the chemical-potential level. When μ is crossed by the energy levels of the l_0th shell, the intensity of the absorption peak changes but the peak position remains unchanged. If $m_0 = l_0$ (the l_0th shell is closed) or $m_0 = l_0 - 1$, then, as follows from Eq. (21), $I_\pi^{(1)} = 0$ and the absorption curve exhibits only one resonance peak, at frequency $\omega = \Omega(l_0 + 1)$. If the energy levels of the $(l_0 + 1)$th shell cross the chemical potential with increasing magnetic field, then a new peak arises in the absorption curve (Fig. 6).

As in the case of the Faraday geometry, the positions of jumps of the first type are determined by Eq. (16). From this equation, it is seen that the position of the jump $(l, 0)$ is independent of the magnetic field. Since the spacing between adjacent jumps of an individual series is $\omega_c/2$, the positions of jumps with $m > 0$ shift to lower frequencies relative to the jump $(l, 0)$, while the positions of jumps with $m < 0$ shift to higher frequencies, with increasing magnetic field. Note that the series of jumps with $l = l_0 - 1$ occurs in the region of the first resonance peak, while the other series appear on the higher frequency slope of the second peak. It should be

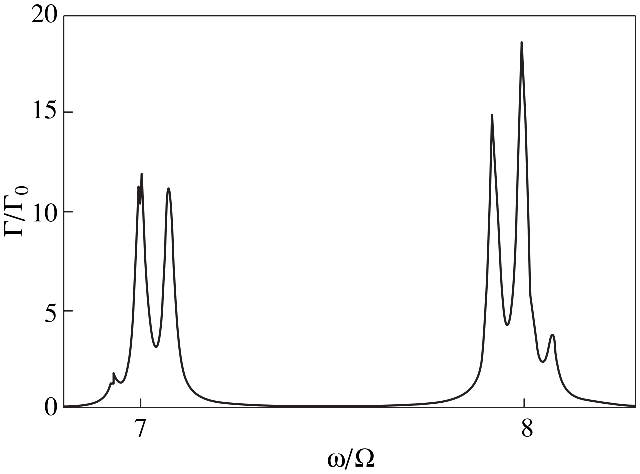

Fig. 7. Dependence of radiation absorption by a nanosphere on the radiation frequency in the Voigt geometry. $R = 10^{-5}$ cm, $T = 0$, $\tau = 4 \times 10^{-10}$ s, $\mu = 5.1 \times 10^{-15}$ erg, $\omega_c/\Omega = 0.15$, $\alpha = \pi/4$, and $l_0 = 7$.

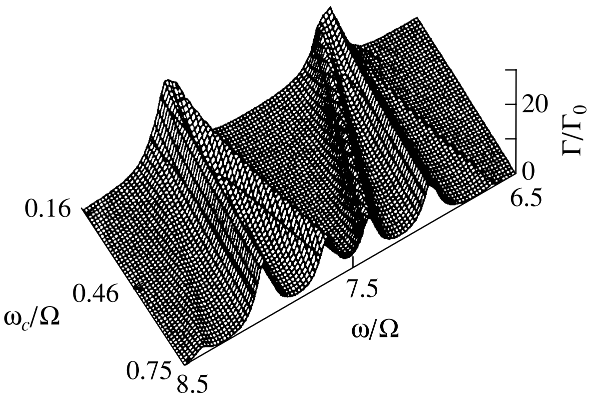

Fig. 8. Dependence of radiation absorption by a nanosphere on the frequency of radiation and magnetic field strength in the Voigt geometry. $R = 10^{-5}$ cm, $T = 0$, $\tau = 10^{-10}$ s, $\mu = 5.12 \times 10^{-15}$ erg, $\alpha = \pi/4$, and $l_0 = 7$.

noted that the jumps are progressively smoothened with increasing temperature (Fig. 5).

Now, we consider the series of jumps associated with the $(l_0 - 1)$th shell levels crossing the $(\mu - \hbar\omega)$ level. From Eq. (16) and the definition of the quantum number m_0 ($E_{l_0, m_0} \le \mu < E_{l_0, m_0 + 1}$ for $m_0 \ne l_0$), we find that the jumps appear at frequencies satisfying the conditions

$$\Omega l_0 + \omega_c(m_0 - m)/2 \le \omega_{\text{jump}}(l_0 - 1, m) < \Omega l_0 + \omega_c(m_0 - m + 1)/2. \tag{23}$$

From Eq. (23), it follows that the $(l_0 - 1)$th series of jumps appears in the region of the first resonance peak: the jumps with $m \le m_0$ are located on the higher frequency side of this peak $[\omega_{\text{jump}}(l_0 - 1, m) \ge \Omega l_0]$, while the jumps with $m > m_0$ are located on the lower frequency side $[\omega_{\text{jump}}(l_0 - 1, m) < \Omega l_0]$.

When the levels of the l_0th shell cross the chemical potential, we have $\omega_{\text{jump}}(l_0 - 1, m_0) = \Omega l_0$. Therefore, the quantum number m_0 and the peak intensity are changed when the position of a jump of the $(l_0 - 1)$ series passes through the first resonance frequency with increasing magnetic field. For $m_0 = 0$ and -1, the jumps with $m > 0$ move to the left of the first resonance frequency and the jumps with $m < 0$ move to the right (the position of the jump with $m = 0$ remains unchanged) with increasing magnetic field.

The relative magnitude of a first-type jump $\Delta^{(1)}_{l,m}$ at temperatures close to zero can be approximated by the expression

$$\Delta^{(1)}_{l,m} \approx \frac{4\Omega l^2[(l+1)^2 - m^2]}{[\mu/\hbar - \Omega l(l+1)/2 - \omega_c m/2](2l+1)(2l+3)} \times \frac{1}{1 + \tau^2[\mu/\hbar - \Omega(l+1)(l+2)/2 - \omega_c m/2]^2}. \tag{24}$$

It follows from Eq. (24) that the closer a jump of the $(l_0 - 1)$th series to the first resonance frequency, the larger the magnitude of the jump. If jumps are shifted toward the resonance frequency with increasing magnetic field, the magnitude of such jumps increases with the field, while the magnitude of the other jumps decreases. For $m_0 > 0$, the position of the jump $(l_0 - 1, m_0)$ passes through the first resonance frequency as the magnetic field is increased. In this case, as follows from Eq. (24), the magnitude of the jump at the first resonance frequency $[\omega_{\text{jump}}(l_0 - 1, m_0) = \Omega l_0]$ is equal to

$$\Delta^{(1)}_{l_0 - 1, m_0} \approx \frac{4(l_0 - 1)^2(l_0^2 - m_0^2)}{l_0(2l_0 - 1)(2l_0 + 1)}. \tag{25}$$

The number of jumps in the intensity of the first peak equals $m_0|_{B=0}$.

For $m_0 < -1$, the position of the jump $(l_0 - 1, m_0 + 1)$ passes through the first resonance frequency with increasing magnetic field, the magnitude of the jump at this frequency being equal to $-\Delta^{(1)}_{l_0 - 1, m_0 + 1}$ in this case. The number of jumps in the first-peak intensity equals $-m_0|_{B=0} + 1$.

Now, let us consider the second-type jumps, which appear in the magnetic-field dependence of absorption when energy levels of the l_0th shell cross the chemical potential. At such crossings, the quantum number m_0 changes by unity. Note that, in Eq. (20), only the first

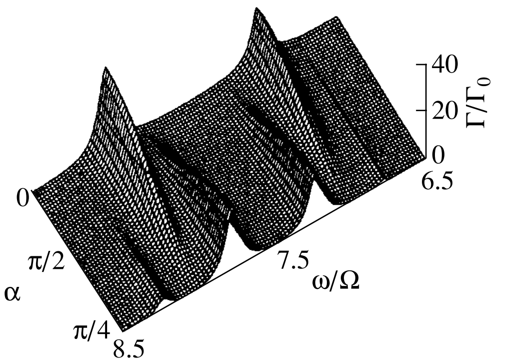

Fig. 9. Dependence of radiation absorption by a nanosphere on the radiation frequency and the angle between the magnetic field direction and the photon polarization vector in the Voigt geometry. $R = 10^{-5}$ cm, $T = 0$, $\tau = 10^{-10}$ s, $\mu = 5.12 \times 10^{-15}$ erg, $\omega_c/\Omega = 0.46$, and $l_0 = 7$.

term (responsible for the formation of the second resonance peak) is dependent on the quantum number m_0; the second term, corresponding to the first resonance peak, does not depend on m_0. Therefore, the second-type jumps are significant only in the region of the second resonance peak.

From Eqs. (21) and (22), it can be seen that at $T = 0$, the intensities of the peaks do not vary with magnetic field in the range where the energy levels do not cross the chemical potential. For $m_0 = 0$ and –1, the chemical potential is not crossed by the energy levels (the quantum number m_0 does not change) and, hence, the peak intensities are independent of the field (in the field range in question).

If $m_0 > 0$, the quantum number m_0 decreases by unity as the chemical potential is crossed by an energy level of the l_0th shell. From Eq. (21), it follows that the relative magnitude of the second-type jump at the second resonance frequency is

$$\Delta^{(2)}_{l_0, m_0} \approx -\frac{4l_0^2[(l_0+1)^2 - m_0^2]}{(l_0+1)(2l_0+1)(2l_0+3)}. \qquad (26)$$

It can be seen from Eqs. (25) and (26) that for $m_0 > 0$, the intensity of the first peak increases and the intensity of the second peak decreases with increasing magnetic field. The number of second-type jumps in the intensity of the second resonance peak equals $m_0|_{B=0}$.

If $m_0 < -1$, the quantum number m_0 increases by unity as an energy level of the l_0th shell crosses the chemical potential. In this case, the absorption at the ith resonance frequency undergoes a jump $-\Delta^{(i)}_{l, m_0+1}$. Therefore, for $m_0 < -1$, the intensity of the first absorption peak decreases, while the intensity of the second peak increases, with increasing magnetic field. The number of second-type jumps in the intensity of the second resonance peak is equal to $-m_0|_{B=0} + 1$.

In the general case of the Voigt geometry, where the photon polarization vector is oriented arbitrarily relative to the magnetic field, it follows from Eqs. (8) and (9) that the absorption curve exhibits six resonance peaks: two peaks in the π component of absorption [at frequencies $\omega_2 = \Omega l_0$ and $\omega_5 = \Omega(l_0 + 1)$] and four peaks in the σ component [$\omega_{1,3} = \Omega l_0 \mp \omega_c/2$ and $\omega_{4,6} = \Omega(l_0 + 1) \mp \omega_c/2$] (Fig. 7). Therefore, the positions of the π components (of the second and fifth resonance peaks) do not vary with field, whereas the frequencies $\omega_2 - \omega_1 = \omega_3 - \omega_2 = \omega_5 - \omega_4 = \omega_6 - \omega_5 = \omega_c/2$ are dependent on the field (Fig. 8).

It is seen from Fig. 7 that there are two triplets in the absorption curve for low magnetic fields. As the magnetic field is increased, the spacings between the peaks of a triplet increase (Fig. 8) and, when $\omega_c = \Omega$, the third and fourth peaks merge into one peak.

The peak intensities are $I_1 = \sin^2\alpha I_\sigma^{(1)}$, $I_2 = \cos^2\alpha I_\pi^{(1)}$, $I_3 = \sin^2\alpha I_\sigma^{(2)}$, $I_4 = \sin^2\alpha I_\sigma^{(3)}$, $I_5 = \cos^2\alpha I_\pi^{(2)}$, and $I_6 = \sin^2\alpha I_\sigma^{(4)}$ (when the peaks are well resolved, i.e., when $\omega_c\tau/2 \gg 1$, $\omega_c \neq \Omega$). The dependence of the absorption on the angle α and frequency ω is shown in Fig. 9.

In the case where the peaks are well resolved, the intensities of the second and fifth peaks do not vary with magnetic-field strength, while the behavior of the other peaks is the same as in the Faraday geometry; that is, the intensities of the first and fourth peaks decrease, whereas those of the third and sixth peaks increase, with increasing magnetic field.

As indicated above, the absorption curve in the Faraday geometry exhibits four peaks, with the spacing between the first and second peaks and between the third and fourth peaks being equal to the cyclotron frequency and with the peak positions varying linearly with magnetic field.

In the Voigt geometry, where the magnetic field is oriented arbitrarily relative to the photon polarization vector, the absorption curve exhibits six resonance peaks: two peaks in the π component (associated with electron transitions $m \longrightarrow m$) and four σ-component peaks (due to electron transitions $m \longrightarrow m \pm 1$).

In the particular case of the Voigt geometry, where the photon polarization vector is parallel to the magnetic field, the absorption curve at low temperatures exhibits only two π-component peaks, whose positions are independent of the magnetic field. At low temperatures, the peak intensities do not vary with magnetic field in the range where there are no energy levels crossing the chemical potential.

4. CONCLUSIONS

For all configurations of the magnetic field and the photon polarization vector considered in this paper, the absorption has been shown to undergo jumps of two types. The first type of jump is associated with electronic energy levels crossing the level $\mu - \hbar\omega$; the positions of these jumps depend on the frequency of the electromagnetic radiation and on the magnetic field [see Eq. (16)]. Jumps of the second type arise when electronic energy levels cross the chemical potential μ; the positions of these jumps depend only on the magnetic field and are determined by the condition $\mu = E_{l,\,m}$.

First-type jumps appear in series. Each series of jumps is associated with the electronic energy levels of an electron shell crossing the level $\mu - \hbar\omega$; the number of jumps in each series is equal to the number of energy levels in the corresponding electron shell. The $(l_0 - 1)$th series of jumps arises in the region of the first and second resonance peaks in the Faraday geometry and in the region of the first, second, and third resonance peaks in the Voigt geometry. The other series appear on the higher frequency slope of the last resonance peak.

Second-type jumps are significant only when they arise in the region of the third and fourth resonance peaks in the Faraday geometry and in the region of the fourth, fifth, and sixth peaks in the Voigt geometry, with the magnitudes of the jumps being maximum at the resonance frequencies. The jumps of the second type can be both positive or negative, depending on the sign of the quantum number m_0.

It should be noted that jumps of both types are significantly smoothened even at fairly low temperatures.

A numerical analysis revealed that, in the case of an isolated nanosphere, the dependence of the chemical potential on the magnetic field B is such that the electronic energy levels do not cross the chemical-potential level. Therefore, as the field B is varied, the quantum numbers l_0 and m_0 remain unchanged. For this reason, when the number of particles is fixed, the absorption undergoes only jumps of the first type. The position of the jump (l, m_0) does not change with varying the magnetic field, whereas the jumps with $m > 0$ are shifted to lower frequencies and the jumps with $m < 0$, to higher frequencies, relative to the jump (l, m_0), as the magnetic field is increased. Due to the dependence of μ on T, the positions of first-type jumps can vary with temperature, in contrast to the case of a constant chemical potential, where the temperature causes the jumps only to smoothen.

ACKNOWLEDGMENTS

This study was supported by the Russian Foundation for Basic Research, project no. 01-02-16564.

REFERENCES

1. C. B. Murray, D. J. Norris, and M. G. Bawendi, J. Am. Chem. Soc. **11**, 8706 (1993).
2. R. C. Salvarezza, L. Vázquez, H. Miguez, *et al.*, Phys. Rev. Lett. **77** (22), 4572 (1996).
3. Yu. A. Vlasov, V. N. Astratov, O. Z. Karimov, *et al.*, Phys. Rev. B **55** (20), R13357 (1997).
4. J.-B. Xia and J. Li, Phys. Rev. B **60** (16), 11540 (1999).
5. S. S. Martinos, Phys. Rev. B **39** (2), 1363 (1989).
6. R. Ruppin, Phys. Rev. B **45** (19), 11209 (1992).
7. B. M. Smirnov and H. Weidele, Zh. Éksp. Teor. Fiz. **116** (6), 1903 (1999) [JETP **89**, 1030 (1999)].
8. G. Mie, Ann. Phys. (Leipzig) **25**, 377 (1908).
9. V. Albe, C. Jouanin, and D. Bertho, Phys. Rev. B **58** (8), 4713 (1998).
10. H. Miguez, A. Blanco, F. Meseguer, *et al.*, Phys. Rev. B **59** (3), 1563 (1999).
11. V. Yannopapas, A. Modinos, and N. Stefanou, Phys. Rev. B **60** (8), 5359 (1999).
12. K. Ohtaka, Y. Suda, S. Nagano, *et al.*, Phys. Rev. B **61** (8), 5267 (2000).
13. M. A. Hines and P. Guyot-Sionnest, J. Phys. Chem. **100** (2), 468 (1996).
14. H. S. Zhou, I. Honma, H. Komiyama, and J. W. Haus, Phys. Rev. B **50** (16), 12052 (1994).
15. R. D. Averitt, D. Sarkar, and N. J. Halas, Phys. Rev. Lett. **78** (22), 4217 (1997).
16. R. D. Averitt, S. L. Westcott, and N. J. Halas, Phys. Rev. B **58** (16), R10203 (1998).
17. J. J. Diao and G. D. Chen, J. Phys. D **34**, L79 (2001).
18. N. Kalyaniwalla, J. W. Haus, R. Inguva, and M. H. Birnboim, Phys. Rev. A **42** (9), 5613 (1990).
19. L. Fu and L. Resca, Phys. Rev. B **56** (17), 10963 (1997).
20. R. Rojas, F. Claro, and R. Fuchs, Phys. Rev. B **37** (12), 6799 (1988).
21. L. Brey, N. F. Johnson, and B. I. Halperin, Phys. Rev. B **40** (15), 10647 (1989).
22. V. A. Margulis, Zh. Éksp. Teor. Fiz. **111** (3), 1092 (1997) [JETP **84**, 603 (1997)].
23. N. G. Galkin, V. A. Margulis, and A. V. Shorokhov, Fiz. Tverd. Tela (St. Petersburg) **43** (3), 511 (2001) [Phys. Solid State **43**, 530 (2001)].
24. V. A. Geyler, V. A. Margulis, and A. V. Shorokhov, Phys. Rev. B **63**, 245316 (2001).
25. V. Ya. Demikhovskiĭ and A. A. Perov, Zh. Éksp. Teor. Fiz. **114** (5), 1795 (1998) [JETP **87**, 973 (1998)].
26. D. N. Aristov, Pis'ma Zh. Éksp. Teor. Fiz. **70** (6), 405 (1999) [JETP Lett. **70**, 410 (1999)].
27. P. Malits and I. D. Vagner, J. Phys. A **32**, 1507 (1999).
28. H. Aoki and H. Suezawa, Phys. Rev. A **46** (3), R1163 (1992).

29. Ju. H. Kim, I. D. Vagner, and B. Sundaram, Phys. Rev. B **46** (15), 9501 (1992).
30. D. N. Aristov, Phys. Rev. B **59** (9), 6368 (1999).
31. D. V. Bulaev, V. A. Geyler, and V. A. Margulis, Phys. Rev. B **62** (17), 11517 (2000).
32. C. L. Foden, M. L. Leadbeater, and M. Pepper, Phys. Rev. B **52** (12), R8646 (1995).
33. A. Wójs and J. J. Quinn, Physica E (Amsterdam) **3**, 181 (1998).
34. M. V. Entin and L. I. Magarill, Phys. Rev. B **64**, 085330 (2001).
35. D. V. Bulaev and V. A. Margulis, Fiz. Tverd. Tela (St. Petersburg) **44** (9), 1557 (2002) [Phys. Solid State **44**, 1632 (2002)].
36. I. V. Komarov, L. I. Ponomarev, and S. Yu. Slavyanov, *Spheroidal and Coulomb Spheroidal Functions* (Nauka, Moscow, 1976).
37. R. K. Bakanas, Fiz. Tverd. Tela (Leningrad) **12** (12), 3408 (1970) [Sov. Phys. Solid State **12**, 2769 (1970)].

Translated by Yu. Epifanov

Physics of the Solid State, Vol. 45, No. 2, 2003, pp. 381–385. Translated from Fizika Tverdogo Tela, Vol. 45, No. 2, 2003, pp. 359–363.

Phonon Scattering from the Boundaries of Small Crystals Embedded in a Dielectric Porous-Glass Matrix

L. S. Parfen'eva*, I. A. Smirnov*, A. V. Fokin*, H. Misiorek, J. Mucha**, and A. Jezowski****

** Ioffe Physicotechnical Institute, Russian Academy of Sciences,*
Politekhnicheskaya ul. 26, St. Petersburg, 194021 Russia
e-mail: igor.smirnov@pop.ioffe.rssi.ru
*** Institute of Low-Temperature and Structural Research, Polish Academy of Sciences, Wroclaw, 50-950 Poland*

Received April 25, 2002; in final form, May 23, 2002

Abstract—The thermal conductivity of porous glass with randomly distributed connecting pores ~70 Å in size (glass porosity ~25%), as well as of a porous glass + NaCl composite, was measured in the temperature range 5–300 K. NaCl filled one fourth of the pores in the composite. The experimental results on the composite thermal conductivity can be accounted for only by assuming that phonons scatter from the boundaries of NaCl nanocrystals embedded in channels of the porous glass. © *2003 MAIK "Nauka/Interperiodica".*

The physical properties of small particles of metals and semiconductors embedded in nanovoids (nanochannels) of porous dielectric matrices, such as zeolites, opals, asbestos, and porous glass, have become a topic of broad interest in recent years all over the world. Research in this area is aimed at studying the fundamental properties of micro- and nanoparticles with the aim of applying them in technology and nanoelectronics [1–5].

In this paper, we deal with nanocomposites based on porous glasses.

Porous glass is produced in the chemical reaction of acids with a starting sodium borosilicate glass subjected preliminarily to a specific thermal treatment [6]. The composition of sodium borosilicate glasses is as follows: 80–96% SiO_2, 3–13% B_2O_3, and 0.5–1.5% Na_2O. Reaction with acids taken in various concentrations etches sodium and boron oxides out of the starting glass, leaving porous glass as the final product. The size of the randomly distributed pores (channels) varies from 30 to 150 Å [6]. The porosity (number of pores per unit volume) and the degree of pore uniformity in size are determined by the composition of the starting glass and the actual conditions of its heat treatment, both before and in the course of etching. A porous glass obtained in this way can be conceived of as an array of densely packed SiO_2 spheres of various diameters [7, 8]; the space between these spheres (the porosity) in such glasses amounts to ~25–27% of the sample volume.

The glass pores can be filled by metals, semiconductors, or insulators. Liquids that wet the glass enter its voids easily, so that the loading of compounds dissolved into pores in such liquids does not present any difficulties. To do this, one simply immerses the porous glass into the required solution and dries the impregnated glass. Nonwetting liquids are introduced into glass pores using high-pressure injection.

The above techniques were employed to introduce Ga, Hg, In, NaCl, ferroelectrics, etc., into porous glasses, and their physical properties (changes in the superconducting transition temperature and in the melting and solidification points, specific features in the behavior of the electrical resistivity, heat capacity, thermal conductivity, optical characteristics, neutron scattering, etc.) were studied [2].

Of particular interest for the physics of small particles are studies of the behavior of phonons in them, including phonon scattering from nanocrystal boundaries [9] and estimation of the part played by surface vibrations [10, 11] and by variation of the phonon spectrum [12, 13]. Unfortunately, studies of the thermal conductivity of nanocomposites based on porous glasses are scarce. This study attempts to fill this gap by investigating the thermal conductivity of a porous glass + NaCl nanocomposite. We measured the thermal conductivity of porous glass with randomly distributed and fairly uniform (in size) pores ~70 Å in diameter, the total volume of the pores being ~25% of that of the sample. The composition of the starting sodium borosilicate glass was 91.7% SiO_2, 7.3% B_2O_3, and 0.5% Na_2O.

A 5 × 5 × 12-mm sample dried by heating to 250°C was immersed in a water solution containing NaCl and kept there until impregnation was complete. After the impregnation, the sample was taken out of the solution and dried and the NaCl macrocrystals formed on its surface were mechanically removed. Weighing of the sample before and after NaCl loading showed that 1/4 of the pore volume was filled by NaCl.

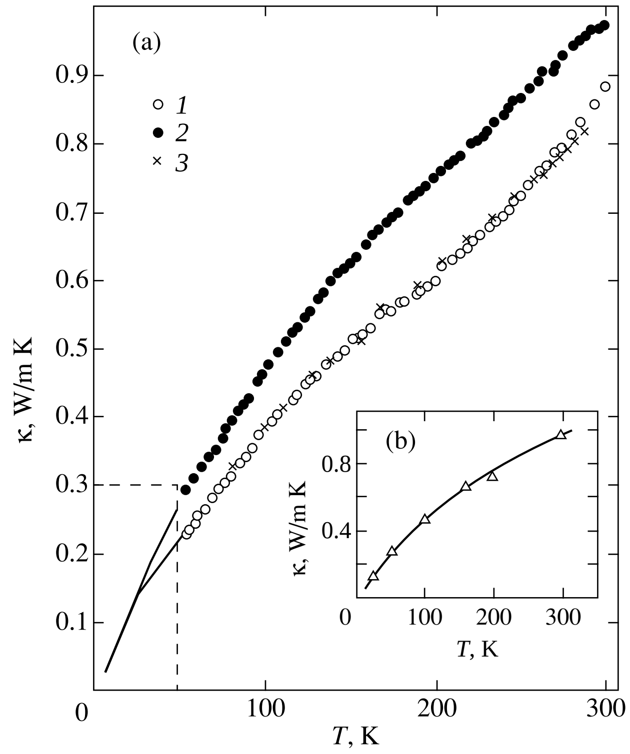

Fig. 1. (a) Temperature dependences of the thermal conductivity of (*1*) porous glass, (*2*) porous glass + NaCl composite, and (*3*) a sample of the composite from which NaCl was removed by dissolution in water. (b) Temperature dependence of the thermal conductivity of the porous glass + NaCl composite (solid curve obtained using curve *2* in Fig. 1a) and the thermal conductivity calculated for this composite from Eq. (2) (triangles) [15] assuming the κ of NaCl nanocrystals embedded in channels of porous glass to be substantially smaller than the κ of a bulk single crystal [16] due to phonon scattering from the nanocrystal boundaries.

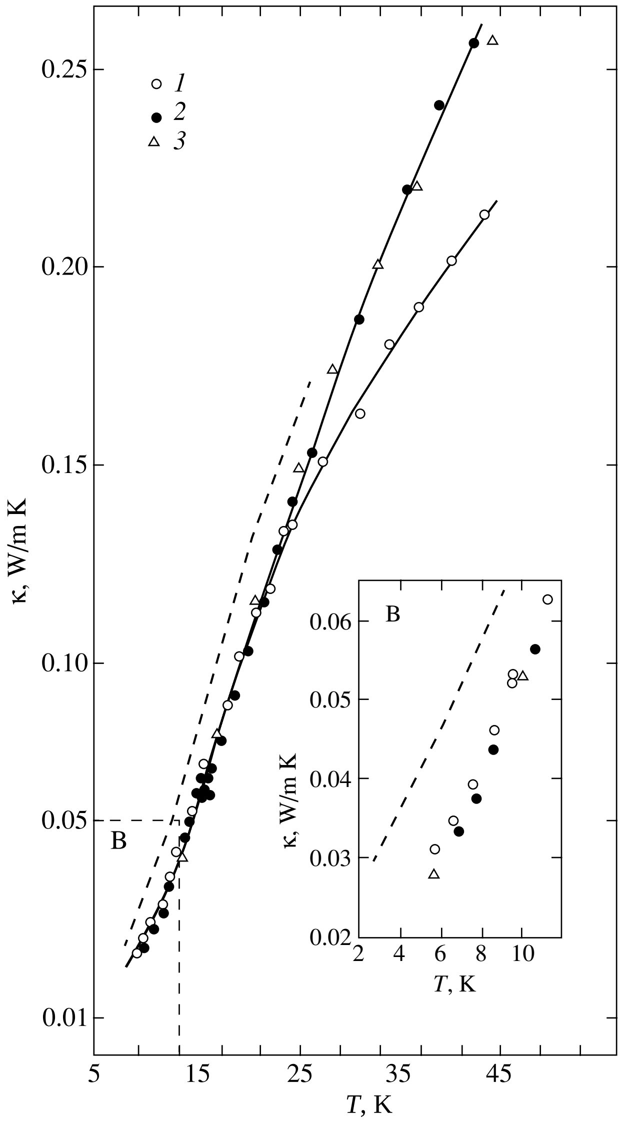

Fig. 2. Temperature dependences of the thermal conductivity of (*1*) porous glass and (*2*) porous glass + NaCl composite. (*3*) κ_{eff} of the nanocomposite calculated from Eq. (2) [15] with due account of phonon scattering from the boundaries of nanocrystals embedded in glass channels. Inset B: expanded low-temperature part. Dashed curves in the figure and inset B are κ_{eff} calculated from Eq. (2) [15] under the assumption of the thermal conductivity of the filler (NaCl) being equal to that of a bulk single crystal [16].

The thermal conductivity κ was measured within the temperature interval 5–300 K on a setup similar to that used in [14].

The results obtained for κ of the starting porous glass and of the porous glass + NaCl composite are presented in Figs. 1a and 2. After the κ measurements on the composite, the sample was placed in water and the NaCl contained in it was completely washed off, which was verified by weighing the washed and dried sample. After thorough drying, the κ(*T*) of the sample was measured again (from 80 to 300 K). The thermal conductivities of the starting and washed porous glass were found to completely coincide (Fig. 1a).

The porous glass and composite studied are insulators; therefore, the thermal conductivity measured in the experiment is that of the crystal lattice, κ_{ph} ($\kappa = \kappa_{ph}$).

We note two interesting features revealed by us in the behavior of κ(*T*) of the composite:

(1) Within the temperature interval 25–300 K, κ of the composite is noticeably in excess of κ of the starting porous glass, although NaCl fills only ~6% of the available pores in the glass.

(2) In the 5- to 25-K interval, κ of the composite is equal to κ of the starting porous glass.

The first feature does not raise any questions, although it seems remarkable that a small filling of the pores by sodium chloride is capable of producing such a noticeable effect on the κ of the composite.

The second feature is somewhat unusual. A zero contribution from the embedded NaCl to the κ of the composite can be expected only if the κ of the filler

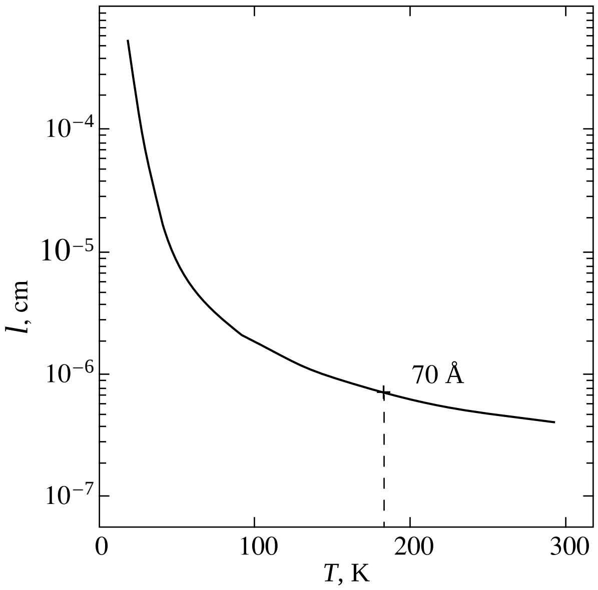

Fig. 3. Temperature dependence of phonon mean free path in bulk NaCl single crystals [17].

(NaCl in our case) is approximately equal to the κ of the matrix (porous glass) or is substantially smaller than it (filler $\kappa \lesssim$ matrix κ). The observed effect cannot be explained given the fact that the κ of NaCl in the glass is the same as that in the bulk material. For instance, at 5 K, the κ of bulk NaCl is ~600 W/m K according to [15],whereas the thermal conductivity of the composite and of the matrix is, according to our data (Figs. 1, 2), only ~0.03 W/m K.

The low-temperature thermal conductivity of NaCl in the channels of porous glass can be of the order of (or lower than) that of the matrix only if the NaCl nanocrystals in the channels of porous glass are subject to the size effect, for which the phonon mean free path (l) is limited by the size of the NaCl nanocrystals.

The mean free path of phonons in a bulk NaCl single crystal can be estimated as [17]

$$l = \frac{3\kappa_{ph}}{C_v \bar{v}}. \quad (1)$$

Here, C_v is the specific heat at constant volume [18–20] and $\bar{v}$ is the average sonic speed [21]. The values of l calculated from Eq. (1) for a bulk NaCl single crystal are shown graphically in Fig. 3.

We shall assume the NaCl nanocrystals embedded in channels of porous glass to have the same transverse dimensions as the channels (70 Å).[1] In this case, the value of l for NaCl nanocrystals in glass will be 70 Å and the maximum in $\kappa(T)$ for them will lie at ~180 K (Fig. 3).

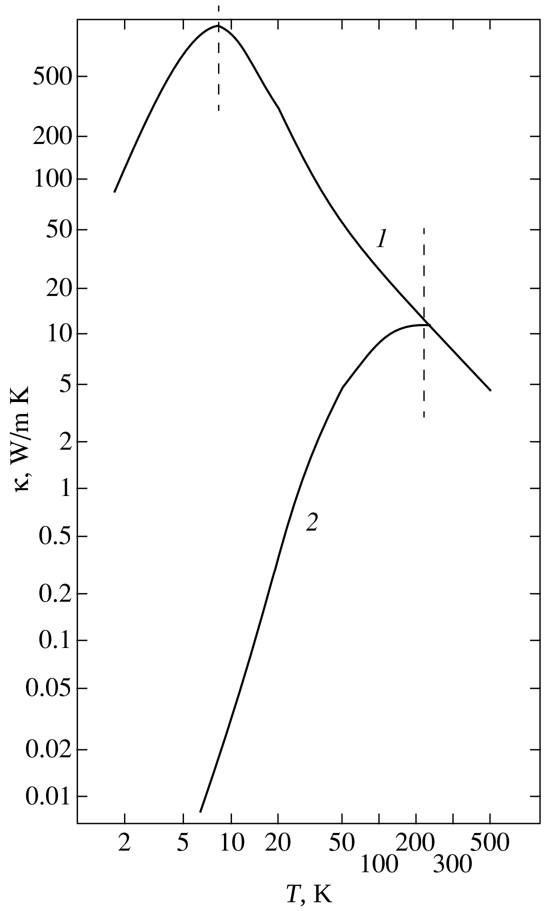

Fig. 4. Temperature dependence of the thermal conductivity of the (*1*) NaCl single crystal [15] and (*2*) NaCl assuming $\bar{v} \simeq$ const and l = const = 70 Å.

Equation (1) can be used to calculate $\kappa_{ph}(T)$ for NaCl nanocrystals in channels of porous glass (curve *2* in Fig. 4) accepting l = const = 70 Å, $C_v(T)$ and $\bar{v}$ = const for the interval 180–5 K [18–21]. Now, by taking these values of κ_{ph} for NaCl in porous glass, we find that in the interval 5–35 K, the κ of NaCl in channels of porous glass is smaller than or of the order of the κ of the matrix (porous glass) (see Figs. 1, 2, 4 and table).

This provides an explanation for the κ of the composite being approximately equal to that of the matrix in the temperature interval 5–35 K.

The above conclusion is qualitatively supported by our estimation of the thermal conductivity of the composite under study. The thermal conductivity of the composite κ_{eff} was calculated from the well-known formula obtained by Odelevsky [15] for a standard nanocomposite:

$$\frac{\kappa_{eff}}{\kappa_{mat}} = 1 - \frac{m}{\left(\frac{1}{1-\nu} - \frac{1-m}{3}\right)}, \quad (2)$$

---

[1] The transverse dimensions of NaCl nanocrystals may be less than 70 Å [11].

Thermal conductivity κ (in W/m K) of a bulk NaCl single crystal, of NaCl nanocrystals embedded in channels of porous glass, of porous glass, and of a porous glass + NaCl nanocomposite in the low-temperature region

T, K	κ of NaCl + porous glass composite	κ of porous glass	κ of NaCl single crystal	κ of NaCl nanocrystals embedded in porous glass
5	0.03	0.03	600	0.004
10	0.05	0.05	900	0.032

where $\nu = \frac{\kappa_{\text{fill}}}{\kappa_{\text{mat}}}$, m is the volume occupied by the filler, and κ_{fill} and κ_{mat} are the thermal conductivities of the filler (NaCl) and matrix (porous glass), respectively.

For κ_{fill}, we took the data available for bulk single-crystal NaCl [16] and our data obtained for NaCl nanocrystals embedded in channels of porous glass (curve *2* in Fig. 4).

As seen from Fig. 2, the calculation made for the κ_{fill} taken equal to the κ of bulk NaCl (dashed curve) for the low-temperature region $T < 35$ K, where the experiment showed the κ of the composite to be equal to the κ of the matrix, fails to fit to the experiment; conversely, good enough agreement between the calculated and experimental data for the whole temperature range covered, 5–300 K, was reached when the data on the thermal conductivity of nanocrystals embedded in channels of porous glass (curve *2* in Fig. 4) were substituted for κ_{fill} in Eq. (2).

It should be pointed out that we carried out only a qualitative analysis of the obtained data. The real behavior of the κ of the nanocomposite based on porous glass and of the material loaded in its channels follows a much more complicated pattern. We considered phonon scattering from the sample boundaries assuming the NaCl nanocrystals to be free. In actual fact, one should take into account that rather than being free, the nanocrystals are embedded in a matrix, which can also affect the behavior of the thermal conductivity of the filler considerably. In addition, our analysis disregarded the possible effect exerted on the κ of small crystals by surface vibrations[2] [10, 11] and by changes in the phonon spectrum [12, 13].

One can, however, draw the conclusion that phonon scattering from the boundaries of nanocrystals embedded in matrix channels probably dominates over the behavior of the κ(*T*) of small objects.

In conclusion, we point out another possible interpretation of our results for the κ of the porous glass + NaCl nanocomposite.

Both the experimental and theoretical studies reported in [22–25] and in other publications considered the possibility of the onset, at low temperatures $T < 20$–10 K, of additional phonon scattering in composites whose matrix (epoxy resin, polymers, etc.) was loaded by sufficiently large particles, 1 to 100 μm in size, of crystalline quartz, diamond, corundum [22], copper [24], etc., as well as by crystallized particles of the matrix (semicrystalline materials) [23] and of amorphous glass. In order to discriminate these materials from nanocomposites, we refer to them as microcomposites.

The additional phonon scattering giving rise to a decrease in the thermal conductivity of these composites at low temperatures appeared because of the contact thermal resistance r_b between the crystals (or amorphous particles) of the filler and the amorphous matrix.[3] According to [23–25], $r_b \sim T^{-3}$ and depends on the relative magnitude of the acoustic parameters and the filler and matrix densities.

In our case, however, there are some points that do not fit into the model considered in [23–25]. According to [22–24], as the temperature is lowered, κ_{eff} crosses κ_{mat} at one point and, as the temperature is lowered still further, falls off rapidly, following a law close to $\kappa_{\text{eff}} \sim T^{+3}$, until κ_{eff} becomes significantly smaller than κ_{mat}. No such behavior was observed, however, in our nanocomposite. This nanocomposite does not have the crossing point mentioned above; instead, one observes $\kappa_{\text{eff}} = \kappa_{\text{mat}}$ in the interval 4–35 K and κ_{eff} does not decrease with further lowering of the temperature (for $T < 30$–35 K).

That our experiment does not reveal the effect observed in [22–24] is possibly accounted for by the fact that the acoustic parameters and densities of the materials making up the nanocomposite (amorphous quartz and crystalline NaCl) do not differ very much from one another [21–25]. Thus, either r_b becomes insignificant compared to the contribution to κ that derives from phonon scattering by the boundaries of NaCl nanocrystals embedded in the channels of the porous glass matrix or the relation for r_b in nanocomposites is different from that observed in the microcomposites.

---

[2] The influence of surface modes on the κ of small particles can probably be felt above room temperature, because surface modes in small NaCl crystals, according to [11], appear in the gap between the limiting frequencies of longitudinal and transverse optical vibrations.

[3] At low temperatures, this thermal resistance is sometimes referred to in the literature as the Kapitza resistance [24].

ACKNOWLEDGMENTS

The authors are indebted to Yu.A. Kumzerov for valuable discussions.

This work was conducted within bilateral agreements between the Russian Academy of Sciences and Polish Academy of Sciences and was supported by the Russian Foundation for Basic Research, project nos. 02-02-17657 and 00-02-16883.

REFERENCES

1. V. N. Bogomolov and T. M. Pavlova, Fiz. Tekh. Poluprovodn. (St. Petersburg) **29** (5), 826 (1995) [Semiconductors **29**, 428 (1995)].
2. Yu. A. Kumzerov, in *Nanostructured Films and Coatings*, Ed. by Gan-Moog Chow, I. A. Ovid'ko, and T. Tsakalakos (Kluwer Academic, Dordrecht, 2000); NATO ASI Ser. 3: High Technology, Vol. 78, p. 63.
3. V. N. Bogomolov, Usp. Fiz. Nauk **124** (1), 171 (1978) [Sov. Phys. Usp. **21**, 77 (1978)].
4. I. D. Morokhov, V. I. Petinov, L. I. Trusov, and V. F. Petrunin, Usp. Fiz. Nauk **133**, 653 (1981) [Sov. Phys. Usp. **24**, 295 (1981)].
5. É. L. Nagaev, Usp. Fiz. Nauk **162** (9), 49 (1992) [Sov. Phys. Usp. **35**, 747 (1992)].
6. I. P. Grebenshchikov and T. A. Favorskaya, Tr. Gos. Opt. Inst. **7**, 72 (1931).
7. J. H. P. Watson, J. Appl. Phys. **37**, 516 (1966).
8. P. Levitz, G. Ehret, S. K. Sinha, and J. M. Drake, J. Chem. Phys. **95**, 6151 (1991).
9. Th. F. Nonnenmacher and R. Wunderle, Phys. Status Solidi B **82**, 257 (1977).
10. V. V. Bryksin, Yu. M. Gerbshteĭn, and D. N. Mirlin, Fiz. Tverd. Tela (Leningrad) **13** (6), 1603 (1971) [Sov. Phys. Solid State **13**, 1342 (1971)].
11. M. I. Abaev, V. N. Bogomolov, V. V. Bryksin, and N. A. Klushin, Fiz. Tverd. Tela (Leningrad) **13** (6), 1578 (1971) [Sov. Phys. Solid State **13**, 1323 (1971)].
12. V. N. Bogomolov, N. A. Klushin, N. M. Okuneva, *et al.*, Fiz. Tverd. Tela (Leningrad) **13** (5), 1491 (1971) [Sov. Phys. Solid State **13**, 1248 (1971)].
13. A. Balandin, Phys. Low-Dimens. Semicond. Struct. **1/2**, 1 (2000).
14. A. Jezowski, J. Mucha, and G. Pompe, J. Phys. D: Appl. Phys. **20** (5), 739 (1987).
15. G. N. Dul'nev and Yu. P. Zarichnyak, *Thermal Conductivity of Mixtures and Composite Materials* (Énergiya, Leningrad, 1974).
16. *Handbook on the Thermal Conductivity of Solids*, Ed. by A. S. Okhotin (Énergoatomizdat, Moscow, 1984).
17. V. N. Bogomolov, N. F. Kartenko, D. A. Kurdyukov, *et al.*, Fiz. Tverd. Tela (St. Petersburg) **41** (2), 348 (1999) [Phys. Solid State **41**, 313 (1999)].
18. K. Clusius and J. Goldmann, Z. Naturforsch. A **4**, 424 (1949).
19. J. H. Barkman, R. L. Anderson, and T. E. Brackett, J. Chem. Phys. **42** (3), 1112 (1965).
20. T. H. Kwon and J. H. Henkel, Can. J. Phys. **49**, 20 (1970).
21. *Acoustic Crystals*, Ed. by M. P. Shaskol'skaya (Nauka, Moscow, 1982).
22. K. W. Carret and H. M. Rosengerg, J. Phys. D: Appl. Phys. **7**, 1247 (1974).
23. C. L. Choy and D. Greig, J. Phys. C: Solid State Phys. **8**, 3121 (1975).
24. C. Schmidt, Cryogenics **15**, 17 (1975).
25. W. A. Little, Can. J. Phys. **37**, 334 (1959).

Translated by G. Skrebtsov

Physics of the Solid State, Vol. 45, No. 2, 2003, pp. 386–390. Translated from Fizika Tverdogo Tela, Vol. 45, No. 2, 2003, pp. 364–368.
Original Russian Text Copyright © 2003 by Korovaĭ, Khadzhi.

LOW-DIMENSIONAL SYSTEMS AND SURFACE PHYSICS

Nonlinear Surface Waves in a Symmetrical Three-Layer Structure Caused by the Generation of Excitons and Biexcitons in Semiconductors

O. V. Korovaĭ and P. I. Khadzhi
Dniester State University, ul. Dvadtsat' Pyatogo Octyabrya 128, Tiraspol, MD 3300 Moldova
e-mail: tdsu@tirastel.md

Received February 20, 2002

Abstract—A theory of nonlinear TE-polarized surface waves propagating along the flat interfaces of a symmetric flat three-layer structure with a linear core and nonlinear coatings is developed. The coatings are nonlinear due to the optical exciton–biexciton conversion. The dispersion laws of the propagating waves are found and analyzed. *© 2003 MAIK "Nauka/Interperiodica".*

1. INTRODUCTION

In view of the rapid development of integrated optics, investigation of the properties of surface, interface, and waveguide modes directed by the interfaces of nonlinear media and nonlinear light guides are of particular interest [1, 2]. The demonstration of the fact that *s*-polarized nonlinear surface waves can, in principle, propagate along the boundary between a crystal and vacuum [3–5] or between two nonlinear media [6] is a significant experimental result. The spatial distributions of the fields of nonlinear surface waves propagating in nonlinear media characterized by different modeling dielectric functions were studied in [7, 8]. The properties of nonlinear surface waves are usually studied by using the dielectric function of a crystal whose dependence on the field of the propagating wave can be represented by a quadratic (Kerr) correction with respect to the field. However, the use of such a dielectric function is valid only in the range of moderate fields. Furthermore, such a function carries almost no information on the model of the nonlinear medium and the type of quantum transitions involved. Nevertheless, the properties of nonlinear surface waves have been studied for non-Kerr media in a number of papers [9–13]. In a consistent theory, the dielectric function of a medium should be determined self-consistently from constitutive equations of the Bloch type with due regard for the specific mechanisms of the nonlinearity and quantum-transition type.

In this paper, we present the results of theoretical investigations of the properties of nonlinear surface waves (to be more specific, of nonlinear interface waves) propagating along an interface of a symmetrical three-layer structure (Fig. 1).

2. STATEMENT OF PROBLEM AND BASIC EQUATIONS

Let us consider nonlinear TE-polarized surface waves propagating in a symmetrical three-layer structure consisting of a flat $2d$ thick layer ($-d \le z \le +d$) surrounded by semi-infinite nonlinear semiconductors on both sides (Fig. 1). Suppose that the layer is characterized by a dielectric constant ε_0 and the coatings are semiconductors in which a propagating light wave can generate excitons from the ground state of the crystal and simultaneously transform them into biexcitons through optical exciton–biexciton conversion. This may occur in crystals, such as CdS and CdSe, in which the biexciton binding energy is vanishingly small. In these crystals, the giant oscillator strength corresponding to the optical exciton–biexciton conversion makes it possible to consider nonlinear propagation of laser radiation at moderate excitation levels. To solve the problem, we need to obtain the dielectric function of the nonlinear medium ε depending on the frequency ω

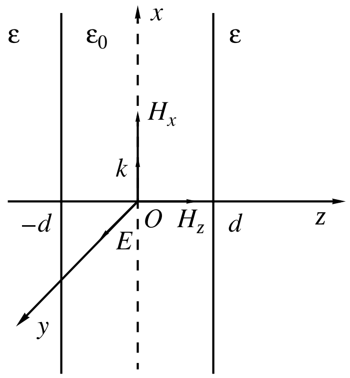

Fig. 1. Configuration of the problem and the directions of the field components.

1063-7834/03/4502-0386$24.00 © 2003 MAIK "Nauka/Interperiodica"

and amplitude E of the electromagnetic field of the propagating wave originating from the interaction between the light and the excitons and biexcitons in the crystal. The interaction Hamiltonian has the form

$$H = -\hbar g(a^+E^+ + aE^-) - \hbar\sigma(b^+aE^+ + a^+bE^-), \quad (1)$$

where E^+ and E^- are the positive- and negative-frequency components of the field of the electromagnetic wave, respectively; a and b are the amplitudes of the exciton and biexciton waves of the crystal polarization, respectively; g is the exciton–photon interaction constant; and σ is the optical exciton–biexciton conversion constant. The Heisenberg equations for the amplitudes a and b have the form

$$i\dot{a} = \omega_0 a - gE^+ - \sigma bE^-, \quad (2)$$

$$i\dot{b} = \Omega_0 b - \sigma aE^+, \quad (3)$$

where ω_0 and Ω_0 are the exciton- and biexciton-transition frequencies, respectively. In a stationary regime, a and E are proportional to $e^{-i\omega t}$ and b is proportional to $e^{-2i\omega t}$. Solutions to Eqs. (2) and (3) can be easily found in this case; then, we can find the polarization and the crystal dielectric function:

$$\varepsilon = \varepsilon_\infty\left(1 - \frac{\omega_{LT}}{\Delta}\frac{E_s^4}{(E_s^2 - E^2)^2}\right), \quad (4)$$

where $E_s^2 = 2\Delta^2/\sigma^2$, $\Delta = \omega - \omega_0$ is the detuning of the resonance between the frequency ω of the propagating radiation and the exciton transition frequency ω_0, $\omega_{LT} = 4\pi\hbar g^2/\varepsilon_\infty$ is the longitudinal–transverse splitting frequency of the exciton state, and ε_∞ is the background dielectric constant. It should be noted that Eq. (4) has been previously used in considering the properties of surface waves propagating along the boundary between semi-infinite linear and nonlinear media [9], optical bistability [14], and the self-reflection effect [15].

We use Eq. (4) to investigate the stationary propagation of TE-polarized surface waves in the geometry shown in Fig. 1. Suppose that the electromagnetic wave propagates along the x axis and is characterized by wave vector k. The wave field contains the transverse electric E (parallel to the y axis) and the transverse magnetic component H_z, as well as the longitudinal component of the magnetic field H_x. From the Maxwell equations, we derive the following wave equations to describe the spatial distribution of the electric field of the electromagnetic wave in the stationary regime:

$$\frac{d^2E}{dz^2} = \frac{\omega^2}{c^2}\left(n^2 - \varepsilon_\infty\left(1 - \frac{\omega_{LT}}{\Delta}\frac{E_s^4}{(E_s^2 - E^2)^2}\right)\right)E, \quad (5)$$
$$|z| \ge d,$$

$$\frac{d^2E}{dz^2} = \frac{\omega^2}{c^2}(n^2 - \varepsilon_0)E, \quad |z| \le d, \quad (6)$$

where $n = ck/\omega$ is the effective index of refraction of the medium and c is the speed of light in vacuum. We look for spatially confined surface waves whose energy is localized in the vicinity of the interface $|z| = d$. For this reason, a solution to Eq. (5) must satisfy the conditions

$$\lim_{z \to \pm\infty} E \longrightarrow 0, \quad \lim_{z \to \pm\infty} dE/dz \longrightarrow 0. \quad (7)$$

Introducing a new variable $\bar{z} = \frac{\omega}{c}x$ and integrating Eq. (5) with due regard for conditions (7) yields the following equation in the region $|\bar{z}| > D = \frac{\omega}{c}d$:

$$\left(\frac{dE}{d\bar{z}}\right)^2 + W(E) = 0, \quad (8)$$

where

$$W(E) = -E^2\left(n^2 - \varepsilon_\infty + \varepsilon_\infty\frac{\omega_{LT}}{\Delta}\frac{E_s^2}{E_s^2 - E^2}\right). \quad (9)$$

Here, $W(E)$ is the potential energy of a nonlinear oscillator, whose motion is described by the first integral in Eq. (8).

It should be noted that for an optically linear medium, we have $W(E) = -E^2(n^2 - \varepsilon_0)$, where ε_0 is the dielectric constant of the middle layer. Extending this to the nonlinear case, one can write $W(E)$ as $W(E) = -E^2(n^2 - \varepsilon^*)$, where, according to Eq. (9), we have

$$\varepsilon^* = \varepsilon_\infty\left(1 - \frac{\omega_{LT}}{\Delta}\frac{E_s^2}{E_s^2 - E^2}\right). \quad (10)$$

Below, ε^* is referred to as the effective dielectric function of the medium. It follows from Eq. (8) that solutions to this equation in the form of surface waves exist only for the amplitudes of the field $E(z)$ satisfying the condition $W(E) \le 0$. This condition significantly restricts the range of values of the parameters in which the desired solutions exist. An analysis shows that solutions exist at $\Delta < 0$ and for $n^2 > \varepsilon_{\text{ex}} = \varepsilon_\infty\left(1 - \frac{\omega_{LT}}{\Delta}\right)$ and the amplitudes of the corresponding waves lie in the range

$$0 \le E^2 \le E_m^2 = \frac{n^2 - \varepsilon_{\text{ex}}}{n^2 - \varepsilon_\infty}E_s^2. \quad (11)$$

Here, ε_{ex} is the dielectric function of the linear medium in the vicinity of the exciton transition and E_m is the maximum possible amplitude of the field in the surface wave. Hence it follows that the nonlinear surface waves can exist only in the long-wavelength range with respect to the frequency of the exciton transition and under the condition that $n^2 \geq \varepsilon_0$ or $n^2 \geq \varepsilon^*$. The spatial distribution of the field $E(\bar{z})$ of this wave has a maximum in the region $|\bar{z}| > D$. Integrating Eq. (8) yields the following solution for the profile of the field $E(z)$ outside the layer (for $|\bar{z}| > D$):

$$\ln\frac{\sqrt{E_s^2-E^2}+\sqrt{E_m^2-E^2}}{\sqrt{E_s^2-E_0^2}+\sqrt{E_m^2-E_0^2}} + \frac{E_s}{E_m}\ln\left(\frac{E}{E_0}\frac{E_s\sqrt{E_m^2-E_0^2}+E_m\sqrt{E_s^2-E_0^2}}{E_s\sqrt{E_m^2-E^2}+E_m\sqrt{E_s^2-E^2}}\right) = q(\bar{z}-D) \tag{12}$$

in the region $D \leq \bar{z} \leq \bar{z}_m$ and

$$\ln\frac{\sqrt{E_s^2-E_m^2}}{\sqrt{E_s^2-E^2}+\sqrt{E_m^2-E^2}} + \frac{E_s}{E_m}\ln\left(\frac{E_s\sqrt{E_m^2-E^2}+E_m\sqrt{E_s^2-E^2}}{E\sqrt{E_s^2-E_m^2}}\right) = q(\bar{z}-\bar{z}_m) \tag{13}$$

for $\bar{z} \geq \bar{z}_m$. Here, the position $\bar{z} = \bar{z}_m$ of the maximum of the field $E(\bar{z}) = E_m$ is determined from the expression

$$q(\bar{z}_m-D) = \ln\frac{\sqrt{E_s^2-E_m^2}}{\sqrt{E_s^2-E_0^2}+\sqrt{E_m^2-E_0^2}} + \frac{E_s}{E_m}\ln\left(\frac{E_s\sqrt{E_m^2-E_0^2}+E_m\sqrt{E_s^2-E_0^2}}{E_0\sqrt{E_s^2-E_m^2}}\right), \tag{14}$$

where $q = \sqrt{n^2-\varepsilon_\infty}$ and E_0 is the field amplitude at the boundary of the light guide at ($\bar{z} = D$). It follows from Eq. (12) that, in the region $\bar{z} \gg \bar{z}_m$, where $E \ll E_m$, the field decays exponentially: $E \sim \exp(-\sqrt{n^2-\varepsilon_{\text{ex}}}(\bar{z} - \bar{z}_m))$.

First, we consider the properties of symmetrical (even) nonlinear surface waves. In this case, the solution to Eq. (6) has the form

$$E = \frac{C}{q_0}\cosh(q_0\bar{z}), \tag{15}$$

where $q_0 = \sqrt{n^2-\varepsilon_0}$ and C is a constant of integration, which defines the field amplitude at the center of the layer in this case. From the condition that the tangential components of the electric and magnetic fields be continuous at the boundary $\bar{z} = D$, the following relationship can be obtained using Eqs. (15) and (8):

$$q_0\tanh(q_0D) = \sqrt{n^2-\varepsilon_\infty-\varepsilon_\infty\frac{\omega_{LT}}{|\Delta|}\frac{E_s^2}{E_s^2-E_0^2}}. \tag{16}$$

This formula can be considered to be a dispersion relation determining the $\omega(k)$ dependence or, in this case, the effective index of refraction n of the medium depending on the detuning from the resonance Δ at fixed values of the layer thickness d and the parameter E_0, which is the amplitude of the wave field at the boundary between the media at $\bar{z} = D$. It should be noted that the field amplitude E_0 cannot be controlled experimentally; the energy flow P transferred by the propagating wave is experimentally determined in this case. The total energy flux through the cross-sectional area of the wave guide P can be written as the sum of the linear flux P_L in the core and the nonlinear flux P_{NL} in the coatings:

$$P_L = \frac{c^2n}{4\pi\omega}\frac{E_0^2}{4q_0\cosh^2(q_0D)}(\sinh(2q_0D)+2q_0D), \tag{17}$$

$$P_{NL} = \frac{c^2n}{8\pi\omega}\frac{1}{q}\left\{E_sE_m+\sqrt{(E_s^2-E_0^2)(E_m^2-E_0^2)} + (E_s^2-E_m^2)\ln\frac{\sqrt{E_s^2-E_0^2}+\sqrt{E_m^2-E_0^2}}{E_s-E_m}\right\}. \tag{18}$$

Using Eq. (16) to eliminate E_0 from Eqs. (17) and (18), we find the $P(n, \Delta)$ dependence or the dependence of the effective index of refraction n of the nonlinear light guide on the energy flow transferred by the wave.

Now, we consider antisymmetric (odd) nonlinear surface waves. For the internal region ($|\bar{z}| \leq D$), the solution has the form

$$E = \frac{C}{q_0}\sinh(q_0\bar{z}) \tag{19}$$

for the external region: the solution is defined by Eqs. (12)–(14) and (18), as in the case of symmetric waves. The energy flux in the layer in this case is

$$P_L = \frac{c^2n}{4\pi\omega}\frac{E_0^2}{4q_0\sinh^2(q_0D)}(\sinh(2q_0D)-2q_0D), \tag{20}$$

and the dispersion law is expressed by the formula

$$q_0\coth(q_0D) = \sqrt{n^2-\varepsilon_\infty-\varepsilon_\infty\frac{\omega_{LT}}{|\Delta|}\frac{E_s^2}{E_s^2-E_0^2}}. \tag{21}$$

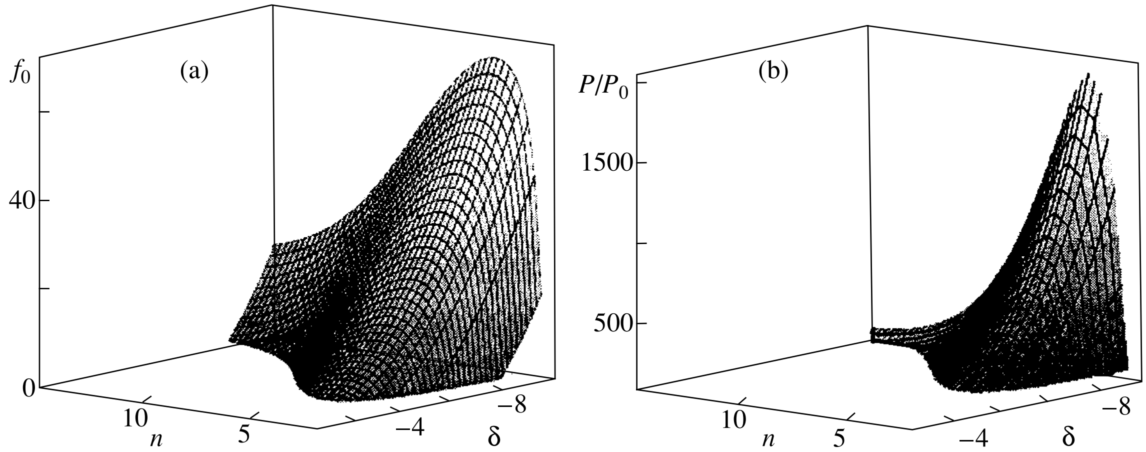

Fig. 2. Dispersion law of symmetrical TE-polarized surface waves at $\varepsilon_0 = 5.6$, $\varepsilon_\infty = 5$, and $D = 1/3$.

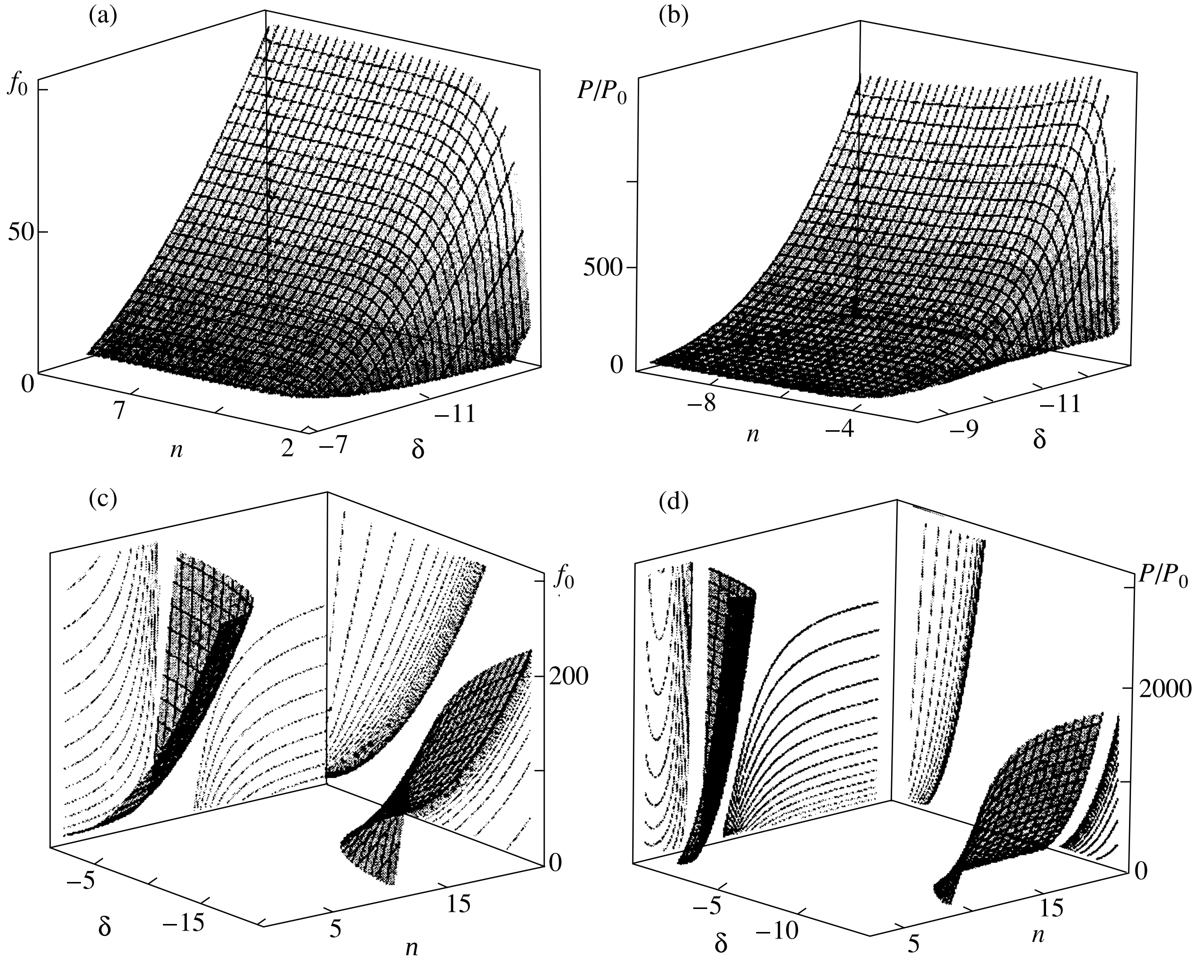

Fig. 3. Dispersion laws of antisymmetrical TE-polarized surface waves at $\varepsilon_0 = 5.6$ and $\varepsilon_\infty = 5$ for the cases of (a, b) $D = 1$ and (c, d) 1/3.

3. DISCUSSION

For simplicity, we will use the resonance detuning Δ and the Rabi frequency σE_0 normalized to the longitudinal–transverse splitting ω_{LT}: $\delta = \Delta/\omega_{LT}$ and $f_0 = \sigma E_0/\omega_{LT}$. First, we consider the dispersion law for even modes and, according to Eq. (15), study the behavior of the $n(\delta, f_0)$ dispersion curves. It follows from Eq. (16)

that $n^2 > \varepsilon_0$, ε^* is larger than ε_0 and ε^*, where $\varepsilon^* = \varepsilon_\infty(1 + |\delta|/(\delta^2 - f_0^2/2))$. The nonlinear surface waves exist only in the spectral range $\delta < 0$. At a fixed value of f_0, the $\delta(n)$ curve begins at the point $n = \sqrt{\varepsilon_0}$, where $|\delta| = |\delta_0| = (1 + \sqrt{1 + 2f_0^2})/2$. Then, the function $\delta(n)$ monotonically increases with $n = \sqrt{\varepsilon_0 + x_m^2 D^{-2}}$, reaching a maximum value $|\delta_m| = \left(1 + \frac{x_m^2 - 1}{4D^2}\right)^{-1}$ at n, where x_m is determined from the equation $x \tanh x = 1$. As n increases further, the function $\delta(n)$ decreases and asymptotically approaches $|\delta| = |\delta_0|$. There are two values of n corresponding to a given value of $|\delta|$. With increasing D, the maximum point approaches $n = \sqrt{\varepsilon_0}$. The $n(\delta, f_0)$ surface is shown in Fig. 2a. As f_0 increases, the region of existence of the nonlinear surface waves shifts towards longer wavelengths; thus, the long-wavelength part is pulled into the spectrum of the light guide, whereas the short-wavelength parts are expelled from it. At a fixed value of $|\delta| > |\delta_m|$, the function $f_0(n)$ has a maximum at $n = (\varepsilon_0 + x_m D^{-2})^{1/2}$ and the position of the maximum does not depend on $|\delta|$. The smaller the $|\delta|$, the higher the maximum of the function $f_0(n)$.

Figure 2b shows the $P(n, \delta)$ dependence for symmetric nonlinear surface waves. It is seen that at a fixed value of $|\delta|$, the energy flux increases rapidly with n and then, reaching a maximum, monotonically decreases. At fixed n, the energy flux decreases rapidly with increasing $|\delta|$. It should be noted that there are two different values of the effective index of refraction n corresponding to the same energy flux.

Figures 3a–3c show the dispersion law of the antisymmetrical nonlinear surface waves for two values of the normalized thickness of layer D. It follows from Eq. (21) that, at $D > (\varepsilon_0 - \varepsilon_\infty)^{-1/2}$, the dispersion relation describes a surface in (n, δ, f_0) space which is bound with respect to δ and n (Fig. 3a). At $D < (\varepsilon_0 - \varepsilon_\infty)^{-1/2}$; however, the dispersion law defines two different surfaces, because there is a gap in the dispersion law (Fig. 3c). One of these surfaces is restricted to values of n within the limits $\sqrt{\varepsilon_0} \le n \le n^*$, where n^* is a solution to the equation $(\varepsilon_0 - \varepsilon_\infty)\sinh^2(q_0 D) = q_0^2$. It is seen that the limit values of the effective index of refraction n^* depend on ε_0, ε_∞, and D but are independent of the resonance detuning δ. The more distant region of the dispersion law is defined by the inequality $n \ge n^{**}$, where n^{**} is a solution to the equation $(\varepsilon_0 - \varepsilon_\infty - \varepsilon_\infty/|\delta|)\sinh^2(q_0 D) = q_0^2$ and depends not only on the parameters ε_0, ε_∞, and D but also on the resonance detuning δ. At $|\delta| \gg 1$, the gap in n (the interval of the forbidden values of n) decreases and $n^{**} \longrightarrow n^*$.

It can be seen from Figs. 3b and 3d that the dispersion law depends on the energy flux and also exists in one or two separate regions, depending on the value of the parameter D.

4. CONCLUSIONS

Thus, the properties of *s*-polarized nonlinear surface waves arising from the interaction of excitons and biexcitons with light differ significantly from the properties of nonlinear surface waves propagating in Kerr media. The resonance character of the nonlinear dielectric function is of crucial importance for the existence of the waves considered in the present paper. The region of existence of the antisymmetrical nonlinear surface waves is split into two independent subregions separated from each other at certain values of the parameters. The dispersion laws obtained depend significantly on the value of the energy flux.

REFERENCES

1. *Surface Polaritons: Electromagnetic Waves at Surfaces and Interfaces*, Ed. by V. M. Agranovich and D. L. Mills (North-Holland, Amsterdam, 1982; Nauka, Moscow, 1985).
2. N. L. Dmitruk, V. G. Litovchenko, and V. L. Strizhevskiĭ, *Surface Polaritons in Semiconductors* (Naukova Dumka, Kiev, 1989).
3. V. M. Agranovich, V. S. Babichenko, and V. A. Chernyak, Pis’ma Zh. Éksp. Teor. Fiz. **32** (8), 532 (1980) [JETP Lett. **32**, 512 (1980)].
4. W. I. Tomlinson, Opt. Lett. **5** (7), 323 (1980).
5. A. A. Maradudin, Appl. Phys. B **41** (4), 341 (1980).
6. A. I. Lomtev, Pis’ma Zh. Éksp. Teor. Fiz. **34** (2), 64 (1981) [JETP Lett. **34**, 60 (1981)].
7. P. I. Khadzhi and E. S. Kiseleva, Zh. Tekh. Fiz. **57** (2), 395 (1987) [Sov. Phys. Tech. Phys. **32**, 242 (1987)].
8. A. D. Boardman and T. Twardowski, J. Opt. Soc. Am. B **5** (2), 523 (1988).
9. P. I. Khadzhi and E. S. Kiseleva, Phys. Status Solidi B **147** (2), 741 (1988).
10. P. I. Khadzhi, Fiz. Tverd. Tela (Leningrad) **29** (9), 2721 (1987) [Sov. Phys. Solid State **29**, 1566 (1987)].
11. P. I. Khadzhi and L. V. Fedorov, Zh. Tekh. Fiz. **61** (5), 110 (1991) [Sov. Phys. Tech. Phys. **36**, 564 (1991)].
12. L. S. Aslanyan and Yu. S. Chilingaryan, Pis’ma Zh. Tekh. Fiz. **20** (9), 1 (1994) [Tech. Phys. Lett. **20**, 765 (1994)].
13. V. G. Bordo, Pis’ma Zh. Tekh. Fiz. **14** (13), 1172 (1988) [Sov. Tech. Phys. Lett. **14**, 512 (1988)].
14. P. I. Khadzhi, G. D. Shibarshina, and A. Kh. Rotaru, *Optical Bistability in a System of Coherent Exitons and Biexcitons in Semiconductors* (Shtiintsa, Kishinev, 1988).
15. P. I. Khadzhi and K. D. Lyakhomskaya, Kvantovaya Élektron. (Moscow) **29** (1), 43 (1999).

Translated by A. Poushnov

Physics of the Solid State, Vol. 45, No. 2, 2003, pp. 391–399. Translated from Fizika Tverdogo Tela, Vol. 45, No. 2, 2003, pp. 369–376.
Original Russian Text Copyright © 2003 by Kosachev, Gandurin.

LOW-DIMENSIONAL SYSTEMS AND SURFACE PHYSICS

Rayleigh Wave Dispersion and Attenuation on a Statistically Rough Free Surface of a Hexagonal Crystal

V. V. Kosachev and Yu. N. Gandurin

Moscow Engineering Physics Institute, Kashirskoe sh. 31, Moscow, 115409 Russia

e-mail: kosachev@pc1k32.mephi.ru

Received October 30, 2001; in final form, March 11, 2002

Abstract—Dispersion and attenuation of Rayleigh surface acoustic waves on a statistically rough free surface of a *Z*-cut hexagonal crystal were analytically studied using a modified mean-field method within the perturbation theory. Numerical calculations were carried out in the frequency range accessible for the perturbation theory using expressions for the real and imaginary parts of the complex frequency shift of Rayleigh waves caused by a slight surface roughness. The Rayleigh wave dispersion and attenuation in the *Z*-cut hexagonal crystal were shown to coincide qualitatively with those in an isotropic medium, differing only quantitatively. In the long-wavelength limit $\lambda \gg a$, where a is the lateral roughness correlation length, explicit analytical expressions for the relative change in the phase velocity and the inverse damping depth of Rayleigh waves were derived and used in numerical calculations. © *2003 MAIK “Nauka/Interperiodica”*.

1. INTRODUCTION

Over the past twenty-five years, a great number of theoretical and experimental studies have been dedicated to the propagation of surface acoustic waves (SAWs) along a statistically rough solid surface. This attention can be explained by the high sensitivity of SAWs to various perturbations of the surface along which they propagate. Random roughness is one of the most commonly encountered perturbations existing at the surface of a sample and arising during sample preparation. SAWs have found many technical applications in seismology, ultrasonic defectoscopy, and acoustoelectronics.

Emphasis has been placed on the Rayleigh waves, which, as is known [1], can exist in a semi-infinite elastic medium that is bounded by a plane surface and propagate along it with no dispersion or attenuation. When the surface is only slightly rough (the characteristic roughness heights are small in comparison with the wavelength of the wave under study), a small roughness-caused addition (a complex frequency shift) arises in the dispersion law of the Rayleigh wave. In this case, the real part of the frequency shift describes the phase velocity dispersion of the Rayleigh wave, while the imaginary part characterizes wave attenuation.

The dispersion relation for the Rayleigh SAW propagating along the statistically rough free surface of an isotropic solid was first found theoretically in [2]. The dispersion law was derived in an integral form using the mean-field (Rayleigh) method. Since the authors of [2] failed to calculate the integral in an explicit form, they made an order-of-magnitude estimate of the imaginary part of the frequency shift, i.e., of the attenuation. In [3–5], the Rayleigh SAW attenuation was studied in the framework of the scattering theory using the Green’s function method. We note that the mean-field method, in contrast to the scattering theory, allows one to determine not only the imaginary part of the frequency shift but also its real part. In [6–8], the dispersion law of a Rayleigh wave propagating along a statistically rough surface was derived by solving the Dyson equation for the average Green’s function. In this case, the dispersion relations also had an integral form and only order-of-magnitude estimates of the dispersion and attenuation were made in the extreme cases of short and long (in comparison with the lateral roughness correlation length) Rayleigh waves.

In our opinion, the dispersion and attenuation of a Rayleigh SAW propagating along a slightly rough free surface of an isotropic elastic half-space were most comprehensively studied in [9]. The authors of [9] derived explicit analytical expressions for the real and imaginary parts of the frequency shift using the mean-field method. Since the expressions for the phase velocity dispersion and the attenuation coefficient were rather intricate and contained integrals, the authors of [9] calculated them numerically in a wide frequency range. The approach advanced in [9] was generalized in [10] to the case of stratified media by taking into account the piezoelectric effect. We note that, in [2–10], the three-dimensional roughness $x_3 = \zeta(x_1, x_2)$ was mostly considered. An important class of problems related to the Rayleigh wave dispersion and attenuation caused by two-dimensional roughness $x_3 = \zeta(x_1)$ was considered in [10–14].

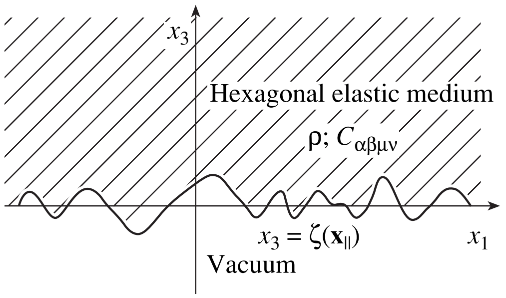

Fig. 1. Geometry of the semi-infinite homogeneous elastic medium with a free surface $x_3 = \zeta(\mathbf{x}_{\parallel})$ exhibiting three-dimensional roughness.

An analysis of [2–14] shows that their results often seriously differ and sometimes contradict each other. This is true for both conclusions made on the basis of different methods and within the same technique. To clarify the situation, the use of a modified mean-field method was suggested in [15] to calculate the dispersion and attenuation. The expressions derived in [15], along with the relations from [5], confirmed the results of [9].

We note that only isotropic media were considered in most of the above-mentioned studies. As for [10, 15], where the results involved the Green's tensor for an anisotropic elastic medium occupying the half-space $x_3 > 0$, numerical calculations were carried out only for the isotropic case. However, the overwhelming majority of materials in applications of SAWs are anisotropic crystals. In contrast to isotropic media, computational complications emerge even for ideally smooth surfaces in this case. The study in [16] seems to be the first to derive frequency dependences for the Rayleigh SAW dispersion and attenuation in the long-wavelength limit. The dependences of the relative variation in the phase velocity in the Rayleigh SAW on the propagation angle were numerically constructed for various anisotropic-medium cuts.

This study is dedicated to the Rayleigh SAW propagation along the statistically rough free surface of a hexagonal crystal (three-dimensional roughness). The statistical roughness is assumed to be slight; the surface $x_3 = 0$ coincides with the crystal basal plane (Z cut). The modified mean-field method [15] is applied; this method allows derivation of the dispersion relations for SAWs of various polarizations propagating along a free slightly rough solid surface of any symmetry. We analytically derive a dispersion relation for the frequency shift of Rayleigh waves and study this relation numerically in the whole frequency range accessible for the perturbation theory. Furthermore, we derive analytical expressions for the phase velocity dispersion and the attenuation coefficient of Rayleigh waves in the long-wavelength limit and compare them to the results of [16]. The dispersion and attenuation of Rayleigh waves propagating in any direction along the rough Z-cut surface $x_3 = \zeta(x_1)$ of a hexagonal elastic medium will be studied in a separate paper.

2. STATEMENT OF THE PROBLEM. EFFECTIVE BOUNDARY CONDITIONS FOR AN ELASTIC SEMI-INFINITE HEXAGONAL MEDIUM BOUNDED BY A FREE SLIGHTLY ROUGH SURFACE

The geometry of the problem is shown in Fig. 1. A hexagonal crystal, considered in the elastic-continuum approximation with the hexad axis parallel to the x_3 axis, is bounded by a free rough surface $x_3 = \zeta(\mathbf{x}_{\parallel})$ and occupies the half-space $x_3 > \zeta(\mathbf{x}_{\parallel})$, where $\mathbf{x}_{\parallel} = (x_1, x_2, 0)$. The hexagonal elastic medium is characterized by the mass density ρ and the elastic-moduli tensor $C_{\alpha\beta\mu\nu}$. A Rayleigh wave propagates along the statistically rough surface of the hexagonal medium (Z cut). It is required to determine the phase velocity dispersion and attenuation of the Rayleigh wave caused by the surface roughness.

For a randomly rough surface, the surface profile function $\zeta(\mathbf{x}_{\parallel})$ is not known exactly; therefore, we describe the surface statistically as

$$\langle\zeta(\mathbf{x}_{\parallel})\rangle = 0, \quad \langle\zeta(\mathbf{x}_{\parallel})\zeta(\mathbf{x}'_{\parallel})\rangle = \delta^2 W(|\mathbf{x}_{\parallel} - \mathbf{x}'_{\parallel}|). \quad (1)$$

Here, $\delta = \sqrt{\langle\zeta^2\rangle}$ is the root-mean-square roughness amplitude, the angular brackets indicate averaging over the ensemble of profile function $\zeta(\mathbf{x}_{\parallel})$ realizations, and $W(|\mathbf{x}_{\parallel}|)$ is the correlation function, hereafter assumed to be a Gaussian,

$$W(|\mathbf{x}_{\parallel}|) = \exp(-|\mathbf{x}_{\parallel}|^2/a^2), \quad (2)$$

where a is the lateral roughness correlation length characterizing the average distance between sequential surface peaks or hollows.

The surface roughness is assumed to be slight; i.e., we consider the characteristic roughness height δ to be small in comparison with the wavelength of the wave under study $(\delta/\lambda) \ll 1$. The temporal dependence of the displacement field $u(\mathbf{x}, t)$ is assumed to be harmonic,

$$u(\mathbf{x}, t) = u(\mathbf{x}|\omega)\exp(-i\omega t).$$

Taking into account the above assumptions, the equations of motion of the medium are written as

$$\left(\omega^2\delta_{\alpha\mu} + \frac{1}{\rho}C_{\alpha\beta\mu\nu}\frac{\partial^2}{\partial x_\beta \partial x_\nu}\right)u_\mu(\mathbf{x}|\omega) = 0, \quad x_3 > \zeta(\mathbf{x}_{\parallel}), \quad (3)$$

where the Greek subscripts α, β, γ, … run through 1, 2, and 3; repeated subscripts indicate summation.

The boundary conditions at the free surface are given by

$$C_{\alpha\beta\mu\nu}\hat{n}_\beta \left.\frac{\partial u_\mu(\mathbf{x}|\omega)}{\partial x_\nu}\right|_{x_3 = \zeta(\mathbf{x}_{\parallel})} = 0, \quad a = 1, 2, 3, \quad (4)$$

where $\hat{n}$ is the unit normal vector to the surface dependent on the two-dimensional vector $\mathbf{x}_\parallel$.

To derive the dispersion relation for the SAW (it can be both a Rayleigh SAW and an SAW of shear horizontal (SH) polarization), equations of motion (3) should be solved in the half-space $x_3 > \zeta(\mathbf{x}_\parallel)$, taking into account boundary conditions (4) at the free surface $x_3 = \zeta(\mathbf{x}_\parallel)$. We solve this problem using the modified mean-field method advanced in [15]. As shown in [15], in the case of slightly rough surfaces, this problem can be reduced to a simpler one, namely, to the same equations of motion (3), but in the half-space $x_3 > 0$, and to effective boundary conditions at the plane surface $x_3 = 0$. These effective boundary conditions for the Fourier components of the displacement field were obtained in [1] to the second order with respect to ζ (see [1, Eqs. (2.19)]).

As indicated in [15], only the assumption of a slight surface roughness was used when deriving the effective boundary conditions and the medium symmetry was not concretized. Thus, the effective boundary conditions are also valid for the *Z*-cut hexagonal elastic medium under consideration.

3. SET OF EQUATIONS FOR THE MEAN DISPLACEMENT FIELD

To derive the dispersion equation for Rayleigh waves, we preliminarily write a set of equations for the mean displacement field. To this end, it is convenient to pass over from the set of differential equations of motion (3) in the half-space $x_3 > 0$ and the effective boundary conditions at the plane surface $x_3 = 0$ to a set of integral equations. With this object in view, we introduce the Green's function $D_{\alpha\beta}(\mathbf{x}, \mathbf{x}'|\omega)$, satisfying the equation

$$\left(\omega^2\delta_{\alpha\mu} + \frac{1}{\rho}C_{\alpha\beta\mu\nu}\frac{\partial^2}{\partial x_\beta \partial x_\nu}\right)D_{\mu\beta}(\mathbf{x}, \mathbf{x}'|\omega) = \delta_{\alpha\beta}\delta(\mathbf{x} - \mathbf{x}'), \quad x_3, x_3' \geq 0 \tag{5}$$

and the boundary conditions at the plane $x_3 = 0$ and at infinity

$$C_{\alpha 3\mu\nu}\frac{\partial}{\partial x_\nu}D_{\mu\beta}(\mathbf{x}, \mathbf{x}'|\omega)\big|_{x_3 = 0} = 0,$$

$$D_{\alpha\beta}(\mathbf{x}, \mathbf{x}'|\omega)\big|_{x_3 \to \infty} = 0.$$

Then, using the fact that the displacement field diminishes with distance from the surface, as well as the symmetry property of the Green's tensor

$$D_{\alpha\gamma}(\mathbf{x}, \mathbf{x}'|\omega) = D_{\gamma}(\mathbf{x}, \mathbf{x}'|\omega),$$

we invoke Green's integral theorem to arrive at

$$\theta(x_3)u_\alpha(\mathbf{x}|\omega) = \int d^2x'_\parallel\left\{D_{\alpha\gamma}(\mathbf{x}, \mathbf{x}'|\omega)\frac{1}{\rho}C_{\gamma 3\mu\nu}\frac{\partial u_\mu(\mathbf{x}|\omega)}{\partial x'_\nu}\right\}_{x'_3 = 0}, \tag{6}$$

where $\theta(x_3)$ is the Heaviside step function.

The hexagonal crystal is assumed to be oriented such that the surface $x_3 = 0$ coincides with the crystal basal plane (*Z* cut). All the directions in the basal plane of the hexagonal crystal are equivalent for elastic waves. In other words, the hexagonal crystal in the plane $x_3 = 0$ is characterized by translational invariance in the directions parallel to the plane $x_3 = 0$. Therefore, we have

$$D_{\alpha\beta}(\mathbf{x}, \mathbf{x}'|\omega) = D_{\alpha\beta}(\mathbf{x}_\parallel - \mathbf{x}'_\parallel; x_3, x'_3|\omega)$$

and the Green's function can be conveniently represented in the form of a Fourier integral,

$$D_{\alpha\beta}(\mathbf{x}, \mathbf{x}'|\omega) = \int\frac{d^2k_\parallel}{(2\pi)^2} \times \exp(i\mathbf{k}_\parallel(\mathbf{x}_\parallel - \mathbf{x}'_\parallel))D_{\alpha\beta}(\mathbf{k}_\parallel\omega|x_3x'_3).$$

Then, the set of integral equations (6) in the Fourier representation is written as

$$\theta(x_3)u_\alpha(\mathbf{k}_\parallel\omega|x_3) = D_{\alpha\gamma}(\mathbf{k}_\parallel\omega|x_3 0) \times\left\{\frac{1}{\rho}\left[C_{\gamma 3\mu\Phi}ik_\Phi + C_{\gamma 3\mu 3}\frac{\partial}{\partial x'_3}\right]u_\mu(\mathbf{k}_\parallel\omega|x'_3)\right\}_{x'_3 = 0}, \tag{7}$$

where the subscript Φ takes on the values 1 and 2.

The braced expression in the right-hand side of Eq. (7) coincides with the left-hand side of the expression for the effective boundary conditions. Thus, we come to a homogeneous integral equation for $u_\alpha(\mathbf{k}_\parallel\omega|x_3)$ to the second order with respect to ζ:

$$\begin{aligned}\theta(x_3)u_\alpha(\mathbf{k}_\parallel\omega|x_3) &= \int\frac{d^2q_\parallel}{(2\pi)^2}D_{\alpha\gamma}(\mathbf{k}_\parallel\omega|x_3 0) \\ &\times\zeta(\mathbf{k}_\parallel - \mathbf{q}_\parallel)M_{\gamma\mu}(\mathbf{q}_\parallel, \mathbf{k}_\parallel|\omega)u_\mu(\mathbf{q}_\parallel\omega|0) \\ &+ \int\frac{d^2q_\parallel}{(2\pi)^2}D_{\alpha\gamma}(\mathbf{k}_\parallel\omega|x_3 0)\zeta^{(2)}(\mathbf{k}_\parallel - \mathbf{q}_\parallel) \\ &\times N_{\gamma\mu}(\mathbf{q}_\parallel, \mathbf{k}_\parallel|\omega)u_\mu(\mathbf{q}_\parallel\omega|0).\end{aligned} \tag{8}$$

Expression (8) can be significantly simplified by introducing a real orthogonal 3 × 3 matrix $S(\mathbf{k}_\parallel)$ and its inverse $S^{-1}(\mathbf{k}_\parallel)$,

$$S(\hat{\mathbf{k}}_\parallel) = \begin{pmatrix} \hat{k}_1 & \hat{k}_2 & 0 \\ -\hat{k}_2 & \hat{k}_1 & 0 \\ 0 & 0 & 1 \end{pmatrix}, \quad S^{-1}(\hat{\mathbf{k}}_\parallel) = \begin{pmatrix} \hat{k}_1 & -\hat{k}_2 & 0 \\ \hat{k}_2 & \hat{k}_1 & 0 \\ 0 & 0 & 1 \end{pmatrix}, \tag{9}$$

$$\hat{k}_\Phi = \frac{k_\Phi}{k_\parallel}, \quad \Phi = 1, 2,$$

as well as the following notation:

$$F_\alpha(\mathbf{k}_\parallel\omega|x_3) = S_{\alpha\mu}(\hat{\mathbf{k}}_\parallel)u_\mu(\mathbf{k}_\parallel\omega|x_3), \tag{10}$$

$$d_{\alpha\beta}(\mathbf{k}_\parallel\omega|x_3x_3') = S_{\alpha\mu}(\hat{\mathbf{k}}_\parallel)D_{\mu\nu}(\mathbf{k}_\parallel\omega|x_3x_3')S^{-1}_{\nu\beta}(\hat{\mathbf{k}}_\parallel), \tag{11}$$

$$X_{\alpha\beta}(\mathbf{q}_\parallel, \mathbf{k}_\parallel|\omega) = S_{\alpha\mu}(\hat{\mathbf{k}}_\parallel)M_{\mu\nu}(\mathbf{q}_\parallel, \mathbf{k}_\parallel|\omega)S^{-1}_{\nu\beta}(\hat{\mathbf{q}}_\parallel), \tag{12}$$

$$Y_{\alpha\beta}(\mathbf{q}_\parallel, \mathbf{k}_\parallel|\omega) = S_{\alpha\mu}(\hat{\mathbf{k}}_\parallel)N_{\mu\nu}(\mathbf{q}_\parallel, \mathbf{k}_\parallel|\omega)S^{-1}_{\nu\beta}(\hat{\mathbf{q}}_\parallel). \tag{13}$$

Using the symmetry properties of the elastic-moduli tensor $C_{\alpha\beta\gamma\delta} = C_{\gamma\delta\alpha\beta}$, the matrices X and Y can easily be shown to possess the properties

$$\begin{aligned} X^T(\mathbf{k}_\parallel, \mathbf{q}_\parallel|\omega) &= X(\mathbf{k}_\parallel, \mathbf{q}_\parallel|\omega), \\ Y^T(\mathbf{k}_\parallel, \mathbf{k}_\parallel|\omega) &= -Y(\mathbf{k}_\parallel, \mathbf{k}_\parallel|\omega), \end{aligned} \tag{14}$$

where the symbol T implies the transposition operation. The matrices X and Y are identical in form to expressions in [15, Eqs. (A.7a)–(A.8e)] and depend on ω and the components of the elastic-moduli tensor for the hexagonal medium. By multiplying both parts of Eq. (8) from the left into $S(\hat{\mathbf{k}}_\parallel)$ and taking into account Eqs. (9)–(13), we arrive at

$$\begin{aligned} \theta(x_3)F_\alpha(\mathbf{k}_\parallel\omega|x_3) = &\int\frac{d^2q_\parallel}{(2\pi)^2}\zeta(\mathbf{k}_\parallel-\mathbf{q}_\parallel)d_{\alpha\beta}(k_\parallel\omega|x_30) \\ &\times X_{\beta\mu}(\mathbf{q}_\parallel, \mathbf{k}_\parallel|\omega)F_\mu(\mathbf{q}_\parallel\omega|0) \\ &+\int\frac{d^2q_\parallel}{(2\pi)^2}\zeta^{(2)}(\mathbf{k}_\parallel-\mathbf{q}_\parallel)d_{\alpha\beta}(k_\parallel\omega|x_30) \\ &\times Y_{\beta\mu}(\mathbf{q}_\parallel, \mathbf{k}_\parallel|\omega)F_\mu(\mathbf{q}_\parallel\omega|0). \end{aligned} \tag{15}$$

Relation (15) is valid for all values of $x_3 = 0+$. Having put $x_3 = 0+$ in Eq. (15), we come to a set of equations for the displacement field components $F_\alpha(\mathbf{k}_\parallel\omega|x_3)$ near the crystal surface:

$$\begin{aligned} F_\alpha(\mathbf{k}_\parallel\omega|0) = &\int\frac{d^2q_\parallel}{(2\pi)^2}\zeta(\mathbf{k}_\parallel-\mathbf{q}_\parallel)d_{\alpha\beta}(k_\parallel|\omega) \\ &\times X_{\beta\mu}(\mathbf{q}_\parallel, \mathbf{k}_\parallel|\omega)F_\mu(\mathbf{q}_\parallel\omega|0) \\ &+\int\frac{d^2q_\parallel}{(2\pi)^2}\zeta^{(2)}(\mathbf{k}_\parallel-\mathbf{q}_\parallel)d_{\alpha\beta}(k_\parallel|\omega) \\ &\times Y_{\beta\mu}(\mathbf{q}_\parallel, \mathbf{k}_\parallel|\omega)F_\mu(\mathbf{q}_\parallel\omega|0), \end{aligned} \tag{16}$$

where

$$d_{\alpha\beta}(k_\parallel|\omega) = d_{\alpha\beta}(k_\parallel\omega|0+, 0). \tag{17}$$

An explicit form of the surface profile function $\zeta(\mathbf{x}_\parallel)$ is not known; only its statistical properties are known. Therefore, the set of equations (16) should be averaged over an ensemble of function $\zeta(\mathbf{x}_\parallel)$ realizations. To this end, according to [9], we introduce the operator $\hat{P}$, which averages all the quantities on which it operates over an ensemble of realizations of the profile function, $\hat{P}f = \langle f\rangle$, as well as the operator $\hat{Q} = I - \hat{P}$, where I is the unit operator.

We apply the operators $\hat{P}$ and $\hat{Q}$ sequentially to both parts of Eq. (16) and then substitute the second obtained equation into the first. Taking into account the equality

$$\hat{P}\zeta^{(2)}(\mathbf{k}_\parallel-\mathbf{q}_\parallel) = \delta^2(2\pi)^2\delta(\mathbf{k}_\parallel-\mathbf{q}_\parallel)$$

and properties (14) of the matrix X, we arrive at a homogeneous set of linear algebraic equations for the mean-field components:

$$\begin{aligned} \langle F_\alpha(\mathbf{k}_\parallel\omega|0)\rangle = \delta^2&\int\frac{d^2q_\parallel}{(2\pi)^2}g(|\mathbf{k}_\parallel-\mathbf{q}_\parallel|)d_{\alpha\beta}(k_\parallel|\omega) \\ \times X_{\beta\gamma}(\mathbf{q}_\parallel, \mathbf{k}_\parallel|\omega)&d_{\gamma\mu}(\mathbf{q}_\parallel|\omega)X^T_{\mu\nu}(\mathbf{q}_\parallel, \mathbf{k}_\parallel|\omega)\langle F_\nu(\mathbf{k}_\parallel\omega|0)\rangle \\ &+\delta^2d_{\alpha\beta}(k_\parallel|\omega)Y_{\beta\mu}(\mathbf{k}_\parallel, \mathbf{k}_\parallel|\omega)\langle F_\mu(\mathbf{k}_\parallel\omega|0)\rangle. \end{aligned} \tag{18}$$

The Green's function $d_{\alpha\beta}$ was determined in [17] for any values of x_3 and x_3' in the Z-cut hexagonal crystal with a plane boundary. Green's function (17) at the crystal surface appears in Eq. (18). Therefore, after simple algebraic transformations, the Green's function becomes much simpler in comparison with that in [17].

4. DISPERSION RELATION FOR RAYLEIGH WAVES

It can be shown by performing integration over the angle in Eq. (18) that the components $\langle F_1(\mathbf{k}_\parallel\omega|0)\rangle$ and $\langle F_3(\mathbf{k}_\parallel\omega|0)\rangle$ are separate from $\langle F_2(\mathbf{k}_\parallel\omega|0)\rangle$. In this case, surface waves of sagittal polarization (Rayleigh SAWs) are described by the matrix equation

$$\begin{pmatrix} \langle F_1(\mathbf{k}_\| \omega|0)\rangle \\ \langle F_3(\mathbf{k}_\| \omega|0)\rangle \end{pmatrix} = \delta^2 \int \frac{d^2 q_\|}{(2\pi)^2} g(|\mathbf{k}_\| - \mathbf{q}_\||)$$

$$\times \begin{pmatrix} d_{11}X_{11}^2\tilde{d}_{11} + d_{11}X_{12}^2\tilde{d}_{22} + d_{13}X_{33}X_{11}\tilde{d}_{31} & d_{11}X_{11}X_{33}\tilde{d}_{13} + d_{13}X_{33}^2\tilde{d}_{33} \\ d_{31}X_{11}^2\tilde{d}_{11} + d_{31}X_{12}^2\tilde{d}_{22} + d_{33}X_{33}X_{11}\tilde{d}_{31} & d_{31}X_{11}X_{33}\tilde{d}_{13} + d_{33}X_{33}^2\tilde{d}_{33} \end{pmatrix} \begin{pmatrix} \langle F_1(\mathbf{k}_\| \omega|0)\rangle \\ \langle F_3(\mathbf{k}_\| \omega|0)\rangle \end{pmatrix} \quad (19)$$

$$+ \delta^2 \begin{pmatrix} d_{13}Y_{31} & d_{11}Y_{13} \\ d_{33}Y_{31} & d_{31}Y_{13} \end{pmatrix} \begin{pmatrix} \langle F_1(\mathbf{k}_\| \omega|0)\rangle \\ \langle F_3(\mathbf{k}_\| \omega|0)\rangle \end{pmatrix},$$

where $X_{\alpha\beta} \equiv X_{\alpha\beta}(\mathbf{q}_\|, \mathbf{k}_\||\omega)$, $Y_{\alpha\beta} \equiv Y_{\alpha\beta}(\mathbf{k}_\|, \mathbf{k}_\||\omega)$, and $d_{\alpha\beta} \equiv d_{\alpha\beta}(k_\||\omega)$; the tilde means that the corresponding quantity should be taken at an argument equal to $q_\|$, e.g., $\tilde{d}_{\alpha\beta} \equiv d_{\alpha\beta}(q_\||\omega)$.

The dispersion law for Rayleigh waves is derived from the condition for a nontrivial solution to matrix equation (19). To make the algebra simpler, we use the relation

$$\det(A + \delta A) = \det A + \det A \operatorname{Tr}(A^{-1}\delta A) + O(\delta A^2)$$

(in this case, A is the 2×2 unit matrix). Thus, the dispersion relation for Rayleigh waves takes the form

$$1 = \delta^2 \int \frac{d^2 q_\|}{(2\pi)^2} g(|\mathbf{k}_\| - \mathbf{q}_\||)\{d_{11}X_{11}^2\tilde{d}_{11} + d_{11}X_{12}^2\tilde{d}_{22} + d_{13}X_{33}X_{11}\tilde{d}_{31} + d_{31}X_{11}X_{33}\tilde{d}_{13} + d_{33}X_{33}^2\tilde{d}_{33}\} + \delta^2(d_{31} - d_{31})Y_{13}. \quad (20)$$

Using the explicit expressions for the function $d_{\alpha\beta}$, we rewrite Eq. (20) as

$$\Delta(k_\||\omega) = \delta^2 Z(k_\||\omega), \quad (21)$$

where $\Delta(k_\||\omega)$ is the Rayleigh determinant, which is reduced to [15, Eq. (4.11)] in the case of an isotropic medium. We omit explicit expression of function $Z(k_\||\omega)$, because it is cumbersome.

In the limiting case of $\delta = 0$, Eq. (21) describes the dispersion law of Rayleigh waves propagating along the plane surface of the hexagonal crystal parallel to the basal plane:

$$\Delta(k_\||\omega_R) = 0. \quad (22)$$

Its solution [17] is $\omega_R(k_\|) = k_\| c_R$, where c_R is the Rayleigh wave velocity at the plane surface of the hexagonal crystal (Z cut). It is convenient to introduce the notation

$$\rho\omega_R^2 = c_{44}k_\|^2\varepsilon. \quad (23)$$

Then, we have $c_R = \sqrt{\frac{c_{44}}{\rho}}\varepsilon$, where ε depends only on the components of the elastic-moduli tensor and, under the condition $0 < \varepsilon < \min(1, a_1)$, is defined by the equation [following from Eq. (22)]

$$\left(1 - \frac{c_{44}}{c_{33}}\right)\varepsilon^3 + \left(\frac{c_{11}}{c_{33}} - 1 - 2a_1\right)\varepsilon^2 + a_1(2 + a_1)\varepsilon - a_1^2 = 0, \quad (24)$$

$$a_1 = \frac{c_{11}c_{33} - c_{13}^2}{c_{33}c_{44}}.$$

Since only the terms $O(1)$ and $O(\delta^2)$ are retained in the above calculations, we can put $\omega = \omega_R(k_\|) = k_\| c_R$ in the right-hand side of Eq. (21). Expanding $\Delta(k_\||\omega)$ into a Taylor series in the vicinity of $\omega = \omega_R$, the dispersion law of Rayleigh waves propagating along a statistically rough surface can be written as

$$\omega(k_\|) = \omega_R(k_\|) + \Delta\omega(k_\|) = \omega_R(k_\|) + \delta^2\left[\frac{Z(k_\||\omega)}{\partial\Delta/\delta\omega}\right]_{\omega = \omega_R}. \quad (25)$$

If we now substitute the surface scattering factor $g(|\mathbf{k}_\||)$ in the form of Gaussian (2) into $Z(k_\||\omega)$, pass over to the polar coordinates, and integrate over the angle θ, we arrive at

$$Z(k_\||\omega_R) = \frac{a^2}{2}\exp(-k_\|^2a^2/4)\int_0^\infty dq_\| q_\| \frac{\exp(-q_\|^2a^2/4)}{\Delta(q_\||\omega_R)} \times \sum_{n=0}^{4} C_n(q_\|, k_\||\omega_R) I_n\left(\frac{k_\| q_\| a^2}{2}\right) - 2Y_{13}d_{13}\Delta(k_\||\omega_R), \quad (26)$$

where $I_n(z)$ is the modified Bessel function of the nth order and the coefficients $C_n(q_\|, k_\||\omega_R)$ are

$$C_n(k_\|, q_\||\omega_R) = k_\|^8\varepsilon\alpha_t(k_\|, \omega_R)C_n(\eta), \quad (27)$$

with $\eta = q_\|/k_\|$. The denominator $\Delta(q_\||\omega_R)$ in the integrand in Eq. (26) should be understood as $\Delta(q_\||\omega_R + i\alpha)$ as $\alpha \longrightarrow 0+$. As follows from Eq. (22), $\Delta(q_\||\omega_R + i\alpha)$ vanishes at $\eta = 1$ and $\alpha = 0$. Considering $\Delta(q_\||\omega_R + i\alpha)$

formally as a function of the variables $q_{\|}$ and ω_R, we expand Δ into a Taylor series in the vicinity of $q_{\|} = k_{\|}$ and $\alpha = 0$:

$$\Delta(q_{\|}, \omega_R + i\alpha) = k_{\|}\frac{\partial\Delta(q_{\|}, \omega_R)}{\partial q_{\|}}\bigg|_{(k_{\|}, \omega_R)}\left(\eta - 1 - i\frac{\alpha}{\omega_R}\right). \tag{28}$$

Using the well-known relation

$$\frac{1}{x + i\nu} = P\frac{1}{x} - i\pi\,\mathrm{sgn}(\nu)\delta(x), \tag{29}$$

where the symbol P indicates the Cauchy principal value of the integral and $\mathrm{sgn}(\nu) = \pm 1$ for $\nu \gtrless 0$, we can write

$$\frac{1}{\Delta(q_{\|}|\omega_R + i\alpha)} = P\frac{1}{\Delta(q_{\|}|\omega_R)} + i\pi\frac{\delta(\eta - 1)}{k_{\|}\left(\dfrac{\partial\Delta(q_{\|}|\omega_R)}{\partial q_{\|}}\right)_{q_{\|} = k_{\|}}}. \tag{30}$$

Then, it is convenient to pass over to the dimensionless function ω_{12} defined by the equality

$$\frac{\Delta\omega(k_{\|})}{\omega_R} = \frac{\delta^2}{a^2}\omega_{12}(\xi), \tag{31}$$

where $\xi = k_{\|}a$. Taking into account Eq. (30) and replacing the variable of integration in Eq. (26) by $t = \eta^2/\varepsilon$, we arrive at the dispersion law $\omega_{12}(\xi)$ in the final form

$$\omega_{12}(\xi) = -\frac{d}{2}\xi^4\exp(-\xi^2/4) \times [A(\xi) + B(\xi) + E(\xi)] + \xi^2 l, \tag{32}$$

where the coefficients $A(\xi)$, $B(\xi)$, $E(\xi)$, l, and d are given in Appendix A. Expression (32) is complex; therefore, $\omega_{12}(\xi)$ can be written as

$$\omega_{12}(\xi) = \omega_1(\xi) - i\omega_2(\xi), \tag{33}$$

where $\omega_1(\xi)$ and $\omega_2(\xi)$ are real functions. The real and imaginary parts of $\omega_{12}(\xi)$ define the phase velocity dispersion

$$\frac{\Delta c}{c_R} = \frac{d^2}{a^2}\omega_1(\xi), \tag{34}$$

and the inverse damping depth of Rayleigh waves

$$\frac{1}{l} = \frac{\delta^2}{a^3}2\xi\omega_2(\xi), \tag{35}$$

respectively.

Expression (32) contains the complex functions $\tilde{\alpha}_{t1,\,t2}(t)$, which appear in an expression for the Green's function in [17]. Since the surface wave should vanish at an infinite depth and go away from the surface, the following conditions are imposes on these functions in [17]:

$$\mathrm{Re}\,\tilde{\alpha}_{t1,\,t2}(t) > 0, \quad \mathrm{Im}\,\tilde{\alpha}_{t1,\,t2}(t) < 0. \tag{36}$$

Inequalities (36) can be met only in the case where $\tilde{\alpha}^2_{t1,\,t2}(t)$ are real functions, which imposes the following conditions on the elastic moduli:

$$\frac{c_{11}}{c_{33}}\left(1 + \frac{c_{44}}{c_{11}}\right)^2 + \left(1 - \frac{c_{44}}{c_{33}}\right)^2 - \left(1 + \frac{c_{44}}{c_{11}}\right)\left(1 + \frac{c_{44}}{c_{33}}\right)\left(a_1 - 2\frac{c_{13}}{c_{33}}\right) \le 0$$

if

$$\left(a_1 - 2\frac{c_{13}}{c_{33}}\right)^2 > 4\frac{c_{11}}{c_{33}}, \tag{37}$$

$$2\frac{c_{11}}{c_{33}}\left(1 + \frac{c_{44}}{c_{11}}\right) - \left(a_1 - 2\frac{c_{13}}{c_{33}}\right)\left(1 + \frac{c_{44}}{c_{33}}\right) \ge 0$$

if

$$\left(a_1 - 2\frac{c_{13}}{c_{33}}\right)^2 - 4\frac{c_{11}}{c_{33}} = 0.$$

Conditions (37) are met for most of the known hexagonal crystals (see table). In the case of an isotropic medium, where

$$\begin{gathered} c_{11} = c_{33} = \rho c_l^2, \quad c_{44} = \rho c_t^2, \\ c_{12} = c_{13} = \rho(c_l^2 - 2c_t^2), \end{gathered} \tag{38}$$

dispersion law (32) reduces to [15, Eq. (4.16)].

The functions $\omega_1(\xi)$ and $\omega_2(\xi)$ calculated numerically for ZnO are shown in Figs. 2 and 3, in which dashed curves correspond to polycrystalline ZnO with the Poisson ratio $\sigma = 0.356$. A method for calculating the Poisson ratio for a polycrystalline material from the data for single crystals was suggested in [18]. An analysis of Figs. 2 and 3 and their comparison with the corresponding figures for the isotropic case considered in [15] and for the other hexagonal crystals listed in the table show that such curves are qualitatively similar for all single crystals and are similar to the corresponding curves for isotropic media, differing only quantitatively.

5. LONG-WAVELENGTH LIMIT $\lambda \gg a$

The relations

$$c_{11} > c_{12}, \quad c_{11} > c_{44} \tag{39}$$

are met for all known hexagonal crystals. From the inequality $c_{11} > c_{12}$, it follows that $h > 0$. The expression for $\tilde{\alpha}^2_{t1,\,t2}$ contains the square root $\sqrt{z^2 - 4y_2} \ge 0$, which is

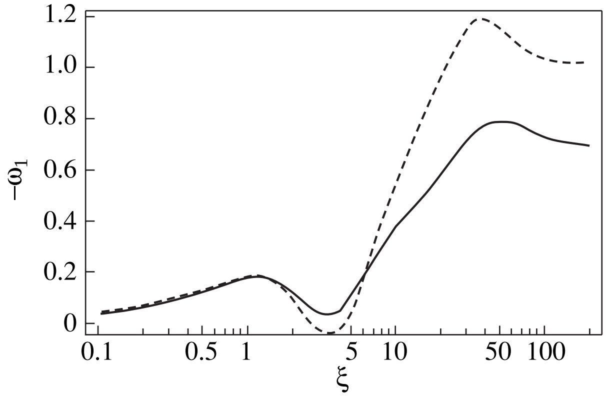

Fig. 2. $\omega_1(\xi)$ dependence for single-crystal (solid curve) and polycrystalline (dashed curve) ZnO; the Poisson ratio for the polycrystal is $\sigma = 0.356$ [18].

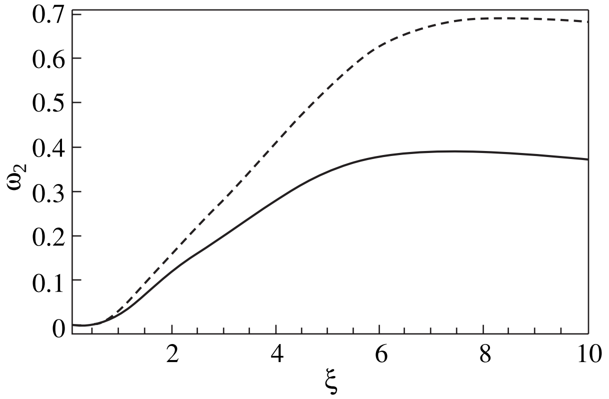

Fig. 3. $\omega_2(\xi)$ dependence for single-crystal (solid curve) and polycrystalline (dashed curve) ZnO; for the polycrystal, $\sigma = 0.356$ [18].

positive according to condition (37). Therefore, if $z = 0$, we have $y_2 \le 0$ and, hence,

$$\frac{c_{44}}{c_{11}} \le \frac{1 + c_{44}/c_{33}}{a_1 - 2c_{13}/c_{33}} \le 1. \tag{40}$$

Taking into account Eqs. (39) and (40), one readily sees that $\tilde{\alpha}(t)$ is a pure imaginary quantity in the range $0 < t < \frac{c_{44}}{c_{11}}$ and $\tilde{\alpha}_{t2}(t)$ is purely imaginary in the range $0 < t < 1$; in the remaining region, $\tilde{\alpha}_{t1,\,t2}(t)$ are real. Let us consider $\omega_{12}(\xi)$ in Eq. (32) in the long-wavelength limit $\lambda \gg a$ ($\xi = ka \ll 1$). In this case, only the coefficients of I_0 will contribute to $\omega_{12}(\xi)$, since $I_0(0) = 1$ and $I_n(0) = 0$ at $n = 1, 2, \ldots$. The result can be conveniently written using the following notation:

$$\omega_1(\xi) = -\Phi\xi, \quad \omega_2(\xi) = \frac{\xi^4}{2}\Lambda, \tag{41}$$

where Λ and Φ are constants independent of ξ;

$$\Phi = \frac{d\sqrt{\pi}}{2a_1} \times \{a_1 h^{3/2} + (2(a_1 - h)^2 + h^2)(\sqrt{m+n} + \sqrt{m-n})\}, \tag{42}$$

Numerical values of Φ, Λ, and c_R for numerous hexagonal crystals*

Medium	Temperature, K	ρ, g cm^{-3}	c_R, km s^{-1}	Φ	Λ
Be	293	1.816	7.203	0.4125	0.1262
CdS	293	4.825	1.700	0.3073	0.05179
Co	298	8.836	2.808	0.3572	0.06368
Ice	257	0.960	1.768	0.3624	0.07435
Ice	248	0.960	1.730	0.3448	0.05929
Ice	263	0.960	1.703	0.3437	0.05832
Ice	268	0.960	1.702	0.3470	0.05892
Mg	0	1.799	3.006	0.4100	0.09836
SiO_2	873	2.517	3.516	0.4257	0.1136
SiO_2	873	2.533	3.516	0.4178	0.1159
ZnO	293	5.676	2.615	0.3587	0.07057
Y	4	4.472	2.285	0.4700	0.1149
Y	75	4.472	2.276	0.4704	0.1124
Y	200	4.472	2.225	0.4607	0.1082
Y	300	4.472	2.177	0.4479	0.1095
Y	400	4.472	2.139	0.4374	0.1045

* The elastic moduli involved in the expressions for c_R, Φ, and Λ, were taken from [18].

$$\Lambda = d(A + B + E). \tag{43}$$

The coefficients m, n, A, B, and E are given in Appendix B.

The numerical values of Λ and Φ for some crystals are listed in the table.

6. CONCLUSIONS

Thus, the Rayleigh SAW propagation along a statistically rough free surface $x_3 = \xi(x_1, x_2)$ of a hexagonal crystal, whose hexad axis is normal to its surface such that the Rayleigh wave propagates in the basal plane (Z cut), has been theoretically studied. Since the solid has been considered as an isotropic medium in the overwhelming majority of studies dedicated to the problem under consideration [2–15], we attempted to generalize the “isotropic” consideration. The surface roughness was assumed to be slight ($\delta/\lambda \ll 1$), and the problem was solved using the modified mean-field method [15] within the perturbation theory. This method was chosen because the results obtained using this method involve the Green’s tensor, which is currently known only for an isotropic medium [3] and for a Z-cut hexagonal crystal [17].

Dispersion relation (32) for the Rayleigh SAW was derived; this relation has an explicit analytical integral form and reduces to [15, Eq. (4.16)] in the isotropic limit. As in the isotropic case, the expressions for the real $\omega_1(\xi)$ and imaginary $\omega_2(\xi)$ parts of the complex frequency shift $\omega_{12}(\xi)$ were derived in an explicit analytical form. However, these expressions are cumbersome and are not presented in this paper.

The $\omega_1(\xi)$ and $\omega_2(\xi)$ curves were calculated numerically for all hexagonal crystals listed in the table. The calculated results for the typical hexagonal crystal ZnO are shown in Figs. 2 and 3.

The long-wavelength approximation of most interest in the experimental aspect, $\lambda \gg a$, was studied analytically and numerically. In this case, $\omega_1 \sim \omega$ and $\omega_2 \sim \omega^4$; therefore, the relative change in the phase velocity and the inverse damping depth are $\Delta c/c_R \sim \omega$ and $1/l \sim \omega^5$, respectively. A comparison shows that the results calculated for ZnO in this study and the results of [16] are identical. In closing, we note that the results of this study are applicable to hexagonal crystals belonging to classes 6, $\bar{6}$, 6/*m*, 6*mm*, $\bar{6}m2$, 622, and 6/*mmm* in the Hermann–Mauguin notation.

APPENDIX A

$$A(\xi) = \int_0^\infty \varepsilon\frac{dt}{2}\frac{\exp(-\xi^2\varepsilon t/4)}{\tilde{\alpha}_{tt}(t)}\left\{\frac{\sqrt{\varepsilon}}{2}(\varepsilon + th^2)I_0\left(\frac{\xi^2\sqrt{\varepsilon t}}{2}\right)\right.$$
$$-\varepsilon\sqrt{t}hI_1\left(\frac{\xi^2\sqrt{\varepsilon t}}{2}\right) - \frac{\varepsilon^{3/2}}{2}I_2\left(\frac{\xi^2\sqrt{\varepsilon t}}{2}\right) \tag{A.1}$$
$$\left.+ h\varepsilon\sqrt{t}I_3\left(\frac{\xi^2\sqrt{\varepsilon t}}{2}\right) - \frac{h^2\sqrt{\varepsilon t}}{2}\left(\frac{\xi^2\sqrt{\varepsilon t}}{2}\right)\right\},$$

$$B(\xi) = -P\int_0^\infty \frac{dt\varepsilon^2}{2\sqrt{\varepsilon}}\frac{\exp(-\xi^2\varepsilon t/4)\tilde{\alpha}_p(t)}{\tilde{\alpha}_m(t) + (1 - a_1 t)\sqrt{t-1}}$$
$$\times\sum_{n=0}^{4}\Phi_n(t)I_n\left(\frac{\xi^2\sqrt{\varepsilon t}}{2}\right), \quad \text{pole} \quad t = \frac{1}{\varepsilon}, \tag{A.2}$$

$$E(\xi) = i\pi d\exp\left(-\frac{\xi^2}{4}\right)\left\{\left(a_1^2 - 2a_1h + \frac{3}{2}h^2 + \frac{\varepsilon^2}{2}\right.\right.$$
$$\left. + (a_1 - \varepsilon)^2 - (a_1 - h)\gamma\right)I_0\left(\frac{\xi^2}{2}\right)$$
$$+ \varepsilon(\gamma + h - 2a_1)I_1\left(\frac{\xi^2}{2}\right)$$
$$+ \left(\frac{\varepsilon^2}{2} + 2h(a_1 - h) - h\gamma\right)I_2\left(\frac{\xi^2}{2}\right)$$
$$\left. - h\varepsilon I_3\left(\frac{\xi^2}{2}\right) + \frac{h^2}{2}I_4\left(\frac{\xi^2}{2}\right)\right\},$$

$$l = -\frac{d}{\alpha_p\varepsilon\sqrt{\varepsilon}}\left(\varepsilon\left(1 + \frac{c_{13}}{c_{33}}\right) - a_1\right)\left(\varepsilon\left(\frac{c_{13}}{c_{33}} - 1\right) + a_1\right), \tag{A.3}$$

$$d = \frac{(1-\varepsilon)\left(\frac{c_{11}}{c_{44}} - \varepsilon\right)\alpha_p\sqrt{\varepsilon}}{\left(2a_1 - \frac{c_{11}}{c_{44}} + 1\right)\varepsilon^2 - \varepsilon a_1\left(\frac{c_{11}}{c_{44}} + 3\right) + 2a_1\frac{c_{11}}{c_{44}}}, \tag{A.4}$$

$$\Phi_0(t) = t\sqrt{t-1}\frac{2(a_1 - h)^2 + h^2}{2} + \frac{\varepsilon\sqrt{t-1}}{2}$$
$$+ \frac{2t(a_1 - h)}{\varepsilon\alpha_p\tilde{\alpha}_p(t)}\left(\varepsilon\frac{c_{33} + c_{13}}{c_{33}} - a_1\right)\left(\tilde{\alpha}_m(t) - \frac{c_{13}}{c_{33}}\sqrt{t-1}\right) \tag{A.5}$$
$$+ \tilde{\alpha}_m(t)(a_1 - \varepsilon),$$

$$\Phi_1(t) = -\frac{2\sqrt{t}}{\sqrt{\varepsilon}\alpha_p\tilde{\alpha}_p(t)}\left(\varepsilon\frac{c_{33}+c_{13}}{c_{33}} - a_1\right) \times\left(\tilde{\alpha}_m(t) - \frac{c_{13}}{c_{33}}\sqrt{t-1}\right) - \sqrt{\varepsilon t(t-1)}(2a_1 - h), \tag{A.6}$$

$$\Phi_2(t) = \frac{\varepsilon}{2}\sqrt{t-1} + 2h(a_1-h)t\sqrt{t-1} + \frac{2ht}{\varepsilon\alpha_p\tilde{\alpha}_p(t)}\left(\varepsilon\frac{c_{33}+c_{13}}{c_{33}} - a_1\right)\left(\tilde{\alpha}_m(t) - \frac{c_{13}}{c_{33}}\sqrt{t-1}\right), \tag{A.7}$$

$$\Phi_3(t) = -h\sqrt{\varepsilon t(t-1)}, \quad \Phi_4(t) = \frac{h^2}{2}t\sqrt{t-1}, \quad h = \frac{c_{11}-c_{12}}{2c_{44}}, \tag{A.8}$$

$$\gamma = \frac{2\varepsilon\left(\varepsilon\left(1+\frac{c_{13}}{c_{33}}\right) - a_1\right)^2}{a_1^2(1-\varepsilon) - \left(1 + \frac{2c_{13}+c_{11}}{c_{33}} - a_1\right)\varepsilon^2}, \tag{A.9}$$

$$\tilde{\alpha}_p(t) = \tilde{\alpha}_{t1}(t) + \tilde{\alpha}_{t2}(t), \quad \alpha_p = \tilde{\alpha}_p(1/\varepsilon),$$

$$\tilde{\alpha}_{t1}^2(t) = 1/2\left(z(t) + \sqrt{z^2(t) - 4y_2(t)}\right), \quad \tilde{\alpha}_{t2}^2(t) = 1/2\left(z(t) - \sqrt{z^2(t) - 4y_2(t)}\right), \tag{A.10}$$

$$\tilde{\alpha}_m(t) = \frac{\tilde{\alpha}_{t1}(t)\tilde{\alpha}_{t2}(t)}{\sqrt{t-1}}, \quad \tilde{\alpha}_{tt}(t) = \begin{cases}\sqrt{ht-1}, & ht-1 \geq 0,\\ -i\sqrt{1-ht}, & ht-1 < 0,\end{cases} \tag{A.11}$$

$$y_2(t) = (c_{11}/c_{33})(t-1)(t-c_{44}/c_{11}), \quad z(t) = (a_1 - 2c_{13}/c_{33})t - (1 + c_{44}/c_{33}), \tag{A.12}$$

where c_{11}, c_{12}, c_{13}, c_{33}, and c_{44} are the independent components of the elastic-moduli tensor of the hexagonal crystal.

APPENDIX B

$$m = \frac{a_1}{2} - \frac{c_{13}}{c_{33}}, \quad n = \sqrt{m^2 - \frac{c_{11}}{c_{33}}}, \quad A = \frac{\varepsilon^{3/2}}{2h}\left(\varepsilon + \frac{2}{3}h\right), \tag{B.1}$$

$$B = -\mathrm{Im}\int_0^1 \frac{dt}{2\sqrt{\varepsilon}\tilde{\alpha}_m(t) + (1-a_1t)\sqrt{t-1}} \varepsilon^2\tilde{\alpha}_p(t) \times\left\{t\sqrt{t-1}\frac{2(a_1-h)^2+h^2}{2} + \frac{\varepsilon\sqrt{t-1}}{2} + \frac{\varepsilon\sqrt{t-1}}{2} + \frac{t2(a_1-h)}{\varepsilon\alpha_p\tilde{\alpha}_p(t)}\left(\varepsilon\frac{c_{33}+c_{13}}{c_{33}} - a_1\right) \times\left(\tilde{\alpha}_m(t) - \frac{c_{13}}{c_{33}}\sqrt{t-1}\right) + \tilde{\alpha}_m(t)(a_1-\varepsilon)\right\}, \tag{B.2}$$

$$E = \pi d\left(a_1^2 - 2a_1h + \frac{3}{2}h^2 + \frac{\varepsilon^2}{2} + (a_1-\varepsilon)^2 - (a_1-h)\gamma\right). \tag{B.3}$$

REFERENCES

1. Lord Rayleigh, Proc. London Math. Soc. **17**, 54 (1887).
2. E. I. Urazakov and L. A. Fal’kovskiĭ, Zh. Éksp. Teor. Fiz. **63** (6), 2297 (1972) [Sov. Phys. JETP **36**, 1214 (1972)].
3. A. A. Maradudin and D. L. Mills, Ann. Phys. (NY) **100** (2), 262 (1976).
4. V. G. Polevoĭ, Akust. Zh. **29** (1), 91 (1983) [Sov. Phys. Acoust. **29**, 52 (1983)].
5. V. V. Kosachev, Yu. N. Lokhov, and V. N. Chukov, Zh. Éksp. Teor. Fiz. **94** (9), 162 (1988) [Sov. Phys. JETP **67**, 1825 (1988)].
6. Nguen van Chong, Ukr. Fiz. Zh. **28** (11), 1699 (1983).
7. V. V. Krylov and V. E. Lyamov, Zh. Tekh. Fiz. **49** (11), 2514 (1979) [Sov. Phys. Tech. Phys. **24**, 1424 (1979)].
8. V. V. Kosachev, Yu. N. Lokhov, and M. V. Polikarpov, in *Abstracts of XIII All-Union Conference on Acoustic–Electronics and Quantum Acoustics* (1986), Vol. 1, p. 131.
9. A. G. Eguiluz and A. A. Maradudin, Phys. Rev. B **28** (2), 728 (1983).
10. A. P. Mayer and M. Lehner, Waves in Random Media **4** (3), 321 (1994).
11. X. Huang and A. A. Maradudin, Phys. Rev. B **36** (15), 7827 (1987).
12. V. V. Kosachev, Yu. N. Lokhov, and V. N. Chukov, Fiz. Tverd. Tela (Leningrad) **32** (7), 2045 (1990) [Sov. Phys. Solid State **32**, 1189 (1990)].
13. V. V. Kosachev, Yu. N. Lokhov, and V. N. Chukov, Solid State Commun. **73** (8), 535 (1990).
14. S. Z. Dunin and G. A. Maksimov, Preprint No. 032-88, MIFI (Moscow Engineering Physics Institute, 1988).
15. V. V. Kosachev and A. V. Shchegrov, Ann. Phys. (NY) **240** (2), 225 (1995).
16. A. V. Shchegrov, J. Appl. Phys. **78** (3), 1565 (1995).
17. L. Dobrzynski and A. A. Maradudin, Phys. Rev. B **14** (6), 2200 (1976); Erratum: Phys. Rev. B **15** (4), 2432 (1977).
18. O. L. Anderson, Phys. Acoust. B **3**, 80 (1965).

Translated by A. Kazantsev

Physics of the Solid State, Vol. 45, No. 2, 2003, pp. 400–407. Translated from Fizika Tverdogo Tela, Vol. 45, No. 2, 2003, pp. 377–383.
Original Russian Text Copyright © 2003 by Rashkovich, Petrova, Shustin, Chernevich.

LOW-DIMENSIONAL SYSTEMS AND SURFACE PHYSICS

Formation of a Dislocation Spiral on the (010) Face of a Potassium Hydrogen Phthalate Crystal

L. N. Rashkovich, E. V. Petrova, O. A. Shustin, and T. G. Chernevich
Moscow State University, Vorob'evy gory, Moscow, 119992 Russia
e-mail: rashk@polc49.phys.msu.su

Received February 21, 2002; in final form, March 28, 2002

Abstract—The atomic-force microscopy method is used to study the structure of the surface and the formation of a dislocation spiral on the (010) face of a potassium hydrogen phthalate crystal grown from a water–alcohol solution. It is shown that the face grows according to the dislocation mechanism. Channels surrounding dislocation sources with a large Burgers vector are discovered. The density of kinks at the steps was so high that no smooth regions were observed between kinks. The velocity of a step fluctuates, with the fluctuations growing in proportion to the fourth root of time. During the formation of a spiral, a segment of a step acquires a constant velocity independent of its length after attainment of the critical length. *© 2003 MAIK "Nauka/Interperiodica".*

1. INTRODUCTION

Immediately after Frank's discovery of the dislocation mechanism of crystal growth, Burton, Cabrera, and Frank [1] used the Gibbs–Thomson relation to prove that the separation λ between the turns of an isotropic dislocation spiral must be equal to 19 times the radius r_c of a two-dimensional critical nucleus. The radius r_c and the above-mentioned relation (for small supersaturation) can be written in the form

$$r_c = \Omega\alpha/\Delta\mu, \qquad V = V_\infty(1 - r_c/r), \tag{1}$$

where Ω is the volume of a building unit of the crystal; α is the free surface energy of the step riser; $\Delta\mu$ is the difference in the chemical potentials of particles in the medium and in the crystal; r and V are the radius of curvature and the velocity of a step, respectively; and V_∞ is the velocity of a direct step. In the case of a polygonal spiral, $r_c/r = l_c/l$, where l is the length of a side of an m-gonal spiral and $l_c = 2r_c\tan(\pi/m)$.

For almost 50 years following this discovery, the separation between the turns of isotropic, elliptic, and polygonal spirals was calculated using various methods [2–7]. In those publications, relation (1) was used and values approximately equal to $19r_c$ were obtained. At that time, the theory had not been verified experimentally; the above estimate was assumed to be correct and was used to calculate, for example, the free linear energy of steps. However, as early as in 1973, Voronkov [8] proved that a polygonal spiral should satisfy, instead of Eq. (1), the equation

$$\frac{l}{l_c} - 1 = A\frac{V/V_\infty}{\sqrt{1-(V/V_\infty)^2}}\left(1 - \frac{2}{\pi}\arcsin V/V_\infty\right), \tag{2}$$

where $A = \pi kTh/2\Omega\alpha$ for a square critical nucleus and h is the separation between the rows of building units. A distinguishing feature of Eq. (2) is that, for $A < 1$, the value of V increases with l/l_c much more rapidly than follows from Eq. (1). It was also proved in [8] that the velocity of a side of the polygon is independent of its length for a small supersaturation. The distance between the turns of the spiral is equal to the product of the time T it takes for one spiral turn to form and the velocity V_∞ of a side; for a square spiral, we have $T = 4l_c/V_\infty$ and, consequently, $\lambda = 4l_c$. Therefore, for a large supersaturation, when l_c is smaller than the mean distance between kinks, the value of λ must be of the order of this distance and be independent of supersaturation [8]. It should be noted that, for a large density of kinks, the latter condition may be violated. Relation (2) has not been verified experimentally either.

The contradiction to the Gibbs–Thomson formula was noted for the first time in [9], where it was found that the velocity of steps on a face of a growing calcite crystal increases with the length of the steps at a rate much higher than that predicted by formula (1). Higgins *et al.* [10] studied the growth of barium sulfate under hydrothermal conditions by using an atomic-force microscope (AFM) and also proved that formula (1) was inconsistent with their results. In [9], as well as in [10], an explanation was sought on the basis of the concepts developed by Voronkov [8, 11], but Higgins *et al.* were likely unaware of Eq. (2). The discrepancy with formula (1) was observed in [12, 13], where crystallization of the rhombic and monoclinic modifications of lysozyme was investigated.

Our study was also aimed at verification of the generally accepted (so far) relation (1) from an analysis of the formation of a new turn of a dislocation spiral on a face of a potassium hydrogen phthalate (KAP) crystal.

In contrast to barium sulfate and lysozyme, whose steps contain a small number of kinks and are displaced through the formation of one-dimensional nuclei (the density of kinks in calcite is unknown), the density of kinks in KAP is high.

PBP crystals have been grown for a long time [14], and their structure is well known. These crystals belong to the rhombic-pyramidal class with a well-developed lateral pinacoid face (010) possessing a perfect cleavage. The lattice parameters are a = 0.9609 nm, b = 1.3857 nm, c = 0.6466 nm, and z = 4; the space symmetry group is $Pca2_1$; and c is a polar axis [15, 16]. The evolution of growth spirals on the (010) face was observed *in situ* at 2-s intervals using the phase contrast method, but the velocity of steps was too high to trace the process in detail [17, 18]. The energy of strong link chains was calculated in [15]; it was concluded that the steps on the (010) face are predominantly oriented in the [101] and [102] directions. The same authors determined the kinetic coefficient (the proportionality factor between the velocity of steps and supersaturation) of rapidly moving steps in the [101] direction, which was found to be equal to 50 μm/s. The velocity of steps with the same orientation, but moving in the opposite direction relative to the c axis, was smaller by a factor of 10 [19].

The large velocity of steps even for small supersaturation did not allow the authors of recent publications [20–23] to study the growth of the (010) face *in situ* with the help of AFM. They obtained *ex situ* perfect images of spirals in crystals grown for different supersaturations in nominally pure solutions, as well as in solutions containing various impurities. By assuming that $\lambda = 19r_c$, those authors determined the free surface energy of the end faces of rapidly and slowly growing steps (50 and 4 erg/cm^2, respectively) from the dependence of the distance between the spiral turns on the degree of supersaturation.

2. EXPERIMENTAL TECHNIQUE

Crystals with a size up to 5 mm were obtained by spontaneous crystallization from an aqueous solution. Owing to perfect cleavage over the (010) face, the surface of this face can easily be renewed with the help of an adhesive tape to which a layer of thickness of a few tens of micrometers is stuck.

Experiments were made in the contact regime in a Digital Instruments Nanoscope-3 liquid cell of an AFM using silicon nitride tips. As in [20–23], we could not make reliable *in situ* measurements in the aqueous solution. For this reason, crystallization was carried out from a water–alcohol solution consisting of eight parts (by weight) 96% ethyl alcohol and two parts saturated aqueous solution of PBP in order to reduce the solubility and the growth rate. The solvent with crystals in it was held for several days at 30°C; the obtained saturated solution was placed in an air thermostat, from which it flowed by gravity to the measuring cell. The pressure and flow rate were held constant by placing the solution into a Mariotte vessel. The flow rate was chosen such that the crystal growth rate was independent of the velocity of the solution flow. The experiments were made at a temperature 5°C higher than room temperature. The degree of supersaturation was varied by changing the solution temperature and was maintained constant in the course of measurements. The temperature dependence of solubility of KAP in the water–alcohol solution is not known; therefore, the degree of supersaturation could not be determined.

3. MORPHOLOGY OF THE GROWING SURFACE AND STEP VELOCITY FLUCTUATIONS

The sources of growth were screw dislocations generating spiral hillocks with steps of height equal to the unit-cell parameter b (Fig. 1). At the points of emergence of dislocations, channels were observed (Fig. 2); this was predicted by Frank in [24] and detected for the first time on a face of potassium dihydrophosphate in [7]. The radius of the channels was approximately proportional to the square of the Burgers vector of the dislocation source. However, the channels could not be seen in all cases (e.g., there is no channel in Fig. 1a or in Fig. 2 at the sources of single-thread spirals).

Using a large magnification, we visualized unit cells on the surface. The distances between the cells match the x-ray data diffraction (Fig. 3). A fragment of a step with such a magnification is strongly rugged and occupies the entire field of vision. This indicates a high density of kinks, as well as considerable fluctuations in the velocity of individual parts of steps.

We recorded the image of a small region of a step in the single-row-scanning regime. In this regime, slow motion of the AFM scanner (along the vertical) is terminated and a change in the position of a small segment on a step (equal to one scan, which is ~0.6 nm long in our case; Fig. 4) with time is observed. The coordinate of this segment was measured in each of 512 scans at a time interval of 0.1 s. The obtained $x(t)$ dependence is presented in Fig. 5. It can be seen that, in addition to the displacement of a step as a whole with an average velocity of the order of 0.3 nm/s, the segment of the step moves back and forth over a distance $dx \approx \pm 4$ nm (~±7 lattice parameters).

In an analysis of fluctuations in the position of a segment on a step, we assumed, in the first approximation, that the velocity of the step was constant and approximated the data depicted in Fig. 5 by a linear dependence. The fluctuations δx of the step position from its mean value as a function of time was calculated by subtracting the coordinate of the actual position of the step from the coordinate of the corresponding point on the approximating straight line. Then, we constructed the

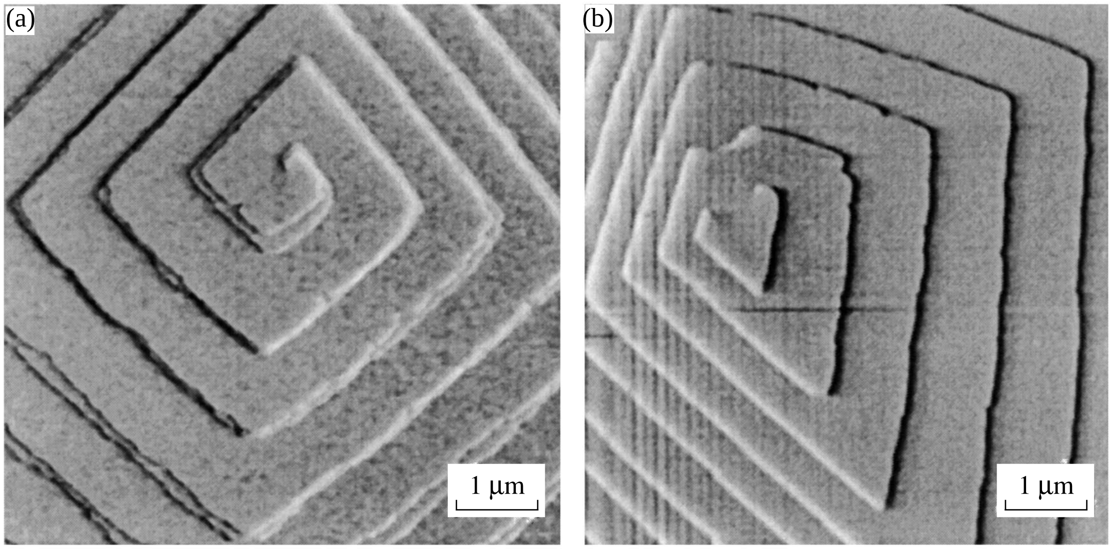

Fig. 1. AFM image of dislocation hillocks on the (010) face of a KAP crystal: (a) double spiral and (b) Frank–Read source. The step height is 1.4 nm. The angles between the segments of the steps are distorted due to the small difference between the velocities of the steps and the measuring tip. The number of scans is 512, and the scanning frequency is (a) 10 and (b) 20 Hz.

autocorrelation function $\langle(\delta x)^2\rangle$ for the dependence on time Δt:

$$\langle(\delta x)^2\rangle = \langle[\delta x(t) - \delta x(t + \Delta t)]^2\rangle. \qquad (3)$$

This expression defines the mean square change in the amplitude of fluctuations in the position of the step over time Δt: for each instant t, the change in the coordinate of the step during the time interval Δt is calculated, and the obtained values are averaged over all values of the running time t. In view of the poor approximation of the results presented in Fig. 5 by a linear dependence, we had to confine the analysis to the maximal value of $\Delta t \approx 3$ s, since the motion of the step as a whole starts to be manifested for $\Delta t > 4$ s. When plotted on the log–log scale, dependence (3) turned out to be linear with a slope equal to 0.54 ± 0.02, i.e., close to 0.5. Consequently, we can assume that $\langle(\delta x)^2\rangle$ increases in proportion to the square root of time Δt (Fig. 6). This fact is reflected in the following dependence, in which we write t instead of Δt, indicating now the time characterizing the rate of fluctuations buildup:

$$\langle(\delta x)^2\rangle = (\chi t)^{1/2}. \qquad (4)$$

The proportionality factor was determined from the slope of the straight line in Fig. 6: $\chi = 61.2 \pm 0.3$ nm^4/s = $(6.12 \pm 0.3) \times 10^{-27}$ cm^4/s. The proportionality of δx to the fourth root of the time was predicted by Voronkov [25] and discovered by us earlier for steps on the faces of potassium dihydrophosphate [26] and of rhombic [27] and monoclinic [13] lysozyme. A number of fundamental parameters of crystallization could be determined from the value of χ if we could ascertain the structural unit of the crystal and determine its size.

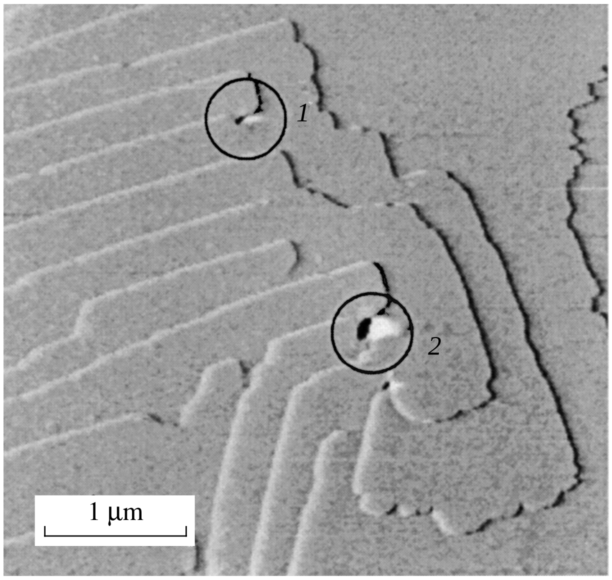

Fig. 2. Region on a face with the emergence of several dislocations. Channels surrounding the sources of (*1*) double and (*2*) triple spirals can be seen.

4. FORMATION OF A DISLOCATION SPIRAL

Figure 7 shows the AFM images of several frames obtained by us that characterize the evolution of a turn of a dislocation spiral. The images were recorded under the following conditions. The frame size was 5 × 5 μm, and only the half of the frame containing 64 scans at a scanning frequency of 30.5 Hz was recorded. The time of recording of one image was 2.097 s, and the error in the measurement of distances (discretization step) was 39 nm. The choice of such conditions was dictated by the compromise that had to be achieved between the minimal recording time and the maximal possible accuracy of measurements. We could not improve the accuracy, since an insufficiently large segment of a spiral was in the frame in the case of large magnification. The velocity of slow movement of the measuring needle was 1192 nm/s. It will be proved below that this value is approximately 50 times as large as the velocity of steps. In spite of such a difference, the orientation of steps in the consecutive upward and downward scanning was slightly distorted. For this reason, Fig. 7 shows images obtained for the same direction of scanning. In frame *6*, the numbering of step segments is indicated; the designations of the angles between the segments are shown in frame *1*.

The main difference in the shape of the spiral observed by us from the images obtained earlier [20–23] lies in a much smaller (by a factor of ~5) difference in the separations between the turns along the positive and negative directions of the *c* axis. In all probability, this is due to the fact that a water–alcohol solution was used as the solvent instead of water.

In order to illustrate the mechanism of formation of a new turn of the dislocation spiral more distinctly, Fig. 8 shows the superposition of the frames depicted in Fig. 7. Each new segment emerging on the step is elongated first due to the motion of the neighboring segment and then itself starts moving after attaining a critical length. At this instant, a new segment appears. When the latter segment attains its critical length and starts moving, the rate of elongation of the former segment increases and is determined by the displacement of two neighboring segments. This process can be recorded as follows. Let us denote the length of the segments and their velocity by l_i and v_i, respectively, where the values of $i = 1, 2, 3, 4$ correspond to the numbering of segments in Fig. 7; $l_{c,i}$ is the critical length; and t is the time. In this case, $l_i = 0$ as long as $l_{i+1} < l_{c,i+1}$ and $l_i = l_{c,i}$ for $l_{i-1} = 0$:

$$\begin{aligned} dl_i/dt &= v_{i+1}, \quad l_{i-1} < l_{c,i-1}, \\ dl_i/dt &= v_{i+1} + v_{i-1}, \quad l_{i-1} > l_{c,i-1}. \end{aligned} \tag{5}$$

It should be noted that, for $i = 1$, the index $i - 1$ corresponds to the fourth segment of the next turn, while for $i = 4$, the index $i + 1$ corresponds to the first segment of the preceding turn.

The time dependence of the segment lengths measured from the images of the step (Fig. 7) is shown in Fig. 9. These results characterize the formation of a turn and the beginning of the formation of the next turn. The

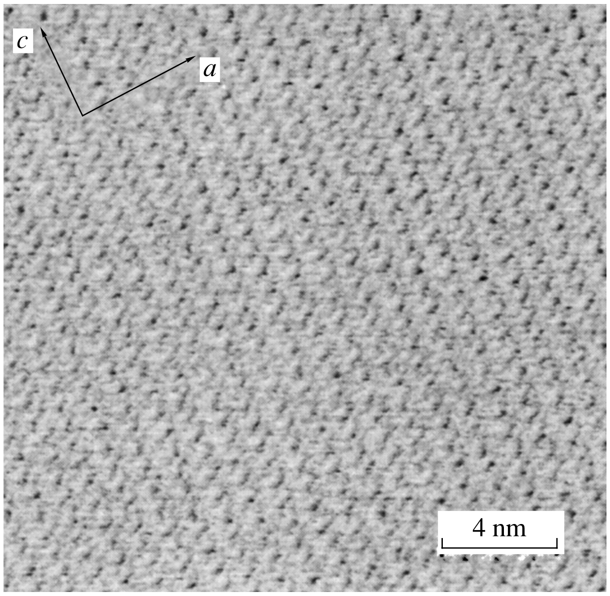

Fig. 3. Structure of a face with high resolution. Unit cells are clearly seen even without noise filtration by using Fourier transforms. The number of scans is 512, and the scanning frequency is 60 Hz.

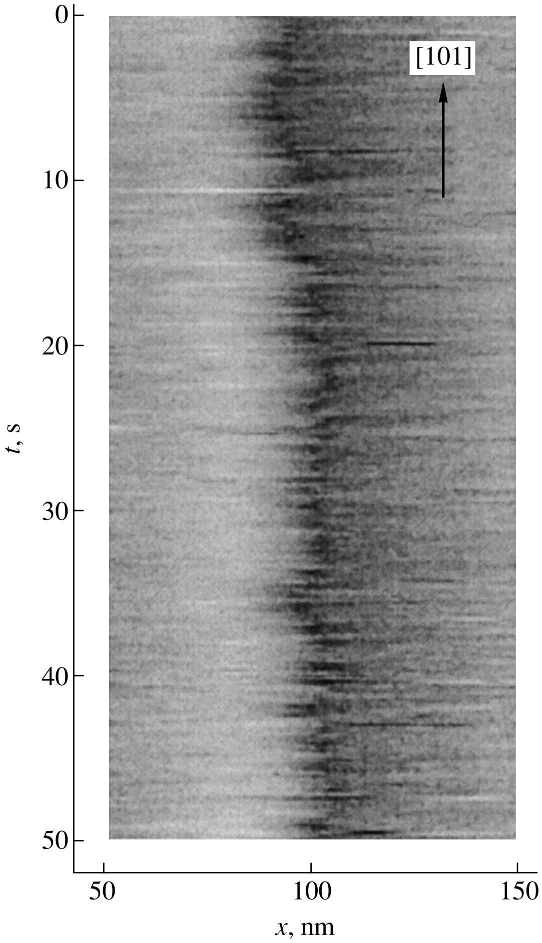

Fig. 4. Time variation of the coordinate of a segment of a step moving from left to right. There are 512 scans; and the scanning frequency is 10 Hz.

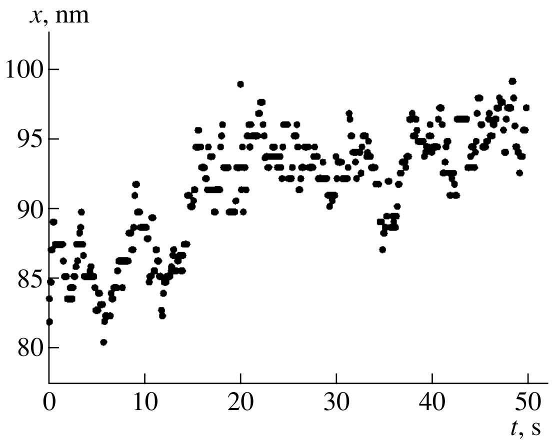

Fig. 5. Time dependence of $x(t)$ plotted according to the results presented in Fig. 4.

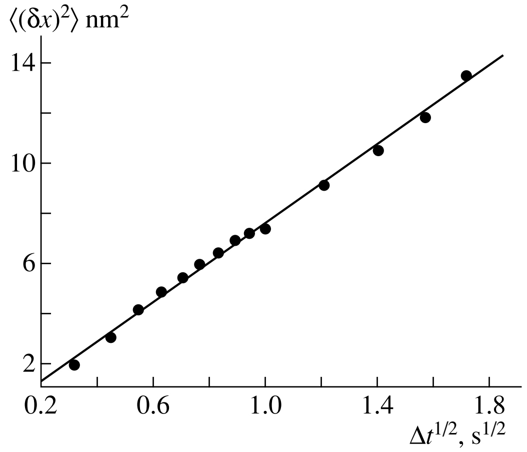

Fig. 6. Autocorrelation function given by Eq. (4), describing the time dependence of fluctuations of the position of a segment of a step. The slope of the straight line is 7.82 ± 0.15 nm^2/s$^{1/2}$.

time during which one turn of the spiral is completed is $T = 36 \pm 1$ s.

It can be seen from Fig. 9 that all experimental points fit straight lines (5) to within the measuring error (±20 nm). In crystals of the rhombic-pyramidal class, the mirror symmetry plane passes along the c axis perpendicularly to the (010) face; consequently, the relations

$$\alpha = \beta, \quad v_1 = v_4, \quad v_2 = v_3, \qquad v_1 + v_3 = v_2 + v_4 \tag{6}$$

should hold and the slopes of the corresponding straight lines in Fig. 9 should be identical. Relations (6) hold quite accurately if we take into account the fact that the actual angle θ between a segment and the horizontal axis in Figs. 7 and 8 depends on the direction of motion of the measuring tip ($\theta_\uparrow$ or $\theta_\downarrow$): $\cot\theta = (\cot\theta_\uparrow + \cot\theta_\downarrow)/2$. Moreover, the depicted lengths of the second and third segments in the case of downward motion of the tip are smaller than the true length, while those for the first and fourth segments are larger than the true length. The opposite situation is observed in the case of upward motion of the tip. Taking into account these corrections and the errors in our measurements, it was found that

$$\alpha = \beta = 85°, \quad \gamma = 107°, \quad \delta = 83°,$$

$$v_1 = v_4 = 38 \text{ nm/s}, \quad v_2 = v_3 = 19 \text{ nm/s},$$

$$l_{c,1} = l_{c,4} = 240 \text{ nm}, \quad l_{c,2} = l_{c,3} = 180 \text{ nm}.$$

Judging from these values of the angles, the orientation of the second and third segments differs slightly from the directions ⟨101⟩, for which $\gamma = 112°$. The orientations of the first and fourth segments are close to the ⟨102⟩ directions but also differ from them ($\delta = 73°$ for these directions).

The main feature of Fig. 9 is that the quantity dl/dt is the same for all segments. Let us consider, by way of example, the elongation of the fourth segment. This segment appears when the first segment attains its critical length, and its length starts to increase immediately at a constant rate equal to the growth rate of the first segment. This means that the velocity of the first segment for $l_1 > l_{c,1}$ is independent of its length. Subsequently, the elongation of the fourth segment is accelerated sharply but then proceeds at a constant rate (equal to $v_1 + v_3$). Acceleration takes place when the third segment attains its critical length (and the second segment appears); consequently, the velocity of this segment is also independent of its length (for $l_3 > l_{c,3}$). The same applies to other segments.

If the velocity of segments is independent of length, the time during which a spiral completes a turn is the sum of the times over which each segment attains its critical length:

$$T = l_{c1}/v_2 + l_{c4}/v_1 + l_{c3}/v_4 + l_{c2}/v_3.$$

Substituting the above values of l_{ci} and v_i into this formula, we obtain $T = 33.1$ s, which is only 7% smaller than the actual time it takes for one turn of the spiral to form. For a square spiral, the pitch would be equal to $\lambda = 4l_c$. In our case, $\lambda_i = Tv_i$; these values for the first and fourth segments differ from those for the second and third by a factor of two. This corresponds to the values $\lambda_{2,3} \approx 680$ nm (=35.6 s × 19 nm/s) and $\lambda_4 \approx 1350$ nm (=35.6 s × 38 nm/s), measured from the data presented in Fig. 7.

Let us compare these findings with expressions (1) and (2). Let us suppose that $l/l_c = 1.5$, which is observed approximately 4.2 s after the attainment of the critical

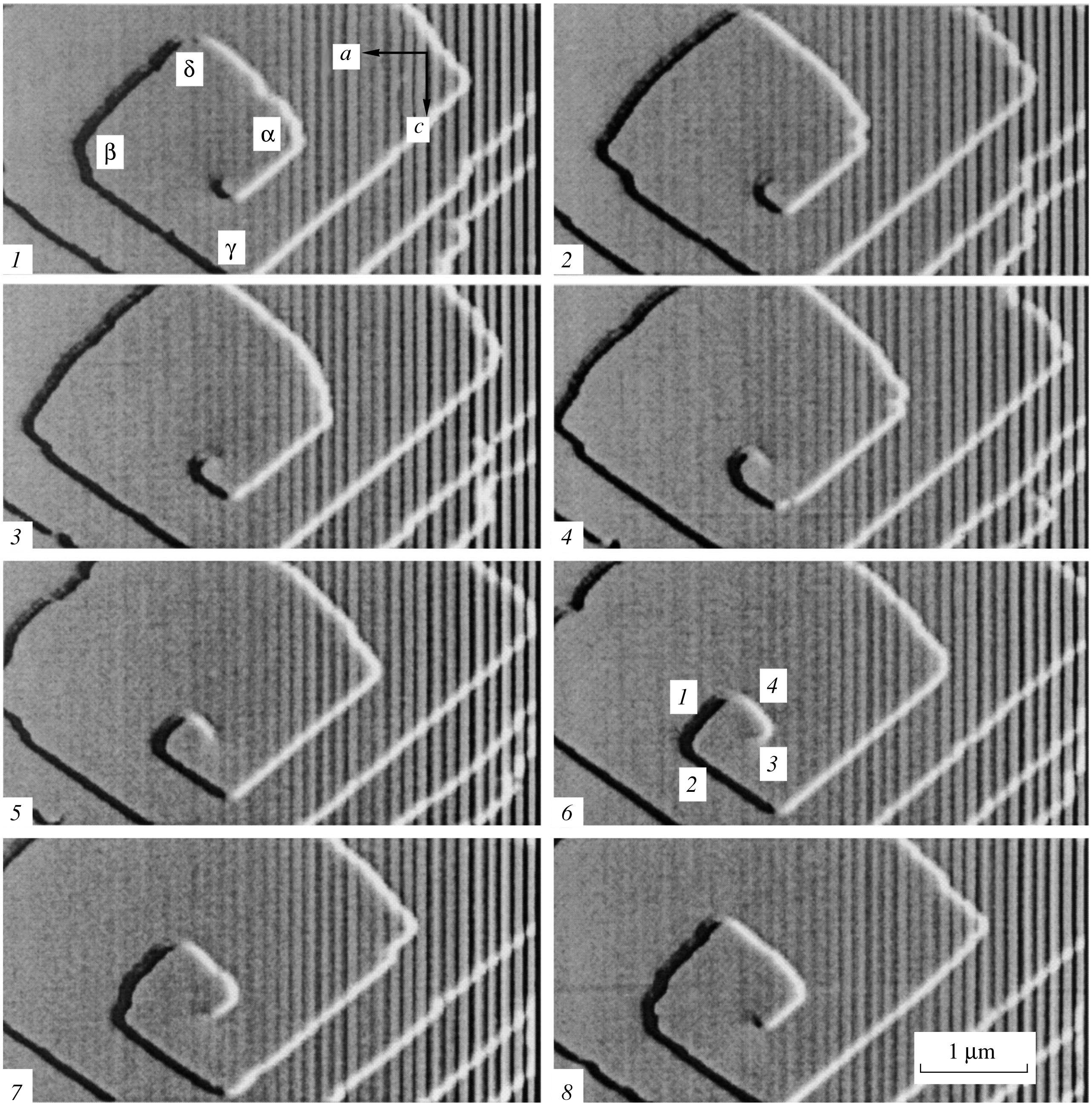

Fig. 7. AFM images of consecutive stages of formation of a new turn of a dislocation spiral. The time interval between the frames is 4.2 s; 64 scans with a scanning frequency of 30.5 Hz. Frame *1* shows the beginning of motion of the second segment and the emergence and elongation of the first segment. After the critical length is reached (frame *2*), the first segment starts to move and the fourth segment emerges in frame *3*. In frame *4*, the fourth segment attains its critical length. Frames *5* and *6* illustrate the formation of the third segment. In frames *7* and *8*, the second segment is formed and attains its critical length. The turn is completed, the hillock height increases by the thickness of a unit step, and then the process is repeated. The formation of the turn is completed 2.1 s after the shooting of frame *8*, which explains the large distance between the first and last positions of the spiral in Fig. 8.

length by the segments (Fig. 8). Then, relation (1) gives $V/V_\infty = 0.33$. We assume that, for $l/l_c = 1.5$, $V/V_\infty \sim 0.95$, in accordance with the results of experiments, and find $A = 0.813$ from relation (2). Knowing A, we can determine the surface energy $\alpha = \pi kTh/2\Omega A$. Assuming that the volume of a building unit is equal to the unit-cell volume $\Omega = 0.861 \times 10^{-21}$ cm^3 and that the distance between the rows of building units along the [101] direction is $h = 0.537 \times 10^{-7}$ cm, we obtain $\alpha = 4$ erg/cm^2 for $T = 300$ K ($k = 1.38 \times 10^{-16}$ erg/K). If, however, the building unit is a molecule, then the value of Ω is a fourth and the value of h is half as large as the

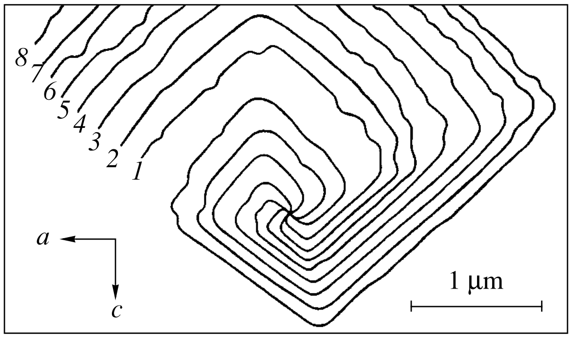

Fig. 8. Change in the position of a spiral over 4.2 s. The numbers correspond to frames in Fig. 7.

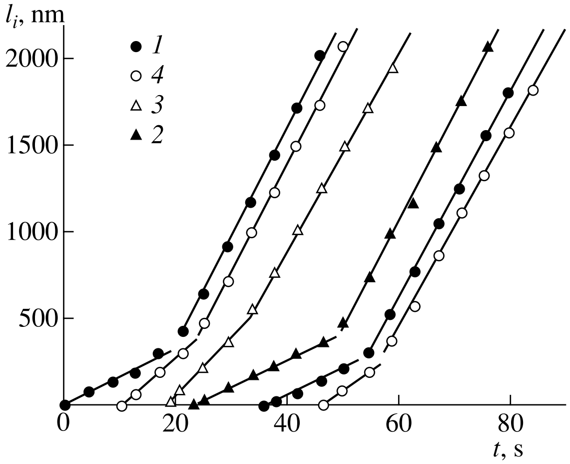

Fig. 9. Time dependence of the length of segments of a step. The designations of the curves correspond to those of the segments.

above values and $\alpha = 8$ erg/cm^2. Both values of α are regarded as the minimum possible values for the interface with a solution of low-molecular compound crystals. If the surface energy is higher than these values, the value of A will be even smaller and the ratio V/V_∞ will be even closer to unity.

Thus, the experimental results confirm the validity of Eq. (2). It should be noted that the derivation of Eq. (2) is based on the fact that, for a high density of kinks, a segment of critical length has an equilibrium shape and is bent. Only a small central part of the segment with low Miller indices deviates from the equilibrium shape. When the length of the segment increases, its central part has the smallest curvature and determines the velocity. The length of the central part increases much more rapidly than the length of the segment; for this reason, the velocity attains its maximum value after a short time [8]. It can clearly be seen from Figs. 7 and 8 that the segment of critical length has the shape of a rounded curve, as predicted by the theory; the angles between adjacent segments are also rounded.

5. CONCLUSIONS

The main results of this study can be formulated as follows.

(1) It has been shown experimentally that the dependence of the velocity of segments of steps on their length in the case of a polygonal dislocation spiral with a high density of kinks does not obey the Gibbs–Thomson formula (1); it is determined by relation (2) derived by Voronkov. This conclusion requires a revision of the prevailing concepts concerning not only the relation connecting the spiral pitch with the surface energy and the degree of supersaturation but also the interaction of a step with an array of impurity stoppers absorbed at the crystal surface.

(2) KAP is the fourth crystal for which fluctuations in the velocity of steps have been studied. It has been shown that the fluctuations increase in proportion to the fourth root of time. An analysis of the fluctuations makes it possible to determine the phenomenological and microscopic parameters of crystallization. The analysis is complicated by the lack of information on the building unit of the crystal.

ACKNOWLEDGMENTS

This study was supported by the Russian Foundation for Basic Research (project no. 00-02-16701).

REFERENCES

1. W. K. Burton, N. Cabrera, and F. C. Frank, Philos. Trans. R. Soc. London, Ser. A **243**, 299 (1951).
2. N. Cabrera and M. M. Levine, Philos. Mag. **1** (5), 450 (1956).
3. E. Budevski, G. Staikov, and V. J. Bostanov, J. Cryst. Growth **29** (3), 316 (1975).
4. A. A. Chernov and L. N. Rashkovich, J. Cryst. Growth **84** (3), 389 (1987).
5. G. T. Avanesyan, Kristallografiya **33** (6), 1492 (1988) [Sov. Phys. Crystallogr. **33**, 888 (1988)].
6. A. S. Mikhaĭlov, L. N. Rashkovich, V. V. Rzhevskiĭ, and A. A. Chernov, Kristallografiya **34** (2), 439 (1989) [Sov. Phys. Crystallogr. **34**, 260 (1989)].
7. J. J. De Yoreo, T. A. Land, L. N. Rashkovich, *et al.*, J. Cryst. Growth **182** (3–4), 442 (1997).
8. V. V. Voronkov, Kristallografiya **18** (1), 32 (1973) [Sov. Phys. Crystallogr. **18**, 19 (1973)].
9. H. H. Teng, P. M. Dove, Ch. A. Orme, and J. J. De Yoreo, Science **282**, 724 (1998).
10. S. H. Higgins, D. Bosbach, C. M. Eggleston, and K. G. Knauss, J. Phys. Chem. B **104** (30), 6978 (2000).
11. V. V. Voronkov, Kristallografiya **15** (1), 13 (1970) [Sov. Phys. Crystallogr. **15**, 8 (1970)].

12. L. N. Rashkovich, N. V. Gvozdev, M. I. Sil'nikova, *et al.*, Kristallografiya **46** (5), 934 (2001) [Crystallogr. Rep. **46**, 860 (2001)].
13. L. N. Rashkovich, N. V. Gvozdev, M. I. Sil'nikova, and A. A. Chernov, Kristallografiya **47** (5), 935 (2002) [Crystallogr. Rep. **47**, 859 (2002)].
14. L. M. Belyaev, G. S. Belikova, A. B. Gil'varg, and I. M. Sil'vestrova, Kristallografiya **14** (4), 645 (1969) [Sov. Phys. Crystallogr. **14**, 544 (1969)].
15. M. H. J. Hottenhuis and C. B. Lucasius, J. Cryst. Growth **94** (3), 708 (1989).
16. P. Murugakoothan, R. M. Kumar, P. M. Ushasree, *et al.*, J. Cryst. Growth **207** (4), 325 (1999).
17. W. J. P. van Enckevort and L. A. M. J. Jetten, J. Cryst. Growth **60** (2), 275 (1982).
18. L. A. M. J. Jetten, B. van der Hoek, and W. J. P. van Enckevort, J. Cryst. Growth **62** (3), 603 (1983).
19. M. H. J. Hottenhuis and C. B. Lucasius, J. Cryst. Growth **91** (4), 623 (1988).
20. G. R. Ester, R. Price, and P. J. Halfpenny, J. Cryst. Growth **182** (1), 95 (1997).
21. G. R. Ester and P. J. Halfpenny, J. Cryst. Growth **187** (1), 111 (1998).
22. R. Price, G. R. Ester, and P. J. Halfpenny, Proc. R. Soc. London, Ser. A **456**, 4117 (1999).
23. G. R. Ester, R. Price, and P. J. Halfpenny, J. Phys. D: Appl. Phys. **32** (10), A128 (1999).
24. F. C. Frank, Acta Crystallogr. **4** (6), 497 (1951).
25. V. V. Voronkov, in *Crystal Growth, Properties and Application*, Ed. A. A. Chernov and H. Muller-Krumbhaar (Springer, Berlin, 1983), Vol. 9, p. 7.
26. L. N. Rashkovich, O. A. Shustin, and T. G. Chernevich, Fiz. Tverd. Tela (St. Petersburg) **42** (10), 1869 (2000) [Phys. Solid State **42**, 1921 (2000)].
27. L. N. Rashkovich, T. G. Chernevich, N. V. Gvozdev, *et al.*, Surf. Sci. Lett. **492** (1–2), L717 (2001).

Translated by N. Wadhwa